



# NSLS-II

Providing High Brightness Synchrotron Radiation

Proposal for approval of Conceptual Design (CD-0)  
Submitted to the U.S. Department of Energy  
Office of Basic Energy Sciences



## List of Contributors

Peter Abbamonte<sup>13</sup>, James Ablett<sup>13</sup>, Harald Ade<sup>50</sup>, Radoslav Adzic<sup>13</sup>, Ian Affleck<sup>16</sup>, Marc Allaire<sup>13</sup>, Dario Arena<sup>13</sup>, Robert Austin<sup>25</sup>, William Bailey<sup>5</sup>, Nitash Balsara<sup>27</sup>, Alfred Baron<sup>54</sup>, Lonny Berman<sup>13</sup>, Simon Bare<sup>21</sup>, Ron Beauman<sup>13</sup>, Michael Becker<sup>13</sup>, Richard Biscardi<sup>13</sup>, Kent Blasie<sup>28</sup>, Al Boerner<sup>13</sup>, Benjamin Bostick<sup>23</sup>, Angela Bowden<sup>13</sup>, Scott Buda<sup>13</sup>, Christian Burger<sup>9</sup>, Steven Burley<sup>41</sup>, Wolfgang Caliebe<sup>13</sup>, Larry Carr<sup>13</sup>, Mark Chance<sup>1</sup>, Chris Channing<sup>13</sup>, Praveen Chaudhari<sup>13</sup>, Stephen Cheng<sup>10</sup>, Ben Chu<sup>9</sup>, Noel Clark<sup>29</sup>, John Dabrowski<sup>13</sup>, Denis Danseglio<sup>13</sup>, Frank de Groot<sup>14</sup>, Steve Dierker<sup>13</sup>, Elaine DiMasi<sup>13</sup>, Adnan Doyuran<sup>13</sup>, Martine Duff<sup>24</sup>, Paul Dumas<sup>43</sup>, Ove Dyling<sup>13</sup>, Charles Eddy<sup>20</sup>, Tom Ellenberger<sup>40</sup>, Ken Evans-Lutterodt<sup>13</sup>, Marty Fallier<sup>13</sup>, Jeffrey Fitts<sup>13</sup>, Paula Fitzgerald<sup>42</sup>, Conrad Foerster<sup>13</sup>, Mark Fuhrmann<sup>13</sup>, Yang Gao<sup>52</sup>, Doon Gibbs<sup>13</sup>, Sol Gruner<sup>12</sup>, Jonathan Hanson<sup>13</sup>, Ed Haas<sup>13</sup>, Zahid Hasan<sup>25</sup>, Randy Headrick<sup>15</sup>, Paul Heiney<sup>28</sup>, Russel Hemley<sup>3</sup>, Wayne Hendrickson<sup>5</sup>, John Hill<sup>13</sup>, B. J. Hinch<sup>22</sup>, Chris Homes<sup>13</sup>, Jan Hrbek<sup>13</sup>, Benjamin Hsiao<sup>9</sup>, Eugene Hu<sup>13</sup>, Huey Huang<sup>8</sup>, Steve Hulbert<sup>13</sup>, Bob Hwang<sup>13</sup>, Eric Isaacs<sup>35</sup>, Chris Jacobsen<sup>9</sup>, Jiangsheng Jiang<sup>13</sup>, Erik Johnson<sup>13</sup>, Peter Johnson<sup>13</sup>, Jean Jordan-Sweet<sup>6</sup>, Leemor Joshua-Tor<sup>4</sup>, Chi-Chang Kao<sup>13</sup>, Lindsay Kelley<sup>44</sup>, Valery Kiryukhin<sup>22</sup>, Janos Kirz<sup>9</sup>, C. Kloc<sup>36</sup>, Ken Koebel<sup>13</sup>, Steve Kramer<sup>13</sup>, Satyendra Kumar<sup>7</sup>, F. Lamelas<sup>38</sup>, Antonio Lanzirrotti<sup>19</sup>, Carolyn Larabell<sup>49</sup>, George Leskody<sup>13</sup>, David Litster<sup>30</sup>, Timothy Lodge<sup>31</sup>, Henrik Loos<sup>13</sup>, Mathias Losche<sup>32</sup>, Kathy Loverro<sup>13</sup>, Karl Ludwig<sup>16</sup>, P. J. Lyman<sup>37</sup>, Don Lynch<sup>13</sup>, Rod MacKinnon<sup>39</sup>, Ho-Kwang Mao<sup>3</sup>, Tefvik Mendes<sup>13</sup>, Corinne Messina<sup>13</sup>, Rich Michta<sup>13</sup>, Lazslo Mihaly<sup>9</sup>, Laura Miller<sup>13</sup>, Lisa Miller<sup>13</sup>, Andrew Millis<sup>5</sup>, Jim Mills<sup>13</sup>, Jim Misewich<sup>13</sup>, John Mitchell<sup>35</sup>, Simon Mochrie<sup>33</sup>, Paul Montanez<sup>13</sup>, Eileen Morello<sup>13</sup>, Payman Mortazavi<sup>13</sup>, David Mullins<sup>45</sup>, Jim Murphy<sup>13</sup>, Satish Myneni<sup>25</sup>, Christie Nelson<sup>13</sup>, Charlie Nielson<sup>13</sup>, Joseph Nordgren<sup>17</sup>, Cev Noyan<sup>6</sup>, Benjamin Ocko<sup>13</sup>, Rick Osgood<sup>5</sup>, Satoshi Ozaki<sup>13</sup>, Peter Paul<sup>13</sup>, Pauline Pearson<sup>13</sup>, James Penner-Hahn<sup>53</sup>, Ron Pindak<sup>13</sup>, Sal Pjerov<sup>13</sup>, Boris Podobedov<sup>13</sup>, George Rakowsky<sup>13</sup>, Susila Ramamoorthy<sup>13</sup>, Art Ramirez<sup>5</sup>, Richard Reeder<sup>9</sup>, Richard Register<sup>25</sup>, Denise Robinson<sup>13</sup>, Howard Robinson<sup>13</sup>, Ian Robinson<sup>34</sup>, Jose Rodriguez<sup>13</sup>, Jim Rose<sup>13</sup>, Christoph Rose-Petruck<sup>2</sup>, Jeff Rothman<sup>13</sup>, Thomas Russell<sup>11</sup>, Cecelia Sanchez-Hanke<sup>13</sup>, Sergei Savrasov<sup>48</sup>, George Sawatzky<sup>18</sup>, Dieter Schneider<sup>13</sup>, Timur Shaftan<sup>13</sup>, Lawrence Shapiro<sup>5</sup>, Peter Siddons<sup>13</sup>, Boris Sinkovic<sup>55</sup>, John Skaritka<sup>13</sup>, Kevin Smith<sup>16</sup>, Jack Soo<sup>51</sup>, Donald Sparks<sup>26</sup>, Tom Steitz<sup>33</sup>, Peter Stephens<sup>9</sup>, Paul Stevens<sup>47</sup>, Vivian Stojanoff<sup>13</sup>, Helmut Strey<sup>9</sup>, Steve Sutton<sup>19</sup>, Robert Sweet<sup>13</sup>, Yong Tang<sup>13</sup>, David Tanner<sup>46</sup>, Cheo Teng<sup>13</sup>, Frank Terrano<sup>13</sup>, Ned Thomas<sup>30</sup>, Mark Toscano<sup>13</sup>, Nathan Towne<sup>13</sup>, John Tranquada<sup>13</sup>, Trevor Tyson<sup>48</sup>, Veena Venkatagiriappa<sup>13</sup>, Ellio Vescovo<sup>13</sup>, Tom Vogt<sup>13</sup>, Jiunn-Ming Wang<sup>13</sup>, Xijie Wang<sup>13</sup>, Peter Weber<sup>2</sup>, Donald Weidner<sup>9</sup>, Lin Yang<sup>13</sup>, Lihua Yu<sup>13</sup>, Zhong Zhong<sup>13</sup>, Emil Zitvogel<sup>13</sup>, Pete Zuhoski<sup>13</sup>

<sup>1</sup> Albert Einstein College of Medicine

<sup>2</sup> Brown University

<sup>3</sup> Carnegie Institutions of Washington

<sup>4</sup> Cold Spring Harbor Laboratory

<sup>5</sup> Columbia University

<sup>6</sup> IBM

<sup>7</sup> Kent State University

<sup>8</sup> Rice University

<sup>9</sup> Stony Brook University

<sup>10</sup> University of Akron

<sup>11</sup> University of MA at Amherst

<sup>12</sup> Cornell University

<sup>13</sup> Brookhaven National Laboratory

<sup>14</sup> University of Utrecht

<sup>15</sup> University of Vermont

<sup>16</sup> Boston University

<sup>17</sup> Uppsala University

<sup>18</sup> University of British Columbia

<sup>19</sup> University of Chicago

<sup>20</sup> Naval Research Laboratory

<sup>21</sup> UOP

<sup>22</sup> Rutgers University

<sup>23</sup> Dartmouth College

<sup>24</sup> Westinghouse Savannah River Co.

<sup>25</sup> Princeton University

<sup>26</sup> University of Delaware

<sup>27</sup> University of California at Berkeley

<sup>28</sup> University of Pennsylvania

<sup>29</sup> University of Colorado

<sup>30</sup> Massachusetts Institute of Technology

<sup>31</sup> University of Minnesota

<sup>32</sup> Johns Hopkins University

<sup>33</sup> Yale University

<sup>34</sup> University of Illinois at Urbana-Champaign

- <sup>35</sup> Argonne National Laboratory
- <sup>36</sup> Bell Laboratories
- <sup>37</sup> University of Wisconsin at Milwaukee
- <sup>38</sup> Washington State University
- <sup>39</sup> Rockefeller University
- <sup>40</sup> Harvard University
- <sup>41</sup> Structural GenomiX Corporation
- <sup>42</sup> Merck Corporation
- <sup>43</sup> Centre National de la Recherche Scientifique
- <sup>44</sup> National Aeronautics & Space Administration
- <sup>45</sup> Oak Ridge National Laboratory
- <sup>46</sup> University of Florida
- <sup>47</sup> ExxonMobil
- <sup>48</sup> New Jersey Institute of Technology
- <sup>49</sup> Lawrence Berkeley National Laboratory
- <sup>50</sup> North Carolina University
- <sup>51</sup> University at Buffalo
- <sup>52</sup> General Electric
- <sup>53</sup> University of Michigan
- <sup>54</sup> SPring-8
- <sup>55</sup> University of Connecticut

In addition to the individuals listed above, we have benefited greatly from the input of many more people who attended a series of workshops (see Appendix C) organized by the user community to help define the scientific case for, and requirements to be met by, NSLS-II.

# Table of Contents

List of Contributors.....	iii
Table of Contents.....	v
<b>1 OVERVIEW OF THE BNL NSLS-II .....</b>	<b>1</b>
<b>1.1 Introduction and Scientific Overview .....</b>	<b>1</b>
1.1.1 Goals and Proposal Precis .....	1
1.1.2 Scientific Opportunities .....	1
<b>1.2 Institutional Context .....</b>	<b>9</b>
1.2.1 National Synchrotron Light Source.....	9
1.2.2 Brookhaven National Laboratory.....	10
<b>1.3 National and Regional Context .....</b>	<b>11</b>
<b>1.4 U.S. Scientific Work Force and Participation of Under-represented Minorities and Women .....</b>	<b>17</b>
<b>2 SCIENCE OPPORTUNITIES.....</b>	<b>18</b>
<b>2.1 Macromolecular Crystallography.....</b>	<b>19</b>
2.1.1 Overview .....	19
2.1.2 Scientific Challenges and Opportunities .....	21
2.1.2.1 Large Molecular Assemblies .....	21
2.1.2.2 Membrane Proteins .....	24
2.1.2.3 Structural Genomics .....	25
2.1.2.4 Drug Design.....	27
2.1.3 Impact of NSLS-II.....	28
<b>2.2 Structure and Dynamics in Solutions and Membranes.....</b>	<b>32</b>
2.2.1 Overview .....	32
2.2.2 Scientific Challenges and Opportunities .....	32
2.2.2.1 Protein Folding .....	32
2.2.2.2 Structural Kinetics in Biological Macromolecular Complexes.....	33
2.2.2.2 Extension of Solution Scattering to Membrane Proteins .....	34
2.2.2.3 Counterion Cloud.....	35
2.2.2.4 Study of Metalloproteins with X-ray Absorption Spectroscopy.....	35
2.2.2.5 Electron Delocalization in Biomolecules.....	36
2.2.3 Impact of NSLS-II.....	37
2.2.3.1 Time resolved Studies in Micro-fabricated Flow-cell Mixers .....	37
2.2.3.2 X-ray Footprinting.....	38
2.2.3.3 High-throughput Characterization of Biomolecules .....	38
<b>2.3 Biological Imaging.....</b>	<b>41</b>
2.3.1. Overview .....	41
2.3.2 Scientific Challenges and Opportunities .....	42
2.3.2.1 Imaging Molecular Machines .....	42
2.3.2.2 Fundamental Basis of Disease .....	43

2.3.2.3 Early Disease Detection.....	45
2.3.3 Impact of NSLS-II.....	47
2.3.3.1 Soft X-ray Microscopy and Nanotomography.....	47
2.3.3.2 Diffraction Imaging.....	48
2.3.3.3 Hard X-ray Microprobe.....	49
2.3.3.4 Infrared Imaging and Microspectroscopy.....	49
2.3.3.6 Diffraction-Enhanced Imaging.....	50
2.3.3.7 User Demand.....	51
<b>2.4 Nanoscience.....</b>	<b>54</b>
2.4.1 Overview.....	54
2.4.2 Scientific Challenges and Opportunities.....	54
2.4.2.1 Nanoelectronics.....	54
2.4.2.2 Nanomagnetics.....	56
2.4.2.3 Nanoscale Functional Materials.....	57
2.4.2.4 Nanoscale Strongly Correlated Systems.....	59
2.4.2.5 Polymer Nanocomposites.....	61
2.4.2.6 Biomimetic Devices.....	61
2.4.3 Impact of NSLS-II.....	62
2.4.3.1 X-Ray Nanoprobes.....	63
<b>2.5 Soft Matter and Biomaterials.....</b>	<b>68</b>
2.5.1 Overview.....	68
2.5.2 Scientific Challenges and Opportunities.....	69
2.5.2.1 Hierarchical Structures in Polymers.....	69
2.5.2.2 Complex Phases in Block Polymers.....	70
2.5.2.3 Liquid Crystals and Colloids.....	70
2.5.2.4 Liquid and Soft Matter in Confinement.....	71
2.5.2.5 Complex Solutions.....	72
2.5.2.6 Hierarchical Biological Systems.....	72
2.5.2.7 Signal Transduction, Neuron Plasticity and Structural Changes in Membranes.....	73
2.5.2.8 Synthetic Biomolecular Systems.....	74
2.5.3 Impact of NSLS-II.....	75
2.5.3.1 X-Ray Photon Correlation Spectroscopy - Fluctuations.....	75
2.5.3.2 Resonant X-Ray Scattering - Orientational Order.....	76
2.5.3.3 Time-Resolved SAXS - In-Situ Processing.....	77
2.5.3.4 Time-Resolved GISAXS – Nanostructured Organic Films.....	77
2.5.3.5 Strategies for Studying Radiation Sensitive Materials.....	78
<b>2.6 Strongly Correlated Electron Systems.....</b>	<b>81</b>
2.6.1 Overview.....	81
2.6.2 Scientific Challenges and Opportunities.....	82
2.6.2.1 Surface Science.....	82
2.6.2.2 Fluctuating Order.....	82
2.6.2.3 Dynamics.....	83
2.6.2.4 Quantal Correlations.....	83
2.6.3 Impact of NSLS-II.....	84
2.6.3.1 Hard X-ray Inelastic X-ray Scattering.....	85
2.6.3.2 Soft X-ray Inelastic X-ray Scattering.....	86
2.6.3.3 Angle Resolved Photoemission Spectroscopy.....	87
2.6.3.4 Anomalous Soft X-ray Scattering.....	88
2.6.3.6 Coherent X-ray scattering.....	89
2.6.3.7 Infra-Red Studies.....	91
2.6.3.8 Materials Synthesis.....	91
2.6.3.9 High Pressure.....	91
2.6.3.10 High Magnetic Field.....	92

2.6.3.11 Ultra-low Temperature.....	92
<b>2.7 Magnetism.....</b>	<b>95</b>
2.7.1 Overview.....	95
2.7.2 Scientific Challenges and Opportunities.....	95
2.7.2.1 Low Dimensional Magnetism.....	95
2.7.2.2 Complex Magnetic Materials.....	98
2.7.2.3 Magnetic X-ray Microscopy.....	101
2.7.2.4 Magneto-Dynamic Phenomena.....	103
<b>2.8 Growth and Processing of Advanced Materials.....</b>	<b>107</b>
2.8.1 Overview.....	107
2.8.2 Scientific Challenges and Opportunities.....	108
2.8.2.1 Pulsed Laser Deposition.....	108
2.8.2.2 Self-organized Nanoscale Features on Surfaces.....	109
2.8.2.3 MBE Growth.....	110
2.8.2.4 Atomic Layer Deposition.....	111
2.8.2.5 MOCVD of AlGaN for Energy Conserving Solid-State Lighting.....	113
2.8.2.6 Thin Film Organic Crystal Growth.....	114
2.8.2.7 Growth in Fluids.....	115
2.8.3 Impact of NSLS-II.....	115
2.8.3.1 Full Field Reflectance X-ray Microscopy.....	115
2.8.3.2 Scanning Reflectance X-ray Microscopy.....	116
2.8.3.3 Oversampling Methods for Surfaces and Interfaces.....	116
2.8.3.4 Powder Diffraction.....	117
<b>2.9 Catalysis and Energy Science.....</b>	<b>120</b>
2.9.1 Overview.....	120
2.9.2 Scientific Challenges and Opportunities.....	121
2.9.2.1 Nanocatalysis.....	121
2.9.2.2 Hydrogen Storage.....	122
2.9.2.3 Battery Materials.....	125
2.9.2.4 Electrocatalysis and Fuel Cells.....	126
2.9.3 Impact of NSLS-II.....	127
2.9.3.1 Quick EXAFS and Dispersive EXAFS.....	127
2.9.3.2 High Resolution Powder Diffraction Studies.....	128
2.9.3.3 High Resolution X-ray Emission Spectroscopy.....	129
2.9.3.4 Anomalous Small Angle X-ray Scattering & Diffraction Anomalous Near Edge Structure.....	130
2.9.3.5 Inelastic X-ray Scattering.....	131
2.9.3.6 Photoemission and Surface Microscopies.....	131
2.9.3.7 Carbon K-edge Fluorescence Yield Near Edge X-ray Absorption Fine Structure.....	131
<b>2.10 Earth and Planetary Science.....</b>	<b>134</b>
2.10.1 Overview.....	134
2.10.2 Scientific Challenges and Opportunities.....	134
2.10.2.1 Elastic Properties at Pressure and Temperature.....	134
2.10.2.2 Rheology Challenges.....	136
2.10.2.3 Study of Melt Property and Liquid-liquid Phase Transition at High Pressures.....	137
2.10.2.4 Phase Transformations at High Pressures.....	138
2.10.2.5 Oxidation and Spin States.....	139
2.10.2.6 Amorphous Materials and Nanomaterials.....	140
2.10.2.7 Hydrous Minerals and the Deep Earth.....	141
2.10.2.8 Oxides and Silicates of Earth's Interior.....	142
2.10.3 Impact of NSLS-II.....	142
<b>2.11 Environmental Science.....</b>	<b>145</b>

2.11.1 Overview .....	145
2.11.2 Scientific Challenges and Opportunities .....	145
2.11.2.1 Speciation of Contaminants in Complex Natural Systems .....	145
2.11.2.2 Contaminant fate, Wasteforms, Remediation, and Long-term Stewardship .....	147
2.11.2.3 Biogeochemical Processes, Rates, and Element Cycling .....	148
2.11.2.4 Structure and Chemical Properties of Environmental Nanoparticles .....	149
2.11.2.5 Environmental Genomics and Toxicology .....	150
2.11.3 Impact of NSLS-II .....	151
<b>3 PROPOSED FACILITY .....</b>	<b>154</b>
<b>3.1 Capability Requirements .....</b>	<b>155</b>
3.1.1 Requirements for NSLS-II .....	155
3.1.2 Capabilities of Present NSLS .....	155
<b>3.2 Design Alternatives.....</b>	<b>160</b>
3.2.1 Free Electron Lasers.....	160
3.2.2 Energy Recovery Linacs .....	160
3.2.3 Third Generation Storage Rings.....	163
<b>3.3 NSLS-II: An Advanced Medium Energy Storage Ring .....</b>	<b>165</b>
<b>3.4 Design Considerations and Challenges .....</b>	<b>173</b>
3.4.1 Introduction .....	173
3.4.2 Lattice .....	175
3.4.2.1 Lattice Magnets .....	178
3.4.3 Stored Current .....	178
3.4.4 X-ray Pulse Length .....	179
3.4.5 Collective Effects .....	179
3.4.5.1 Coupled Bunch Instabilities .....	179
3.4.5.2. Single Bunch Instabilities .....	180
3.4.5.3 Intra-Beam Scattering .....	181
3.4.5.4 Ion-related Instabilities .....	181
3.4.6 Effects of Insertion Devices .....	181
3.4.7 Electron Beam Lifetime .....	182
3.4.7.1 Quantum Lifetime.....	182
3.4.7.2 Gas-Scattering Lifetimes .....	182
3.4.7.3 Touschek Lifetime .....	183
3.4.7.4 Total Lifetime .....	184
3.4.8 Heat Loads .....	184
3.4.9 RF.....	185
3.4.9.1 Third Harmonic Superconducting RF Cavity for Bunch Lengthening: .....	186
3.4.10 Injection System.....	187
3.4.10.1 Booster Synchrotron .....	187
3.4.10.2 Full Energy Linac Injector .....	189
3.4.11 Photon Beam Stability.....	190
3.4.12 Insertion Devices.....	191
3.4.12.1 High-Energy Undulator Sources.....	191
3.4.12.2 In-Vacuum Permanent Magnet Undulators .....	192
3.4.12.3 Consideration of Radiation Damage in Permanent Magnets .....	193
3.4.12.4 Superconducting Undulators.....	193
3.4.12.5 Soft X-ray Undulators.....	195
3.4.12.6 Ultraviolet Sources .....	196
3.4.12.7 Superconducting Wigglers.....	196

<b>3.5 Future Upgrade Opportunities.....</b>	<b>197</b>
3.5.1 Storage Ring Upgrades .....	197
3.5.2 Compatibility with Future Upgrade to Operation as an Energy Recovery Linac.....	197
<b>3.6 Facility Siting and Compatibility with BNL’s Master Plan.....</b>	<b>199</b>
<b>4 EXPERIMENTAL FACILITIES .....</b>	<b>200</b>
<b>4.1 Beamlines .....</b>	<b>200</b>
4.1.1 X-ray Beamlines.....	201
4.1.1.1 X-ray Scattering/Crystallography Beamlines .....	201
4.1.1.2 Small Angle X-ray Scattering.....	203
4.1.1.3 Nanoprobes .....	204
4.1.1.4 High-resolution Inelastic X-ray Scattering .....	205
4.1.1.5 Superconducting-wiggler-based High Energy Beamlines .....	207
4.1.2 Soft X-ray Beamlines .....	209
4.1.3 High-K-undulator-based VUV Beamlines .....	211
4.1.4 Infrared.....	211
<b>4.2 Extreme Sample Environments.....</b>	<b>215</b>
4.2.1 High Pressures.....	215
4.2.2 High Magnetic Fields .....	217
4.2.3 Ultra-Low Temperatures .....	218
<b>4.3 Automation and Robotics .....</b>	<b>219</b>
<b>4.4 Detectors.....</b>	<b>222</b>
4.4.1 Overview .....	222
4.4.2 Advances.....	222
4.4.2.1 Architecture .....	222
4.4.2.2 Sensors .....	224
4.4.2.3 Readout Electronics .....	225
4.4.2.4 Software.....	226
<b>5 BUDGET FOR CONCEPTUAL DESIGN OF NSLS-II AND PRELIMINARY BUDGET FOR THE PROJECT .....</b>	<b>227</b>
<b>5.1 Project and Operating Costs .....</b>	<b>227</b>
<b>5.2 Schedule.....</b>	<b>228</b>
<b>5.3 Acquisition Plan.....</b>	<b>228</b>
<b>5.4 Environment, Safety, and Health.....</b>	<b>229</b>
5.4.1 Integrated Safety Management System.....	229
5.4.2 National Environmental Policy Act .....	229
5.4.3 Fire Hazard Analyses .....	229
5.4.4 Safety Assessment Document .....	229
<b>APPENDIX: LIST OF WORKSHOPS .....</b>	<b>230</b>



# **1 Overview of the BNL NSLS-II**

## **1.1 Introduction and Scientific Overview**

### **1.1.1 Goals and Proposal Precip**

This proposal is to construct and then operate a new National Synchrotron Light Source, NSLS-II, at Brookhaven National Laboratory. NSLS-II will be an advanced, highly optimized, third generation, medium energy storage ring with full energy injection for top-off mode operation. NSLS-II will replace the current NSLS facility, which is presently 22 years old and will be 30 years old when we propose NSLS-II to become operational. The X-ray brightness and flux of NSLS-II will be world leading, exceeding that of any other synchrotron light source currently existing or under construction. It will be 10,000 times brighter and have 10 times higher flux than the present NSLS. NSLS-II will meet the nation's need for a high brightness medium energy X-ray source. It will enable structural studies of the smallest crystals in structural biology and provide a wide range of nanometer resolution probes for nanoscience. It will make possible coherent beam scattering studies of the dynamics of condensed matter systems in an otherwise inaccessible regime of low frequencies and short length scales. It will introduce new methods for imaging the structure of disordered materials and of biological systems, and greatly increase the applicability of inelastic X-ray scattering. NSLS-II will be situated in close proximity to the present NSLS building and the new BNL Center for Functional Nanomaterials, forming a research cluster for materials science, condensed matter, biology, and chemistry. NSLS-II will serve the cutting edge science of the nation, and will have a particularly dramatic impact as a vital resource for the strong academic and industrial research community of the Northeast United States.

Section 1 of this proposal presents highlights of the scientific opportunities enabled by NSLS-II. The main focus of this proposal is to describe those scientific opportunities in detail, and that is done in Section 2. Section 1 also provides the institutional and regional context that supports the determination that a new facility is vital to the needs of the scientific community. Sections 3 and 4 describe the new storage ring facility and associated instrumentation required for the cutting edge science in Section 2. Section 5 summarizes the preliminary budget and schedule for the project.

### **1.1.2 Scientific Opportunities**

The unprecedented brightness and flux of NSLS-II in combination with anticipated developments in optics, detectors, and computing power will lead to many advanced experimental capabilities that are not possible today. Access to these new capabilities and the unique infrastructure envisioned for this new facility will have profound impact on a wide range of scientific disciplines and initiatives and lead to many exciting discoveries in the coming decades. Section 2 outlines the grand challenges in these scientific disciplines and the impact that NSLS-II will have upon them. Here we present just a few examples, selected from the hundreds of outstanding challenges described in Section 2, which illustrate the breadth, excitement, and importance of the advances that NSLS-II will lead to.

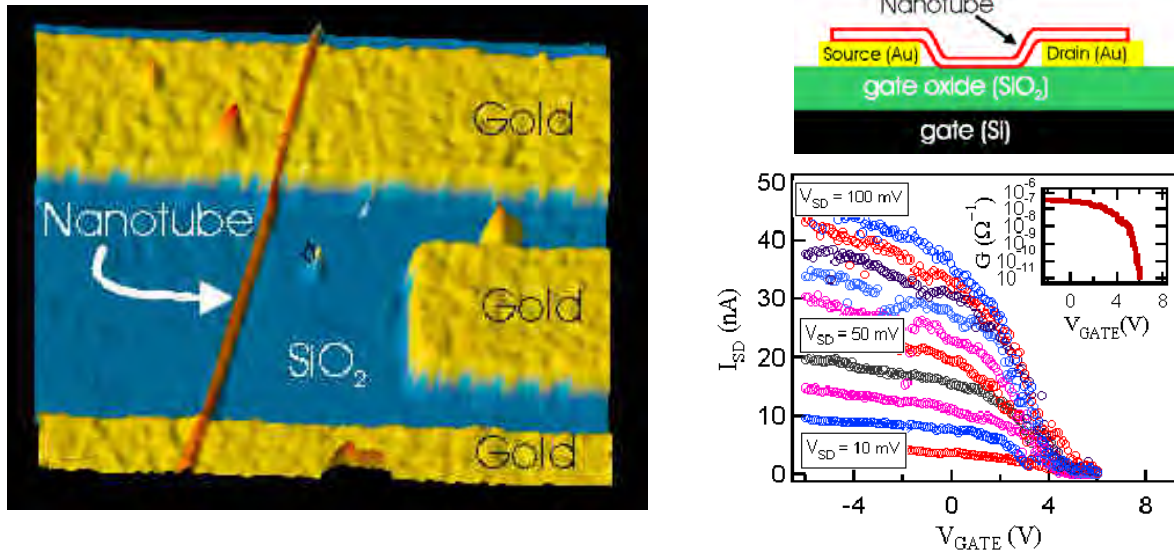


**Figure 1.1.1.** (a) Left: Micrograph of carbon nanotube-based field effect transistor (FET). (b) Top right: Schematic of carbon nanotube FET. (c) Bottom right: Demonstration of gate-controlled conductance. The conductance changes by a factor of 100,000 with the application of the gate voltage.

### Nanoscience

The rapid advances in Nanoscience and Nanotechnology promise to revolutionize our ability to control matter on the nanometer length scale and lead to the creation of nanostructures or assemblies that exhibit novel physical, chemical, and biological properties and phenomena. The scientific challenges ahead of us are to understand the unique properties of the individual nanometer-sized building blocks as well as the larger structures and assemblies and to understand the principles of self-assembling so that we can learn to exploit those unique properties and efficiently manufacture and employ the structures.

One exciting example is the possibility of using carbon nanotubes in future electronic and photonic devices. Due to their small size and high aspect ratios (single-walled carbon nanotubes have a diameter of 1.4 nanometer while their length can extend for microns), carbon-based nanotubes are ideal structures to incorporate into FETs and other basic components in advanced nanotechnologies, as shown in Figure 1.1.1(a). However, the electrical and optical properties of the nanotubes are intimately linked with their structure. When the nanotube is stressed, as in the bridging architecture used in the FET depicted in Figure 1.1.1(b), the nanotube electrical characteristics can change considerably. Detailed knowledge of the nanotube structure and electronic configuration will be essential. The unparalleled brightness of NSLS-II combined with recent advances in X-ray focusing optics and new coherent X-ray imaging techniques will enable position-resolved diffraction and spectroscopic investigations of the atomic structure and chemical composition of nanometer-scaled objects such as single-walled carbon nanotube FETs under realistic device operating conditions.

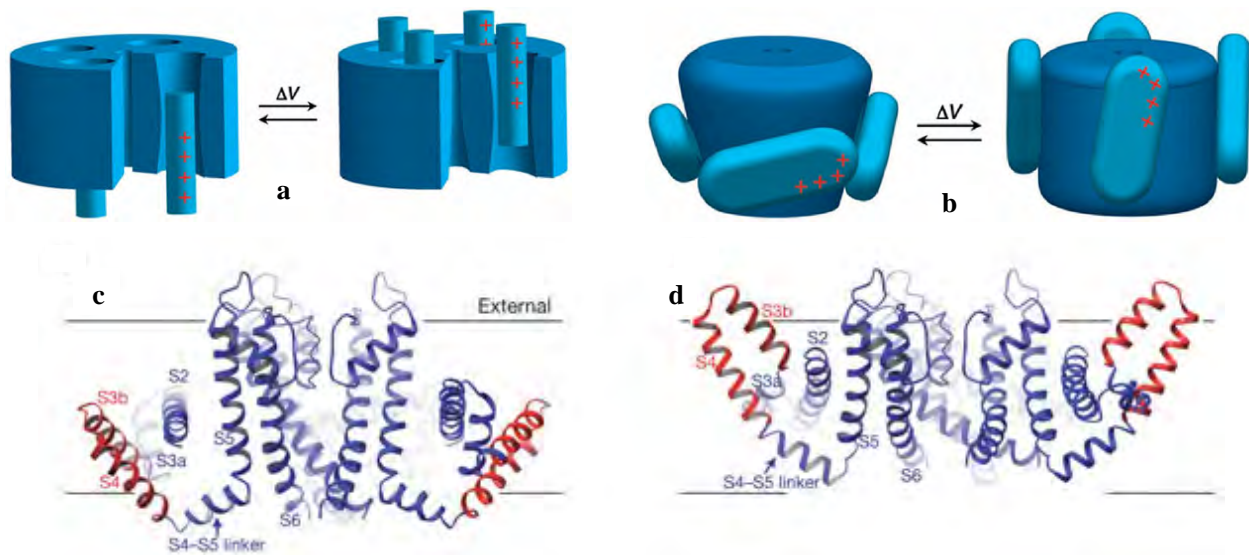


**Figure 1.1.2** Hypothesis for gating charge movements for voltage-dependent K<sup>+</sup> channel. a) and b) The conventional and the newly proposed model for gating activation, c) and d) The structure of the channel with the voltage sensor paddles (red) moving across the lipid membrane.

### Structural Biology

Atomic resolution protein structures obtained by macromolecular crystallography are indispensable in advancing many important areas of biological science. The world-leading brightness of NSLS-II will enable researchers to solve increasingly difficult problems.

The work on the voltage-dependent K<sup>+</sup> channel (Figure 1.1.2), for which Prof. Roderick MacKinnon, Rockefeller University, was co-awarded the 2003 Nobel Prize in Chemistry, is a perfect illustration of the dramatic impact that X-ray crystallography based structural studies have made in structural biology. Voltage-dependent cation channels open and allow ion conduction in response to changes in cell membrane voltage. Among other processes, these “life’s transistors” control electrical activity in nerve and muscle.

MacKinnon’s work also provides a glimpse into the future, where the most exciting and challenging structural studies will focus on understanding the biological functions of the large number of membrane proteins and large biomolecular assemblies. For example, the largest asymmetric molecular assembly whose atomic structure has been determined to date is that of the whole 70S ribosome, which consists of nearly 100,000 atoms in 53 proteins and 3 chains of ribosomal RNA. Future structural studies will focus on capturing the structure of the ribosome in various functional states in order to fully understand the process of protein synthesis, as well as to determine the structure of the ribosome complexed with antibiotics to facilitate drug design.

With the ultra-high source brightness of NSLS-II, studies such as MacKinnon’s will go beyond static structure to exploration of the dynamics of molecular machines functioning in their natural environments of solutions and membranes, where flexibility of the molecule and water, pH, and ion concentration play determinant roles. Time-resolved studies of macromolecular dynamics and interactions down to microsecond time scales will be possible. These experimental advances, combined with large-scale computer simulations, will provide new insights into the function of molecular machines that carry out critical cellular functions.

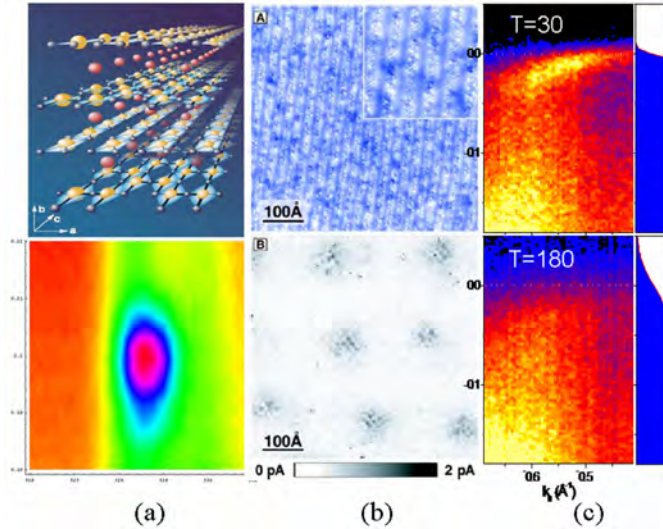


**Figure 1.1.3** (a) (top) 3D model of the spin ladder compound,  $\text{Sr}_{14}\text{Cu}_{24}\text{O}_{41}$  [1]; (bottom) Direct observation of the proposed charge density wave in  $\text{Sr}_{14}\text{Cu}_{24}\text{O}_{41}$  using oxygen K-edge resonant scattering. [2]; (b) STM images of vortices in  $\text{Bi}_2\text{Sr}_2\text{CaCu}_2\text{O}_{8+\delta}$ , clearly showing modulation with  $\sim 2.6$  nm wavelength. Soft x-ray resonant scattering at NSLS-II will be able to provide direct evidence of the underlying electronic modulation. (c) ARPES studies of  $\text{Bi}_{0.5}\text{Pb}_{0.5}\text{Ba}_3\text{Co}_2\text{O}_{9+\delta}$  show that at low temperatures a two- to three-dimensional crossover in the transport properties occurs [3].

### Strongly Correlated Electron Systems

Understanding the electronic behavior of strongly correlated electron systems is arguably the most challenging problem in condensed matter physics today - one that is driving a revolution in the prevailing paradigm of Fermi-liquid behavior of solids. Since the controlling degrees of freedom in these systems are electronic in nature, probes that couple directly to the electrons are uniquely suited to their study. Further, since these systems are characterized by competing interactions and frequently display inhomogeneous ground states, probes on a number of different length, energy, and time scales are required to fully elucidate their behavior. As a result, the full gamut of synchrotron techniques, including X-ray diffraction, resonant scattering, IR spectroscopy, and high-resolution angle-resolved photoelectron spectroscopy, have provided data which has been critical to understanding these systems.

However, the field is far from mature and surprising new phenomena appear on a regular basis, such as the recent discovery of superconductivity in cobaltate materials, the unusual superconductivity in  $\text{Sr}_2\text{RuO}_4$  and the realization of “spin liquids”. The transport, thermodynamic, magnetic, and spectroscopic characteristics of these systems are essentially unknown on short length scales and near surfaces. The advances in nanofabrication technology and materials synthesis will for the first time enable researchers to explore low dimensional and finite-size effects in these systems, which might provide the basis for future device applications. For example, one might be able to develop novel sensors and electronic devices based on the metal-insulator, superconductor, and magnetic phase transitions induced by small changes in strain, external fields, and composition.

In coming years, the key to advancing the field will be a strong effort in materials synthesis coupled with the development of new and improved measurement techniques. NSLS-II will significantly enhance the capability of a wide range of experimental techniques, including:  $\sim 1$  meV high-resolution photoemission using high-energy photons will be possible so that this powerful technique can be applied to a wide range of samples; inelastic X-ray scattering with  $\sim 10$  meV resolution in the study of electronic excitations will be possible, providing access to an energy scale relevant to, for example, high temperature superconductivity; and it will be possible to use coherent X-rays to study the dynamics as well as image the complex domain structure in these systems.

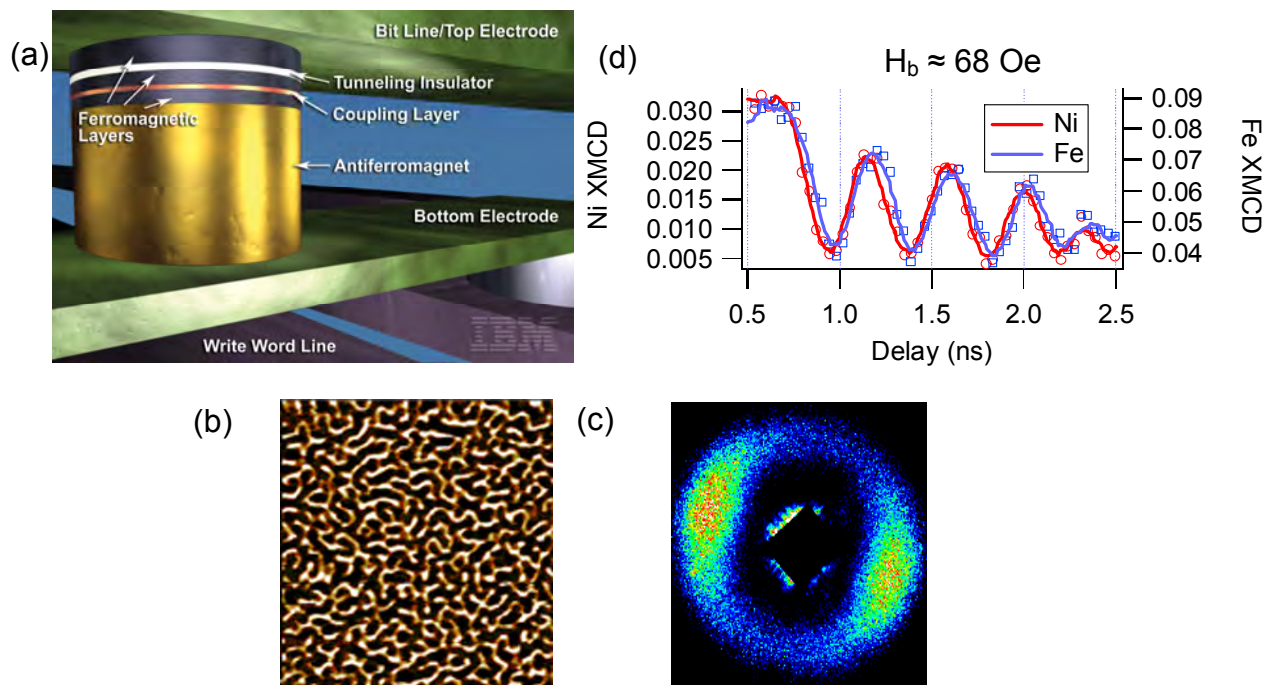


**Figure 1.1.4** (a) Multilayer MRAM structure from IBM. (b) Magnetic Force Microscopy image of the domain structure in a Co/Pt multilayer film. (c) Magnetic speckle pattern from the same sample produced by coherent diffraction of circularly polarized x-rays at the Co L3 edge. The element-specific domain structure can be reconstructed from these diffraction patterns. (d) Element-specific and time-resolved x-ray magnetic circular dichroism measurements of the magnetization rotation for a 50 nm thick permalloy film after application of a fast magnetization pulse. These measurements provide researchers with new insights into magnetization dynamics [4].

### Spintronics

Microelectronic devices which exploit the spin of the electron are still in their infancy in comparison with semiconductor devices. However, they have already had tremendous impact in the area of high-density magnetic storage. Future spintronic devices are under active development and will consist of complex materials, such as the multilayer magnetic random-access memory (MRAM) structure from IBM shown in Figure 1.1.4, spin-polarized field-effect transistors, and fully programmable all-spintronics microprocessors. As element sizes in these advanced magnetic devices approach the nanometer scale and switching speeds surpass the GHz range, designers will be forced to consider fundamental issues such as the magnetic domain structure and the dynamics of magnetization reversal. A thorough understanding of these processes and solution of a number of critical materials issues, such as the development of room temperature magnetic semiconductors, improvements in the spin-injection efficiency across an interface, and understanding spin de-coherence processes, must be achieved before these novel devices can be successfully implemented.

The need to characterize and understand these novel magnetic materials, devices and processes has motivated the development of a wide range of experimental tools using synchrotron radiation over the last decade. The high brightness of NSLS-II in combination with elliptically polarized IDs or polarization conversion optics will significantly improve the sensitivity as well as spatial and timing resolution of these techniques. They will enable study of (1) magnetic interfaces, which play a crucial role in giant magneto-resistance, exchange-bias, and many other important phenomena, (2) nano-scale self-assembled and fabricated magnetic structures, (3) novel magnetic materials, such as molecular magnets, half-metallic materials and magnetic semiconductors, and (4) magnetic switching dynamics.

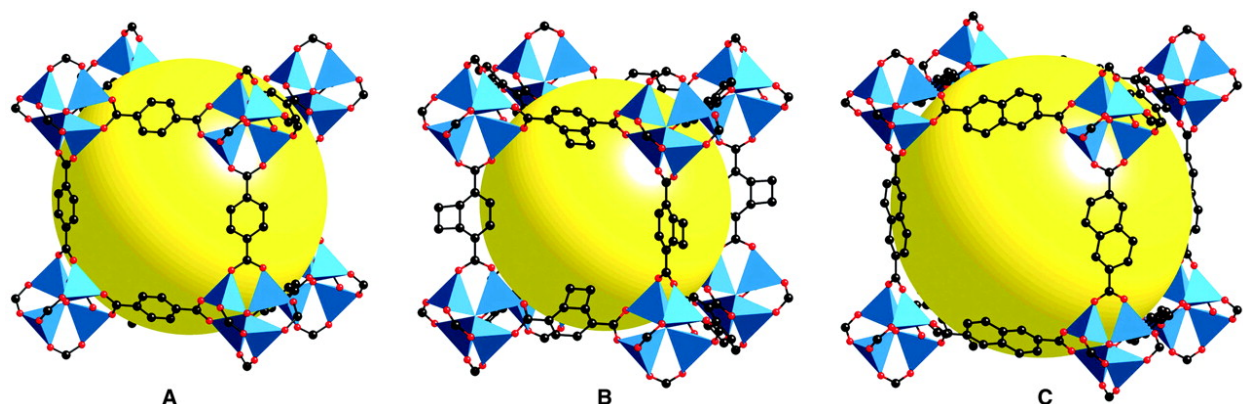


**Figure 1.1.5** An example of a novel metal-organic framework nanostructure used for hydrogen storage. Over 90 % of the crystal volume is open space (yellow ball) which can be used for gas storage ( $H_2, CH_4, N_2$ ). These are the most porous, and have the highest specific surface area, of any known material. (a) Single-crystal x-ray structures of metal-organic framework-5 (MOF-5) of composition  $Zn_4O(BDC)_3$  ( $BDC = 1,4$ -benenedicarboxylate) with a cubic three-dimensional extended porous structure which can adsorbed up to 4.5 weigh percent of hydrogen (17.2 hydrogen molecules per formula unit) at 78 k. The topologically similar isorecticular MOF-6 (b) and MOF-8 (c) having cyclobutylbenzene and naphthalene linkers, respectively, give approximately double and quadruple the uptake found for MOF-5.

#### *Energy Research – Hydrogen Storage*

In response to the Presidential Hydrogen Fuel Initiative, the Department of Energy's Office of Basic Energy Sciences convened a workshop on hydrogen production, storage, and use in May 2003. The report of that workshop, "Basic Research Needs for the Hydrogen Economy" identified several grand challenges which the scientific community must solve in order to develop and demonstrate viable hydrogen storage technologies for transportation and stationary applications. Among the most important of these are (1) development of novel low-density nanomaterials, which have high hydrogen storage capacity at ambient temperature and low pressure, (2) detailed understanding of the processes by which hydrogen is taken up and released by these complex materials, and (3) development of improved catalytic materials and performance for increased fuel cell efficiency, faster storage kinetics, and increased production capacity. Many promising approaches and materials (Figure 1.1.5) are under intense investigation worldwide, including hydrogen driven metallurgical reactions, chemically bonded complex hydrides, and nanoporous materials such as carbon fibers and nanotubes.

Catalysis and energy science represent perhaps the ultimate challenge for characterization, with reactions occurring at specific atomic sites in a complex system, on short time scales, and at high temperatures and pressures. Nevertheless, it is extremely important to have high-resolution atomic and electronic structures of these materials and their transformation under operating conditions at different stages of the hydrogen uptake/release cycle to aid the search for new materials and understand the adsorption/desorption and reaction/catalytic kinetics.

The unprecedented brightness and flux of NSLS-II will enable measurements with the high spatial, energy, and time resolution necessary to fully characterize these complex systems. Advanced capabilities will include: spectromicroscopy characterization of novel nanocomposite catalytic systems, as well as their active sites and adsorbate-substrate interactions, with better than 10 nm spatial resolution; time-resolved in-situ studies of the kinetics of materials synthesis and catalytic processes on millisecond timescales or faster; application of new experimental techniques, such as high-resolution x-ray emission spectroscopy and x-ray Raman scattering, to provide new spectroscopic information; and the use of combinatorial methods for large scale screening of novel materials.

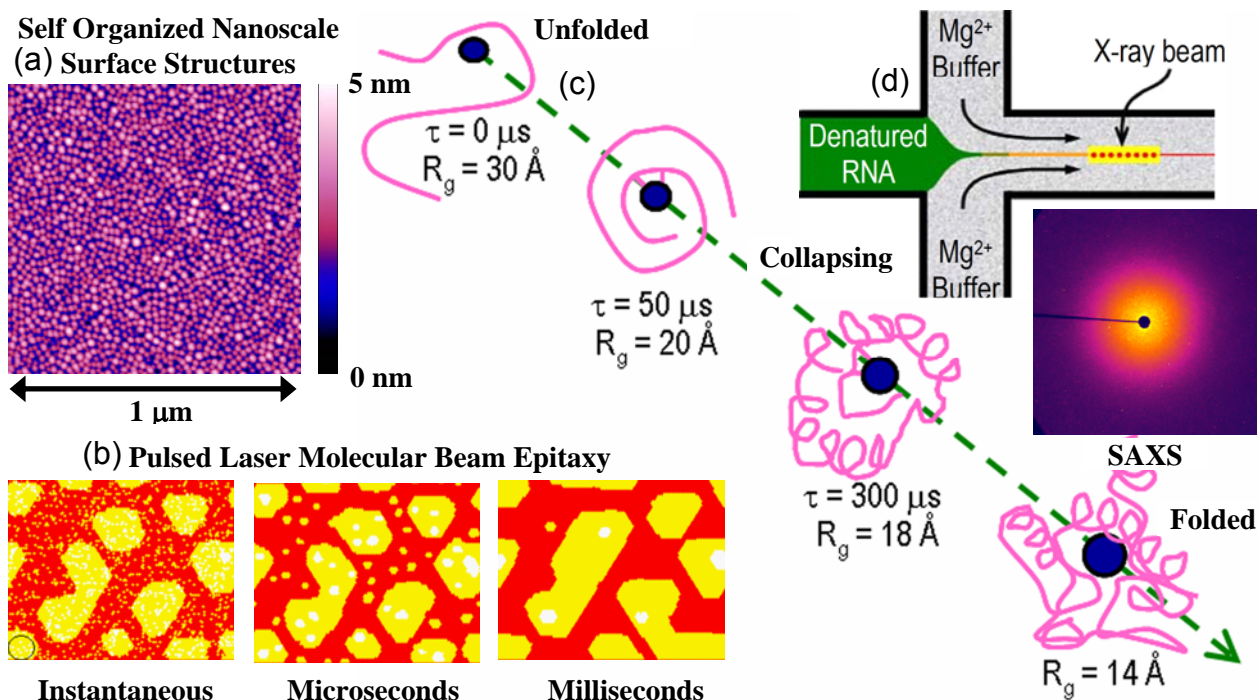


**Figure 1.1.6** NSLS-II will extend studies of many important kinetic processes from the millisecond range possible today down to the microsecond range, providing a region of overlap where computations and experiments can be compared. This will have impact in fields as diverse as growth of advanced materials (a and b above) and understanding of protein folding (c). The high brightness and flux of NSLS-II together with advanced detectors and new experimental techniques such as micro-fabricated flow-cell mixers (d) are key to this advance.

#### Kinetics – From Advanced Materials to Protein Folding

Understanding kinetics is the key to unraveling the mysteries of how systems evolve. With current sources, synchrotron experiments are able in many important cases to determine the structural, electronic, chemical, and magnetic evolution of materials with only millisecond time resolution. The high brightness and flux of NSLS-II will extend studies of kinetics into the microsecond regime, providing new insight into a variety of kinetic problems as diverse as protein folding and growth of advanced materials.

For example, understanding how proteins fold is a key to understanding how they perform their biological function. The time scale of the folding process varies from picoseconds to nanoseconds, when the initial secondary structure starts to form, to milliseconds to seconds, when the folding process is complete. Advances to petaflop computational ability will lengthen the time over which folding can be calculated to microseconds. The high brightness of NSLS-II together with advances in micro-fabricated flow-cell mixers will extend the time range over which small angle x-ray scattering measurements can observe folding down from milliseconds, currently, to microseconds. Computations and experiments will then overlap and provide better tests of our understanding of the physics of the underlying interactions.

Similarly, it is crucial to understand materials growth kinetics in order to design materials with ever more advanced properties. In the example of pulsed laser molecular beam epitaxy, deposited atoms diffuse on surfaces on picosecond time scales but surface morphology (islands, terraces, etc) evolves on time scales of microseconds to seconds. NSLS-II together with advanced detectors will allow x-ray scattering techniques to follow the evolution of these nanoscale surface morphologies on microsecond time scales rather than the millisecond time scales possible today. Once again, advanced computations are only able to reach microsecond time scales and so NSLS-II will provide a critical bridge, joining the results of advanced computation with experimental observation.

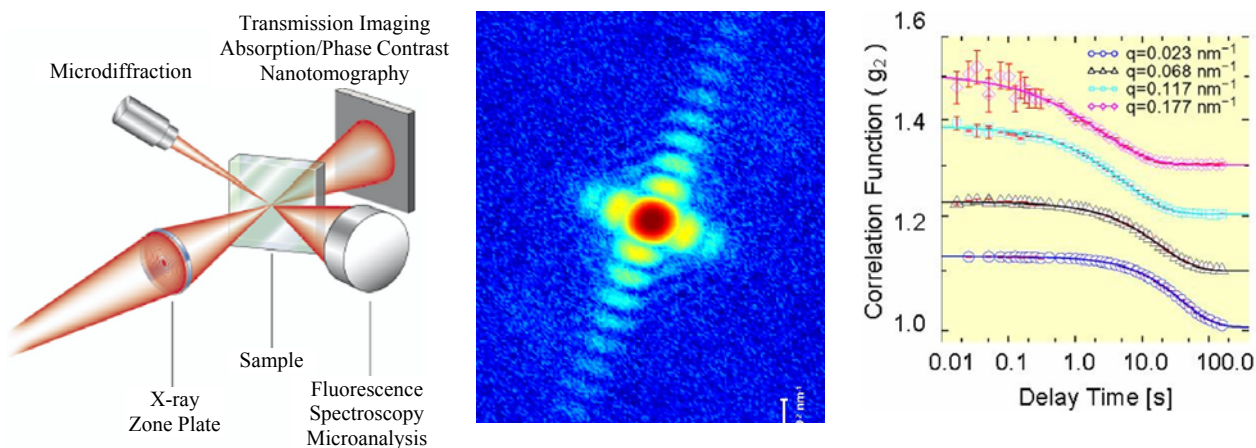


**Figure 1.1.7** (left) NSLS-II will enable nanoprobe to reach 10 nm resolution. (center) Speckle pattern from a 160 nm Ag nanocube. With NSLS-II, coherent diffraction images such as this will provide sufficient information to reconstruct real space images of objects with nanometer spatial resolution. (right) Intensity-intensity autocorrelation functions for an  $L_3$ -phase sample of P(SEBS) triblock copolymer in short-chain PS homopolymer. NSLS-II will revolutionize XPCS, pushing the time resolution of studies of the dynamics of soft matter systems from time scales of 10 msec today down to 100 nanoseconds and vastly increasing the diversity of dynamical processes which can be studied.

#### *Nanoprobes, Diffraction Imaging, and X-ray Photon Correlation Spectroscopy*

A hallmark of NSLS-II will be its unprecedented brightness. This singular feature will enable dramatic advances in three particular techniques which find application across all of the scientific areas outlined in Section 2. These are nanoprobe, diffraction imaging, and X-ray photon correlation spectroscopy (XPCS). All require high coherent flux to reach their ultimate potential.

Synchrotron-based X-ray microprobe, with micron and sub-micron spatial resolution, have proven themselves to be extremely valuable research tools. However, by further improving the spatial resolution to 10 nanometers or below, X-ray nanoprobe will, for the first time, allow the characterization of individual nanoparticles or nanometer-sized grains in complex nanomaterials by their density, elemental composition, elemental oxidation state and spin state, strain, texture, magnetization, and atomic and electronic structure and dynamics. This exciting prospect requires the high brightness of NSLS-II to provide a sufficiently high flux of x-rays in the resulting small focal spot.

Diffraction-based (lensless) imaging has the potential to go beyond the resolution of nanoprobe, which are ultimately limited by the laws of optics. With NSLS-II, it will be possible to reconstruct 3D real space images of non-crystalline specimens with a resolution of a few nm. By combining this technique with chemical and magnetic contrast unique to x-rays 3D chemical and magnetic imaging will be possible with similar resolution. Diffraction imaging depends on coherent illumination, and so the high brightness of NSLS-II is essential.

One of the most exciting scientific opportunities offered by the unprecedented brilliance of NSLS-II is its revolutionary impact on our ability to carry out X-ray photon correlation spectroscopy (XPCS) experiments. XPCS experiments at NSLS-II will yield exciting new insights into the dynamics of equilibrium fluctuations of myriad systems, occurring on shorter length scales than can be reached in light scattering and longer time scales than can be reached with the neutron spin echo technique. The ultra-high brightness of NSLS-II together with improvements in experimental technique will revolutionize XPCS, pushing the time resolution from the current state-of-the-art of 10 msec for soft matter systems down to the hundred nanosecond range, vastly increasing the diversity of dynamical processes which can be studied.

## 1.2 Institutional Context

### 1.2.1 National Synchrotron Light Source

Designed in the 1970's and commissioned in 1982, the two NSLS storage rings were the first Double Bend Achromat (DBA) lattices and the first second generation storage ring sources in the world. Their design emphasized the production of high flux synchrotron radiation from bending magnets and included only a small number of straight sections for insertion devices. The smaller 800 MeV VUV/IR ring covers the photon energy range from far infrared (IR) to soft X-ray. Continually updated over more than 20 years, the X-ray ring today operates at 2.8 GeV, with brightness several orders of magnitude higher than the initial design value. However, its performance has reached its theoretical limit and its brightness cannot be increased significantly beyond its current value. Additionally, the eight-fold periodicity of the lattice severely limits the number of insertion devices, which are crucial today for producing high brightness radiation.

The NSLS and its successes served as a springboard for 'third-generation' storage ring facilities around the world, many of which scaled up the ground-breaking NSLS lattice. Built with many more cells and insertion devices, these machines today surpass the technical performance of the NSLS.

Today's most challenging and important problems at the scientific frontier demand photons with a broad spectrum of wavelengths and a broad range of dramatically enhanced capabilities, especially higher average brightness with nearly DC time structure, exquisite position stability, and easy energy tunability for each beamline independent of other beamlines. As described in Section 2, the great majority of the cutting edge scientific problems require photons across the energy spectrum up to  $\sim 20$  keV.

In order to address these compelling scientific challenges, the NSLS proposes development of a new facility that will provide a dramatic upgrade in capabilities relative to the present NSLS. Dubbed NSLS-II, the new facility seeks to preserve the cross-cutting nature of the research that characterizes the present NSLS, while providing the advanced capabilities that are essential to enable the large user community to solve the most challenging scientific problems. This goal can be best realized through the construction of the highly advanced medium energy storage ring proposed here. It will take advantage of the latest advances in storage ring technology, including superconducting undulators, top-off operation, superconducting RF cavities, and others, to achieve world-leading average brightness and flux and set a new performance standard. It will be designed to be upgradeable to operation as an energy recovery linac for even greater performance, should that technology become feasible in the future. Relocating the present VUV/IR storage ring to the new facility to serve as a dedicated IR ring will also provide world-leading high brightness in the important near- to far-IR spectral region. NSLS-II will thus continue to provide one of the unique strengths of the present NSLS, i.e., the broadest range of wavelengths available to users in a single facility, extending from the hard X-rays ( $0.1 \text{ \AA}$ ), to the far-infrared (10 mm). The wide array of analytical techniques that is currently available to the NSLS users due to this broad spectral range will thus continue in the new facility, with greatly advanced capabilities.

The NSLS scientific and technical staff is highly qualified to carry out this task. The breadth and depth of experience it has gained in operating one of the most successful and heavily used scientific user facilities in the world for the past two decades gives it a keen understanding of the needs of the user community and how to best serve them. With NSLS-II, we will take advantage of the lessons learned at NSLS and other facilities and develop a new paradigm for operating an outstanding user program, including optimization of the respective roles of the facility and users in constructing and operating beamlines. NSLS has routinely operated both storage rings for more than more than 5500 hours/year and with greater than 95% reliability for many years. The NSLS staff has also made pioneering contributions in the pertinent areas of accelerator physics, including development of the first in-vacuum undulators, the first digital feedback systems for beam position stabilization, and many other innovations. The specifications we propose for NSLS-II are ambitious and pose a number of technical challenges. We are confident that we will meet these challenges.

## 1.2.2 Brookhaven National Laboratory

This proposal builds upon the many strengths of BNL in designing, constructing and operating large accelerator complexes, in developing advanced instrumentation, in carrying out myriad complementary research programs, many of which synergistically interact with and depend upon synchrotron radiation facilities, and in engaging in strong collaborations with the academic community.

BNL has a distinguished history of accomplishments as an accelerator laboratory. Besides the NSLS, other accelerators designed, constructed, and operated at BNL in support of DOE and national missions include the Alternating Gradient Synchrotron (AGS) and the Relativistic Heavy Ion Collider (RHIC), one of the world's largest high energy particle accelerators. Each of these broke new technical ground. All of the expertise, experience, and infrastructure of BNL in executing large scientific construction projects will be available to support the NSLS-II project.

BNL's strength in instrumentation is focused in its Instrumentation and Superconducting Magnet Divisions, which have world class programs in development of new detectors and magnet systems, respectively. The present NSLS has enjoyed a long-standing collaboration with the Instrumentation Division, which has resulted in development of several advanced detectors in use at NSLS today. Even more advanced detectors will be necessary to take full advantage of the high intensity X-ray beams of NSLS-II and continued collaboration with the Instrumentation Division will be central to meeting this challenge. One of the objectives for NSLS-II is to develop and employ superconducting undulators to provide fully tunable radiation from this medium-energy ring. Active development to meet this challenge is underway at the NSLS in collaboration with the Superconducting Magnet Division, Argonne National Laboratory (ANL), Lawrence Berkeley National Laboratory (LBNL), and Stanford Linear Accelerator Laboratory (SLAC).

BNL maintains outstanding research programs in its Physics, Chemistry, Materials Science, Biology, Medical, Energy Science and Technology, and Environmental Sciences Departments as well as hosting exceptional user facilities such as the NSLS, the Center for Functional Nanomaterials (CFN), the Laser Electron Acceleration Facility (LEAF), and others. Many of these research programs either depend directly upon access to the NSLS or interact synergistically with programs that use the NSLS.

For example, BNL's strength in non-synchrotron imaging and other complementary techniques for biological and medical applications, including Positron Emission Tomography (PET), Magnetic Resonance Imaging (MRI), Cryo-Electron Microscopy, Scanning Transmission Electron Microscopy, macromolecular NMR, and mass spectrometry, provide an ideal synergistic environment for structural biological studies and biomedical research that uses synchrotron radiation; several examples are given in Section 2.1-2.3. NSLS-II will stimulate collaboration at every level of biomedical structural study from molecules, to cells, to tissue, to the whole organism, and a vibrant community of researchers will assemble with NSLS-II serving as one of its core facilities.

The Center for Functional Nanomaterials at BNL is a key institutional asset that will benefit NSLS-II both synergistically and directly. The high brightness of NSLS-II is absolutely essential to fully characterize the novel nanomaterials that will be fabricated in the CFN, as described in Section 2.4 and several other parts of Section 2. At the same time, the ability to probe nanomaterials on nanometer length scales will require that the high brightness of NSLS-II be combined with equally advanced X-ray optics to permit the beams to be focused to spots of  $\sim 10$  nm or less. BNL has benefited greatly from a strong collaboration in X-ray optics research, based on advanced electron beam lithography, with Stony Brook University and Bell Labs. The establishment of the CFN will further strengthen this collaboration. In particular, the CFN will house a state-of-the-art electron beam lithography facility that will accelerate the development of a wide range of novel X-ray focusing optics, including zone plates, waveguides, and refractive optics.

## 1.3 National and Regional Context

In the last decade, there has been tremendous growth in the national synchrotron user community as synchrotron techniques have developed into powerful tools with broad applicability across diverse disciplines. This has been especially dramatic in the Life Sciences, where there has been a large increase in the use of synchrotron radiation in structural biology studies. Structural biology has gained widespread importance, and X-ray crystallography in particular plays a key role in providing physical descriptions of the macromolecular complexes that embody the integrated nature of cellular and functional biology. In coming years, a similar increase in synchrotron usage is likely in the Nanoscience community.

The increasing demand for state-of-the-art synchrotron resources is driven not only by the challenges of highly complex samples, but also by the general growth in the number of researchers who use synchrotron techniques in their research. These trends in growth and usage are shown in Figure 1.3.1 for the collective user population supported by the four DOE synchrotrons: the Advanced Light Source (ALS) and Stanford Synchrotron Radiation Laboratory (SSRL) in California, the Advanced Photon Source (APS) in Illinois, and the National Synchrotron Light Source (NSLS) in New York. Similar trends in growth of users and shifts in usage have been observed at all four facilities. There is every reason to expect this growth to continue and indeed current projections are that the number of synchrotron users nationwide will grow to ~ 11,000 annually in coming years.

At the NSLS, a uniquely diverse and productive scientific community has grown up around it over the last two decades. The wide range of photon energies available at the NSLS brought together researchers from many fields in a comparatively compact environment, fostering collaborations that otherwise might not have come about. Encouraged by BNL and the NSLS, the community blossomed, drawing its strength from the fabric of science and technology throughout the Northeastern US.

Today, the NSLS provides essential scientific tools for about 2400 scientists per year, which is about one third of the total user community for the DOE synchrotrons. These users come from more than 400 academic, industrial, and government institutions. The NSLS user community has gained a well earned reputation for synchrotron based research that is both novel and of high impact. The myriad research

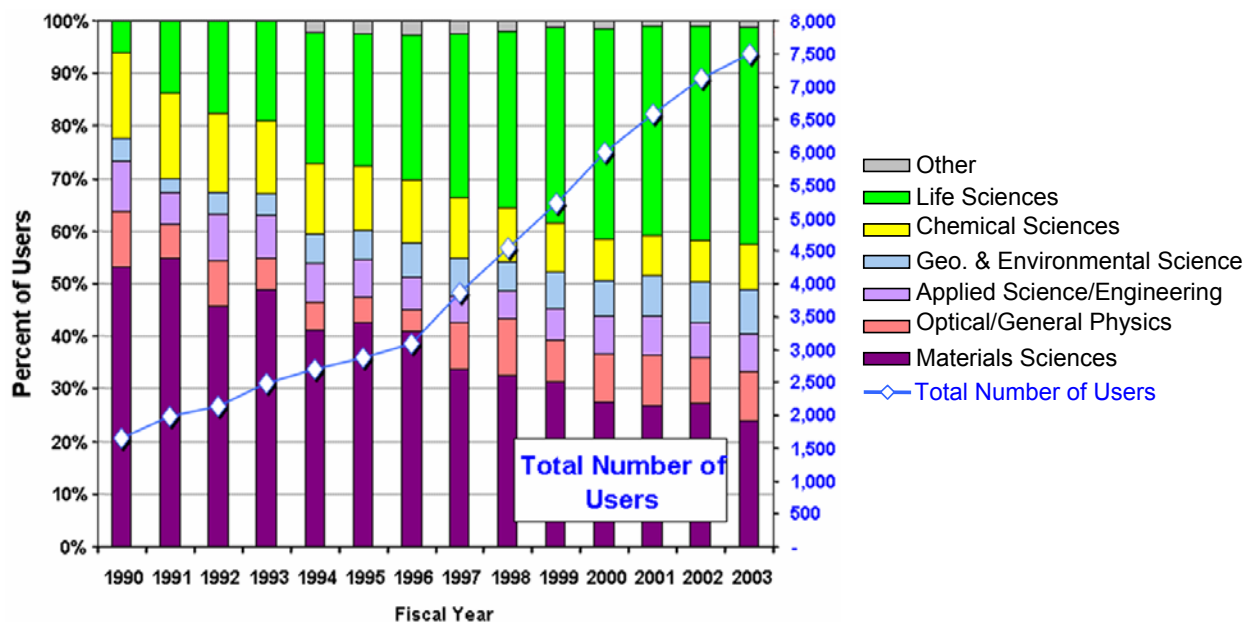


**Figure 1.3.1** User profile by discipline of experiments and total number of users for the four DOE synchrotrons (ALS, APS, NSLS, SSRL). This shows the strong increase in the percentage of users in the life sciences as well as the dramatic growth in total number of users. Current projections are that the total number of users will grow to ~ 11,000 annually in coming years.

	<u>FY2000</u>	<u>FY2001</u>	<u>FY2002</u>
<b>Total Publications</b>	<b>824</b>	<b>806</b>	<b>707</b>
Physical Review Letters	23	18	13
Science	18	12	16
Nature	10	20	18
Cell	11	15	7
EMBO J.	14	20	14
Nature Str. Bio.	15	23	28
Proc. Nat. Acad. Sci.	2	7	18
Structure	5	13	11
Applied Physics Letters	10	10	9
<b>Total Premier Journal Articles</b>	<b>108</b>	<b>138</b>	<b>134</b>

**Table 1.3.1** Research at the NSLS has had high impact. One measure of that is the number of publications appearing in so-called premier journals. These are listed above with the number of publications appearing in each based on work done at the NSLS for FY2000-FY2002.

programs of its large user community produce about 800 publications per year, of which about 130 appear in the ‘premier’ group of international scientific journals, as shown in Table 1.3.1.

In addition to their contribution to the national effort in synchrotron radiation, each of the four DOE facilities also plays a critical role as a vital resource for their region. This is clearly illustrated in Figure 1.3.2, which shows the distribution of users by US State who use each of the four facilities. Almost all users from California use either ALS or SSRL. Almost all users from Illinois use the APS. And almost all users from New York State use the NSLS.

The dominance of the NSLS in the Northeast region is further illustrated in Figure 1.3.3, which shows the geographical distribution of NSLS users. In fact, NSLS is a critical resource not only for New York

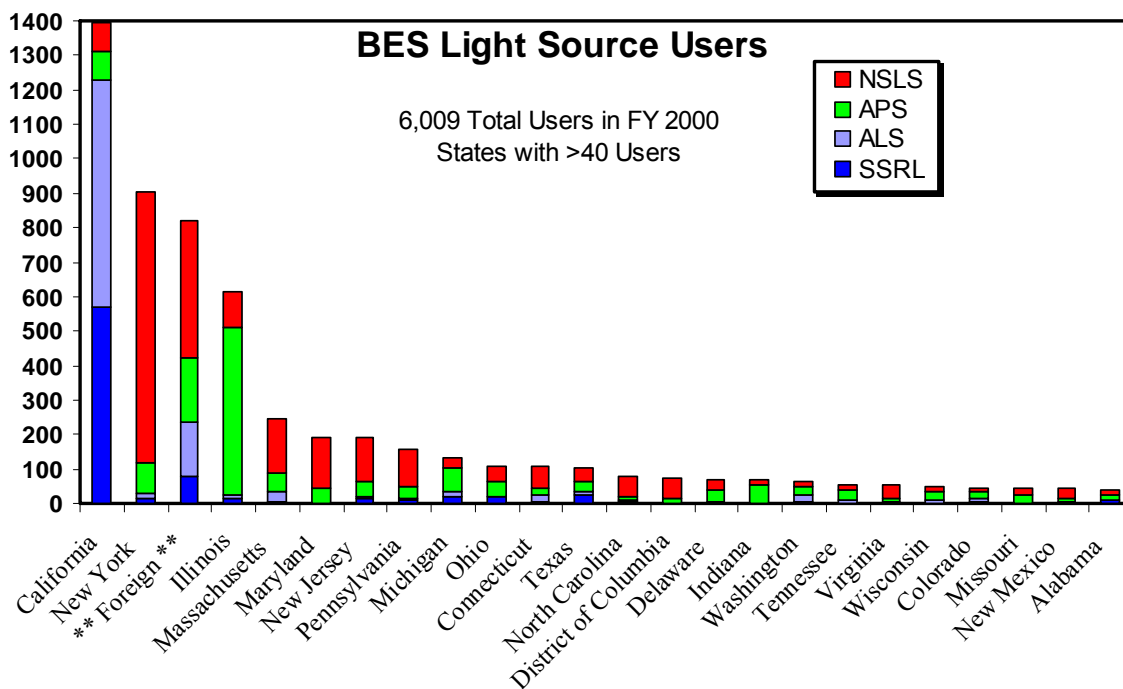


**Figure 1.3.2** Geographical distribution of NSLS users in FY02.

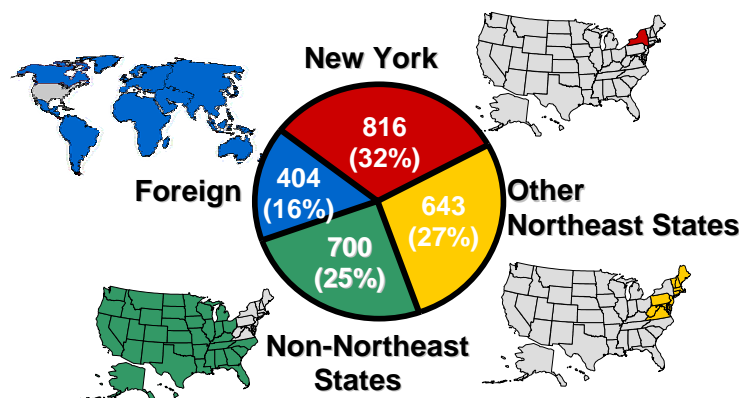


**Figure 1.3.3** Geographical distribution of NSLS users in FY02.

State, but indeed for the entire Northeastern United States. About 60% of all NSLS users come from Northeast States, with about one third of all users coming from New York State. This illustrates the critical role that NSLS plays as a major resource for this strong research community and as a provider of essential scientific tools to strategic programs at BNL and to neighboring universities. Interestingly, NSLS also draws the largest number of foreign users among the four facilities, representing about 16% of all NSLS users. The remaining 25% of NSLS users come from throughout the rest of the US.

A particularly pointed example of the regional importance of the NSLS is illustrated by the macromolecular crystallography community. As shown in Figure 1.3.4, the NSLS is geographically well positioned to provide resources to a large community of macromolecular crystallographers. One finds that there are about 175 principal investigators from this discipline in these northeastern states, representing 48 universities, 22 companies (mostly pharmaceuticals), and seven other research institutions (hospitals, NIH, etc). As described in a front-page New York Times article on December 30, 2002, the Northeast is “the nation’s health care epicenter... stretching from Boston to Bethesda, Md.” This regional transformation is reported to have provided the Northeast corridor with a crucial economic cushion during the recent downturn. The Northeast is the site of research facilities for most of the world’s major drug

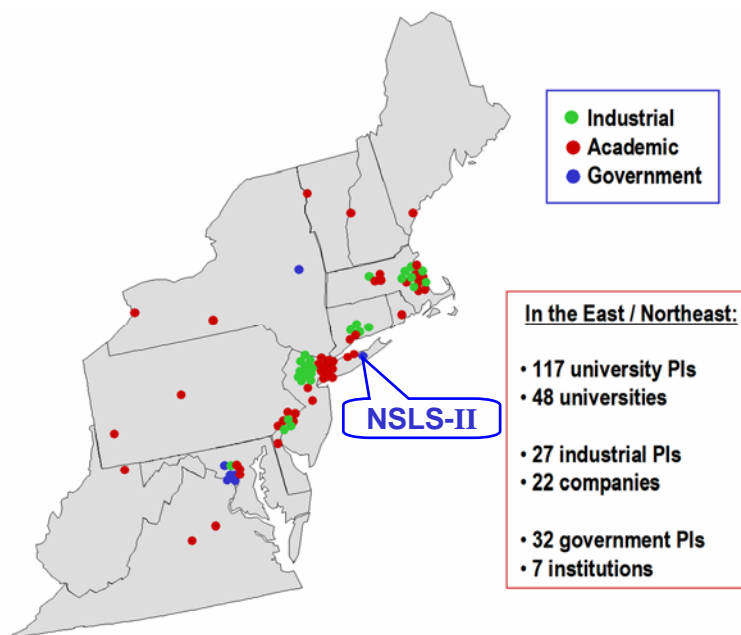


**Figure 1.3.4** Distribution of home institutions of the macromolecular crystallography user community of the NSLS.

<b>Days of Beam Use</b>	<b>SSRL 2001</b>	<b>CHESS 2001</b>	<b>NLSL 2000</b>	<b>ALS 2001</b>	<b>APS 2001</b>	<b>Row Sums</b>
Canada	3	6	31	0	26	66
Mexico	3	0	0	0	0	3
Midwest	79	0	67	4	366	516
Northeast	39	80	672	5	160	956
Northwest	13	0	124	24	4	165
Southeast	44	2	48	0	33	127
Southwest	34	0	16	1	8	59
<u>West</u>	<u>284</u>	<u>13</u>	<u>32</u>	<u>282</u>	<u>14</u>	<u>625</u>
<b>Totals</b>	<b>499</b>	<b>101</b>	<b>990</b>	<b>316</b>	<b>611</b>	<b>2517</b>

**Table 1.3.2** *Synchrotron usage and home institution location, 2000-2001. Taken from the 2002 BioSync Report.*

companies, a very high concentration of academic, government, and private research centers, and biotech companies, most of which are actively engaged in macromolecular crystallography. As part of the Northeastern “health epicenter”, NSLS-II will serve as a coalescence site for the biological and biochemical communities in this thriving geographical region.

Data regarding the way investigators tend to employ nearby synchrotron sources is collected in Table 1.3.2. The conclusion is clear: macromolecular crystallographers prefer, and in many cases find it necessary, to collect data close to home. This reduces travel costs and time spent and, importantly, is essential for some cutting-edge projects. The table also shows that in 2000-2001, ~40% of the days used for crystallographic data collection in the US were consumed by groups based in the Northeast. These needs were met largely by NSLS and CHESS, the two increasingly obsolete synchrotrons located in their area. The value of proximate and timely access is very clear to investigators in the region. As was pointed out recently by R. MacKinnon (Rockefeller University), the proximity with the NSLS, and the way this allowed frequent visits to optimize crystal preparation, was absolutely essential for the successful elucidation of the structure of the potassium channel, for which he won the 2003 Nobel Prize in Chemistry. The same sort of iteration argument was made clearly by the Steitz and Moore group (Yale University) a few years earlier concerning their work on the large 50S ribosomal subunit.

The availability of the NSLS to this large research community has dramatically enhanced its productivity. From 1995-2003, there were 4040 X-ray structure depositions to the Protein Data Bank (PDB) from US synchrotrons, of which 1300 came from the NSLS. In 2002 alone, one third of the 880 PDB depositions from US synchrotrons came from research performed at the NSLS. During the last four years, there has been roughly one new structure submitted to the Protein Data Bank *every working day of the year* from data measured at an NSLS beam line. Pharmaceuticals express their productivity in a different way: last year seven different companies, mostly from the Northeast, paid for 35 full days of beam time devoted to their proprietary work.

A similar regional need is increasingly being felt in the growing field of Nanoscience. A large number of current NSLS users are engaged in Nanoscience research and this number is expected to increase significantly in the coming decade. As shown in Figure 1.3.5, the Northeast is home to twenty-four major Nanoscience research centers, established by the National Science Foundation, other federal government agencies and various state governments. BNL is poised to be a focal point for much of this research, with the creation of the DOE funded Center for Functional Nanomaterials (CFN) at BNL. With current synchrotron sources, synchrotron radiation techniques are uniquely able to probe the structural, electronic, chemical, and magnetic state of materials on length scales of hundreds of nanometers. NSLS-II will extend the ability of these techniques to probe materials to length scales of 10 nm or less and will be increasingly essential for progress in all aspects of Nanoscience research. In anticipating this demand, several new beamlines and endstations are planned at the present NSLS in close collaboration with the CFN, including small angle X-ray scattering, micro-beam diffraction, and Low Energy Electron and

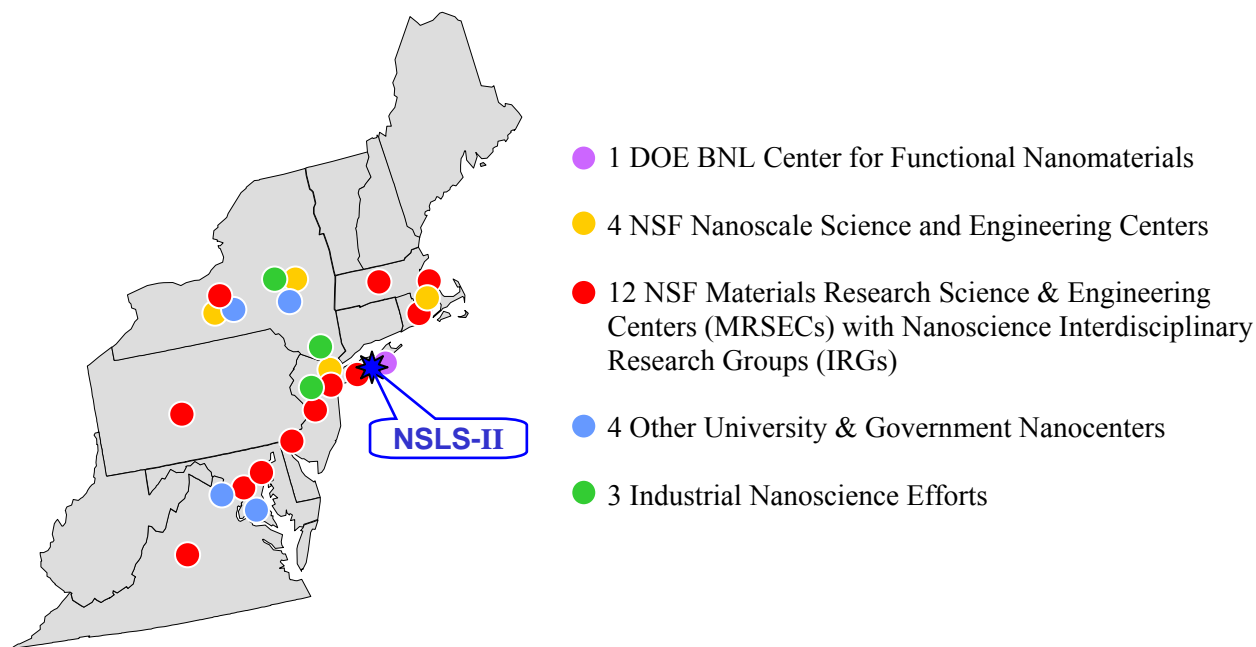


**Figure 1.3.5** *Distribution of home institutions of the Nanoscience user community of the NSLS.*

Photoelectron Microscope (LEEM/PEEM). The proximity and strong link between CFN and the NSLS also encourages collaborations among university, government, and industrial researchers.

Demand for synchrotron beamtime is expected to continue to grow across the range of disciplines displayed in Figure 1.3.1. Examples of this are everywhere. The demand for soft X-ray beamtime, particularly for scattering experiments, is expected to grow significantly in the future as resonant techniques are further developed. Advances in coherent scattering and magnetic scattering will also generate larger user communities, particularly in Nanoscience where such techniques will be the only ones capable of probing the electronic behavior with the appropriate resolution. Further, inelastic X-ray scattering techniques to be developed in the coming years will generate communities with the potential to be as active and large as the present angle resolved photoemission community. The soft X-ray undulator at the present NSLS is overwhelmed with proposals unable to satisfy even the existing demand, which even without growth of the community could take the capacity of three dedicated undulators. About 25% of synchrotron experiments in the life-sciences area are non-crystallographic, and this community continues to grow. The techniques that are new and whose value is just being realized, like time-resolved solution scattering, footprinting, and scattering from membranes, will become routine and more widely used as they become more mature. X-ray spectroscopy on transition metals in proteins is an exquisitely sharp tool for dissecting certain information from biological systems, and its popularity will remain strong. The number of user groups that use multiple imaging techniques at the NSLS is a rapidly growing user community, having approximately tripled in the past few years. With the broad spectral range available at the NSLS, the wide range of imaging tools can be combined easily to provide complementary information for sample characterization. This is a feature unique to the NSLS; no other facility in the world has such a wide wavelength range available for imaging. Since synchrotron-based imaging techniques are rather new, this complementarity is just being realized. NSLS-II will continue in this tradition. These are but a small subset of the many examples of increasing demand for not just synchrotron beamtime but also increased capabilities from synchrotron techniques.

Realizing the full potential of these many techniques and scientific collaborations, and enabling even more advanced techniques that are not possible today, requires more than just additional capacity or beamtime. What is critically needed, especially to tackle the most important and challenging problems, is a synchrotron source with greatly increased capabilities.

The capabilities of the present NSLS have been far surpassed by the other three DOE synchrotrons, which are either newer third-generation designs, such as the ALS and the APS, or have been upgraded to third generation capabilities, as at SSRL with its recent SPEAR3 upgrade. The NSLS contribution has continued to be significant in large part because of the sizeable community of Northeast researchers who depend on it. However, the restricted capabilities of the present NSLS are increasingly limiting the productivity and impact of its user community. For the scientific productivity of the large and formidable Northeast research community to continue and even increase, and to tackle the “grand challenge” problems of tomorrow, it is essential that the NSLS be upgraded to provide world leading brightness and higher flux. NSLS-II will accomplish this goal.

## 1.4 U.S. Scientific Work Force and Participation of Under-represented Minorities and Women

The construction of, and eventually the research performed at, a facility as complex and advanced as NSLS-II will be enhanced by the inclusion of scientists, scientists-in-training, engineers, and technicians from a variety of backgrounds. There will also be substantial training and research opportunities for students and post-doctoral researchers. A healthy exchange of scientific ideas and viewpoints will be fostered by participation of individuals of diverse age, gender, religion, national origin and social backgrounds. NSLS has been the training ground for many of the nations' synchrotron radiation engineers and technicians.

The DOE has a stated mission of providing a workforce of well qualified individuals who meet the specific needs for future scientists and engineers in key technology areas. An integral component of NSLS-II with its advanced technology will be the education of the next generation of U.S.-trained scientists, engineers, and technicians as the Laboratory fulfills this DOE mission. These goals will be accomplished with the assistance of programs administered by the BNL Diversity Office, in concert with similar programs at our collaborating universities.

### REFERENCES

- [1] G. Blumberg, P. Littlewood, A. Gozar, B. S. Dennis, N. Motoyama, H. Eisaki, and S. Uchida, *Science*, 297, 584 (2002).
- [2] P. Abbamonte et. al., unpublished data
- [3] T. Valla, P. D. Johnson, Z. Yusof, B. Wells, Q. Li, S. M. Loureiro, R. J. Cava, M. Mikamik, Y. Morik, M. Yoshimurak, and T. Sasakik, *Nature*, 417, 627 (2002).
- [4] W. E. Bailey, E. Vescovo, C. C. Kao, and D. A. Arena, unpublished results.

## 2 Science Opportunities

The proposed NSLS-II facility, a state-of-the-art medium-energy high brightness X-ray storage ring and a high brightness IR ring, will

- play a critical role in the success of DOE's Genomes-to-Life, NIH's structural genomics, and other major initiatives;
- provide a wide range of nanometer-resolution probes to meet the needs of the nation's rapidly growing nanoscience programs;
- alter dramatically the capability and variety of experimental probes of materials sciences, allowing access to new energy regimes and time-scales through inelastic and coherent scattering techniques;
- enable measurements with the high spatial, energy, and time resolution necessary to fully characterize new catalysts and to advance energy science;
- offer new insights into geophysical processes that determine the evolution of the Earth and planets;
- provide critical capabilities to study complex molecular-scale environmental processes, and to design remediation technology.

This Section outlines the outstanding scientific challenges and opportunities in the fields of Life Science, Nanoscience, Materials and Chemical Science, and Geoscience and Environmental Science and describes the impact that the superlative characteristics and combination of capabilities of NSLS-II will make in advancing research in them. The specific areas considered within each of these broad disciplines are:

- Life Science
  - Macromolecular Crystallography
  - Structure and Dynamics in Solutions and Membranes
  - Biological Imaging
- Nanoscience
- Materials and Chemical Science
  - Soft Matter and Biomaterials
  - Strongly Correlated Electron Systems
  - Magnetism
  - Growth and Processing of Advanced Materials
  - Catalysis and Energy Research
- Geoscience and Environmental Science
  - Earth and Planetary Science
  - Environmental Science

## 2.1 Macromolecular Crystallography

### 2.1.1 Overview

X-ray crystallography has transformed our understanding of biological processes. It was X-ray diffraction that provided the first clues to the structure of the DNA double helix 50 years ago, giving profound insights into how DNA is replicated. The reality that knowledge of biological structure imparts deep insights into the mechanism of action of molecules and assemblies [1,2,3,4,5], and the increasing difficulty in determining those structures as they get larger, has been one of the major driving forces in the continuing development of synchrotron radiation facilities world wide [6]. The Nobel Prizes in Chemistry awarded to Sir John Walker of the MRC in 1997 and to Professor Roderick MacKinnon of Rockefeller University in 2003 both depended on readily available synchrotron X-rays, and are proof of the crucial role synchrotron radiation facilities play in our understanding of the mechanisms of life.

The routine use of synchrotron radiation for single crystal diffraction studies has revolutionized macromolecular structural biology. With the availability of brighter X-ray sources, the size and complexity of macromolecules that can be studied has increased by an order of magnitude, or three orders of magnitude in mass (Figure 2.1.1). On the other hand, the size of the crystals that can be produced almost always decreases as the complexity of the macromolecule increases. The advancements observed for the past 15 years in the development of cloning, expression, purification, and crystallization methods have been impressive. However, crystals of the most complex structures that are suitable for diffraction are often scarce and difficult to obtain. Therefore, continuing advances in synchrotron radiation sources, detectors, and software are required to tackle the most challenging problems, which are the ones most likely to make a significant impact on our knowledge of the functioning of living systems [4].

The impact of synchrotron radiation on macromolecular crystallography must be regarded in the context of developments in molecular biology, cell biology, genomics, and bio-molecular crystallography. Crystallography is the dominant method for determining the three-dimensional atomic structure of any molecule. It is the only method for large and complex molecular structures. A current survey of the Protein Data Bank (PDB) shows that 69% of the structures deposited in 2002 were derived from synchrotron data (Figure 2.1.2). The US synchrotrons contributed over half of these, accounting for one third of all depositions. The source of this increasing role of synchrotron radiation is the large energy band width to help with phasing, the high collimation to resolve diffraction patterns from very large molecules, and the high overall intensity to make the measurements go quickly, even for small, weakly diffracting crystals. As a consequence, a larger and more diverse group of researchers are benefiting from diffraction studies at synchrotron light sources.

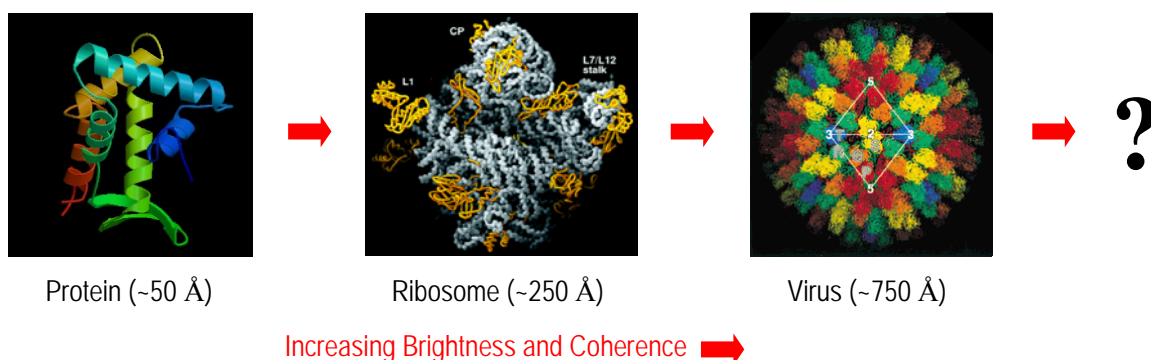


**Figure 2.1.1** *Molecular complexes and assemblies are the challenge of the 21<sup>st</sup> century [5]. Conventional macromolecular crystallography has benefited from nearly every improvement in synchrotron sources. The possibilities offered by increased brightness have driven researchers to attempt increasingly difficult scientific problems, especially structures of large asymmetric molecular assemblies, which is where the cutting edge of structural biology currently lies.*

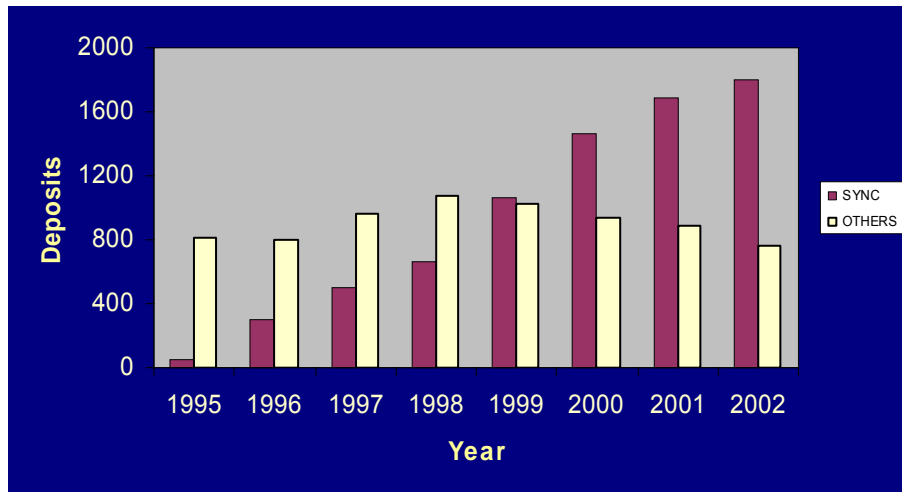


**Figure 2.1.2** Structures deposited in the Protein Data Bank originating from synchrotron radiation data and from other sources as of October 2003. Other sources include NMR and home sources. The use of synchrotron radiation has revolutionized structural biology and consequently allowed for an increased understanding of molecular functions.

The growing use of synchrotron sources for macromolecular crystallography has increased the pressure on existing facilities to upgrade existing, or construct new, sources and beamlines. This problem is particularly acute in the Northeastern United States, where aging synchrotron sources at Brookhaven National Laboratory and Cornell University find it increasingly difficult to meet the experimental demands of a large group of crystallographers working in this region. Quoting from the 2002 BioSync report: “Much of the growth in beam line number, quality and capability in recent years has occurred at the APS, ALS and SSRL, i.e. in the mid-west and the Bay area. While these developments are welcomed by all because of their positive impact on the nation’s scientific capabilities, they pose a significant logistical problem for investigators based on the east coast, who increasingly find themselves having to travel long distances to collect data hands-on at state-of-the-art beam lines.” This proposal to construct NSLS-II at Brookhaven National Laboratory is intended to respond to user pressure in the Northeast well into the future.

Biological and biomedical research has entered a new era, with an increasing emphasis on understanding the functional and physical connections between macromolecules. Integrative biology is a broad conceptual paradigm for discovery of how the molecular components of cells and tissues are connected in biochemical pathways, cellular responses, and functioning organs. Once the structures of these molecular components are known, deeper insights into specificity and mechanisms may be obtained similar to those achieved for individual enzymes and recognition proteins.

During the molecular biology era, structural biologists created an enduring legacy of atomic structures of many fundamental building blocks of the cell. Structural biology is now poised to make invaluable contributions to our understanding of integrated assemblies of interacting macromolecules. A taste of what is to come was unveiled recently with the structures of the ribosome and ribosomal subunits [3,4,5]; mitochondrial F1 ATPase [1] (Figure 2.1.3); both the eukaryotic and prokaryotic cytochrome c oxidases and b/c complex [9,10,11]; the potassium channel [2,12,13]; the HIV gp120 envelope protein complex with CD4 receptor and antibody [14]; the GroEL/GroES/ADP chaperone complex [15] and the eukaryotic and bacterial RNA polymerases [16].

The first step in the understanding of these multi-protein complexes will require direct structural analysis. These complexes are very difficult to express and to purify, especially in the quantities required for crystallization experiments. The major challenges in this work will be biochemical. The challenges will be not only to handle the large size and complexity of the assemblies, but also perhaps to trap unstable short-lived complexes that exist for only a few minutes in the cell. These might include signaling

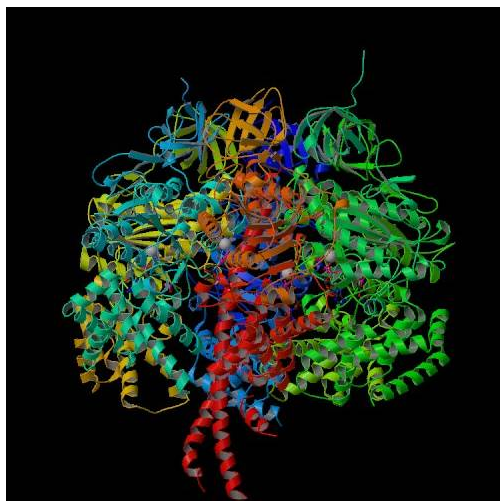


**Figure 2.1.3** *The 3D molecular structure determination of FIATPase was only possible through access to a synchrotron radiation facility [1]. Synchrotron radiation will play a crucial role in the determination of the molecular structure of complex assemblies, which is the major challenge for this century.*

complexes, where weak binary interactions contribute cooperatively to tight but often transient multi-component systems, and DNA replication, mediated by transient assemblies of polymerases, clamps, *etc.* If crystals can be obtained, they are often small and fragile, and require considerable optimization, guided by the results of diffraction experiments that can be achieved only with direct access to a bright source. Furthermore, they are difficult to stabilize for shipment, and diffraction from such crystals is generally weak, with successful data collection often requiring the intensity and fine collimation of a third-generation synchrotron source. *NSLS-II is needed to meet the needs of scientists who will accomplish this difficult work.*

## **2.1.2 Scientific Challenges and Opportunities**

### **2.1.2.1 Large Molecular Assemblies**

Several past successes in molecular structure determination of large complexes and assemblies are indicative of the critical role of high brilliance, high flux synchrotron sources in these studies. Early applications were the structure determination of virus particles, consisting of 180 or more proteins with a total mass of 8-9 Mdalton (including the RNA genome). These studies illustrated the difficulties in working with crystals of large complexes. Weak diffraction, close spacing of the reciprocal lattice, and radiation sensitive crystals, all conspired to make X-ray data collection possible only at synchrotron radiation sources. Recent successes with the determination of the structure of the core of much larger viruses, reovirus [17] and bluetongue virus [18], have shown the enormous potential of modern X-ray crystallography to reveal vast amounts of information. These and application of crystallography to large asymmetric complexes, the ribosome and the RNA polymerase transcription complexes being prime examples, were critically dependent on routine and frequent access to synchrotron radiation facilities.

The largest asymmetric molecular assembly whose atomic structure has been determined is the whole 70S ribosome [19] (Figure 2.1.4), consisting of nearly 100,000 atoms in 53 proteins and 3 chains of ribosomal RNA. In addition, this model also contains the three tRNA molecules bound to the A-, P-, and E-sites and a small piece of mRNA. The ribosome has two multi-protein/RNA subunits and is the site of protein synthesis. While the smaller, 30S subunit decodes messenger RNA, the large, 50S subunit catalyzes peptide bond synthesis. The model of the 70S ribosome has been constructed using the atomic

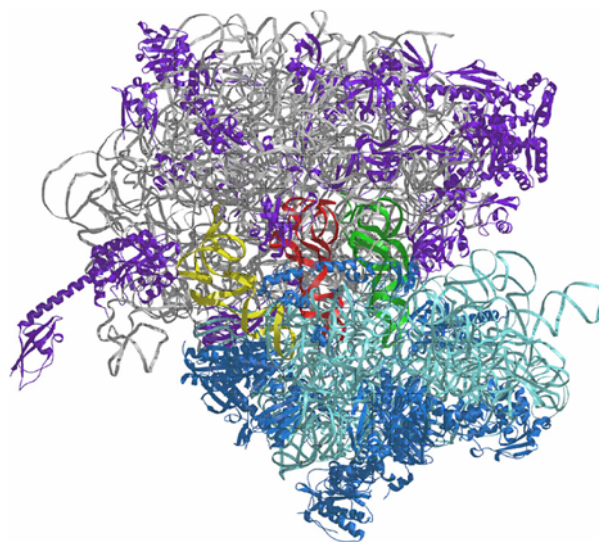


**Figure 2.1.4** View of the structure of the *T. thermophilus* 70S ribosome from the back of the 30S subunit; after Noller [19]. Structures like the 70S ribosome have relied both on synchrotron studies and cryo-electron microscopy results.

coordinates of the separate higher resolution structures of the large [3] and small subunits [4, 5], solved at 2.4 and 3.1 Å resolution, respectively and a 5.5 Å resolution electron density map of the whole ribosome. This was an amazing “tour de force” that would not be possible without constant sample optimization at a bright synchrotron source.

As is characteristic of all structural studies intended to illuminate biological function, the initial structure determination of the ribosomal components is only the beginning of structural studies of many complexes with substrates and antibiotics. Future structural studies will reveal the functional states of the ribosome during protein synthesis. The approximately dozen structures of the *Haloarcula marismortui* 50S ribosomal subunit complexed with various antibiotics (Figure 2.1.5.) are having a major impact on the design of new antibiotics that target the ribosome. These account for about one half of all antibiotics used clinically, and amount to tens of billions of dollars in sales per year.

Other large assemblies comprised of proteins and nucleic acids are continuously being identified and

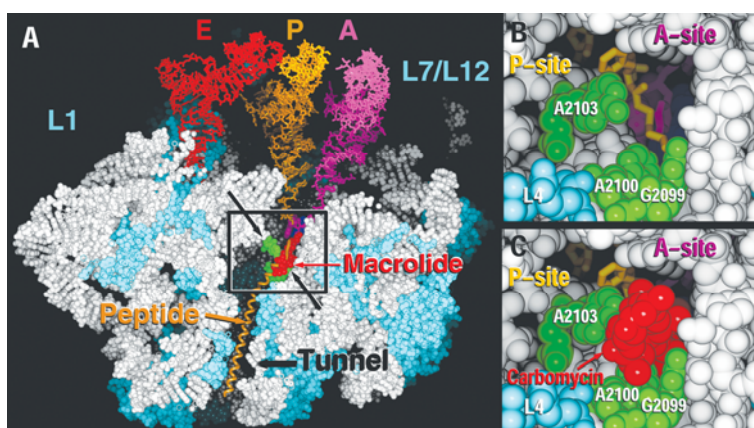


**Figure 2.1.5** The 50S ribosome: global view of the macrolide binding site for antibiotics showing how they block the peptide exit tunnel. A) The binding site for Macrolide antibiotics. B) and C) Close-up on the exit tunnel. The determination of the atomic molecular structure of large macromolecules have required years in the optimization of the crystallization process of the individual proteins and X-ray structure determination. High brightness sources can reduce significantly the time frame of such process.

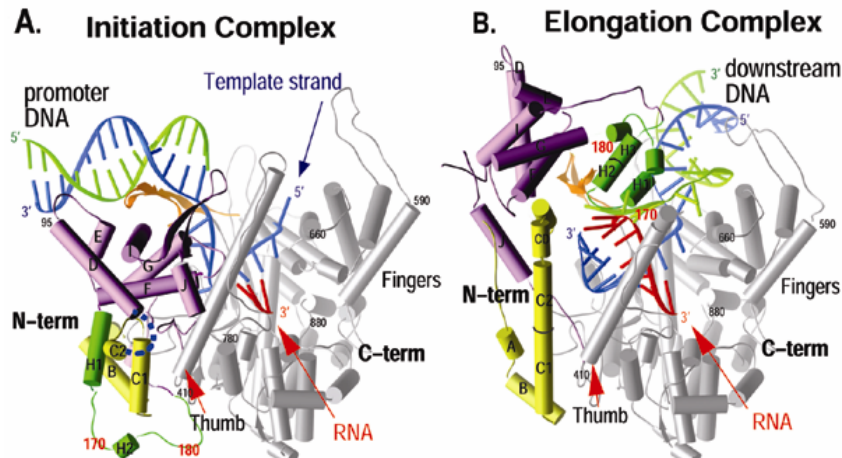


**Figure 2.1.6** Comparison of the structures of the T7 RNAP initiation and elongation complexes. The initiation complex (A) and elongation complex (B) have been orientated equivalently.

will be the target of high resolution crystallographic studies in the future. A recent landmark where synchrotron radiation played a crucial role is the structure elucidation of eukaryotic, prokaryotic, and viral RNA polymerase complexes in various stages of transcribing DNA into RNA [16, 20, 21]. The purification, crystallization, and subsequent structure determination of RNA polymerase II from yeast, a 12 subunit, relatively unstable complex, is the prime example of the type of molecular machinery that the field is now able to tackle given regular and frequent access to high-brightness sources [20].

Many structure determinations of RNA polymerases, caught while forming RNA transcripts, are required to provide a complete structural description of transcription. The four-subunit bacterial *Thermus aquaticus* enzyme [22] and the transcribing RNA polymerase from phage T7 provide a modest sized assembly of protein, DNA, and RNA for these studies. Numerous separately determined crystal structures for both the bacterial, yeast and T7 RNAP have been captured in various states of the process [21, 23]. The T7 RNAP structures, for example, show a dramatic alteration in the structure of T7 RNAP between the initiation phase of transcription and the elongation phase (Figure 2.1.6). Significant changes are also seen in the structure during the cycle of nucleotide incorporation. The establishment of structures that include not only the polymerase but large assemblies of transcription factors that carefully regulate this important basic cellular process, particularly in eukaryotic cells, is the next frontier in structural studies of in the field of transcription.

Presently, the large macromolecular complexes to be studied by X-ray crystallography are purified from naturally occurring sources. However, many biologically important complexes are not sufficiently abundant and/or stable to be purified from a natural source, and instead they will have to be produced by co-expression of all the components in an overproducing strain or by reconstitution *in vitro* from purified components. One example of this approach is an ongoing effort to crystallize the DNA replication complexes encoded by several model replication systems, including those from bacteriophage T7 and the Herpes Simplex Virus. Many of the protein components have been crystallized individually and their structures determined (Figure 2.1.7) [24]. However, the overall arrangement of proteins within any replication complex is unknown. The physical associations of these enzymes coordinate their activities within the complex to ensure efficient replication. Current efforts are directed toward forming stable, stalled replication complexes that can be crystallized. It is very likely that crystals of the resulting complexes will be weakly diffracting and require analysis at synchrotron radiation sources. Many of the individual enzymes in the complex are highly flexible and may further degrade the quality of diffraction that can be recorded. A high brilliance X-ray source will be essential to make progress with these challenging projects.

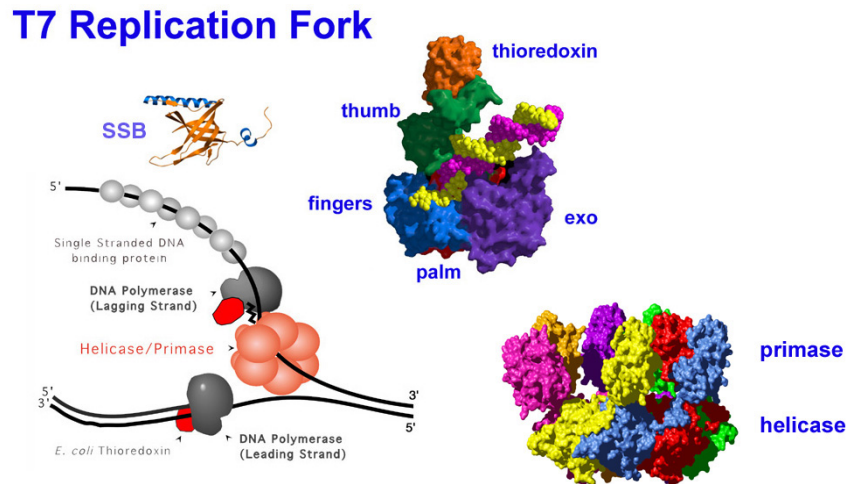


**Figure 2.1.7** DNA replication complexes: several individual protein components have been crystallized and structures determined yet the overall structure of any replication complex remains unknown. It is expected that weakly diffracting crystals from such complexes will require high brilliance synchrotron sources if any progress is to be made.

#### 2.1.2.2 Membrane Proteins

Membrane proteins are ubiquitous and essential to all living cells. They are found in eukaryotes and prokaryotes, as well as some viruses, and correspond to a sizable fraction of the entire genome. Membrane proteins are involved in every aspect of cellular function. Examples are the production of energy (e.g. the ATPase complex), the transmission of signals in nerve and muscle (e.g. the ion-channels), and cellular responses (e.g. the family of G-protein coupled receptors). Because of their ubiquity, membrane proteins are tempting targets within the pharmaceutical industry for the development of new therapeutics. Structural characterization of membrane proteins, notoriously known to be difficult to crystallize, can revolutionize our understanding of the molecular machinery of the cell.

The work on voltage-dependent  $K^+$  channel [2, 12, 13], just awarded the 2003 Nobel Prize in Chemistry, is a perfect example of the dramatic impact that structural studies of membrane proteins have in the understanding of cellular function<sup>1</sup>. Voltage-dependent cation channels open and allow ion conduction in response to changes in cell membrane voltage. Among other processes, these “life’s transistors” control electrical activity in nerve and muscle. The voltage-dependent  $K^+$ -channels are most often found as tetramers of molecules comprising six hydrophobic helical segments S1-S6, where (S5-S6)<sub>4</sub> forms the pore and defines the ion selectivity and S1-S4 forms the voltage sensors. In the conventional model (Figure 2.1.8a) the voltage-dependent gating charges on S4 are supposed to be driven through the protein core to open the channel. The S4 helices would lie in the interior of the protein secluded from the membrane.

MacKinnon’s structural work suggests a different model, that shown in Figure 2.1.8c wherein a tetramer of segments S5-S6 line the pore and S1-S4 form “voltage-sensor paddles” [2]. Obviously the disposition of these structural elements differs completely from the conventional model. The S4 with the S3 helices are found in the outer perimeter of the channel and most likely lie at the interface of the cytoplasmic side of the membrane. Functional studies of the gating mechanism reveal a movement of the voltage-sensor paddles by 20 Å across the lipid membrane (Figure 2.1.8d), and the travel of S4 would be associated to the S5-S6 segment in opening the pore.

<sup>1</sup> Note that the Nobel Prize in Chemistry was given also in 1988 for determination of the structure of a membrane-bound protein, and in 1997 for work that depended on another such structure.

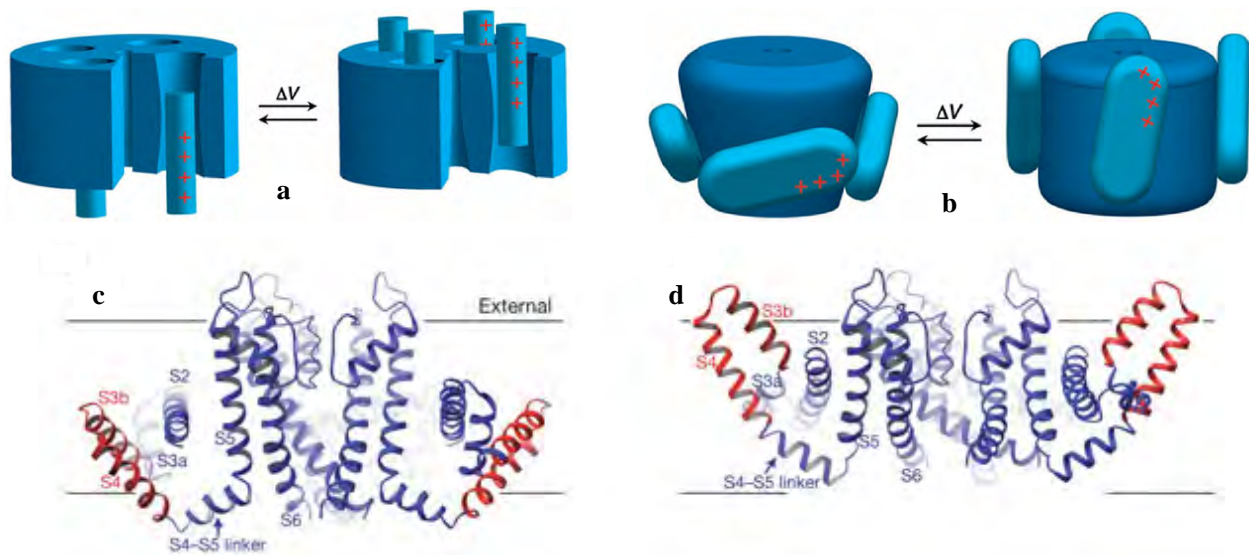


**Figure 2.1.8** Hypothesis for gating charge movements for voltage-dependent  $K^+$  channel. a) and b) The conventional and the newly proposed model for gating activation, c) and d) The structure of the channel with in red the voltage sensor paddles moving across the lipid membrane. Frequent access to synchrotron sources was essential to the insight gained to the function of the  $K^+$  channel [30].

The successful story of the voltage-dependent  $K^+$  channel also exemplifies some of the difficulties associated with membrane-protein structure determination. MacKinnon's group often explored expression of multiple members of this family of membrane proteins to obtain sufficient quantities. In most cases the channel aggregated during concentration and never crystallized. However, they were able to express and purify the  $K^+$  channel from *Aeropyrum pernix*, an extreme thermophile that remained unaggregated in a variety of detergents. Crystals of this channel could be grown, but only in the presence of a monoclonal Fab fragment that stabilized the voltage-sensor paddles. At that point the major limitation was that the crystals were often small, and of poorer quality than "soluble" protein crystals. Local access to an extremely bright source of X-rays was critical.

Our understanding of membrane proteins is far behind that of other proteins. Only a few dozen structures of such molecules are known, a small fraction of one percent of the total. The major limitation to membrane-protein structure determination is still difficulty in production of crystals. However, some of these problems may be overcome through molecular biology; new expression systems, advances in detergent biochemistry, and new crystallization approaches such as monoclonal Fab-mediated crystallization, increase success. Nonetheless, repeated examples show us, firstly, that the rewards for structure determination of membrane-bound proteins can be great, and secondly that this work depends strongly on frequent access to a bright X-ray source to provide the constant feedback between the synchrotron and the biochemistry lab that is essential.

### 2.1.2.3 Structural Genomics

The availability of complete genome sequences for many organisms stimulates the imagination of all biologists. Confronted with several tens of thousands of genes, nearly all coding for cellular proteins, a structural biologist may want to crystallize them all. That is not far from the motivation behind the different approaches to this lode of protein-sequence information, each being a facet of Structural Genomics. Certainly, since proteins are central to almost all aspects of biology and disease, Structural Genomics will have an impact on the way biological problems are addressed (Figure 2.1.9). A completely different goal might be to obtain a global view of the "protein structure universe" through the identification of the total protein-folding "space" (Figure 2.1.10).

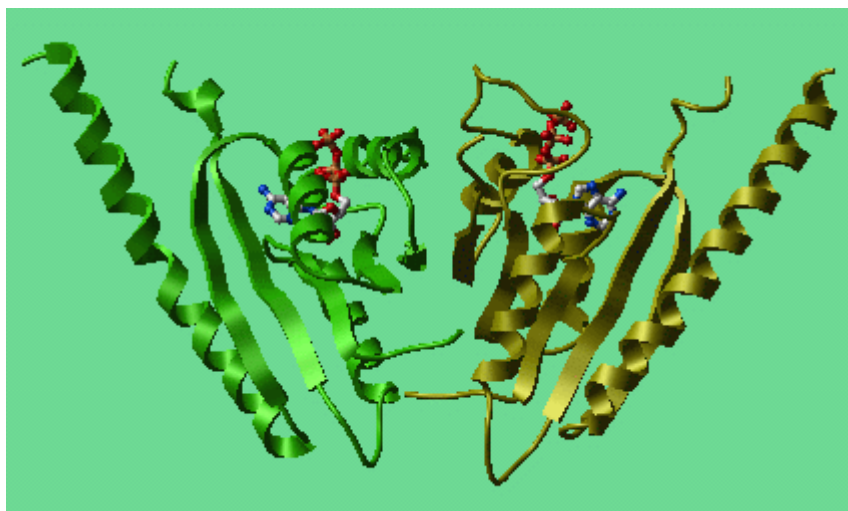


**Figure 2.1.9** *The three dimensional structure of protein MJ0577 from Methanococcus jannaschii revealed bound ATP, suggesting a putative function as an ATPase or an ATP-mediated molecular switch, thus giving functional insights to all members of this family of homologous proteins [25].*

The Protein Structure Initiative (PSI), a structural genomics program funded by the National Institutes of Health - National Institute of General Medical Sciences (NIH-NIGMS), aims ultimately to provide structural information for all proteins in all naturally occurring protein sequences using a combination of experiment and comparative protein structure modeling. The goal is to carry out a pan-genomic clustering of protein sequences and determine representative structures for each sequence family. Once sufficient structures have been determined by experiment, mostly synchrotron-based crystallography, it will be possible to calculate all the rest. Currently, the NIH-NIGMS is funding nine centers to conduct a five-year pilot study to examine the feasibility of this approach. Although the first cycle of funding is nearing an end, the NIH-NIGMS Council approved, in principle, the renewal of the funding program for a second five-year term.

Different approaches to target selection are being attempted. These range from a focus on only novel protein folds, to selecting all proteins encoded by the genome of a model organism. Other target-selection strategies are biologically based, including all members of an enzymatic pathway, every protein in a macromolecular complex, interacting partners of related proteins, or gene products that are either up- and

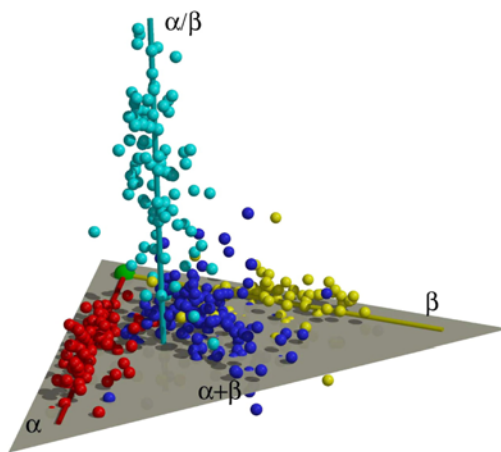


**Figure 2.1.10** *A representation of the protein fold space, condensed to only three dimensions. Each sphere represents a protein fold family [26]. The determination of the atomic structure of a protein will allow to understand and to predict functions of other members of the same family.*

down-regulated during a given biological process, or proteins of unknown function and structure that are important for microbial survival.

Even with a large scale structural determination effort, the goal of the PSI is to determine sufficient structures that other closely related proteins can be modeled. The accuracy of homology models decreases sharply below 30% amino acid sequence identity. This cutoff implies that structure determination of 16,000-32,000 new proteins will allow most proteins to be modeled from 90% of all protein structure families, including membrane proteins. Once this initial set of target structures is substantially complete, structural information (experimental and computational) will be available for many proteins found in nature. Thereafter, attention will turn to structural studies of engineered proteins of industrial and pharmaceutical importance, macromolecular complexes and assemblies, and protein-ligand complexes.

NSLS-II will play a major role during and after the production phase of the NIH-NIGMS-funded Protein-Structure Initiative. Two distinct experimental activities are anticipated: crystal screening and definitive structural determination. Crystal-growing is such that approximately 20 crystals are screened *per* target protein to identify the truncated and/or mutated form, and the cryo-preservation scheme, that yields the best diffraction. Each optimally productive undulator beam line has the capacity to examine approximately 250 to 500 crystals during each 24-hour day when equipped with bar-coded, automated, cryogenic sample changing and crystal centering. NSLS-II undulator beam lines dedicated to structural biology can be used to handle this load: crystals will be screened for quality; if quality is adequate, sufficient data to solve the structure will be measured and all results recorded in an experiment-tracking database.

#### 2.1.2.4 Drug Design

The development of new drugs in pharmaceutical companies has tended to be a rather linear process, from target identification to the selection of a drug candidate and compound optimization, with fixed criteria for passing to the next stage [27]. Although over the last twenty five years crystallographic studies have made significant contributions to the identification of a number of new ligands and inhibitors, targeting such major diseases as HIV infection (Figure 2.1.11), high blood pressure, and diabetes, X-ray crystallography has not yet realized its full potential as part of the drug-design process [28]. Mostly, current approaches to empirical screening and rational design benefit from fast high throughput methods developed for structural genomics initiatives, both for target selection and for structure determination.

Today virtually every large pharmaceutical company has a crystallography group, and many companies have one at each of their major research centers. Recognizing the need for rapid and frequent

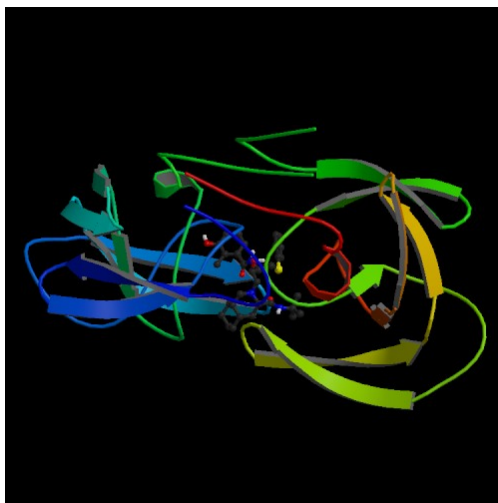


**Figure 2.1.11** *The structure of the HIV-1 protease, with a model of Viracept, a potent, orally bioavailable inhibitor, in the active site. This structure was published by workers at Agouron Pharmaceuticals [31].*

access to synchrotron radiation, twelve of these companies have for years operated their own beam line at the Advanced Photon Source, and several others companies have demonstrated an interest in other beam lines worldwide.

Crystallography as performed in the pharmaceutical industry is much like the structural studies carried out in academic laboratories, with some important differences [29]. A critical challenge faced by pharmaceutical crystallographers is that the macromolecules studied are very often human proteins, since the aim is to treat human diseases. Human proteins can be very difficult to work with, and the growth of large single crystals can be daunting. Another distinct feature of pharmaceutical crystallography is the time course. Only after the first structure is determined can one begin the cyclic sequence of structures typically used to hone the chemistry of the lead compound, hoping to generate the potency, solubility, and pharmacokinetic properties required of a drug. In this phase of the program, crystallographic feedback must be rapid and accurate. Synchrotron-based crystallography helps not only with optimization of crystallization methods, but also to solve new structures easily. The synergy between the needs for automation and high throughput within both pharmaceutical research and structural genomics is clear. Each can benefit from the other's automation developments in genomics, crystal formation, and X-ray data collection. The development of convenient access to efficient synchrotron facilities is central to both efforts.

An interesting development is the emergence of a large number of start-up biotech companies that fulfill at least initially a particular niche in the drug-design process. Focused on a small, special biochemical feature these small biotechs usually have fewer resources than the large companies, and rely mainly on general-user time or on collaborations with the synchrotron facilities for their crystallographic needs. An example of such a start-up is Rib-X Pharmaceuticals, Inc. who is using the structure of the 50S ribosomal subunit for the development of new antibiotics. Especially in the case of an enterprise like Rib-X, access to a bright synchrotron is a must if for any sort of progress at all. The NSLS-II should be a magnet for small ventures like Rib-X.

### 2.1.3 Impact of NSLS-II

The NSLS has played a major role in the advancement of macromolecular crystallography in the US but there is a critical need to improve the capabilities of the NSLS for macromolecular crystallography. Knowing the time course of construction of high brightness macromolecular crystallography beam lines is one way to put this in perspective. Table 2.1.1 shows the commissioning dates of U.S. high brightness beam lines in chronological order; this expression of the nation's *capacity* of such beam lines might shed light on the *needs* for expansion. An original five beam lines available by 1997 was followed by thirteen more during the seven-year interval 1997-2003 (at a steady pace of about two per year). Looking ahead, eight or so beam lines now under construction (mostly at the APS, one at the NSLS, and one at the SSRL) will be commissioned during the next five years, a pace of about two beam lines per year. By 2008, about twenty-six high brightness beam lines will be in operation nationwide. Half of the nationwide brightest beam lines, of the kind that will be available at NSLS-II, will be at the APS. Just two high brightness beam lines will be in operation at the NSLS then, neither of which with exceptionally high brightness of the kind that is associated with the APS and NSLS-II undulator beam lines.

Beyond 2008, the prospect for further expansion of capacity of exceptionally high brightness beam lines is dismal. At present, just four sectors remain to be formally assigned at the APS. It seems possible, because of interest that has been expressed from other disciplines, that in the end none may be developed for macromolecular crystallography. If this is true, no further expansion of such beam lines nationwide is envisioned beyond 2008. If the need for high-brightness beam lines follows the linear slope that has been observed, these beam lines will be oversubscribed, nationwide, after this date. To make things worse, still only two moderately high brightness beam lines will be in operation at NSLS. The situation will be grim for Northeastern structural biologists. The availability of a number of beam lines at NSLS-II, perhaps in a staged expansion, would alleviate this situation, particularly for Northeast users. It goes without saying

<u>Beamline</u>	<u>Device</u>	<u>Commissioned</u>
CHESS A1	wiggler	before 1997
CHESS F1	wiggler	before 1997
CHESS F2	wiggler	before 1997
NLSL X25	wiggler	before 1997
SSRL 7-1	wiggler	before 1997
APS 19-ID	undulator	1997
SSRL 9-1	wiggler	1997
ALS 5.0.2	wiggler	1998
APS 17-ID	undulator	1998
APS 5-ID	undulator	1999
APS 14-ID	wiggler	1999
SSRL 9-2	wiggler	1999
ALS 5.0.1	wiggler	2000
APS 32-ID	undulator	2000
ALS 5.0.3	wiggler	2001
SSRL 11-1	wiggler	2001
APS 22-ID	undulator	2002
APS 31-ID	undulator	2003

**Table 2.1.1** *Insertion device beamlines dedicated to macromolecular crystallography in operation in the US. A beamline is considered commissioned for macromolecular crystallography upon the first PDB deposition of a structure resulting from data collected at the beamline.*

that many of the experiments would benefit greatly from the fact that the brightness of NSLS-II will surpass existing NSLS beam lines by a huge factor.

The future impact of NSLS-II can be assessed in terms of the science that its user community will be able to explore. The high brightness of NSLS-II will foster research in:

- *Molecular Complexes and Machines*: crystals are small and weakly diffracting, large unit cells are not uncommon. Molecular structure determination will be possible from crystals 20  $\mu\text{m}$  or smaller.
- *Structural Genomics and Proteomics*: high throughput crystal screening through improved automation will allow the assessment of crystal quality even of small crystals for molecular structure determination.
- *Drug Design*: fast screening for new drug candidates in pace with medicinal chemistry will allow the rational design of drugs to fight diseases.
- *Novel techniques*: novel applications to structure determination from 2D crystals and development of new approaches to molecular structure determination.

NSLS-II will impact the user community:

- *Increased availability*: the US capacity of high brightness beam lines will increase significantly.
- *Demand*: an increase in the number of beam lines dedicated to structural biology will allow for dedicated beam time for difficult problems such as the study of large assemblies and high throughput.
- *Diversity of techniques*: macromolecular crystallography will not be the only method available at the NSLS-II to study biological interesting molecules. Other methods will allow biochemist and molecular biologist to gather information on the tertiary and quaternary molecular structures, study molecular kinetics and dynamics.

- *Location*: the geographical location will affect directly all researchers in the Northeast of the United States. These researchers in the academic, government, and pharmaceutical environments can also benefit from other facilities such as cryo-electron microscopy, nuclear magnetic resonance (NMR) and mass spectrometry, at Brookhaven and SUNY Stony Brook.

NSLS-II will become integrated to biological communities that will explore techniques and methods to advance the understanding of the mechanisms of life.

## REFERENCES

- [1] J. P. Abrahams, A. G. W. Leslie, R. Lutter, and J. E. Walker, "Structure at 2.8 Å resolution of F<sub>1</sub>-ATPase from bovine heart mitochondria", *Nature* 370, 621-628 (1994)
- [2] Y. Zhou, J. Morais-Cabral, A. Kaufman, R. MacKinnon, "Chemistry of ion coordination and hydration revealed by a K<sup>+</sup> channel-Fab complex at 2.0 Å resolution", *Nature* 414, 43-48 (2001)
- [3] N. Ban, P. Nissen, J. Hansen, P. Moore, T. Steitz. "The complete atomic structure of the large ribosomal subunit at 2.4 Å resolution" *Science* 289, 905-920 (2000)
- [4] B. Wimberly, D. Brodersen, W. Clemons, A. Carter, R. Morgan-Warren, C. Vonrhein, T. Hartsch, V. Ramakrishnan, "Structure of the 30S ribosomal subunit", *Nature* 407, 327-339 (2000)
- [5] Bashan, H. Bartels, I. Agmon, F. Franceschi, A. Yonath, "Structure of functionally activated small ribosomal subunit at 3.3 angstroms resolution" *Cell* 102, 615-23 (2000)
- [6] W.A. Hendrickson, "Synchrotron Crystallography," *Trends Biochem. Sci.* 12, 637-643 (2000)
- [7] S.S. Hassain, J. R. Helliwell and H. Kamitsubo, "Synchrotron radiation and structural biology", *J. Synchrotron Rad.* 6, 809-811 (1999)
- [8] Genomes to Life web site: <http://doegenomestolife.org/>
- [9] T. Tsukihara, H. Aoyama, E. Yamashita, T. Tomizaki, H. Yamaguchi, K. Shinzawa-Itoh, R. Nakashima, R. Yaono, S. Yoshikawa, "Structures of metal sites of oxidized bovine heart cytochrome c oxidase at 2.8 Å", *Science* 269 1063-1064 (1995)
- [10] S. Iwata, J. W. Lee, K. Okada, J. K. Lee, M. Iwata, B. Rasmussen, T. A. Link, S. Ramaswamy, B. K. Jap, "Complete structure of the 11-subunit bovine mitochondrial cytochrome bc<sub>1</sub> complex", *Science* 281, 64-71(1998)
- [11] D. Xia, C. A. Yu, H. Kim, J. Z. Xia, A. M. Kachurin, L. Zhang, L. Yu, J. Deisenhofer, "Crystal structure of the cytochrome bc<sub>1</sub> complex from bovine heart mitochondria", *Science* 277, 60-66 (1997)
- [12] Y. Jiang, A. Lee, J. Chen, M. Cadene, B. Chait, R. MacKinnon, "Crystal structure and mechanism of a calcium-gated potassium channel", *Nature* 417, 515-522 (2002)
- [13] J. Jiang, A. Lee, J. Chen, V. Ruta, M. Cadene, B. Chait, R. MacKinnon, "X-ray structure of a voltage-dependent K<sup>+</sup> channel", *Nature* 423, 33-41 (2003)
- [14] P. Kwong, R. Wyatt, J. Robinson, R. Sweet, J. Sodroski, W. Hendrickson, "Structure of an HIV gp120 envelope glycoprotein in complex with the CD4 receptor and a neutralizing human antibody" *Nature* 393, 648-659 (1998)
- [15] Z. Xu, A. Horwich, P. Sigler, "The crystal structure of the asymmetric GroEL-GroES-(ADP)<sub>7</sub> chaperonin complex" *Nature* 388, 741-750 (1997)
- [16] K. Murakami, S. Masuda, E. Campbell, O. Muzzin, S. Darse "Structural basis of transcription initiation: An RNA polymerase holoenzyme/DNA complex" *Science* 296, 1285-1290 (2002)
- [17] K. M. Reinisch, M. L. Nilbert and S. C. Harrison, "Structure of the reovirus core at 3.6 angstroms resolution", *Nature* 404, 960 (2000)
- [18] J. M. Grimes, J. N. Burroughs, P. Gouet, J. M. Diprose, R. Malby, S. Zientara, P. P. Mertens, D. L. Stuart, "The atomic structure of the bluetongue virus core", *Nature* 395, 470 (1998)
- [19] M.M. Yusupov, G. Zh. Yusupova, A. Baucom, K. Lieberman, T.N. Earnest, J.H.D. Cate and H.F. Noller, "Crystal structure of the ribosome at 5.5 Å resolution" *Science* 292, 883-896 (2000)

- [20] P. Cramer, D. A. Bushnell, R. D. Kornberg, "Structural Basis of Transcription: RNA Polymerase II at 2.8 Ångstrom Resolution" *Science* 292, 1863-1876 (2001)
- [21] G. M. T. Cheetham, and T. A. Steitz, "Structure of a transcribing T7 RNA polymerase initiation complex", *Science* 286, 2305-2309 (1999)
- [22] Y. Kim, S. H. Eom, J. Wang, D. S. Lee, S. W. Suh, T. A. Steitz, "Crystal structure of *Thermus aquaticus* DNA polymerase", *Nature* 376, 612-6 (1995)
- [23] P. Cramer, D. A. Bushnell, R. D. Kornberg, "Structural Basis of Transcription: RNA Polymerase II at 2.8 Ångstrom Resolution", *Science* 292, 1863-1876 (2001)
- [24] S. Doublé, S. Tabor, A. Long, C. C. Richardson, T. Ellenberger, "Crystal Structure of a Bacteriophage T7 DNA Replication Complex at 2.2 Ångstrom Resolution", *Nature* 391, 251-258(1998)
- [25] T. I. Zarembinski, L. W. Hung, H. J. Mueller-Dieckmann, K. K. Kim, H. Yokota, R. Kim, S. H. Kim, "Structure-based assignment of the biochemical function of a hypothetical protein: a test case of structural genomics", *Proc. Natl. Acad. Sci.* 95, 15189-15193 (1998)
- [26] J. Hou, G. E. Sims, C. Zhang and S-H. Kim, "A global representation of the protein fold space", *PNAS* 100 2386-2390 (2003)
- [27] R. Pauptit, "Drug design: trends and strategies", *From Genes to Drugs via Crystallography*, 33<sup>rd</sup> crystallography course at the E. Majorana Center, Erice, Italy, 45-54(2002)
- [28] Scharff and H. Jhoti, "High-throughput crystallography to enhance drug discovery", *Curr. Opin. Chem. Biol* 6, 704-710 (2003)
- [29] P. Fitzgerald, private communication.
- [30] R. MacKinnon private communication
- [31] Kaldor, S. W., Kalish, V. J., Davies 2nd, . 2., Shetty, B. V., Fritz, J. E., Appelt, K., Burgess, J. A., Campanale, K. M., Chirgadze, N. Y., Clawson, D. K., Dressman, B. A., Hatch, S. D., Khalil, D. A., Kosa, M. B., Lubbehusen, P. P., Muesing, M. A., Patick, A. K., Reich, S. H., Su, K. S., Tatlock, J. H.: Viracept (nelfinavir mesylate, AG1343): a potent, orally bioavailable inhibitor of HIV-1 protease. *J Med Chem* 40 pp. 3979 (1997).
- [32] [http://biosync.sdsc.edu/BioSync\\_Report\\_2002.pdf](http://biosync.sdsc.edu/BioSync_Report_2002.pdf)

## **2.2 Structure and Dynamics in Solutions and Membranes**

### **2.2.1 Overview**

Macromolecular crystallography has been enormously successful in elucidating the structure of proteins and other biomolecules. An increasingly complete collection of atomic resolution protein structures is becoming available, and a growing catalog of cellular assemblies has been identified. These data are being combined with emerging genetic and biochemical information on pathways to suggest temporal, spatial, and functional relations controlling cellular function.

However, the central question in biophysics still remains: What is the connection between structure and function of biological macromolecules such as protein, DNA, RNA, polysaccharides, and their complexes? Answering this question requires understanding the dynamics of macromolecular structures in their natural environment, where flexibility of the molecules and water, pH, and ion concentration play determinant roles. Examples include protein and nucleic acid folding and unfolding, multimeric association and disassociation, polymer collapse upon change of solvent, ligand binding and unbinding, receptor binding, force generation, electron transfer, phosphorylation events and large-scale fluctuations in macromolecules.

Studies of the structure and dynamics of molecules in solutions and membranes are an essential complement to macromolecular crystallography. Such studies are poised to provide new insights into the function, control, and dynamics of individual macromolecules and large molecular complexes. Solutions and membranes are the media where many of the most intriguing and complex biological processes take place, including molecular recognition, signal transduction, chemical sensing, transport, synthesis, degradation, replication, and defense.

Techniques such as solution scattering, spectroscopy, and footprinting provide valuable information regarding how biomolecules and molecular machines function. Time resolved X-ray studies of biomolecules in solution have evolved so that with present synchrotron sources, scattering studies at millisecond time resolution are feasible in favorable cases.

The high brightness of NSLS-II will give X-ray scattering and spectroscopy studies of biomolecules and membranes unparalleled sensitivity and time resolution, enabling more precise structure determinations and extending measurements of dynamics down to the microsecond time range.

### **2.2.2 Scientific Challenges and Opportunities**

#### **2.2.2.1 Protein Folding**

Understanding protein folding, i.e. how a protein achieves its stable functional three-dimensional structure from a linear string of amino acids, is a key to understanding how the protein performs its biological functions. Time resolved solution scattering now allows researchers to follow the structural changes of the protein as folding proceeds.

The time scale that is characteristic of the folding process varies from picoseconds to nanoseconds, when the initial secondary structure starts to form, to milliseconds to seconds, when the folding process is completed. With the development of more accurate force fields that simulate the interactions that govern the folding process, and construction of more powerful computers (e.g. the Blue Gene project [1]), computational biologists are lengthening their calculations to the time scale of microseconds [2]. The high brightness of NSLS-II will extend the time resolution of solution-scattering measurements down to this time scale. Computations and experiments will then overlap and provide better tests of our understanding of the physics of the underlying interactions. Combined with complementary methods, especially NMR, solution scattering and computer simulation will provide a complete time course for how proteins fold.

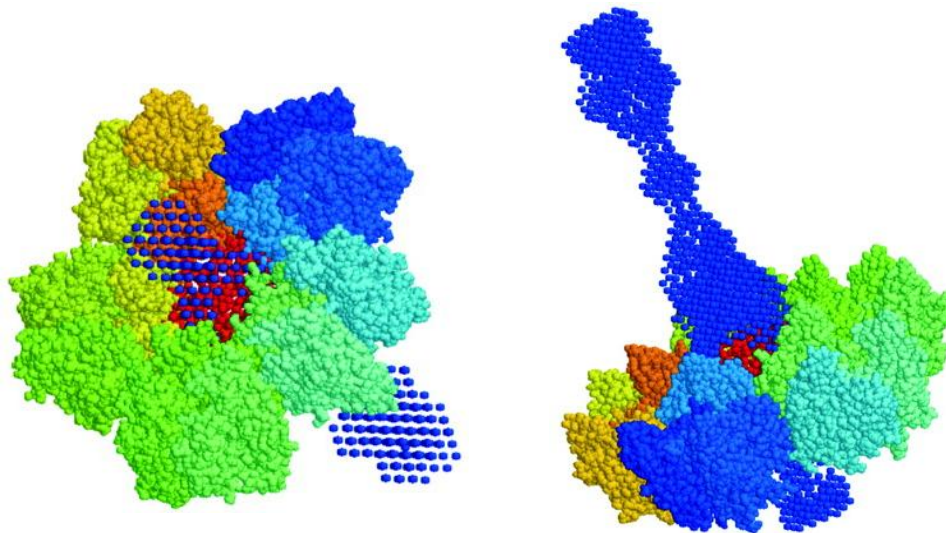


**Figure 2.2.1** *Low-resolution structural model of the bacteriophage PRD1 vertex complex restored from solution scattering data [5], viewed from different angles. Both the structures of the individual components and the overall structure of the complex are obtained from analysis of solution scattering data.*

### 2.2.2.2 Structural Kinetics in Biological Macromolecular Complexes

High-resolution methods, both X-ray crystallography and NMR, have difficulties dealing with macromolecular complexes, where changes in shape may accompany the biological function that is under study. These structures are difficult to crystallize and are too large for NMR studies. Also, even if the complex does crystallize, the crystal structure may be misleading because shape changes are constrained.

In contrast, small angle solution scattering can provide structural information that reveals global conformation changes in biomolecules and molecular complexes in solution, and is thus complementary to protein crystallography. Traditionally used to characterize the radii of gyration and the folding states of proteins in solution, newly developed shape-reconstruction algorithms [3, 4] have transformed solution scattering into an effective technique for determining the low-resolution, basic shape of these complexes [5] (Figure 2.2.1). This approach also holds great potential for resolving the structural kinetics of macromolecular complexes using time resolved solution scattering to produce low-resolution movies of events such as the assembly and operation of molecular machines.

The idea behind these methods is that although the molecules in solution are randomly oriented, and much of the structural information is lost in the isotropic average, some information that is characteristic of the shape envelope of the biomolecules remains in the measured one-dimensional scattering curve. In many cases the subunits that make up a protein complex are rigid and their atomic structures are known. Solution scattering provides a useful tool for putting the pieces of this puzzle together to reveal the functional structure of the protein complex. Because knowing the shape of components reduces the degrees of freedom in the model, overall shape determination becomes much simpler and more reliable. This may suffice to define a low-resolution shape envelope. This low-resolution structure information is often invaluable, especially when combined with other experimental evidence. The low-resolution structures obtained also can be used to help determine phases in the analysis of crystallographic data [6].

These shape-determination algorithms operate by iterative modification and evaluation of a model against experimental data with a pre-defined penalty function. As with all optimization problems, quick convergence to an unambiguous solution depends not only on the selection of the model and the optimization algorithm, but also on the quality of the data. Data quality can be especially important for solution scattering since the scattering signal is weak in general, and varies by two to four orders of magnitude within the interesting  $q$  range.

The high brightness of NSLS-II will provide high intensity, highly collimated, and small X-ray beams for SAXS measurements, resulting in high quality data necessary for accurate shape determinations. Together with the flow-cell mixers discussed in Section 2.2.3.1 and fast detectors, NSLS-II will also enable time resolved measurements at microsecond time resolution to become routinely achievable.

### 2.2.2.2 Extension of Solution Scattering to Membrane Proteins

By analogy to protein solution scattering, non-crystalline membrane structures can also be studied with X-ray scattering. Under native conditions, individual membrane protein molecules, and supra-molecular structures such as self-assemblies of membrane-active antimicrobial peptides, diffuse within the confinement of the lipid bilayer. This is much like a two dimensional (2D) liquid, and can be investigated with SAXS by probing the in-plane correlations. Neutron scattering studies on these 2D liquids already exist [7], owing to the use of deuterated components that enhance the contrast in the sample (Figure 2.2.2). X-ray studies have so far been limited to nearly crystalline systems [8] and studies of multiple-layers.

All of the solution scattering techniques used for proteins are equally applicable to the 2D liquid of membrane proteins, including low-resolution shape determination and time resolved measurement. They have the similar advantage that one isn't limited in the quantity of the specimen one can get in the X-ray beam by the size of a crystal. In particular, in the case of the 2D membrane, a glancing-angle beam might illuminate a patch of several square millimeters to produce a significant scattering signal. Just as solution scattering can provide shape and kinetic information to complement protein crystallography, X-ray scattering from single-layered membranes will provide the opportunity to study the structure transitions within membranes.

The high brightness of NSLS-II will enable solution scattering experiments to provide information about these structural transitions, such as the conformation change of receptors upon binding of a ligand. These phenomena are related directly to the function of the membrane proteins, and therefore are central to many branches of life-science research.

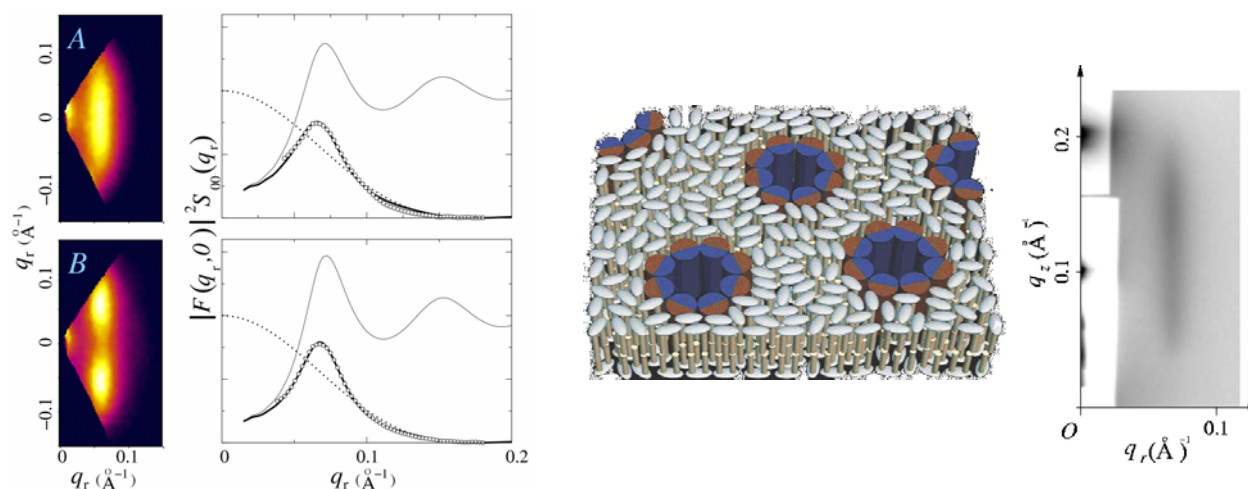


**Figure 2.2.2** Scattering from a two-dimensional liquid of membrane pores formed by antimicrobial peptides (model shown in the middle). Owing to the contrast enhanced by deuteration, neutron scattering can easily detect these structure in multiple-layered model membranes (left), whereas only much more ordered liquids were observed by X-rays (right). The increased beam intensity of NSLS-II will make up for the contrast disadvantage of X-ray scattering. Observation of fluid membrane structure will be possible, even in single-layered membranes.

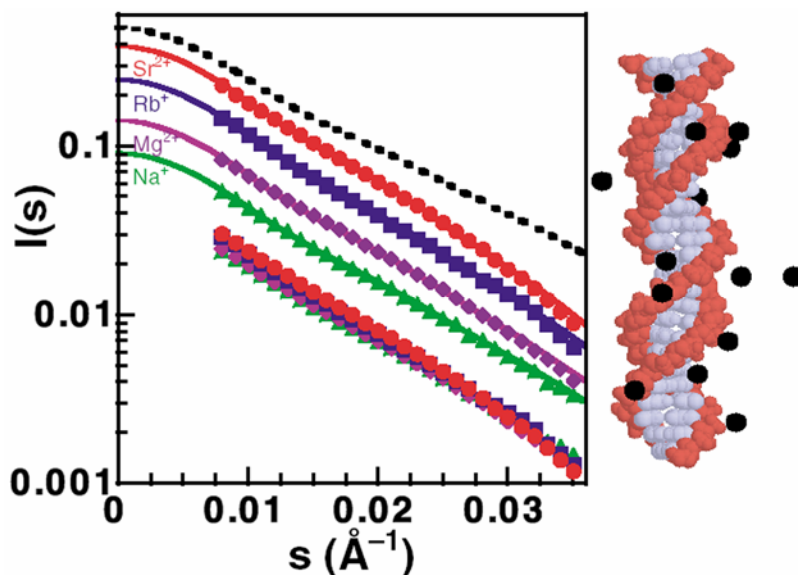


**Figure 2.2.3** Monovalent and divalent counterion clouds around negatively charged DNA double helices in solution are probed using anomalous small-angle x-ray scattering [9]. The spatial correlation of surrounding counterions to DNA was directly measured.

### 2.2.2.3 Counterion Cloud

In their native environment biomolecules are surrounded by water and ions. It has long been recognized that the availability of water and ions is an important factor in protein structure and function but little is known about the structure of “ordered” water and the distribution of counterions around biomolecules. By using synchrotron radiation it is possible to specifically probe the counterion cloud by anomalous scattering while keeping the biomolecules in solution. Multivalent ions are particularly interesting because they are present at much lower concentrations in biology and are often used to trigger biological events, such as opening or closing a channel or enzyme activation. Multi-valent ions are also responsible for DNA condensation inside the cell nucleus, in sperm heads and virus capsids. Recent efforts to employ solution anomalous X-ray scattering techniques to address such questions had to resort to exotic ions such as  $\text{Rb}^+$  and  $\text{Sr}^{2+}$  with K edges of 15.2 keV and 16.1 keV [9] (Figure 2.2.3).

The high brightness of NSLS-II in the 1 to 4 keV energy range makes it very well suited to use anomalous scattering techniques on biologically relevant ions such as Na (1.07 keV), Mg (1.3 keV), Cl (2.8 keV), K (3.6 keV), Ca (4.0 keV), S (2.5 keV) and P (2.1 keV). Because biological materials including water absorb strongly at these low energies high photon flux is essential and this high flux must be in a small spot to use flow-cell mixers to follow triggered events in time resolved experiments.

### 2.2.2.4 Study of Metalloproteins with X-ray Absorption Spectroscopy

X-ray absorption spectroscopy (XAS) can be used to measure the transition of core electronic states of a metal atom to excited electronic states or continuum states. Spectral analysis near the electronic transition, so-called X-ray absorption near-edge structure, or XANES, provides information on the metal’s charge state and geometry. Spectral analysis above the absorption edge (from the edge to 10-15% above the edge in energy), so called Extended X-ray Absorption Fine Structure, or EXAFS, provides complementary structural information, such as numbers, types, and distances of ligands or neighboring atoms. Both spectroscopies are valuable techniques for studying a variety of metal sites in biological systems [10]. Recent experiments where X-ray crystallography and X-ray spectroscopy are used in combination have provided information that was not available from either technique alone [11].

Traditionally, XAS, like most other spectroscopies, has been used as a static probe of structure. NSLS-II provides the opportunity to extend X-ray absorption measurements into the time resolved realm, potentially revolutionizing the study of biochemical and bioinorganic systems. The importance of real-time structural information for mechanistic studies is apparent, and has led to a blossoming of interest in time resolved XAS. Although hundreds of papers have been published on time resolved XAS, until now these have focused mostly on questions of materials-science and catalysis. This is because the best method for measuring time resolved XAS is to use a “dispersive” geometry, in which a polychromatic X-ray beam is focused onto the sample of interest. Unfortunately, the dispersive geometry is limited to relatively high metal concentrations (> 10 mM for modest time resolution; higher for ms time resolution) and is thus not practical for most biological samples.

To study dilute samples such as metalloproteins, one must measure the data as fluorescence excitation spectra. For slow reactions occurring over several hours, time resolved XAS was used as early as 1995 in a study of reaction of the enzyme carboxypeptidase [12]. With recent advances in rapid-scanning monochromators, it has proven possible to measure XAS spectra with scan times as short as 50 ms [13], although typical scan times are several seconds [14]. NSLS-II will allow much faster time scales to be probed.

Since the biomolecular system being studied evolves continuously during the reaction, with many different species potentially being present, one cannot take a literal “snapshot” of intermediates that form. However, use of sophisticated mathematical approaches such as principal-component analysis [15], allows one to come close to this ideal. Combining the information from tens or hundreds spectra, each measured at a different time after mixing, makes it possible for one to deconvolve the component spectra, even for relatively minor components. With the bright X-ray beams provided by NSLS-II, the continuous flow mixing technology discussed above will enable time resolution close to one microsecond.

### 2.2.2.5 Electron Delocalization in Biomolecules

The wave nature of the electron determines almost all of the properties of simple condensed matter, for example its color, mechanical hardness, electrical resistivity, thermal conductivity, thermal expansion, dielectric constant, melting and boiling points, etc. It is therefore worth investigating the degree to which delocalization underlies protein function, since proteins are, after all, a form of condensed matter. NSLS-II will enable a new class of such phenomena to be studied for the first time.

As an example, consider the light harvesting complex (LHC) protein-chromophore (Figure 2.2.4) of the photosynthetic bacterium *rhodospira rubra*. Light is first absorbed by a circular aggregate of bacteriochlorophyll molecules and carotenoids held together by proteins, LH-II. Energy is then transferred to a circular antenna complex, LH-I, surrounding the reaction center, and finally to the reaction center (RC) where it starts the respiratory cycle of the cell. The structures of LH-II and RC are

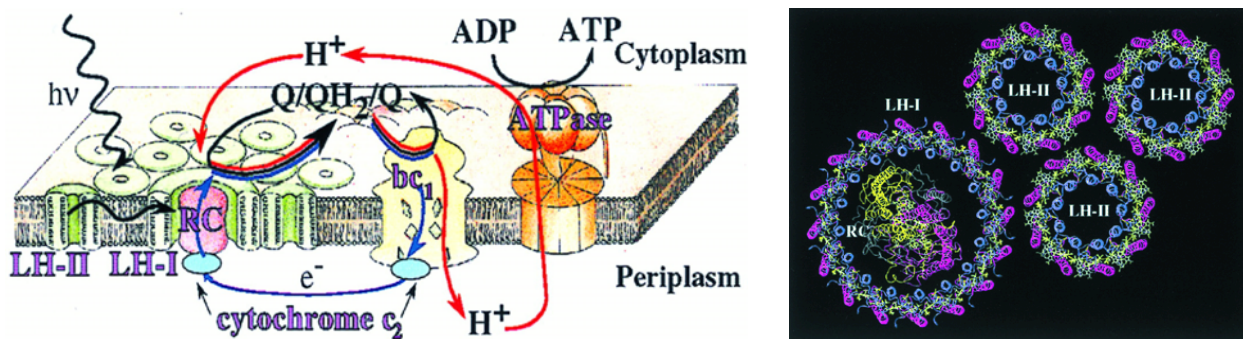


**Figure 2.2.4** (Left) Schematic representation of the photosynthetic apparatus in the intra-cytoplasmic membrane of purple bacteria. (right) A model for the pigment-protein complexes in the modeled bacteria *rhodospira rubra* [16].

known to atomic resolution from x-ray diffraction experiments. However, the mechanism and dynamics of electron energy transfer remains a mystery.

For example, the quantum efficiency of LHC is  $\sim 95\%$ , raising questions about how it is able to avoid fluorescence losses when transmitting energy over large distances. LHC possesses a high degree of circular symmetry, a property conjectured by Hu *et. al.* [17] to suppress fluorescence by making the lowest excited states of LHC dipole forbidden. For Hu's arguments to be correct, the electronic states must be coherently delocalized over the entire molecule, a prediction with profound implications since it suggests quantum delocalization played a crucial role in the evolutionary history of this organism. So far, efforts to indirectly estimate the coherence length optically, however, have yielded mixed results [18, 19].

Inelastic X-ray scattering (IXS) is a direct probe of quantum coherence. Specifically, the momentum spread of excited states as they appear in the dynamic structure factor  $S(\mathbf{k}, \omega)$ , gives the exciton mean-free-path, i.e. the distance over which it propagates before losing phase coherence. The energy scale is set by the electronic excitations in the photosynthetic unit, the first dipole allowed transition is  $\sim 1.4$  eV. However, because of the poor quality of these sample, elastic scattering background is going to a severe problem. To overcome this problem, an energy resolution of a few meV will be needed.

The high brightness and flux of NSLS-II, together with new optical schemes, will enable IXS experiments with an energy resolution of a few meV at 8 to 10 keV, and open up a new window into the electronic properties of biomolecules.

## 2.2.3 Impact of NSLS-II

### 2.2.3.1 Time resolved Studies in Micro-fabricated Flow-cell Mixers

The development of micro-fabricated lamellar flow-cell mixers (Figure 2.2.5) provides a way to initiate dynamical events in micron-scale jets of solution on microsecond time scales, while requiring only extremely small quantities of specimen [20-22]. These continuous-flow diffusion mixers [23, 24] produce thin laminar flow sheets of solutions and dynamical events are triggered as the solutions mix by diffusion between the solution sheets. They can potentially enable us to watch dynamical events unfold by making measurements at different positions downstream. For instance, to generate a protein-folding

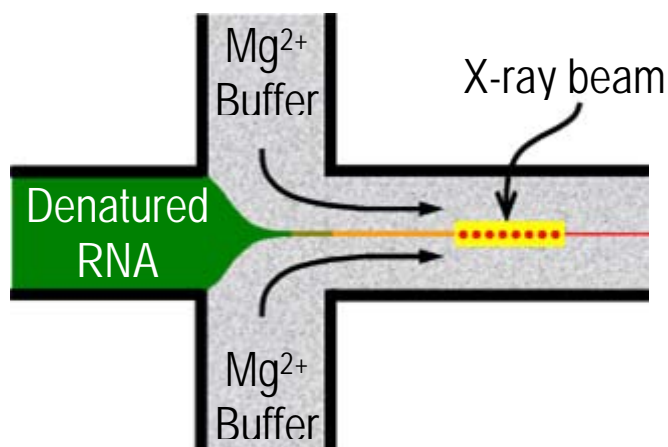


**Figure 2.2.5** Principle of operation of the flow cell, showing a cross section through the center and indicating one possible location of the X-ray beam. In this case, denatured RNA solution was mixed with side-streams of  $Mg^{++}$  to initiate folding. Because the time-scale of diffusional equilibrium of the central solution jet with the side-streams varies as the square-root of the central jet width, the time scales for equilibrium can be on the order of microseconds for jets less than a micron wide. The X-ray beam is moved downstream to access later times after the initiation of mixing. The high brightness of NSLS-II will revolutionize mixer experiments.

event, denatured protein is injected into the central channel, sandwiched between buffer solutions. As the protein and buffer solutions flow downstream, the denaturant diffuses out of the protein layer. Once the denaturant concentration drops below a threshold, the protein folds back to its functional conformation. The solution mixer also could trigger other biochemical reactions by a similar mixing of reactants. The solution-mixer technology can be combined with X-ray solution scattering, spectroscopy, or footprinting techniques to study a wide range of problems in life science.

The high brightness X-ray beams of NSLS-II will have a dramatic impact on mixer experiments. Achieving the ultimate time resolution requires the very small and intense beams that NSLS-II will excel at producing, since, for a given solution velocity the time resolution is directly determined by the beam size. Small beams will also allow smaller overall dimension of the solution layers, reducing sample consumption. Because the solution that is exposed to the X-ray beam is constantly replenished, radiation damage is not a limitation. Finally, the small beams will enable measurements to include as little of the side solution streams as possible, providing enhanced signal-to-noise for the weak X-ray signals from the small volumes.

NSLS-II combined with micro-fabricated flow-cell mixers will revolutionize solution studies in much the same way that earlier synchrotron sources enhanced the possibilities of macromolecular crystallography.

### **2.2.3.2 X-ray Footprinting**

Hydroxyl radicals cleave the phosphodiester backbone of nucleic acids. In sections where the RNA is folded, however, the backbone is inaccessible to solvent, and therefore protected from radical cleavage. X-ray footprinting employs the very intense and ionizing white (polychromatic) X-ray beam to generate hydroxyl radicals. One then analyzes the pattern of fragments after X-ray exposure by gel electrophoresis; the protected sections of the RNA that are not cleaved yield a "footprint", a general illustration of which is in Figure 2.2.6. One can follow the protections as a function of time, showing the tertiary contacts formed as the RNA folds. X-ray footprinting also works for proteins. In this case, hydroxyl radicals modify the amino acid side chains that are exposed to the solvent. The oxidized samples are digested with proteases and analyzed by LC-mass spectrometry to determine the extent and sites of modification.

Time resolved footprinting measurements can be achieved with a solution mixer to induce cleavage after a delay relative to the triggering of a dynamic event. This is an ideal method for gaining insight into dynamic processes of large RNA and protein assemblies. It provides detailed structural information (at the single-nucleotide and single side-chain level) on biologically relevant timescales. Current time resolved footprinting measurements are limited to millisecond time resolution. The high beam brightness provided by NSLS-II will make the time scale that is accessible by this technique significantly shorter, certainly by a factor of ten. This improvement is not only because of the better time resolution of the smaller-scale solution mixers enabled by NSLS-II, but also owing to the shorter X-ray exposure time that is necessary to generate the hydroxyl radicals that cleave the biomolecules. All of this would benefit from use of microcapillary focusing that could produce a 10  $\mu\text{m}$  spot with high intensity. Achieving an understanding of conformational dynamics in macromolecules and their complexes during processes as diverse as ligand binding, folding, catalysis, and macromolecular assembly is a challenging and important step towards providing detailed molecular descriptions of biological systems.

### **2.2.3.3 High-throughput Characterization of Biomolecules**

Whereas the undulator-based beamlines at NSLS-II will offer the opportunity to overcome a number of exceedingly difficult and important problems in life science, the lower intensity bending magnet-based beamlines will contribute by performing relatively simple tasks that are time consuming today. The duration of static measurements will be greatly reduced even on bending magnet beamlines as the source brightness increases. This provides the possibility of high-throughput characterization of large numbers of

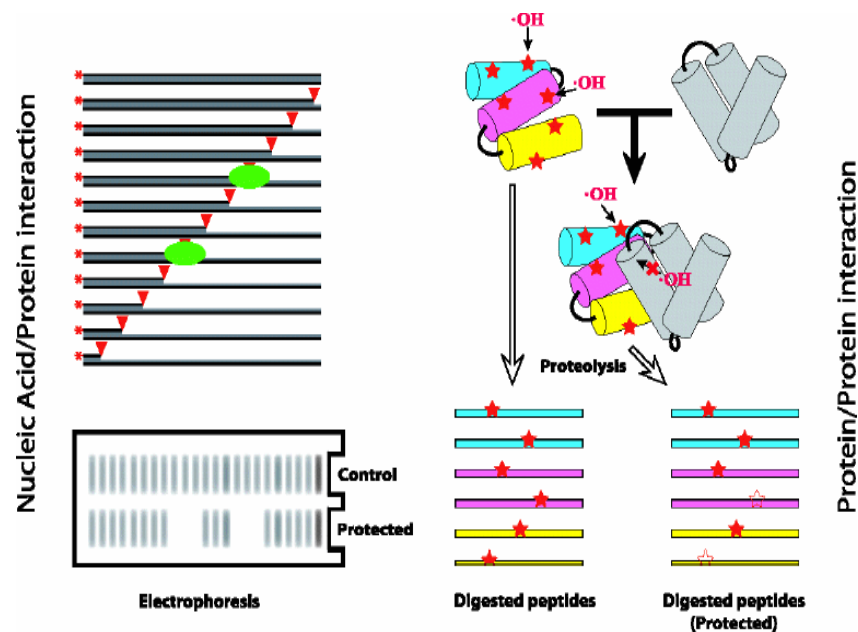


**Figure 2.2.6** Synchrotron X-ray footprinting uses a white X-ray beam to generate hydroxyl radicals to cleave RNA backbone or protein side chains that are exposed to water. Analysis of the cleaved/modified products provides structural information on the single nucleotide/side chain level. This capability is very useful for studying the dynamic processes of large RNA and protein assemblies when combined with time-resolved measurements.

samples. Automatic sample handlers will be constructed to feed samples, and many, perhaps even hundreds, of samples will be characterized each hour by solution scattering and X-ray spectroscopy.

High-throughput solution-scattering measurements will be useful as a quality-control and diagnostic tool during the genome-scale expression of proteins that accompanies the Structural Genomics programs mentioned in Section 2.1 on macromolecular crystallography. For example, many proteins cannot be expressed in *E. coli*, or are unable to fold in these bacterial cells. Therefore the quality of the expressed proteins must be monitored, and some of their physical characteristics can be discovered, for example by solution scattering and IR/UV spectroscopy. High-throughput measurement is necessary to match the scale of the whole structural genomics effort.

Another potential application of high-throughput measurements is for crystallization screening. The interaction between individual protein molecules can be measured far before nucleation occurs [25]. Measuring the protein-protein interaction under a spectrum of conditions therefore can serve as a tool for searching for the optimal condition under which proteins can nucleate and continue to grow into large crystals.

## REFERENCES

- [1] F. Allen et.al, IBM Systems Journal, 40, 310 (2001)
- [2] Y. Duan and P. A. Kollman, Science 282, 740 (1998).
- [3] D.I. Svergun, Biophys. J. 76, 2879 (1999)
- [4] P. Chacon, F. Moran, J.F. Diaz, E. Pantos, J.M. Andreu Biophys. J. 74: 2760 (1998)
- [5] Sokolova, M. Malfois, J. Caldentey, D.I. Svergun, M.H. Koch, D.H. Bamford and R. Tuma, J. Biol. Chem. 276, 46187 (2001)
- [6] Q. Hao, F.E. Dodd, J.G. Grossmann, S.S. Hasnain, Acta Cryst., D55, (1), 243-246, 1999
- [7] Yang, T.M. Weiss, T.A. Harroun, W.T. Heller, and H.W. Huang, Biophys. J. 77, 2648 (1999)

- [8] Koltover, J.O. Raedler, T. Salditt, K.J. Rothschild and C.R. Safinya, *Phys. Rev. Lett.*, 82, 3184, (1999)
- [9] R. Das, T. T. Mills, L. W. Kwok, G. S. Maskel, I. S. Millett, S. Doniach, K. D. Finkelstein, D. Herschlag L. , Pollack, *Phys. Rev. L ett.* 90, 188103 (2003).
- [10] R.A. Scott, D.L. Rousseau, ed. p. 295, Academic Press, Orlando, Florida (1984)
- [11] Ascone, R. Fourme, S. Hasnain, *J. Synch. Rad.*, 10, 1 (2003).
- [12] Zhang, J. Dong and D.S. Auld, *Physica B* 209, 719 (1995).
- [13] M. Richwin, R. Zaeper, D. Lutzenkirchen-Hechtand R. Frahm, *Rev. Sci. Instrum.* 73, 1668-1670 (2002).
- [14] M. Haumann, M. Grabolle, T. Neisius and H. Dau, *FEBS Lett.* 512, 116 (2002).
- [15] Frenkel, O. Kleinfeld, S.R. Wasserman and I. Sagi, *J. Chem. Phys.* 116, 9449 (2002).
- [16] X. Hu, A. Damjanovic, T. Ritz, K. Schulten, *Proc. Natl. Acad. Sci.*, 95, 5935 (1998)]
- [17] X. Hu, T. Ritz, A. Damjanovic, and K. Schulten, *J. Phys. Chem. B*, 101, 3854 (1997).
- [18] D. Leupold, et. al., *Phys. Rev. Lett.*, 77, 4675 (1996).
- [19] R. Jimenez, F. van Mourik, J. Y. Yu, and G. R. Fleming, *J. Phys. Chem. B*, 101, 7350 (1997).
- [20] R. Russell, I. S. Millett, M. W. Tate, L. W. Kwok, B. Nakatani, S. M. Gruner, S. G. J. Mochrie, V. Pande, S. Doniach, D. Herschlag & L. Pollack, *Proc. Natl. Acad. Sci.* 99 , 4266 (2002).
- [21] L. Pollack, M. W. Tate, N. C. Darnton, J. B. Knight, S. M. Gruner, W. A. Eaton, R. H. Austin, *Proc. Natl. Acad. Sci.* 96, 10115 (1999).
- [22] L. Pollack, M. W. Tate, A. C. Finnefrock, C. Kalidas, S. Trotter, N. C. Darnton, L. Lurio, R. H. Austin, C. A. Batt, S. M. Gruner & S. G. J. Mochrie *Phys. Rev. Lett.* 86, 4962 (2001).
- [23] J.B. Knight, A. Vishwanath, J.P. Brody, and R.H. Austin, *Phys. Rev. Lett.* 80, 3863 (1998)
- [24] L. Pollack, M.W. Tate, A.C. Finnefrock, C. Kalidas, S. Trotter, N.C. Darnton, L. Lurio, R.H. Austin, C.A. Batt, S.M. Gruner, and S.G.J. Mochrie *Phys. Rev. Lett.* 86, 4962 (2001)
- [25] Tardieu, S. Finet and F. Bonnete, *J. Crys. Growth*, 232, 1 (2001).

## 2.3 Biological Imaging

### 2.3.1. Overview

The high brightness of NSLS-II will make it possible to tightly focus the beam to create very intense nanoprobes for high-resolution cellular imaging and sensitive trace element mapping in biological specimens. The brightness will also provide highly collimated beams of high intensity and large transverse dimensions for novel forms of medical imaging and tomography [1]. In addition to high brightness, NSLS-II will also provide the broadest range of wavelengths to users in a single facility, extending from hard X-rays to the far-infrared and enabling a wide array of analytical techniques, including: X-ray microscopy (hard and soft; scanning and full-field), diffraction imaging, X-ray tomography, X-ray microprobe, diffraction-enhanced imaging (DEI), and infrared imaging. These diverse imaging tools will span the resolution scale from nanometers to millimeters, allowing non-destructive analysis of biological subjects ranging from sub-cellular structures to humans.

Synchrotron facilities worldwide, including the NSLS, demonstrate the value of using a synchrotron for biological and medical imaging. Information that could once be obtained only on pure, spatially homogeneous samples is now obtained from heterogeneous natural and complex biological samples on length scales of tens of nanometers. NSLS-II will extend this to less than 10 nm, enabling studies of nanoscale phases and compositional variations and providing deeper insight into nature (Figure 2.3.1).

The ultra-high brightness of NSLS-II will have significant impact:

- For the highest resolution, radiation with spatial and temporal coherence is required. NSLS-II will increase the coherent flux available by at least two orders of magnitude. Combined with advanced X-ray optics, NSLS-II will make  $\sim 10$  nm spectromicroscopy routinely available. Higher spatial resolution ( $\sim 10$  nm) for imaging whole cells ( $>10$   $\mu\text{m}$  thick) will enable imaging substructures such as cell membranes, protein complexes (e.g. ribosomes), and cytoskeleton components (microtubules, actin filaments).
- Combined with new techniques in reconstruction of diffraction data, NSLS-II will make sub-10 nm spatial resolution possible, improving the image resolution of subcellular components.
- With NSLS-II, the spatial resolution of X-ray microprobes and DEI will be reduced to below 1  $\mu\text{m}$ . This spatial resolution will enable the imaging of plant and animal tissues on the sub-cellular level, and importantly, in their natural state.

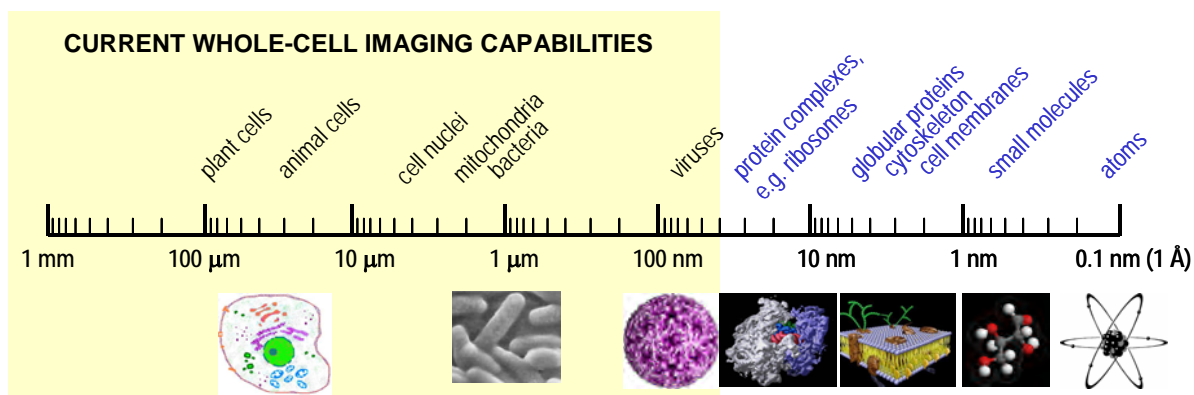


**Figure 2.3.1** The size scale of biological materials. Current visible-light imaging capabilities are diffraction-limited at  $\sim 200$  nm. Using synchrotron X-rays, imaging is extended to 30-40 nm. With the high brightness and coherence of NSLS-II, this limit will be extended to  $\sim 10$  nm, permitting intact imaging of subcellular structures such as protein complexes, cytoskeleton components, and cell membranes.

## 2.3.2 Scientific Challenges and Opportunities

The requirement for increased efficiencies in the health care system and global trends toward an aging demographic are stimulating investments in biomedical imaging research. NIH and DOE are keenly interested in developing and improving the ability to image macromolecular machines. In 2000, NIH established the National Institute of Biomedical Imaging and Bioengineering, which “coordinates with biomedical imaging and bioengineering programs of other agencies and NIH institutes to support imaging and engineering research.” In addition, the first goal of the DOE Genomes-to-Life initiative is to “identify and characterize the molecular machines of life,” where “imaging will help define interactions between proteins and other components in the complex interacting networks of living cells.”

Recent discoveries in synchrotron X-ray and infrared imaging sciences have spawned the development of new imaging techniques that provide unprecedented resolution of nature’s small details. NSLS-II will enable greatly enhanced capabilities for forefront integrated biomedical research that will lead to dramatic breakthroughs in both basic scientific understanding and human health.

### 2.3.2.1 Imaging Molecular Machines

Biological cells are composed of complex macromolecular assemblies that work together in functional networks that characterize the dynamic life of a cell. These machines execute important metabolic functions, mediate information flow within and among cells, and build cellular structures. Imaging of whole cells, and the macromolecular assemblies within cells, is critical for understanding these interactions.

For example, one of the outstanding problems in cellular biology is the way the mammalian cell packages its genetic material under different conditions. How is the chromosome assembled and organized? How are errors in this organization related to disease? One specific example involves how the organization of genetic material is different in the sperm cell where, instead of histones, protamines are attached to DNA. The ability to image hidden abnormalities in the composition of sperm nuclei, including damaged DNA, impaired chromatin condensation, alteration in the chemical composition and concentration of sperm proteins is important in order to understand how the morphology of the sperm cell affects male fertility.

Recently X-ray microscopy was introduced for the evaluation of a single sperm (Figure 2.3.2). Sperm have a size in the 1-2 micron range, and the structures of interest are typically 30 nm, well matched to the capabilities of soft X-ray microscopes. Soft X-ray spectromicroscopy with a cryo scanning transmission X-ray microscope can evaluate both qualitative and quantitative abnormalities in sperm ultrastructure and composition. The chemical sensitivity of XANES spectroscopy allows the identification of the major constituents (protein, DNA, etc.), and the ability to image frozen hydrated specimens assures that the specimen is as close to its natural state as possible.

The high brightness of NSLS-II will improve the resolution of sperm imaging to ~10 nm. At this size scale, the packaging of genetic material will be imaged. Specifically, the small protamine-DNA complexes will be visualized within the sperm. Chromosomes and abnormalities in chromatin condensation will also be seen. Moreover, spectroscopic imaging of sperm will enable the study of sperm cell chemistry at ultra high resolution, such as the concentration of sperm proteins and nucleic acids.

As another example, the budding yeast, *Saccharomyces cerevisiae*, has long been a valuable model system for genetic, molecular, and biochemical analyses, and continues to be important for modern proteomics investigations. Hundreds of distinct multiprotein complexes have been identified and new cellular roles for several hundred other proteins, most of which had no previous functional annotation, have been proposed. An important method for gaining insight into the function of a protein is to determine its location in cells. Kumar et al recently conducted a high throughput immunofluorescent localization of tagged gene products in the budding yeast [2]. They concluded that the entire yeast

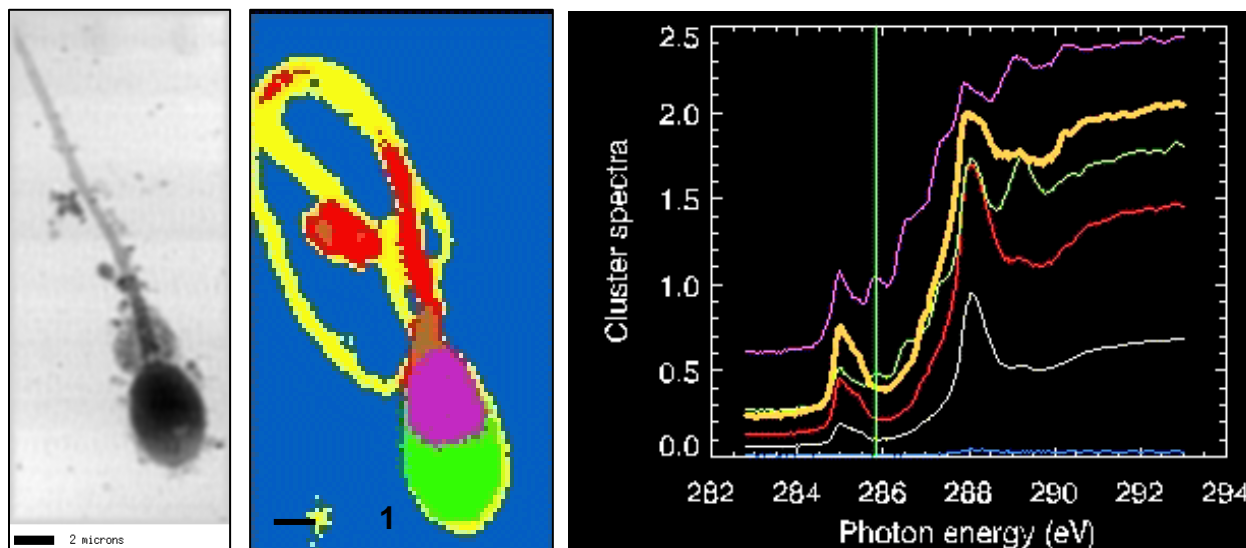


**Figure 2.3.2** *Soft X-ray spectromicroscopy imaging of human sperm: wet image (left), and cluster analysis image (center) of spectral data set (right) demonstrating biochemical mapping. Such studies can correlate morphological types with biochemistry.*

proteome encompasses about 5100 soluble proteins and more than 1000 transmembrane proteins. This is a remarkable undertaking that begins to provide insight into protein locations and their associated function. However, if the yeast proteome encompasses 30,000 protein interactions, many of which change during the organism's life cycle [3], more precise information about the location of each protein throughout the cell cycle will be required. This information is beyond the level of resolution of existing light microscopy techniques and is unattainable using electron microscopy, given the time-consuming nature of the requisite specimen preparation.

X-ray tomography has the potential to accomplish these goals and make significant contributions to our understanding of protein function in cells. Using this approach, superb structural information can be obtained from whole, hydrated cells at better than 35 nm resolution. In addition, immunogold labeling techniques similar to those used for TEM can be used to localize proteins in whole cells [4, 5]. These capabilities, combined with tomographic procedures, offer unique three-dimensional views of cells.

Transmission X-ray microscopy has been used to examine whole cells, revealing superb images of cytoplasmic and nuclear structures at 35-40 nm resolution (Figure 2.3.3). The high brightness of NSLS-II coupled with improvements in zone plate technology will enable even higher resolution. This promises to be a remarkably fertile line of research for which NSLS-II is a critical and necessary requirement.

### 2.3.2.2 Fundamental Basis of Disease

Biological tissues are composed of individual cells and a complex extracellular matrix that holds the cells together to make a tissue. Many diseases involve alterations in the chemistry of the cells and extracellular matrix. For example, cancerous tumors, scar tissue, and atherosclerotic (blood vessel) and neuritic (brain) plaques all form through some combination of irregular cell growth, and breakdown and remodeling of the extracellular matrix around them. Imaging of whole tissues, encompassing the interactions between cells and the extracellular matrix, is critical for understanding these disease processes.

As a prime example, a growing number of neurodegenerative diseases, including Alzheimer's disease (AD), Parkinson's disease, Huntington's disease, amyotrophic lateral sclerosis (ALS) and Creutzfeldt-Jakob disease, involve the misfolding of normal proteins in the brain, which has recently been associated

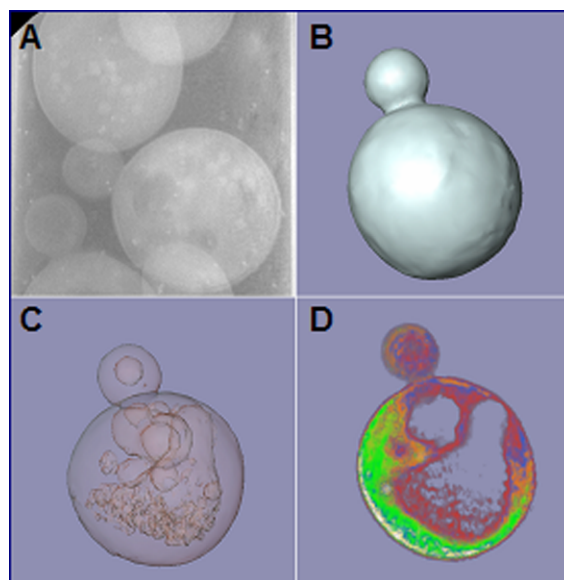


**Figure 2.3.3** X-ray tomograph of the budding yeast, *Saccharomyces cerevisia*. (A) Projection image of yeast in the capillary; arrows indicate 60 nm gold balls used as fiducial markers for alignment of all images for tomographic reconstruction. (B and C) Computer generated sections from the reconstructed data; X-ray dense lipid droplets (small white circles) are now easily distinguished as distinct organelles and large vacuoles that are less dense appear dark. Yeast cell is 5 microns in diameter.

with the binding of metal ions such as iron, copper, and zinc. Yet, the functions of these metal ions and the misfolded proteins in the disease process are not well understood.

To date, metal concentrations in brain tissue are generally measured via macroscopic (bulk) techniques that cannot provide any spatial information on localized metal accumulation. Traditional histochemical (staining) methods for localizing metals in tissue are insufficient. Stains and/or fluorescently-tagged antibodies are also used to identify misfolded proteins in tissue, but do not provide direct information on the protein's structure.

Using X-ray microspectroscopy, the metal ion distribution, concentration, oxidation state, and local structure as a function of disease severity can be imaged in intact brain tissue. By combining fluorescence microscopy and infrared microspectroscopy, the location and secondary structure of the associated misfolded proteins are imaged (Figure 2.3.4). By combining these results, it is possible to identify the metal ions that accumulate before, concurrently, or after protein misfolding, in order to develop a possible mechanism for the complex formation and toxicity.

Current limitations for X-ray microprobe imaging of neuritic plaques include spatial resolution and beamtime availability. Although many neuritic plaques are large (e.g. AD plaques are 50-200 microns in diameter), others are much smaller (e.g. ALS) and more diffuse (e.g. mad cow disease and scrapie). The higher brightness and coherence of NSLS-II, including increased insertion device capacity, will enable X-ray microprobe analysis at below 1 micron resolution, and even zone plate microscopy at 70-100 nm resolution. In addition to high resolution, the quantity of beamtime required for X-ray microprobe analysis as well as infrared imaging is also a limiting factor. Large areas of tissue need to be imaged and a large number of samples are necessary for good statistics. With NSLS-II, array-detector infrared imaging will be possible, increasing data collection rates by a factor of at least 20.

NSLS-II will also allow longitudinal in-vivo studies to track disease progression and/or evolution of pathology during treatment of neurodegenerative diseases. For example, DEI and X-ray Microtomography will be able to penetrate the skull of animal models of Alzheimer's disease.

Another important example is that of osteoarthritis (OA), which affects over 40 million Americans. Important questions remain as to the relationship between underlying (subchondral) bone and joint

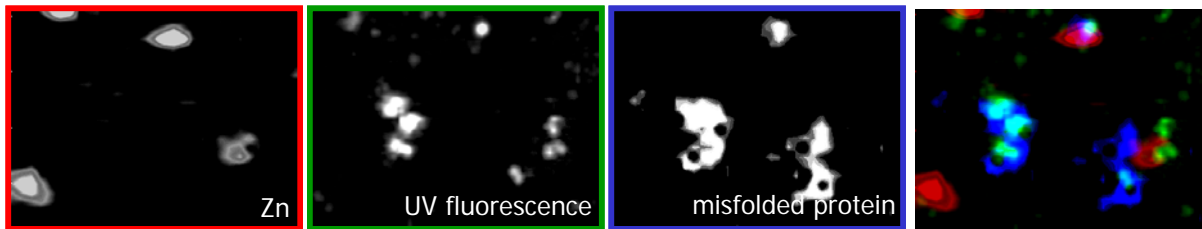


**Figure 2.3.4** Grayscale images of zinc (left), amyloid plaque (left, center), and misfolded protein (right, center) in a single specimen of Alzheimer's brain tissue. The Zn image and the misfolded protein image were collected with X-ray fluorescence microprobe and infrared microspectroscopy, respectively. The UV-fluorescence image of the amyloid plaque identifies their location based on a fluorescence stain, but does not provide protein structural information. (Right) An RGB image containing overlays of the three grayscale images: red = zinc; green = amyloid; blue = misfolded protein.

cartilage changes in OA, partly because of the difficulty in studying this calcified tissue. DEI is able to simultaneously detect both cartilage and bone changes in the progression of OA (Figure 2.3.5) [6]. The spatial resolution of these images is limited by the present NSLS source size to about 50 microns. However, NSLS-II will extend this to below 1 micron with enhanced sensitivity.

Very little is known about the composition of the mineralized plate beneath the articular cartilage in OA. Presently, infrared microscopy is limited in its ability to examine the chemical composition (e.g. mineralization, carbonate content, collagen structure) of intact sections of joints. Advances in array detector technology will soon enable access to the low wavelength range necessary to image some of the mineral modes in bone, and these detectors will be best suited to a synchrotron source such as NSLS-II with a wide acceptance angle.

### 2.3.2.3 Early Disease Detection

Challenges remain in clinical diagnostic and screening imaging, despite recent advancements in mammography, MRI, CT, PET, and SPECT. The rate of false negative in mammography is still about 10%; cartilage is difficult to visualize by radiological means; and the contrast of chest X-ray is too low to detect early stages of emphysema and edema. Since early intervention of these diseases is typically life-saving, development of new radiography methods for diagnosis and screening is of great interest.

DEI is advantageous for mammography because its refraction contrast mechanism [7] provides increased sensitivity to soft-tissue contrast. Figure 2.3.6 shows images of breast tissue with invasive lobular carcinoma that extends to the edge [8]. It illustrates the improved visualization of spiculations

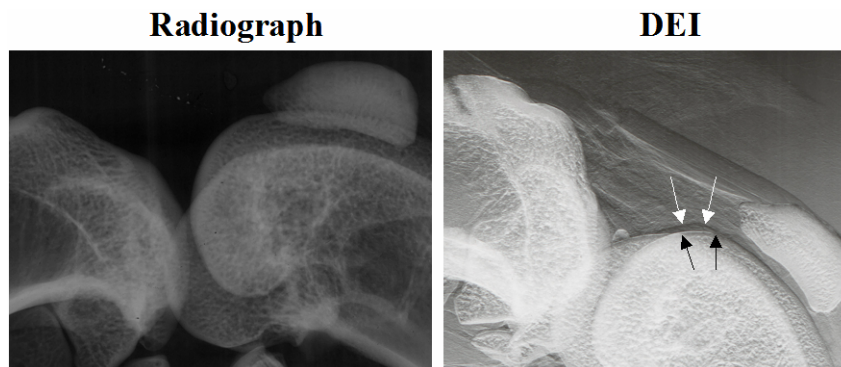


**Figure 2.3.5** Conventional X-ray (left) and DEI image (right) of an intact rabbit knee joint. Notice that even though the DEI contrast allows visualization of cartilage, the resolution of the image does not yet allow detailed study of early stage cartilage damage or the bone-cartilage interface. NSLS-II will extend the resolution from 50 microns today to below 1 micron and make this possible.

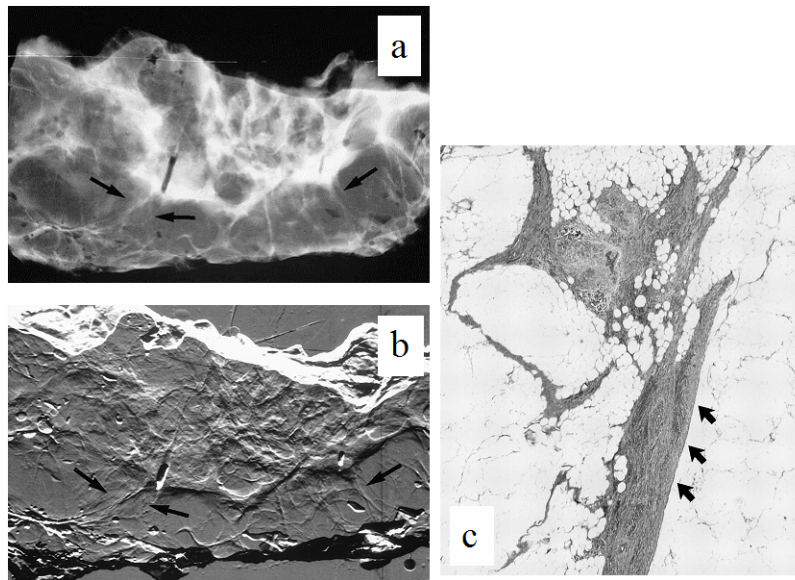


**Figure 2.3.6** Specimen with invasive lobular carcinoma, which typically grows in single files of cells. (a) Digital radiograph of the specimen. Note the vague linear densities along the inferior margin of the lesion. (b) Diffraction-enhanced image of the same specimen. Note the increased prominence and number of lines that extend from the inferior border of the lesion at the arrows. (c) Photomicrograph of the spiculations identified between the two arrows on the left in b shows a band of fibrous tissue with invasive lobular carcinoma.

representing tumor extension by DEI, compared to standard radiographs. The DEI apparent absorption image was found to have 8 to 33 times greater contrast than that of a normal radiograph [9]. DEI breast images are currently limited to a spatial resolution of about fifty microns and it is important to visualize smaller calcifications and small spiculations. NSLS-II will provide a major advance by extending this to below one micron. The increased resolution and sensitivity allowed by NSLS-II will enable study of the cancer biology and morphological features of animal models of breast cancer and other cancers that are typically too small to be reliably detected by the current DEI resolution and will guide the design of a clinically-relevant DEI system.

As another example, degeneration of joint cartilage in OA is among the leading causes of immobilization and affects 85% of elderly people. Joint pain is one of the first signs of disease, but by the time pain becomes a symptom, successful treatment leading to regeneration of the tissue is too late.

Conventional radiography is the first and most frequently used imaging method to detect joint abnormalities. However, cartilage tissue has little X-ray absorption contrast and cannot be easily seen so that conventional radiography is sensitive only in cases of advanced disease. A high-resolution radiographic method to directly visualize early defects in cartilage is thus desirable.

The ragged face of damaged cartilage produces substantial changes in X-ray refraction as well as small angle scattering. Studies have shown that DEI is able to visualize damage typical of early degenerative disease in cartilage, tendons and other soft tissues in intact joints [10]. Cartilage is thin, especially in animal models of OA, and is usually obstructed by overlaying bone structures in a projection image. Multiple high resolution DEI images, and their reconstruction by CT, are thus necessary.

NSLS-II, with its small source size and top-off filling mode, will allow DEI imaging of cartilage at spatial resolution of less than 1 micron and much better sensitivity to reveal subtle changes in cartilage of animal models. The thermal stability will also allow the longer exposures necessary for routine CT imaging and reconstruction of phase contrast.

## 2.3.3 Impact of NSLS-II

### 2.3.3.1 Soft X-ray Microscopy and Nanotomography

Soft X-ray microscopy generates 3-D, quantifiable, structural and molecular information at better than 40-nm resolution. It is fast, relatively easy to accomplish, produces high-resolution, absorption-based images, and is naturally combined with small-spot spectroscopy for chemical identification at high spatial resolution. When operating between the K-edges of carbon and oxygen, it has good intrinsic contrast between organic material and water, and good penetration in micron-thick specimens. By taking images at photon energies near an element's absorbance resonances, regions of high concentration of certain bonding states of the element can be highlighted. Whole, hydrated cells (between 10-15 microns thick) can be examined, eliminating the need for time-consuming, and potentially artifact-inducing, embedding and sectioning procedures, and yet it is possible to localize proteins using simple immunolabeling protocols (Figure 2.3.7).

Obtaining the highest resolution in soft X-ray microscopy requires that the zone plate be coherently illuminated. Hence, the technique is brightness-limited. The high brightness of NSLS-II will provide unprecedented spatial resolution, faster data collection, and improved signal to noise.

The goal of obtaining high resolution 3D nanotomographic images on whole cells is an important one. Electron microscopes are able to obtain 6-8 nm resolution 3D images of regions of frozen hydrated cells but only when the sample thickness is less than 300-400 nm. Soft X-ray tomography demonstrations at the NSLS, BESSY, and ALS have obtained 60-100 nm resolution 3D images of cells up to about 8 microns thick (Figure 2.3.8). To prevent radiation damage, the cells must be rapidly frozen and maintained at low temperatures. Remarkably, cryo-fixation enables collection of hundreds of successive images with no detectable radiation damage. This technique should enable, for the first time, an absolute measurement of the full 3-D structure of small single cells. However, depth of focus decreases as the square of improvements in transverse resolution in microscopes, so that soft X-ray microscopes with better resolution will be limited to even thinner cells.

An important approach to this problem is to use 3-5 keV x rays for phase contrast imaging, where one can push towards 10 nm 3D resolution with good penetrating power and little limit due to depth of focus [13, 14]. The high brightness of NSLS-II at these energies is crucial for phase contrast nanotomography at higher resolution.

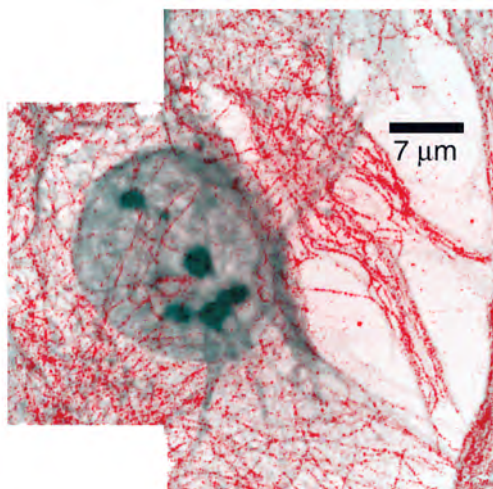


**Figure 2.3.7** STXM image of a fibroblast that has been antibody labeled with gold particles for tubulin (a cytoskeleton component) [11].

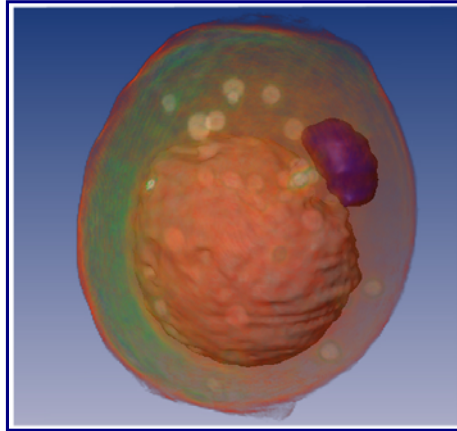


**Figure 2.3.8** *Soft X-ray nanotomograph (50 nm resolution) combined with volume rendering of Saccharomyces cerevisiae (a yeast cell). The nucleus is colored blue, lipid droplets appear white, and the surface of a large vacuole in the center of the yeast is color-coded pink. The yeast is 5 microns in diameter. [12]*

Scanning transmission X-ray microscopes are presently quite slow compared to full-field transmission X-ray microscopes (TXMs): it can take several minutes to acquire one high resolution image, several hours to acquire a spectromicroscopy data set, or a day to acquire a 100 nm voxel resolution tomography data set [15]. At the same time, scanning microscopes offer important advantages: the 10-20% efficient zone plate is located upstream of the specimen in the beam path so that its efficiency affects only exposure time but not radiation dose to the sample. Also, the small phase space required for zone plate illumination leads to simpler designs for high energy resolution monochromators, and segmented detectors can be used to simultaneously acquire absorption and phase contrast images in one scan [16]. The NSLS hosts a group from Stony Brook that has pioneered zone plate scanning microscopy, and a large community already uses zone plate scanning microscopy for scientific research in biology and environmental science.

The higher brightness of NSLS-II, combined with laser interferometer position feedback, will enable over two orders of magnitude improvement in spatial resolution and greatly reduced data collection times in TXM measurements.

### 2.3.3.2 Diffraction Imaging

The resolution of X-ray microscopes is limited by our ability to fabricate high-resolution optics. It was pointed out by David Sayre that one should be able to record the diffraction pattern of small, isolated non-crystalline specimens, such as small cells or organelles, and reconstruct the image at a resolution not limited by optics. The diffraction pattern of such objects is continuous, and can be sampled on a fine raster to obtain the information necessary to retrieve the phase lost in the recording process. Diffraction imaging, illustrated in Figure 2.3.9, was first demonstrated at the NSLS in 1999. The ultimate resolution limit is set by radiation damage to the specimen. A full 3D reconstruction can be performed if diffraction patterns are collected from a complete range of angular orientations.

Scientists using the NSLS pioneered the reconstruction of X-ray diffraction data to yield real-space images of non-crystalline specimens [17], and a development program is nearing completion [18] to allow these experiments to be carried out on cryogenic specimens to minimize radiation damage, and to allow the specimen to be rotated through a 160° tilt range. Experiments underway at the NSLS are using a zone plate to obtain an already-phased image at low spatial frequencies, and collecting diffraction data without the transfer function loss of the zone plate at higher spatial frequencies, and thus extend X-ray imaging beyond the zone plate resolution limit.

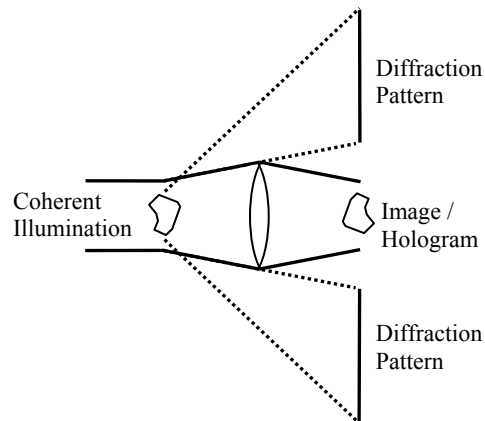


**Figure 2.3.9** *Diffraction-based imaging. A zone plate is used to obtain an image at low spatial frequencies, diffraction data yields image at higher spatial frequencies beyond the zone plate resolution limit. NSLS-II provides the essential coherent illumination.*

The diffraction technique depends on coherent illumination, and hence on the brightness of the source. NSLS-II will be the ideal source for diffraction imaging, providing the high brightness required for routine 3D imaging by this technique.

In the push to higher resolution, it is inevitable that radiation damage is increased: one is attempting to illuminate and collect signal from a smaller mass. Scientists using the NSLS have pioneered the development of cryo methods for scanning microscopy [19], and have shown a  $10^4$  decrease in damage relative to room temperature hydrated specimens, consistent with cryo TXM studies [20]. It is worthwhile noting that timescales play an important role in high resolution imaging: for 10 nm resolution imaging one must either collect the entire dataset in a time much less than 100 fsec to avoid hydrodynamic blurring, or greater than about 1 msec to allow for heat conduction.

### 2.3.3.3 Hard X-ray Microprobe

X-ray absorption spectroscopy (XAS), including X-ray fluorescence (XRF), has been widely used for probing metal content and structure within biological systems. The XAS spectrum provides information such as metal oxidation state, metal spin state, number and type of ligands bound to the metal, and bond distances. Using focusing mirrors, XAS and XRF imaging can be used to non-destructively provide the distribution of trace element content and structure with a resolution of 1-10 microns and elemental sensitivities in the sub-mg kg<sup>-1</sup> range. Applications have included the characterization of heavy metal contamination in soils, the uptake of metals in plants (i.e. phytoremediation), and the role of metal ion accumulation in neurological diseases [21]. Analyses can be done on standard microscopic sections, rock fragments, powders, soils, and biological materials; samples can be in solution, liquids, amorphous solids, aggregates, plant roots, surfaces, etc.

The greatly increased brightness of NSLS-II will make it possible to use zone plate focusing optics to improve the resolution to 50 – 100 nm [22]. The resulting nanoprobe will be used for high resolution mapping of trace elements in cells, tissues, and bacteria by XRF, and the mapping of the chemical state of more abundant metals by XAS.

### 2.3.3.4 Infrared Imaging and Microspectroscopy

Infrared microspectroscopy (IRMS) enables the microscopic chemical distribution in materials to be probed through their vibrational spectra. It has been used to study numerous plant and animal tissues, single biological cells, minerals and soils, etc. For complex samples such as human tissues, an IR

spectrum provides a direct indication of sample biochemistry. For example, as discussed in Section 2.3.2, aggregates of misfolded proteins, i.e. amyloid plaques, have been identified in the brain tissue of Alzheimer’s disease patients. Spectral evidence of cervical cancer, heart disease, and bone diseases such as osteoarthritis, osteoporosis, and osteogenesis imperfecta (i.e. “brittle bone disease”) have been identified [23-25]. In addition, contaminants in human tissue, such as silicone in breast tissue and narcotics in human hair have also been observed.

The primary advantage of synchrotrons over conventional IR sources is their 100-1000 times greater brightness. This high brightness allows smaller regions to be probed with acceptable signal to noise ratio [26, 27]. Indeed, aperture settings smaller than the wavelength of light can be used, in which case diffraction controls the available spatial resolution [28].

NSLS-II will provide world leading brightness throughout the infrared and will make near-field techniques possible, improving the spatial resolution beyond the diffraction limit to below 1 micron. NSLS-II will provide wide opening angles capable of imaging sixteen or more synchrotron source points onto imaging array detectors, which have not yet been utilized on synchrotron beamlines. This will improve the signal to noise ratio of the data and greatly reduce the data collection time over current, single-point, synchrotron-based microscopes.

### 2.3.3.6 Diffraction-Enhanced Imaging

Diffraction enhanced imaging (DEI) is a phase-contrast radiography method developed at the NSLS in 1995 that introduces fine selectivity for the angular deviation of x rays traversing an object. It uses collimated X-rays produced by a perfect crystal monochromator, and an analyzer crystal positioned between the subject and the detector. The high angular sensitivity of DEI allows measurement of the gradient of the X-ray index of refraction and ultra-small-angle scattering, as well as the X-ray attenuation. Since the contrast mechanism for DEI does not rely on absorption, it is ideally suited for soft-tissue imaging of biological subjects, where better contrast and lower dose are both important [29], as discussed in Sections 2.3.2 and 2.3.3. And by imaging at higher X-ray energies, the radiation dose is reduced significantly without much degradation of image contrast.

DEI has great potential for high resolution imaging. The gain in contrast in DEI images compared with absorption images increases as the feature size decreases (Figure 2.3.10). However, the resolution of DEI at the current NSLS is currently limited by the source size to about 50 microns. The full advantage of phase contrast imaging can only be realized with a bright X-ray source. The increased brightness of NSLS-II will enable DEI imaging and other phase-contrast X-ray imaging of animals and tissues at a sub-cellular resolution of below 1 micron. This will lead to in vivo investigation of biological processes in small cell populations deep within the tissues of the body [1].

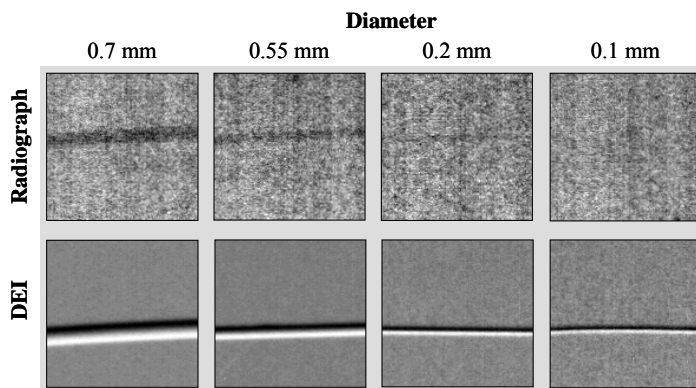


**Figure 2.3.10** Conventional radiograph vs. DEI image (on shoulder of rocking curve) of a nylon fiber, which simulates density variation in soft tissue. With conventional radiography, smaller objects show less contrast, a drawback that is not seen in the DEI images.

### 2.3.3.7 User Demand

The number of user groups that use multiple imaging techniques at the NSLS is a rapidly growing user community [22], having approximately tripled in the past few years.

With the broad spectral range available at the NSLS, the wide range of imaging tools can be combined easily to provide complementary information for sample characterization. This is a feature unique to the NSLS; no other facility in the world has such a wide wavelength range available for imaging. Since synchrotron-based imaging techniques are rather new, this complementarity is just being realized.

Despite the success and productivity of the current facility, with a limited number of insertion devices on the existing NSLS storage rings, these imaging techniques are currently brightness-limited. The proposed new facility will provide a significantly brighter source, while maintaining the broad wavelength range familiar to NSLS users.

The NSLS hosts a group from Stony Brook that has pioneered zone plate scanning microscopy and many developments with it, and a large community already uses soft X-ray zone plate scanning microscopy for scientific research in biology and environmental science. In addition, there is also a rapidly growing IR spectromicroscopy, and X-ray microprobe/microdiffraction community for materials, environmental, and biomedical applications. The power of combining the complementary information obtained with all these imaging tools, from IR to hard X-ray, has also begun to be realized.

All these imaging efforts have benefited greatly by a strong collaboration in X-ray optics research, based on advanced electron beam lithography, between Stony Brook University and Bell Labs. The establishment of the BNL Center for Functional Nanomaterials (CFN) will further strengthen this collaboration. In particular, the proposed CFN will house a state-of-the-art electron beam lithography facility that will accelerate the development of a wide range of X-ray focusing optics.

Zone plates act as lenses with a Rayleigh resolution equal to 1.22 times the outermost zone width for incoherent bright field imaging; with a 30 nm zone plate, the Rayleigh resolution is 37 nm while in coherent imaging the contrast transfer has a hard-edged cutoff at a spatial frequency of  $1/(2 \cdot 30 \text{ nm}) = 17 \mu\text{m}^{-1}$  and in incoherent imaging there is a smooth decline in spatial frequency response to  $1/(30 \text{ nm}) = 33 \mu\text{m}^{-1}$ . With deconvolution [30], it is quite possible to study structures to spatial frequency at least three-quarters of that limit, i.e.,  $25 \mu\text{m}^{-1}$ , corresponding to a 20 nm half-period width. This is representative of soft X-ray zone plate imaging at the present time, and it is reasonable to expect that zone plates at 5-10 keV will begin to approach this performance level as well [31]. To do so will require considerable research and development, but NSLS is well positioned for this by building upon a collaboration between Stony Brook University and Bell Labs in 100 keV electron beam lithography that has already yielded 20 nm zone width zone plates [32], and ultimately using the e-beam capabilities that will be part of the BNL Center for Functional Nanomaterials building. It is not impossible to foresee zone plates with 15 nm outermost zone width (giving 10 nm structural information), and furthermore waveguide effects may act to improve their efficiency if the zones can be oriented properly [33].

The NSLS has 2 soft X-ray microscopy beamlines, both of which operate on an undulator (X1A1, X1A2). Even with the undulator, the beamlines' brightness is slightly more than a factor of 10 below the brightness of undulators at the ALS. They utilize two of the best zone plates available for soft X-ray microscopy, providing a spatial resolution of about 30 nm. The demand for this very high spatial resolution, despite the lower brightness, makes these beamlines oversubscribed.

The high brightness of NSLS-II, combined with the increased insertion device capacity, will also improve the quality and quantity of X-ray microprobe beamlines. Currently, the NSLS has one microprobe beamline (X26A) and it operates on a bending magnet port, where the spatial resolution is limited to 10-15  $\mu\text{m}$  in order to provide sufficient flux to the sample. Even so, the demand for this beamline is tremendous; it is >200% oversubscribed.

Demand for medical imaging beamlines is strong. Currently there are only three dedicated synchrotron-based medical beamlines in the world, the ESRF in France, the Spring-8 in Japan and the

ELETTRA in Italy. Although one facility is planned for the new Canadian Light Source, currently under construction, no such facility currently exists in North America. The user schedules for the three dedicated medical beamlines are fully subscribed.

NSLS-II allows systematical investigation of the applicability of DEI, pioneered at the NSLS, to clinical imaging, by concentrating on three cases that have been shown by the preliminary studies to be promising: breast, lung imaging and cartilage imaging. There will be substantial expansion of the user base for DEI made possible by the NSLS-II.

The improvement in spatial resolution achieved by using a synchrotron IR source has only been realized recently, and applications to biological systems are growing rapidly. In 1999, the NSLS had one infrared microscope and ~5 user groups. Today, the NSLS has 4 infrared microscopes and over 50 biological/geological/environmental user groups. Each beamline is fully or over subscribed, one by more than 200% (U10B). In addition, only one other DOE-operated synchrotron has IR microspectroscopy capabilities (ALS has 1 IR microscope). Indeed, the NSLS is the premier facility for this type of research in the world. Thus, the NSLS needs to expand its IR microspectroscopy capabilities to accommodate a rapidly growing user community.

## REFERENCES

- [1] P. Suortti and W. Thomlinson, "Medical applications of synchrotron radiation", *Phys. Med. Bio.* 48 (2003), R1-R35.
- [2] Kumar, P.M. Harrison, K.H. Cheung, N. Lan, N. Echols, P. Bertone, P. Miller, M. B. Gerstein and M. Snyder, "An integrated approach for finding overlooked genes in yeast", *Nature Biotechnology* 20 (2002) 58-63.
- [3] Kumar and M. Snyder, "Protein complexes take the bait", *Nature* 415 (2002) 123-124.
- [4] W. Meyer-Illse, D. Hamamoto, A. Nair, S.A. Lelievre, G. Denbeaux, L. Johnson, A.L. Pearson, D. Yager, M.A. Legros, C.A. Larabell, "High resolution protein localization using soft X-ray microscopy", *J. Microscopy-Oxford* 201 (2001) 395-403.
- [5] J.W. Miao, K.O. Hodgson, T. Ishikawa, C.A. Larabell, M.A. LeGros, Y. Nishino, "Imaging whole *Escherichia coli* bacteria by using single-particle X-ray diffraction", *Proc. Nat. Acad. Sci. USA* 100 (2003) 110-112.
- [6] Muehleman, L.D. Chapman, K. E. Kuettner, J Rieff, J A. Mollenhauer, K. Massuda, and Z. Zhong, "Radiography of Rabbit Articular Cartilage with Diffraction Enhanced Imaging", *Anatomical Record* 272A (2003) 392-397.
- [7] Chapman, W. Thomlinson, R. E. Johnston, D. Washburn, E. Pisano, N. Gmür, Z. Zhong, R. Menk, F. Arfelli, and D. Sayers, "Diffraction Enhanced X-ray Imaging". *Phys. Med. Biol.*, 42 (1997) 2015-2025.
- [8] D. Pisano, et. al., "Human Breast Cancer Specimens: Diffraction Enhanced Imaging with Histologic Correlation - Improved Conspicuity of Lesion Detail Compared with Digital Radiography", *Radiology*, 214 (2000) 895-901.
- [9] M. Z. Kiss, D. E. Sayers and Zhong Zhong, "Measurement of image contrast using diffraction enhanced imaging", *Phys. Med. Bio.* 48 (2003) 325-340.
- [10] J. Li, Z. Zhong, R. Litdke, K. E. Kuettner, C. Peterfy, E. Aleyeva, and C. Muehleman, "Radiography of Soft Tissue of the Foot and Ankle with Diffraction Enhanced Imaging", *J. Anatomy* 202 (2003) 463-470.
- [11] H. Chapman, C. Jacobsen, and S. Williams, *Ultramicroscopy* 62, 191 (1996).
- [12] C. Larabell, M. LeGros, unpublished.
- [13] R. Grimm, H. Singh, R. Rachel, D. Typke, W. Zillig and W. Baumeister, "Electron tomography of ice-embedded prokaryotic cells", *Biophysical J.* 74 (1998) 1034-1042.
- [14] Medalia, et al. "Macromolecular Architecture in Eukaryotic Cells Visualized by Cryoelectron Tomography", *Science* 298 (2002) 1209-1213.

- [15] Y. Wang, C. Jacobsen, J. Maser, J. and A. Osanna, "Soft X-ray microscopy with a cryo STXM: II. Tomography". *J. of Microscopy* 197 (2000) 80-93.
- [16] M. Feser et al., in *X-ray micro- and nano-focusing: applications and techniques II* (ed. McNulty, I.) 117-125 (SPIE, Bellingham, WA, 2001).
- [17] J. Miao, P. Charalambous, J. Kirz and D. Sayre, "An extension of the methods of X-ray crystallography to allow imaging of micron-size non-crystalline specimens". *Nature* 400 (1999), 342-344.
- [18] T. Beetz, et al., in *Seventh International Conference on X-ray Microscopy* (eds. Susini, J., Polack, F. & Joyeux, D.) (*Journal de Physique IV*, Grenoble, France, 2002).
- [19] J. Maser et al., "Soft X-ray microscopy with a cryo STXM: I. Instrumentation, imaging, and spectroscopy". *J. Microscopy* 197 (2000), 68-79.
- [20] G. Schneider, "Cryo X-ray microscopy with high spatial resolution in amplitude and phase contrast". *Ultramicroscopy* 75 (1998), 85-104.
- [21] Lanzirotti, "Yttrium zoning in metamorphic Garnets", *Geochimica et Cosmochimica Acta.* 59 (1995) 4105-4110.
- [22] Lanzirotti and L. M. Miller, "Imaging and Microspectroscopy at the National Synchrotron Light Source", *Syn. Rad. News* 15(6) (2003), 17-26.
- [23] L. M. Miller, C.C. Carlson, D. Hamerman and M.R. Chance, « Chemical differences in subchondral osteoarthritic bone observed with synchrotron infrared microspectroscopy», *Bone* 23 (1999) S458.
- [24] L.M. Miller, P. Dumas, N. Jamin, J.L. Teillaud, J. Miklossy and L. Forro, "Combining IR spectroscopy and fluorescence imaging in a single microscope: Biomedical applications using a synchrotron infrared source", *Rev. Sci. Instrum.* 73 (2002) 1357-1360.
- [25] L. M. Miller, V. Vairavamurthy, M.R. Chance, E.P. Paschalis, F. Betts, A.L. Boskey, R. Mendelsohn, "In Situ Analysis of Mineral Crystallinity and Environment in Bone using Infrared Microspectroscopy", *Biochim. Biophys. Acta.* 1527 (2000) 11-19.
- [26] G. L. Carr, J. A. Reffner, G.P. Williams, "Performance of an infrared microspectrometer at the NSLS", *Rev. Sci. Instrum.* 66 (1995) 1490-1492.
- [27] J. A. Reffner, P.A. Martoglio, and G.P. Williams, "Fourier transform infrared microscopical analysis with synchrotron radiation: The microscope optics and system performance", *Rev. Sci. Instrum.* 66 (1995) 1298-1302.
- [28] G.L. Carr and G.P. Williams, "Infrared microspectroscopy with synchrotron radiation", *SPIE Conf. Proc.* 3153 (1997) 51-59.
- [29] Z. Zhong, W. Thomlinson, D. Chapman and D. Sayers, "Implementation of Diffraction Enhanced Imaging Experiments: at the NSLS and APS", *Nucl. Instrum. Meth. in Phys. Res. A.* 450 (2000) 556-567.
- [30] Jacobsen, et al., "Diffraction-limited imaging in a scanning transmission X-ray microscope". *Optics Communications* 86 (1991), 351--364.
- [31] W. Yun, et al. « Nanometer focusing of hard x rays by phase zone plates". *Rev. of Sci. Instrum.* 70 (2000), 2238-2241.
- [32] S. Spector, C. Jacobsen, C. and D. Tennant, "Process optimization for production of sub-20 nm soft X-ray zone plates". *Journal of Vacuum Science and Technology B* 15 (1997), 2872—2876.
- [33] C. Jacobsen, G. Flynn, S. Wirick, S. and C. Zimba, "Soft X-ray spectroscopy from image sequences with sub-100 nm spatial resolution". *J. Microscopy* 197 (2000), 173-184.

## 2.4 Nanoscience

### 2.4.1 Overview

Nanoscience is one of the most dynamic and rapidly developing areas of interdisciplinary research. It addresses the unique physical and chemical properties of nanometer-sized (< 100 nm) materials as well as novel phenomena occurring at the nanoscale. It provides a natural link between physical sciences and life sciences, since nanometer length scales also characterize molecular machines and the basic building blocks in living organisms. The excitement in Nanoscience is driven not only by the potential to revolutionize a wide range of scientific and technical fields, but also the possible economic and societal impact. These can be illustrated by the grand challenges identified by the National Nanotechnology Initiative.

- Nanostructured Materials by Design
- Manufacturing at the Nanoscale
- Chemical-Biological-Radiological-Explosive Detection, and Protection
- Nanoscale Instrumentation, and Metrology
- Nano-Electronics, -Photonics, and -Magnetics
- Healthcare, Therapeutics, and Diagnostics
- Efficient Energy Conversion and Storage
- Microcraft and Robotics
- Nanoscale Processes for Environmental Improvement

In order to understand, and eventually design, the properties of materials at the nanoscale, a full complement of materials synthesis, manipulation, characterization, and theory / modeling / simulation tools need to be developed. In the area of characterization, over the last two decades, a wide range of synchrotron radiation based diffraction, scattering, spectroscopy, and imaging tools have been developed for materials research. These tools have played an essential role in our understanding of bulk materials, thin films, surfaces, and interfaces, by providing atomic resolution structures and unique electronic, chemical, and magnetic information that cannot be obtained otherwise.

There is a compelling need to extend the reach of these synchrotron-based tools to the nanoscale to obtain essential information which is either not accessible with, or is complementary to that provided by, scanning probes and electron microscopy. To do so requires the high brightness of NSLS-II. It will enable these techniques to be applied on nanometer length scales by focusing the x-rays down to ~ 10 nm or below, and by the development of novel full-field x-ray imaging techniques. This unprecedented combination will clearly enable completely new experiments. For example, one can imagine performing in-situ experiments on a single nanometer-sized catalyst in actual reaction conditions (described in section 2.9.2.1); or performing x-ray experiments on a single carbon nanotube while electric current is passing through the nanotube (described in section 2.4.2.1).

### 2.4.2 Scientific Challenges and Opportunities

#### 2.4.2.1 Nanoelectronics

Today's microelectronic industry is the result of advances in nanoscale materials research. Gate widths are 45 nm and the equivalent gate oxide thickness is 1.1 to 1.4 nm. The International Technology Roadmap for Semiconductors predicts that gate widths should reach 13 nm and that the gate oxide should reach an equivalent thickness of 0.4 to 0.6 nm in the next decade. However, for many needed device

characteristics, there are no known processes or solutions that will allow us to reach the required dimensions and material properties. As the limits of electronics scaling are pushed further, there are increasingly difficult challenges in silicon technology and an urgent need to develop novel materials with new scaling properties.

For example, as the critical line widths of microelectronics circuits decreased below 100 nm, two new material challenges appeared immediately. First, the feature size became comparable to the size of non-uniformities in polycrystalline materials, which leads to drastic negative effects on device performance due to changes in the material characteristics. Second, the pace of size reduction was reduced (and should reach a limit in the next decade or two), so that size reduction alone is no longer sufficient to maintain the standard rate of improvement that has been observed in past decades (Moore's law).

This led to the introduction of drastic changes in the materials and substrates. After a major research effort, the on-chip interconnections were changed from an Al based metallurgy to a Cu based one. This was shortly followed by an important modification to the original silicon substrate where only a thin semiconductor layer, isolated from the thicker silicon substrate by a buried oxide layer, is used in device fabrication. This technology is known as silicon on insulator (SOI). Recently, to reduce the capacitive coupling between the interconnections and further increase the speed, the standard silicon oxide dielectric was replaced by a low permittivity dielectric.

The NSLS has proven to be an extremely valuable tool for the microelectronics industry in this major materials research effort. Using in-situ X-ray techniques, with particular emphasis on X-ray diffraction, numerous studies crucial to electronics technology have been possible because of the NSLS. Recent examples include studies of copper films [1], silicide formation [2], diffusion barriers [3], contacts to carbon nanotubes [4], and electromigration [5] (Figure 2.4.1). This research addresses fundamental technological questions ranging from conventional silicon CMOS issues such as finding suitable materials for high speed interconnects, materials for contacts, and control of interdiffusion, to the evaluation of new nanoscale materials that will scale beyond the limits of silicon technology.

Finding materials and process solutions to the current and future limitations of CMOS devices will require controlling the properties of materials that are only a few atoms wide. The high brightness of NSLS-II will enable probing material properties on nanometer length scales at higher speed and with increased sensitivity. This will allow us to reach the level of understanding necessary to design the

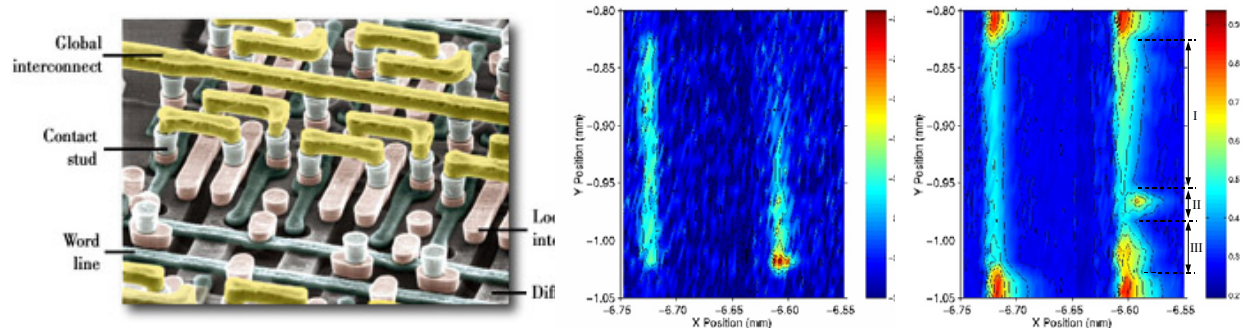


**Figure 2.4.1** (Left) Interconnect in a typical device. To achieve workable devices, a large array of dissimilar materials in very small quantities is used in close proximity. The various processes that are used to deposit these substances can cause very large stresses in very small domains. Such stresses can be due to epitaxial mismatch, phase changes, material densification, and electromigration during device operation. (Right) Real-time in-situ x-ray microbeam diffraction measurements of electromigration-induced Cu redistribution and the concurrent local stress variation in Al (0.25 at. % of Cu) conductor lines. The lines are 10  $\mu\text{m}$  wide, 200  $\mu\text{m}$  long and 0.5  $\mu\text{m}$  thick. (Color) Intensity contours of Cu  $K\alpha$  fluorescence and Si(004) diffraction over an area containing two Al(Cu) wires, with the electromigrated wire on the right and the control sample on the left [5].

properties of materials having nanometer length scales, control the microstructure and texture of very thin films, control strain and heat transfer in complex structures, and control stresses to avoid generation of dislocations. This is essential if the many materials challenges faced by the microelectronics industry in the coming decades are to be overcome. Examples of essential advanced capabilities enabled by the high brightness and flux of NSLS-II include:

- Nanoscale spatial resolution and elemental sensitivity necessary to enable the study of individual nanoscale structures, devices, and defects.
- Time resolved measurements of material properties during increasingly rapid anneal processing, as the microelectronics industry evolves toward ramp rates of thousands of degrees per second.
- Measurements of the evolution of crystallization and texture, including complete texture maps, during phase formations, as well as phase formation mechanisms, such as nucleation, diffusion, and activation energies, in very thin films at very high temperature (or high temperature ramp rates). One could even imagine following the bonding of a fraction of a monolayer through time resolved x-ray spectroscopy.
- Greatly increased throughput, allowing use of combinatorial approaches to material synthesis in the search for new materials.

#### 2.4.2.2 Nanomagnetism

Nanomagnetism, the study and use of nanoscaled magnetic materials, has undergone tremendous growth over the last decade. It is quite broad, and covers topics such as molecular magnets [6], chemically-synthesized nano-magnets [7], biologically-inspired magnetic materials with nano-scale dimensions [8], and Spintronics. Research and development efforts in Spintronics have been particularly intense as a result of the potential impact in information technology [9]. The most notable example is the use of the giant magneto-resistance (GMR) effect, first observed in 1988 [10], in the current generation of read head sensors. This new technology has already made an enormous impact on ultra-high density magnetic storage, resulting in an increase of storage areal density from 1 Gb/in<sup>2</sup> in 1996 to 100 Gb/in<sup>2</sup> in 2003 [11]. Many more applications and novel concepts are being developed, including Magnetic Random Access Memory (MRAM), active Spintronic devices, spin-injection, manipulating spins in semiconductors, and quantum computing.

The key to all current and emerging devices are intricate magnetic nano-structures (Figure 2.4.2). As the dimension of individual magnetic elements shrink below 100 nm, their magnetic microstructures change from simple multiple domain structures to more complex structures, dominated by magnetization vortices or domain walls, and eventually to single domains for elements smaller than 10 nm. As a result, the physics of the switching mechanisms of the elements, the thermal stability of their magnetization, and interactions between elements must all be re-examined. To achieve this will require new synthesis and fabrication processes, new materials with tailored nanoscale properties, and especially new experimental techniques that are sensitive to the magnetization of nanoscale materials.

The high brightness synchrotron radiation of NSLS-II is critical to advancing the field of Nanomagnetism. NSLS-II will make possible chemical element specific magnetic measurements with nanometer spatial resolution and extremely high sensitivity. It will enable study of the magnetic structure and behavior of individual nanomagnetic elements as well as the interactions among collections of elements. The detection of the magnetic structure of buried interfaces and induced moments in non-magnetic metals and semiconductors will become possible. This will be crucial in understanding interfacial magnetic phenomena such as exchange bias, spin-dependent interface scattering, and spin injection. Time-resolved studies with ~10 picosecond resolution will be possible, allowing study of the mechanism of switching dynamics.

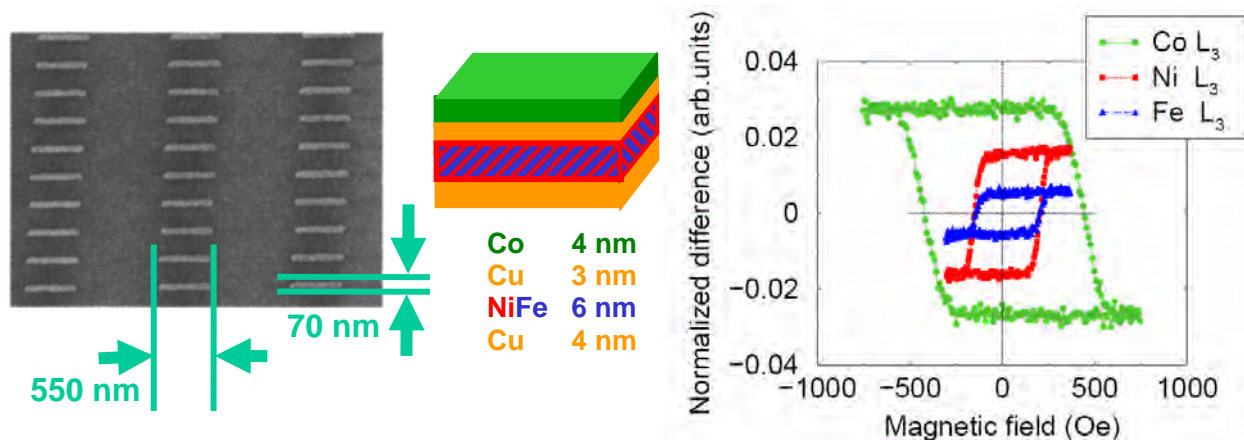


**Figure 2.4.2** Future high-density MRAM devices will require layered magnetic elements with thickness below a few tens of nanometers and in-plane dimensions in the sub-100 nm regime. (Left) SEM image of a large area array of NiFe/Cu/Co pseudo-spin-valves, fabricated using a combination of interference lithography, reactive ion etching, and ion milling. (Center) Schematic of individual spin-valve layer compositions and thicknesses. (Right) Element specific hysteresis loops recorded using x-ray magnetic circular dichroism [12].

### 2.4.2.3 Nanoscale Functional Materials

Advances in organic and inorganic synthetic chemistry are providing an abundance of new nanoscale materials that have promising characteristics for a wide array of applications. Perhaps the best known of these are carbon nanotubes, which have remarkable electrical, optical, and mechanical properties and can be functionalized or combined with other materials for novel applications. Perovskite oxide nanotubes have also been synthesized recently [13]. In bulk form, perovskite oxide materials exhibit a wide variety of useful properties, including high temperature superconductivity, colossal magnetoresistance, and ferroelectricity. It is very likely that these will be modified, perhaps even enhanced, in the nanoscale form of these materials.

However, synthesizing novel nanomaterials is only the first step in making functional devices. New fabrication and characterization techniques are needed in order to understand the effect of structure on the properties of these nanomaterials as well as to integrate them into working devices. For example, carbon nanotubes have the ability to carry current densities of  $10^9$  A/cm<sup>2</sup> [14], much larger than the current densities carried in silicon devices. Moreover, the carbon nanotubes can survive such current densities for a long time, which make them an attractive candidate for future electronic devices. A prototype field effect transistor structure with a single carbon nanotube as the channel material was fabricated recently at the Center for Functional Nanomaterials (CFN) at Brookhaven National Laboratory (Figure 2.4.3). The crucial element in this structure is the fabrication of  $\sim 100$  nm separations between the source and drain electrodes so that the nanotube can be contacted. It would be very important to have the ability to characterize the structure of carbon nanotubes under the operating condition of the device to fully understand its performance. For example, the diameter and/or the length of the nanotube might change under operating condition, and affect the transport properties of the nanotubes.

In another example, very small (70 nm x 70 nm) ferroelectric columns were recently fabricated at the CFN from oxide materials using focused ion beam techniques (Figure 2.4.4). Even in these small dimensions, the piezoelectric response of the 70 nm square island is found to be just as large (0.1 nm/V) as that of the 1 mm square island despite its nanoscale dimensions [15]. This nanometer scaling of the piezoelectric properties of the ferroelectric can be combined with nanolithography [16] and oxide based processing of materials [17] to make new structures with integrated electrodes for applying voltages to nanoscale piezoelectric materials (Figure 2.4.4) and achieve nanometer changes in column height with

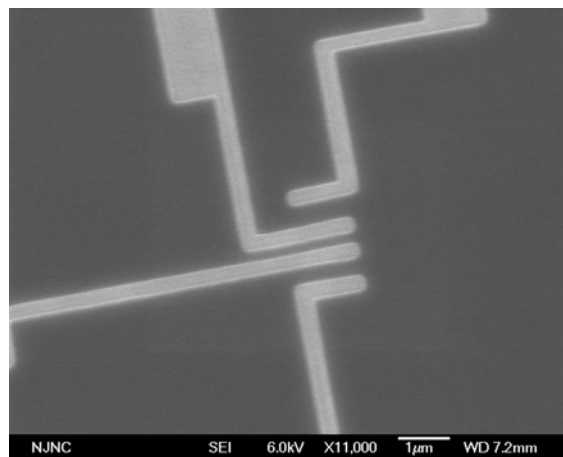
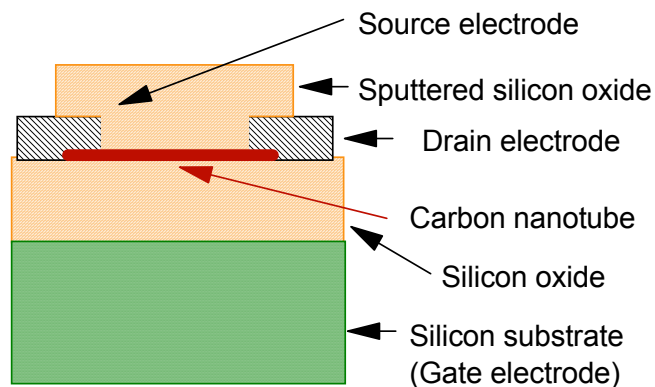


**Figure 2.4.3** (left) Field effect transistor (FET) structure for measuring field dependent electrical transport properties in a single nanotube. The nanotube is dispersed on silicon oxide on a silicon substrate. Metallic source and drain electrodes are evaporated and the tube is optionally encased in a sputtered oxide. (right) Electron micrograph, showing the electrodes with spacings of 300 nm, 100 nm, and 200 nm, which make contact with the nanotube. These lines fan out to larger pads (100  $\mu\text{m}$  x 100  $\mu\text{m}$ ) where probe tips connect the device to test equipment. A one micron scale bar is shown at the bottom.

modest voltages ( $\sim 10$  V). The electrical control of the column height on a nanoscale range allows one to place a material, such as a nanotube or nanowire, on the column through standard shadow evaporation techniques and then apply a strain to it. Again, it would be very important to have the ability to characterize the structure of the nanotubes or nanowire, in particular the lattice spacing, using x-ray scattering or spectroscopy, under real device operating conditions to fully understand its performance.

The high brightness of NSLS-II, combined with enhanced focusing capabilities, will, for the first time, allow x-ray scattering and x-ray spectroscopic experiments to be performed on individual nanotube or nanowire. These two examples also demonstrate the synergy between NSLS-II and the Center for Functional Nanomaterials at Brookhaven National Laboratory.

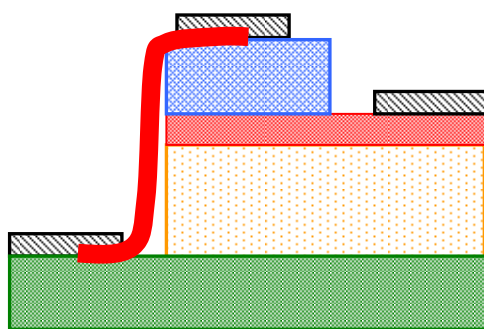
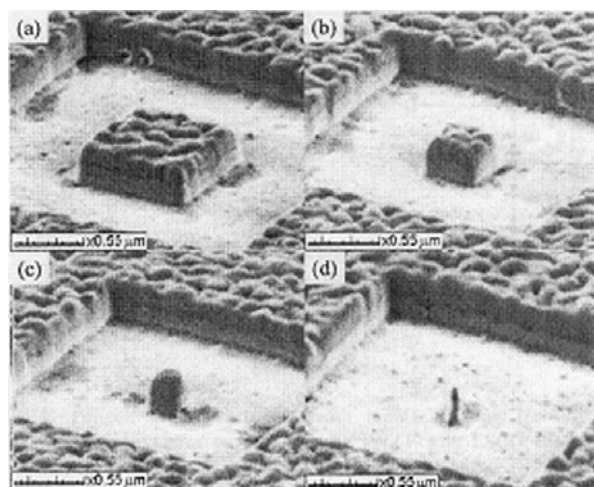


**Figure 2.4.4** (left) Series of focused ion beam fabricated ferroelectric islands ranging from 1  $\mu\text{m}$  x 1  $\mu\text{m}$  base area (a) to 70 nm x 70 nm base area (d). (right) Side view of columnar structure for controllable strain measurements on individual nanotubes (shown in red). The substrate is green, the piezoelectric is orange, the pink layer is a conducting oxide, and the blue layer is a dielectric. Metallic electrodes are gray, allowing for independent application of voltage to the piezoelectric, and simultaneous measurement of the nanotube transport properties.

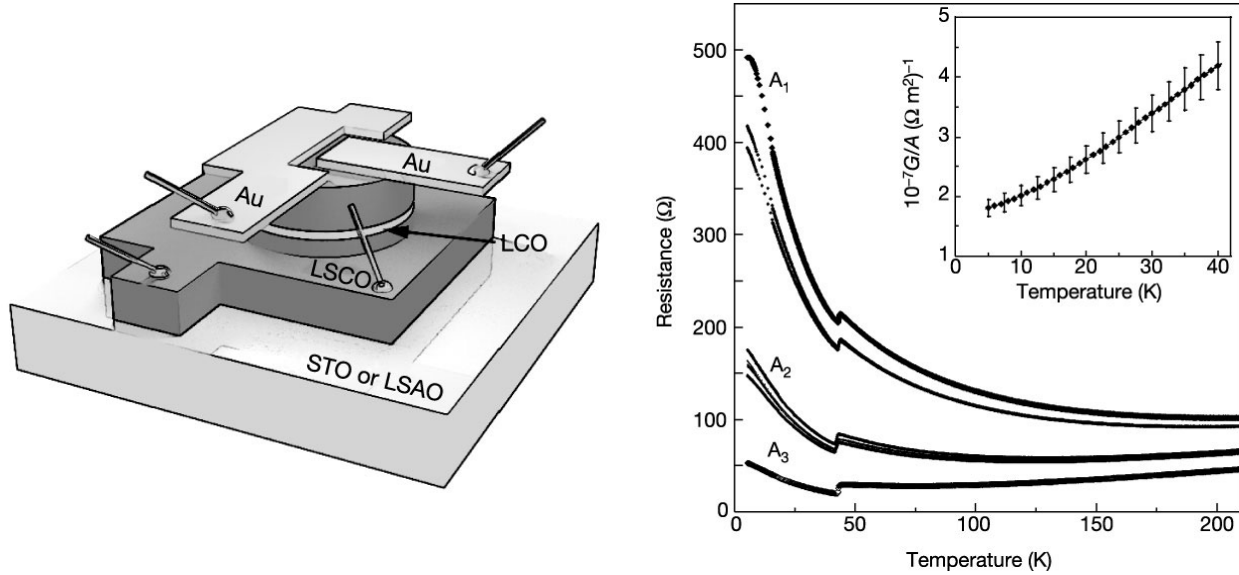


**Figure 2.4.5** The structure of an SIS junction (left) and its transport properties (right). Either  $\text{LaSrAlO}_4$  or  $\text{SrTiO}_3$  were used for the substrate. The top and the bottom high  $T_c$  superconductor electrodes are made of  $\text{LaSrCuO}_4$ . The barrier, only 1 unit cell thick, is made of  $\text{La}_2\text{CuO}_4$ . The mesa diameter was varied from 10 to 80  $\mu\text{m}$  [18].

#### 2.4.2.4 Nanoscale Strongly Correlated Systems

The field of artificially nano-structured strongly correlated electron systems, such as transition metal oxides and rare-earth compounds, is one that is presently untapped but holds great promise. Strongly correlated electron systems are intrinsically inhomogeneous, exhibiting spontaneous charge, spin, and orbital correlations on the length scale of a few to a few tens of nanometers. Understanding and manipulating the interplay of the various phenomena on these length scales are outstanding challenges. It is an area in which NSLS-II will have enormous impact. Precisely engineered nano-structured correlated electron systems could provide critical tests for competing theories. New phenomena might occur by confining these systems in one or more dimensions, or due to the presence of surfaces and interfaces.

Strongly correlated electron systems are also characterized by the presence of a range of ground states in a single specimen, including high- $T_c$  superconductivity, charge and orbital ordering, as well as ferro- and antiferro-magnetism. Thus, small changes in composition, extrinsic applied fields, temperature, or pressure make it possible to switch between many of these ground states, and could lead to dramatic changes in their response for device applications. Understanding the interplay between these ground states, their possible coexistence on nanometer length scales, and the effects of strain and compositional inhomogeneities will be an important key in unlocking the mysteries of strongly correlated systems.

In order to realize this tremendous potential, we need to understand the consequences of spatial confinement for strongly correlated systems, and the interplay between the available ground states and external parameters. New methods for artificially fabricating and controlling structures and correlations in these systems will play an important part in these efforts. For example, advanced molecular beam epitaxy was used to fabricate superconductor-insulator-superconductor junction to test the possible mixing of superconducting phase and antiferromagnetic phase in a high  $T_c$  superconductor (HTS), see Figure 2.4.5. The authors found that even one unit cell thick of the barrier layer, 1.3 nm of  $\text{La}_2\text{CuO}_4$ , is sufficient to completely block the supercurrent, indicating that these two phases do not mix. The ability to fabricate the structure with precise chemical composition and atomically smooth interfaces is critical for the success of the experiment.

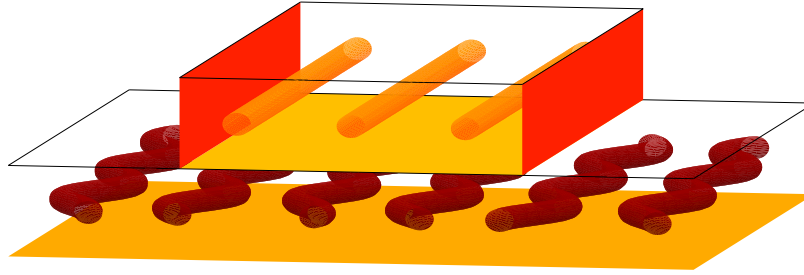


**Figure 2.4.6** Could nano-engineered layer boundaries (indicated in red) induce static stripe order in a material that would otherwise be a metallic stripe liquid?

New nanofabrication techniques will allow lateral nanopatterning of strongly correlated systems with resolution approaching the same length scale as their relevant electronic correlations, i.e., a few nm. This might involve controlling the physical dimensions of the sample, as suggested in Figure 2.4.6, or nanopatterning provided by, for example, variations in the doping levels or some other parameter. A promising approach is shown in Figure 2.4.7, where the polarization of piezoelectrics is used to pull charge into or out of a transition metal oxide. Writing a voltage onto the piezoelectric with an STM tip will allow nanopatterning of the doping levels. Such structures have the potential to enable direct manipulation of the correlations that are responsible for the exotic, and potentially useful, behavior of these systems. Examples of such correlations include the charge and magnetic stripes in the cuprates (1.2 nm periodicity) and the nanoscale charge/orbital correlations responsible for the high resistance phase in the colossal magnetoresistance manganites. This will provide a whole new avenue of research in patterning correlations in strongly correlated systems.

Progress in this field will depend critically on the availability of experimental probes that can quantitatively characterize the structure, strain, composition, and magnetic order with nanometer scale resolution and high sensitivity. With the high brightness of NSLS-II together with advanced x-ray optics,

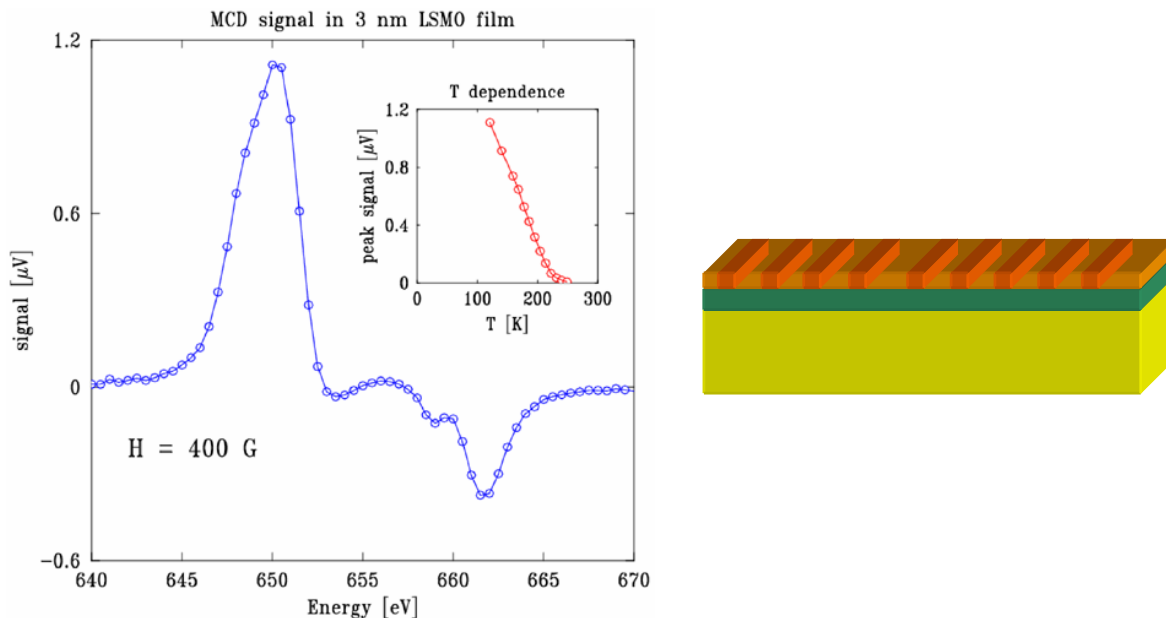


**Figure 2.4.7** XMCD signal measured at NSLS beamline X13B on a 3 nm film of  $\text{La}_{1-x}\text{Sr}_x\text{MnO}_3$  (LSMO). Schematic of the film is shown above with the LSMO layer in green on a STO substrate (yellow). Future experiments will allow the decoration of such films with a piezoelectric, PZT, (orange). Applying a voltage to this PZT (i.e., with an STM tip) “writes” changes of doping into the LSMO below. NSLS-II will enable measurement of the effects of such nano-engineering in manipulating the correlations in strongly correlated systems.

it will be possible to measure charge, magnetic and orbital ordering on a 10 nm length scale and thus to directly probe the effects of applying boundary constraints or patterning induced modulations. This will likely require soft X-ray resonant scattering techniques for which the wavelength is well matched to these length scales and the strong resonances help in providing the required sensitivity. For non-periodic structures, imaging techniques are required, either direct microscopy or inversion of coherent scattering patterns. In both cases, the high-brightness of NSLS-II will play a crucial role in extending the state-of-the-art in this promising new field.

#### **2.4.2.5 Polymer Nanocomposites**

Nanocomposites are a broad family of materials consisting of two or more component phase, at least one of which has dimensions between 1 and 100 nm. Polymer nanocomposites represent a special class of materials, consisting of a soft condensed matter matrix (such as synthetic and natural polymeric or biological templates) and nanoscale inorganic particles. These materials can exhibit markedly improved mechanical and other properties compared to the neat matrix materials or conventional composites, and they may supplant more traditional materials for many applications where high strength-to-weight or high surface-to-weight ratios are required to satisfy extreme conditions.

Recently, polymer nanocomposite materials have attracted a great deal of interest because many new and innovative preparation techniques have been demonstrated that generate novel inorganic/organic hybrid materials. These methods can be divided into several categories: (1) the dispersion of nanometer-scale inorganic particles or molecular clusters (such as layered silicates and carbon nanotubes) in the polymer matrix [19], (2) the growth of inorganic crystals in synthetic nanostructured templates (such as block copolymer/surfactant micelles and structured gels) [20], and (3) the in-situ biomineralization in natural or biomimetic superstructure templates (such as collagen) that can simulate the process of bone growth [21].

The nanoscale structures in polymer nanocomposites can be thoroughly characterized by microscopic means, such as scanning electron microscopy (SEM), transmission electron microscopy (TEM) and atomic force microscopy (AFM). However, the sample preparation schemes for these techniques are often tedious and difficult. In-situ determination of the structure that develops during material preparation and processing, which is critical for optimization of the properties, is particularly challenging using these microscopic techniques.

The high brightness of NSLS-II will enable time-resolved SAXS/WAXD experiments [22] with a small beam size ( $\sim 1 \mu\text{m}$ ) on very small specimens to be carried out. This will significantly advance the development of these unique materials.

#### **2.4.2.6 Biomimetic Devices**

Biomimetic systems that implement self-organization principles encoded in biomolecular structures – with biomacromolecules or synthetic supramolecular complexes as building blocks for a nanoscopic construction set – will play an overwhelmingly important role in the design of functionalized interfaces and the self-assembly of molecular machines. The biochemical, pharmaceutical, sensoric or catalytic properties of such nanoscopic systems integrated in devices are naturally controlled at the molecular level. Utilizing such systems, solid-state surfaces will be functionalized with adsorbed lipid/protein membranes whose optimization requires a deep and detailed comprehension of their structure and dynamics, as well as the molecular-level interactions between their constituents.

The potential of the molecular construction set approach for surface-functionalization is demonstrated in Figure 2.4.8 (left), which shows only a limited set of possibilities on the basis of merely one particular biomacromolecular species, bacterial S-layer proteins (which has been particularly well studied in the recent past). Once the construction of biomimetic membrane structures based on S-layer technology has

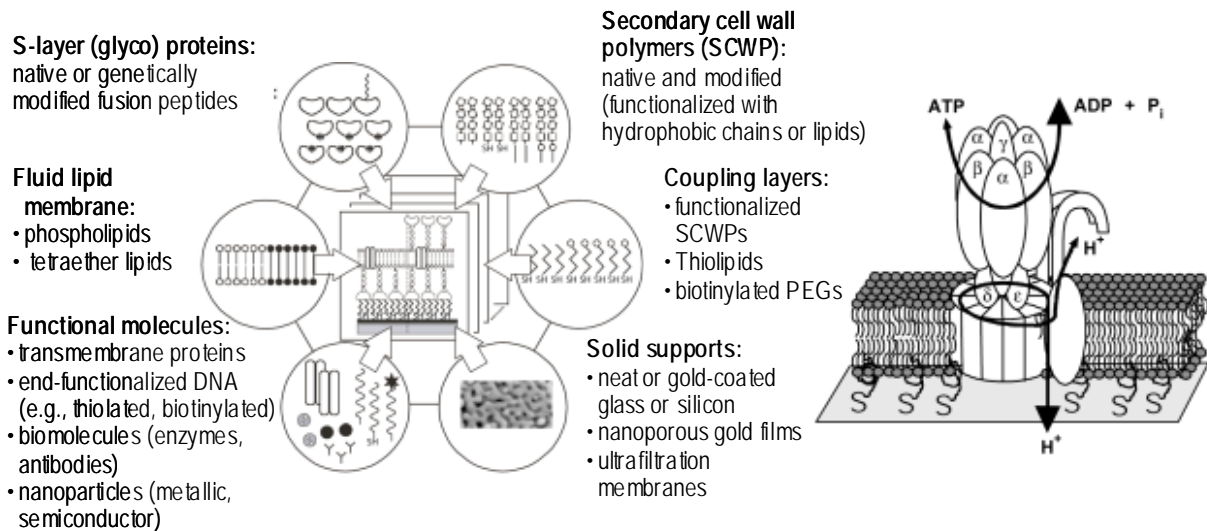


**Figure 2.4.8** A supramolecular construction set for interface functionalization based on bacterial S-layer proteins. A molecular machine based on an ATPase might be reconstructed in an interfacial membrane mimic (right). The ability to implement these concepts requires the high brightness of NSLS-II to enable molecular-level surface characterization (left) [23].

matured, functionalization with membrane proteins as 'molecular machines' is the next logical step, again resulting in a plethora of different possibilities as illustrated in Figure 2.4.8 (right).

The X-ray characterization of a miniscule amount of biomolecules on an infinitely large background of bulk molecules is achieved with well-established techniques in which the excitation of radiation fields is confined at a surface or interface. Challenges in the next decade include the surface-sensitive diffraction from  $\mu\text{m}$ -sized monodomains of 2D protein crystals, as well as their in-situ micro-manipulation and handling; the measurement of form factors of membrane-bound peptides, proteins and supramolecular complexes in a laterally disordered state; determination of the location and spatial distribution of specific atomic constituents via anomalous scattering; or the sequential preparation of complex hierarchical structures as flexible matrices in which biomolecular processes such as signal transduction and amplification may be studied at the molecular length scale. Examples of future device applications may include the electrogenic sequencing of DNA in molecular pores suspended in interface-stabilized membranes or the implementation of stochastic sensors.

To exploit the possibilities in this field, new experimental capabilities are needed that permit surface-sensitive scattering, both in horizontal or vertical scattering geometry (beam directed down toward a horizontal fluid sample surface at a grazing incidence angle), together with micro-focusing of the x-rays for in-plane diffraction from micron sized monodomains of 2D crystals. This capability is also required for surface-sensitive characterization of samples in micro-fluidic applications, e.g. in high-throughput screening. X-rays with energy of 20 keV will permit the characterization of buried interfaces and there is also an urgent need for a tunable, low-energy ( $E = 2 - 8 \text{ keV}$ ), highly monochromatic ( $\Delta E \sim 1 \text{ eV}$ ), high brightness beam in this sample geometry for the species-specific interrogation of surfaces in anomalous scattering experiments. NSLS-II is needed for these experiments.

### 2.4.3 Impact of NSLS-II

The high brightness of NSLS-II will offer the scientific community a unique opportunity to develop a wide range of novel experimental tools for nanoscience and nanotechnology by combining the detailed structural and spectroscopic information obtained from x-rays with nanometer spatial resolution. In this section, several exciting developments are outlined.

### 2.4.3.1 X-Ray Nanoprobes

Synchrotron-based X-ray microprobes, with micron and sub-micron spatial resolution, have proven themselves to be extremely valuable research tools. However, by further improving the spatial resolution to 10 nanometers or below, X-ray nanoprobes will, for the first time, allow the characterization of individual nanoparticles or nanometer-sized grains in complex nanomaterials by their density, elemental composition, elemental oxidation state and spin-state, strain, texture, magnetization, and atomic and electronic structure and dynamics. This exciting prospect has stimulated x-ray optics development efforts worldwide, with four main types of x-ray focusing optics attracting the most attention. All of these approaches require the high brightness of NSLS-II to provide a high flux of x-rays in the resulting small focal spot.

#### 2.4.3.1.1 Reflective Optics

Sub-micron diameter X-ray beams have been made using single hollow tapered capillaries, with the greatest performance obtained using parabolic or ellipsoidal shaped capillaries. A decade ago [24], 50 nm beams at energies of 5-8 keV were produced. Recently, Bergmann et al [25] performed a full wave optics treatment of the confinement of an X-ray beam within narrowly tapered capillaries and suggested that there is a theoretical minimum beam size on the order of 10 nm (FWHM). Although the theoretical minimum is still controversial, there is a general consensus that ~10 nm focus is within reach.

The Kirkpatrick-Baez (KB) mirror system focuses hard X-rays using grazing incidence reflecting surfaces and consists of two orthogonal crossed mirrors. One mirror focuses the X-ray beam in the horizontal plane while the second focuses it in the vertical plane. At the European Synchrotron Radiation Facility (ESRF) on beam line ID19, spot sizes of 100 x 100 nm<sup>2</sup> have been measured at 20.5 keV [26]. There are several promising approaches, including novel polishing techniques and adaptive optics, which suggest that the figure error of these mirrors can be improved to 0.1  $\mu$ rad in the near future. Combining the extremely low figure errors and the superior source properties of NSLS-II, ~10 nm focus with substantial x-ray flux will be possible.

#### 2.4.3.1.2 Refractive Optics

Snigirev, et al [27] have shown that cylindrical and crossed cylindrical X-ray lenses based on X-ray refraction can be made with a focal length in the meter range and a focal spot size in the micrometer range. More recently, parabolic lens have been shown to provide superior focusing. As a consequence of the very weak refraction by matter of hard X-rays one needs to make a stack of many lenses. The focal length of such a parabolic compound refractive lens (PCRL) is given by  $f=R/2N\delta$ , where N is the number of stacked lenses, R the radius of curvature at the apex of the parabola and  $\delta$  the real-part decrement of the index of refraction ( $n=1-\delta-i\beta$ ). The limits on resolution of a PCRL are due to the absorption limited, finite aperture of the lens, and by the surface roughness of each individual lens. Therefore choosing a more transparent material such as lithium, beryllium, boron or diamond should improve the resolution. However, to fabricate lenses with extremely small radii of curvature, nanofabrication techniques, such as electron-beam lithography and deep trench reactive ion etching, need to be used. Schroer et al [28] demonstrated that horizontal and vertical FWHM beam sizes of 380 nm and 210 nm, respectively, with a parabolic refractive lens made of silicon. Extrapolations using a Be lens suggest that a lateral size of 70 nm x 70 nm could be obtained.

#### 2.4.3.1.3 Diffractive Optics

In the soft X-ray spectral region zone plates with a focal spot size close to 20 nm are under development using electron-beam lithography fabrication techniques. Figure 2.4.9 shows a SEM image of a soft x-ray zone plate fabricated through collaboration between Christopher Jabobsen (SUNYSB and

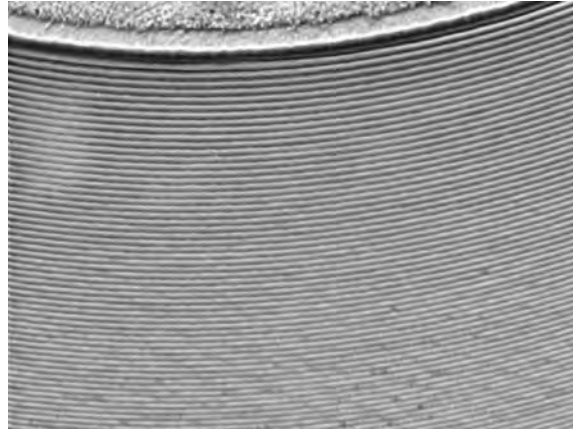


**Figure 2.4.9** *Soft X-ray zone plate.*

BNL/CFN) and Don Tennant (Lucent/NJNC). For hard X-ray applications, Xradia, a new Silicon Valley Start-up, has developed a technology to provide zone plates that currently achieve a focus of 50 nm. We anticipate significant improvement in this technology in the near future with the availability to researchers of new advanced electron lithography facilities through DOE funded nanoscience centers, such as BNL CFN. With these advances, sub-10 nm focus beam size will be achieved by using higher orders of these zone-plates.

#### 2.4.3.1.4 Hybrid Optics

One way around the limited aperture of purely refractive optic is to fabricate a hybrid optic that one can think of as zone plate with the analog profile of a refractive lens. By choosing to work at a fixed wavelength, and removing material that contributes to multiples of  $2\pi$  phase shifts while maintaining the lens shape, the optical focusing properties of the lens are maintained. In exchange for working at a fixed wavelength, absorption is no longer a limitation on the lens aperture, and hence no longer a constraint on the lens resolution. Using the e-beam and etching facilities of Lucent/NJNC, Evans-Lutterodt, et al [29]

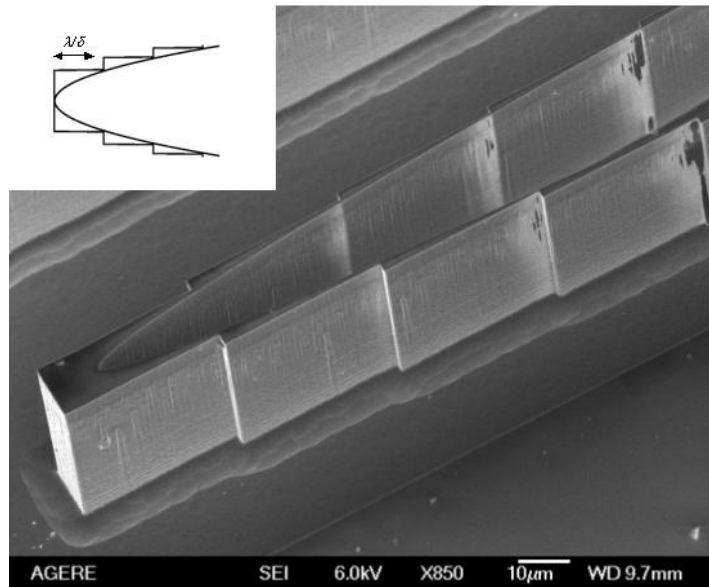


**Figure 2.4.10** *Single element kinoform lens with elliptical profile for 12 keV X-rays. Steps are seen where materials was removed which originally contributed to  $2\pi$  phase-shifts [28].*

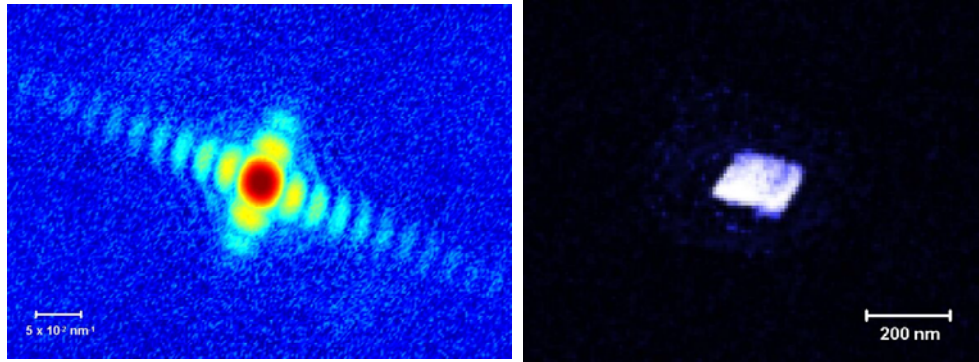


**Figure 2.4.11** *Left -- CXD diffraction pattern of a 160 nm Ag nanocube. The experiments were carried out at the ID-34-C beamline at the APS. Right -- Image of the reconstructed nanocrystal obtained from the diffraction pattern using a variant of Fienup's hybrid input-output inversion algorithm [33].*

recently fabricated a single element kinoform lens in silicon with an elliptical profile for 12 keV X-rays (Figure 2.4.10). This novel approach holds promising for providing sub-10 nm X-ray focusing.

### 2.4.3.2 Full-field Imaging

With NSLS-II, X-ray imaging with nanometer spatial resolution can be achieved straightforwardly by scanning the sample under the nanometer-sized x-ray probes outlined in the previous section. In addition, there are two classes of full-field imaging techniques that show great promise to provide sub-10 nm spatial resolution. Full-field imaging techniques also offer researchers the opportunity to follow fast dynamic processes in time-resolved imaging experiments.

#### 2.4.3.2.1 Diffraction Imaging

It was first pointed out by Sayre in 1980 that with the advent of synchrotron radiation sources, it might be possible to sample the continuous diffraction pattern of non-crystalline specimens to provide the oversampling necessary for solving the phase problem [30]. After two decades of development, Maio, Charalambous, Kirz and Sayre recently succeeded in recording and reconstructing the diffraction pattern of an artificial microstructure with 75 nm resolution [31]. This pioneering work was followed by a demonstration of three-dimensional imaging of Ag and Au nano-crystals using hard X-rays by Robinson et al [32], where subtle internal structure was revealed (Figure 2.4.11).

Since this is diffraction-based lensless imaging, the ultimate achievable resolution does not depend upon developments in optics. The highest resolution achieved to date is already 8 nm in 2D and 50 nm in 3D [34]. For non-biological samples, where radiation damage is not a concern, 2-4 nm resolution for 3D samples should be achievable with NSLS-II. It is also possible to combine this technique with chemical and magnetic contrast unique to x-rays to provide 2D or 3D chemical and magnetic imaging with similar resolution [35].

#### 2.4.3.2.2 Low Energy Electron and Photoelectron Microscopy

Synchrotron-based Low-Energy Electron Microscopy and Photoelectron Emission Microscopy (LEEM/PEEM) generates high image contrast between sample regions having different chemical composition and/or atomic order in the topmost atomic layers (Figure 2.4.12). In LEEM mode, the imaging contrast is provided by the interaction and diffraction properties of the low energy electrons (0 – 100 eV) with the surface. In this energy range, the technique is highly sensitive to the surface crystal structure and surface morphology. Furthermore, with the use of spin-polarized electrons, magnetic domain imaging can be achieved. In the PEEM mode, secondary electrons or photoelectrons are imaged

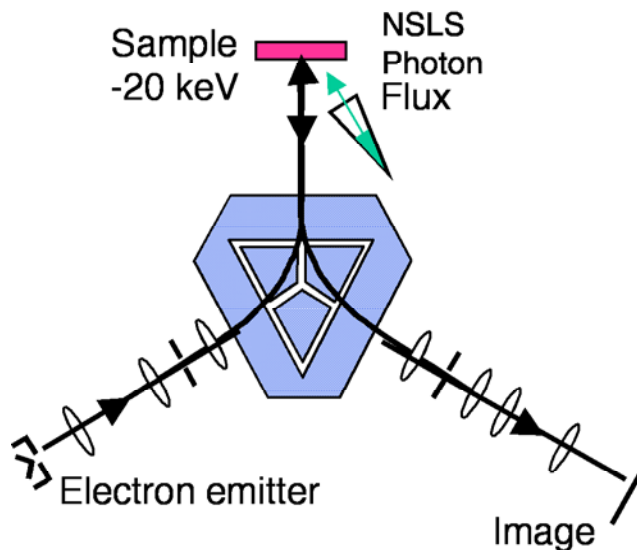


**Figure 2.4.12** Schematic illustration of low-energy-electron microscope and photoelectron emission microscope (LEEM/PEEM). Images are formed using electrons reflected from the surface. Contrast comes from surface morphology, crystal structure, and chemical composition.

in a variety of chemically sensitive modes. It is a uniquely versatile tool with the potential to provide an unprecedented combination of spatial ( $\sim 10$  nm laterally and atomic vertically), temporal ( $\sim 10$  msec), structural (short range ordering or amorphous), and compositional (element and oxidation state) information. It can be designed to image at variable temperatures (170 to 1870 K) and during processes such as material deposition and gas phase chemical reactions. As a result, it can revolutionize our understanding of problems as diverse as surface-assembly, in situ pattern formation, and catalysis. The versatility of LEEM/PEEM is especially crucial for catalysis, since the complex nature of catalytic systems demands simultaneous acquisition of data characterizing the catalyst and the catalytic process in a complex multi-parameter space.

At present there is only one working synchrotron-based LEEM/PEEM instrument in the world, located at ELETRA in Trieste, Italy. Aberration corrected instruments are being developed at BESSY-II in Berlin, Germany and at the present NSLS. The ultra-high brightness of NSLS-II is crucial if the instrument is to achieve its ultimate spatial and temporal resolution as well as take full advantage of the chemical information available.

## REFERENCES

- [1] C. Detavernier et al., *J. Appl. Phys.* **94**, 2874 (2003).
- [2] C. Detavernier, C. Lavoie, and F.M. d'Heurle, *J. Appl. Phys.* **93**, 2510 (2003).
- [3] H. Kim et al., *J. Vac. Sci. Technol. B* **20**, 1321 (2002).
- [4] R. Martel et al., *Phys. Rev. Lett.* **87**, 256805 (2001).
- [5] P.C. Wang, I. C. Noyan, S. K. Kaldor, J. L. Jordan-Sweet, E. G. Liniger, and C.-K. Hu, *Appl. Phys. Lett.*, **78**, 2712 (2001).
- [6] A. Caneschi, D. Gatteschi, C. Sangregorio, R. Sessoli, L. Sorace, A. Cornia, M.A. Novak, C. Paulsen, W. Wernsdorfer, *Journal of Magnetism and Magnetic Materials* **200**, 182 (1999).
- [7] S. Sun, C.B. Murray, D. Weller, L. Folks, A. Moser, *Science* **287**, 1989 (2000).
- [8] T. Douglas and M. Young, *Advanced Materials*, **11**, 679 (1999).

- [9] “Spintronic” stands for spin transport electronics. It was first introduced in the mid-1990s for a Defense Advanced Research Projects Agency (DARPA) program, directed to the development of advanced magnetic memory and sensors.
- [10] M. Baibich, J. Broto, A. Fert, F. Nguyen Van Dau and F. Petroff, *Phys. Rev. Lett.*, **61**, 2472 (1988).
- [11] S.Parkin, X.Jiang, C. Kaiser, A. Panchula, K. Roche, and M. Samant, *Proceeding of IEEE*, **91**, 661 (2003).
- [12] F. J. Castaño, Y. Hao, S. Haratani, C. A. Ross, B. Vögeli, Henry I. Smith, C. Sánchez-Hanke, C.-C. Kao, X. Zhu, and P. Grütter, *J. Appl. Phys.* **93**, 7927 (2003).
- [13] Yuanbing Mao, Sarbajit Banerjee, and Stanislaus S. Wong, *Chem. Commun.*, (3), 408-409 (2003).
- [14] Ph. Avouris, *Acct. Chem. Res.* **35**, 1026 (2002).
- [15] C. Ganpule et al., *Appl. Phys. Lett.* **75**, 3874 (1999).
- [16] Nanofabrication, specifically electron-beam lithography, is available at Brookhaven National Lab through the Center of Functional Nanomaterials
- [17] A.G. Schrott, J.A. Misewich, V. Nagarajan, and R. Ramesh, *Appl. Phys. Lett.* **82**, 4770 (2003)
- [18] I. Bozovic, G. Logvenov, M.A. Verhoeven, P. Caputo, E. Goldobin, and T.H. Geballe, *Nature*, **422**, 873 (2003).
- [19] D. R. Paul, *Proceedings of the American Society for Composites, Technical Conference*, 227 (2001).
- [20] H. Coelfen, M. Antonietti, *Langmuir*, **14**, 582 (1998).
- [21] J. D. Hartgerink, E. Beniash, S. I. Stupp, *Science* **294**, 1684 (2001).
- [22] B. Chu, B. S. Hsiao, *Chemical Reviews (J. Michl, Ed.)* **101**, 1727 (2001).
- [23] W. Knoll, C. W. Frank, C. Heibel, R. Naumann, A. Offenhäusser, J. Rühle, E. K. Schmidt, W. W. Shen and A. Sinner, *Rev. Molec. Biotechn.*, **74**, 137 (2000).
- [24] D.H. Bilderback, S.A. Hoffman, P.J. Thiel, *Synchrotron radiation News* **7**, 27 (1994)
- [25] C. Bergmann, H. Keymeulen, J.F. van der Veen *PRL* **91**, 204801 (2003)
- [26] *ESRF Newsletter* **37**, page 20, July 2003
- [27] A. Snigirev, V. Kohn, I. Snigieva, and B. Lengeler *Nature(London)* **384**, 49 (1996)
- [28] C.G Schroer et al *Appl. Phys Lett.* **82(9)**, 1485 (2003)
- [29] K. Evans-Lutterodt, J.M Ablett, A. Stein, C. Kao, D.M. Tennant, F. Klemens, A. Taylor, P.L. Gammel, H. Huggins, S. Ustin, G. Bogart, L. Ocola *Optics Express* **11** (8), 919-926 (2003)
- [30] D. Sayre, “Prospects for long-wavelength X-ray microscopy and diffraction”, in *Imaging Processes and Coherence in Physics*, M. Schlenker, Editor. 1980: Berlin. p. 229--235.
- [31] J. Miao, C. Charalambous, J. Kirz and D. Sayre, *Nature* **400**, 342 (1999)
- [32] G. J. Williams, M.A. Pfeifer, I.A. Vartanyants, I.K. Robinson, *Phys. Rev. Lett.* **90**, 175501 (2003)
- [33] J. R. Fienup, *Applied Optics* **21**, 2758 (1982).
- [34] J. Miao, T. Ishikawa, B. Johnson, and B.L. E. H. Anderson, K. O. Hodgson, *Phys. Rev. Letters*, **89**, 088303 (2002).
- [35] T.O. Mentess, C. Sanchez-Hanke, and C.C. Kao, *J. Synch. Rad.*, **9**, 90-95 (2002)

## 2.5 Soft Matter and Biomaterials

### 2.5.1 Overview

Soft matter, such as polymers, complex-fluids, liquid-crystals, and colloids, are materials that readily respond to perturbations, from mechanical stress to applied electric and magnetic fields, can be solution-processed utilizing self-assembly into thin, conformal coatings, and form nanoscale ordered structures that can serve as templates or porous membranes. In the related and increasingly important field of biomaterials, the hard tissues (composites of biopolymers and minerals) created by living organisms provide structural support, protective shells, magnetic sensing, and chemical reservoirs that store nutrient. These serve as an inspiration to the design of new functional materials and synthetic biocompatible materials that either do not stimulate host reaction (e.g. in the case of implants) or can trigger a specific cellular reaction (e.g. controlled drug delivery systems). Both classes of materials have hierarchical structures, where the molecular building blocks assemble into supramolecular structures, which in turn form microscopic structures with multiple length scales from a few nanometers to tens of microns.

The study of soft materials has been one of the most rapidly developing areas of condensed matter science. Despite the diversity of their constituents, they share many of the same physical and chemical features: a large number of internal degrees of freedom, relatively weak interactions between the structural elements, hydrocarbon-based building blocks, and substantial entropic contribution to the free energy. These properties give rise to a broad multiplicity of forms, large thermal fluctuations, sensitivity of the equilibrium configuration to external boundary conditions, macroscopic “softness” and different metastable states.

Soft materials are opening exciting new directions in the fundamental physics and chemistry of materials, and provide a wide variety of novel technological applications, such as flexible displays, photonic devices, information storage media, anisotropic properties, biomedical materials, drug delivery, electronics and optics, membranes, porous materials, superior blends, and nanostructured templates. The challenges in soft materials studies include incorporating multiple components to tailor properties, overcoming thermodynamic immiscibility, tuning dimensions from nanometers to microns, utilizing both equilibrium and metastable structures, controlling interfacial properties, prescribing a distribution of functionality, and utilizing self assembly to create hierarchical structures.

The increasing sophistication and successes achieved in soft materials research in recent years promises dramatic progress in the decade ahead. However, progress will require currently unavailable enhanced structural analysis capabilities, the need for which is being felt even now. Application of these materials requires understanding of their kinetics, which often plays a determinate role in how they form.

The ultra-high brightness of NSLS-II is required to effectively address many of these challenges. The high brightness and well collimated beam is absolutely required for measuring the scattering from ultra-small samples such as those in confined geometries and from materials with large intrinsic length scales (0.1 to 1000 nm); for imaging of microstructures especially for systems containing weak scattering contrast or at the initial stages of different forms of phase transitions; for measuring fast processing kinetics, typically on time scales from seconds to microseconds; and for determining the structural evolution in relevant processing conditions, such as shear and elongation flow. The proposed SAXS, USAXS, coherent and surface scattering beamlines at NSLS-II, spanning the nanometer through micron scales (i.e., overlapping the optical regime), and enabling dynamic scattering and effective microscopy, will provide essential tools in the study of soft matter and biomaterials. The high brightness and flux of NSLS-II is absolutely essential to achieve a fundamental understanding of the behavior of these highly complex and technologically important systems.

## 2.5.2 Scientific Challenges and Opportunities

The research opportunities that NSLS-II will open to the soft matter and biomaterials research communities are described in this section. We first describe scientific opportunities in polymers. Because polymer films are self-supporting and robust, applications abound. We next describe the scientific opportunities in materials based on colloids, liquid-crystals and related composite soft systems that exhibit the anisotropic properties of a solid while retaining the processing advantages of a fluid. We conclude by describing the exciting scientific opportunities that result from using biosynthetic techniques to engineer new organic-inorganic complexes that exhibit tailored functionality. The complexity of the processing intermediates and final composite structures, often in the form of thin films or fibers with only partial order, provide a considerable challenge for achieving the X-ray characterization crucial for technological advances.

### 2.5.2.1 Hierarchical Structures in Polymers

Many synthetic block copolymers have distinct hierarchical structures. The phase behavior in these structures is of great scientific and technological interests. For example, an effective way to construct well-defined and uniformly oriented nano-environments uses diblock copolymers as templates. Diblock copolymers are well known to form various ordered phase morphologies, such as lamellae, double gyroid, cylinders and spheres, on a length scale of a few tens of nanometers. These ordered structures are formed because of microphase separation of the dissimilar components below the order-disorder transition temperature ( $T_{ODT}$ ) and they are well suited as the template to provide the nano-scale confinement.

For example, recent studies have been carried out at the NSLS based on a series of poly(ethylene oxide)-b-polystyrene (PEO-b-PS) diblock copolymers with different molecular weights and different compositions as the confinement templates (Figure 2.5.1) [1]. After the PS component was vitrified, the subsequent crystallization of PEO was completely confined within the ordered nano-environments. Using simultaneously time-resolved synchrotron SAXS and WAXD techniques, path-dependent PEO crystal orientations with respect to the lamellar surface normal were observed on the oscillating shear-aligned sample and the lamellar morphology of the block copolymer was found to be perfectly aligned with their lamellar layers parallel to the shear plane.

This phenomenon has also been observed in other nano-confined environments and raises important questions. What is the formation mechanism of mechanical shear to generate different phase morphology

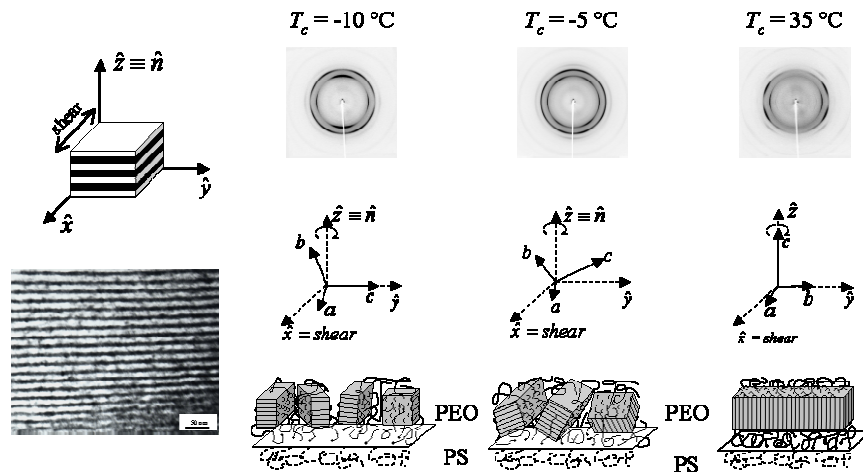


**Figure 2.5.1** PEO blocks crystallized in a lamellar confined environment. At the low  $T_c$ , the  $c$ -axis of the crystals are perpendicular to the  $\hat{n}$ . With increasing the  $T_c$ , The  $c$ -axis is tilted with respect to the  $\hat{n}$ . At the high  $T_c$ , the  $c$ -axis of the crystals are parallel to the  $\hat{n}$ .

on the nanometer scale? Why do the crystals formed in these nano-confined environments behave so differently from those crystallized in unconfined bulk samples? Solving these questions is practically important since these nano-phase structures are potentially useful in photonic band gap materials.

The high brightness SAXS facility at NSLS-II will be ideal for investigation of these and related important fundamental questions.

### **2.5.2.2 Complex Phases in Block Polymers**

Multiblock copolymers, such as ABC triblocks, offer unprecedented opportunities for preparing nanostructured materials with high degrees of internal organization. For example, recent experiments have shown that small variations in composition (e.g., by homopolymer dilution) can provide access to several three-dimensionally tri-continuous network phases from a single parent polymer. Such structures provide a means to incorporate several different functionalities into one material. For example, in ionic conductivity applications, such as fuel cell membranes, one block could provide mechanical integrity, another the transport pathway, and the third a regulatory or buffering role. However, with increasing complexity in both the ingredient molecules and the resulting phase structures, the challenge of morphological characterization becomes acute. Even in "pristine" ABC copolymers, for example, it has sometimes taken 2-3 years of combined painstaking scattering, microscopy, and calculation just to be able to assign the correct space group! Over 30 different structures have already been identified for ABC copolymers, with no obvious limit in sight, so "process of elimination" is not a viable strategy. Add in further ingredients, the inevitable kinetic effects, spatial heterogeneity, distorted unit cells due to processing or previous stress, etc., and it becomes clear that progress will be painstakingly slow without substantial advances in technique.

Although theory and microscopy will continue to play key roles, the SAXS facilities proposed at NSLS-II will offer the greatest potential for significant improvements. In particular, the ability to gain high signal-to-noise scattering from ever-smaller sample volumes will lead to the ability to access single crystal patterns from macroscopically polydomain samples. Furthermore, it will be possible to gain rapid information on sample structural uniformity/heterogeneity and the presence of defects, as well as response to external fields (especially flow); both will play key roles in the future applicability of such complex phases.

### **2.5.2.3 Liquid Crystals and Colloids**

The self-assembly of nanometer sized organic and inorganic molecules can lead to exotic hierarchical structures on very long length scales, often extending to thousands of times the molecular size (Figure 2.5.2). A variety of methods for assembling colloidal nanoparticles, phase segregating composites, or liquid crystals into mesoscopic two and three-dimensional structures are producing an exciting new class of photonic bandgap-based optical materials. Examples include Bragg switches, or self-organized organic nanostructures with controlled optoelectronic properties [2], and a variety of self-assembly schemes that are being explored [3] to produce tailored, defect-free materials. Liquid crystals provide an ever-broadening palate of fascinating systems that self-organize on multiple length scales, serving for example as templates for making novel mesoporous catalysts [4], and spontaneously organizing nanoporous structural elements over micron length scales, as in the twist grain boundary phases [5], and polarization-modulated smectics [6]. Exploring the meso/micro range is also of crucial importance for understanding and controlling "disordered" behavior, such as the flocculation of colloids, the gel forming process exploited in manufacturing such products as diverse as cheese, cosmetics, and ceramics.

To effectively study these and other such hierarchical structures, it will be necessary to integrate scattering and multiple microscopies into beamline instrumentation in completely novel ways. Microprobe SAXS, for which the high brightness of NSLS-II is essential, will be required for decisive studies. The study of the delicate intrinsic local structure in such systems, crucial to understanding their most basic properties, such as elasticity, will benefit from fast ultra-high resolution dynamic SAXS, as

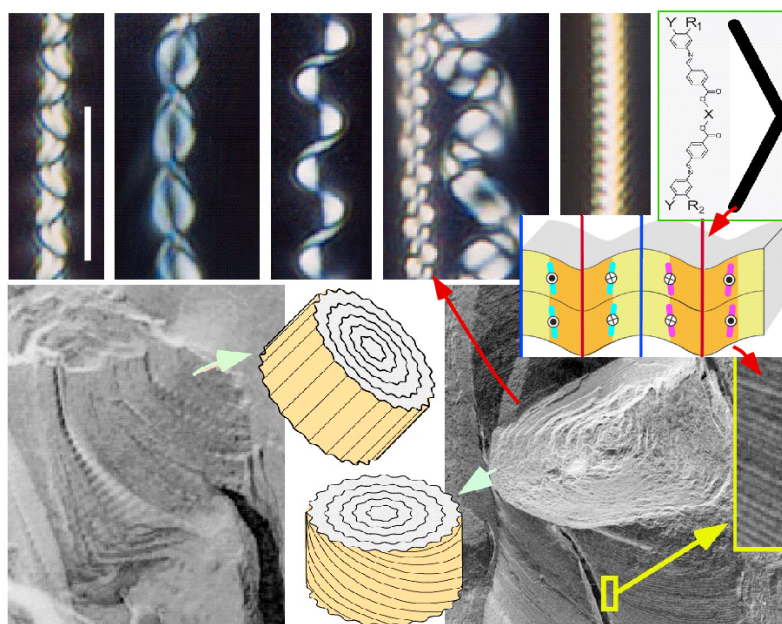


**Figure 2.5.2** Hierarchical filamentary liquid crystal structures formed by the smectic layering of bent-core molecules. The layers are periodically undulated on the 100 nm length scale (yellow box) by polarization modulation and the resulting two dimensional ordering forms micron scale helical filaments.

well as the ability to carry out X-ray PCS on weak scatterers. The rapidly developing research pursuing the use of hierarchical colloidal and liquid crystal organization employing biomolecular components, such as complexes of DNA with cationic lipids [7] or dendrimers [8], will have similar instrumentation needs.

#### 2.5.2.4 Liquid and Soft Matter in Confinement

An important and challenging problem in interfacial science is the behavior of liquids in the vicinity of both hard and soft walls, specifically how the structural properties differ from that of the bulk liquid. For molecular liquids and liquid metal, the broken symmetry imposed by the wall modifies the structure of liquid relative to the underlying bulk [9-11] and in the case of liquid metals gives rise to surface layering [9, 10]. Further, in binary or tertiary liquids, one component may preferentially wet the wall while other components are repelled. Understanding the nanoscale behavior of liquid interfaces is relevant to many fields of science and technology, including sensors, biological interfaces, liquid crystal displays, electrochemistry, and wetting phenomena.

Technical advances, such as very thin, submicron liquid channel cells [11, 12] and the use of high-energy (20 keV), penetrating X-rays allows one the possibility of exploring a new class of problems by reducing the otherwise strong diffuse scattering signal. Sinha and coworkers have demonstrated the technique at the APS for the organic liquid, octamethylcyclotetrasiloxane under confinement [12]. For this system, they have shown that the gap and the number of molecular layers decreased in a quantized fashion with increasing pressure, from a gap size of 25.2 Å containing three close-packed layers to a gap size of 19.9 Å at the highest pressures containing two non-close-packed layers.

Using this approach, it may be possible to study the structure of single membrane bilayers in-vitro. Such studies will greatly benefit from the ultra-focused, micron sized beams provided at NSLS-II. A significant biological problem that would benefit from this advance is that of cholesterol rafts and the micro-phase separation of membrane proteins that occurs at the interface of cells due to the rafts formation. Using the confined geometry it should be possible to study the detailed structure and composition of individual rafts within the biomembrane.

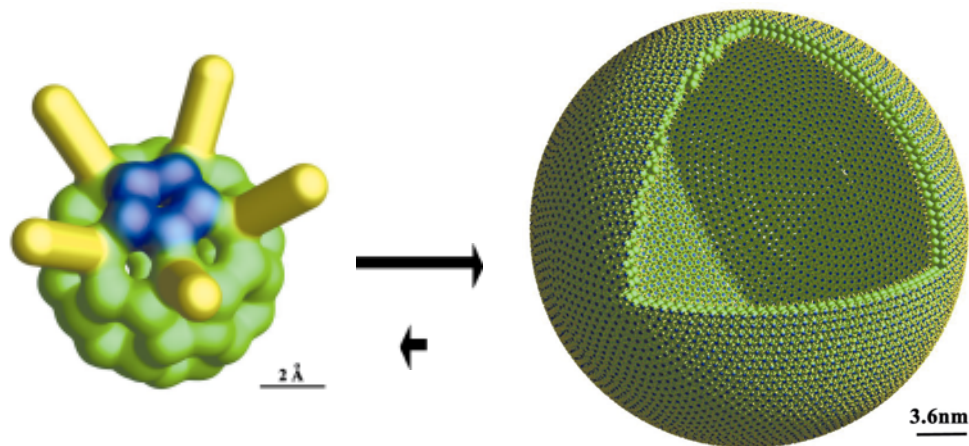


**Figure 2.5.3** Left: Polymer-Surfactant Complexes (PSC's) such as this  $\text{Ph}_5\text{C}_{60}^-$  molecule can form highly ordered superassemblies due to the interplay of electrostatic and hydrophobic interactions, which can be fine-tuned by the degree of hydration. The phenyl group, represented as a stick, reduces the constraint on the inner bilayer curvature. Right: Simulated image of a spherical bilayer vesicle of fullerene surfactants  $\text{Ph}_5\text{C}_{60}^- \text{K}^+$ , with a cutaway view showing the inner layer packing.

### 2.5.2.5 Complex Solutions

Polyelectrolyte-surfactant complexes (PSCs) are microphase-separated systems containing hydrophilic domains (surfactant head groups and polyelectrolyte charges) and hydrophobic regions (surfactant tails and hydrophobic parts of the polyelectrolyte) [13]. The interactions of polyelectrolytes with oppositely charged surfactants are quite strong and can generate complexes having highly ordered structures. The two most important driving forces for the self-assembly of surfactant molecules in PSCs are the electrostatic interactions between the charged components and the hydrophobic interactions between the polymer backbone and the alkyl chains of the surfactant. The well-defined supramolecular structures have unusual properties that may find application in gene therapy, cosmetics, food, paints, coatings, enhanced oil recovery, and other technologies.

For example, as shown in Figure 2.5.3, a PSC in the form of a modified fullerene molecule has recently been described:  $\text{Ph}_5\text{C}_{60}^- \text{K}^+$ , with Ph denoting the phenyl group, self-assembles into bilayer vesicles, with a radius of 17 nm and an aggregation number of close to thirteen thousand modified fullerene molecules [14]. These well-defined and relatively non-toxic fullerene-based surfactants have a distinct feature, i.e., instead of flexible hydrophobic chain(s), the  $\text{Ph}_5\text{C}_{60}^-$ , or the hydrophobic part of the “surfactant”, is a rigid hydrophobic ball. Furthermore, organic chemistry permits rational design of the chemical nature of these functionalized fullerenes, resulting in the establishment of a new class of surfactant systems. These differ not only in hydrophobicity and geometrical constraints (size and shape) from existing surfactants, but can also control the charge (cationic, anionic, or neutral; univalent or multivalent) as well as the spacing between the charges and the hydrophobic  $\text{C}_{60}$  ball.

Improved SAXS capabilities, as promised by NSLS-II, enabling higher intensities measured in small detection volumes, are required for further progress in properly characterizing newly developed PSCs.

### 2.5.2.6 Hierarchical Biological Systems

Understanding the structure of hierarchical biological systems is not only of fundamental importance but can also have substantial medical consequences. Biomineralization processes lead to particularly interesting hierarchical biological systems that can be considered as composite materials consisting of an

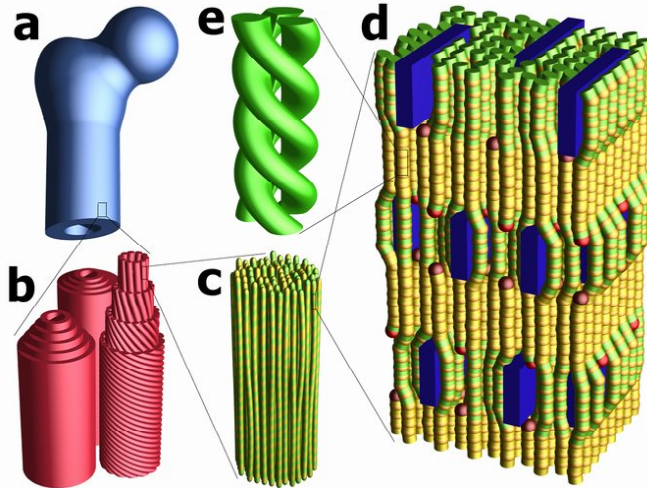


**Figure 2.5.4** *Schematic representation of the hierarchical structures in bone: (a) Macroscopic bone. (b) Osteons (~100 $\mu$ m) with circular arrangements of differently oriented collagen fibers. (c) Collagen fiber (~5 $\mu$ m lateral) consisting of bundles of collagen fibrils (~500nm lat.). (d) Striped collagen fibril (period ~68nm longitudinal) consisting of a staggered arrangement of collagen molecules (~1.5nm lat.) with embedded mineral crystals (~ 2...20 nm lat., 30nm long.). (e) Collagen molecule triple helix.*

organic matrix embedding a nanoscopically dispersed inorganic phase. The mechanical properties, especially the toughness, of such natural composite materials are still unparalleled in the synthetic world.

An important example is given by bone (Figure 2.5.4). The central challenges are to understand the dynamics of the mineralization process, from nucleation to the final stages of mineralization, the localization, size, shape and orientation of mineral crystals, as well as their effect on the order of the collagen matrix, the redissolution of mineral crystals when acting as a calcium ion reservoir, intrafibril versus interfibril mineralization; and the role of non-collagenous proteins.

Synchrotron techniques such as wide-angle scattering, small-angle scattering, and ultra-small-angle scattering, can contribute significantly to the structural analysis on several of the length scales over which these hierarchical structures extend. Imaging techniques and micro-focus scanning probes can be used to investigate structural heterogeneities on even larger length scales. The combination of poor order with poor contrast and strong background scattering that characterizes these materials, makes a highly brilliant source necessary, especially when employing multi-wavelength measurements for anomalous scattering studies. Studying the local dynamics of biomineralization will be photon flux driven and will require the development of a beamline that can span USAXS to WAXS measurements, using a micron size parallel beam to scan across the samples. NSLS-II will make such measurements possible.

### 2.5.2.7 Signal Transduction, Neuron Plasticity and Structural Changes in Membranes

Biological membranes contain rafts of proteins that act as critical elements in many biological processes. For example, in bacteria such as *E. coli* there exists a “nanobrain” consisting of a 100 nm x 100 nm ordered raft containing 5 different chemoreceptor proteins. Due to chemical-mechanical changes in the receptor structure, binding of a signaling agent to one receptor changes the response of adjacent receptors. An even more important example is the puzzle of neuron plasticity. Neuronal plasticity is the activity-dependent structural and functional changes of dendrites, axons, and synapses that plays an important role in the brain function under both physiological and pathological conditions. One of the great challenges is to be able to probe the local protein structural organization and changes in such signaling complexes. A combination of X-ray microprobe scattering coupled with labeling of the receptors and proteins using high-Z multivalent ions could help us untangle this sophisticated and vital signaling path on the membrane.

### 2.5.2.8 Synthetic Biomolecular Systems

Many polypeptides, consisting of a sequence of hydrophobic and hydrophilic amino acids, fold into specific protein shapes when dissolved in water. This is a consequence of the fact that water is an incompatible solvent for the hydrophobic units and the folding is a way in which the polymer acts to shield the hydrophobic units from exposure to water. There is growing evidence that many polymers, consisting of a sequence of monomers that are soluble in incompatible solvents, will spontaneously fold into a specific 3-dimensional shape when inserted into one of the solvents. This is true for polymers that are not based on amino acids and for solvents other than water. The synthesis of such polymers is a tremendous challenge, but we can foresee a day in the not so distant future when such syntheses are more common. It is now well recognized that the 3-dimensional shape of a folded polypeptide is the key to enzymatic activity. For example, the protein might form a channel that is specific to the shape of one end of a specific substrate molecule with a reactive atom, such as a strained-bond transition metal atom, at the bottom of the channel. In this way the protein creates tremendous specificity for chemical reactions at the end of the substrate molecule. The continued progress of polymer synthetic chemistry and of the protein-folding problem will some day allow the creation of “artificial enzymes” with very unusual chemistries. For example, one can envision such artificial enzymes made of polymers that are stable in pH or temperature environments that would destroy proteins. This would open an era of synthetic chemistry of materials using “artificial enzymes” that is vastly greater than now possible. Such developments would have a huge impact on our world. Determination of 3-dimensional structure will be important to understanding artificial enzymes, and it is quite likely that initial quantities of test polymers will be very small. In these circumstances, it will be necessary to perform crystallography on very small crystals of complex macromolecules. The high brightness of NSLS-II will be invaluable for this task.

There also exist strategies to design artificial peptides, based on both  $\alpha$ -helical bundle and  $\beta$ -sheet structural motifs, so as to incorporate biological cofactors, compounds that confer function to many biological proteins, including catalysis [15]. The design of artificial peptides with synthetic non-biological cofactors could lead to peptide-based systems with novel properties not exhibited by biological systems. For example, extended  $\pi$ -electron systems can now be designed and tailored, with appropriate donors, acceptors and constituents, to exhibit selected nonlinear optical responses and light-induced electric charge separation over large distances. Importantly, the interior of the artificial peptide scaffolding can be used to control the solubility, position, orientation, and indeed the properties of the cofactor within the peptide (Figure 2.5.5).

The exterior of the artificial protein scaffolding can be used to control the peptide’s supramolecular assembly into sufficiently ordered nanophase materials whose macroscopic behavior arises from such novel properties. The protein scaffold can thus be employed to control the degree of interaction/non-interaction between neighboring cofactors in the ordered nanophase material [16].

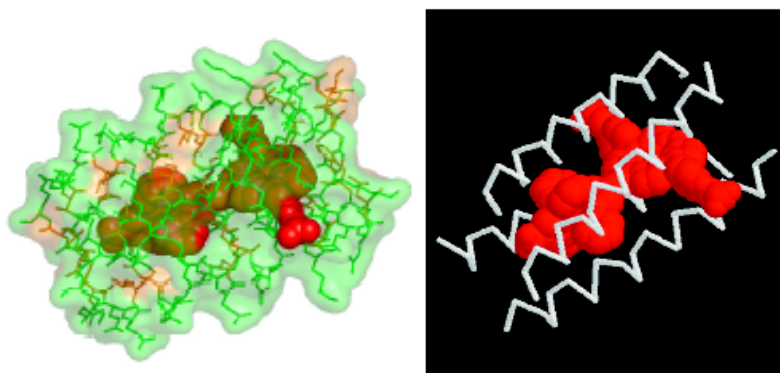


**Figure 2.5.5** Model of statistically designed 4-helix bundle peptide (green/white) to incorporate a novel, non-biological extended  $\pi$ -electron system (red) – an enlarged rendition is shown to the right.

The structural motifs chosen for the artificial peptides can be significantly more stable than the natural protein. However, the interior of the scaffold may not be so stable to the supramolecular assembly process that is required to form a sufficiently ordered material. Thus, it is important to monitor structurally the various stages of the self-assembly process starting from the designed peptide, e.g. a particular  $\alpha$ -helical bundle, to the incorporation of the non-biological cofactor, through to the supramolecular assembly of the peptide-cofactor complexes to a material ordered on a macroscopic scale. Since the desired material properties need not require long-range periodic order, as opposed to orientational order, in one, two or three dimensions, structural determination in the absence of such “crystallinity” is essential.

The high brightness of NSLS-II will enable advances in techniques that are critical for these studies, including X-ray absorption spectroscopy, inelastic X-ray scattering and both non-resonant and resonant elastic X-ray scattering.

### 2.5.3 Impact of NSLS-II

The NSLS-II facility will incorporate a suite of beamlines optimized to implement the X-ray techniques crucial for addressing the scientific challenges in soft matter and biomaterials research described in the preceding section. The X-ray scattering-based techniques utilized in soft matter and biophysics research include X-ray photon correlation spectroscopy (XPCS), time-resolved SAXS and GISAXS, and X-ray resonant scattering. The most dramatic enhancements in capabilities enabled by the high brightness and coherence of NSLS-II will involve coherent X-ray techniques such as XPCS and X-ray focused-beam techniques such as SAXS or GISAXS applied to small samples or used to probe spatial inhomogeneities. The high X-ray flux provided by NSLS-II will benefit flux-limited techniques such as time-resolved SAXS and GISAXS. NSLS-II will also have high brightness and flux at the lower X-ray energies (1-4 keV), which are difficult to access at higher energy synchrotron sources. This will enhance the application of resonance x-ray techniques at the Si, S, P, and Cl k-edges that are of interest in soft matter and biomaterials research. In the following sections, the impact of the enhancements in these X-ray techniques is illustrated by specific examples, and strategies are described to handle the radiation sensitivity of soft matter and biomaterial systems.

#### 2.5.3.1 X-Ray Photon Correlation Spectroscopy - Fluctuations

One of the most exciting scientific opportunities offered by the unprecedented brilliance of NSLS-II is its revolutionary impact on our capability to carry out XPCS experiments. XPCS experiments at NSLS-II will yield exciting new insights into the dynamics of equilibrium fluctuations in soft condensed matter, occurring on shorter length scales than can be reached in light scattering and longer time scales than can be reached with the neutron spin echo technique. Specifically, by illuminating the sample under study with a partially coherent X-ray beam, XPCS reveals the characteristic times of the sample via autocorrelation of its (speckled) scattering pattern [17-20]. The resultant intensity-intensity autocorrelation function  $[g_2(Q, t)]$  is related to the intermediate scattering function (ISF)  $[S(Q, t)]$  of the sample via  $g_2(Q, t) = 1 + \beta [f(Q, t)]^2$ , where  $\beta$  is the optical contrast,  $f(Q, t) = S(Q, t)/S(Q)$  is the normalized ISF, and  $S(Q) = S(Q, 0)$  is the static structure factor. The ISF is a key quantity of interest for any condensed matter system, but as for any method, the issue for XPCS is the range of length and time scales over which it may be applied. In this regard, the crucial aspect of an XPCS experiment is the signal-to-noise ratio (SNR), and, to maximize the SNR, the source should be as brilliant as possible.

Figure 2.5.6 shows representative correlation functions, plotted versus time on a logarithmic scale. They were obtained at the APS for a block copolymer-homopolymer blend at 140° C that forms a so-called sponge (L3) phase, in which amphiphiles self-assemble into extended, random, multiply-connected bilayer membranes [21]. These data extend over 4 decades from a minimum delay time of 17 ms to 200 s. They represent the current state-of-the-art, i.e., 10 millisecond time scales and length scales to 60 nm.

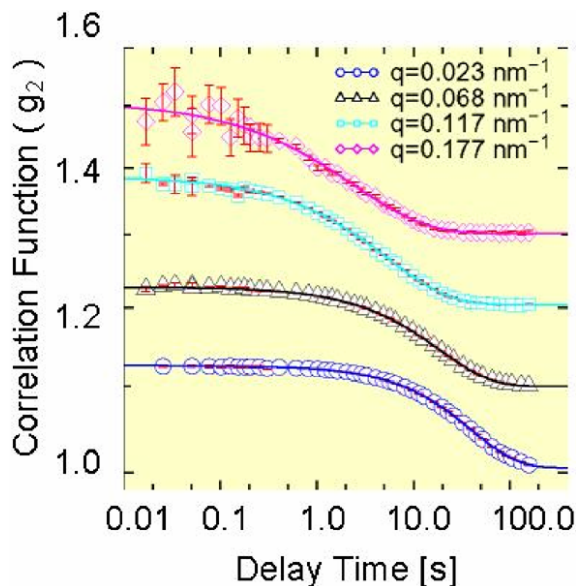


**Figure 2.5.6** Intensity-intensity autocorrelation functions ( $g_2$  vs. delay time for an  $L_3$ -phase sample of  $P(\text{SEBS})$  triblock copolymer in short-chain  $\text{PS}$  homopolymer at  $140^\circ\text{C}$  at wavevectors of 0.023, 0.068, 0.117, and  $0.177\text{ nm}^{-1}$ . For clarity, the  $g_2$ s are displaced by 0.3, 0.2, 0.1, and 0.0, respectively.

Improvements in vertical beam focus, X-ray window quality, and use of a wider energy bandpass would provide at least a 10-fold increase in coherent flux at existing facilities; coupled to the 30-fold enhancement in source brightness at NSLS-II (see Figure 3.3.4), this will yield a net gain of 300. Because of the way XPCS signal-to-noise depends on intensity and accumulation time, a factor of 300 in coherent flux enables the study of processes  $10^5$  times faster! This will revolutionize XPCS, permitting measurements with a time resolution in the hundred nanosecond range, vastly increasing the diversity of kinetic processes to which XPCS may be sensibly applied.

Beyond studies of the dynamics of bulk complex fluids, grazing-incidence scattering at NSLS-II will also permit studies of the dynamics of complex fluids confined in thin films at comparable time scales. In part, this is because of the large increase in sample dimension along the beam direction that occurs at grazing incidence. In addition, there exists the opportunity for an additional enhancement in the scattering signal when studying thin films, due to wave guiding [22].

### 2.5.3.2 Resonant X-Ray Scattering - Orientational Order

In soft matter systems, orientational order plays a crucial role since it impacts the electro-optic anisotropies that are utilized in device applications. Resonant X-ray scattering is a unique probe for measuring these orientational correlations when they occur on nanometer length scales [23]. As an example, Figure 2.5.7 illustrates the nanoscale interlayer and intralayer orientational correlations that can develop in tilted, layered, smectic-C liquid-crystal phases. When the incident X-ray beam is tuned in energy to the resonant edge of one of the atoms in the core of a constituent molecule, the off-diagonal components in the tensor X-ray structure factor become significant and orientational periodicities will diffract X-rays and can change the polarization state. Since the molecules in soft matter systems often contain atoms like S, Si, P, and Cl, with K-edges in the 1 to 4 keV range, this technique requires a soft X-ray beamline.

The high brightness of NSLS-II in this energy range offers the potential to use focused beam to measure orientational periodicities within liquid-crystalline fibers, helical ordering of biomolecules in solution, and an extension of XPCS to the study of orientational fluctuations.

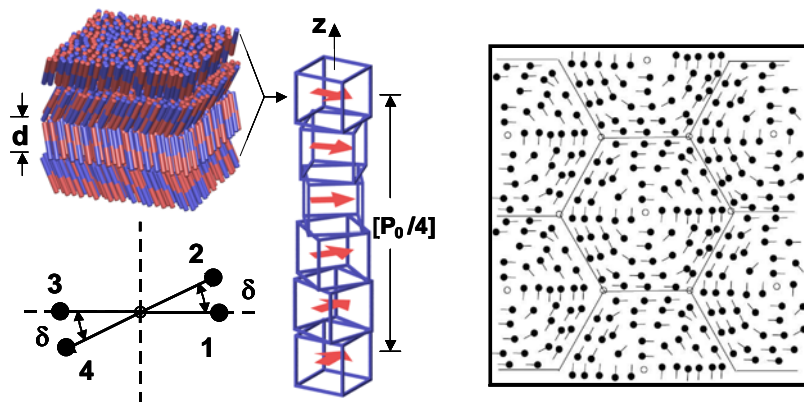


**Figure 2.5.7** *Orientational periodicities in tilted, layer liquid crystal phases. Left: a phase with a uniform in-plane molecular tilt direction, which varies between layers exhibiting a 4-layer unit cell of size 1.2 nm. This unit cell helically rotates with a 1.5  $\mu\text{m}$  pitch ( $P_0$ ) – both periodicities can be observed by RXRD [23]. Right: a proposed phase with an in-plane periodicity of the molecular tilt direction [24].*

### 2.5.3.3 Time-Resolved SAXS - In-Situ Processing

Over 80% of the polymers produced in the world are crystalline polymers. It is well known that during polymer processing, the crystallization kinetics and the final morphology are deeply influenced by molecular orientation induced by flow (in the molten state) and deformation (in the solid state). Understanding and quantifying these effects is extremely important, both scientifically and technologically. Synchrotron X-ray scattering techniques can play a key role in investigations of the molecular orientation in the deformed melt and the resultant morphological changes during the rapid crystallization process under processing flow.

For example, in-situ synchrotron SAXS and WAXD techniques were recently carried out at the NSLS to study the effects of shear and elongational flow fields on orientation and crystallization of polymer chains in undercooled melts [25]. Results suggest that a scaffold (or network) of primary nuclei can be induced by flow at the very early stages of crystallization and that this dictates the morphology of the crystallized polymer. A stable network structure forms, consisting of microfibrillar “shish” with extended chain conformation along the flow direction (form first) superimposed by the crystalline layered structure of “kebabs” with folded chain conformation perpendicular to the flow direction (form second) (Figure 2.5.8). However, the exact nature of the shish-kebab structure (crystalline, mesomorphic and amorphous) remains elusive.

With the present NSLS, information on these precursor structures can only be obtained with a time resolution of seconds (the scattering contrast is quite weak). The high brightness and flux of NSLS-II together with high speed area detectors will allow obtaining structural information with submillisecond or, for stronger scatterers, even microsecond resolution. The proposed NSLS-II SAXS facility will be particularly suitable to explore new insights into the subject of flow-induced polymer crystallization during processing.

### 2.5.3.4 Time-Resolved GISAXS – Nanostructured Organic Films

The high brightness and high flux of NSLS-II will enable grazing-incidence SAXS (GISAXS) on supported polymer thin films (order 100 nm thick) that are themselves nanostructured. Examples include block copolymer thin films (Figure 2.5.9), where the phase-separated domains can act as templates for surface patterning or for the growth of nanoparticles [26, 27] and organic optoelectronic devices (Figure 2.5.10), such as the elements of electroluminescent flat-panel displays, where the distribution of the carrier-transport and luminescent species governs the device performance [28]. The use of a high-

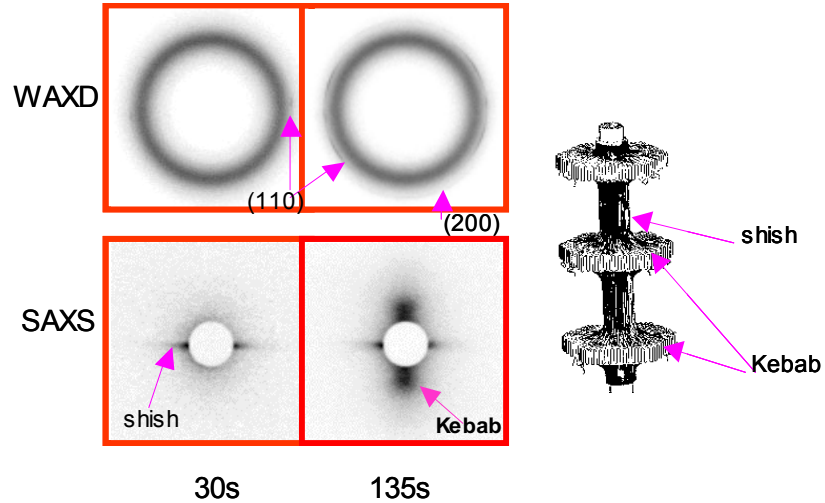


**Figure 2.5.8** Microfibrillar “shish” with extended chain conformation along the flow direction (form first) superimposed by the crystalline layered structure of “kebabs” with folded chain conformation perpendicular to the flow direction (form second) prior to full scale crystallization.

brightness beam and area detection will produce a modest beam footprint on the sample while enabling the simultaneous collection of data over a wide range of scattering and azimuthal angles, in a time-resolved fashion (e.g., during annealing of a block copolymer film, or during the operation of an electroluminescent device).

Small spot size will enable microbeam SAXS/WAXS in a scanning probe mode that will be particularly useful for composite materials. It could, for example, resolve the structure that develops around reinforcing fibers, including ones that nucleate particular structures in the matrix [29]. By decreasing the probe size below 1 micron (e.g., 100 nm), this approach could be extended to nanocomposites, e.g., with layered or exfoliated silicates, that also strongly influence the structure of semi crystalline polymer matrices; and to composites incorporating advanced nanofibers produced through electro spinning. In addition, continuous energy tunability will permit “anomalous reflectivity” measurements on supported polymer thin films. Tuning the X-ray energy to slightly below the absorption edge of one of the constituent elements will permit the direct location of a particular element within the structure from the electron density (index) profile.

### 2.5.3.5 Strategies for Studying Radiation Sensitive Materials

It is evident from the annual reports of the ESRF, APS, and Spring-8 that the high brightness of third

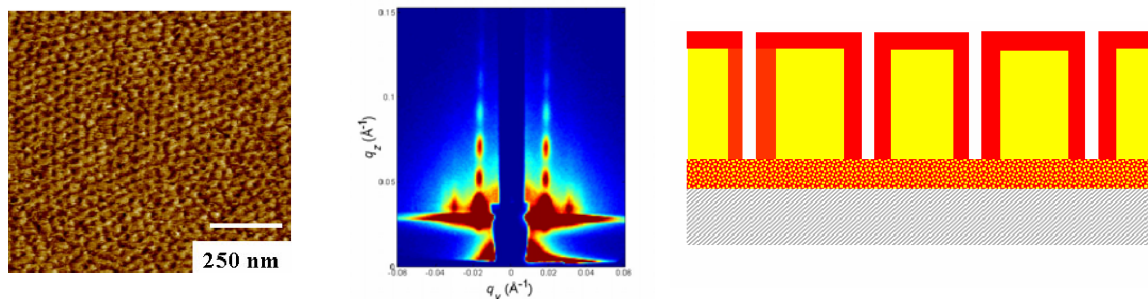


**Figure 2.5.9** A thin polymer film of *P(S-b-MMA)* deposited on a silicon substrate, modified with random copolymer. After rinsing in an acetic acid solution, a local hexagonal pattern emerges as shown in the AFM image (left). The GISAXS spectrum (middle) supports the hexagonal structure and establishes that the film is porous with pores extending the entire depth of the film (right).

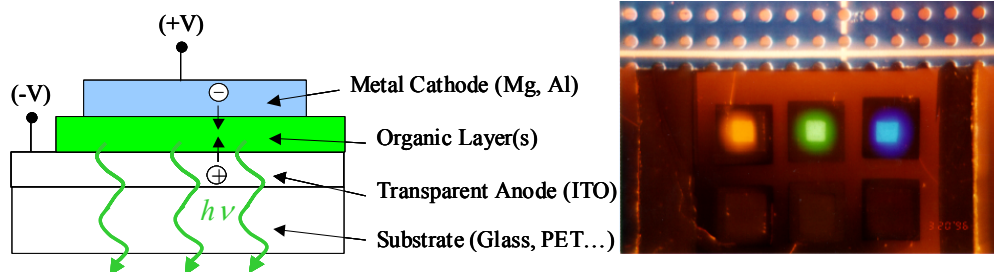


**Figure 2.5.10** Left: schematic of an organic electroluminescent device, where the thickness of the active organic layer is typically 100 nm. Right: photo of an integrated three-color organic device based on dye-doped polyvinylcarbazole; individual subpixels are 2 mm on a side.

generation sources is being widely applied to the study of soft matter systems. Nonetheless, from unpublished comments at synchrotron workshops, it is equally clear that there were a number of cases where attenuation was required to prevent radiation damage. Hence, it is fair to ask whether the substantially higher brightness of NSLS-II can be fully utilized in studies of soft matter.

Clearly, the avoidance of radiation damage at NSLS-II will require careful attention. Researchers who have succeeded in studying soft matter at current third generation sources invariably applied a few of the following strategies. When possible, samples were selected that were composed of radiation robust constituents such as cyclohexane, benzene, biphenyl, rather than constituents known to be susceptible to radiation damage such as COOH,  $-\text{SO}_2-$ ,  $\text{NH}_2$ , and  $\text{C}=\text{C}$ . Since there is considerable evidence that radiation damage is due to cumulative dose, care must be taken to make every photon count, for example, through parallel detection or on-the-fly scans. In some cases, the X-ray beam was rastered and data taken from equivalent sample areas or, when in solution, samples were flowed through the X-ray beam (see the very exciting development of flow-cell mixers in Section 2.2.3.1). Samples were usually kept in vacuum or an inert gas environment. In some cases, samples were freely suspended to avoid interaction with photoelectrons ejected from a substrate and kept thin and studied at grazing incidence to avoid heating from X-ray absorption.

When such precautions are taken, the full range of soft matter and biomaterials applications described in this section will be open for exploration with the ultra-high brightness beams at NSLS-II.

## REFERENCES

- [1] L. Zhu, S.Z.D. Cheng, Q. Ge, R.P. Quirk, E.L. Thomas, B. Lotz, B. Hsiao, F. Yeh, and L. Liu, *Advanced Materials* 14, 31 (2002).
- [2] V. Percec, J. Glodde, T. K. Bera, Y. Miura, I. Shiyonovskaya, K. D. Singer, V. S. K. Balagursamy, P. A. Heiney, I. Schnell, A. Rapp, H. W. Spiess, S. D. Hudson, and H. Duan, *Nature* 419 384 (2002).
- [3] J. Zhang, A. Alsayed, K. H. Lin, S. Sanyal, F. Zhang, W. J. Pao, V.S. K. Balagurusamy, P. A. Heiney, A. G. Yodh, *Appl. Phys. Lett.* 81 3176 (2002).
- [4] S.Y. Lin, E. Chow, V. Hietala, P. R. Villeneuve, J. D. Joannopolous, *Science* 282, 274 (1998).
- [5] K. J. Ihn, J. Zasadzinski, R. Pindak, A. J. Slaney, J. Goodby, *Science*, 258, 275 (1992).
- [6] D. A. Coleman, J. Fernsler, N. Chattham, M. Nakata, Y. Takanishi, E. Korblova, D. R. Link, R. F. Shao, W. G. Jang, J. E. Maclennan, O. Mondainn-Monval, C. Boyer, W. Weissflog, G. Pelzl, L. C. Chien, J. Zasadzinski, J. Watanabe, D.M. Walba, H. Takezoe, N.A. Clark, *Science* 301, 1204 (2003).
- [7] G. C. Wong, J. X. Tang, A. Lin, Y. L. Li, P. A. Janmey, C. R. Safinya, *Science* 288 2035 (2000).
- [8] H. M. Evans, A. Ahmad, K. Ewert, T. Pfohl, A. Martin-Herranz, R. F. Bruinsma, C. R. Safinya, *Phys. Rev. Lett.* 91, 075501 (2003).
- [9] S. Granick, *Physics Today* 26, (July 1999) and references therein
- [10] O. M. Magnussen, B. M. Ocko, M. J. Regan, K. Penanen, P. S. Pershan, and M. Deutsch, *Phys. Rev. Lett.* 74, 4444 (1995).

- [11] C.-J. Yu, A. G. Richter, A. Datta, M. K. Durbin, and P. Dutta, *Phys. Rev. Lett.* 82, 2326 (1999).
- [12] O. H. Seeck, H. Kim, D. R. Lee, D. Shu, I. D. Kaendler, J. K. Basu, and S.K. Sinha, *Europhys. Lett.* 60, 376(2002).
- [13] C. Burger, S. Zhou, B. Chu, in “Handbook of Polyelectrolytes and Their Applications”, Vol. 3, (Eds. S. Tripathy, J. Kumar and H. S. Nalwa), Amer. Sci. Pub., Chapter 7, pp.125, 2002.
- [14] S-Q. Zhou, C. Berger, B. Chu, M. Sawamura, N. Nagahama, M. Toganoh, U. E. Hackler, H. Isobe, E. Nakamura, *Science* 291, 1944 (2001).
- [15] L. Di Costanzo, H. Wade, S. Geremia, L. Randaccio, V. Pavone, W.F. DeGrado, and A. Lombardi, *J. Amer. Chem. Soc.* 123, 12749 (2001).
- [16] T. Swager, *Nat. Mater.* 1, 152 (2002).
- [17] S. B. Dierker, R. Pindak, R. M. Fleming, I. K. Robinson, and L. E. Berman, *Phys. Rev. Lett.* 75, 449 (1995).
- [18] C. Price, L. B. Sorensen, S. D. Kevan, J. Toner, A. Poniewierski, and R. Holyst, *Phys. Rev. Lett* 82, 755 (1999).
- [19] L. B. Lurio, D. Lumma, P. Falus, M. A. Borthwick, S. G. J. Mochrie, J.-F. Pelletier, M. Sutton, A. Malik, and G. B. Stephenson, *Phys. Rev. Lett* 84, 785 (2000).
- [20] H. J. Kim, A. Ruehm, L. B. Lurio, J. Basu, J. Lal, D. Lumma, S. G. J. Mochrie, and S. K. Sinha. *Phys. Rev. Lett* 90, 1212 (2003).
- [21] D. Roux, C. Coulon, and M. E. Cates, *J. Phys. Chem.* 96, 4174 (1992).
- [22] J. Wang, M. J. Bedzyk, and M. Caffrey, *Science* 258, 775 (1992).
- [23] A. Cady, J. A. Pitney, R. Pindak, L. S. Matkin, S. J. Watson, H. F. Gleeson, P. Cluzeau, P. Barois, A.-M. Levelut, W. Caliebe, J. W. Goodby, M. Hird, and C. C. Huang, *Phys. Rev. E – Rapid Comm.* 64, 50702 (2001).
- [24] R. B. Meyer and R. Pelcovits, *Phys. Rev. E* 65, 61704 ( 2002 ).
- [25] R. H. Somani, B. S. Hsiao, A. Nogales, S. Srinivas, A. H. Tsou, I. Sics, F. J. Balta-Calleja, and T. A. Ezquerra, *Macromolecules* 33, 9385 (2000).S. G. J. Mochrie, A. M. Mayes, A. R. Sandy, M. Sutton, S. Brauer, G. B. Stephenson, D. L. Abernathy, and G. Grüber, *Phys. Rev. Lett.* 78, 1275 (1997).
- [26] E. Huang, L. Rockford, T. P. Russell, C. J. Hawker, J. Mays, *Nature* 395, 757 (1998).
- [27] M. Park, P. M. Chaikin, R. A. Register, and D.H. Adamson, *Appl. Phys. Lett.* 79, 257 (2001).
- [28] X. Jiang, R. A. Register, K. A. Killeen, M.E. Thompson, F. Pschenitzka, T. R. Hebner, and J. C. Sturm, *J. Appl. Phys.* 91, 6717 (2002).
- [29] D. M. Dean and R. A. Register, *J. Polym. Sci. B: Polym. Phys.* 36, 2821 (1998).

## 2.6 Strongly Correlated Electron Systems

### 2.6.1 Overview

Understanding the electronic behavior of strongly correlated electron systems is one of the most important problems in condensed matter physics – one that is driving a revolution in the prevailing paradigm of Fermi-liquid behavior of solids. As their name suggests, it is their electronic degrees of freedom that give rise to their exotic properties. In materials with poor screening properties, such as the doped transition metal oxides, the interaction energy between valence electrons can overwhelm their kinetic energy, giving rise to a strongly coupled many-body ground state. As a result of this strong electron correlation, these materials display a range of exotic and useful behaviors, including high-temperature superconductivity, colossal magnetoresistance and a general extreme sensitivity to external perturbations. An example is shown in Figure 2.6.1.

However, in these materials the independent electron framework of solid state physics is not applicable. In our effort to understand the physics of, for example, high  $T_c$  materials, there is thus more at stake than simply the mechanism behind superconductivity – the language we use to discuss condensed matter is itself at issue. J. R. Schrieffer has said: “When high temperature superconductivity is solved we will have to rewrite the textbooks on solid state physics.” This monumental theoretical task is one of the “Grand Challenges” in physics today.

Of particular relevance in this field is the need to go beyond the conventional picture of ordered ground states with weakly interacting (linear) excitations to identify and understand more exotic phases, which may be characterized by unusual correlation functions (orbital currents, topological order, etc). Identifying and characterizing these new phases will require extended phase space in which to search (ultra-low temperatures, high-magnetic fields and high-pressures) closely coupled with materials synthesis (including especially nanoscale structures) together with X-ray techniques (scattering, imaging and local probes) to fully elucidate the electronic behavior.

The high-brightness of NSLS-II will drive advances in energy and real-space resolution of these techniques that, when coupled with the extremes of sample environment and novel materials synthesis, will dramatically advance the field of strongly correlated electron systems, announcing a new era in condensed matter physics.

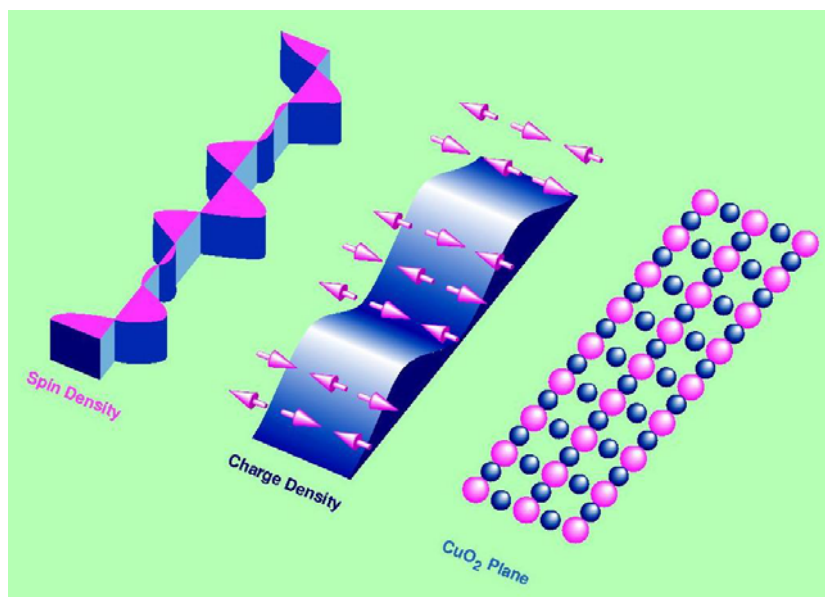


**Figure 2.6.1** Schematic of charge and spin stripes in a high  $T_c$  superconductor. Such exotic electronic orderings, frequently observed in strongly correlated electron systems, remain poorly understood.

## 2.6.2 Scientific Challenges and Opportunities

Correlated Electron Materials Science is a frontier field, currently dominating hard-condensed matter physics. Yet it is far from mature and surprising new phenomena appear on a regular basis, such as the recent discovery of superconductivity in cobaltate materials. While it is believed that the possible phases of one-dimensional electronic systems have been completely classified and characterized theoretically, no such characterization is available for two- and three-dimensional systems. We have recently learned that 'spin liquids' exist in well-defined, non-artificial theoretical models. It has been proposed that they can occur in real metallic systems. The key to finding new phenomena will be a strong effort in materials synthesis, in characterization, and in measurement techniques, including more and better spectroscopies.

To illustrate the importance of this problem in the coming decades, a number of emergent directions that open new avenues for exploration and raise new challenges to present measurement and calculation abilities are highlighted. It is clear that this topic will remain amongst the most fertile and surprising in physics for the foreseeable future.

### 2.6.2.1 Surface Science

The surface science of correlated electron systems is a crucial but surprisingly little-studied issue, practically begging for attention. The motivations are both practical and fundamental. On the fundamental side, the issue is this: correlated electron materials exhibit a multiplicity of interesting electronic phases. It is natural to ask: how do the electronic phases at surfaces or interfaces differ from those in the bulk? On the practical side, one hopes to exploit the interesting electronic properties (such as superconductivity, 'half-metallic' or 'colossal' magnetoresistance) of strongly correlated systems. However, most applications involve getting electrons into or out of a device, and therefore necessarily involve a surface or interface, whose electronic properties are vital to the performance of the device. Very little is actually known about changes in electronic properties near surfaces and interfaces.

Traditional surface science focuses on where the atoms are and why they are there. Correlated electron surface science will focus on the properties of the electrons, asking "what is the electronic phase, and why". This is basic science for possible future correlated electron devices.

Key probes will include photoemission, X-ray Magnetic Circular Dichroism (XMCD), grazing-incidence X-ray scattering, and X-ray resonant scattering. High quality sample preparation will also be crucial, including fabrication of near-ideal interfaces and nano-scaled architectures.

### 2.6.2.2 Fluctuating Order

Fluctuating Order and its consequences are a key open area. One of the traditional questions in materials theory has been the effects of long ranged order on the electronic spectrum (i.e., ordering of atoms into a lattice, ordering of electrons into superconducting or magnetic states). However, we are now learning that many materials exhibit wide regimes in which substantial short-ranged (in space and time) correlations exist that dramatically affect physical properties.

For example, the physical mechanism underlying the magnetic field induced insulator-metal transition and the associated large change in the electrical resistivity in perovskite manganites has been the subject of intense experimental and theoretical investigation since its discovery in 1993. A recent diffuse x-ray scattering study found a strong correlation between the presence of nanoscale charge/orbital ordered regions and the increased electrical resistivity in the paramagnetic phase of these materials, suggesting that nanoscale inhomogeneity plays an essential role in these phase transitions (Figure 2.6.2)

Our ability to detect, normalize and interpret these fluctuations lags far behind our ability to detect, normalize and interpret the Bragg peaks associated with long ranged order. Taking the next step in understanding materials properties will require great improvements in our spectroscopic abilities. In particular, correlation functions beyond the usual two-point correlation functions may be central to the

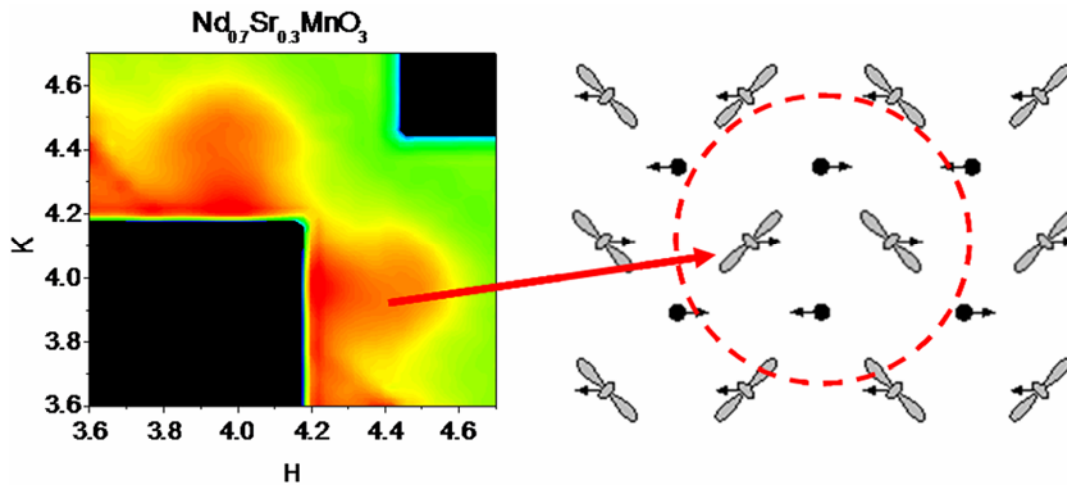


**Figure 2.6.2** Diffuse x-ray scattering (left) in a perovskite manganite resulting from nanoscale charge/orbital ordered regions, shown schematically on the right [1]

problem (i.e., beyond the usual density-density correlations). New scattering experiments will need to be devised to probe such objects, perhaps using resonances or the enhanced coherent properties of the beam.

### 2.6.2.3 Dynamics

Density functional-based band theory has revolutionized our understanding of materials. We are now able to calculate with great accuracy, for a very wide range of systems, anything that can be related to static, ground-state properties. For dynamics we are in much worse shape: for example, even for moderately correlated materials, density functional methods over-predict quasiparticle velocities by factors of two or more. This of course does not cast doubt upon the successes of the methods: the theorems on which the methods are based make no guarantees about excited state properties. However, it does show that additional methods are needed. Recent developments (i.e., the development of the “dynamical mean field method” and its marriage to band theory) suggest that progress is now possible on these issues. The challenge will be to compute dynamical response functions (transport coefficients, single-electron dispersions and linewidths, dynamical structure factors, etc) and to refine our ability to measure these quantities using emerging techniques such as inelastic X-ray scattering and X-ray correlation spectroscopy and advances in more well-established techniques such as angle resolved photoemission spectroscopy.

### 2.6.2.4 Quantal Correlations

Although nature is inherently quantum-mechanical, most of what is measured, calculated, or thought about is fundamentally classical: particle positions, velocities, two-particle correlations, etc. However, we know that the combination of quantum mechanics and interactions leads to correlations that are subtle and surprisingly long ranged in space and time. A well-known example is the phase correlations of superconductors. A very recent example is provided by the work of Rosenbaum, Aeppli and co-workers on the diluted LiHo/YF<sub>4</sub> system in which quantum entanglement was observed in the spin system. The challenge is to measure the quantal correlations more directly, and to find ways to exploit them. Resonant scattering techniques will be able to make unique contributions here.

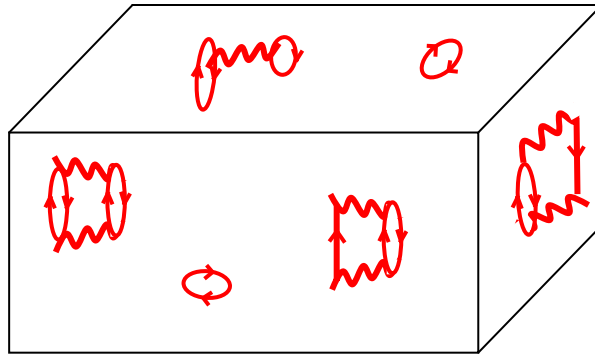


**Figure 2.6.3** *A given system consists of the ground state and its excitations. The excitations “dress” the particles. To completely understand a system one needs to understand the excitations of that system. It is these excitations which determine the response of the system to perturbations.*

### 2.6.3 Impact of NSLS-II

The controlling degrees of freedom in strongly correlated electron systems are electronic in nature and therefore probes that couple directly to the electrons are uniquely suited to their study. Furthermore, these systems are characterized by competing interactions and frequently display inhomogeneous ground states. Thus, probes on a number of different length, energy, and time scales are required to fully elucidate their behavior. As a result, the full gamut of synchrotron techniques has impact in the study of strongly correlated electron systems.

In recent years, progress has been made in characterizing the unusual electronic ground states of these materials, such as stripe order in high-temperature superconductors and charge and orbital order in the manganites. Of particular importance have been basic structural studies, such as X-ray powder diffraction, electronically sensitive local probes, including EXAFS and XANES, and diffraction probes of electronic correlation, including especially resonant X-ray scattering.

However, for complete understanding, the excitations must also be understood (Figure 2.6.3), and it is in measurements of the electronic excitation spectrum where the greatest opportunities lie. The scientific challenge will be to understand the charge dynamics in the vicinity of the gap, which are the prime signature of a strongly correlated electron system. Phenomenon such as spin-charge separation and holon dynamics, charge dynamics associated with striping behavior, charge Goldstone modes (symmetry breaking collective modes), effects of orbital degeneracies as well as charge dynamics in new emergent classes of Mott compounds all remain poorly understood due to a lack of relevant experimental data.

There are two main probes of electron dynamics in the energy domain: inelastic X-ray scattering (IXS) and angle-resolved photoemission spectroscopy (ARPES). IXS measures a two-particle correlation function,  $S(k, \omega)$ , and is bulk sensitive. However, it is presently limited to fairly moderate energy resolution ( $\sim 0.3$  eV), even at today’s third generation synchrotron sources. Thus, the technique is constrained to study the high-energy physics of the electrons. Conversely, ARPES measures the single-particle spectral function  $A(k, \omega)$ , with resolutions of  $\sim 1$  meV, but it is intrinsically surface sensitive. ARPES has had an enormous impact in probing the excitations of high-temperature superconductors, in particular in the vicinity of the Fermi surface.

All of these techniques will continue to be of vital importance in addressing this and related problems and all will benefit dramatically from NSLS-II. In the following, we highlight a few areas where the impact will be particularly great.

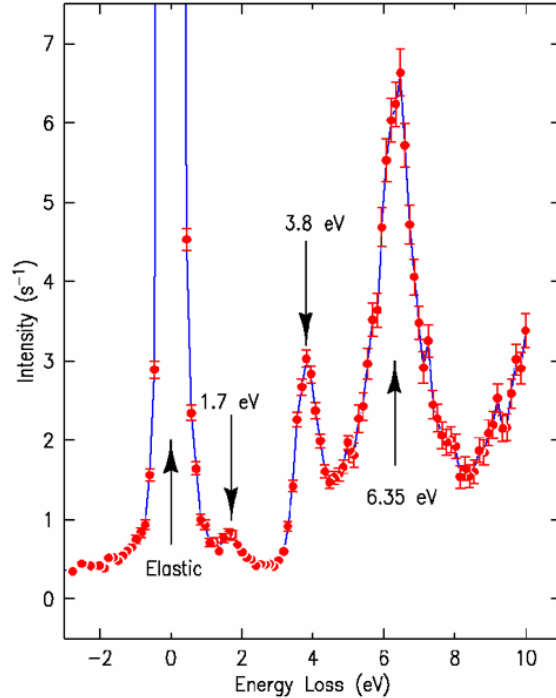


**Figure 2.6.4** *Inelastic X-ray scattering spectrum from  $\text{CuGeO}_3$ , a 1D cuprate. These data were taken at the hard X-ray Cu K-edge with 0.4 eV resolutions at CMC-CAT at APS. With NSLS-II, such experiments will have ten times greater signal strength and improved energy resolution.*

### 2.6.3.1 Hard X-ray Inelastic X-ray Scattering

Over the past few years, IXS has begun to establish itself as a bulk-sensitive, momentum-resolved probe of charge dynamics. Pushing the resolution of IXS down to  $\sim 100$  meV is presently underway at several different synchrotron facilities. In the past decade, enormously improved resolution and experimental geometries have elevated angle-resolved photoemission from a band mapping tool to an important many-body spectroscopy. Inelastic X-ray scattering holds a similar promise.

Hard X-ray inelastic scattering studies of charge dynamics are performed near the transition metal K-edges for 3d transition metals, to take advantage of the large resonant enhancements (Figure 2.6.4). For such edges, the perturbation on the d-orbitals is relatively weak but a large momentum transfer is possible, allowing measurement of dispersion relations. The anisotropy of the Mott gap and studies of holon dynamics are two recent examples of such studies [2-4]. This pioneering work has provided a new window into these strongly correlated systems. However, the large quasielastic scattering in the hard X-ray regime tends to mask out the interesting low-energy physics and it is not possible to separate the valence electron contribution from that of diffuse scattering with the current resolution. Improving the resolution of hard RIXS to the sub 50-meV level would allow it to play a key role in elucidating the charge dynamics of these systems.

For IXS then, the challenge is to reach energy resolutions such that excitations of direct relevance are accessible, namely  $\Delta E \sim 10$  meV. Such resolutions, and better, are presently accessible only by working at high incident photon energies. However the flux is such that one is only able to study collective dynamics of the ion cores (i.e., phonons). While important in the study of electron-phonon effects, this precludes the study of electronic excitations. The ability to obtain meV type resolution at medium incident energies (5-10 keV) would transform this field, making accessible the transition metal resonances (K-edges) that

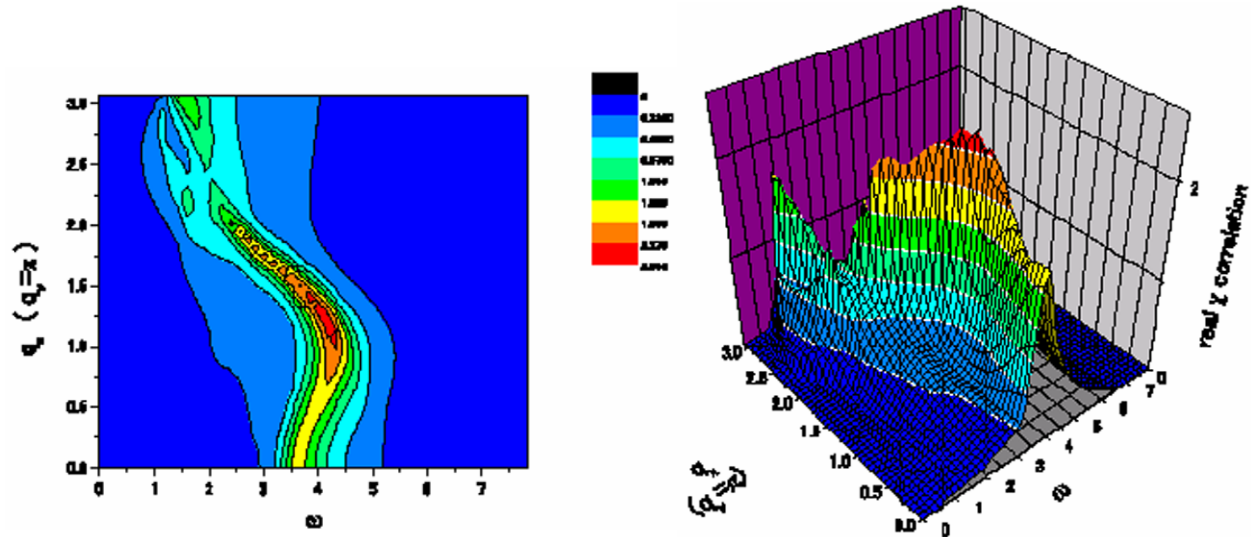


**Figure 2.6.5** Spectral function predicted for the correlation of the kinetic operator in a recent theory of dynamics in a high- $T_c$  superconductor [5]. With NSLS-II, such a correlation function will be measurable by inelastic X-ray scattering at the Cu L-edges, and the validity of the model determined. Energy units ( $\omega$ ) are  $3/8J \sim 60$  meV.

greatly enhance the inelastic scattering, and allowing one to probe the electron dynamics with unprecedented resolution.

This will require both very high brightness beams, and the development of new analyzers. The latter is presently underway at the Advanced Photon Source (APS), with preliminary work being performed on sapphire. The former will be provided by NSLS-II. Compared to existing beamlines at APS, NSLS-II will be 35 times brighter in the 5-10 keV range (see Figure 3.3.4), providing more than a factor of 10 more photons in the same bandpass. Presently, it takes about 6 hours to take a single scan. This will be reduced to less than 30 minutes at NSLS-II, transforming what will be possible and making studies of the charge dynamics in strongly correlated systems routine. Comprehensive studies as a function of doping, temperature, and momentum transfer will become possible.

Important experiments will include probing the charge dynamics of stripe order in cuprates, searching for dynamic, hidden order parameters of the type recently proposed in high-temperature superconductors (Figure 2.6.5), probing orbital excitations (“orbitons”) in manganites, and investigating the superconducting gap in transition metal oxide superconductors. There are also a number of significant mysteries in the “mid-gap” states as revealed by infra-red (IR) studies, where changes in spectral weight appear to violate sum rules [6] and shed light on the condensation energy. NSLS-II will enable enhanced momentum-resolved IXS studies, which will be tremendously important in understanding these results.

Finally, it is important to stress that the same inelastic techniques would have immediate applicability in a variety of other scientific disciplines, including for example organic semi-conductors, heavy fermion systems, quantum critical points (e.g.,  $V_x\text{Cr}_{1-x}$ ) and essentially all other hard condensed matter systems. In addition, geophysics (systems under pressure), biology (protein and membrane dynamics, electronic charge transfer in photosynthetic compounds) and soft condensed matter (polymer dynamics, thin film dynamics etc) all benefit in similar ways.

### 2.6.3.2 Soft X-ray Inelastic X-ray Scattering

Soft X-ray (0.5-2 keV) inelastic X-ray scattering at the L-edges of transition metal compounds complements hard X-ray IXS in probing electronic excitations (Figure 2.6.5). Valence excitations exhibit enhancements of several orders of magnitude near an L-edge and the quasielastic scattering is relatively

low (in many cases lower than the inelastic signals). This would allow studies of the low-energy electron physics of many systems.

Another exciting prospect offered by the use of L-edges is to take advantage of the strong spin-orbit coupling present in the 2p core-hole created in the intermediate state to gain access to magnetic excitations. By changing the helicity of the photon (on an elliptically polarizing undulator (EPU) beamline) one can couple to such excitations. Magnetic inelastic X-ray scattering will open up an entirely new window on spin dynamics that will complement existing neutron scattering techniques. Together, these techniques will allow studies of the magnetic and charge dynamics with the same probe for the first time.

While the use of soft X-ray energies limits the available momentum transfer, near the Cu-L edges (950 eV) there is enough momentum to reach the zone boundary. This is sufficient, for example, for both cuprates and manganites where the pseudogap has its maximum value near the zone boundary. It is also sufficient for studying dynamic charge-stripe correlations for which the ordering vector is small. A big advantage of L-edge resonances is that they involve the d-states directly and are thus highly sensitive to the orbital fluctuations. Mott systems, such as colossal magnetoresistance (CMR) manganites, where orbital degrees of freedom play a role would thus be a perfect match for such a scattering technique. The CMR effect itself is a field effect and hence one needs to have a momentum-resolved probe of electronic structure in the presence of a magnetic field, which is not possible in an ARPES experiment. Inelastic X-ray scattering at the soft edges will be the perfect match for this.

However, in order to achieve these capabilities, the energy resolution must be improved by at *least* an order of magnitude [7, 8]. The current state-of-the-art is 0.25 eV at 500 eV. NSLS-II will be a factor of 60 times brighter than the ALS at 500 eV (see Figure 3.3.4). The extreme brightness of NSLS-II in this spectral range will make it possible to achieve 10 meV at 500 eV and will revolutionize soft X-ray measurements. With such resolution, soft X-ray IXS will directly complement ARPES, which has been so instrumental in advancing our understanding of the very low energy phenomena in these systems.

### 2.6.3.3 Angle Resolved Photoemission Spectroscopy

Dramatic improvements in the photoemission technique have allowed it to become a powerful probe of condensed matter in general and strongly correlated systems in particular. Very high energy resolution (1 - 5 meV) combined with excellent momentum resolution ( $0.01 \text{ \AA}^{-1}$ ) have allowed the study of the electron interaction with phonons, CDWs, and spin fluctuations. Such studies have, for instance, had an important place in the overall discussion of the mechanism behind high- $T_c$  superconductivity. In the latter materials, the magnitude of the superconducting gap is approximately  $8 kT_c$  and has proven relatively easy to observe with existing resolutions. The gap of about  $3.5 kT_c$  in the traditional phonon mediated superconductors puts more demands on the experiment, but even so there have been reports of its observation. However, at the typical photon energies used for these studies, the technique is very surface sensitive.

The challenge is to use higher photon energies where the escape depth would be larger: At 1000 eV, 86 % of the electrons come from the first 15 layers, rather than the first 4 layers at 20 eV. How feasible is the possibility of doing angle resolved photoemission at the higher energies? Clearly it is possible to design an instrument with high-energy resolution at high energies but because the momentum resolution,  $\Delta k_{\parallel}$ , reflects the kinetic energy according to  $\Delta k_{\parallel} = 0.5123 \Delta E^{1/2} \Delta \theta$ , where  $\Delta \theta$  represents the angular resolution, it requires a dramatic improvement in the angular resolution to maintain the same momentum resolution. For example, increasing the kinetic energy from 10 eV to 1000 eV requires an order of magnitude increase in the angular resolution. This is difficult to imagine in the large hemispherical analyzers used at the present time but may be possible in time-resolved instruments where the energy resolution,  $\Delta E/E$ , equals twice the time resolution,  $2\Delta t/t$ .

As discussed in Section 3.4.4, NSLS-II will have a bunch length of only 11 psec (rms) in fast timing mode. The slower the electrons in the drift tube the better the resolution. However, the drift tube should not be too long since stray fields then make it more difficult to retain the angular information. Retarding

the electrons from 1 keV to 1 eV and allowing them to drift down a 1 meter length tube leads to an achievable energy resolution of 10 meV, which matches the current “state of the art” achievable in photon monochromators. A similar instrument in the form of a photoelectron microscope has in fact already been built and tested. It has the possibility of switching its mode of operation from microscopy to spectroscopy and will be well matched to the time structure of NSLS-II.

If the electrons are retarded, it becomes necessary to take phase space considerations into account in considering the angular resolution. Assuming a source size on the sample of 0.1 mm and an acceptance angle of 10 degrees, retarding the photoelectrons to 1 eV with a 1 degree divergence in the drift tube leads to a required spatial resolution of 10 microns in the detector to give an angular resolution of 0.01 degrees. The latter would be an order of magnitude better than currently available.

Such an instrument operated at higher photon energies offers the possibility of more bulk sensitive measurements in the spectroscopy mode or the possibility of examining much smaller samples in the microscope mode. The high brightness of NSLS-II will make such an instrument possible and will enable ARPES experiments to be carried out at high photon energies with the energy and angular resolution required for strongly correlated systems for the first time.

### 2.6.3.4 Anomalous Soft X-ray Scattering

In weakly interacting electron systems, the dominant length scales are the lattice parameter,  $a$ , and, under some circumstances, the inverse Fermi-momentum,  $1/k_F$ . In correlated systems, however, a variety of spontaneous symmetry-broken ground states may occur, with characteristic length scales determined, in general, by a competition between interactions and geometric frustration.

To learn about such ground states one requires a probe that can detect ordering in the carrier liquid directly, even in cases where such ordering is not accompanied by a structural (lattice) distortion. In general if translational symmetry is broken by many-body interactions, rather than for example the electron-phonon interaction as in a charge density wave material, there is no reason to expect the crystal structure to reflect this, except perhaps passively.

The magnetic aspect of such ground states has been studied extensively with neutron diffraction. An example is the “stripe” correlations seen in nickelates and cuprates, which are sometimes accompanied by a crystallographic distortion [9, 10] but more often are not [11-13]. A good probe of the charge

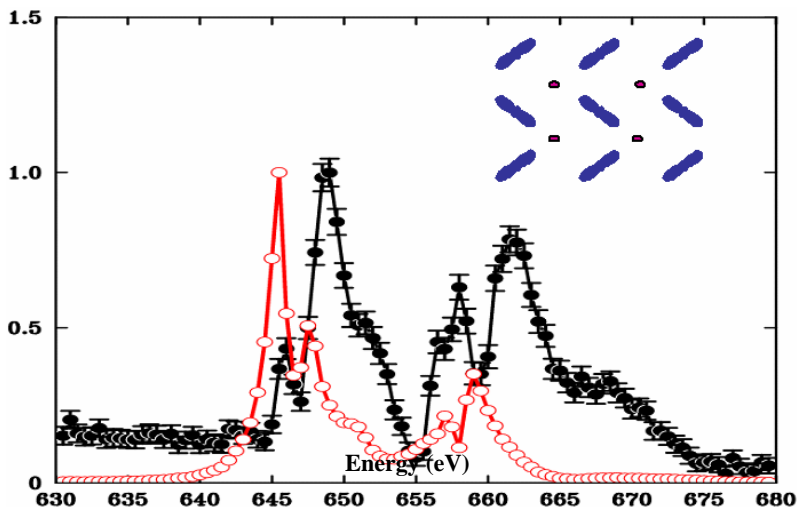


**Figure 2.6.6** Soft X-ray resonant scattering in a doped manganite,  $Pr_{0.6}Ca_{0.4}MnO_3$ . Red data is magnetic scattering, black data are due to orbital order. Inset is an idealized schematic of the orbital and charge order. These data were taken at NSLS beamline X1B. NSLS-II will be 1000 times brighter at this energy and will radically transform such studies.

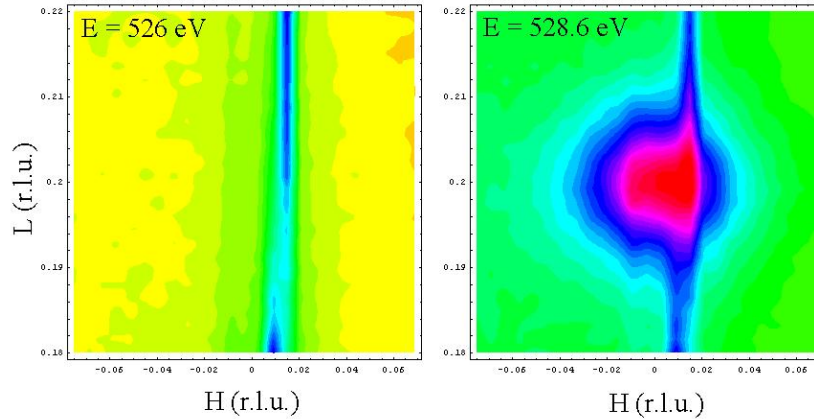


**Figure 2.6.7** Appearance of charge-density wave superstructure reflection from the spin ladder material  $\text{Sr}_{14}\text{Cu}_{24}\text{O}_{41}$ . This feature is visible only on-resonance as it forms from many-body effects rather than via the electron-phonon interaction. The vertical rod at  $H \approx 0$  is the specular reflection from the surface.

component of such phases has been lacking as charge sensitive probes such as X-rays or electrons couple mainly to the core electrons in the former case, and to both the core electrons and the nuclei in the latter.

It was recently demonstrated that the charge channel can be accessed by exploiting anomalous scattering factors in the soft X-ray regime, so called anomalous soft X-ray scattering (ASXS) [14]. In addition, magnetic scattering at transition metal L-edges is known to be extremely strong. Recent experiments at NSLS beamline X1B demonstrate the ability to measure spin and orbital correlations in the same sample at the same time (Figure 2.6.6). Being able to study such correlations simultaneously will be crucial in unraveling the interactions and competing behaviors of these important degrees of freedom.

Soft X-ray resonant scattering has also proved fruitful in studying valence modulations in  $\text{YBa}_2\text{Cu}_3\text{O}_{6.5}$  [15],  $\text{La}_2\text{CuO}_{4+y}$  [16],  $\text{La}_{2-x}\text{Sr}_x\text{NiO}_4$  [17], and  $\text{Pr}_{1-x}\text{Ca}_x\text{MnO}_3$  [18]. For example, Figure 2.6.7 shows a scan through a superlattice reflection from  $\text{Sr}_{14}\text{Cu}_{24}\text{O}_{41}$ . This peak occurs at  $[0,0,0.2]$ , very close to  $4k_F$ , and demonstrates the existence of a Wigner crystalline state in the spin ladder plane of this material. This feature is visible only on resonance, as it forms via many-body effects rather than through the electron-phonon interaction and can only be studied with ASXS.

With the increased brightness and flux of NSLS-II, it will be possible to tackle significantly more challenging problems, such as searching for dynamic stripes in high- $T_c$  superconductors, i.e., charge stripes whose positions with respect to the crystal lattice are fluctuating in time. This problem is particularly difficult because the superlattice peaks corresponding to the ordered state are very weak already. However, with NSLS-II, dynamic stripes should be observable.

### 2.6.3.6 Coherent X-ray scattering

Coherent X-ray scattering is a powerful tool for the study of domain structure because of its sensitivity to the exact spatial arrangement of the domains. Upon illumination by a coherent beam, a sample composed of a mosaic of domains introduces a set of different phases into the scattered beam. The interference of these phases, which are related to the position of individual domains, gives rise to a “speckle” pattern. In principle, this speckle pattern can be inverted to obtain a real-space image of the domains. Such a reconstruction is quite challenging, but has been accomplished in a number of systems.

Another promising use of coherent X-ray scattering is in the study of dynamics. If the spatial arrangement of the domains changes with time, the phases of the scattered beam will be affected and the speckle pattern will also change. Measurements of these changes can therefore be used to study the dynamics of fluctuations.

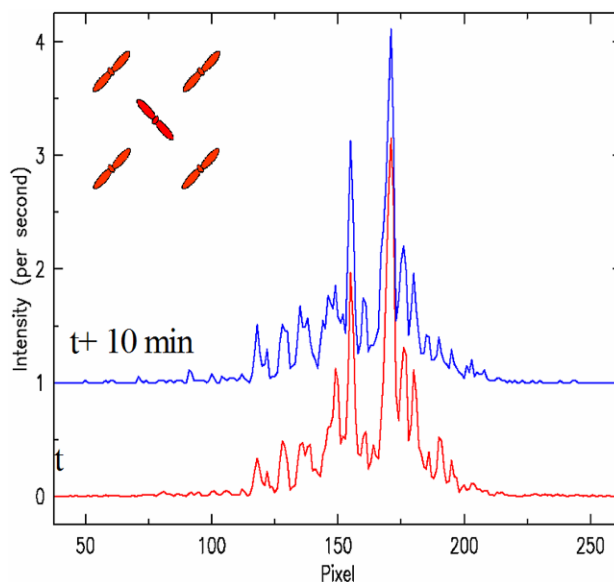


**Figure 2.6.8** “Speckle” pattern resulting from orbital order in  $\text{LaMnO}_3$  [19]. The two curves, taken ten minutes apart, demonstrate that the orbital order is static. The high brightness of NSLS-II will enable speckle experiments to probe the dynamics of orbital domains.

One example where such techniques will profitably be applied is the study of the dynamics of orbital domain walls in the manganites. Domain walls are observed on a number of length scales in these systems, but there is no understanding of the origin of these domains. Elucidating the dynamics of such structures would be an important step in approaching an understanding of this apparent glass-like behavior. Demonstration experiments performed at the Mn K-edge revealed static orbital speckle patterns in a test system,  $\text{LaMnO}_3$  (Figure 2.6.8). However, these experiments, performed at the ESRF, lacked sufficient coherent flux to study the formation of orbital domain walls.

The greatly increased coherent flux at NSLS-II, combined with the large resonant enhancements at the L-edges, as shown in Figure 2.6.9, will allow entirely new classes of experiments to be performed for the first time, including the statistics of orbital and magnetic domains, imaging in real space of the inhomogeneous state and the study of nanostructured materials. It is also possible that in certain temperature ranges, orbital dynamics will be accessible with this technique.

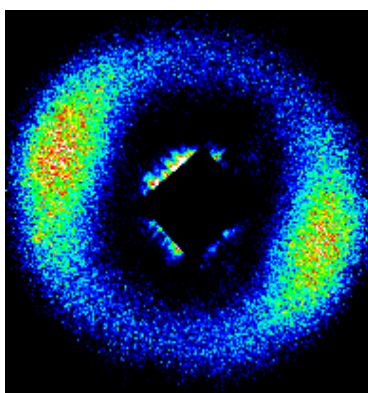


**Figure 2.6.9** Magnetic speckle pattern from a magnetized  $\text{CoPt}$  multilayer taken with the incident X-ray energy tuned to the Co L-edge at 780 eV. Such images provide microscopic real space information on the magnetic state of a sample with nanometer spatial resolution. With the increased coherent flux available at NSLS-II, these techniques will be able to explore both the statics and dynamics of magnetic domains.

### 2.6.3.7 Infra-Red Studies

Infrared beamlines at NSLS-II will have world leading brightness throughout the near to far IR, as discussed in Section 3.4.13. This will be a tremendous advantage in high-resolution IR microscopy utilizing near-field techniques, as well as in ultra-high pressure studies on solids. To achieve the highest-possible working pressures generated in diamond anvil cells, very small gaskets are required, which necessarily entails the ability to focus down to extremely small spot sizes of 100 microns or less. The high IR brightness of NSLS-II will translate directly into more photons on the sample and will make it feasible to look for metal-insulator transitions in highly-correlated systems and for metallic hydrogen. Another area ripe for investigation will be time-resolved spectroscopy of collective excitations in highly-correlated electron systems. The short bunch length at NSLS-II will allow systems with very fast relaxation times to be studied using pump-probe techniques. This will be particularly useful in some of the cuprate materials, where there is considerable evidence for dynamically-fluctuating stripes and infrared anomalies have been observed.

### 2.6.3.8 Materials Synthesis

Strongly correlated electron materials are often doped compounds and synchrotron facilities can improve materials growth by advancing in situ studies of crystal growth in tools such as floating-zone furnaces or high-pressure ovens. The growth of crystals in the former apparatus has been tremendously successful and of considerable impact in the correlated electron field. Yet growing large, single-grain, homogeneous crystals often remains a "trial and error" activity. The ability to track grain growth, phase evolution, and growth orientation in situ would bring a new level of scientific understanding to this crystal growth process.

The study of small (~micron size) samples, and in particular the exploration of magnetism of small samples, would be a tremendous advance for the field. In the growth of doped crystals, composition gradients are inevitable, and indeed an essential aspect of the zone-melting process. Studying small samples will obviously reduce the impact of such distributions. Furthermore, it may be possible to exploit the natural composition gradient of the zone-refining process to map out properties diagrams in a compact, efficient way akin to "combinatorial" studies in thin films. In the case of crystals grown at high pressure, large crystals of the kind required for neutron scattering experiments will be impossible and X-ray scattering techniques will be the only ones of utility.

In the particular case of transition metal oxides (TMOs), the condensed matter field has concentrated on the effects of cation substitution, e.g.,  $\text{La}_{1-x}\text{Sr}_x\text{MnO}_3$  while trying to minimize the impact of nonstoichiometry on the anion sublattice. Modification of this oxide sublattice is known to have dramatic impact on electronic and magnetic states of TMOs, for instance the Y-123 superconductor and the cobaltite  $\text{RBaCo}_2\text{O}_{5+\delta}$  (R=rare earth). However, large, homogeneous crystals are extremely difficult to come by (the nickelates are a notable exception that require considerable precision in the control of T,  $p\text{O}_2$  in their synthesis and cooling to generate homogeneous oxygen distributions).

NSLS-II will enable researchers to fully characterize small single crystal samples in ways comparable to neutron scattering in large, cation-doped materials, opening a new realm of possibilities in TMOs.

### 2.6.3.9 High Pressure

When pressure is applied to matter, atoms are brought closer together, ultimately altering a material's structural, electronic and mechanical properties in radical and often unexpected ways. There are countless examples: metal-insulator transitions occur; some materials reach their yield strength while others become superhard; phase transitions, such as ferroelectric, magnetoresistive, and superconducting, occur; normally unreactive transition metals form alloys with alkali metals; electronic, magnetic, structural and dynamical properties of materials can be determined and tuned for a wide range of technological, defense,

and energy applications; both the highest temperature superconductivity on record and entirely new superconductors have been produced under pressure.

Variations in composition and temperature also change the structural state and the properties of materials. However, changes in these variables are not "clean" since they may be difficult to model (temperature) or reproduce from one synthesis to the next (composition). Isochemical changes of the unit cell volume at high pressure provide unparalleled tests of fundamental theory.

To understand the complex nature of materials, it is essential to observe their response under pressure. With the development of next generation pressure cells, many of these measurements will be extended to higher pressures. Structural studies by X-ray diffraction are an essential starting point for characterizing materials under high pressure (> 100 GPa). Inelastic X-ray scattering can explore in detail the concomitant changes in electronic structure and bonding. EXAFS and XANES measurements can provide local information to beyond the second coordination shells. An understanding of local structure is seen, for example, as the key to understanding the behavior of complex materials such as the oxide superconductors and CMR materials.

The advanced facilities for high pressure research at NSLS-II, described in Section 4.2.1, will provide the combination of local and long range structural probes together with measurements of electronic structure and bonding that are essential for advancing our understanding of these materials in new domains of pressure and temperature.

#### **2.6.3.10 High Magnetic Field**

A steady-state high-field magnet will be another essential component of the core set of extreme condition facilities at NSLS-II, as described in Section 4.2.2. Magnetic field represents a thermodynamic variable, in addition to temperature and pressure, with which to tune the balance of the competing degrees of freedom in these systems and can therefore often provide vital clues as to the nature of that balance. Many of the properties of correlated systems will only be understood through investigation in an applied magnetic field. Most X-ray techniques are equally applicable in an applied field and it is expected that they will be implemented at the high magnetic field beamline.

The high magnetic field beamline at NSLS-II will be invaluable for studies of an extremely wide range of systems, including charge and orbitally ordered states (manganites, ruthenates, titanates, etc.) and field-induced transitions in these compounds; mixed-valent compounds; magnetic semiconductors; materials with quantum critical points; heavy-fermion materials; high- $T_c$  superconductors, including the normal state at high fields; Mott transitions; oxide and sulfur based compounds (BEDT-TTF based organics, etc); one dimensional magnets such as spin-Peierls compounds ( $\text{CuGeO}_3$ ) and field-induced density waves in the TMTSF-based compounds; materials with commensurate-incommensurate transitions; rare earth compounds; frustrated magnets (spinel, pyrochlores, etc); multiferroic compounds ( $\text{YMnO}_3$ ,  $\text{BiMnO}_3$ ); and Jahn-Teller systems (manganites).

#### **2.6.3.11 Ultra-low Temperature**

The final essential component of the extreme conditions facilities at NSLS-II will be ultra-low temperature facilities, as described in Section 4.2.3. Ultra-low temperatures are crucial for a number of reasons, including providing expanded regimes in which to search for novel phases, the ability to test for quantum critical behavior, and as a test bed for theoretical calculations, which may be rigorous in the zero temperature limit. As with high magnetic fields, most X-ray techniques are equally applicable at ultra-low temperatures and it is expected that they will be implemented at the low temperature beamline.

An example of the impact of ultra-low temperature capabilities at NSLS-II is that of frustrated magnetism. Long-range ordering in magnetic systems is generally well understood when a unique ground state exists. When multiple ground states compete at low temperature, however, novel physics emerges from the spin degrees of freedom and is far from understood. The physical systems of interest can be broadly classified into two categories, quantum critical and geometrically frustrated.

Quantum criticality arises when two different magnetic phases, e.g. antiferromagnetic and spin liquid, meet at zero temperature as a physical parameter is varied. Theoretical understanding of quantum criticality is quite advanced and model experimental systems are being studied.

Geometrical frustration arises when a thermodynamically large number of possible ground states compete at temperatures well below the two-spin interaction energy scale. There are empirical rules that govern frustration in materials and several attractive model systems have been identified. Examples include the compounds  $\text{Gd}_3\text{Ga}_5\text{O}_{12}$ ,  $\text{Gd}_2\text{Ti}_2\text{O}_7$ , and  $\text{Dy}_2\text{Ti}_2\text{O}_7$ , which display fascinating spin-liquid and spin-ice ordering. These magnetic states appear at temperatures below 1 K and therefore require dilution refrigeration. It is important to note that neutron scattering cannot be employed to study these systems, since both Gd and Dy have enormous neutron capture cross-sections. X-ray magnetic scattering is the only route to probe the full physics of their geometrical frustration and the ultra-low temperature facility at NSLS-II will be crucial for this.

## REFERENCES

- [1] V. Kiryukhim, T. Y. Koo, H. Ishibashi, J. P. Hill, S. -W. Cheong, *Phys. Rev. B* **67**, 064421 (2003).
- [2] M. Z. Hasan, E. D. Isaacs, Z.-X. Shen, L. L. Miller, K. Tsutsui, T. Tohyama and S. Maekawa, “Electronic Structure of Mott Insulators Studied by Inelastic X-ray Scattering”, *Science* **288**, 1811 (2000).
- [3] M. Z. Hasan, P. A. Montano, E. D. Isaacs, Z.-X. Shen, H. Eisaki, S. K. Sinha, Z. Islam, N. Motoyama and S. Uchida, “Momentum-Resolved Charge Excitations in a Prototype One-Dimensional Mott Insulator”, *Phys. Rev. Lett.* **88**, 177403 (2002).
- [4] Y. J. Kim, J. P. Hill, C. A. Burns, S. Wakimoto, R. J. Birgeneau, D. Casa, T. Gog and C. T. Venkataraman, “Resonant Inelastic X-ray Scattering Study of Charge Excitations in  $\text{La}_2\text{CuO}_4$ ”, *Phys. Rev. Lett.* **89**, 177003 (2002).
- [5] Lee and Nagaosa, cond-matt/0211699.
- [6] V. Boris, D. Munzar, N. N. Kovaleva, B. Liang, C. T. Lin, A. Dubroka, A. V. Pimenov, T. Holden, B. Keimer, Y.-L. Mathis, and C. Bernhard, “Josephson Plasma Resonance and Phonon Anomalies in Trilayer  $\text{Bi}_2\text{Sr}_2\text{Ca}_2\text{Cu}_3\text{O}_{10}$ ”, *Phys Rev. Lett.* **89**, 277001 (2002).
- [7] M. Z. Hasan, et al., *ALS Compend. Report*, LBNL, **R-7.0.1** (1999).
- [8] M. Z. Hasan, *SLAC Report* **R-567** (2001).
- [9] J. M. Tranquada, D. J. Buttrey, V. Sachan and J. E. Lorenzo, “Simultaneous Ordering of Spins and Holes in  $\text{La}_2\text{CuO}_{4.125}$ ”, *Phys Rev. Lett.* **73**, 1003 (1994).
- [10] J. M. Tranquada, J. D. Axe, N. Ichikawa, Y. Nakamura, S. Uchida and B. Nachumi, “Neutron-Scattering Study of Stripe-Phase Order of Holes and Spins in  $\text{La}_{1.48}\text{Nd}_{0.4}\text{Sr}_{0.12}\text{CuO}_4$ ”, *Phys. Rev. B* **54**, 7489 (1996).
- [11] M. Matsuda, M. Fujita, K. Yamada, R. J. Birgeneau, M. A. Kastner, H. Hiraka, Y. Endoh, S. Wakimoto and G. Shirane, “Static and Dynamic Spin Correlations in the Spin-Glass Phase of Slightly Doped  $\text{La}_{2-x}\text{Sr}_x\text{CuO}_4$ ”, *Phys. Rev. B* **62**, 9148 (2000).
- [12] S. Wakimoto, G. Shirane, Y. Endoh, K. Hirota, S. Ueki, K. Yamada, R. J. Birgeneau, M. A. Kastner, Y. S. Lee, P. M. Gehring and S. H. Lee, “Observation of Incommensurate Magnetic Correlations at the Lower Critical Concentration for Superconductivity in  $\text{La}_{2-x}\text{Sr}_x\text{CuO}_4$  ( $x=0.05$ )”, *Phys. Rev. B* **60**, R769 (1999).
- [13] Y. S. Lee, R. J. Birgeneau, M. A. Kastner, Y. Endoh, S. Wakimoto, K. Yamada, R. W. Erwin, S.-H. Lee and G. Shirane, “Neutron-Scattering Study of Spin-Density Wave Order in the Superconducting State of  $\text{La}_2\text{CuO}_{4+y}$ ”, *Phys. Rev. B*, **60**, 3643 (1999).
- [14] P. Abbamonte, L. Venema, A. Rusydi, G. Sawatzky, G. Logvenov and I. Bozovic, “A Structural Probe of the Doped Holes in Copper-Oxide Superconductors”, *Science*, **297**, 581 (2002).
- [15] D.-L. Feng, et al., unpublished data.
- [16] P. Abbamonte, et al., unpublished data
- [17] C. Schussler-Langheine, et al., unpublished data

- [18] K. J. Thomas, *et. al.*, cond-matt/0311553.
- [19] C. S. Nelson, *et. al.*, Physical Review B (2002).

## 2.7 Magnetism

### 2.7.1 Overview

Magnetism continues to play an important role in fundamental physics as well as in technological applications. In magnetic materials, superimposed on the spatial charge-order (the crystalline lattice), there is a second spontaneous spatial ordering of the magnetic moments. Why the atomic magnetic moments survive and how they arrange in the solid is the subject of magnetism. Research in magnetic materials can be divided into three principal areas: the study of the microscopic electronic interactions that give rise to the local magnetic moments (the exchange interaction); the study of the long-range interactions of these moments with the resulting formation of macroscopic magnetic domains (the spin-orbit interaction); and finally, the study of the interaction between magnetic domains, which tend to arrange in macroscopic ordered structures to minimize the total energy of the system, including the magnetic energy stored in its surroundings (micromagnetic interactions).

The past 20 years have shown a steady progress in all these three areas. Synchrotron radiation is playing an increasingly important role in this activity, spurring the development of a number of unique spectroscopic techniques especially designed for the study of magnetism.

Initially the high photon-flux was the main motivation for the use of synchrotron radiation; as a result, new techniques such as spin-resolved photoemission suddenly became possible. More recently, the possibility of creating both linear and circular light polarization via extensive use of advanced insertion devices in third generation rings has driven the application of synchrotron radiation in the field of magnetism. Traditional synchrotron-based techniques such as absorption, reflection and light scattering have been adapted to take full advantage of the light polarization control. This has permitted the observation of large magnetic dichroism effects, now routinely employed in magnetic studies.

Synchrotron radiation techniques have become indispensable tools for the investigation of the properties of magnetic materials. For example, spin-polarized electronic band dispersions, magnetic moments (in bulk and/or at surfaces), magnetic anisotropies and susceptibilities, Curie temperatures and critical behavior at phase transitions are routinely determined at synchrotron beamlines.

The extension of spectroscopic methods that are sensitive to the orientation of magnetic moments to the field of microscopy, with nanometer length scale resolution, will permit the simultaneous observation of magnetic-domain and topographical structures with element sensitivity. Application of the time structure of synchrotron radiation to magnetism will allow investigation of the dynamics of magnetic phenomena. The high brightness, short pulse length, and broad spectral coverage of NSLS-II together with advanced insertion devices with full polarization control will dramatically advance our understanding of magnetism.

### 2.7.2 Scientific Challenges and Opportunities

#### 2.7.2.1 Low Dimensional Magnetism

The possibility of direct manipulation of the electronic wavefunctions in artificially engineered materials has opened new and exciting vistas on all aspects of solid state physics. This wavefunction engineering modifies the magnetic properties to such a degree that these nano-engineered systems can be considered entirely new classes of magnetic materials. Much of this fundamental work has been possible because of increased abilities in the preparation and characterization of “exotic” magnetic structures and because of the extremely sophisticated probing capabilities realized at synchrotron radiation facilities.

The fundamental difference between a material in film form rather than bulk is the quantization of electronic levels induced by the film geometry (Figure 2.7.1). The study of the properties of discreet energy levels (Quantum Well States) in two dimensional systems has been crucial in understanding the indirect exchange interaction recently discovered in metallic magnetic multilayers [3]. Magnetic

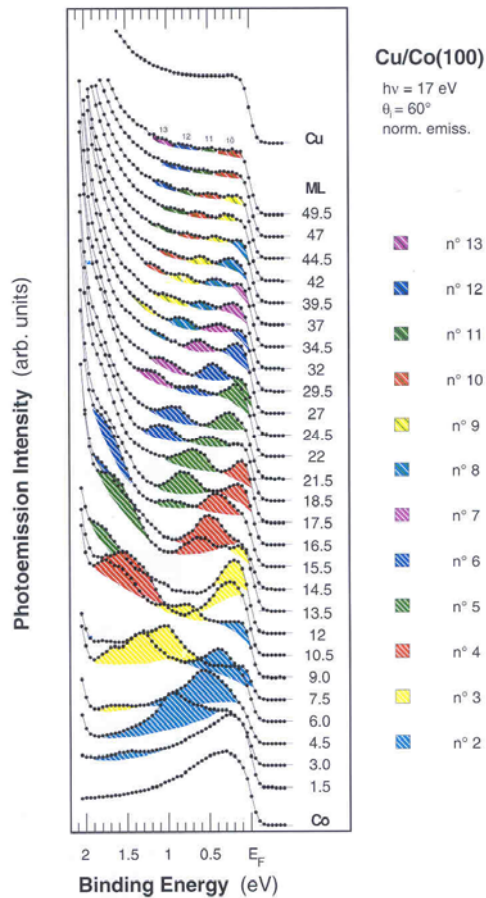


**Figure 2.7.1** Angular-resolved photoemission experiments performed with synchrotron radiation allow the direct sampling of discrete energy levels (colored peaks) in ultra-thin films of Cu (thickness indicated in monolayers units), epitaxially grown on a Co(100) single crystal. The ability to control the light polarization (linear in this case) as well as the photon energy proved essential for this type of experiments [1]. The study of the quantization of states in ultra-thin films not only allows the experimental determination of the bulk band structure with unprecedented precision but it also serves in measuring essential properties of quasi-particles such as lifetime broadening, interfacial reflectivity and phase-shift [2].

multilayers are artificial structures that are prepared by alternate superposition of layers of magnetic and non-magnetic (spacers) metallic materials. The interest in these systems stems from their peculiar physical properties that have no counterpart in bulk: i.e. their properties do not correspond to the superposition of the properties of the constituent materials. Among these - and of great relevance for technological application - are the electronic transport properties (Figure 2.7.2).

The two-dimensional film geometry is clearly the simplest possibility of confining electronic wavefunctions. Modern material science technologies however allow the preparation of structures such as atomic chains and clusters in which electrons are confined in two or even in all three-dimensions. This further confinement has been shown to have spectacular effects in magnetic materials. For example the orbital moments that are effectively quenched in the formation of itinerant magnetic metals can be considerably restored in these lower dimensional systems. At third generation light sources, the high photon flux enables the detection of extremely small quantities of material. Single atomic monolayers and even one dimensional chains become measurable with element-specific magnetic spectroscopy techniques such as magnetic circular dichroism (Figure 2.7.3).

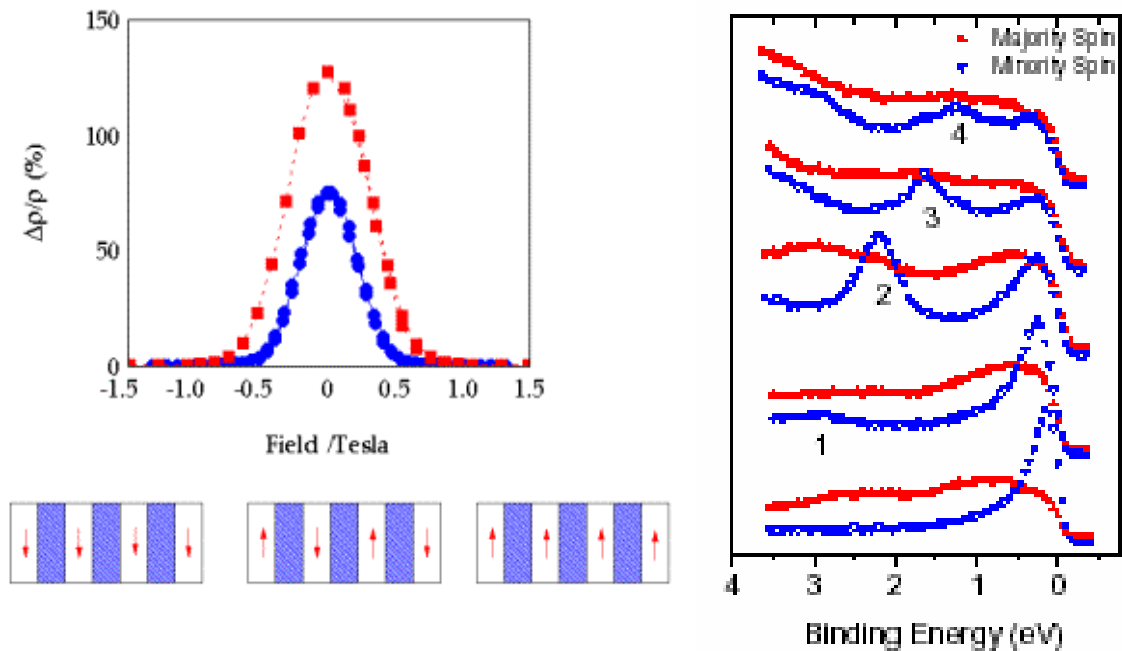


**Figure 2.7.2** In magnetic multilayers with spontaneous anti-parallel alignment, the relative resistance decreases with increasing magnetic field: a conspicuous magnetic phenomenon aptly called Giant Magneto Resistance (left panel). This connection between magnetic and electric properties is technologically significant because it can be used to convert magnetic signals in electrical ones. Magnetic field sensors based on GMR effects in films a few nanometers thick are nowadays routinely employed in industrial application in read-out heads for magnetic memories. The spontaneous alignment, which makes the GMR effect possible, is explained by the existence of spin-polarized QW States in the non-magnetic layers. These states effectively transport the magnetic information from one magnetic layer to the next, thereby enabling the long-range coordination of the single-layer magnetization. An example of these states is shown on the right panel; here quantum well states from 1, 2, 3 and 4 monolayers of Ag grown on an Fe substrate are monitored using Spin-Resolved photoemission. The QW States displays an extremely high degree of (negative) spin-polarization (blue curves: minority spin) [4].

Quite apart from electronic confinement effects, another aspect of low dimensional magnetism has very important technological implications. It is related to the intrinsic anisotropy of these systems. The property that makes magnets so useful in applications is the magnetic anisotropy energy (MAE). MAE describes the tendency of the magnetization to align along specific spatial directions rather than randomly fluctuate over time (Figure 2.7.4).

The quantitative study of this kind of phenomena is usually difficult because the energy differences between competing macroscopic configurations are very small. Nevertheless, low dimensional structures such as films, chains and dots are all highly anisotropic and significant effects on the MAE are expected and are actively investigated in these systems. For example easy-magnetization directions different from those of the bulk materials have been successfully stabilized by MBE deposition of epitaxial films. Even more importantly, perpendicular magnetization in thin film samples has been observed in a number of cases. These systems have the prospect of very high bit-density in magnetic storage memories.

For these reasons the effects of low dimensionality on the anisotropy properties of materials are an important topic of current research in magnetism. These studies require a careful characterization of the system to be investigated (which is a difficult material science research project in itself) and intense radiation sources due to the small amount of material being sampled. For example, recent work at high-flux beamlines at ESRF has demonstrated the possibility of detecting MCD signals from single isolated

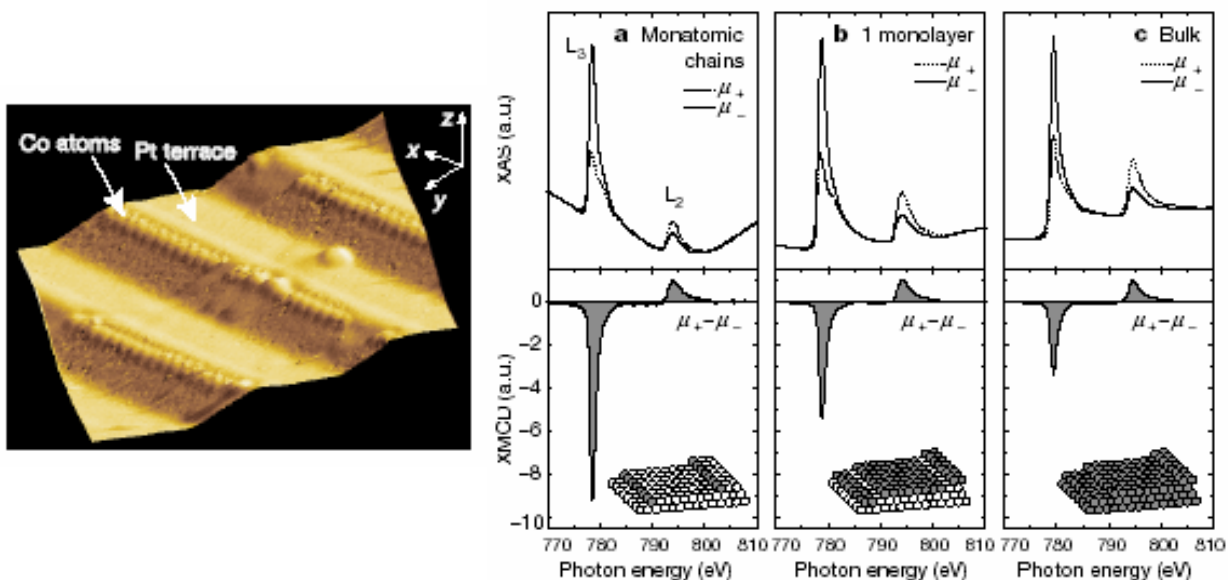


**Figure 2.7.3** Left panel: STM images. Long atomic chains of magnetic material (Co) are obtained by “step-decoration” of a vicinal Pt (111) surface. Right Panel: Corresponding to higher and higher confinement, the Co orbital moment increases substantially, as seen in the MCD spectra of Co on Pt (111) [5].

clusters consisting on the average of only 3 atoms! These results are indeed spectacular and indicate the importance of high brightness, high flux synchrotron radiation for research in magnetism.

The examples of studies on magnetic-multilayers, magnetic films, magnetic chains and magnetic dots just described demonstrate that the opportunities for fundamental as well as applied research in the area of the magnetism of low dimensional structures are vast and still largely unexplored. In this area, synchrotron radiation based spectroscopies constitute unique tools that will continue to be of extreme value in the foreseeable future. Indeed, the high brightness and high flux of NSLS-II are crucial for enabling continued major progress in this field by greatly enhancing the ability to detect small signals from a diminishing number of atoms.

### 2.7.2.2 Complex Magnetic Materials

The notable improvements in sample preparation and characterization techniques over the last 10 years has caused a considerable shift of research in magnetism toward the study of complex materials, often in artificially engineered structures. Spintronic applications, which combine the exquisite control of charges in traditional semiconductor based electronics with the direct manipulation of electronic spin, will have a revolutionary impact on technology.

In a recent article, Wolf and co-authors summarized the potential of new technologies but also pointed out a number of issues that must be understood and overcome before the technology can mature: “It is envisioned that the merging of electronics, photonics, and magnetics will ultimately lead to new spin-based multifunctional devices such as spin-FET (field effect transistor), spin-LED (light-emitting diode), spin RTD (resonant tunneling device), optical switches operating at terahertz frequency, modulators, encoders, decoders, and quantum bits for quantum computation and communication. The success of these ventures depends on a deeper understanding of fundamental spin interactions in solid state materials as well as the roles of dimensionality, defects, and semiconductor band structure in modifying these dynamics. If we can understand and control the spin degree of freedom in semiconductors, semiconductor heterostructures, and ferromagnets, the potential for high-performance

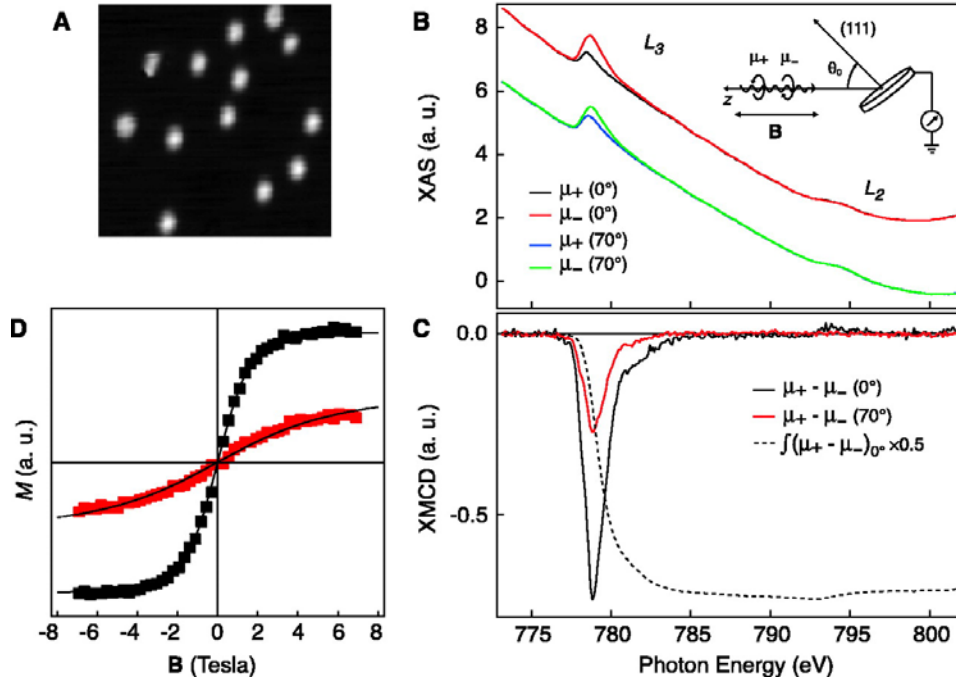


**Figure 2.7.4** Isolated Co atoms deposited on a Pt (111) surface are monitored with MCD techniques using synchrotron light. The MAE is extremely high in this Co atoms: external fields as high as 7 T are not quite enough to align the moments along the substrate plane (panel D: red curve in plane magnetization, black curve out of plane magnetization) [6].

spin-based electronics will be excellent. The most interesting devices will probably be those that we have not even contemplated here!" [7]

At the moment, diluted magnetic semiconductors (DMS) constitute one of the most promising classes of new magnetic materials for spintronic applications. Their principal interest stems from the possibility of (relatively) easily integrating magnetic degrees of freedom in traditional semiconductor technologies. DMS combines its transport and/or optical properties with magnetism, and thereby carries an enormous potential for opening up a path to entirely new devices.

Up to now,  $\text{Ga}_{1-x}\text{Mn}_x\text{As}$  has been a representative DMS with a moderately high Curie temperature ( $T_C$ )  $\sim 100$  K. Therefore, an essential task is to find a DMS with  $T_C$  above the room temperature. Recently, a few DMS based on wide gap II-VI and III-V semiconductors have been reported to have such high  $T_C$ . However, the reproducibility of  $T_C$  is somewhat questionable. More fundamentally, the origin of ferromagnetism in DMS materials is still very much an open question. Synchrotron-based spectroscopies are indispensable tools in unraveling the detailed mechanism that governs the magnetic behavior in DMS.

In DMS, the doped magnetic ions can be either 3d transition metal ions or 4f lanthanide ions, and the typical doping levels are the order of a few percent. Element specific X-ray absorption combined with magnetic circular dichroism (XMCD) provides unique tools to probe the spin and valence states in these systems and to clarify the ferromagnetic origin in DMS [8]. Furthermore the impurity band induced by the Mn-doping in GaAs was recently successfully detected in an angle-resolved photoemission spectroscopy study. As predicted by the theory, the impurity band is localized very near the Fermi level, confirming that the charge carriers in Mn-doped GaAs are governed by this impurity band (Figure 2.7.5).

The efficiency of spintronic devices depends closely on the value of the spin polarization (the imbalance between spin-up and spin-down charge carriers) near the Fermi level. Theoretical predictions for  $\text{Ga}_{1-x}\text{Mn}_x\text{As}$  indicate that it may be a half-metallic ferromagnet (i.e., fully spin polarized) and thus would be a very efficient material for use in spintronic devices. A measurement of the spin polarization of the near-Fermi level states can confirm the half-metallicity as well the ferromagnetic nature of  $\text{Ga}_1$ .

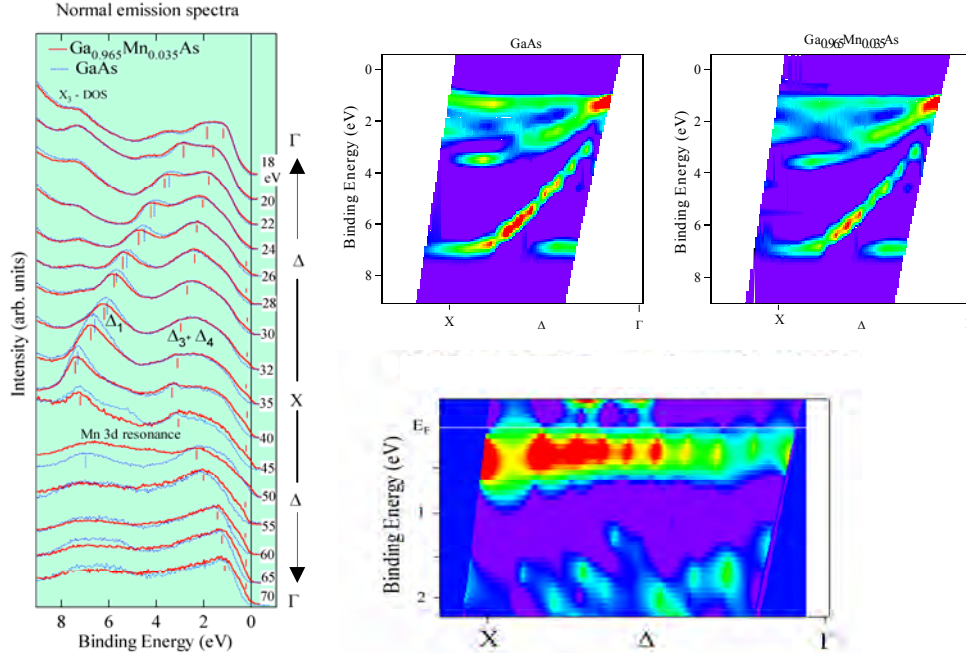


**Figure 2.7.5** Angle resolved photoemission spectra and experimental electronic band structures of pure GaAs and  $Ga_{1-x}Mn_xAs$ . The impurity band induced by the Mn-doping is determined from their difference. At third generation light sources, the extremely high photon flux will allow the spin resolved photoemission measurements of the impurity band and the determination of the spin-polarization of the charge carrier [9].

$xMn_xAs$ . As is shown below in the case of magnetite materials, spin-resolved photoemission spectroscopy is the most direct measurement technique to determine the spin polarization. Unfortunately, its efficiency falls down by about four orders of magnitude in comparison with the conventional photoemission spectroscopy. Considering the fact that the impurity bands have very small spectral weights in DMS systems, one expects that the measurement will require the extremely high photon flux planned for NSLS-II.

Another class of materials of great interest for magnetism research and applications is strongly correlated materials. In these materials the strong electron correlation in partially filled orbitals causes a whole variety of interrelated phenomena such as metal-insulator transitions, orbital ordering, charge ordering, lattice and magnetic polarons, etc. When these complex systems contain magnetic ions, new phenomena, such as the colossal magneto resistance (CMR) effect, result from the interplay between electronic and magnetic degrees of freedom.

An important example of this kind of interplay is offered by films of  $La_{0.7}Sr_{0.3}MnO_3$ . This CMR material can carry electric current only when the spins of the itinerant charges are aligned parallel to the spins of the manganese ions fixed in the crystal lattice. This system then constitutes a natural source of  $\sim 100\%$  spin-polarized current, i.e., it is a half-metallic material. The existence of half-metallic materials was hypothesized long ago to account for magneto-transport properties of bulk  $La_{0.7}Sr_{0.3}MnO_3$ . Their existence was recently verified by spin resolved photoemission at NSLS (Figure 2.7.6).

While DMS and highly correlated materials offer great promise in advancing spintronic technologies, these exotic materials must be incorporated into appropriate device architectures. For example, the use of half-metallic materials will be of great benefit in magnetic tunnel junctions (MTJ), which are three-layer devices with two ferromagnetic metallic layers separated by an insulating layer. Currently, there are great challenges in measuring and controlling parameters such as interface quality, tunnel barrier quality, surface/interface roughness, ferromagnetic electrode quality, magnetic domain walls, and, finally, the

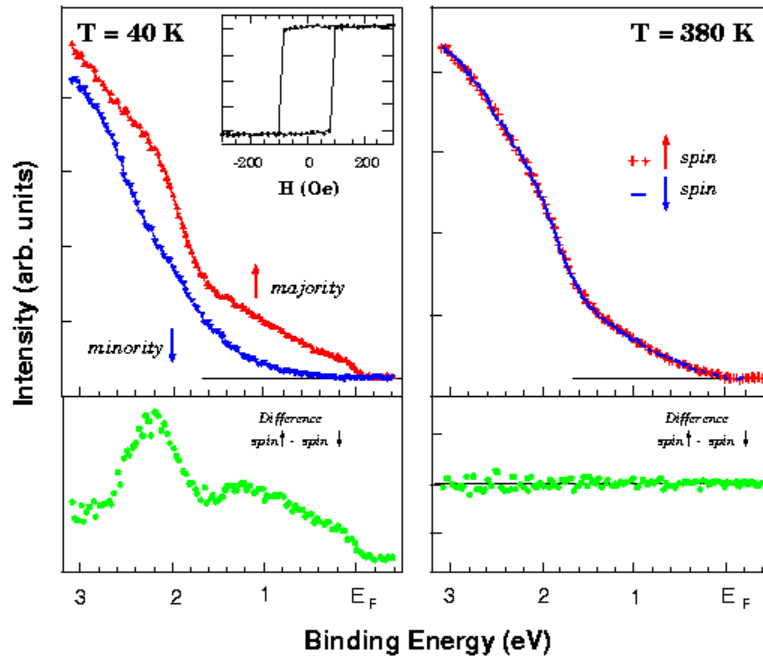


**Figure 2.7.6** *Half-Metallic Material: At low temperature (left panel)  $La_{0.7}Sr_{0.3}MnO_3$  is conducting. Spin-resolved photoemission spectra from the region close to the Fermi level show that the conduction is totally carried by majority spin electrons (red curve). At high temperature (right panel) this material becomes both paramagnetic (blue and red curves superimposed) and insulating (no intensity at  $E_F$ ) [10].*

intrinsic behavior of ferromagnetic surfaces/interfaces. Moreover, as miniaturization of components continues, these potential obstacles must be overcome at the sub-micron and even nanometer length scale.

NSLS-II will greatly help in meeting these challenges. For example, its superior flux in the soft X-ray region will provide the perfect opportunity to extend the technique of valence band spin-resolved photoemission to higher kinetic energies. This will enable the investigation of the electronic structure of highly relevant buried interfaces, such as the ones between a ferromagnet and insulator in MTJs. Moreover, synchrotron based X-ray scattering studies, particularly resonant scattering techniques, provide detailed information on issues such as interface quality and spin-orientations at an interface. As these techniques often deal with processes that have an intrinsically low excitation cross section, the increased flux of NSLS-II will be of crucial benefit. Finally, the greatly increased flux of NSLS-II will enable element-specific core-level spectroscopic investigations of materials such as DMS, which often have small amounts of magnetically active components.

### 2.7.2.3 Magnetic X-ray Microscopy

Current research into magnetic materials focuses on complex, multi-element systems that are often engineered into layered or even more complex geometries. There is a great need to develop analytical tools that can interrogate the magnetic state of a sample with element-specificity as well as nanometer-scale lateral and depth resolution [11]. Real-space imaging techniques based on X-ray microscopies (XRM) such as photoelectron emission microscopy (PEEM) or X-ray transmission microscopy (XTM), combined with an appropriate choice of photon energy and polarization, can provide such a capability on lateral length scales currently around 20 nm, with planned near-term improvements approaching 1 nm [12, 13].

XRM combines a number of features that are found in other forms of magnetic microscopies with capabilities that are unique to synchrotron-based instrumentation. The benefits of XRM for the

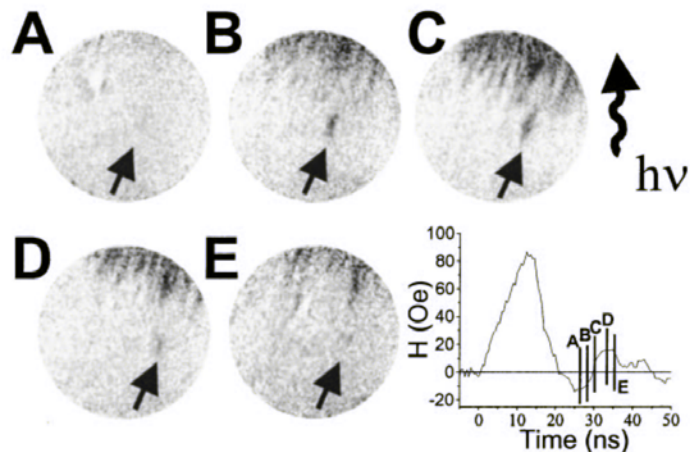


**Figure 2.7.7** Magnetic PEEM domain images of a NiFe layer, taken 13, 15, 17, 20, and 22 ns after the maximum of an 80 Oe field pulse; the field of view is  $\sim 120 \mu\text{m}$ . The arrows indicate a nucleated and subsequently expanding reversed domain. [14]. NSLS-II will enable improvements to both the spatial and temporal resolution.

investigation of magnetic systems are many and include: element specificity; sensitivity to ferromagnetic & antiferromagnetic order (XMCD & XMLD); measurements in applied fields (photon-in, photon out techniques); quantitative analysis of sample magnetization (spin & orbital moments and identification of magnetization vector); high spatial resolution; and high time-resolution. The last two points in particular will benefit greatly from the improvements in X-ray microscopy that will be attained with the superior capabilities of NSLS-II.

As will be seen in the following section, a thorough understanding of the dynamical processes in magnetic systems is crucial for continued development of advanced magneto-electronic devices. Combining these studies with the high spatial resolution of X-ray microscopy will allow investigators to probe fundamental questions involving issues such as the magnetization reversal processes in advanced magnetic materials and the role of reduced dimensionality on the dynamical response of nano-engineered materials.

As an example, Figure 2.7.7 shows time and element resolved (in this case, the images were acquired at the Fe  $L_3$  edge) PEEM images for a  $\text{Ni}_{80}\text{Fe}_{20}$  (5 nm)/Cu (10 nm)/Co (5 nm) spin-valve like trilayer grown on Si (111) [14]. The PEEM images labeled A through E in the figure show the magnetic domain pattern of the NiFe layer with a spacing of approximately 2 ns between frames after the application of a magnetization reversing field pulse. The images, with a field of view of  $\sim 120 \mu\text{m}$ , clearly show domain nucleation (black arrow) and subsequent growth. NSLS-II will improve these types of studies in two areas. First, the greatly increased brightness of the new source will allow a reduction in the field of view and an improvement of the spatial resolution of the time-resolved images. Also, the shorter bunch length of the upgraded machine, currently planned at 30 psec or shorter, will improve the time resolution of the images.

In addition to the direct, real space imaging techniques outlined above, the availability of coherent X-rays from undulator sources has stimulated the development of magnetic speckle imaging. A growing number of research groups worldwide are developing new full-field magnetic imaging techniques and new techniques for the study of magnetic dynamics. For example, an algorithm based on multi-wavelength anomalous diffraction (MAD) has been developed recently at NSLS for reconstruction of magnetic domain pattern from magnetic speckles [15] and an example of the speckle pattern from microscopic domains in a CoPt thin-film is presented in Figure 2.7.8. This technique can be extended to time-resolved measurements for the study of magnetic dynamic processes.

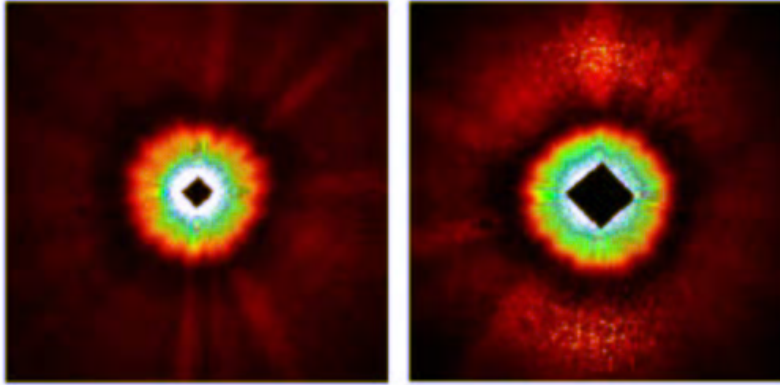


**Figure 2.7.8** Speckle-images measured at the Co L3 edge from a CoPt multilayer (sample from O. Hellwig, IBM Almaden). Left and right panels are the images taken off and on resonance, respectively. On-resonance the magnetic contrast clearly appears as a ring corresponding to the average magnetic domain size ( $\sim 150$  nm) [15].

Magnetic speckle imaging will be of particular importance in examining the interactions within magnetic nanoparticle arrays. Magnetic nanoparticle arrays have been made from monodisperse 3-20 nm particles that self assemble into ordered structures. Just as the exchange and magnetostatic interactions between iron atoms in a crystal lead to the formation of ferromagnetic domains, the magnetic nanoparticle interactions should lead to domain structures. Magnetic speckle techniques using coherent X-rays will enable magnetic domains to be imaged in the nanoparticle arrays. With a smaller interparticle separation or a more conducting matrix between the particles, exchange interactions will become significant [16], and the particle wave function will delocalize over the array, leading to an insulator-to-metal transition [17]. The ability to image magnetic domains while varying the applied field and temperature and while passing spin-polarized currents through the sample would provide a powerful tool for understanding these nanoengineered magnets. Unlike neutrons in SANS or electrons in Lorentz microscopy, the X-ray photons would not be deflected by the external magnetic field. The increased brightness of NSLS-II will greatly improve the signal to noise ratio that is presently a limiting factor in the further development of magnetic speckle imaging.

#### 2.7.2.4 Magneto-Dynamic Phenomena

Dynamic processes, in particular ultra-fast dynamics, are at the forefront of research on magnetic materials [18]. Here the goal is to obtain a detailed description of magnetization reversal processes in magnetic materials subject to external perturbations (magnetic, electric, thermal, or pressure). The detailed understanding of these processes is fundamentally interesting as well as obviously crucial in the development of high-speed recording media as well as other novel magnetic devices (e.g., spin electronics) [19]. Typically, magnetization-reversals in solids (i.e., the transfer of magnetic orientation between atoms) are mediated by spin-lattice relaxations. The relevant time-constants, estimated by considering the emission and lifetime of spin-waves in a crystalline lattice, are in the range of  $10^{-12}$  -  $10^{-10}$  sec [20]. To overcome this limit, several new concepts have been recently suggested such as the possibility of switching the magnetization of metallic nano-particles via injection of spin polarized currents (i.e. via direct exchange scattering) [19]. In this case the relevant time scale would be close to the fundamental dynamics of itinerant ferromagnets (i.e. Stoner excitation  $\sim 10^{-15}$  sec) [21]. The development of experimental probes, capable of high magnetic sensitivity and ultra-fast time-resolution, is then needed for these investigations.

Currently ultra-fast magnetic dynamics can be studied by analyzing the magneto-optical Kerr and Faraday rotations induced in ultra-fast pulsed laser sources. These techniques, an example of which is presented in Figure 2.7.9, have already revealed a wealth of extremely useful information but are sensitive

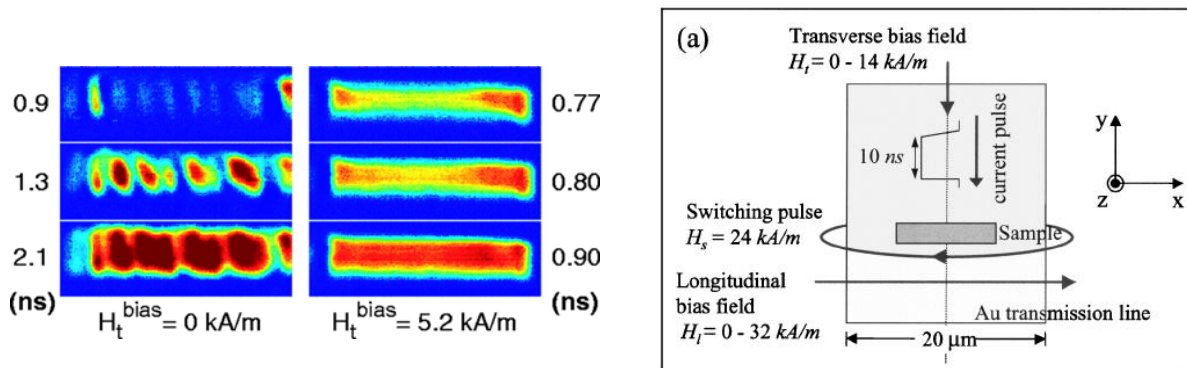


**Figure 2.7.9** a) Schematic configuration of 180 degree magnetization reversal. The magnetization is switched via a current pulse. The presence of bias-fields alters the dynamic mechanisms of the reversal process. MOKE image magnetization reversal in a  $Ni_{80}Fe_{20}$   $12 \times 2 \mu m$  sample exposed to a fast magnetic switching pulse. Note the change in the domain switching dynamics (both in time and space) obtained applying an external bias field [22].

only to the average magnetization, and furthermore limited in their ultimate spatial resolution [22]. However the novel materials now being developed for use in magnetic technologies (such as magnetic tunnel-junction random-access memories) are often complex artificially engineered, multi-element and multi-layer structures [19, 23]. Element-specific probes of magnetic interactions on timescales relevant to the physical processes outlined in Table 2.7.1 are therefore required. Ultra-fast, time resolved core-level spectroscopies at NSLS-II will provide the element-specificity required to separate the contributions from the components of new materials. Furthermore, as many of the samples will be based on small devices and structures, the small spot size and increased brightness of the new source will be indispensable.

The availability of photon pulses as short as 11 psec at NSLS-II will greatly aid the development of elementally resolved investigations of dynamic magnetic processes at ultra-fast time scales, providing investigators with an element-specific strobe light at time scales relevant to most of the physical processes highlighted in Table 2.7.1. NSLS researchers recently demonstrated the feasibility of element-resolved magnetic measurements on fast timescales in measurements at the Advanced Photon Source. The

Excitation / Interaction	Time scale (sec)
Exchange interaction	$10^{-15}$
Stoner excitations	$10^{-15} - 10^{-14}$
Spin Waves	$10^{-12}$ (low q limit)
Precessional rotation and damping	$10^{-9}$
Domain nucleation	$10^{-9}$
Domain wall motion	$10^{-9}$
Spin-lattice relaxation	$10^{-9}$
Magnetic Viscosity	$10^{-6} - 10^{-3}$
Spin injection into semiconductors	TBD
Spin diffusion	TBD
Spin coherence time	TBD

**Table 2.7.1** The dynamical processes in magnetic materials span an impressive breadth of timescales. The successful development of ultra-fast magnetic devices (storage memories are now already operating at GHz rates) must take into account the dynamic behavior of materials on extremely short time-scales. Time-resolved, synchrotron-based experiments feasible at NSLS-II will be particularly useful in this research area. A great advantage of NSLS-II over the present NSLS is the dramatically reduced bunch length of 11 ps. This will enable standard pump-probe techniques on time scales relevant to most of the processes outlined above.

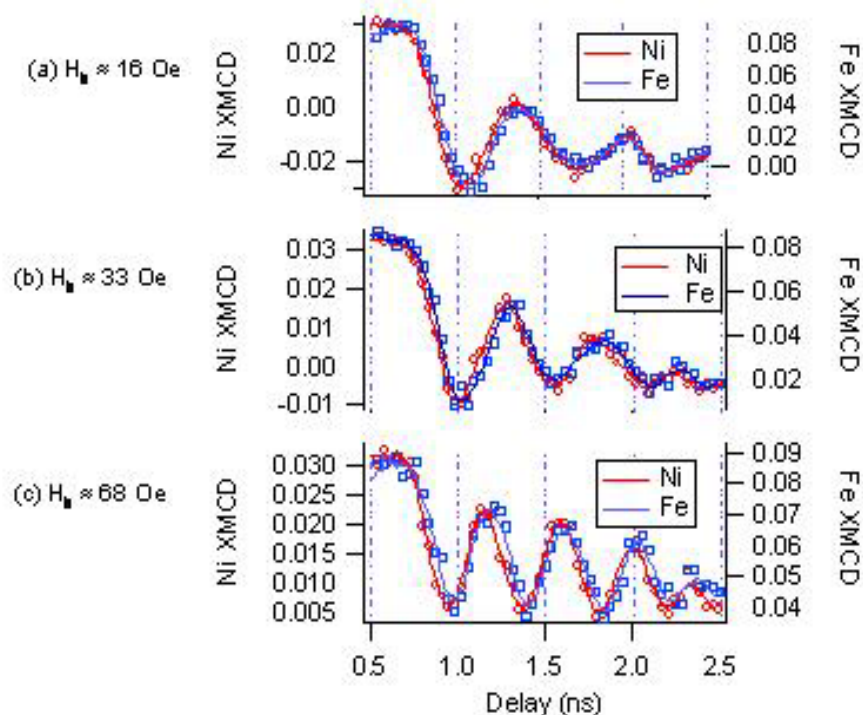


**Figure 2.7.10** Time-resolved X-ray magnetic circular dichroism (XMCD) study in reflection geometry of the relaxation of the magnetization of a 50 nm thick permalloy ( $\text{Ni}_{80}\text{Fe}_{20}$  alloy) film after the application of a fast ( $\sim 100$  psec rise and fall time) magnetization pulse. The measurement was made using standard pump-probe architecture: a variable delay between the magnetization pulse and the photon bunches in the APS storage ring was used to track the horizontal component of the either the Ni (red) or Fe (blue) magnetic moment. After the magnetization pulse, the magnetic moments of the Ni and Fe precess coherently about the bias field ( $H_b$ ) with decaying amplitude, in agreement with the Landau-Lifschitz-Gilbert theory of magnetization dynamics. The frequency of the precession increases with the bias field, as seen in panels (a), (b) and (c) [24].

magnetization dynamics of a 50 nm thick permalloy ( $\text{Ni}_{80}\text{Fe}_{20}$  alloy) film was measured with element specificity on a time scale of  $\sim 100$  psec (Figure 2.2.10) [24]. This proof-of-concept experiment opens up new research areas that will directly address long-standing controversies such as the microscopic origin of ferromagnetic relaxation (e.g. valence exchange, slow relaxer, and fast relaxer models), the interplay between shape anisotropy and demagnetization fields and magnetization reversal mechanisms, and the influence of non-magnetic layers on the dynamical response of ferromagnetic materials. NSLS-II will greatly aid these efforts by providing more intense photon pulses with a time structure almost an order of magnitude shorter than current state-of-the-art storage rings.

Another major advantage of NSLS-II is the dramatic increase in brightness over existing soft X-ray sources. The brightness of the soft X-ray elliptically-polarized undulators will range from  $10^{20}$  (photons/sec/0.1% BW/mm<sup>2</sup>/mrad<sup>2</sup>) at 200 eV (e.g., C K-edge) to  $2 \times 10^{21}$  at 2000 eV (Figure 3.3.3). This represents an increase over the ALS by a factor of 25 at 200 eV to a factor of 3000 at 2000 eV (Figure 3.3.4). This dramatically increased brightness will greatly improve the signal-to-noise ratio of time-resolved experiments. Additionally, it will maximize the data collection efficiency of time-resolved experiments that utilize low-duty cycle pulsers and lasers.

Finally, the soft X-ray insertion devices planned for NSLS-II will have the capability to manipulate the polarization state of the radiation incident on a sample. Switching the polarization between right and left circular polarization forms the basis of many XMCD experiments. Similarly, linearly polarized light will be variable from horizontal to vertical polarization; changes between these polarization states,

combined with appropriate sample geometry, can yield information on anti-ferromagnetic order, or changes in local symmetry due to lattice reconstructions such as the Jahn-Teller distortion in manganites. The soft X-ray range (200-2000 eV) is also particularly well suited to studies of transition metals (L-edges), rare-earths (M-edges) and C, N, O (K-edges). These are the most widely used elements in magnetic systems.

## REFERENCES

- [1] C. Carbone, et. al., *Physical Review Letters* **71**, 2805 (1993).
- [2] J. J. Paggel, et. al., *Science* **283**, 1709 (1999).
- [3] J. E. Ortega, et. al., *Physical Review Lett.* **69**, 844 (1992).
- [4] E. Vescovo, unpublished [NSLS 2003]
- [5] P. Gambardella, et. al., *Nature* **416**, 301 (2002).
- [6] P. Gambardella, et. al., *Science* **300**, 1130 (2003).
- [7] S. A. Wolf, et. al., *Science* **294**, 1488-1495, (2001).
- [8] Kim, et. al., *Physical Review Letters* **90**, 017401 (2003).
- [9] J. Okabayashi, et. al., *Physical Review B* **64**, 125304 (2001).
- [10] J. H. Park, et. al., *Nature* **81**, 1953 (1998).
- [11] M. R. Freeman and B. C. Choi, *Science* **294**, 1484 (2001).
- [12] J. Stöhr, H. A. Padmore, S. Anders, T. Stammler, and M. R. Scheinfein, *Surface Review and Letters* **5**, 1297 (1998).
- [13] P. Fischer, T. Eimüller, G. Schütz, P. Guttman, G. Schmahl, K. Prueg, and G. Bayreuther, *J. Phys. D: Applied Physics* **31** 649 (1998).
- [14] J. Vogel, W. Kuch, M. Bonfim, J. Camarero, Y. Penec, F. Offi, K. Fukumoto, J. Kirschner, A. Fontaine, and S. Pizzini, *Applied Physics Letters*, **82**, 2299 (2003).
- [15] T. O. Mentis, C. Sanchez-Hanke, and C. C. Kao, *Journal of Synchrotron Radiation* **9**, 90-95 (2002).
- [16] V. N. Kondratyev and H. O. Lutz, *Physical Review B* **81**, 4508 (1998).
- [17] C. P. Collier, R. J. Saykally, J. J. Shiang, S. E. Henrichs, and J. R. Heath, *Science* **277**, 1978-1981 (1997).
- [18] M. R. Freeman and B. C. Choi, *Science* **294**, 1484 (2001).
- [19] S. A. Wolf, D. D. Awschalom, R. A. Buhrman, J. M. Daughton, S. v. Molnár, M. L. Roukes, A. Y. Chitchekanova, and D. M. Treger, *Science*, **294**, 1488-1495 (2001).
- [20] S. Blundell, *Magnetism in Condensed Matter*. New York: Oxford University Press (2001).
- [21] L. Berger, *Physical Review B* **54**, 9353 (1996).
- [22] B. C. Choi, M. Belov, W. K. Hiebert, G. E. Ballentine, and M. R. Freeman, *Physical Review Letters* **86**, 728 (2000).
- [23] G. A. Prinz, *Science* **282**, 1660-1663 (1998).
- [24] W. E. Bailey, E. Vescovo, C. C. Kao, and D. A. Arena, unpublished results.

## 2.8 Growth and Processing of Advanced Materials

### 2.8.1 Overview

One of the key scientific challenges in coming decades will be synthesis of advanced materials, ranging from single crystals to thin films and nanoscaled structures. It is clear that in-situ studies will play a central role in understanding synthesis routes and characterizing the samples produced.

Growth of thin films is a non-equilibrium phenomenon governed by a competition between kinetics and thermodynamics. Figure 2.8.1 schematically illustrates common themes that run through all thin film growth processes and methods. The properties of a large fraction of naturally and artificially grown materials depend in detail on the interface between the growing crystal and environment. An important challenge of characterizing growing systems in real time is the wide variation in density in which one finds growing crystal interfaces. It ranges from an ultra-high vacuum environment of less than  $10^{-9}$  Torr through 24 Torr, the vapor pressure of water at room temperature, through to the densest, the liquid/crystal interface. The benefits of photons in the energy range that will be available at NSLS-II for characterizing these interfaces are well understood. The weak electron-photon interaction provides for a deeply penetrating technique that enables the in-situ study of many systems, including the study of many crystal growth systems in real time. The weak photon scattering cross section also results in data that can be interpreted quantitatively.

NSLS-II will take us beyond the study of static surfaces and make the study of dynamically evolving surfaces and interfaces, critical to understanding and optimizing the growth of materials, practical and

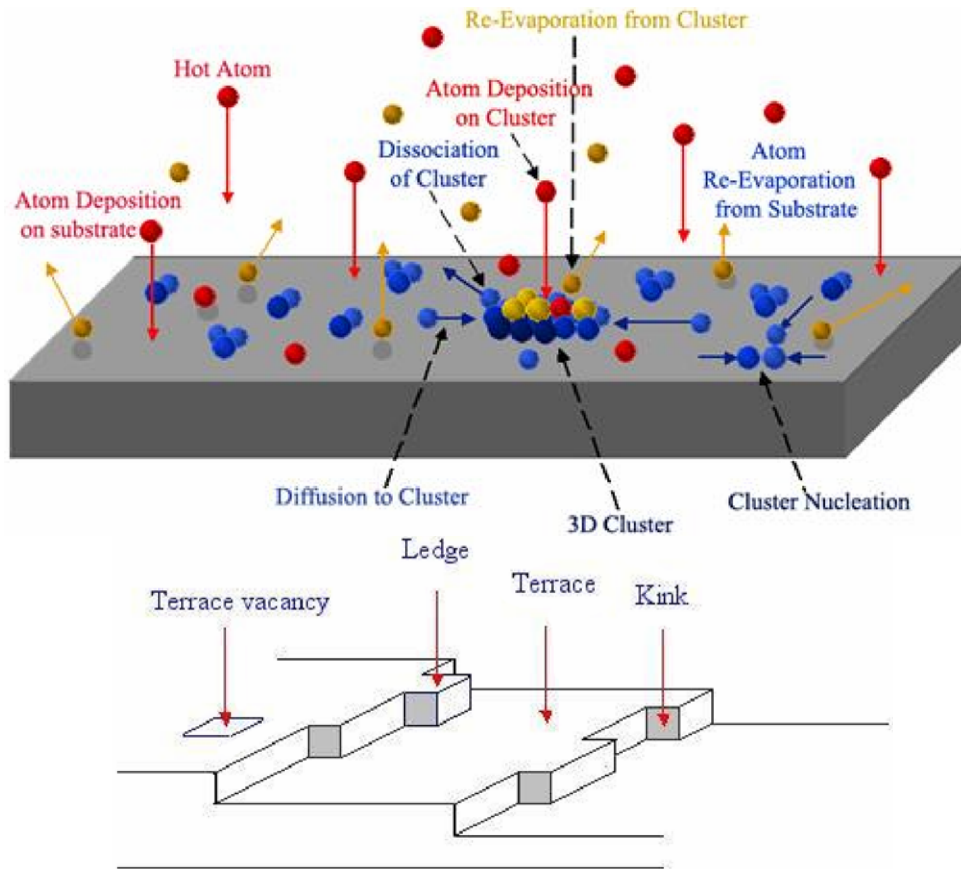


**Figure 2.8.1** In thin film growth, vapor atoms are continuously depositing on the surface. These deposited atoms migrate on the surface and interact with each other, forming 2D and 3D clusters, as well as attaching to the step edges. These interactions determine the morphology of the growing film.

indeed routine. The challenges and opportunities of key materials growth methods are described in this section together with the significant impact that NSLS-II will have in characterizing, understanding, and ultimately tailoring those methods to produce advanced materials for a host of technological applications. In addition to pointing out the general benefits of NSLS-II, several new instruments that will become feasible with the high brightness of NSLS-II are also outlined.

## 2.8.2 Scientific Challenges and Opportunities

### 2.8.2.1 Pulsed Laser Deposition

Pulsed laser deposition (PLD) is a powerful technique for growing thin films from the vapor phase that has increased in importance over the last decade because of its flexibility and advantages for fabricating thin films of complex materials. In PLD, a high power pulsed laser beam is focused onto a target of the material to be grown. As a result, a plume of vaporized material (atoms, ions, molten droplets, and particulates) is emitted and then collected on a substrate to grow the film. Traditional materials systems for PLD are various complex oxides, such as high  $T_c$  superconductors and colossal magnetoresistance materials. However, materials of interest include semiconductors and even metallic films, which often require ultra-high vacuum conditions. PLD performed in ultra-high vacuum conditions is referred to as pulsed laser molecular beam epitaxy, or PL-MBE.

One great advantage of PLD is that multi-element materials are deposited with the same composition as the target material, thus greatly simplifying the deposition of thin films of complex materials. Additionally, since PLD is at the ultimate limit of non-equilibrium vapor deposition, metastable materials and nanoscale structures may be formed that are difficult or impossible to fabricate by other means. The laser plume contains energetic particles that may also promote smoothing of surface roughness (interfaces formed by PLD have been reported with  $< 1 \text{ \AA}$  RMS roughness in several cases).

Atomic diffusion on surfaces occurs on a picosecond time scale. However, surfaces may evolve on times scales of seconds, or even longer in many cases. PLD presents an interesting opportunity, since film growth is accomplished by bursts of particle flux (composed of atoms, ions and small clusters) that last only a few microseconds. The growth surface then continues to evolve until the next pulse arrives on the order of a second later. The time structure of the growth process thus spans six orders of magnitude.

Figure 2.8.2, shows an example of pulsed growth on a Cu (111) surface. A Kinetic Monte Carlo simulation was performed on a 100 by 100 atom surface at 300K. Instantaneous pulses of 0.1 ML are deposited, each followed by a 100 msec “relaxation”. The figure shows the time evolution after the fourth pulse on an initially flat surface. Upon instantaneous deposition, the surface is covered with many monomers and dimers composed of Cu atoms. Since individual atoms and dimers are highly mobile, they

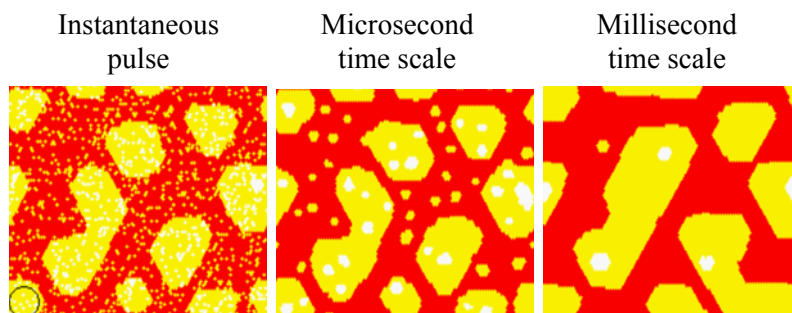


**Figure 2.8.2** Kinetic Monte Carlo simulation of pulsed growth on a Cu(111) surface. The three colors correspond to the initial surface and two incomplete monolayers of deposited copper. The images show that the relaxation of the surface after a deposition pulse spans many orders of magnitude in time. The ability to probe these effects in the time domain with NSLS-II will open up a new window on thin film growth and surface processes.

rapidly coalesce into metastable 2D islands of 10-20 atoms. With time, the smaller islands are absorbed into larger islands on the surface. This dynamic process is then repeated during subsequent pulses.

Complex materials are thought to follow a pattern similar to the simple case of Cu (111). However, it has been widely speculated that there is an additional “assembly” step in which the elements composing the material aggregate into small units with the correct composition and then diffuse around to join up to step edges or large islands. The assembly process probably occurs only at very early time scales, and has thus far not been observed directly.

NSLS-II will be able to access the full range of time scales relevant to the process, down to sub-microseconds. This will allow access to a rich variety of transient phenomena that will be important for the control of thin film growth and ultimately for the fabrication of state of the art materials. The combination of the high intensity of NSLS-II with an area detector with large dynamic range and millisecond readout times will be crucial for the success of these experiments. The high brightness of NSLS-II will also enable new experiments, such as the study of surface evolution on short time scales with photon correlation spectroscopy.

### 2.8.2.2 Self-organized Nanoscale Features on Surfaces

Nanoscale features on surfaces can be obtained by sputter etching, strain effects, Stranski Krastanov growth, Volmer-Weber growth, or by phase separation. There is a great deal of interest in using these effects as the basic technology for the formation of “self-organized” structures that have useful properties. Examples include magnetic dots for thin-film recording media and semiconductor quantum dots. Studies of these effects are relevant to conventional in-situ growth studies, however the emphasis in this field is to create and control nanoscale features during growth and processing.

Figure 2.8.3 shows an example of a cobalt surface with 20-50 nm dots formed by ion erosion. The features formed are on a size scale appropriate for high-density magnetic recording media. Additional examples would include semiconductor quantum dots. In such cases, one would like to be able to locally map elemental composition, and strain distributions, either at the surface, or in a buried layer. Similar capabilities would also be required for a range of other materials such as phase separated GaInN layers, diluted magnetic semiconductors, complex oxides, and silicide layers.

NSLS-II will enable X-ray microscopies with 10 nm resolution or better, extending the uses of such techniques into the realm of surfaces and thin films. NSLS-II end station equipment for in-situ growth and processing will include facilities for surface diffraction and grazing angle small angle scattering to take advantage of scattering experiments requiring high flux. To conveniently study nanoscale surface

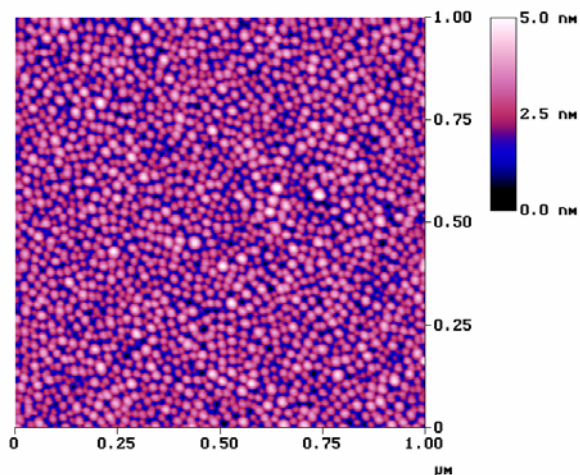


**Figure 2.8.3** AFM image of self-organized mounds formed on a cobalt (0001) surface by 500 eV Ar<sup>+</sup> sputter etching. Similar methods can be used to form nanometer scale quantum dots on surfaces.

features, they will also incorporate complementary microbeam capabilities, facilitating in-situ imaging on length scales of 10 nm or less.

This new capability will address one of the weaknesses of conventional X-ray scattering where fine-scale real space structures are only determined on average, and only in reciprocal space. The very high brightness of NSLS-II will allow the use of local area diffraction or fluorescence mapping, and methods based on back transformation from reciprocal space to obtain nm-scale real-space structural information in non-periodic systems (see Section 2.4.3.2.1). The ability to perform such experiments in-situ will greatly enhance the usefulness of beamline-based growth facilities. Rather than being dependent on the ex-situ analysis of real-space microscopies such as AFM and TEM, the facilities of NSLS-II will approach the ideal of self-contained laboratories for the development of new thin film materials. The high brightness of NSLS-II will enable real-time measurements with many of these techniques and make it possible to study thin film growth, etching, or annealing, as they occur using microbeam-based probes. The natural time scale of these processes is typically  $\sim 1$  second, except for PLD discussed above.

### 2.8.2.3 MBE Growth

Molecular beam epitaxy continues to be a powerful growth technique, particularly for compound semiconductors. Because of its importance, the structure of growth surfaces has been investigated with a number of techniques, each with its own strengths and weaknesses, and much has been learned.

Important information on film microstructure and interface structure has come from careful examination of grown films using transmission electron microscopy (TEM). Atomic force microscopy (AFM) and scanning tunneling microscopy (STM) provide vital information about surface morphology and, in the case of STM, atomic reconstruction. While these can be performed in situ, immediately after deposition and without breaking sample vacuum, they typically require that the sample be cooled to room temperature (versus a growth temperature of order 500-800° C) and cannot easily be used in real time, as the material is deposited. Yet it is known that there is often a significant change in surface reconstruction upon cooling. Moreover, contamination, if present, can fundamentally alter the reconstruction once the growth process is stopped. Finally, scanning probe techniques provide only very limited information about the subsurface structure. Disordered layers often exist on surfaces during growth, particularly in the case of growth with Indium. In addition, ordered reconstructions can sometimes have domain boundaries that move around faster than they can be followed by STM. Thus the STM provides only a time-average of the surface structure, not a snapshot. Finally, while careful AFM and STM experiments can provide important information about step motion on larger length and time scales, they don't provide direct information about the dynamics of atoms on the surface during growth on subsecond or second time scales. Typical atom migration times to steps are on this order.

In-situ RHEED is widely used as a real-time diagnostic tool during growth, and it can provide some important quantitative information, in addition to more qualitative information about surface reconstruction symmetry and flatness. However, dynamical scattering effects can limit its quantitative interpretation. It is not generally used to determine the atomic positions in surface reconstructions, relaxations beneath the surface, or quantitative details of surface step morphology.

NSLS-II will enable investigation of the following important issues.

*Influence and structure of nucleation:* Often a nucleation layer is used to initiate growth, particularly during heteroepitaxy. A detailed understanding of nucleation layer structure and its immediate influence on subsequent growth is often lacking.

*Surface morphology and step dynamics during growth:* The dynamics of atomic motion on surfaces during growth plays a key role in film growth. Step bunching on the evolving surface can be examined by following transverse lineshapes of X-ray scattering truncation rods. GISAXS measurements can track the evolving lateral correlations of the height, both parallel to and perpendicular to the overall direction of substrate miscut. Important information can come from systematic studies of the time evolution of the X-ray signal at the anti-Bragg position following a sudden stop in the flux of deposited atoms [1-4]. Typically an initial rapid (probably millisecond) change in the diffracted signal appears following the

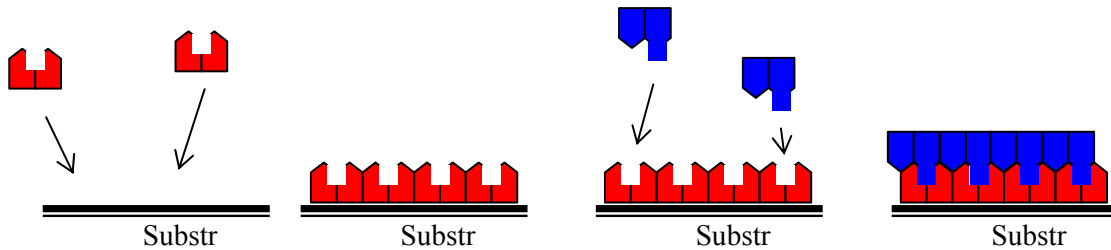


**Figure 2.8.4** Schematic of ALD process. The surface is repeatedly exposed to alternating molecular precursor species (here symbolized by red and blue), typically for approximately 1 sec each. The deposition of each species is self-limiting. A purge and/or carrier gas (not shown) is also typically utilized.

sudden stop, believed to be due to the initial movement of atoms to lattice positions following deposition. There is a much slower (of order 10 sec) relaxation of atoms onto energetically favorable surface step positions. In layer-by-layer growth, where RHEED and anti-Bragg X-ray oscillations can be observed, the relaxation process varies systematically throughout a single layer deposition process.

*Surface reconstruction:* STM and RHEED observations cannot directly confirm the vertical structure of the top layers or adlayers. X-ray diffraction scans along the surface diffraction rods are very sensitive to the surface structure since the scattering from the surface layers interferes with the rod scattering coming from the truncated bulk crystal. This technique can be sensitive to the presence of laterally disordered adlayers that do not appear in RHEED patterns. The width of reconstruction peaks can be examined to better understand the evolution of the lateral correlation lengths at the surface.

*Strain:* Due to the differences in atomic sizes, the strain state of films can play a major role in determining whether the films grow uniformly and with low defect densities. Small strains near the surface will be easily investigated with surface-sensitive X-ray scattering.

*Incorporation of Alloy Components:* The incorporation kinetics of ternary components into III-V structures can be quite complex, with given elements often acting as a surfactant. X-ray scattering can be used to investigate surface segregation.

*Evolution of Surface Structure during Quantum Well Growth:* Although quantum wells form an important component of opto-electronic devices, little is known about how the surface morphology and step structure evolve when there is a sudden change in composition. This can be investigated with real-time X-ray scattering.

## 2.8.2.4 Atomic Layer Deposition

Atomic layer deposition (ALD), a chemically self limiting process, first developed in the 1970's by Suntola [5], is in some aspects similar to chemical vapor deposition (CVD) in that it utilizes chemical reactions between precursor molecules to deposit new material. However, unlike CVD processes, precursor species are introduced individually, in a pulsed mode, as shown schematically in Figure 2.8.4. In conjunction with the proper chemistry limiting the adsorption to a single layer of the reactant molecules, this results in a highly controlled process with inherently atomic-layer resolution.

Typically the beginning of the deposition process, i.e. the nucleation of the film on the substrate, can have rather different kinetics than the subsequent growth. Several layers are often deposited before the film thickness becomes linear in the number of deposition cycles.

Initially, the inherently low growth rates of the technique made it commercially unattractive relative to CVD or physical vapor deposition (PVD) techniques such as sputter, thermal or e-beam deposition. However, with the continued evolution of fabricated structures into the nano-regime, the layer-by-layer growth method characteristic of ALD has come to be seen as a significant advantage. Whereas CVD and PVD rely on precise and uniform control of deposition rate (determined by geometry, temperature and chemical fluxes) and exposure time to determine deposited thickness, ALD is inherently much more forgiving because of its self-limiting nature. Moreover, it can typically operate at significantly lower

temperatures, decreasing unwanted diffusion or thermal degradation of the substrate material. ALD also has excellent conformality in nanostructures with high aspect ratios, much better than PVD or CVD.

Many systems have been grown with ALD, including compound and elemental semiconductors, metals, and ceramics. It is increasingly being used for the creation of nanolaminates on particles [6]. It is also now on the International Technology Roadmap for Semiconductors [7] because of future needs for precise nanoscale deposition of high-k dielectrics, diffusion barriers, and electrodes [8].

In traditional ALD the activation energy for precursor adsorption and reaction comes from the thermal background. To decouple reaction kinetics from substrate temperature, and hence avoid sample damage arising from higher temperatures, plasma-enhanced ALD (PE-ALD) is becoming increasingly important. The use of plasmas to excite molecular hydrogen for the chemical reduction of metal precursors on the sample surface has been particularly promising [9].

Although ALD promises to be important across a spectrum of nanotechnology applications, there are many questions about the detailed processes underlying its success. Chemical species present in the adsorbed molecular film that is a precursor to the adlayer formation have been investigated with infrared spectroscopy. Film thickness has also been monitored in real time using quartz microbalances and optical ellipsometry. The typical pressures of  $10^{-3}$  to  $10^{-1}$  Torr present during the ALD growth process, however, complicate the application of many traditional surface science techniques, particularly those using electrons. In some cases, differential pumping has allowed the use of Auger spectroscopy to examine surface chemical composition. However, none of these techniques offers the ability to examine in real time the detailed atomic and nanometer structure of the growing films, the adsorbed molecular layers or the interface between them.

NSLS-II will enable detailed investigation of the structural evolution of ALD films during both their initial nucleation phase and during their steady state growth phase. Moreover, the millisecond or better time resolution achievable in many of the X-ray techniques will allow examination of the surface evolution as the layer of precursor molecules is adsorbed and/or reacts.

Key issues that will be accessible to such studies at NSLS-II include the following.

*Structure of adsorbed gas layer:* The ALD process typically begins with the self-limiting adsorption of a monolayer of reactant molecules. To what extent is this layer crystalline or amorphous? In-plane X-ray diffraction can be used to examine this question. With the high brightness of NSLS-II, one can monitor with millisecond time resolution, the structural quality of the adsorbed gas layer changes during the adsorption process itself. Where are the atoms relative to the substrate? During the beginning of the nucleation phase, X-ray standing wave fluorescence can be used to identify the vertical position of medium- and high-Z atoms in the adsorbed layer relative to the substrate surface. SEXAFS can also be used to provide information on the local directional chemical environment around these atoms.

*Adsorption and reaction processes:* Are these processes spatially homogeneous or heterogeneous on the surface? Do the absorption and reaction processes begin at definite points on the surface (e.g. at step edges) and then propagate laterally along the film surface, or do they happen relatively randomly as gas atoms hit the surface? If the processes are heterogeneous, the resulting variations in atomic structure will lead to electron density variations on the appropriate length scales (probably tens of nanometers) during precursor deposition/reaction. The evolution of the surface inhomogeneity can then be followed in detail with GISAXS or nanoimaging.

*Composition of adsorbed gas layer(s):* Using X-ray reflectivity, the total electron density profile of the adsorbed layer can be measured. With appropriate modeling, this tells much about the distribution of atoms above the existing film/substrate.

*Surface morphology:* As mentioned above, ALD often leads to relatively rough surfaces. X-ray reflectivity can be analyzed with well-defined approaches to understand the evolution of root-mean square surface and interface roughness. Examination of crystal truncation rods from the substrate also gives information about the interface width. In addition, the lateral size scale of the developing morphologies can be examined with GISAXS or nanoimaging.

### 2.8.2.5 MOCVD of AlGaN for Energy Conserving Solid-State Lighting

The metallo-organic chemical vapor deposition (MOCVD) technique has been applied to the growth of quaternary compounds such as AlGaAsP materials. These materials have composition dependent band gaps and lattice parameters that have found many uses in the telecommunications industry as well as other areas. The future challenge for MOCVD growth will be application of these techniques to other wide band gap materials.

Light-emitting-diodes (LEDs) made from aluminum containing epitaxial materials offer tremendous breakthrough potential for 21<sup>st</sup> century technologies including solid-state lighting and biophotonics. Of the \$50 billion annual production of electricity, fully 20% is used for lighting; even modest improvements in efficiency will have great environmental impact. Solid-state lighting has been identified as a national technology priority because of its impact on the nation's energy reserve, economy and environment. The steady improvement in performance of solid-state lighting is shown in Figure 2.8.5.

Specifically, large bandgap aluminum gallium nitride (AlGaN) alloys permit absorption and high intensity emission of light in the deep blue and UV wavelength ranges enabling development and widespread utilization of energy and cost efficient red-green-blue (RGB) solid-state white lighting technologies.

MOCVD growth of gallium nitride (GaN) has been partially successful. It is the introduction of Al to GaN, however, that permits the manufacture of deep blue and UV wavelength LEDs needed for solid-state, white-lighting and biophotonics applications. However, the application of the older AlGa phosphide MOCVD methods appears not to be successful for the higher processing temperatures required for the wider band gap AlGaN materials. MOCVD depends on a complex interaction between the diffusive and convective heat and mass transport and the chemical reactions at the growing interface and in the growth chamber. Depending on the details of the reactor system, heat transport in the solid reactor walls can influence the deposition process significantly. What limits the AlGaN technologies is the inability to predict and control fluid and thermal instabilities associated with AlGaN MOCVD. Such instabilities lead to non-homogeneous residual stress distributions, spiral shaped thickness variations of the thin film and formation of ~10 nm sized Al particles within the gaseous phase. The challenge is to find new techniques

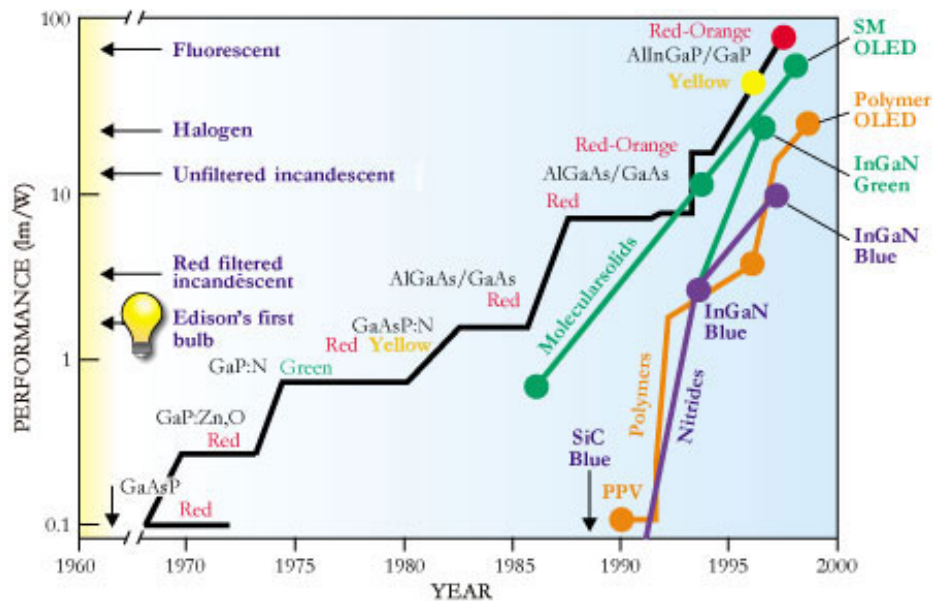


**Figure 2.8.5** Solid state lighting performance has increased dramatically in recent years and has the potential to make an enormous impact in reducing the nation's energy consumption. NSLS-II will contribute to further advances by enabling new techniques for understanding and optimizing methods of growing advanced materials [10].

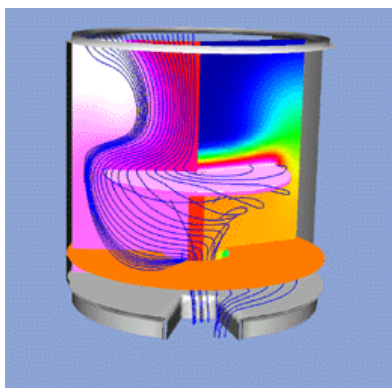


**Figure 2.8.6** Simulation of gas flow in an MOCVD reactor [11].

that can be applied to the analysis of the gas phase, and in particular assess what is controlling the gas phase nucleation of Al particles. Neither the particulate densities, nor the size distributions have been well characterized in the high-pressure 1000° C processing environment.

Application of the high brightness of NSLS-II in scanning this environment will provide vital information on the thermal/fluid stability issues associated with MOCVD AlGaN wafer production. Figure 2.8.6 shows a simulation of the gas flow in such a reactor. The lines are traces of the reactant flows incident onto a rotating sample disk as in commercially available reactors. Using the high brightness of NSLS-II together with nanometer tracer particles and fluorescence techniques, the simulations can be tested and growth conditions optimized. Using EXAFS techniques in the gas phase one can obtain spatial profile information on the chemical state. This will be in addition to the real time imaging of the growing interface and crystal structure. Clearly, NSLS-II will make substantial contributions to this problem.

### 2.8.2.6 Thin Film Organic Crystal Growth

The electrical properties of organic field effect transistors depend on many parameters and in particular, on the properties of the organic single crystalline film. High quality single crystal films are required to characterize the transport properties. Organic molecules are bonded by weak Van der Waals interactions and therefore unfortunately can form many polymorphic crystal structures. Understanding what crystal growth parameters favor one polymorph over another would be an important step forward. Furthermore, some of these polymorphs undergo phase transitions, upon cooling from the growth temperature to room temperature, further complicating the situation. The experimental path forward that is most likely to succeed is to observe in situ the structure during crystal growth, during the subsequent cool down, through to fabrication of electronic devices. The issues here are similar to those for MOCVD. Figure 2.8.7 shows on the left a typical growth chamber, and on the right a typical crystal. Such studies will be possible with NSLS-II and will have large impact on technology of organic field effect transistors as well as on the basic understanding of the electrical transport in this class of materials

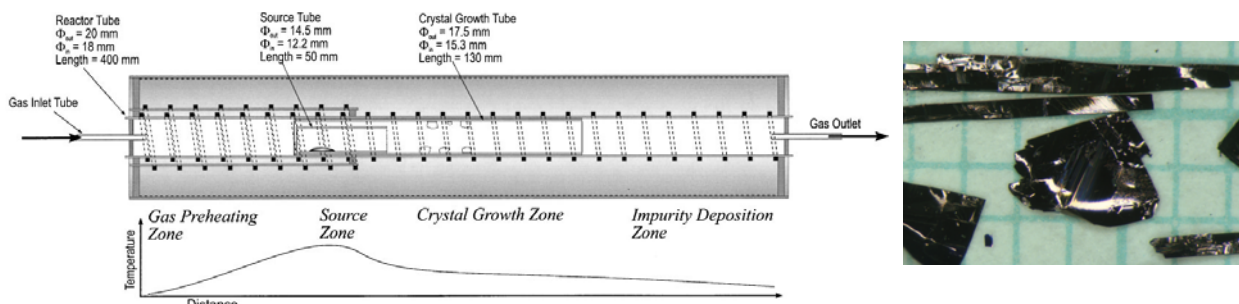


**Figure 2.8.7** Left: Chamber for growing thin film organic crystals. Right: Typical organic crystal [12].

### **2.8.2.7 Growth in Fluids**

In addition to better time resolution, more intense synchrotron beams will facilitate the study of growth and phase transformations in contact with dense fluids. While scattering studies have already been carried out on samples in aqueous environments, the significant absorption of water at moderate X-ray energies ( $\sim 10$  keV) imposes significant limitations on the maximum fluid layer thickness that can be used in an X-ray experiment. In addition to absorption by the fluid itself, in some cases the samples may be contained in pressure cells or other vessels that contribute significantly to the absorption.

Physical systems of interest include heteroepitaxial growth from solution, solidification from the melt, the deposition of polymers from solution, the deposition of metals in supercritical liquids, the electrodeposition of layer structures, and biomineralization. Processes such as these are of great fundamental and technological importance; many are likely to be crucial in the development of novel, low-cost, or environmentally-sound methods. On the whole, given their occurrence in relatively inaccessible (dense, high-pressure, or chemically reactive) fluids, structural studies of such processes have been performed *ex situ*. With the availability of the high flux, penetrating synchrotron beams of NSLS-II, studies of samples in dense fluids will become as routine as current studies of samples in vacuum or relatively low pressure gas environments.

### **2.8.3 Impact of NSLS-II**

Due to the inadequate spatial resolution and low signal rates, there is essentially no full field imaging of surfaces and interfaces performed at second generation sources with the elastic photon in/photon out channel. Inelastic channel imaging methods, such as the photon in/electron out of PEEM, that take advantage of well developed electron imaging optics, can be performed at second generation sources, but this method does not have the penetrating capability of the 2-30 keV photon in/photon out methods. The high brightness of NSLS-II together with improvements in X-ray optics will enable real time X-ray microscopy studies of growing surfaces.

To study thin film growth, it would be useful to simultaneously and in real time perform imaging and diffraction characterization of a growing surface. Two key quality factors for advanced materials growth are the perfection of the crystalline lattice, and the morphology. Electron microscopy techniques can both image the surface morphology and diffract from the underlying lattice, but these methods are generally incompatible with most interesting growth conditions. A new microscope for the study of thin film growth will be enabled by the high brightness of NSLS-II. This microscope will be integrated with a variety of growth chambers and will run in two modes; a full field reflectance microscope, and a high spatial resolution scanning reflectance microscope.

#### **2.8.3.1 Full Field Reflectance X-ray Microscopy**

For the full field mode of the proposed instrument, one can image the morphology of the growing interface in real time, and simultaneously collect the large-angle diffracted beams from the growing crystal. A focused beam is incident onto a growing crystal interface in a crystal growth chamber, with two coexisting downstream detector types, as shown in Figure 2.8.8. The first detector will be a phase preserving, imaging quality optic for hard X-ray photons, configured with a high resolution area detector, to obtain an image with substantial magnification. The second type of detector will be a set of large area detectors to collect the large angle diffracted beams from the lattice. The incident beam focusing optics are at, or near, the 1:1 point to minimize the divergence. The downstream imaging optics and area detectors can coexist because the numerical aperture of the imaging optics is small; even for 10 nm resolution at a wavelength of 0.1 nm the numerical aperture is of order  $10^{-2}$  radians. To enhance sensitivity to the surface, one can orient the incident beam to a fraction of the grazing incidence angle,

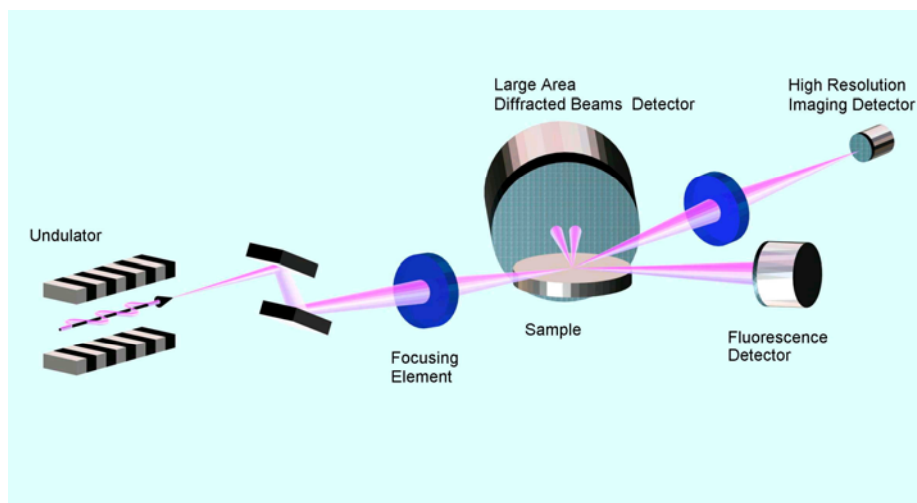


**Figure 2.8.8** Schematic illustration of optics of new microscopy techniques enabled by NSLS-II.

thus limiting the depth penetrated by the incident flux. Thus, one can simultaneously image the morphology of the growing interface and collect the wider angle diffracted beams that are sensitive to the crystalline lattice, all while under typical growth conditions. This tool can be thought of as analogous to an optical full field microscope, combined with a Reflecting High Energy Electron Diffraction (RHEED) or Grazing Incidence Small Angle X-ray Scattering (GISAXS) for the diffraction pattern.

### 2.8.3.2 Scanning Reflectance X-ray Microscopy

The scanning reflectance X-ray microscope (SRXM) uses upstream optics to highly demagnify the incident beam and then raster it across the sample while monitoring the diffraction pattern, the fluorescence yield and the reflected intensity. The SRXM is the reflection hard X-ray analog of the transmission type microscopes, for example the electron based STEM, or the soft X-ray based STXM. The small focal spot enables selection of specific features from the heterogeneous features on growing surfaces, such as nano-sized clusters of atoms, growth facets and terraces. For example, for a surface in the step-flow growth mode, one can imagine measuring the time averaged step edge atomic structure, at growth temperature and pressure, to understand how an adatom incorporates into the crystal.

The SRXM requires the high brightness of NSLS-II, and maximizes the sample flux density and hence sensitivity. The ability to convert from a full field view to a scanned spot view of the same area with high spatial resolution will have great practical benefits. The high brightness of NSLS-II will enable it to efficiently achieve spot sizes of 10 nm or less and makes it the ideal source for an SRXM instrument.

### 2.8.3.3 Oversampling Methods for Surfaces and Interfaces

While there are many existing methods for determining surface crystal structure, a novel and model independent method that is rapidly developing is based on oversampling methods and holds great promise for real time monitoring of growth. A great deal of progress has been made in understanding the nature of molecular adsorption on surfaces by examining highly ordered, reconstructed configurations. These low-energy configurations have then been used to make inferences regarding the typical pathways that occur during departure from equilibrium conditions. For example, CVD growth of an epitaxial layer, which is manifestly a non-equilibrium situation, undoubtedly proceeds by occupation of quasi-equilibrium adsorption sites by diffusing and decomposing surface species. Although knowledge of preferred reaction paths and typical binding sites can aid a great deal in interpreting non-equilibrium structures, the lack of order inherent in such situations greatly compounds the difficulty of measuring their atomic positions. The advent of the scanning tunneling microscope (STM) provided a localized picture of these structures

for a number of favorable cases. However, a STM is a serial instrument, has limited scan rates, cannot operate in all environments, probes only a fraction of the growing surface, and can typically resolve only the outer atoms of the adsorbed molecule. An X-ray based tool is needed that can probe atomic positions within the decomposing molecule as well as determine their locations on surfaces of disordered materials in real time.

The well-known phase problem in crystallography precludes a direct inversion of scattering data. It is necessary to know the phases of the scattered beams to directly determine atomic locations by a simple Fourier transform. However, in favorable cases, scientists have been able to overcome this limitation by oversampling the scattering data (and by using auxiliary information) to assign phases to the scattering data. For the case of surface or interface X-ray diffraction, a continuous intensity distribution is found normal to the surface of a single crystal due to the non-periodicity imposed by the truncation of the crystal (i.e., the crystal truncation rods, or CTR). Recently, it has been shown that by oversampling this distribution, the phase of the scattered intensities can be reliably recovered. This allows a direct inversion showing atomic locations that are occupied in a surface reconstruction.

With present sources, this kind of analysis is limited to well-ordered surfaces. However, surfaces that show limited order, such as molecular precursors and/or reaction products that are adsorbed in preferred sites, could be addressed with the high brightness of NSLS-II. If the adsorbate molecule shows fairly good long-range order, as might be expected for species with an attractive adsorbate-adsorbate interaction, the atomic binding site and internal configuration of the molecular species could be determined. The oversampling would take place along the Bragg CTR rods from the substrate, as has been already demonstrated for the case of well-ordered substrates. However, the signal would be weaker, owing to the imperfect ordering of the adsorbate, necessitating a more intense X-ray source. This powerful application will shed new light on the growth process.

An even more exciting application is the case of fast-decomposing molecular precursors that do not exhibit significant long-range order. This is closer to the situation encountered in actual CVD growth conditions. It is likely that such species occupy a preferred lattice site, but decompose before any adsorbate-adsorbate interactions can foster long-range order. In this case, the lack of long-range order would prevent the use of the methods discussed above, because the overlap of the signal from the adsorbate layer and the Bragg CTR rods would be small. Instead, the diffuse X-ray scattering from the disordered adsorbate layer itself would be exploited, enabling a direct determination of the atomic configuration of adsorbed species. Determination of the structure of metastable species could also be made with suitable growth apparatus. A pulsed beam of precursors could easily be synchronized with the data collection. With an intense X-ray beam, the diffuse signal could be sampled at a particular time after the arrival of the gaseous pulse. If required, statistics could be built up over multiple arriving pulses, but advances in detectors such as those outlined in Section 4.4 could allow a single diffraction pattern to provide a "snapshot" of the surface at a given time.

Finally, we mention the possibility of inverting the data in real time to provide continuous visualization of the species on the growing surface. This advance would require the development of suitable fast area detectors, which is vital to the refinement of many other scattering techniques. Such detectors could record the entire diffuse scattering signal from an overlayer in a single frame. The algorithms currently available can invert a set of CTR data in tens of seconds on a modest workstation or high-end PC. With improved computing power and development of more efficient algorithms, it is reasonable to expect that in ten year's time, such inversions to take less than 100 ms. In concert, it is feasible that diffuse patterns could be recorded and interpreted almost instantaneously, giving the operator of a CVD reactor real-time insight into the growth process.

#### **2.8.3.4 Powder Diffraction**

From advanced structural ceramics to catalysts, from semiconductor technology to the frontiers of biology, and from new magnetic materials and devices to framework compounds used to sequester radioactive waste, crystallography plays a crucial role in our understanding of materials. It is apparent that

the ability of crystallographic techniques to handle smaller samples and more complicated structures has been an important driving force in many areas of science and technology. The distinction between single crystal and powder diffraction measurements is blurring, both as it becomes possible to perform single crystal measurements on samples that are the order of the grains in a powder, and as powder techniques evolve to handle problems of great complexity. NSLS-II presents important opportunities to continue this advance.

For non-protein crystals (unit cell dimensions in the range of 10 to 30 Å), the current state of the art to collect a full diffraction dataset with CCD or imaging plate detection and focused synchrotron beams, is a sample volume on the order of 100  $\mu\text{m}^3$ , generally limited by the ability to mount and handle small samples and maintain reasonable signal to background ratios. Even if one can collect diffraction data from a sample of that size, there are issues of interpretation. Several groups are developing the software and techniques to handle diffraction data sets from a sample consisting of a few crystalline grains in the illuminated X-ray beam, on a transparent backing such as a thin silicon nitride film. One could collect quasi-3D diffraction data by tuning the X-ray energy during data collection so that several thick slices of reciprocal space are sampled, without the need to rotate the sample (and thereby avoid parallax effects of grains translating in and out of the beam). With a very bright X-ray beam provided by NSLS-II and sample grains mounted on transparent film, data will be collected to very large momentum transfers, needed for pair distribution analysis of disorder and deviations from the average crystal structure.

There is growing recognition that it is useful to simultaneously measure physical properties and atomic structure, or to measure the structure of a system under some form of external perturbation. For example, in single crystal work done at NSLS beamline X3A, application of a poling electric field to a nonlinear optical material (2-methyl-4-nitroaniline) rotated the molecule by 0.0045(5) degrees and translated it by 0.0019(3) angstrom [13]. Such precisions could never be achieved by comparing, e.g., a poled with an unpoled crystal; instead they depend on the application of an external field during measurement.

NSLS-II will enable implementation of a beamline optimized *both* for physical property measurements *and* for the determination of accurate and precise crystallographic structures, both for single crystal and for polycrystalline samples. Whole new classes of experiments can be envisioned: As batteries discharge what short-range order-disorder results? What are the changes in fuel cell electrolytes and electrodes under real operating conditions (1000° C) as oxygen site occupancies adjust? The construction of cells suitable for *simultaneous* measurement of potential, resistivity, current and scattering are required to address important questions. These cells will give rise to parasitic scattering and so beamline components, including optics, slits etc will need to be optimized for these “real world” experiments.

## REFERENCES

- [1] T. Shitara, D.D. Vvedensky, M.R. Wilby, J. Zhang, J.H. Neave and B.A. Joyce, Phys. Rev. B **46**, 6815 (1992).
- [2] J. Tischler, G. Eres, M. Yoon, B. Larson, C. Rouleau, D. Lowndes, T.-C. Chiang and P. Zschack, Advanced Photon Source Annual Report 2000,
- [3] P. Smilauer and D.D. Vvedensky, Phys. Rev. B **48**, 17603 (1993).
- [4] R.L. Schwoebel, J. Appl. Phys. **40**, 614 (1968).
- [5] T. Suntola, Mater. Sci. Rep. **4**, 265 (1989).
- [6] J.D. Ferguson, A.W. Weimer, and S.M. George, Thin Solid Films **371**, 95 (2000).
- [7] <http://public.itrs.net/Files/2001ITRS/Home.htm> -- see for instance the Interconnect section.
- [8] For an overview of applications in silicon technology, see H. Kim, IBM Research Report RC22737 (available on the Web at <http://www.research.ibm.com>).
- [9] S.M. Rossnagel, A. Sherman and F. Turner, J. Vac. Sci. Tech. **B18**, 2016 (2000).
- [10] J. Y. Tsao, Editor, Optoelectronics Industry Development Association (2002).

- [11] G. S. Tompa, A. Colibaba-Evulet, J. D. Cuchiaro, L. G. Provost, D. Hadnagy, T. Davenport, S. Sun, F. Chu, G. Fox, R. J. Doppelhammer, and G. Heubner, Structured Materials Industries, <http://www.structuredmaterials.com/>
- [12] R. A. Laudise, Ch. Kloc, P. G. Simpkins, and T. Siegrist, *Journal of Crystal Growth* **187**, 449-454 (1998).
- [13] H. Graafsma, A. Paturle, L. Wu, H.S. Sheu, J. Majewski, G. Poorthuis, and P. Coppens, "Molecular Reorientation in an Electric Field as Studied by Single Crystal X-ray Diffraction," *Acta Cryst.* **A48**, 113-120 (1992).

## 2.9 Catalysis and Energy Science

### 2.9.1 Overview

Catalysis provides a means of changing the rates at which chemical bonds are formed and broken and of controlling the yields of chemical reactions to increase the amounts of desirable products from these reactions and reduce the amounts of undesirable ones. As a result, catalysis is at the heart of the petroleum, chemical, food, and pharmaceutical industries. Today, approximately one third of the U.S. gross national product in materials involves a catalytic process somewhere in the production chain. The proportion of processes using catalysts in the chemical industry is 80% and increasing [1].

Catalysis also plays a crucial role in pollution control and alternative energy technologies. Stabilizing CO<sub>2</sub> emissions is of paramount importance. In the 20<sup>th</sup> century, power consumption increased 16-fold [2]. The concentration of atmospheric CO<sub>2</sub> increased from 275 to 370 ppm and at the current rate of increase will reach ~550 ppm this century. Climate models and paleoclimate data indicate that this could produce global warming comparable in magnitude but opposite in sign to that of the last Ice Age [3]. Power consumption today is ~12 TW, 85 % of which is based on fossil fuels. To stabilize at 550, 450 or 350 ppm atmospheric CO<sub>2</sub> concentrations requires CO<sub>2</sub> emission-free power by mid-century of 15, 25, or 30 TW [4], respectively. The decarbonization of fuels alone will not be able to mitigate global warming. The combined use of fossil fuels from which carbon has been sequestered, solar and wind power, biomass, and nuclear fusion and fission, in combination with efficiency improvements, hydrogen production, storage and transport, and superconducting electricity grids, is necessary. A broad range of research and development in catalysis and energy science is necessary now to create technological options that permit both climate stabilization and sustained economic development.

Catalysis and energy science represent perhaps the ultimate challenge for characterization, with reactions occurring at specific atomic sites in a complex system, on short time scales, and at high temperatures and pressures. Detailed characterization requires imaging combined with spectroscopic measurements to reveal how atomic and electronic structures change during operation and as a function of reaction conditions. For a working catalyst, the elevated pressure and temperature conditions that are typically necessary are often not readily compatible with the probing and detection schemes.

Synchrotron radiation facilities provide unique and powerful tools for characterizing the temporal and spatial evolution of working catalysts [5]. The structure of catalysts, both crystalline and amorphous, and their microstructure, texture, porosity, domain size distribution, defects, etc., can all be studied by X-ray powder and/or single-crystal diffraction, small-angle X-ray scattering, and X-ray microprobe techniques. Information regarding the valence-band and core-level electronic structure of catalysts and adsorbates can be obtained using X-ray Emission Spectroscopy (XES), Ultra-violet Photoelectron Spectroscopy (UPS), and X-ray Photoelectron Spectroscopy (XPS), and that measured data can be compared with first principles electronic structures calculations. A variety of soft and hard X-ray absorption spectroscopies, including Extended X-ray Absorption Fine Structure (EXAFS), and X-ray Absorption Near Edge Structure (XANES), can be used to study the element-specific and symmetry-projected conduction band electronic and geometric structure of catalysts and adsorbates. Vibrational modes of adsorbate-substrate interactions and rotational tunneling of molecules can be studied by IR absorption spectroscopy.

The high brightness and flux of NSLS-II is essential to enable these tools to be applied with the high spatial, energy, and time resolution necessary to fully characterize these complex systems.

## 2.9.2 Scientific Challenges and Opportunities

### 2.9.2.1 Nanocatalysis

The Grand Challenge for catalysis science in the 21<sup>st</sup> century is to understand how to design catalyst structures to control catalytic activity and selectivity. Through a combination of experiment and theory, a fundamental atomic-scale and nanoscale understanding of catalysis must be developed. The ability to control and manipulate atoms using nanotechnology portends major breakthroughs in catalysis. Since catalytic processes are largely controlled by local phenomena, changes in local electronic and physical structure brought about by tunable ‘nanostructuring’ can alter the physical and chemical properties of catalytic systems and powerfully impact their heterogeneous chemistry. The ability to synthesize, and structurally and kinetically characterize, unique and well-defined nanostructured materials presents an opportunity for theoretical and experimental catalysis investigators to progress towards the compelling goal of tunable catalyst design from first principles.

The essence of nanocatalysis can be highlighted by gold’s size-dependent reactivity. Although gold is the least reactive of all metals, it nevertheless becomes a catalyst for the oxidation of CO to CO<sub>2</sub> when deposited as nanoparticles on certain surfaces, such as TiO<sub>2</sub> (Figure 2.9.1). Competing theoretical models suggest that either the substrate-nanoparticle interaction provides highly reactive oxygen atoms or that the inherent “step edges” of nanoparticles provide more reactive sites. Measurements of the static and dynamic physical and electron structure, as can be provided by real space imaging methods, are necessary to resolve these questions.

As another example, nanostructured oxides introduce tunable properties—multiple valences, structural variations, phase diagrams, electronic structure, acid-base and redox functionalities—that, in principle, can be controlled and manipulated through catalyst design. There is also diversity at the surfaces of these materials—ionic to covalent behavior, acidic to basic nature, defect structures, and

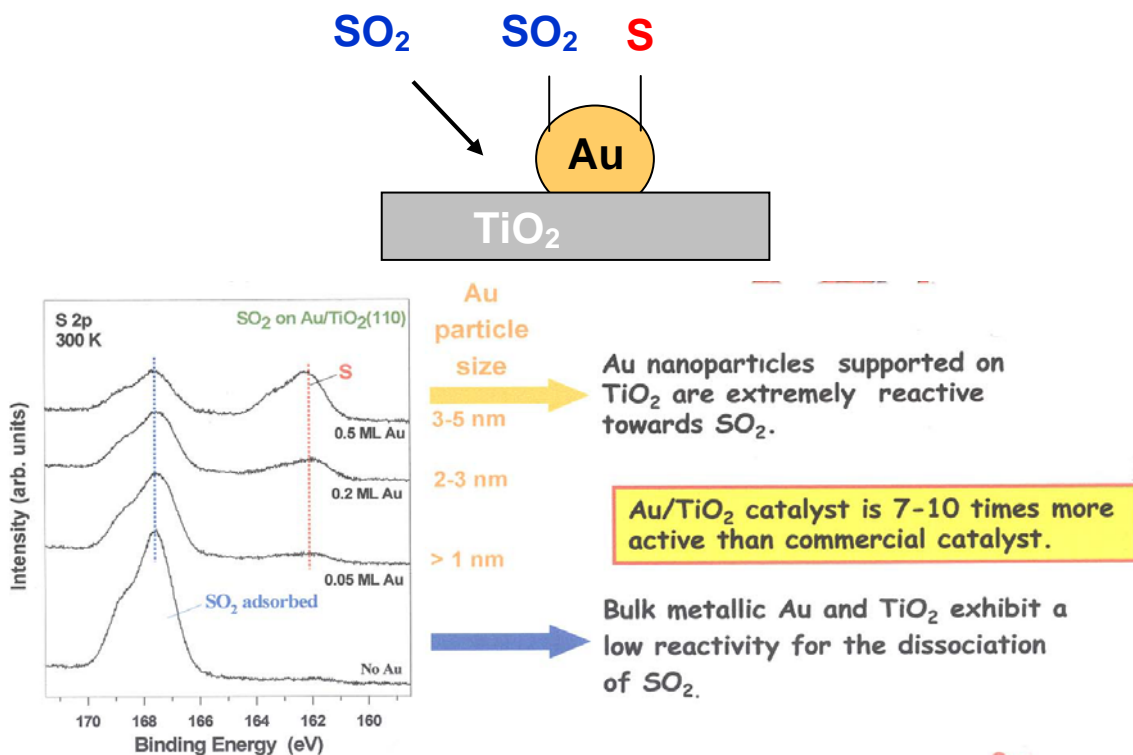


**Figure 2.9.1** Nanocatalytic effect of Au particles supported on TiO<sub>2</sub> as evidenced by the reduction of SO<sub>2</sub> to S as a function of particle size.

oxidative to reductive chemistry.

Understanding of interaction of oxygen, carbon and sulfur with single-crystal surfaces on the nanoscale with sub-second temporal resolution will fill in existing gaps in our understanding of surface chemical transformations. The opportunity to follow simultaneously the evolution of the surface structure, the rate of its growth, the rate of its transformation in presence of reactants, and its thermal and temporal stability will be enormously important for the description and understanding of the kinetics and dynamics of processes occurring on the catalyst surface.

Combining nano and molecular science, synthetic chemists working with catalysis and materials scientists will develop new nanocatalysts based on many different strategies, with the ultimate goal being engineered nanostructured assemblies. One can envision using self-assembly to produce functional microstructures in bound, ready-to-use, form incorporating selective barriers, with engineered porosity and distribution of active sites.

### 2.9.2.2 Hydrogen Storage

The search for materials with high hydrogen storage per unit volume and weight is a very active research area being pursued worldwide. In his January 2003 State of the Union Address, President Bush announced the Hydrogen Fuel Initiative “so that America can lead the world in developing clean, hydrogen-powered automobiles.” Hydrogen storage technology is the bottleneck to carry enough hydrogen on-board a vehicle to provide a 300-mile range. The Department of Energy has issued a Grand Challenge to the scientific community to develop and demonstrate viable hydrogen storage technologies for transportation and stationary applications. The goals are to develop and verify on-board hydrogen storage systems achieving 4.5, 6, and 9 wt% hydrogen storage by 2005, 2010, and 2015, respectively. These technical targets were established through the FreedomCAR partnership between DOE and the U.S. Council for Automotive Research. No existing technology meets these challenging performance criteria to make hydrogen-powered vehicles competitive with traditional vehicles (Figure 2.9.2).

Presently there are three basic routes for the storage of hydrogen in materials: adsorption in metal hydrides, adsorption in carbon-based and microporous materials, and chemical reaction using complex metal and chemical hydrides. Sorptive processes require highly porous materials to maximize the surface area and allow for easy uptake and release of hydrogen. Therefore, basic research is needed on the size effects of adsorptive processes, in particular at the nanoscale.

The use of nanomaterials in energy generation and storage may not only allow for higher storage capacities and higher charge and discharge rates but also for better control over the chemical processes

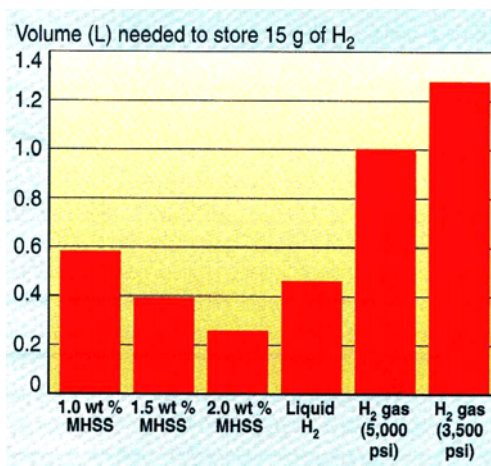


**Figure 2.9.2** Comparison of volume needed to store 15 g of hydrogen. Metal hydride storage systems (MHSS) which can store more than 1.5wt % hydrogen contain more hydrogen than liquid hydrogen. DOE’s Grand Challenge calls for 4.5 wt % by 2005.

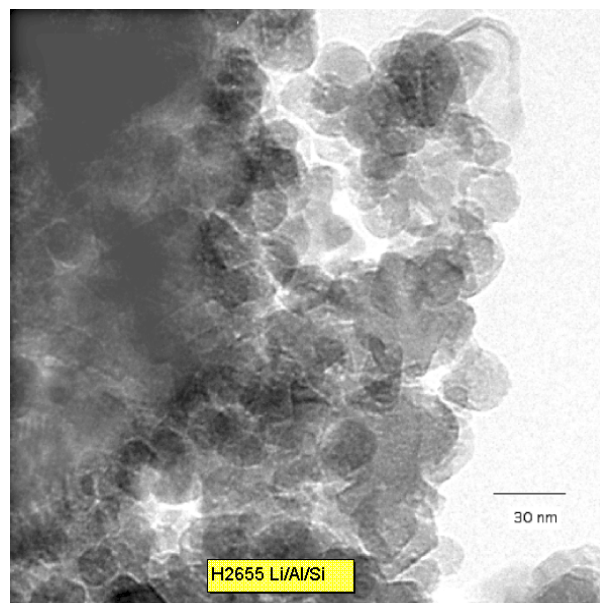


**Figure 2.9.3** TEM of LiAlSi nanocomposite made by a hydrogen-driven metallurgical reaction.

involved (i.e. adsorption, charge transfer). As an example, magnesium and its alloys can store about 7.7 wt % hydrogen, but their adsorption and desorption kinetics are very slow. One approach to remedy this is to increase the surface area by making nanocomposites of Mg and MgNi<sub>2</sub> by ball milling. The addition of MgNi<sub>2</sub> catalyzes the H<sub>2</sub> dissociation and thereby increases the rate of hydrogen adsorption.

An alternative way of making such nanocomposites is to use hydrogen driven, solid state, metallurgical reactions (HDMR) [6]. When a hydrogen storage alloy is subjected to cyclic hydriding-dehydriding (HD) reactions it may undergo large cyclic volume changes that lead to reversible disproportionation into a stable binary metal hydride and other metal components, with the hydride and other components recombining upon removal of the hydrogen. This is a very flexible process that promises to provide novel materials with not only high hydrogen storage capacity, but also other unique properties, such as nanocatalysts, electrodes, and nanomagnets.

X-ray powder diffraction is crucial for the in-situ monitoring of the reaction products and their grain sizes. Figure 2.9.3 shows a TEM of a LiAlSi composite made using a HDMR [7]. The inherent inhomogeneity of nanocomposites requires small X-ray beams to probe specific areas. The high brightness of NSLS-II will significantly enhance the ability to characterize such heterogeneous nanocomposites.

A major breakthrough was achieved when it was observed that in the well-known reaction sequence,  $\text{NaAlH}_4 \rightarrow \frac{1}{2} \text{Na}_3\text{AlH}_6 + \frac{2}{3} \text{Al} + \text{H}_2 \leftrightarrow \text{NaH} + \text{Al} + 1.5 \text{H}_2$ , the dehydrogenation is rapid and reversible under unprecedented moderate conditions when adding a few mole % of selected dopants such as Ti(OBu)<sub>4</sub> [8]. NaAlH<sub>4</sub> has a theoretical reversible H<sub>2</sub> storage capacity of 5.6 wt %. Other potentially viable systems such as LiAlH<sub>4</sub> (7.9 wt %), MgAlH<sub>4</sub> (7.0 wt %), Ca(BH<sub>4</sub>)<sub>2</sub> (8.6 wt %) or Fe(BH<sub>4</sub>)<sub>2</sub> (9.4 wt %) have not yet been made to store hydrogen reversibly. Therefore fundamental studies of the Ti:NaAlH<sub>4</sub> model system must continue in order to provide an understanding of the role of the dopant. Once again, in situ powder diffraction is the ideal tool to follow the reaction kinetics of this and other systems.

Another class of hydrogen storage materials under intensive investigation is nanoporous carbon fibers and nanotubes. Microporous hollow carbon fibers have shown high permeability and selectivity as hydrogen membranes and are currently being scaled up to commercial levels [9-11]. Adsorption of a hydrogen gas monolayer onto a graphite surface occurs at low temperatures and yields an uptake of 4.1 wt % hydrogen. Nanotubes are seen as more useful hydrogen storage materials since they can retain hydrogen at room temperature, and because the nanotube wall curvature increases the binding energy of the H<sub>2</sub> molecules compared to that on a flat graphite surface. When single-wall carbon nanotubes

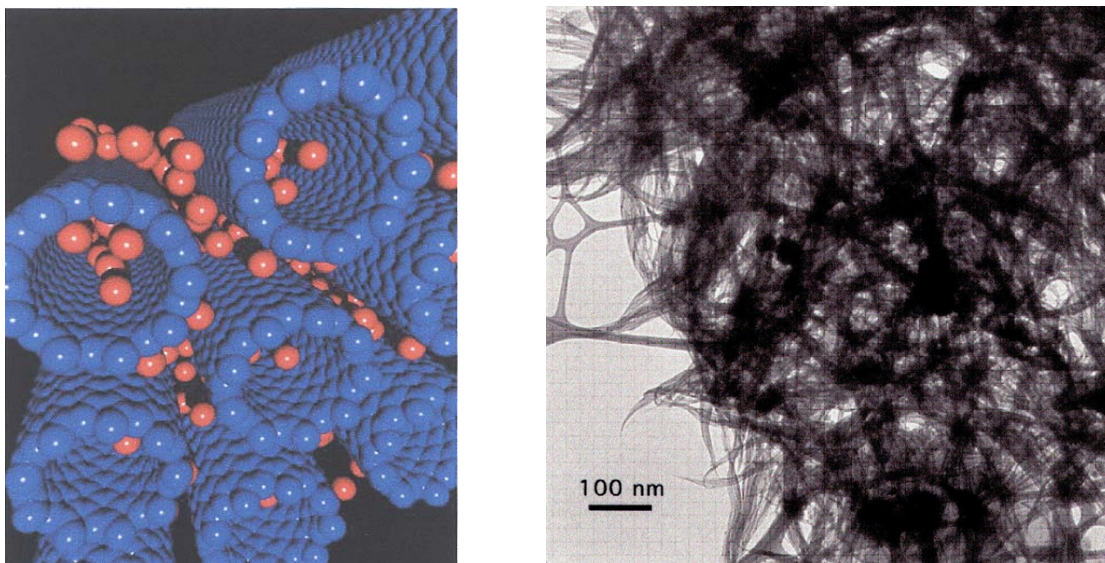


**Figure 2.9.4** TEM image of ropes of single wall nanotubes (SWNT) (left), which allow hydrogen (in red on the right) to be adsorbed into the interstitial spaces.

(SWNT) are synthesized, they form “ropes” that are triangular, close-packed parallel cylinders (Figure 2.9.4). This stacking provides a total hydrogen storage capacity of 4 wt % [12]. New strategies are being devised to increase the hydrogen-to-carbon ratio and achieve even higher hydrogen storage density and faster adsorption/desorption kinetics [13].

Yet another class of novel hydrogen storage materials is “nanocubes” of metal-organic frameworks (MOF). These are very porous materials ( $\sim 3000 \text{ m}^2/\text{g}$ ) that can be synthesized from low-cost starting materials such as zinc oxide and terephthalate, which is a component of plastic (PET) soda bottles (Figure 2.9.5) [14]. With a density of only  $0.59 \text{ g/cm}^3$ , this MOF is one of the most porous materials known. By comparison, carbon nanotubes have a density of  $1.3 \text{ g/cm}^3$ . Furthermore, with  $3000 \text{ m}^2/\text{g}$  specific surface area, these materials exceed the corresponding figures for commercially activated carbons ( $800$  to  $2000 \text{ m}^2/\text{g}$ ), zeolites ( $700 \text{ m}^2/\text{g}$ ), and carbon nanotubes ( $200 \text{ m}^2/\text{g}$ ). Recharge capacities of close to 2 wt % have already been achieved.

Due to their large surface area these materials are polycrystalline powders and their structural characterization relies on high-resolution synchrotron powder diffraction. The high brightness and flux of NSLS-II will allow their adsorption properties to be monitored in real time using fast time-resolved in-situ powder diffraction.

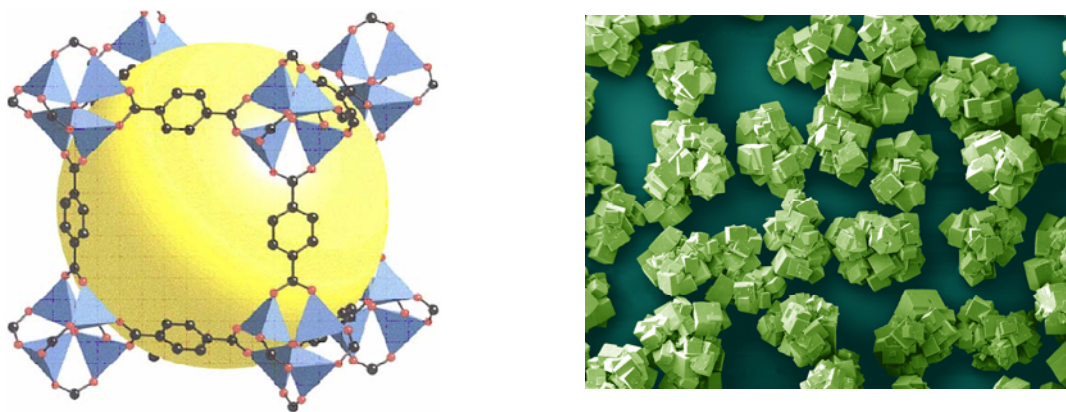


**Figure 2.9.5** An example of a metal-organic framework structure (above) and its microstructure. Over 90 % of the crystal volume is open space (orange ball) which can be used for gas storage ( $\text{H}_2, \text{CH}_4, \text{N}_2$ ).

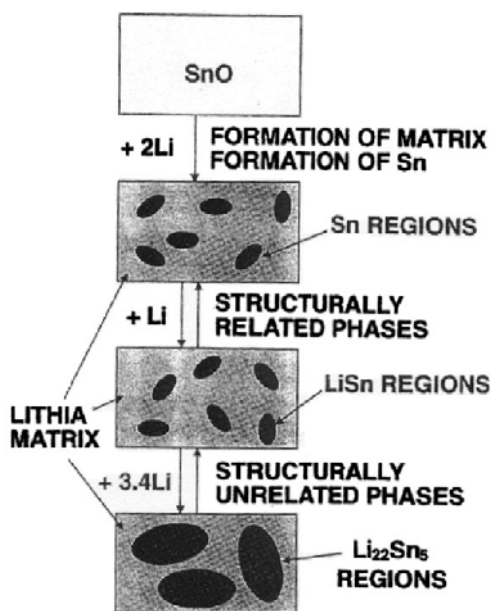


**Figure 2.9.6** *Fuji-type glass for Li battery: 4SnO : 1B<sub>2</sub>O<sub>3</sub> : 1:P<sub>2</sub>O*

### 2.9.2.3 Battery Materials

Rechargeable batteries with high energy and power density and that are also light weight and environmentally friendly are in great demand as energy sources for numerous uses, such as space applications, notebook computers, portable telecommunication devices, and hybrid electric vehicles. The main challenges facing researchers in the field are (1) development of new cathode and anode materials, with high intrinsic discharge voltage, large charge storage capacity, good charge/discharge reversibility, and high rate of charging/discharging; (2) development of new classes of electrolytes that are environmentally friendly and cost effective to replace the toxic salts currently used; (3) understanding the complex material responses under realistic operation conditions.

For example, the current commercial lithium ion battery is based on LiCoO<sub>2</sub> cathode. Due to the high cost of Co, there is great interest in developing cathodes based on V, Mn or Ni. Because of the large structure changes in these layered Li-intercalated oxides during lithiation and delithiation, it is essential to be able to characterize the structural and electronic changes of these new cathode materials during electrochemical cycling. In recent years, synchrotron x-ray diffraction and spectroscopy have played important roles in elucidating the average long-range and local structure changes that accompany the charge/discharge cycle. However, the electronic structure changes associated with the charge compensation mechanism are still not clear. In addition, completely new materials, many of which are based on nano-composites (Figure 2.9.6) due to their increased lithium adsorption capacity and faster kinetics, are also being actively pursued.

With the high brightness and flux of NSLS-II, in-situ x-ray diffraction and spectroscopy studies of individual grains of the cathode materials will be possible. Novel x-ray techniques, such as resonant and non-resonant x-ray Raman scattering, will also be applied to determine the electronic structure by providing shallow core-level absorption spectroscopy information, particularly the K-edge of oxygen and the L edges of 3d transition metals, using hard x-rays.

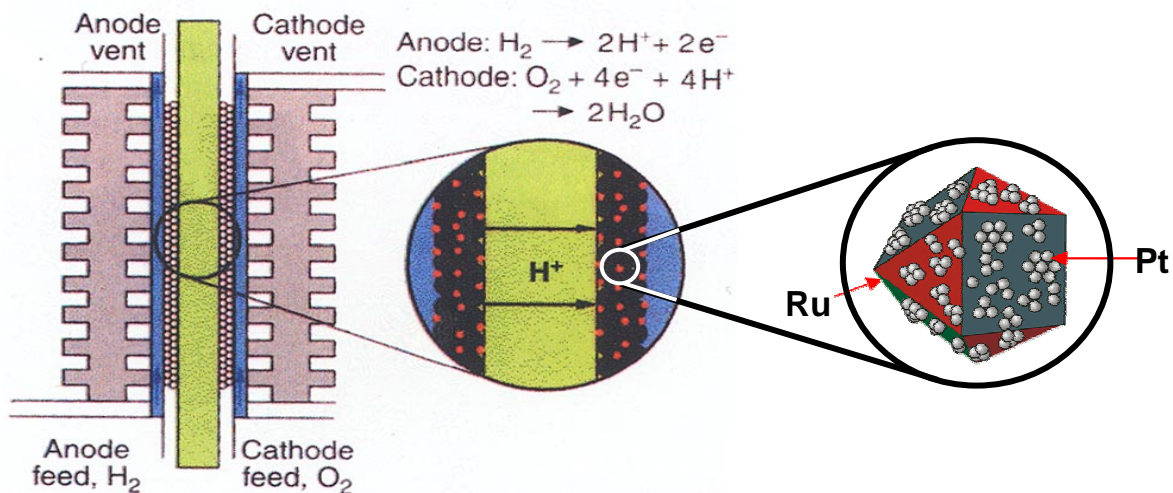


**Figure 2.9.7**  $\text{H}_2/\text{O}_2$  fuel cell and the chemical reactions occurring at the anode and cathode.

### 2.9.2.4 Electrocatalysis and Fuel Cells

Fuel cells represent one of the greatest opportunities for clean and efficient power generation, including electric power for transportation. Continuous progress has been made in electrocatalysis over the last two decades, in particular in areas related to fuel cell research. Fuel cells are soon expected to become one of the major sources of clean energy. Considerable environmental benefits and some preservation of fossil fuels will follow if this direct energy-conversion electrochemical power source becomes an economically viable alternative.

Much research has been devoted to developing electrocatalysts, since the success of fuel cells largely depends on improving their performance. However, despite considerable progress technical challenges must be overcome before fuel cells can be widely used in electromotive and residential applications, including low loading of noble metals, enhanced catalytic activity, and long-term stability [15-17]

To meet these requirements, the development of new electrocatalysts with increased activity and reduced noble metal content is necessary. This challenging task will only be accomplished with atomic level design of electrocatalysts, which requires a new level of characterization of the structural, electronic, and dynamic properties of supported nanoparticle electrocatalysts.

One approach to synthesis of the next generation of electrocatalysts that has been demonstrated consists of a submonolayer-to-monolayer deposition of Pt on carbon-supported metal nanoparticles [18-19]. In this synthesis, all the Pt atoms are placed on the surface of carbon-supported metal nanoparticles, i.e., exactly where they are needed for the reaction. Thus, an ultimate reduction of Pt loading can be achieved since there are no 'bulk' Pt atoms present, as there are in standard electrocatalysts.

An electrocatalyst for a fuel cell anode with 1/8 monolayer of Pt on Ru nanoparticles deposited on carbon (1/10 of Pt loading in standard electrocatalysts) has been shown to have an excellent activity for  $\text{H}_2$  oxidation, good tolerance to CO impurities in  $\text{H}_2$  and excellent long-term performance stability. Figure 2.9.7 shows the schematic of a  $\text{H}_2/\text{O}_2$  fuel cell and a model of the recently developed Pt/Ru electrocatalyst nanoparticles.

The characterization of electrocatalysts requires the high brightness of NSLS-II in combination with high-speed detectors for time-resolved studies of the kinetics of electrocatalytic processes and surface atom mobility. An important feature of the monolayer-level electrocatalysts is that all of the Pt atoms are active. Hence, the observed electronic and structural properties can be unambiguously correlated with their catalytic activity. However, the signal from such samples is weak and high-intensity sources can greatly improve these studies. Again, NSLS-II is needed for these measurements.

Surface segregation is a key to a long-term structural stability of alloy catalysts. To characterize subtle changes in structure and to understand dynamic aspects of these processes requires the power of NSLS-II, which will be especially critical for characterization of metal monolayer electrocatalysts on tailored alloy nanoparticles prepared by the above method, and for catalysts prepared by combinatorial methods for large scale screening of novel materials.

### 2.9.3 Impact of NSLS-II

Modern catalysts acquire a considerable amount of their multifunctionality from their complex multielemental composition. As an example of such a complex chemical “factory”, consider a modern automotive catalytic converter that is typically made up of a porous alumina oxide honeycomb impregnated with nanoparticles of Pt, Rh, ceria, zirconia, lanthana and baria: Pt oxidizes hydrocarbons and CO, Rh reduces NO<sub>x</sub>, ceria and zirconia work as oxygen storage components enabling the oxidation of hydrocarbons and CO while the engine is running fuel-rich, lanthana stabilizes the alumina surfaces, and baria traps the catalyst poison SO<sub>3</sub>. Modern synchrotron-based tools therefore must provide time-resolved elemental information to investigate *in-situ* the complex chemical reactions involved.

The unprecedented brightness and flux of NSLS-II, in combination with high-speed detectors, will extend the existing techniques to include time-resolved studies of the kinetics of catalytic processes on msec timescales or faster and enable the use of combinatorial methods for large scale screening of novel materials. It will also enable the application of new experimental techniques, such as high-resolution X-ray emission spectroscopy and X-ray Raman scattering, to provide new spectroscopic information; allow spectromicroscopy characterization of model systems with better than 10 nm spatial resolution to characterize novel nanometer sized catalytic materials, as well as the active sites and adsorbate-substrate interactions in model systems; and enable high-pressure studies of model systems to help bridge the pressure gap. The impact of these new developments is illustrated below.

#### 2.9.3.1 Quick EXAFS and Dispersive EXAFS

Catalysis is a dynamic phenomenon, with the active phase often only formed in the presence of the reactants and/or products. Gaining detailed knowledge about the electronic and geometric structure of the active phase is paramount to developing a deeper understanding of the active sites necessary for a particular catalytic reaction. With this knowledge, it should be possible to predict the structures necessary for other reactions. While some catalytic structures can be determined under steady-state conditions, there are many cases where it is advantageous to obtain the information about the active structures by perturbing the conditions in some manner, such as by applying a temperature or pressure pulse, or by pulsing the reactants as opposed to continuous flow. This is especially true in partial oxidation reactions, or in catalysts comprised of several different elements, all of which could undergo redox chemistry.

Dispersive EXAFS [20] and quick scanning EXAFS [21], coupled with a reactor supplied by an automated manifold capable of both continuous gas flow and fast switching valves for pulse flow, can be used to follow transformations on the millisecond time scale. With a quick scanning monochromator, full EXAFS scans can be collected in the few second time scale. In this manner, redox changes can be followed using XANES, and once an interesting regime of pressure and temperature is identified, the quick scanning monochromator can be used to obtain detailed local structure information. Figure 2.9.8 shows the time-resolved EXAFS (QEXAFS) data for a heteropolymolybdate catalyst where the evolution of the active phase is clearly identified.

Another important application of a QEXAFS beamline on NSLS-II will be to follow structural transformations in supported bimetallic and trimetallic catalysts. For example, a more rigorous structure determination is obtained if the EXAFS of both edges in a bimetallic catalyst are refined simultaneously. Currently, this data is obtained by collecting the EXAFS data twice, once from one element and then by repeating the entire EXAFS data collection from the second element. Using a quick scanning

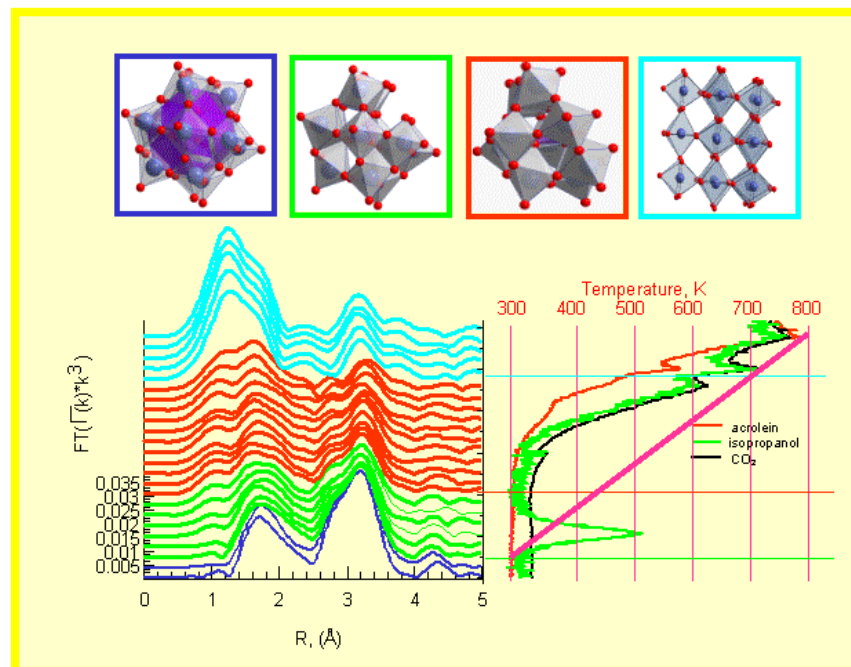


**Figure 2.9.8** FT-EXAFS and in-situ catalysis data of propene oxidation over a  $H_4PVMo_{11}O_{40}$  HPA catalyst. Multiple structure-activity relations for acid catalysed (green) action, for selective oxidation (red) and for deactivation (blue) were found [22].

monochromator, the data can be obtained in a pseudo-simultaneous manner by slewing quickly from one edge to the next. This would then ensure that the data are collected under essentially identical conditions and thereby lead to more reliable data analysis. A typical example application would be measurements of methanol or reformat fuel cell anode catalysts, where it has been demonstrated that the most active catalysts are bimetallic/trimetallic catalysts [23]. This is an area of very active research in which devices are sought that will be economically viable.

With the high brightness of NSLS-II, it will be possible to apply these techniques to reactions on msec time scales, well beyond what would otherwise be possible.

### 2.9.3.2 High Resolution Powder Diffraction Studies

The best of all catalysts for the production of acrylonitrile are mixed metal-oxide molybdenum systems. The first one, patented by Mitsubishi Chem. Ind., is a MoVNbTe-oxides that was claimed to have 59% yield with 63% selectivity. It was found that the active catalyst forms only under mildly reducing conditions and is made up of two prominent phases, denoted M1 and M2. Recently, the structure of the orthorhombic M1 phase was determined by using a combination of TEM, high-resolution synchrotron and neutron powder diffraction [24].

The atomic structure of this catalyst component (Figure 2.9.9) reveals that the sites partially occupied by  $V^{5+}$  (red),  $V^{4+}$  (green), and  $Te^{4+}$  (light blue) cations are isolated and provide sites for the propane ammoxidation catalysis to occur on terminal [001] planes. In particular, the ionicity of the metal-oxygen bonds in corner-sharing octahedra with  $V^{5+}$  and  $V^{4+}/Mo^{4+}$  centers provides particularly nucleophilic bridging oxygen, which is critical to propane activation. The  $Mo^{6+}$  sites have been shown to act as propane adsorption and nitrogen insertion sites in bismuth molybdates, which are also used for propane ammoxidation. This demonstrates how the multifunctionality of complex oxide catalysts is based on their multielemental distribution. High-resolution synchrotron powder diffraction provides unique information about the phase composition of such multicomponent catalysts.

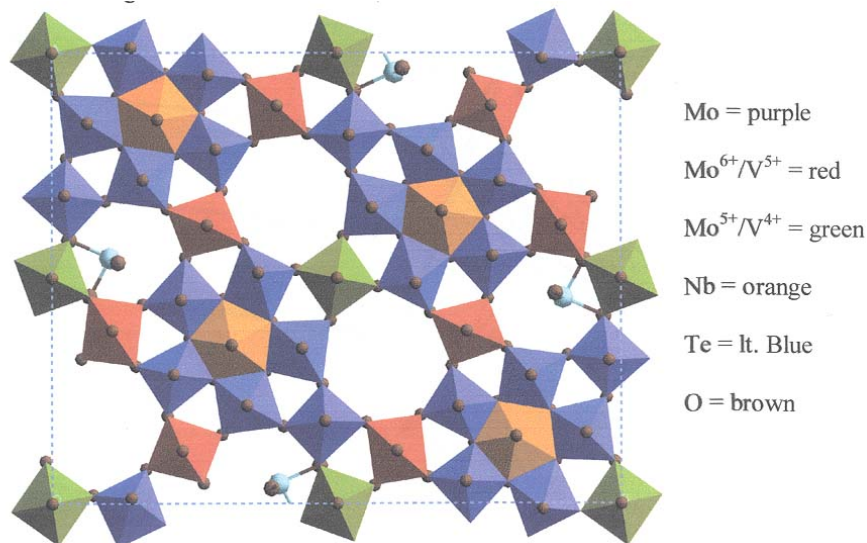


**Figure 2.9.9** The average structure of  $\text{Mo}_{7.5}\text{V}_{1.5}\text{NbTeO}_{29}$ .

By providing even higher flux and smaller beams, NSLS-II will make it possible to isolate diffraction contributions from different phases originating from different grains and thereby unravel the complex structure of individual grains as well as the strain and texture effects that might be beneficial for catalytic processes. In-situ and time-resolved powder diffraction of ‘real’ catalytic processes will provide an unprecedented wealth of understanding that will lead to new approaches to the design of novel multifunctional catalysts. The high brightness of NSLS-II combined with fast position sensitive X-ray detectors will provide a unique opportunity to study industrial catalytic processes at atomic resolution in real time and under real working conditions of pressure and temperature.

### 2.9.3.3 High Resolution X-ray Emission Spectroscopy

The electronic structure of a catalyst is often the overriding factor in determining its activity. Up to now, a common method used by many researchers in catalysis, is to record the XANES “white line” as an indicator of the density of unoccupied states, particularly for the Pt group metals, which are extremely important catalytic elements. In a recent breakthrough, deGroot, et al., [25] using high resolution X-ray emission spectroscopy, showed for bulk Pt metal that the normally accepted model for Pt, that the Pt  $5d_{3/2}$  level is filled, is not true. This has profound impact for our understanding of the chemistry of supported Pt-based catalysts, where it has been taken de facto that this level is filled. de Groot states, “the present spectra are limited by experimental resolution. With the prospect of an improved experimental resolution for X-ray excitation and decay, the Pt edge absorption spectra could be obtained with even better resolution, thus providing a high-resolution hard X-ray probe of the empty density of states with important advantages for *in-situ* and high-pressure studies”. Data collected in this manner, when coupled with reliable user-friendly ab initio XANES codes, e.g. FEFF8, will provide dramatic and powerful insight into the electronic structure of supported metal catalysts.

Currently, a multi-element high-resolution crystal analyzer funded by NSF is being developed at the NSLS. NSLS-II will provide the high brightness and flux necessary to extend this technique to higher energy resolution and to real-time *in-situ* studies. A high-resolution X-ray emission spectrometer can also be used in resonant inelastic X-ray scattering (RIXS) measurements, where the rich soft X-ray spectroscopic information could be obtained using hard X-rays. The feasibility of this technique has been demonstrated in a recent 1s2p RIXS study of  $\alpha\text{-Fe}_2\text{O}_3$ , where the incident energy is tuned to the Fe K edge and Fe  $K\alpha$  emission lines are analyzed with high-resolution spectrometer [26]. Figure 2.9.10 shows the applications of Fe 1s2p RIXS to an important industrial catalyst, Fe-ZSM<sub>5</sub> [27].

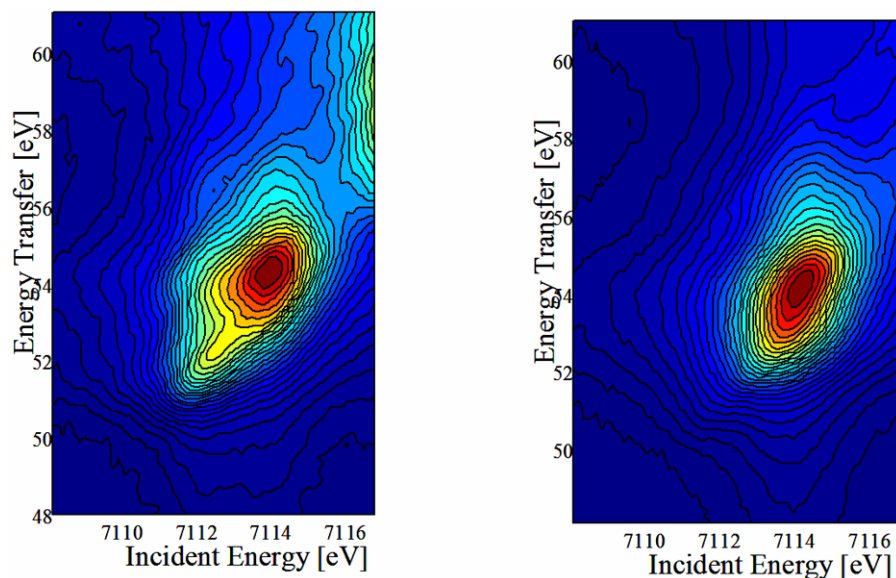


**Figure 2.9.10** *1s2p RIXS spectra of Fe in a ZSM-5 catalyst: The left-hand figure shows the catalyst at partially reduced state and the right-hand figure shows the fully oxidized state.*

### 2.9.3.4 Anomalous Small Angle X-ray Scattering & Diffraction Anomalous Near Edge Structure

One of the most fundamental characteristics of a heterogeneous catalyst is the size distribution of the metal particles, which is traditionally determined using transmission electron microscopy (TEM). However, there are difficulties with TEM characterization of heterogeneous catalysts: the smallest particles, which are of the greatest importance for catalytic chemistry, are difficult to identify; the conclusions are based upon the analysis of extremely small samples; and the technique is very labor intensive and not readily performed *in-situ*.

A technique that removes these shortcomings and complements TEM is anomalous small angle X-ray scattering (ASAXS). Like TEM, small angle X-ray scattering (SAXS) is sensitive to objects with sizes below 10 nm. Because its contrast mechanism originates from electron density differences, SAXS cannot normally directly link features in a scattering profile to specific components in a composite system. For a catalyst this means, for example, that pore structure scattering cannot be separated from scattering from metal particles. However, by taking SAXS data above and below the absorption edge of an element of interest, so called ASAXS, scattering from it can be isolated. Being a photon-in/photon-out technique, ASAXS measurements can be made on catalysts in reactive environments. Thus, one could use ASAXS to understand the resistance of a heterogeneous catalyst to sintering, and hence activity loss, under working conditions, such as temperature and environment.

Diffraction anomalous fine structure (DAFS) is an important development in X-ray absorption spectroscopy [28]. It provides a probe of site-selective local structure for systems with chemically identical atoms. To apply this technique to catalysis problems requires the capability to perform DAFS on dilute powder samples, which is an extremely demanding experiment. The feasibility of performing diffraction anomalous near-edge structure (DANES) was recently demonstrated [29] on a ZSM-5 zeolite catalyst with 3 wt % platinum loading.

With the increased brightness of NSLS-II, DAFS from catalysts with relevant weight loading of metal will be possible and it will be possible to conduct these studies *in-situ*.

### 2.9.3.5 Inelastic X-ray Scattering

Significant progress has been made in understanding the relationship between structure and functionality for heterogeneous catalysts. Because of its ability to provide chemical and physical state information about a catalyst in a reactive environment, hard X-ray absorption spectroscopy has been a crucial tool for obtaining such information. Studies on working catalysts have been complemented with studies on model systems, both single crystal and powders, using VUV radiation. With VUV radiation it is possible to study the first row elements, in particular the carbon K-edge, and the 3d-transition metal L-edges. However, VUV studies of powder catalysts suffer because they are usually limited to pre-natal/post-mortem characterization in vacuum or, at best, in the presence of a few milli-Torr of gas. In principle, inelastic X-ray scattering (X-ray Raman scattering) can provide the same information as VUV and soft X-ray spectroscopy under “real” reaction conditions. The feasibility of using X-ray Raman scattering for this kind of application has been demonstrated recently [30].

The increased brightness and flux of NSLS-II in combination with the development of higher energy and larger area crystal analyzers will increase the sensitivity of this technique by several orders of magnitude and revolutionize our understanding of working catalysts.

### 2.9.3.6 Photoemission and Surface Microscopies

The high brightness and flux of NSLS-II will allow the acquisition of photoelectron spectra down to msec time scale. With current capabilities, these spectra are acquired in a time interval of 5-120 seconds. The improved time-resolution will allow the monitoring of the evolution of surface reactions as a function of time under changing temperature and/or reactant conditions. Another important aspect is the gain in sensitivity that will result from the use of a high brightness X-ray source. Currently, it is extremely difficult to detect low concentration species on a catalytic surface because the data acquisition time is too long to prevent contamination of the sample surface. The increased brightness of NSLS-II will allow the detection of adsorbate concentrations on the order of 0.05 % on the surface of a catalyst.

The increased brightness of NSLS-II will be particularly important for imaging techniques. Given the complex nature of even the simplest catalytic systems, detailed understanding of the relationships between structure and reactivity is difficult to achieve. Genuine comprehension of catalytic processes requires multi-dimensional imaging techniques. For example, serious limitations have come to light by virtue of the discovery of dynamic patterns on catalyst surfaces under reaction conditions. The presence of patterns on crystal facets in supported catalysts is also confirmed. With the further development of photoemission electron microscopy (PEEM), it will be possible to image these intricate patterns *in-situ* with chemical sensitivity and sub-10 nm spatial resolution.

In operation, heterogeneous catalysis at gas-solid interfaces occurs at pressures much higher than those typical of electron-based spectroscopies. New electron energy analyzer designs compatible with ‘high pressure’ sample environments, based on differential pumping and tailored electron optics, are being developed to lower the pressure gap by allowing the surface chemistry to occur at elevated pressures (100 mbar) while tracking the surface electronic structure and composition using X-ray photoelectrons. This is a very exciting development and will allow, for the first time, detailed information on the oxidation states of the elements in the catalyst combined with detailed knowledge of the electronic structure of weakly adsorbed intermediates on the catalyst surface.

### 2.9.3.7 Carbon K-edge Fluorescence Yield Near Edge X-ray Absorption Fine Structure

In heterogeneous catalysis involving carbon-containing species, distinguishing among the electronic states of the carbon atoms is critical to understanding reaction intermediates. While this is not typically revealed in XPS, NEXAFS can make this distinction because it samples the local valence electron density

as excitations from core levels to unoccupied molecular orbitals relax, emitting photons or emitting Auger electrons. On planar model catalysts, the molecular orientation of surface intermediates can be determined under reaction conditions using polarized X-rays. Even though the photon yields are low (~0.0012), this technique provides a photon-in photon-out spectroscopy that can track the concentrations of various forms of carbon under working catalyst conditions. Mixed-element technical catalysts often suffer from background scattering. Rather than increasing the incident X-ray intensity, a process that often damages the sample, it is better to improve the signal-to-noise ratio. In a recent breakthrough, a near-normal-incidence focusing multilayer mirror detection system tuned for carbon-based signals has shown the ability to reject non-carbon background and makes possible the analysis of carbon in technical materials [31]. This detector potentially enables a whole new class of *in-situ* photon-in photon-out soft X-ray absorption measurements.

The high brightness of NSLS-II, together with these advances, will make millisecond time resolution for kinetic analysis a key future direction.

## REFERENCES

- [1] Chemistry & Industry, Jan 21, 2002 p.22
- [2] J.R. McNeill, *Something New Under The Sun : An Environmental History Of The Twentieth Century* (Norton, New York,2000)
- [3] M.I. Hoffert, C. Covey, *Nature* 360, 573 (1992)
- [4] M.I Hoffert et al *Nature* 395, 881 (1998)
- [5] G. Meitzner, G. H. Via, F. W. Lytle, J. H. Sinfelt, *J. Chem. Phys.* 83 4793 (1985)
- [6] "Method for producing electrodes using microscale or nanoscale materials obtained from hydrogen driven metallurgical reactions." US patent No 6,613,213 J.J. Reilly, G.D. Adzic, J.R. Johnson, T. Vogt, J. McBreen Issued Septemer 2, 2003
- [7] J.J. Reilly, J.R. Johnson, T. Vogt, G.D. Adzic, Y. Zhu and J. McBreen *J. of the Electrochemical Society* 148, A636-A641 (2001)
- [8] B. Bogdanovich and M.J. Schwickardi *J. Alloys Compds.* 253, 1 (1997)
- [9] Soffer, J.E. Koresh, ans S. Saggy 1987 US Patent 4,685,940
- [10] C.W. Jones and W.J. Koros *Carbon* 32 , 1419 (1994)
- [11] M.B. Rao and S. Sircar *Gas Separation and Purification* 7, 279 (1993)
- [12] A.C. Dillon, K.M. Jones, T.A. Bekkedahl, C.H. Kiang, D.S. Bethune and M.J. Heben *Nature* 386, 377-379 (1997)
- [13] M.S. Dresselhaus and P.C. Eklund *MRS Bulletin* November (1999)
- [14] Eddaoudi, J. Kim, N. Rosi, D. Vodak, J. Wachter, M. O'Keefe, O.M. Yaghi *Science* 295 , 469 (2002)
- [15] S. Gottesfeld, T. A. Zawodzinski, in *Advances in Electrochemical Science and Engineering*, vol. 5, R. C. Alkire, D. M. Kolb, Eds., Wiley\_VCH, Weinham, (1997).
- [16] N. M. Markovic, P.N. Ross, *Electrochim. Acta*, 45, 4101 (2000).
- [17] T. E. Springer, T. Rockward, T .A. Zawodzinski, S. Gottesfeld, *J. Electrochem. Soc.*, 148, A11 (2001).
- [18] S.R. Brankovic, J .X. Wang, R. R. Adzic, *Electrochem. Solid-State Lett.*, 4 (2001) A217.
- [19] S.R. Brankovic, J.Wang, R.R. Adzic, *Surf. Sci.* 470 (2001) L173.
- [20] G. W. Coulston, S. R. Bare, H.H. Kung, K. E.Birkeland, G. Bethke, R. Harlow, N. Herron, P. L. Lee, *Science*, 275 191 (1997).
- [21] G. S. Clausen L. Graabaek, G. Steffensen, P. L. Hansen, P. H. Topsoe, *Catal. Lett.* 20 23 (1993); T. Ressler, O. Timpe, T. Neisius, J. Find, G. Mestl, M. Dieterle, R. Schlögl, *J. Catal.* 191 75 (2000).
- [22] R. Schlogl, private communication.
- [23] R. Viswanathan, G. Hou, R. Liu, S. R. Bare, F. Modica, G. Mickelson, C. U. Segre, N. Leyarovska, E. S. Smotkin, *J. Phys. Chem. B*, 106 3458 (2002).

- [24] P. DeSanto Jr, D. J. Buttrey, R. K. Grasselli, C. G. Lugmair, A. F. Volpe, B. H. Toby, T. Vogt  
Topics in Catalysis Vol 23 No1-4, 23, (2003)
- [25] F. M. F. de Groot, M. H. Krisch, J. Vogel; Phys. Rev. B66, 195112 (2002)
- [26] W. A. Caliebe, C.-C. Kao, J. B. Hastings, M. Taguchi, A. Kotani, T. Uozumi, F. M. F. de Groot;  
Phys. Rev. B58, 13452 (1998).
- [27] F. M. F. de Groot, private communication
- [28] H. Stragier, J. O. Cross, J. J. Rehr, L.B. Sorensen, C. E. Bouldin, J. C. Woicik; Phys. Rev. Lett, 69,  
(1992) 3064.
- [29] D. Sayers, H. Renevier, J. L. Hodeau, J. F. Berar, J.M. Tonnerre, D. Raoux, A. Chester, D. Bazin  
and C. Bouldin, ESRF, newsletter January 1997.
- [30] “Chemical Applications of Inelastic X-ray Scattering”; Hayashi, Udagawa, Gillet, Caliebe, C.-C.  
Kao; chapter 18 in “Chemical Application of Synchrotron Radiation”, Advanced Series in Physical  
Chemistry Vol. 12, editor Tsun-Kong Sham, World Scientific (2002).
- [31] D. A. Fischer, S. Sambasivan, A. Kuperman, Y. Platonov, J. L. Wood, Rev. Sci. Instrum. submitted  
(2002).

## 2.10 Earth and Planetary Science

### 2.10.1 Overview

The evolution of the Earth and other planets is a vast process lasting billions of years, involving huge amounts of materials (crystalline and molten silicates, metals, and volatile constituents), at temperatures from near absolute zero to several thousand degrees, and pressures from a fraction to millions of atmospheres. The present state of the Earth, as well as its evolution through time, is governed by the properties of these materials. Their properties at the relevant conditions of pressure, temperature, and stress dictate the red and blue regions of a seismic tomographic image (Figure 2.10.1), or control the depth and time history of earthquakes (Figure 2.10.2). These materials also define the frequencies of the oscillations of the Earth and the rate that plates slide over the surface.

With the symbiotic development of synchrotron radiation and high-pressure techniques, experimental studies of earth materials are experiencing an unprecedented surge of breakthroughs that were deemed inconceivable a decade ago. Synchrotron sources have fundamentally altered the nature of high-pressure experimentation, from reconnaissance study with limited capabilities to high-precision study with comprehensive material characterization over a wide range of pressures and temperatures. In particular, rheological properties, phonon related properties, and dynamics of chemical reactions can now be investigated at very high pressures and temperatures. By studying the materials of which the Earth is made, high-pressure research using synchrotron high-energy X-ray and infrared radiation has contributed significantly to understanding of the phenomena, processes, and state of the Earth. This information allows addressing issues that range from the chemical heterogeneity of the Earth's interior to the processes responsible for deep focus earthquakes.

### 2.10.2 Scientific Challenges and Opportunities

#### 2.10.2.1 Elastic Properties at Pressure and Temperature

Elasticity measurements on minerals are the bridge between the observed seismic velocity structure of the Earth and properties at depth, such as chemical composition and temperature. The sound velocity

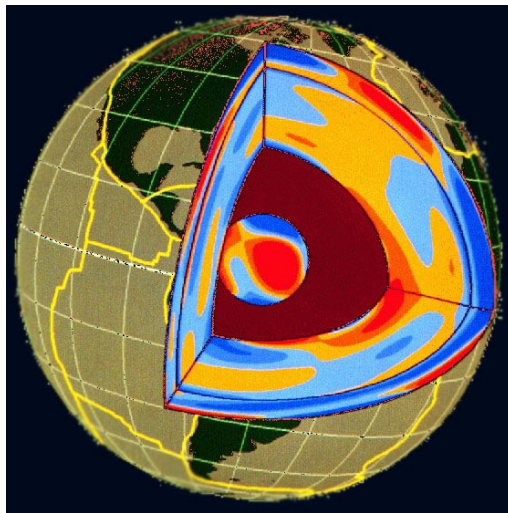


**Figure 2.10.1** A seismologist's view of the Earth. Red regions indicate slow sound wave velocities, blue are fast. This structure may represent the flow patterns of hot (slow) material rising with sinking cold (fast) regions. Actual association of fast with either thermal or chemical variations requires high pressure laboratory data.

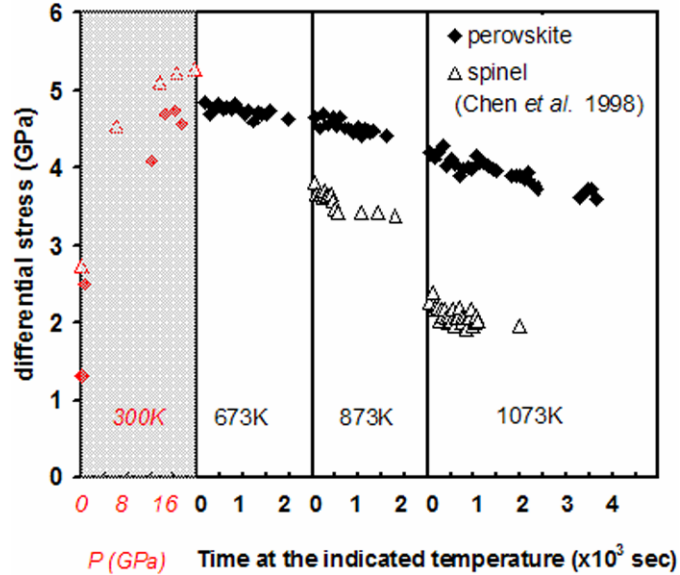


**Figure 2.10.2** Data acquired on the large-volume press at NSLS X17B1. Time-resolved EDXRD shows that perovskite is stronger than other minerals at high P-T. Data explains why no earthquakes start in earth's lower mantle [1].

structure of the Earth is known from the surface to the center of the core, through seismological studies. Tomographic studies of 3-D velocity structure are providing detailed images of fast and slow regions that relate not only to our notions of the current compositional state of the mantle, but to convective flow and mixing over time [2]. Observations now reveal the penetration of some slabs into the lower mantle, the stagnation of other slabs in the transition zone, and broad differences in velocity structure beneath continents and oceans. In other studies of reflected and converted seismic phases, subtle undulations in the depths of seismic discontinuities are being mapped and being related to the properties of phase transformations that likely causes them. Elastic anisotropy, reflecting the single crystal elastic properties coupled with large deformations, traces out the stress-strain history of the planet. At the core-mantle boundary, astonishing degrees of heterogeneity and complex velocity structure are observed that may be related to chemical reactions between the mantle and core, and/or the recycling of subducted material in a slab graveyard.

Synchrotron X-rays are a vital part of acoustic velocity measurements in multi-anvil apparatus at high pressure and temperature. The travel times for elastic waves traveling through a sample are measured, from which wave speeds and elastic moduli are calculated. This technique provides relatively high precision data, it can be used with transparent or opaque samples, and it yields the bulk elastic properties without the need for single crystals. The direct measurement of sample length by X-ray imaging greatly reduces errors in velocities and elastic moduli. In the future, capabilities will be expanded from measurements at pressures of 14 GPa and temperatures of 1300° C to pressures greater than 20 GPa and temperatures of more than 2000° C using the state-of-the-art high pressure systems.

Measurement of velocities and elastic properties allow the raw information provided by seismology to be interpreted in terms of physically meaningful quantities such as chemistry, temperature, dynamics and stress history. Without accurate information on the variation of mineral acoustic velocities with temperature, pressure, and composition, it is not possible to form a realistic picture of Earth's interior.

The ambitious challenge facing the mineral physics community is to develop the ability to measure sound velocities on any Earth material throughout the entire range of pressure-temperature (P-T) conditions in Earth's interior and to recover both aggregate elastic properties and single crystal properties.

The dynamics and processes associated with texture development in the inner core represent a major problem in geophysics. Seismic anisotropy reflects oriented texture in elastically anisotropic minerals. To address this question, the technique of radial X-ray diffraction was pioneered at the NSLS [3, 4]. In these

measurements, strain anisotropy was observed that corresponded to variations in diffraction intensities and suggest the presence of preferred crystallographic orientations. These deformation experiments at inner core pressures provide information about flow processes within the Earth and are relevant to the possible development of anisotropy during outer core convection. It is now essential to extend these studies to alloys and compounds of iron with hydrogen, carbon, oxygen, silicon, sulfur, and nickel. Studies at high temporal, spatial, and wavelength resolution require a dedicated facility that is capable of quantitative texture analysis. Empirical modeling techniques have been developed to extract elasticity information from such X-ray diffraction studies on textured polycrystals.

With NSLS-II, a new generation of direct in situ investigations of the rheology and texture of materials at extreme pressures will be carried out in entirely new domains of pressures and temperature. In situ structure, equation of state, and phase equilibria studies of light element alloys will be possible at extreme conditions. Inelastic scattering of X-rays promises to provide a new leap in elasticity data. The facility will provide an important means to extend inelastic X-ray scattering measurements for high pressure phonon studies. Phonon scattering contains crucial information about not only the acoustic velocity of the polycrystal, but also information about the single-crystal elastic moduli. Recovery of this information will provide new insights into the deep Earth by allowing interpretation of seismically defined elastic anisotropy. Phonon density of states reflects thermal properties of the material. Measurements of this property with pressure and temperature will give better interpretations of the thermal state within the Earth. This is currently one of the poorest, yet important physical parameters for the deep Earth.

NSLS-II will provide the flux and energy range that is needed for these experiments in both multi-anvil cells and diamond anvil cells. Through these studies, the entire region of the Earth's interior can be explored.

### 2.10.2.2 Rheology Challenges

It is no more than a decade since synchrotron radiation has been applied to the understanding of rheology of polycrystals at high pressure and temperature. With the rapid development of high pressure facilities and techniques, progress in probing the rheological properties of deep Earth materials has enhanced understanding of the dynamics of the Earth and other terrestrial planets. For example, two new types of high-pressure apparatus, a modified cubic apparatus (D-DIA) (Figure 2.10.3) capable of providing quantitative rheological information and a rotational Drickamer apparatus (RDA) able to produce very large plastic strains, are now becoming available to users. With synchrotron radiation, these tools can be used for quantitative measurements of stress ( $\pm .01$  GPa) and strain ( $\pm 10^{-4}$ ) at high pressure and high temperature (15~25 GPa, 2000 K). Results have been as fundamental as giving us an improved

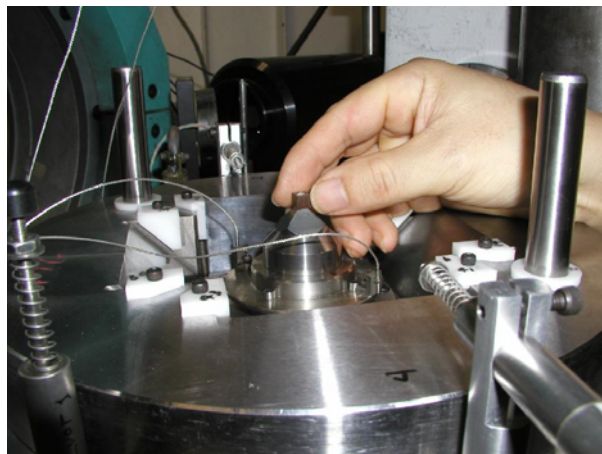


**Figure 2.10.3** Sample being loaded into the D-DIA high-pressure deformation device.

understanding of mantle convection and dynamic processes such as deep earthquakes.

The remaining frontier that needs exploration in connecting seismic studies with laboratory experiments is the time scale. Seismic studies use millihertz acoustic waves to probe the Earth, while laboratory studies use megahertz acoustic waves. Differences in these time scales are expressed in the attenuation, or the  $Q$  (quality factor), of the stress-strain relationship. With the newly developed synchrotron tools, unprecedented flexibility in controlling the stress and strain during the deformation process at mantle pressure and temperature is feasible. Knowledge gained will bring important constraints on the thermal, velocity, and density structure of the Earth.

To measure  $Q$ , we need to measure stress relaxation times and strain retardation times as a function of frequency. In particular, to describe seismic wave attenuation and related transient creep, we need to resolve strain with a precision of  $10^{-6}$  [5]. Current techniques in NSLS beamline X-17B2 allow a precision of  $10^{-4}$ , good for plasticity studies, yet two orders of magnitude lower than what is need for anelasticity study. Improvements on both X-ray source and detection instrumentation are essential to reach the strain precision of  $10^{-6}$ . NSLS-II will be able to offer an intensive high energy X-ray beam with source size two orders of magnitude smaller than current beam size. This makes the increase in strain precision possible. Instrumentation improvements include use of asymmetrical cut single crystal analyzer, phase contrast imaging, and the development of a hard X-ray microscope.

NSLS-II, together with the new high resolution strain instrumentation, will enable measurement for earth materials of  $Q$  at high pressure and temperature and measurement of quantitative flow laws using multi-anvil cell to 20 GPa and 2000K and using diamond anvil cell to 100 GPa and 1200K.

### **2.10.2.3 Study of Melt Property and Liquid-liquid Phase Transition at High Pressures**

Liquid silicates have shaped the surface of the planet that we live on. It has been the most significant chemical filter in the history of the planet and it still plays a role in dictating its future. The earth's core is predominantly liquid and creates the magnetic field. Whether liquids sink or float is determined by the local structure of the melt and the chemical partitioning between the melt and residual solid. Liquids have long been ignored because adequate tools have not been available for providing insight.

While pressure-induced phase transformations in crystalline solids are common and have been extensively studied, phase transitions in liquids or melts have caught scientists' attentions only very recently. As almost all solids transform to a denser phase when pressure is applied, it is very reasonable to expect that local structure changes also occur when a liquid is subject to high pressures. The lack of understanding of melt phase transitions is mainly due to experimental difficulty. Crystalline phase transitions can be very well characterized using in situ X-ray diffraction. X-ray scattering by noncrystalline materials, however, is much less straight forward. In addition, in-situ measurements while the specimen is maintained simultaneously at high pressure and high temperature make the study even more technically difficult. Nevertheless, study of liquid-liquid phase transitions has gained rapidly growing interest. Materials that reportedly show a liquid-liquid phase transition so far include C, Si, P, Ge, I, Bi, Se, Te,  $H_2O$ ,  $SiO_2$ ,  $GeO_2$  and  $S_{12}O_3$ - $Y_2O_3$  melt [6-16]. Experimental techniques used in these studies include X-ray scattering, X-ray absorption spectroscopy and melt density measurement through X-ray absorptions.

The pressure-induced local structure transition is a new class of phase transformations. It is undoubtedly important in terms of pure physics. In addition, understanding melt behavior and structure under high pressures has been a dream of the scientists in national defense programs as well as Earth and planetary sciences. Melt properties are essential information for simulations of a nuclear explosion, and for understanding volcanism and the role of partial melting in the Earth mantle. More significantly, the liquid outer core portion of Earth's interior (Figure 2.10.4) is still mysterious. It likely gives rise to the Earth's magnetic field, but is least understood by scientists. It consists of mostly liquid iron but little is known about its local structure and phase transitions. Studies of liquid local structure and phase transitions at elevated pressures (<100 GPa) are likely to become one of the hottest topics in condensed

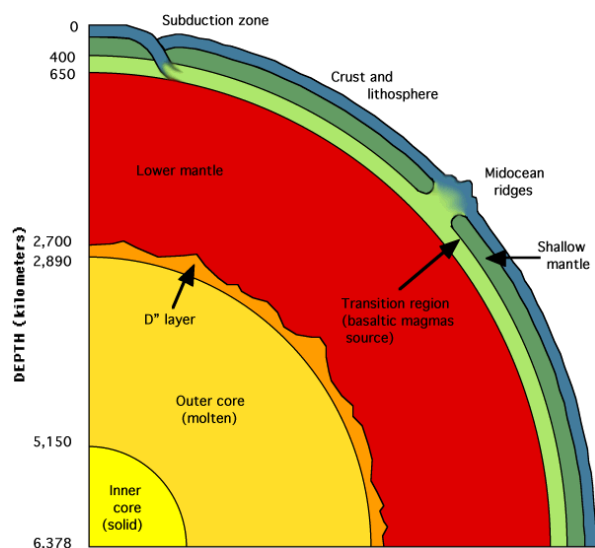


**Figure 2.10.4** Illustration of the Earth's interior (Courtesy of *Windows to the Universe*, <http://www.windows.ucar.edu>). The molten outer core is the least known portion of the Earth's interior.

matter physics, and understanding the melt structure of the Earth's outer core at pressures  $> 135$  GPa will be a great challenge for the next decade and beyond.

At the NSLS superconductor wiggler beamline X17B, experiments have been carried out to study liquid properties (density and viscosity) at high pressures in a multi anvil press using high energy X-rays. An X-ray radiograph imaging technique has been developed to measure density of melts [17]. Figure 2.10.5 demonstrates a melting volume measurement of a very important Earth core material, FeS. Studies of radial distribution function of melts are also on the way. Although X-ray absorption spectroscopy is a very powerful tool to study the local structure of melts, energies of the absorption edges of the most important elements to Earth science (e.g. Si and Al) are too low. Photons with those low energies are completely absorbed by the high pressure cell, even through Be gaskets. Study of local structure around these light atoms at high pressures is currently impossible.

The above challenging scientific issues require an improved brilliant high-energy X-ray source, and integrated X-ray optics and measurement techniques. NSLS-II will offer these capabilities, and enable the following scientific challenges to be met with great impact on physics and Earth science: X-ray scattering at extremely high pressures ( $>100$  GPa) for deriving radial distribution function of melts; expanding all current phase diagrams of elements and compounds into the field of melts; mapping local structures around light atoms in melts using X-ray Raman spectroscopy; and understanding property and structure of the melts existing in the Earth outer core.

### 2.10.2.4 Phase Transformations at High Pressures

Studies of mineral phase transformations at high pressures are the key for understanding the Earth and planetary interiors. For example, the Earth's mantle is marked by two prominent seismic discontinuities at 410 and 660 km depth, where abrupt jumps in seismic velocities have been detected through the analysis of seismic waves created by earthquakes. It is now widely believed that both discontinuities are related to the phase transformations in olivine, the most abundant mineral in the Earth's upper mantle. With the detailed phase relations in olivine mapped out in the laboratory, the seismic determinations of the discontinuities can be translated into chemical composition and temperature for the mantle. Because of their importance to our quest of knowledge about the Earth's interior, phase relations in relevant silicate systems have been the subjects of the most extensive investigation in high-pressure research in the past half-century.

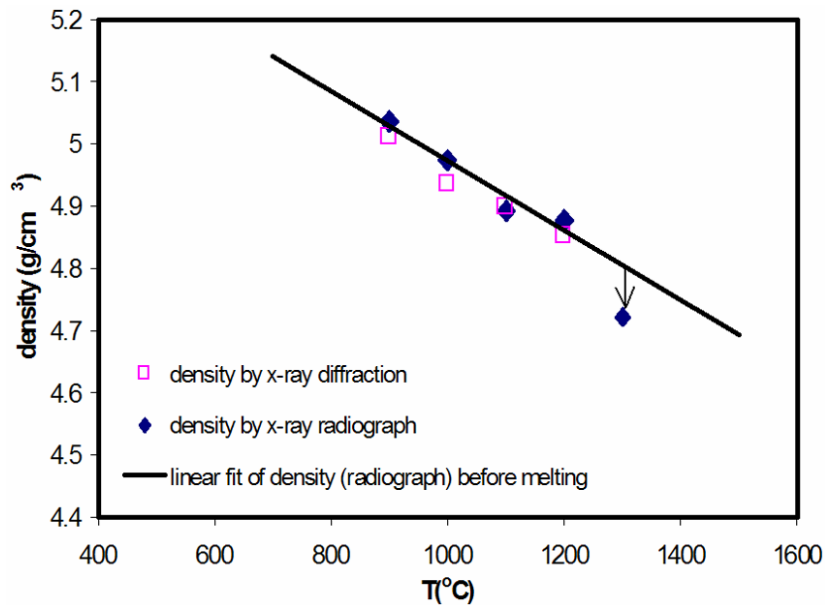


**Figure 2.10.5** Measured densities of FeS as function of temperature at 4 GPa. Melting causes a significant density drop.

In situ synchrotron X-ray measurements have been used to study mineral phase transformations at high pressures. Compared to the conventional quench/recovery method, synchrotron-based techniques provide much better environmental control. For example, precision in pressure measurements is about ten times higher than in quench experiments. Furthermore, important variables related to phase transitions, such as pressure and deviatoric stress, can be monitored throughout each experiment. This has led to much needed improvement in the determination of phase boundaries, which is critical to deciphering the detailed structures of seismic discontinuities, hence the Earth models, and to the determination of thermodynamic properties of minerals. Synchrotron-based techniques also provide the only reliable method for studying phase transitions that involve unquenchable phases, such as Ca-silicate perovskite.

Synchrotron X-rays allow time-resolved studies of phase transformation processes at high pressures, a fundamental problem in solid-state physics. Kinetics and mechanisms of phase transitions in the silicate system are also important for understanding the Earth's dynamic interior. Much like metamorphism that occurs in the Earth's crust over geological time, similar processes also occur in the Earth's mantle owing to the mantle convection. That is, materials in the mantle are subjected to constant changes in pressure and temperature, and hence the physical and chemical states of the mantle are not only depth-dependent, but also time-dependent. Phase transition kinetics could play an important role in defining the properties of convective currents in the mantle.

There are several shortcomings for present measurements that will be solved using the higher brightness of NSLS-II. One is that it is difficult to introduce various metal capsules and pressure-transmitting materials to control fugacities of oxygen and other volatile components within the sample charge. Thus the effects of these volatiles on the phase transitions can not be investigated quantitatively. The second is that it is not possible to investigate the local structure change during phase transitions using techniques such as EXAFS and XANES. The current X-ray acquisition time necessary for identification and characterization of the phases under high pressure and temperature also needs to be reduced in order to capture kinetics of fast phase transformations and transition characteristics near phase boundaries.

### 2.10.2.5 Oxidation and Spin States

The application of pressure often dramatically affects magnetic properties. While measurements of the magnetic susceptibility provide the magnetic moment, diffraction can provide the three dimensional

structure in magnetically ordered materials. Theoretically predicted pressure-induced magnetic collapse [18] is important for transition-element ions that, with their variable valence and magnetic states, control major geochemical and geophysical processes, such as oxidation and reduction, chemical differentiation, elasticity, geomagnetism, conductivity, and radiative heat transfer.

Depending on temperature and pressure the deceptively simple composition FeS crystallizes in at least five modifications with structures related to the NiAs-type. The spin state of iron in FeS can be determined from the Fe  $K_{\beta}$  spectrum by X-ray emission spectroscopy (XES) [19]. In the 2+ oxidation state of iron, the low-spin state is characterized by a total magnetic moment equal to zero. This collapse of the 3d magnetic moment has a distinct signature, since the exchange interaction vanishes and the resulting spectrum consists of a single narrow line. Measurements on troilite (FeS) show a high-spin to low-spin transition at 7 GPa coinciding with the FeS II-III structural transition [19]. Such studies have also been applied to FeO, indicating that there must be a maximum  $T_N$  above 300 K and 40-60 GPa with re-entrant behavior back to the paramagnetic phase above 80 GPa [20]. Likewise, a high-spin to low-spin transition occurs in hematite at 50 GPa [20].

The above mentioned transformations occur over a broad range of conditions up to >100 GPa. Hence direct study of these transitions and the high pressure phases by in situ X-ray diffraction, spectroscopy, and inelastic scattering will require the integrated capabilities of NSLS-II. The new generation of high-pressure devices based on large single crystal CVD diamond [21] will facilitate these studies.

### 2.10.2.6 Amorphous Materials and Nanomaterials

Pressure-induced amorphization transformations and pressure induced amorphous-amorphous transitions have been observed in a growing number of materials. Porous Si is one technologically relevant example and a number of other amorphous materials, including high-silica glasses, can be irreversibly compacted by pressure. A densified form can be retrieved on quenching to ambient conditions. This provides materials with a range of optical properties, densities, and chemical properties, which can be continuously tuned by changing synthesis conditions. Apart from the compaction of liquids and glasses, pressure can also induce certain classes of crystalline material to amorphize if compressed to pressures well outside their stability fields.

In situ diffraction studies of these materials and transitions are critical for understanding these processes. Some samples can be quenched in metastable states at atmospheric pressures and these recovered samples have been studied with standard diffraction techniques. The first high-pressure diffraction experiments with full radial distribution function analysis of amorphous materials were carried out at the NSLS on SiO<sub>2</sub> glass to 28 GPa [22]. This study demonstrated the importance of in situ measurements because the high-pressure structures were not quenchable. The primary barrier to in situ high pressure investigations has been the typically small sample sizes and limited incident beam flux, combined with the complicated data normalization procedure necessary when using high pressure cells.

Intermediate range structural order in permanently densified GeO<sub>2</sub> and SiO<sub>2</sub> glasses has been a subject of debate in recent years. The question as to whether a discontinuous transition takes place over a certain range of pressures and temperatures still appears to be open. Measurements on permanently densified GeO<sub>2</sub> show that although changes in the short range order are small, the intermediate range order is altered substantially. High energy X-ray diffraction measurements performed on normal and permanently densified GeO<sub>2</sub> glass (10 GPa) have revealed in detail the changes in local structure under pressure. The main conclusion from this study is that densification produces a change in the intermediate range order that subsequently causes a change in the short range order in the GeO<sub>2</sub> glass.

Similarly, recent studies on the archetypal glass GeSe<sub>2</sub> have shown that there is a breakdown of intermediate range ordering in liquid GeSe<sub>2</sub> at high pressure that may lead to a liquid-liquid phase transition [23], as seen in glassy GeO<sub>2</sub>. Whereas only corner sharing units are known to exist in GeO<sub>2</sub>, both edge and corner sharing units exist in the network forming GeSe<sub>2</sub> glass, so the situation becomes more complex. In-situ studies of the structure of GeO<sub>2</sub> and GeSe<sub>2</sub> glasses at 6-10 GPa and high

temperatures (1000° C) using diffraction would give critical insight into the structural nature of amorphous-amorphous and liquid-liquid transitions. In addition, isotopic substitution measurements of both the Ge and Se atoms would allow unprecedented structural information to be obtained.

Understanding the structure of magnesium silicate liquids and glasses is important for interpreting the behavior of refractory liquids produced by melting processes of the Earth and Lunar mantles. Although magnesium-rich silicate minerals are primary constituents of the Earth's mantle there is little information available on either the structure of the magmas produced when they melt or the associated thermodynamic properties. This paucity of information is due to the refractory nature of these phases, which makes in situ study of the liquids at high P-T conditions difficult and also because the liquids do not form glasses very easily, which limits the study of quenched phases. There are also important implications for the early history of the earth and moon since low-silica magnesium-rich liquids are considered to have played an important part in development of magma oceans and komatiite volcanism. More fundamentally, the change in liquid behavior could relate to the underlying changes in liquid structure that may be expected to occur as the liquids are compressed at deep Earth conditions.

High-pressure also provides a powerful means for tuning the properties of nanomaterials. A variety of studies of pressure-induced transitions in fullerenes and nanotubes have been reported, including transformations to novel superhard phases [24]. Studies of nanocrystalline chromium [25] indicate that antiferromagnetic order in the body-centered-cubic phase of powder and consolidated ultrafine-grain-size chromium samples can be suppressed to well below the Neel temperature of coarse-grained and single-crystal chromium.

With advances in pressure cells coupled with bright high energy X-ray beams, radial distribution function from in situ pressure amorphized solids will be possible. These investigations can be coupled with detailed vibrational spectroscopic studies carried out with synchrotron infrared spectroscopy over a wide pressure range. Detailed X-ray and infrared investigations of novel properties of nanomaterials will be carried out over a wide P-T range. This includes extensions of recent studies of pressure-induced transitions in nanotubes. It will be possible to examine previously reported but poorly understood transitions in fullerenes at higher pressure. The effects of intercalation of other components to form novel high pressure phases, including potential hydrogen storage and superhard and electronic materials can be explored with the diversity of techniques available.

### **2.10.2.7 Hydrous Minerals and the Deep Earth**

High P-T experiments offer the only practical means to examine directly the chemistry and physical properties of materials that comprise the deep interior of the Earth and other planets [26]. This information is crucial for understanding the Earth's water cycle and the connections between dewatering of the interior, formation of the oceans and recycling of water in subduction zones. Most water held within the crystal structures of minerals is released during subduction of the oceanic slab and then recycled back into the overlying mantle wedge where it can trigger melting or enter into reactions with other minerals. However, some of this water may be transported from the subducted slab into the mantle via dense hydrous magnesium silicates. For example, recent experimental studies [27] have shown that dehydration-rehydration reactions involving OH-clinohumite [ $Mg_9(SiO_4)_4(OH)_2$ ] could be an important mechanism for transporting water into the transition zone (400 km).

Hydrous minerals play a major role in low temperature geochemistry and are increasingly implicated in deep earth processes such as mantle convection and deep focus earthquakes. For example, layered hydrous phyllosilicates such as the clays, amongst the most common minerals at the earth's surface, are thought to be involved in the dehydration of the down going slab in subduction zones. Nominally anhydrous [28] as well as novel high pressure magnesium silicates have been suggested as phases for water storage in the mantle [29, 30]. Finally, the strength and rheological properties of the polymorphs of  $Mg_2SiO_4$  suggest they might provide mechanisms for storage of stress in the mantle and that dewatering processes in these and other hydrous phases may lead to the reactivation of faults in the lithosphere. The properties of these minerals then impacts a variety of surface and deep earth processes. A comprehensive

understanding of the phase relations, structures, elasticity, strength and rheological properties is a useful first step to bounding the mineralogical controls on these processes.

The transformations that clay minerals undergo when exposed to high temperatures and pressures are of great interest for both fundamental and applied science. Clays occur in nature in a variety of environments, and hydrothermal influences on their structures and properties are important for understanding their genesis and geological transformations, including geohazards such as earthquakes. From a fundamental perspective, the response of clay minerals to changes in pressure can shed new insight into understanding of the balance between different interlayer cohesive forces. However, detailed information of such transformations involving interlayer hydrogen bonds requires accurate determination of hydrogen atom positions by single-crystal diffraction. More generally, the presence of hydrogen bonding in solids can determine stability and properties of other materials [31, 32] and pressure provides a particularly "clean" variable for this study.

Dense hydrous phases are a key to efforts to understand the Earth's deep interior. As demonstrated by recent work at the NSLS, the combination of synchrotron X-ray diffraction and infrared spectroscopy has proven essential for investigating these important deep Earth materials [33]. Higher P-T studies using the full complement of integrated synchrotron techniques are essential for understanding these systems. Provided single crystals are available, many of the techniques now used routinely for high pressure single crystal X-ray diffraction will be transferred and implemented with large gem anvil cells.

### **2.10.2.8 Oxides and Silicates of Earth's Interior**

The high P-T behavior of silicates and oxides are particularly important for understanding the nature of the Earth's deep interior [26]. These materials exhibit numerous intriguing equilibrium and metastable transformations under pressure. For example, (Mg,Fe,Al)SiO<sub>3</sub> silicate perovskite is likely to be the most abundant mineral in the planet. The oxygen deficiency and cation-site distribution of silicate perovskite control its physical and chemical properties, including density, bulk modulus, defect mobility, ionic transport, flow behavior, oxidation states, hydration, and minor-element solubility. These properties of perovskite, in turn control the geophysical and geochemical processes of the Earth.

The basic crystallographic characteristics of the silicate perovskite were previously determined by conventional X-ray diffraction techniques [34]. The defect crystallography of silicate perovskite, however, requires a new generation of diffraction, inelastic scattering, and spectroscopic techniques. A new generation of in-situ crystallographic studies of complex silicate perovskites over the entire P-T range of the Earth's lower mantle are required to shed light on long-standing puzzles of the unusual effects on compressibility, the strong P-T-X dependence of iron-magnesium partitioning between the perovskite and magnesiowüstite, the effects of the high-spin/low-spin transition in ferrous and ferric iron, and the controversy surrounding electrical and mass transport properties of perovskite in the lower mantle. Coupled with new large volume megabar devices, accurate measurements will become possible on multicomponent systems to the P-T conditions of the core-mantle boundary.

### **2.10.3 Impact of NSLS-II**

Understanding the behavior of Earth and planetary materials at high pressures and temperatures requires an integrated experimental approach that utilizes a combination of complementary measurements. It is often essential to study the same sample at the same pressure and temperature with a broad range of techniques, including spectroscopy and diffraction. NSLS-II will be unique by virtue of its range of X-ray through infrared capabilities and the proven success of the NSLS in high-pressure geoscience during the past decade.

High-brilliance, high-energy synchrotron radiation provides the non-destructive probe to penetrate through the gaskets or anvils of multi-anvil presses or diamond cells. Newly developed X-ray focusing optics (described in Section 4.1.1.5), detectors and analytical techniques together with NSLS-II, will

enable a myriad of crystallographic and spectroscopic measurements with resolutions rivaling studies at ambient conditions.

With NSLS-II, major advances will be made in understanding the Earth from its surface to its center.

## REFERENCES

- [1] J Chen, D Weidner, M Vaughan, *Nature* **419**, 824 (2002)
- [2] Forte, A M, A M Dziewonski, and R J O Connell, *Science* **268**, 386-388 (1995).
- [3] Mao, H. K. et al., *Nature* **396**, 741-743 (1998).
- [4] Singh, A. K., Mao, H. K., Shu, J. F. & Hemley, R. J. *Phys. Rev. Lett.* **80**, 2157-2160 (1998).
- [5] Karato, S.-i. and H. Jung, *Earth and Planetary Science Letters* **157**: 193-207 (1998).
- [6] Y. Katayama, T. Mizutani, W. Utsumi, O. Shimomura, M. Yamakata, and K. Funakoshi, *Nature* **403**, 170-173 (2000).
- [7] D. J. Lacks, *Physical Review Letters* **84**, 4629-4632 (2000).
- [8] P. H. Poole, T. Grande, C. A. Angell, and P. F. McMillan, *Science* **275**, 322-323 (1997).
- [9] J. N. Glosli and F. H. Ree, *Physical Review Letters* **82**, 4659-4662 (1999).
- [10] O. Mishima and H. E. Stanley, *Nature* **396**, 329-335 (1998).
- [11] Y. Katayama, K. Tsuji, H. Kanda, H. Nosaka, K. Yaoita, T. Kikegawa, and O. Shimomura, *Journal of Non-Crystalline Solids* **207**, 451-454 (1996).
- [12] V. V. Brazhkin, S. V. Popova, and R. N. Voloshin, *High Pressure Research* **15**, 267-305 (1997).
- [13] S. Harrington, R. Zhang, P. H. Poole, F. Sciortino, and H. E. Stanley, *Physical Review Letters* **78**, 2409-2412 (1997).
- [14] S. Aasland and P. F. McMillan, *Nature* **369**, 633-636 (1994).
- [15] P. H. Poole, F. Sciortino, U. Essmann, and H. E. Stanley, *Nature* **360**, 324-328 (1992).
- [16] E. G. Ponyatovsky and O. I. Barkalov, *Materials Science Reports* **8**, 147-191 (1992).
- [17] J. Chen, D. Weidner, and M. T. Vaughan, in *Density measurements of molten minerals at high pressure using synchrotron X-ray radiography*, Beijing, 2001.
- [18] Cohen, R. E., Mazin, I. I. & Isaak, D. E. *Magnetic collapse in transition metal oxides at high pressure: Implications for the Earth.* *Science* **275**, 654-657 (1997).
- [19] Rueff, J. P. et al. *Pressure induced high-spin to low-spin transition in FeS evidenced by X-ray emission spectroscopy.* *Phys. Rev. Lett.* **82**, 3284-3287 (1999).
- [20] Badro, J. et al. *Magnetism in FeO at megabar pressures from X-ray emission spectroscopy.* *Phys. Rev. Lett.* **83**, 4101-4104 (1999).
- [21] Yan, C., Vohra, Y. K., Mao, H. K. & Hemley, R. J., *Proc. Nat. Acad. Sci.* **99**, 12523-12525 (2002).
- [22] C. Meade, R. J. Hemley, and H. K. Mao, *Phys. Rev. Lett.* **69**, 1387-1390 (1992).
- [23] W. A. Chrichton, M. Mezouar, T. Grande, S. Stolen, and A. Grzechnik, *Nature* **414**, 622 (2001).
- [24] *High-Pressure Phenomena, Proceedings of the International School of Physics, "Enrico Fermi" Course CXLVII*, R. J. Hemley, G.L. Chiarotti, M. Bernasconi and L. Ulivi (Eds.), IOS Press, Amsterdam; Vol., edited by R. J. Hemley, G. Chiarotti, M. Bernasconi, and L. Ulivi (2002).
- [25] M. R. Fitzsimmons, J. A. Eastman, R. B. Von Dreele, and L. J. Thompson, *Phys. Rev. B* **50**, 5600 (1994).
- [26] Hemley, R. J. (ed.) *Ultrahigh-Pressure Mineralogy*, *Rev. Min.*, **37** (Mineralogical Society of America, Washington, D.C., 1998).
- [27] Stalder, R. U., *P. Contributions to Mineralogy and Petrology* **140**, 670-679 (2001).
- [28] Bell, D. R. & Rossman, *Science* **255**, 1391-1397 (1992).
- [29] Ahrens, T. J. *Nature* **342**, 122-123 (1989).
- [30] Kagi, H., Inoue, T., Weidner, D. J., Lu, R. & Rossman, G. *Japan Earth Planet. Sci., Joint Meet. Abstract G42-09*, 506 (1997).
- [31] Greenwood, N. N. & Earnshaw, A. *Chemistry of the Elements* (Pergamon Press, Oxford, 1984).
- [32] Hamilton, W. C. & Ibers, J. A. *Hydrogen Bonding in Solids* (W. A. Benjamin, Inc., New York, 1968).

- [33] Liu, Z., Hu, J., Yang, H., Mao, H. K. & Hemley, R. J. *J. Phys.: Condens. Matter* **14**, 10641-10646 (2002).
- [34] Ross, N. L. & Hazen, R. M. *Phys. Chem. Minerals* **17**, 228-237 (1990).
- [35] Z. Zhong, C.C. Kao, D.P. Siddons and J. B. Hastings, *J. Appl. Cryst.* **34**, 504-509 (2001).
- [36] Z. Zhong, C. Kao, D.P. Siddons, H. Zhong, and J.B. Hastings, *Acta. Cryst. A* **59**, 1-6 (2003).

## **2.11 Environmental Science**

### **2.11.1 Overview**

Identification of the chemical form and the chemical, physical and biological processes that control the distribution of contaminants in our environment is a core mission of the Department of Energy (DOE), one of the leading sponsors of cutting-edge research in the environmental sciences. Such research is focused on developing a better understanding of how contaminants are distributed, bound and react in the environment. Whether they are heavy metal toxins such as mercury or lead, radioactive contaminants such as uranium, plutonium or radon, or greenhouse gases such as sulfur dioxide; DOE's commitment to the clean-up of impacted sites and long-term stewardship of the environment is reflected in its funding of environmental research at DOE facilities.

Without a detailed knowledge of contaminant behavior, remediation of highly impacted sites will likely be less effective and far more costly than needed. The major questions involving environmental contaminants concern their speciation, distribution, reactivity, transformations, mobility, biogeochemical cycling, and bioavailability. These issues ultimately depend on molecular-scale structure and properties, best determined using spatially-resolved spectroscopic techniques. Basic understanding at this scale is essential for development of clean-up strategies and risk assessments for both local and global scale pollution problems. Such basic spectroscopic studies will lead to new techniques to remediate contaminated soils, natural waters, and the atmosphere and novel approaches to safely isolate from the biosphere hazardous wastes from past U.S. weapons production, agricultural activity, energy production, manufacturing, and mining.

One of the major challenges to understanding fundamental biogeochemical processes in earth's near-surface environment is the characteristically heterogeneous nature of the impacted materials. Soil, sediment, and rock samples commonly contain multiple solid phases, as well as liquids, air, and complex biomaterials. Relevant particle size distributions extend into the sub-micron range, which hinders characterization by conventional bulk methods. The low concentrations that are typical for many contaminants make their detection difficult without high sensitivity analytical techniques. The high brightness of synchrotron radiation sources allow small, intense X-ray beams to be produced. Synchrotron-based methods have allowed a new level of characterization by offering element and chemical state specificity, high spatial and energy resolution, excellent detection sensitivity at ppb levels, and the ability to work in-situ, for example with wet samples safely sequestered within environmental cells. These types of studies have led to unique information on many of the chemical processes that affect contaminant elements, particularly those occurring at solid-water interfaces.

The high brightness and flux of NSLS-II will provide much enhanced capabilities in environmental science research and enable continued advances in this critical area of research.

### **2.11.2 Scientific Challenges and Opportunities**

The wide range of scientific challenges in environmental science is reflected in the inter-disciplinary nature of this field of study, which draws scientists from soil and agricultural sciences, geochemistry, chemistry, physics, biology, microbiology, hydrology, ocean sciences, climatology and atmospheric sciences. The following broadly defined scientific challenges and opportunities in environmental science demonstrate how the new capabilities made available by NSLS-II will play a critical role in shaping the future of environmental science research and its contributions to society.

#### **2.11.2.1 Speciation of Contaminants in Complex Natural Systems**

The speciation of toxic elements is a critical factor in controlling their mobility, bioavailability, and toxicity in aqueous and terrestrial environments. Speciation refers to the chemical and physical form of an

element in a geochemical setting and includes the following components: the identity of the contaminant of concern or interest, the oxidation state of the contaminant, the associations and complexes to solids and dissolved species (surface complexes, metal-ligand bonds, surface precipitates), and molecular geometry and coordination environment of an element. The more of these parameters that can be identified, the better one can predict the potential risk of contaminants to humans and make sound decisions about remediation. Natural materials such as soils and sediments are very complex and heterogeneous, being composed of an array of primary and secondary minerals, phyllosilicates, hydrous metal oxides, and humic substances. The processes and reactions that occur at the interfaces between minerals, water, organic matter, and microbes dictate the speciation and species transformations over a wide range of spatial and temporal scales.

Traditionally, bulk elemental analysis, sequential chemical extraction, and analytical techniques such as X-ray diffraction (XRD), X-ray photoelectron spectroscopy (XPS), electron microprobe analysis (EMPA), and scanning electron microscopy (SEM) have been employed to glean information about speciation, mineralogy, elemental chemical state and spatial distributions, including elemental associations. These approaches, however, do not directly give information about the speciation of elements and can have other drawbacks including poor detection sensitivity and spectral artifacts due to ex-situ analysis. The use of micro-focused X-ray absorption and fluorescence spectroscopies, micro-diffraction, micro-tomography, and multielement spectromicroscopy can provide the means to determine such parameters in-situ, which is critical in such heterogeneous natural systems. These techniques allow us to evaluate the speciation of toxic elements over a range of environmentally relevant spatial and temporal scales.

An example of the type of nanoscale heterogeneity commonly observed is shown in Figure 2.11.1. In this example, a scanning transmission X-ray microscope (STXM) was used to acquire a series of images over the oxygen K edge (giving a spectrum at each pixel) in order to study lutetium (a homologue for the actinide americium) incorporation into iron oxide phases as amorphous ferrihydrite crystallizes into hematite. Such measurements contain considerable information but it can be difficult to recognize the key themes due to complexity. By using cluster analysis methods, one can simplify this information into an image shown in the top left panel. The red areas correspond to lutetium enrichment and indicate that the crystallization process excludes lutetium from the hematite structure. These results suggest that lutetium-substituted hematite might not be thermodynamically stable, and therefore, the abundance of iron oxides in soils and sediments may not protect against long-term actinide mobility.

The increased brightness of NSLS-II is required for this type of research to take advantage of advances in beam focusing optics and detectors that will enable spectroscopy studies at lower detection limits with nanoscale spatial resolution.

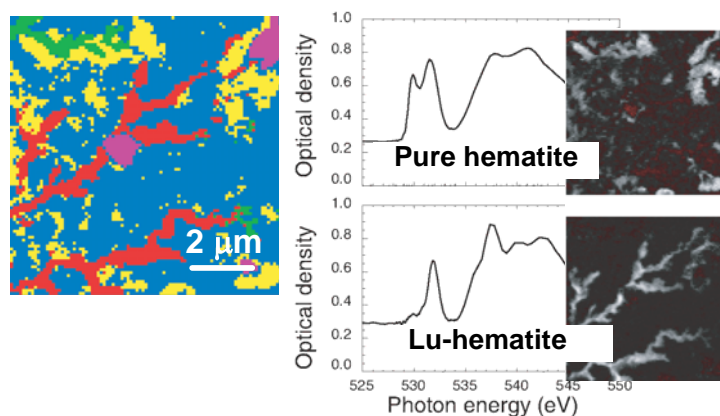


**Figure 2.11.1** STXM images and oxygen K-edge  $\mu$ -NEXAFS spectra showing regions of lutetium enrichment in hematite. Work conducted at the NSLS beamline X1A2.

### 2.11.2.2 Contaminant fate, Wasteforms, Remediation, and Long-term Stewardship

The cradle-to-grave strategy for management and disposal of environmental wastes from point sources such as nuclear fuel production and spent fuel disposal, industrial and agricultural wastes and from non-point sources such as suburban pollution poses a tremendous burden to regulators, scientists, engineers and the public. Developing remediation strategies is complicated because of the incredibly diverse forms such wastes represent, the differences in approaches to short- and long-term waste storage and treatment, the inherent heterogeneity of contaminated environmental media (e.g., soil, biota, rock) and the laws that strictly govern the classification and disposition of such waste. Long-term environmental stewardship and waste management activities require a thorough knowledge of the contaminants and their interactions (i.e., fate) with their environment.

Synchrotron-based techniques are uniquely suited to providing the detailed knowledge required to support the decision-making process for selecting remediation strategies, optimizing waste treatment processes and evaluating nuclear waste form stability in geologic repositories. A prominent example is that of high-level waste (HLW) residing in aging subsurface tanks at DOE sites. HLW is a high volume (several tens of millions of gallons) waste form that is highly radioactive, exists in multiple forms (e.g., sludge, salt cake and solution) and contains fissionable actinide elements such as plutonium. Its management and treatment alone is estimated to be in the hundreds of billions of dollars. When vitrified, this material is ultimately intended for long-term geologic storage in a repository such as Yucca Mountain, NV.

To ensure the isolation of long-lived radionuclides within the repository, scientists need to understand how the repository's geologic material will interact with the waste. X-ray micro-Fluorescence (micro-XRF) images shown in Figure 2.11.2 reveal that Pu sorption on heterogeneous tuff rock occurs preferentially on manganese oxide rich areas and not on iron oxide rich areas. In addition, Pu L-edge micro X-ray Absorption Near Edge Structure (micro-XANES) spectra (data not shown) indicate that localized regions of Pu enrichment are comprised of a mixture of Pu(V) and Pu(VI) oxidation states. [1] The oxidation state and mineral phase associations observed here would not have been possible without synchrotron-based micro-analytical techniques. The improved spatial resolution and lower detection limits achievable at NSLS-II will significantly improve the quality of information derived from this type of study. Furthermore, the higher beam brightness will significantly reduce data collection time and thereby allow greater sample thru-put that is critical to improving the statistical significance of physicochemical parameters used to predict contaminant behavior in highly variable field-scale settings.

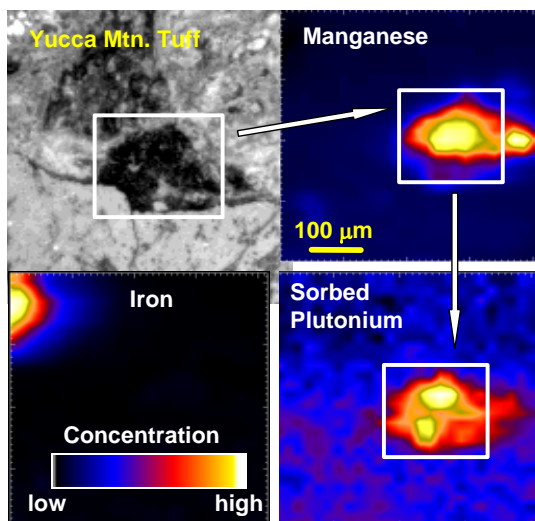


**Figure 2.11.2** Micro-XRF image map of Mn, Fe and Pu distribution in Yucca Mountain Tuff. Images collected at the NSLS X26A.

### 2.11.2.3 Biogeochemical Processes, Rates, and Element Cycling

Among the most important biogeochemical processes are dissolution and precipitation, reduction and oxidation, sorption, and the complex reactions associated with the metabolism of micro-organisms. Ultimately, understanding these biogeochemical processes requires that we identify the rates and mechanisms of the most important reactions that occur between each component in the system. While this level of understanding seems fundamental, it is lacking for most environmental systems. The greatest barrier to understanding such processes is the inherent complexity and heterogeneity of natural systems. While synchrotron-based studies of complex real-world samples have proven invaluable in providing a great deal of information about the distribution and speciation of contaminants, environmental scientists have long-since recognized the need to study model systems of varying degrees of complexity to explore fundamental aspects of important biogeochemical processes. Results from these model system studies have proved to be essential for interpreting studies of contaminant behavior in complex environmental systems.

Synchrotron-based model system studies have provided fundamental information about aqueous solute complexes, poorly crystalline materials, solid-liquid interfaces, mineral-aqueous solution interactions, microbial biofilm-heavy metal interactions, heavy metal-plant interactions, complex material microstructures, and nanomaterials, all of which are important components or processes in the environment. [2] These studies range from standard bulk X-ray absorption fine structure (XAFS) spectroscopy measurements of contaminants in suspensions of model oxide colloids to X-ray and VUV investigations of contaminants on atomically flat single crystal oxide surfaces.

One topic of significant interest concerns the role of micro-organisms in biogeochemical processes. Figure 2.11.3 shows a STXM and  $\mu$ -NEXAFS study of how OSY3 bacteria (isolated from sediment at a DOE site) reduce aqueous Cr(VI) to the less toxic and sparingly soluble Cr(III) species. The Cr L-edge  $\mu$ -NEXAFS spectra collected at intervals across a single bacterium (transect a-b in lower STXM image) reveal that the reduction process is localized at the bacteria-water interface. The ability to explore microbe-driven processes is essential for designing and implementing microbial remediation strategies. Studies of metabolic processes require high brightness in the energy range from 100 eV to 5 keV to probe

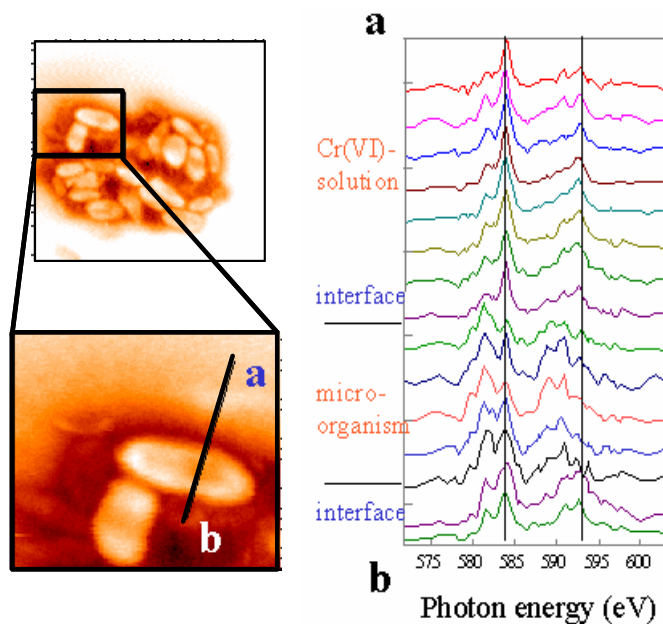


**Figure 2.11.3** STXM images and Cr L-edge  $\mu$ -NEXAFS spectra collected at intervals along the transect a-b drawn in the lower left panel show Cr(VI) reduction on the bacteria surface. From ALS beamline 11.0.2.

both contaminant L-edges and biologically relevant elements such as C, N, P, S, Cl, and Ca.

The high brightness of NSLS-II will significantly enhance the tools used to explore biogeochemical processes in model systems. For example, studies of contaminant speciation and transformations in solution will finally extend to environmentally-relevant micro- and nano-molar concentrations. Moreover, the increased brightness will greatly advance our ability to explore biogeochemical processes in increasingly complex systems that more closely resemble real-world conditions by adding thick water layers, biofilms and competing chemical species. Finally, NSLS-II will enable time-resolved spectroscopic studies on time-scales relevant to important biogeochemical processes. Understanding the kinetics of biogeochemical processes is essential for predicting contaminant behavior.

#### 2.11.2.4 Structure and Chemical Properties of Environmental Nanoparticles

Nano- and micron-sized particulates generated by weathering of geological materials, biological processes, and the emissions of industries and automobiles are ubiquitous in the environment. The role of environmental nanoparticles (Figure 2.11.4) in the solubility, transport and bioavailability of aqueous contaminants is well established, but the composition and structure of these particles and their influence on the aforesaid processes are poorly understood. The mineralogical and associated organic molecule composition of such particles in the atmosphere influence light scattering, and water adsorption, condensation and particle growth, which in turn modify global temperatures and climates. Composition and reactivity of these particulates also influence the chemistry of rainwater. At present, attempts to model climate fluctuations are limited by the lack of specific mineralogical and chemical characteristics of these particles. Several atmospheric particulates, such as asbestos and other mineral dust, have deleterious effects on human health, and a correlation between health effects and particulate composition is yet to be established.

Properties that dictate the behavior of nanoparticles in the environment are their composition, morphology, and bulk and surface structure. A majority of environmental nanoparticles possess complex composition and consist of inorganic constituents, such as iron oxides (e.g. magnetite produced by bacteria) and oxyhydroxides (e.g. ferritins common in several organisms), aluminum oxyhydroxides (e.g. acid soils and waters), metal sulfides (e.g. all reducing sediments and soils), and organic molecules of



**Figure 2.11.4** Iron oxyhydroxides precipitated from acid waters through biotic and abiotic processes play a central role in controlling the solubility of several toxic elements, such as As, Cu, Cd. Such acid environments are common around abandoned and active coal and sulfide mines all over the world. The picture on the left shows the precipitation of iron oxide nanoparticles in a stream in Eastern Pennsylvania. Electron microscopy studies of sediments collected from a sulfide mine (picture on the right) shows the existence of ZnS nanoparticles (green) in the biofilm matrix (blue). [3]

different sizes and functional groups (e.g. humic substances). Their small size and sensitivity to the surrounding chemical environment make them very reactive and structurally labile. Thus sample drying and characterization with vacuum methods, such as electron microscopes, are not suitable for examining a majority of environmental nanoparticles because of changes such as the loss of volatile constituents from samples. Consequently, the ability to do experiments in environmental cells at synchrotron facilities provides a powerful approach to study nanoparticles under environmentally realistic conditions.

Information on the compositional and structural heterogeneity of nanoparticles is central to predicting their reactivity, stability, and structural lability in the environment. Element-specific methods (e.g. X-ray absorption spectroscopy) are ideal for examining the chemistry of environmental nanoparticles in their pristine state. At present, the composition and structural characterization of particles below ~500 nm cannot be examined at any facility in the world. Availability of spatially resolved chemical and structural information on these nanoparticles could contribute significantly to the understanding of the chemistry of nanoparticles in the environment.

Spectromicroscopy facilities with a broad energy range, from a few eV to several keV to allow simultaneous probing of organic molecule functional groups and metal ions, and with facilities for structural characterization are essential if significant progress is to be made in this important research area. While radiation damage will provide the ultimate limit on studies of organic molecules, NSLS-II will provide sufficient brightness for studies of 10 nm colloidal particles where optics and sample damage considerations allow.

### **2.11.2.5 Environmental Genomics and Toxicology**

To fully model the interaction of toxins with the environment, it is important to not only determine the physicochemical processes that control their mobility, but also understand their bioavailability to micro-organisms, plants, animals, and even humans. But fully assessing a toxin's bioavailability requires a detailed understanding of the complex interrelationship between factors such as toxin speciation, its metabolic pathways in organisms, and how gene expression influences biological interactions with not only the toxin but also nutrients, soil and water. For the environmental scientist, this defines a challenging new discipline that has been referred to as Environmental Genomics [4], the study of the inter-relationship between environmental changes and the gene expression of organisms. With synchrotron-based techniques it may be possible, in real time, to explore how toxin speciation varies with changes in gene expression in plants and micro-organisms, with the eventual goal of engineering gene expression to promote toxin sequestration from contaminated environments. Although in its infancy, there is a strong appreciation both among the environmental sciences community and the U.S. government of the potential importance of studies in environmental genomics. For example, in July 2002 DOE announced that funding would be made available from the Genomes to Life program to "support post-genomic research in new technologies for generating energy from biological sources, sequestering carbon, and cleaning up the environment." The EPA has similarly expanded its investment in genomics research.

The unique capabilities provided by synchrotron radiation, and especially the greatly enhanced capabilities enabled by NSLS-II, will play a critical role in shaping and advancing the emerging field of environmental genomics. For example, researchers at the NSLS are involved in several phytoremediation studies to determine how contaminant uptake and speciation in selected plant species respond to changes in soil and atmospheric chemistry. Contaminant and micronutrient element uptake by plants is controlled by complex formation with organic molecules that are in part produced in the root exudates of plants. Figure 2.11.5 reveals how complexing organic molecules can dramatically alter contaminant uptake and translocation in plants. The micro-XRF images in the upper and lower right panels show high lead concentrations in the tobacco plant stem only when EDTA, an organic molecule that readily complexes cations, is added to the contaminated soil. Synchrotron investigations probing changes in speciation as metal ions or radionuclides are sorbed by roots, translocated through the plant, and then returned to the soil as the plant dies are possible but the quality of the spectroscopic information is currently limited by beam brightness and flux. The development of transgenic plants to remediate certain metals in soils and to

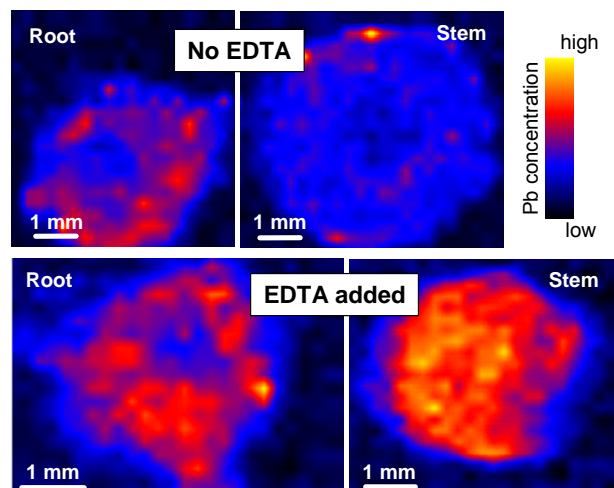


**Figure 2.11.5** *Micro-XRF images of lead distribution in tobacco roots and stems with and without EDTA added to a contaminated soil. Images collected at NSLS beamline X26A.*

better use mineral nutrients is becoming a possibility but confirming the expected effects of genetic manipulation on element chemistry is critical. This can be done in part at synchrotron facilities, and such studies should reveal the relationships between certain genes (perhaps through “knock out experiments”) and metal speciation.

Although studies in this area of environmental science have been remarkably successful, this research requires improvements in beam brightness, flux, and spatial resolution. In many of these biological systems the elemental abundances are low, ppm to sub-ppm levels, requiring higher brightness to provide improved detection sensitivity. NSLS-II will allow for detection levels to be improved by at least an order of magnitude. Concurrently, better detection sensitivity and higher count-rates at NSLS-II will also provide order of magnitude improvements in data acquisition time and quality for X-ray absorption spectroscopic studies. As we endeavor to understand contaminant interactions at bacterial and cellular levels, improvements in spatial resolutions are also required and will be provided by NSLS-II.

### 2.11.3 Impact of NSLS-II

As we have seen from the above examples, the goals in environmental science research are to obtain information on the speciation of contaminants in the natural environment, and to use this understanding to obtain improved and lower cost methods of environmental cleanup. It is increasingly apparent that this information must be obtained on sub-micrometer length scales, because at larger size scales one may obtain misleading interpretations based on an average over distinctly different structures in a specimen.

Most methods in synchrotron-based environmental science research involve not just simple imaging, but collection of signals from a microprobe beam on the sample. It is therefore of prime importance to have as many photons as possible in as small a spot as can be achieved. As was first pointed out at Brookhaven Lab a quarter of a century ago, [5] this is intrinsically linked to the brightness of a synchrotron source. Therefore, the improvement in brightness of NSLS-II by 10,000 times over the present brightest beamline at NSLS should lead to the ability to understand contaminants in the environment at size scales 100 times smaller than can be studied at the present NSLS. This can lead to fundamental improvements in the understanding of environmental science problems, because it should make it possible to distinguish (for example) between surface and bulk interactions of environmental nanoparticles.

To understand the impact of NSLS-II for these types of environmental analyses, consider the X26A hard X-ray microprobe beamline at the NSLS, a beamline historically dedicated to environmental science research and one of the most heavily over-subscribed beamlines at the NSLS. Given the anticipated

source characteristics of NSLS-II, the same endstation optics (Kirkpatrick Baez microfocusing mirrors) will achieve *minimally* an order of magnitude improvement in detection sensitivity and at least 10X improvement in spatial resolution. Thus, techniques such as XRF, XANES, and EXAFS will have sensitivities in the range of 100 ppb, 1-10 ppm, and 100-1000 ppm, respectively, or better.

Focusing mirrors that are commercially available today typically have about 1  $\mu$ rad slope errors. It should be noted that recent studies of mirrors manufactured using numerically controlled plasma chemical vaporization techniques reportedly achieve line focusing widths of 0.12 and 0.2  $\mu$ m FWHM at 15 keV. [6] Zone plates also show great promise for focusing hard X-ray beams to sub-micron resolution. They have been demonstrated to focus 8 keV X-rays to 150 nm FWHM focal spot size in the first-order focus and to 90 nm in the third-order focus. Their effective use at X26A is hampered by the significant loss of flux density relative to the Kirkpatrick-Baez. But with the significantly higher brightness of NSLS-II, such optics become an attractive and viable choice for hard X-ray microspectroscopy.

Such highly focused, high intensity beams will allow environmental scientists to apply micro-spectroscopic analysis in-situ at much higher spatial resolution than previously available, directly probing the interface of contaminant species with grain surfaces or biological organisms. For example, using the hard X-ray microprobe, scientists from the University of Wisconsin-Madison have found compelling evidence that micro-organisms play a central role in the formation of certain mineral deposits (see Figure 2.11.6). These results shed light on the basic question of biology's function in the formation of some metal ores, and hold out the promise for applications in mining-site remediation. Improved spatial resolution allows for not only analysis of aggregate biofilms, but of individual precipitate minerals on cell walls. NSLS-II will provide much higher flux density in much smaller spot sizes and enable understanding contaminant speciation in nanoparticles using X-ray absorption spectroscopy.

The high flux of NSLS-II will significantly enhance almost every technique critical to environmental research. Reflectivity or bulk EXAFS experiments, for example, would be able to be done in 1/10th the time with potentially order of magnitude improvements in detection sensitivity. These experiments would also be able to make better use of new technologies that allow for "on-the-fly" scanning for kinetics studies that currently are not feasible.

Environmental scientists and geoscientists have made extensive use of NSLS beamlines ever since NSLS began operations in 1982 and estimates indicate that this research currently comprises 10-15% of the total user base at the NSLS. As the user base has evolved to one more dominated by scientists interested in the application of developed techniques, the subscription of beamlines whose core mission is in environmental sciences has risen dramatically. Typically these beamlines are strongly oversubscribed. User statistics show that in the last 10 years earth and environmental sciences research at the NSLS has almost tripled. Such statistical trends are mirrored at the other DOE synchrotron facilities [2] and in the scientific literature. For example, in *Geochimica et Cosmochimica Acta*, a leading international journal focusing on the geochemical sciences, articles referencing synchrotron-based X-ray absorption data increased from 25 in 2000, to 32 in 2001 and 54 in 2002. Similar trends can be seen in the journal

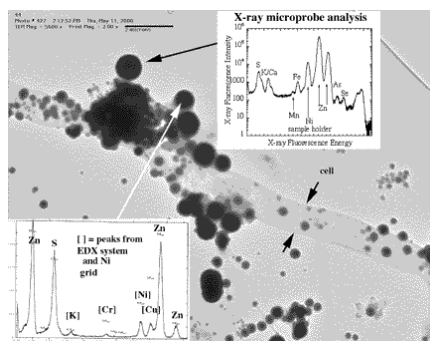


**Figure 2.11.6** Results of EDX (bottom left) and X-ray microprobe fluorescence (top right) analysis of specific biomineralized zinc sulfide precipitates. Scale bar is 2  $\mu$ m. From APS beamline 2-ID-D [3].

*Environmental Science and Technology*, with 11 articles in 2000, 16 in 2001, and 39 in 2002. An important driver for this continuing growth is the generation of new environmental science users from a diverse range of scientific and engineering communities such as soil science, plant biology, microbiology and environmental engineering.

Environmental Sciences research at the NSLS plays a major role in advancing our understanding of contaminant speciation and fundamental biogeochemical processes in nature. This information is an essential contribution to DOE's environmental management decision-making process. NSLS-II is critically needed if the environmental science community is to meet the ever increasing challenges for spectromicroscopy analyses with high spatial resolution of complex environmental samples necessary to meaningfully support regulators and engineers responsible for environmental assessment, remediation and management.

NSLS-II will greatly advance the quality and utility of environmental science research in a number of ways including:

- Ability to explore chemical, biological and mineralogical heterogeneity in complex environmental samples at the nanoscale with soft and hard X-ray probes
- Ability to probe biologically-important elements such as C, N, P, S, Cl, and Ca in fully-hydrated samples
- Ability to probe aqueous contaminant speciation at micro- and nano-molar solution concentrations
- Ability to perform time-resolved spectroscopic studies on times scales relevant to important biogeochemical processes
- Significantly reduce data collection time and thereby enable greater sample throughput

#### REFERENCES

- [1] Duff, M.C., et al., *Environmental Science & Technology*, **33**, 2163-2169 (1999).
- [2] Brown, G.E., Jr., *MOLECULAR ENVIRONMENTAL SCIENCE: An Assessment of Research Accomplishments, Available Synchrotron Radiation Facilities, and Needs*. 2003, White paper prepared on behalf of EnviroSync. p. 50.
- [3] Labrenz, M., et al., *Science* **290**, 1744-1747 (2000).
- [4] See, for example, *Environmental Science & Technology* **35** (2001).
- [5] K. Green, BNL report 50522 (1976).
- [6] Yamamura et al., *Review of Scientific Instruments* **74**, 4549-4553 (2003).

## 3 Proposed Facility

This Section describes the NSLS-II user facility that BNL proposes to design, construct, and operate. Section 3.1.1 summarizes the light source capabilities required to enable the science described in Section 2. Section 3.1.2 summarizes the characteristics and capabilities of the current NSLS X-ray and VUV/IR storage rings to illustrate both the need for a new X-ray source (as opposed to an upgrade of the existing one) and also the tremendous advance that NSLS-II represents. Section 3.2 describes several alternative approaches for meeting the requirements, including free electron lasers, energy recovery linacs, and third generation storage rings. From these considerations, it is clear that an advanced third generation X-ray storage ring, designed to be upgradeable to future operation as an energy recovery linac, is the best choice for NSLS-II. A pre-conceptual design for NSLS-II and its expected performance are described in Section 3.3. The design of NSLS-II will be highly aggressive in order to deliver the necessary superlative characteristics, and will set a new standard for third generation light sources. The various design considerations and challenges necessary to realize this goal are reviewed in Section 3.4. The potential to be upgraded in the future to operate as an energy recovery linac, for even greater performance, is a key distinguishing characteristic of NSLS-II. The design considerations to enable that option are described in Section 3.5. Section 3.6 closes this Section with a discussion of the facility siting considerations and of compatibility with BNL's Site Master Plan.

## 3.1 Capability Requirements

### 3.1.1 Requirements for NSLS-II

In Section 2, we have outlined the range of current and future problems of interest in the many areas of science served by synchrotron radiation, including the most difficult, so-called grand challenge problems. To address those scientific challenges, it is necessary to

- probe materials on ever smaller length scales, down to 10 nanometers or less
- apply a number of new techniques based on utilizing the coherence of the photons
- study elementary excitations with energies ranging from  $< 1$  meV to  $\sim 10$  eV
- access resonance and absorption edges ranging from  $\sim 100$  eV to  $\sim 10,000$  eV

The photon qualities needed to enable these capabilities determine the design goals for the NSLS-II light source. These goals are:

- highest possible time average brightness, 10,000 times more than the current NSLS and more than any other current or planned source in the energy range 0.3 to 20 keV
- highest possible flux, 10x more than the current NSLS, and more than any other current or planned source in the energy range 0.3 to 20 keV
- photon pulse lengths down to 11 psec, 13 times shorter than the current NSLS
- wide spectral coverage, including the far-IR, UV, VUV, soft X-ray, and hard X-ray regions
- exquisite intensity, position, and pointing stability

A light source meeting these design goals will not only exceed the performance of the existing NSLS storage rings by many orders of magnitude but will also be a world leader in many characteristics, including highest average brightness and flux in the 0.3 to 20 keV energy range and exquisite stability.

### 3.1.2 Capabilities of Present NSLS

A photo of the exterior of the present NSLS building is shown in Figure 3.1.1. It houses two electron storage rings and their associated injection system consisting of a linear accelerator and a booster synchrotron. An interior diagram showing their layout and also that of the beamlines and associated laboratories is shown in Figure 3.1.2. The parameters of the X-ray ring and VUV/IR ring are given in Table 3.1.1.

The NSLS facility consists of two so-called second generation storage rings, having begun operation in 1982 as the first facility in the U.S. that was designed expressly for the use of synchrotron radiation. It was designed in the 1970's with the pioneering Chasman-Green lattice, which was developed at BNL, and utilizes double achromatic bends to provide zero-dispersion straight sections for insertion devices. It is optimized for brightness, within the constraints imposed by its small number of cells and small circumference, and includes only a small number of straight sections for insertion devices, which were still quite novel at that time. The two storage rings provide a wide range of photon energies, spanning from the far-IR to the hard X-ray (100 keV) range, that is still unique today.

The injection system consists of a 120 MeV electron linac that injects into a small (28 m circumference) booster synchrotron that accelerates the electrons up to 750 MeV. The booster serves as the injector for the VUV storage ring, which operates at 800 MeV to provide radiation in the infrared to soft X-ray region of the spectrum. The booster is also used to inject electrons into the X-ray storage ring, which operates at 2.8 GeV to provide hard X-rays.



**Figure 3.1.1** Exterior view of the current NSLS facility. The VUV/IR ring is housed in the smaller square section extending out and to the lower right from the circular portion of the building, which houses the X-ray Ring.

The 8 bending magnets and 4 straight sections on the VUV/IR ring host 30 beamlines. All beamlines are numbered clockwise starting from the U1 straight section. Only U5 and U13 host undulator insertion devices, with U1 used for injection and U9 occupied by two RF cavities.

The 16 bending magnets and 8 straight sections on the X-ray ring host 60 beamlines. These are also numbered clockwise starting from the X1 straight section. The beam is injected into the X5 straight, which hosts a nuclear physics gamma ray experiment (LEGS). Five other straights are fitted with insertion devices, feeding beamlines X1, X13, X17, X21, and X25. A total of four RF cavities are used, with two located in each of the X9 and X29 straights.

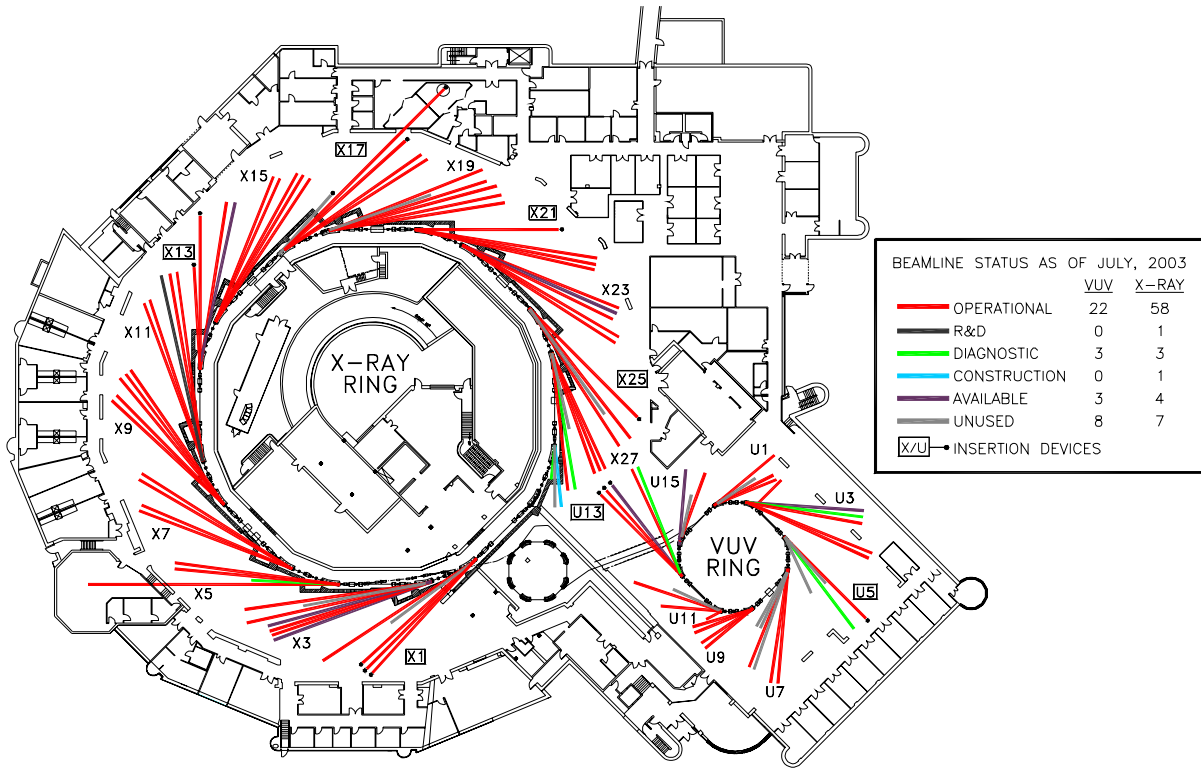


**Figure 3.1.2** Layout of X-ray ring, VUV/IR ring, booster, and experimental floor showing beamlines and associated setup laboratories.

Parameter	X-ray Ring	VUV/IR Ring
Lattice Type	DBA	DBA
Circumference [m]	170	51
Superperiods	8	4
Number of Insertion Devices	5	2
Straight Section Length [m]	5	3
Energy [GeV]	2.8	0.8
Horizontal Emittance, $\epsilon_x$ [nm]	75	160
Emittance coupling, $\chi$	0.002	0.025
Momentum Compaction, $\alpha$	0.004	0.0235
Dipole Radius [m]	6.875	1.91
Bending Magnet Critical Energy [eV]	7091	600
ID Beta Functions, $\beta_x, \beta_y$ [m]	1.60, 0.35	11.1, 5.84
RF Frequency [MHz]	52.88	52.88
Current at fill [mA]	280	1000
Average Current [mA]	238	665
Lifetime [Hours]	20	6
Revolution Frequency [MHz]	1.76	5.88
Orbit Time [nsec]	567	170
Maximum Number of RF Buckets	30	9
Typical Bunch Mode	25	7
Typical Single Bunch Current [mA]	11.2	143
Typical Single Bunch Charge [nC]	6.37	24.3
Bunch Length, $\sigma$ [mm, ps]	43.5, 145	48.5, 162
Natural Energy Spread [%]	0.092	0.05

**Table 3.1.1** Parameters for the current NSLS X-ray and VUV/IR storage rings.

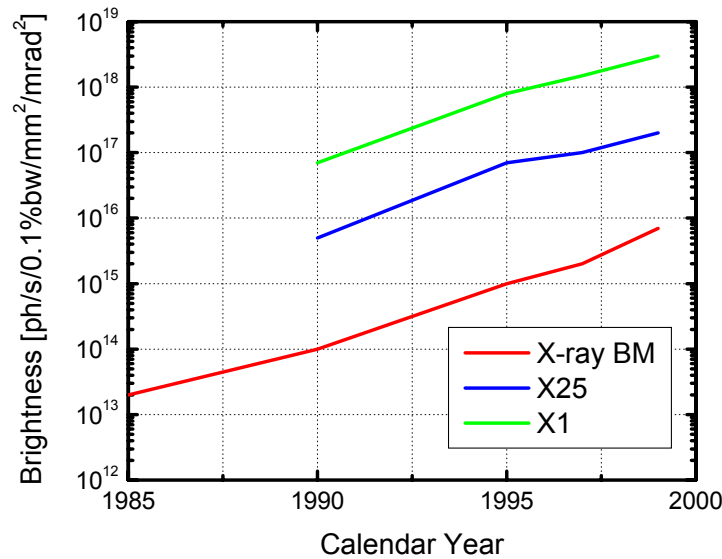


**Figure 3.1.3** Improvement in X-ray brightness over time from bending magnets, wiggler X25, and soft X-ray undulator X1.

A concerted program of accelerator

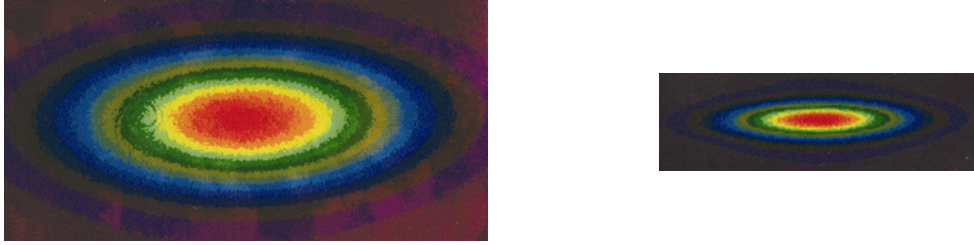


**Figure 3.1.4** *Electron beam profile in the X-ray ring taken in 1990 (left) and in 2000 (right).*

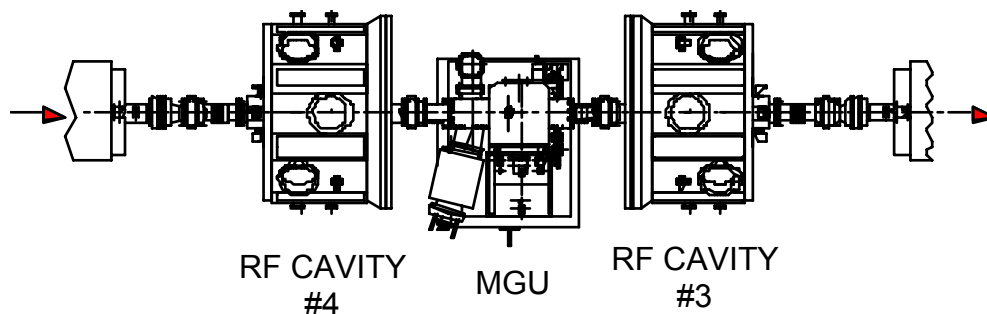
improvements over the last 20 years has steadily upgraded the performance of the NSLS to far surpass its original performance. Figure 3.1.3 shows the dramatic increase of five orders of magnitude in brightness of the brightest X-ray source at the NSLS over that period. About half of this gain was obtained by optimizing the storage ring lattice, resulting in a substantial reduction in electron emittance. For example, Figure 3.1.4 shows the reduction in electron beam size from 1990 to 2000. The other half of the gain in brightness was obtained by introducing advanced insertion devices, many of which were pioneered at the NSLS. These include development of a time varying (1 to 100 Hz) elliptically polarized wiggler and of in-vacuum undulators that operate with a full magnet gap down to 3.3 mm. Most recently, in replacing the RF cavities in the X9 and X29 straight sections with more reliable ones, they were also redesigned to allow room between them for installation of a short (0.3 m) Mini-gap in-vacuum undulator (MGU), as shown in Figure 3.1.5. The X29 MGU has been installed and the X29 beamline should become operational in the summer of 2004. Funding has just recently been provided to install an MGU in the X9 straight and build the X9 beamline.

Table 3.1.2 lists the full complement of insertion devices that the NSLS facility currently hosts or plans to host in the near future. These devices exhaust the useable straight sections and the NSLS is thus unable to add any additional high brightness beamlines beyond this set.

The NSLS and its successes served as a springboard for ‘third-generation’ storage ring facilities around the world. These designs are distinguished by having many more cells to obtain very low emittances and with many more straight sections to host insertion devices.

While the upgrade in performance that has been achieved with the NSLS is impressive, further improvements are not feasible. As outlined in Section 3.4.2, fundamental realities of accelerator physics require that the number of cells of the storage ring lattice be substantially increased in order to realize significant gains. We have considered ripping out the current X-ray storage ring and replacing it with a new lattice with 12 cells. However, this would provide only limited improvement and would require at least a two year shutdown, with a consequential serious negative impact on our large user community.

A new X-ray storage ring with a substantially larger circumference to accommodate many more cells and straight sections is necessary to meet the needs of the science case outlined in Section 2 for much higher brightness and flux in the VUV, soft X-ray, and hard X-ray energy ranges. Furthermore, by taking



**Figure 3.1.5** *Layout of X29 straight section, showing two RF cavities which were redesigned to allow insertion of a 0.3 m Mini-gap Undulator (MGU).*

<b>Straight Section</b>	<b>Usage</b>	<b>Scientific Program</b>
X1	Soft X-ray Undulator	Soft X-ray spectro-microscopy
X5	Injection	LEGS Nuclear Physics Gamma Ray Source
X9	RF plus Planned MGU	SAXS
X13	MGU plus Time Varing EPW	Magnetism plus X-ray Microprobe
X17	Superconducting Wiggler	High Pressure, Geoscience, Materials Science
X21	Hybrid Wiggler	Materials Science
X25	Hybrid Wiggler	Protein Crystallography
X29	RF plus MGU	Protein Crystallography
U1	Injection	Not usable
U5	UV Undualtor	Spin-resolved Photoemission, XES
U9	RF	Not usable
U13	UV Undulator	Photoemission

**Table 3.1.2** *Straight sections on present NSLS X-ray and VUV/IR storage rings, their usage, including existing and planned insertion devices, injection and RF cavities, and the scientific programs they support. With the planned installation of the X9 MGU, straight sections usage will be at full capacity.*

advantage of continued advances in storage ring technology, it is possible to surpass the performance of existing or planned storage rings through the development and construction of a new state-of-the-art medium energy storage ring, serving many users simultaneously with world leading capabilities.

Due to incompatible accelerator physics requirements, it is not possible for the new X-ray storage ring to also provide very high brightness in the near- to far-IR region. Thus, in order to continue to provide world leading high brightness in this important spectral region, we propose relocating the existing VUV/IR storage ring to the area of the new X-ray storage ring and operating it solely as an IR source.

We propose to continue to operate the current NSLS X-ray ring for some period of overlap with the beginning of operations of the new X-ray ring. This will allow users time to move their programs over to the new facility. After all users have moved over, the old X-ray storage ring would be decommissioned and the building made available for other purposes.

## 3.2 Design Alternatives

There are three alternative approaches to generating radiation in the 0.3 to 20 keV energy range that either exist (third generation storage rings), are under development (free electron lasers) or have been proposed (energy recovery linacs). In this section, we consider these alternatives to meeting the needs of the science outlined in Section 2 and argue that a facility based on an advanced third generation storage ring, designed to be upgradeable to future operation as an energy recovery linac, is the best choice.

### 3.2.1 Free Electron Lasers

There are several free electron laser (FEL) projects that are either under construction or in advanced planning stages. In the U.S., DOE is funding the construction of the Linac Coherent Light Source (LCLS), which is being built at the Stanford Linear Accelerator Center (SLAC). In Europe, the XFEL and BESSY FEL projects are in advanced stages of planning. Representative of FELs, when operational in 2008 the LCLS will provide unprecedented peak ( $10^{32}$  ph/sec/0.1%bw/mm<sup>2</sup>/mrad<sup>2</sup>) and time average ( $10^{22}$  ph/sec/0.1%bw/mm<sup>2</sup>/mrad<sup>2</sup>) brightness and ultrashort (230 fsec or less) pulses at a maximum rate of 120 Hz and over an energy range of 0.8 to 8 keV. FELs such as the LCLS are ideally suited for exploring entirely different problems from those outlined in Section 2, i.e., primarily those exploring the science of ultrafast phenomena and the interaction of very high intensity X-ray pulses with matter where the intensity is sufficient to reveal nonlinear interactions or even destroy the material.

FELs as currently envisaged have substantial drawbacks for the science applications emphasized here:

- Although the time average brightness is somewhat higher than can be achieved with a storage ring, it comes in very infrequent, very intense pulses that will either destroy or significantly perturb a great number of the samples described in Section 2.
- The photon energy is not easily or rapidly tunable, especially if one needs multiple, independently tunable beamlines that can simultaneously serve experiments with photons ranging from the VUV (< 100 eV) to the hard X-ray (100 keV).
- FELs may not possess the intensity, energy, and positional stability that many of the experiments outlined here demand.
- FELs typically serve one, or at most a few, beamlines and are not expected to be able to host a user community the size of the present NSLS, which numbers in the thousands.

For these reasons, there is a consensus in the community that FELs will complement rather than replace storage rings and are not an optimal choice to serve the vast majority of the science applications described in Section 2.

### 3.2.2 Energy Recovery Linacs

There are three particularly important time scales that characterize the behavior of the electrons in a storage ring. The revolution time is the time to complete one orbit, and is typically of order 1  $\mu$ sec. As the electrons circulate, they undergo photon emission, suffer gas collisions, interact among themselves and with the vacuum chamber, etc. The small amount of energy they lose from synchrotron radiation is replenished by RF cavities; however their spatial and angular distributions are degraded by these processes. As a result, after  $10^3$  to  $10^4$  orbits, or a time scale of typically 1 to 10 msec, they evolve away from their initial injected phase space into an equilibrium one that is determined by the electron optics of the magnetic lattice. As they continue to circulate, residual gas collisions and other events kick the electrons out of the dynamic, physical, or momentum apertures and they are lost. The rate at which the

stored charge is lost determines the third fundamental time scale, i.e., the lifetime of the stored charge. All existing storage rings have been designed to achieve lifetimes of typically 10 to 20 hours.

An energy recovery linac (ERL) takes a completely new approach to generating synchrotron radiation. It is based on the assumption that one can generate the initial injected electrons with a much smaller emittance than the best equilibrium emittance that can be achieved in a storage ring, and this small emittance can be preserved while the electrons are accelerated in a linear accelerator. The injected electrons are then circulated only once before being thrown away and replaced by a fresh bunch of electrons. Since the circulating electrons are not stored, they do not live long enough to suffer the degradations in beam quality mentioned above. Thus, in principle, this concept has the potential to provide higher brightness than a storage ring. In addition, since the shape of the injected electrons might be easily controlled by a photo-injector, it could be possible to create symmetric (i.e., round) beams as opposed to the very flat beams characteristic of equilibrium in a storage ring, where the vertical emittance is typically 0.1 to 1.0 % of the horizontal emittance. Control of the initial electron bunch duration might also enable photon pulses as short as 100 fsec.

One difficulty with this approach is the energy required to accelerate fresh bunches of electrons equivalent to a current of say 500 mA to an energy of say 3 GeV, which would be 1.5 GW! This is clearly impractical, and requires that the energy of each bunch must be recovered and reused to accelerate succeeding bunches. In its most basic form then, an ERL consists of a very high quality electron source, a linear accelerator, and a magnetic lattice that contains photon radiators and returns the electron beam to the linac, as shown in Figure 3.2.1. The returned electrons enter the linac with a 180° phase shift, whereby they are decelerated, returning their energy to the electric field stored in the linac, before being dumped. In this way, the ERL works on the principle of storing energy (in the linac) rather than storing charge (in the magnetic lattice).

Variations on this basic approach are also possible: N-passes through the same linac coupled with N-arcs can reduce the size of the linac and yield N different energy beams but this requires the linac to support N-times the current in one arc; linac sections can occur on opposite sides of the arc to generate two different energy beams, etc.

Since in many respects an ERL and a storage ring are very similar, an ERL would also be an essentially continuous photon source (as opposed to the slow pulsed nature of an FEL), would have broad spectral coverage, and would permit many beamlines, each easily and independently tunable in energy. The potential performance of an ERL based light source might exceed that of a storage ring with:

- average brightness as high as  $10^{22}$  ph/sec/0.1%bw/mm<sup>2</sup>/mrad<sup>2</sup>
- diffraction limited round electron beams ( $\epsilon_x = \epsilon_y$ ) from photo-injectors
- reduced electron energy spread giving higher brightness from long undulators and high harmonics
- very long insertion devices in the return arcs
- bunch compression to provide sub-picosecond electron bunches
- variable pulse formats for timing experiments

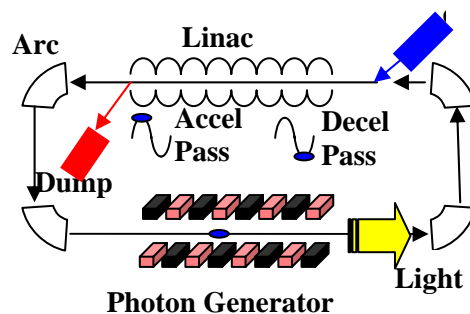


**Figure 3.2.1** Schematic illustration of the major elements of a single turn ERL light source.

While these capabilities are attractive, there are many very formidable technological challenges that must be overcome before a light source based on this principle can be demonstrated. Chief among these is the photo-injector. The world's best photo-injectors have been developed here at BNL and are capable of producing bunches with the required emittance but only operate at  $\sim 10$  Hz rather than the GHz rates necessary for an ERL. To put the magnitude of this jump in perspective, development of a photo-injector capable of delivering similar emittance but operating at a rate of only 120 Hz is one of the chief technical challenges that must be met for the LCLS to operate. A photo-injector suitable for an ERL must operate 10,000,000 times faster than that for the LCLS. Many other challenges also exist, such as demonstration of efficient energy recovery at the high currents and energies necessary for a synchrotron light source based on an ERL and achieving beam position stability that rivals that which can be achieved in a storage ring.

Presently, the most advanced ERLs have been developed at the Thomas Jefferson National Accelerator Facility (TJNAF). The IR FEL Demo ERL is a 50 MeV ERL that has successfully demonstrated an average circulating current of 5 mA in 2000. This ERL has recently been upgraded (2003) to try to achieve 10 mA operations and it is undergoing commissioning. There are several other facilities around the world engaged in the development of similar "low energy prototype" ERLs.

While these low energy prototype ERLs are a far cry from a 3 GeV-500 mA facility, TJNAF has taken another important step forward in ERL development by operating the CEBAF multi-turn accelerator in an energy recovery mode. A beam current of 80  $\mu$ A was successfully accelerated to 1 GeV and energy recovered at 56 MeV. This is the highest energy ERL demonstrated thus far, albeit with a circulating current far below what is available in electron storage rings. What remains is to demonstrate a high average current and high energy ERL.

While a light source based on ERL technology might some day be feasible, there are many technological challenges that must first be overcome. A list of the key R&D issues is as follows:

- development of high average current (at least  $\sim 100$  mA), low emittance electron photoinjectors (at least  $\sim 1$   $\mu$ m normalized emittance or lower)
- robust laser systems and long lifetime, high quantum efficiency, photocathode materials for photoinjectors
- demonstration of high gradient superconducting RF cavities operating in high current mode
- extraction of the higher order mode power excited by the sub-picosecond electron bunches in the superconducting linac
- beam dynamics issues such as coherent synchrotron radiation that arise for short electron bunches
- feedback systems to suppress multibunch beam breakup instabilities
- control of the electron beam halo
- positional stability of the e-beam for all beamlines
- safety systems to detect and prevent beam loss

A thorough investigation and resolution of these key R&D issues is required before the conceptual design of a high energy ( $E \sim 3$  to 6 GeV), high average current ( $I \sim 100$  mA or more) ERL user facility can be initiated and its eventual construction and operation assured of success.

While there are some promising indications that these challenges may one day be overcome, it is not unreasonable to expect that 10 years or more of R&D will be necessary before the feasibility of this approach can be ascertained. The need to dramatically upgrade the capabilities of the NSLS to serve the science needs outlined in Section 2 and the large northeastern research community is urgent. The opportunity cost of waiting until we know whether ERL technology will be feasible is prohibitive. A light source based on ERL technology does not meet the pressing needs outlined in this proposal.

### 3.2.3 Third Generation Storage Rings

Third generation storage rings are distinguished by having many cells to obtain very low emittances and many straight sections to host insertion devices. Together these result in the ability to produce very high brightness photons. Since storage rings are based on mature technology they are an excellent basis for an early project start. At the same time, there have been continued advances in key technologies whereby an advanced design can exceed the performance of existing third generation storage rings substantially. In this section, we summarize the characteristics and performance of existing third generation storage rings throughout the world as well as that of those that are not yet operational but are either under construction or in an advanced development phase.

Currently there are a total of about 50 synchrotron storage rings in operation around the world. Of these, 10 are currently operating as dedicated third generation light sources. Another 12 are either under construction or in varying stages of design. The key characteristics of these 22 machines are shown in Table 3.2.1. Only 3 are high energy machines: Spring-8 in Japan, APS in the U.S., and ESRF in Europe. To achieve high brightness, the high energy machines must have a large circumference, as shown in the table. This makes them quite expensive. The real forte of high energy machines is their ability to produce high brightness X-rays at energies above 20 keV. While there are a handful of problems that require such high energies, the majority of problems studied with synchrotron radiation do not. In addition, high

Name	E [GeV]	Circum [m]	Current [mA]	Emittance [nm-rad]	Cells (i.e., Straights)	Lattice	Full Energy Injection	Year Commis- sioned
SPRING-8	8	1436	100	5.6	48	DBA	Y/Booster	1997
APS	7	1060	100	3.5	40	DBA	Y/Booster	1995
ESRF	6	844	200	3.8	32	DBA	Y/Booster	1994
PLS	2.5	281	180	12	12	TBA	Y/Linac	1995
ANKA	2.5	240	110	70	8	DBA	N/ $\mu$ tron	2000
SLS	2.4	240	400	5	12	TBA	Y/Booster	2001
ELETTRA	2-2.4	260	320	7	12	DBA	N/Linac	1993
NANO-HANA	2	102	300	70	8	DBA	N/Booster	2004
ALS	1.9	197	400	6.8	12	TBA	N/Booster	1993
BESSY-II	1.7-1.9	240	270	5.2	16	DBA	Y/Booster	1998
SPEAR3	3	240	500	18	18	DBA	Y/Booster	2004
CLS	2.9	171	500	18	12	DBA	Y/Booster	2003
SOLEIL	2.85	354	500	3.1	16 + 8	DBA	Y/Booster	2005
DIAMOND	3	560	300	2.7	24	DBA	Y/Booster	2006
AUST. SYNCH.	3	216	200	8.6	14	DBA	Y/Booster	2007
LLS	2.5	252	250	8.5	12	TBA	Y/Booster	?
SSRF	3.5	396	300	4.8	20	DBA	Y/Booster	?
MAX-IV	3	285	500	1.2	12	7BA	Y/?	?
SESAME	2.5	120	400	27	16	DBA	N/Booster	2008
TLS-II	3	240	400	10	16	DBA	N/Booster	?
CANDLE	3	224	350	8.4	16	DBA	Y/Booster	?
INDUS-II	2.5	173	300	58	8	DBA	N/Booster	?

**Table 3.2.1** Key characteristics of third generation light sources around the world. Top group: Existing dedicated machines which were commissioned after 1990, by decreasing order of electron energy. Bottom group: New machines at various stages of construction or development. If a commitment to build the machine has not yet been made, or the commissioning date is uncertain, year commissioned is shown as a question mark.

energy machines are not optimal for producing bright photons in the VUV and soft X-ray energy range. In light of these factors, it is generally viewed as sufficient that each of the major scientific continents have one high energy third generation light source and there are currently no plans anywhere to build another high energy machine.

The 19 remaining machines in Table 3.2.1 are so-called medium energy machines, having energies ranging from 1.7 to 3.5 GeV. Brightness and flux are two of the most important figures of merit for a light source. The electron emittance is proportional to the square of the electron energy, making brightness inversely proportional to the fourth power of the electron energy. The total power of radiation from an undulator at any given photon energy is directly proportional to the current times the square of the electron energy and the power density is proportional to the current times the fourth power of the electron energy. Thus, lowering the storage ring energy can raise the brightness and increase the flux by permitting lower emittance and higher current. Countering this is the fact that the undulator photon energy is proportional to the electron energy squared and producing high energy photons from a medium energy storage ring requires shorter period undulators. However, there have been tremendous advances in undulator technology, leading to short period undulators capable of producing hard X-rays from medium electron energies. Even greater advances are expected in the near future with the development of superconducting undulators. As a result, medium energy third generation storage rings meet or exceed the performance of the high energy machines in the most desired energy range of 0.3 to 20 keV at a significantly lower cost.

The most advanced medium energy machine under construction is the Diamond light source, scheduled to be commissioned in 2006. As indicated in Table 3.2.1, Diamond will have the lowest emittance (2.7 nm) of any existing storage ring when it begins operations in 2007. NSLS-II will go beyond this value to 1.5 nm. Of course, emittance is only one metric of storage ring performance. To most users, the brightness, flux, and stability are of more immediate relevance to the quality of science the facility can support. More detailed comparisons are made between the expected performance of NSLS-II and other facilities in Section 3.3.

### 3.3 NSLS-II: An Advanced Medium Energy Storage Ring

It is clear from the above discussion that only a third generation storage ring can meet the urgent needs of the large user community who demand very high average brightness and flux in the VUV, soft, and hard X-ray energy regions, together with exquisite intensity, position, and energy stability, which are required to enable the scientific opportunities described in Section 2. The centerpiece of the new NSLS-II facility will be an advanced, highly optimized medium energy third generation storage ring. It will take advantage of the latest advances in storage ring technology, including superconducting undulators, top-off operation, superconducting RF cavities, and others, to achieve world-leading average brightness and flux in the target spectral region from 10 eV to 20 keV and set a new performance standard. It will be designed to be upgradeable to operation as an energy recovery linac for even greater performance, should that technology become feasible in the future. Relocating the present VUV/IR storage ring to the new facility to serve as a dedicated IR ring is a cost effective way to also provide world-leading high brightness in the important near- to far-IR spectral region. The IR ring will offer even better performance than the current VUV/IR ring in the IR region by operating in top-off mode using the first 800 meV of the same linac used to perform top-off injection of the X-ray ring.

A detailed conceptual design of the new X-ray ring will be initiated upon approval of this proposal. However, we have already done sufficient analysis to determine the major elements of NSLS-II and its anticipated performance:

- Ultrahigh brightness ( $\sim 10^{21}$  ph/sec/0.1%bw/mm<sup>2</sup>/mrad<sup>2</sup>)
- Ultrahigh flux ( $\sim 10^{16}$  ph/sec/0.1%bw)
- Electron energy of 3.0 GeV
- Circumference in the range of 600 to 700 m
- Ultra-low emittance (horizontal  $\sim 1$  nm; vertical  $\sim 10$  pm, which is diffraction limited at 1 Å)
- Very high stored current of at least 500 mA
- Top-off operation with a full energy injector
- Superconducting small gap undulators for continuous tunability
- Large number of insertion devices ( $> 20$ )
- Potential to be upgraded in the future to operation as an energy recovery linac

Obtaining this level of performance will be challenging. The design considerations and issues that must be overcome to meet these goals are discussed in detail in Section 3.4. Based on those considerations, we have done a preliminary conceptual and engineering design as well as a cost estimate for a 620 m circumference 3 GeV storage ring with a Triple Bend Achromat (TBA) lattice, 24-fold symmetry, and 7 m straight sections. The storage ring is housed in a building that allows room on the experimental floor for all beamlines to extend 60 m from the source to the end of the beamline. The shield wall is 25 m from the source, so a beamline length of 60 m was chosen to accommodate 1:1 imaging of the beam on the sample. While this is expected to be sufficient for the majority of cases, there may be a few special needs for extra long beamlines, for example for coherence experiments. As discussed in Section 3.6, the siting of the facility has been chosen to allow for longer beamlines to be built as extensions coming out of the building, as needed.

Figure 3.3.1 shows a computer rendering of the exterior of the facility and Figure 3.3.2 shows a schematic drawing of major elements of the facility. Table 3.3.1 lists the initial parameters of the design. The injection system will be either a full energy linac or a full energy booster sufficient to operate the storage ring in top-off mode. Figures 3.3.1 and 3.3.2 show a full energy linac. The gross square feet associated with the various elements shown in Figure 3.3.2 are given in Table 3.3.2. Figure 3.4.5 later in the text shows an alternative booster injection system. The new facility will be situated directly across from the current NSLS building and the new Brookhaven Center for Functional Nanomaterials.



**Figure 3.3.1** Computer rendering of the exterior of the NSLS-II storage ring. The main entrance is shown to the lower left, the RF gun chamber is to the lower right outside the ring, and the buildings housing the klystron galleries for the linac injection system (which is itself below ground), are shown in the infield of the ring. The small circular building in the infield is the IR ring, which shares the first portion of the same injection system used to top-off the X-ray ring.

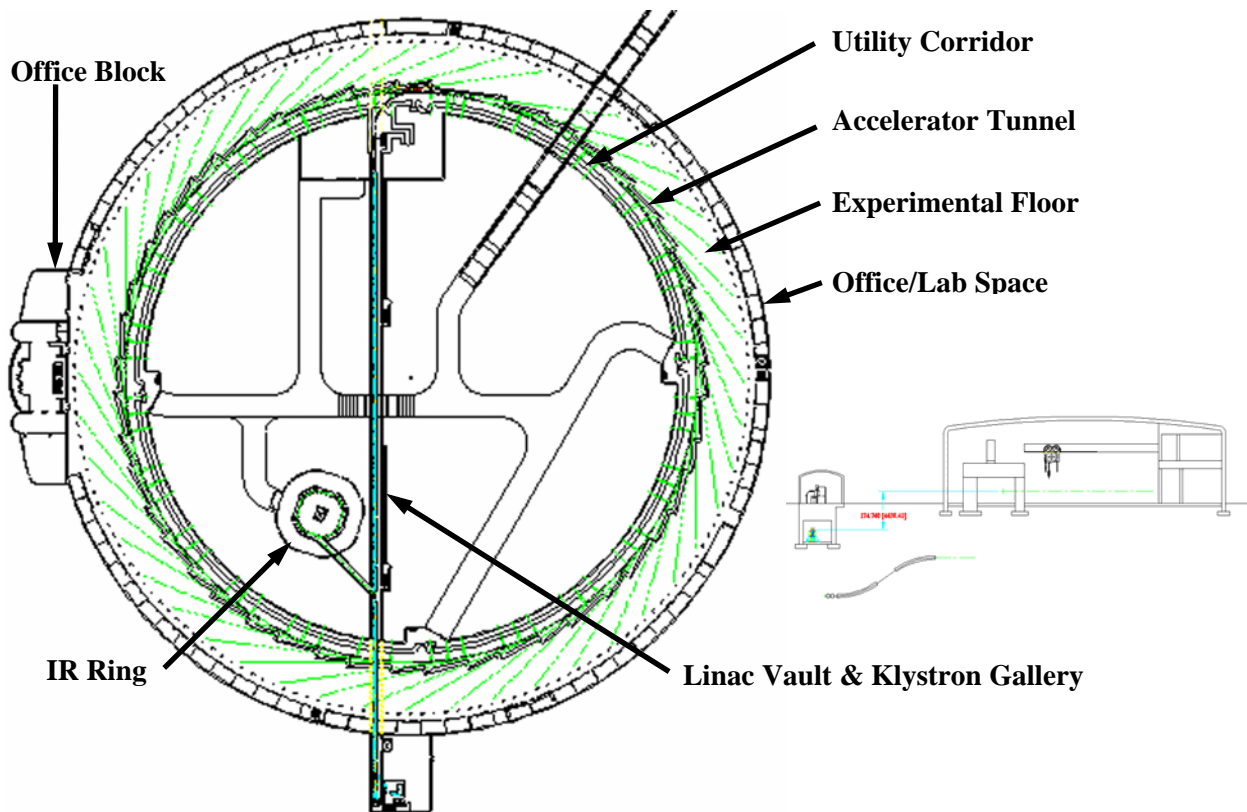


**Figure 3.3.2** Schematic of NSLS-II facility, showing the full energy linac injection system (blue) injecting first the small IR ring and then the much larger X-ray ring, the beamlines (in green) and surrounding lab/office space. A cross-sectional view on the right shows, in order from left to right, the linac tunnel and klystron gallery, utility corridor, accelerator tunnel, experimental floor, and perimeter lab/office space.

### NSLS-II Parameters

Circumference	620 m
Energy	3.0 GeV
Current	500 mA
Emittance ( $\epsilon_x, \epsilon_y$ )	1.5, 0.008 nm
Beam Size ( $\sigma_x, \sigma_y$ )	84.6, 4.3 $\mu\text{m}$
Beam Divergence ( $\sigma_x', \sigma_y'$ )	18.2, 1.8 $\mu\text{rad}$
Pulse Length (rms)	11 psec

**Table 3.3.1** *Main parameters for NSLS-II.*

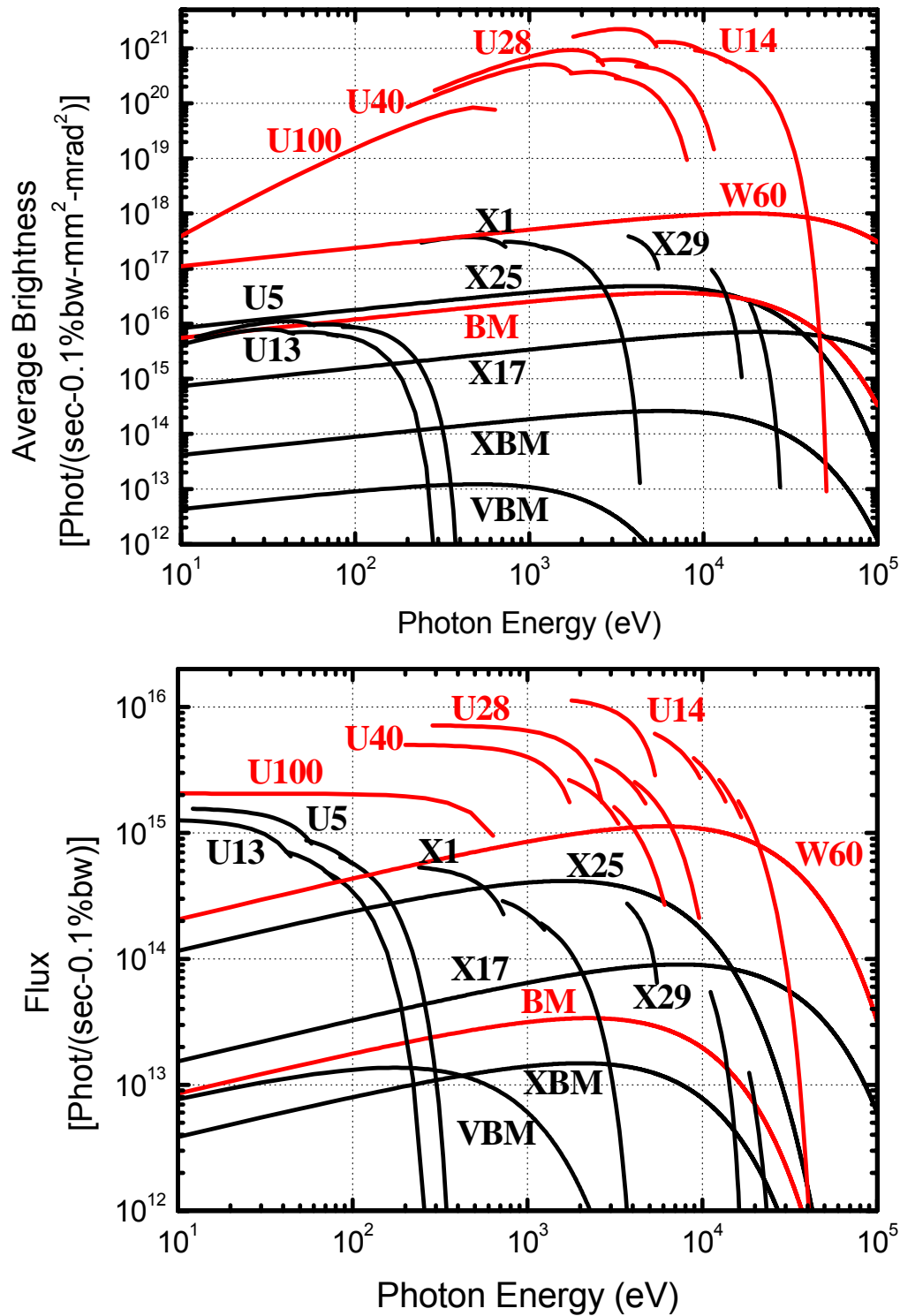
Building Area	Area [SF]		
	First Floor	Second Floor	Total
Linac Vault & Klystron Gallery	12,493	6,068	18,561
Utility Corridor	14,578		14,578
Accelerator Tunnel	51,563		51,563
Experimental Floor	111,230		111,230
Office/Lab	64,173	64,173	128,346
Office Block	11,055	8,945	20,000
<b>TOTAL</b>	<b>265,092</b>	<b>79,186</b>	<b>344,278</b>

**Table 3.3.2** *Gross square feet associated with conventional construction for NSLS-II. The different building areas are indicated in Figure 3.3.2.*

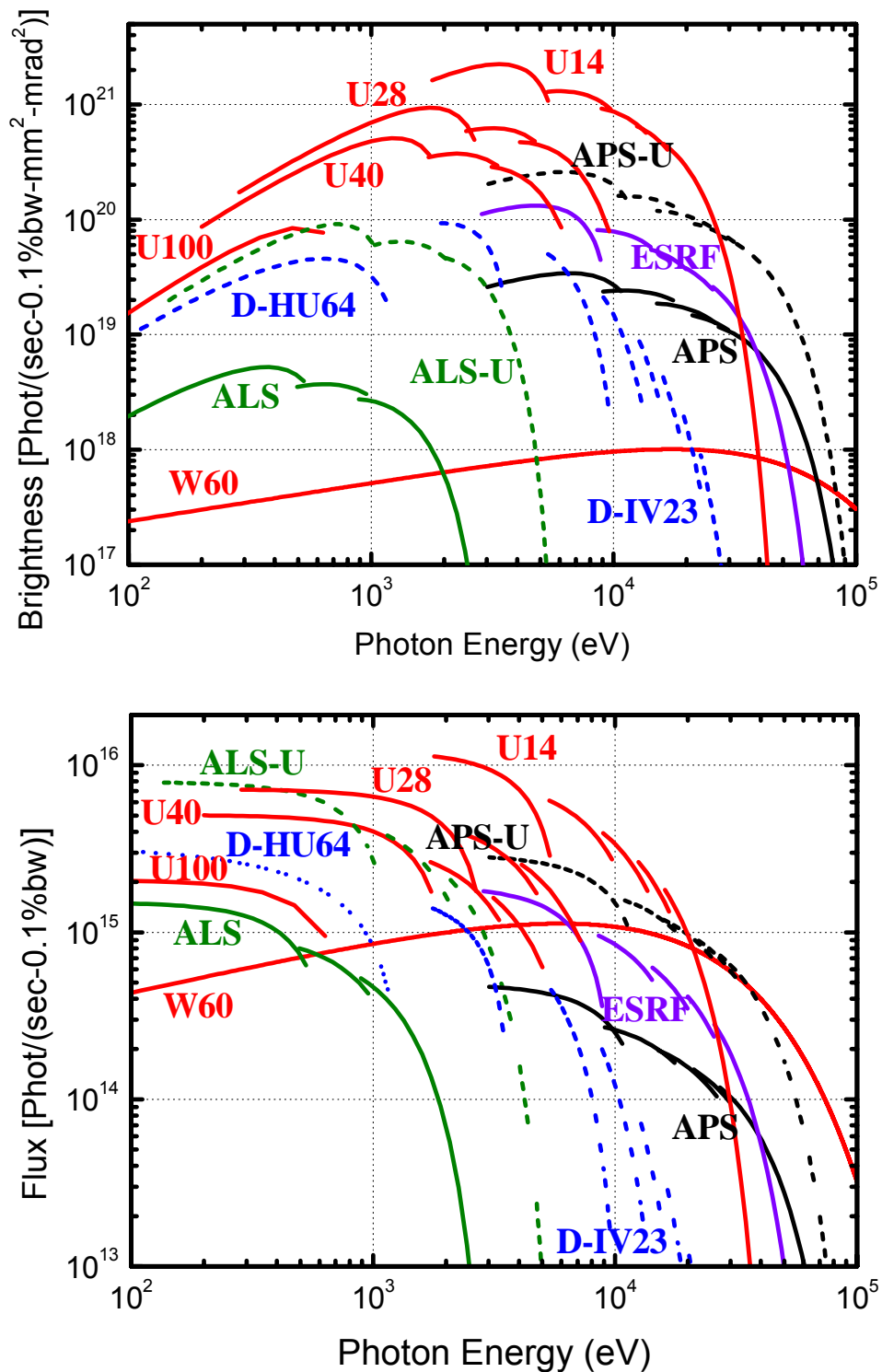
The X-ray storage ring will more than double the number of insertion device beamlines to 21 compared to the combined total of 9 once the remaining straights are built out on the current X-ray and VUV/IR ring (see Table 3.1.2) One straight section is reserved for injection and two are reserved for superconducting RF cavities and a third harmonic RF stretcher cavity. Most of the insertion devices will be superconducting undulators to provide fully tunable radiation from this medium energy ring. More information on insertion devices is given in Section 3.4.12.

Fig. 3.3.3 gives the average brightness and flux of the insertion devices and bending magnets on the NSLS-II X-ray storage ring, and compares them to those on the present X-ray ring and VUV/IR ring. NSLS-II undulators will be more than 10,000 times brighter than the present brightest NSLS beamline, X25, in the hard X-ray region above  $\sim 3$  keV. In the soft X-ray region from  $\sim 200$  eV to  $\sim 3$  keV, NSLS-II soft X-ray undulators will be 1,000 times brighter than the present brightest NSLS beamline, X1. And in the UV and VUV region from 10 to 200 eV, NSLS-II undulators will be 100-1,000 times brighter than the brightest VUV undulator, U5, on the present VUV/IR ring. The flux from the undulators will also increase substantially, especially in the soft and hard X-ray energy regions, where there will be  $\sim 20$  times greater flux from  $\sim 200$  eV to  $\sim 60$  keV. The 24 bending magnet beamlines will have more than 100 times higher brightness and several times higher flux than the present NSLS bending magnet beamlines throughout the entire energy range from 10 eV to more than 60 keV.

The brightness and flux of the NSLS-II X-ray storage ring will also be significantly greater than that of any other storage ring in the US or abroad. Figure 3.3.4 compares the brightness and flux of NSLS-II to that of other leading synchrotrons around the world, including the present Advanced Photon Source (APS), Advanced Light Source (ALS), and European Synchrotron Radiation Facility (ESRF). NSLS-II will be 10-100 times brighter than these facilities from  $\sim 2$  keV to  $> 20$  keV and from 10-1000 times brighter from 10 eV to 2 keV. The flux from NSLS-II undulators will be 1.5-100 times higher than from these other machines throughout the energy range from 10 eV to  $> 20$  keV.



**Figure 3.3.3** Average brightness (top) and flux (bottom) of insertion devices and bending magnets on NSLS-II (red) compared to the existing NSLS (black). U = Undulators, W = Wiggler, BM = Bending Magnet. The parameters of the NSLS-II undulators and wiggler are given in Section 3.4.12.



**Figure 3.3.4** Average brightness (top) and flux (bottom) of insertion devices at NSLS-II compared to devices at APS, ALS, ESRF, and Diamond (which is expected to be operational in 2007). The performance of proposed upgrades of APS [1] and ALS [1, 2] are also shown for comparison. The performance of NSLS-II will be world leading in both brightness and flux

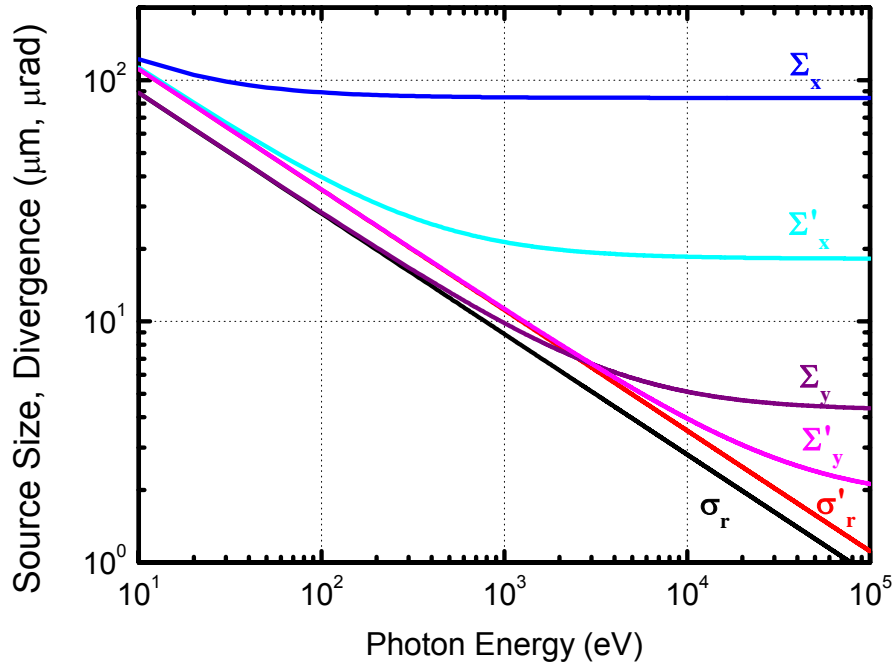


**Figure 3.3.5** Photon beam source sizes,  $\Sigma_{x,y}$ , and divergences,  $\Sigma'_{x,y}$ , for radiation emitted from a 5 m long undulator at NSLS-II compared to the natural, diffraction limited, photon source size,  $\sigma_r$ , and divergence,  $\sigma'_r$ . This shows that the photon beam size and divergence will be essentially diffraction limited in the vertical, and have a high degree of coherence in the horizontal, at photon energies of  $\sim 10$  keV and below.

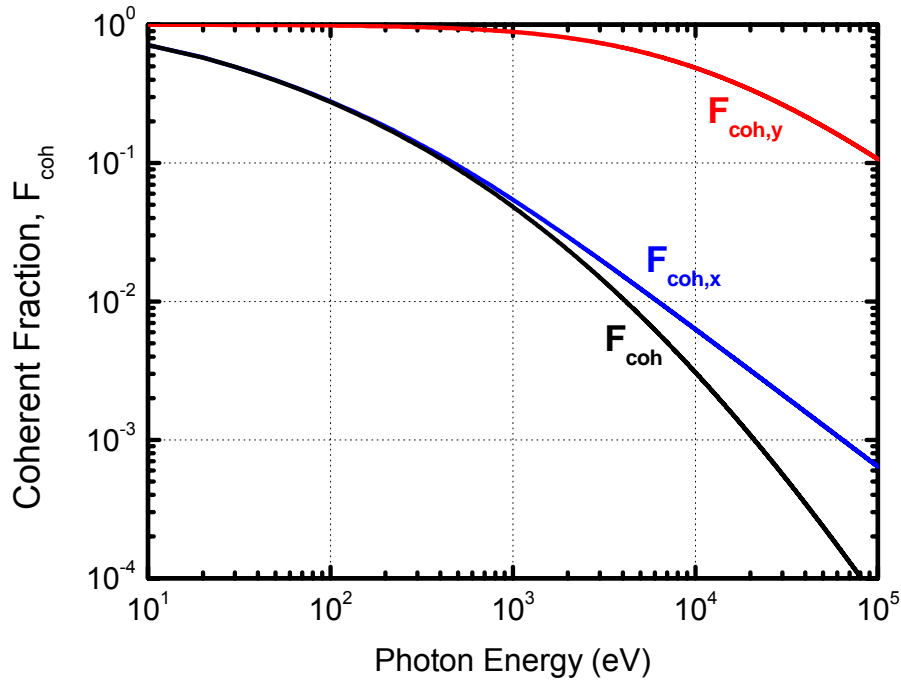


**Figure 3.3.6** Vertical, horizontal, and overall coherent fraction for photons emitted by 5 m long undulators at NSLS-II. This shows the nearly diffraction limited quality of the photons in the vertical, and high coherence in the horizontal, at photon energies of  $\sim 10$  keV and below.

As discussed in Section 3.4.1, the very low emittance of the electron beam in the NSLS-II X-ray ring results in very small photon beam source sizes and divergences and a high degree of coherence of the radiated photons, especially in the vertical direction. These photon properties are crucial for many of the most challenging problems described in Section 2. Figure 3.3.5 shows the effective source size and divergence of photons emitted by a 5 m long undulator as a function of energy from 10 eV to 100 keV and Figure 3.3.6 shows the corresponding coherence fraction (defined in Section 3.4.1) in the vertical and horizontal directions, as well as the overall coherence fraction. These curves show that the radiation from NSLS-II will be essentially diffraction limited in the vertical direction below about 10 keV and have a high degree of transverse coherence in the horizontal direction.

NSLS-II will continue to be world-leading in brightness and flux for many years after it begins operations in 2012. Among future machines listed Table 3.2.1, the Diamond facility is among the most advanced. As shown in Figure 3.3.4, NSLS-II will significantly surpass the performance of Diamond in both brightness and flux throughout the spectral range. In addition to future new machines, there may also be future upgrades of existing machines. Upgrades of both the APS [1] and the ALS [1, 2] have been proposed. The expected performance if those upgrades do take place is also shown in Figure 3.3.4. Again, NSLS-II significantly exceeds the performance of both the ALS and APS upgrades throughout the spectral range. Thus, we conclude that NSLS-II will continue to be a world-leading synchrotron in both brightness and flux for many years after it becomes operational.

As mentioned above, the existing VUV/IR ring will be relocated to the new facility to serve as a dedicated IR ring and support science at near- to far-IR photon energies. The ring will be upgraded to have a 500 MHz RF system to enable it to share the NSLS-II injection system. The first 800 meV of the linac injector will serve as a full energy injector for the IR ring, allowing it to run in top-off mode with 1000 mA stored current. This high stored current plus the very large opening angles ( $90 \text{ mrad}^2$ ) possible

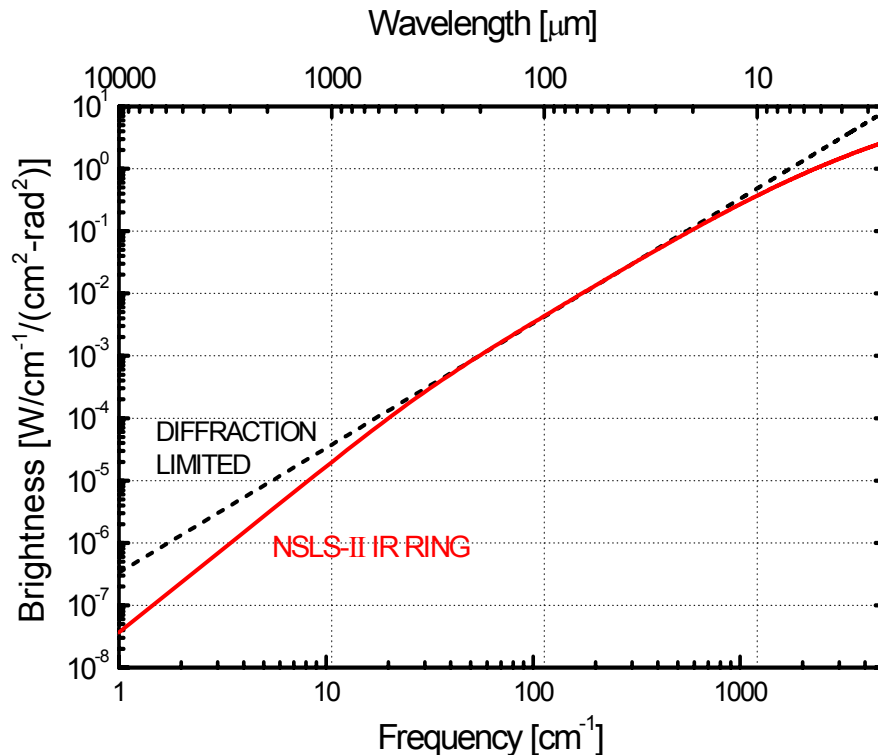


**Figure 3.3.7** Calculated brightness for the NSLS-II IR ring at 1000 mA and a  $90 \times 90 \text{ mrad}^2$  extraction aperture, compared to the brightness of an ideal diffraction limited source at 1000 mA. The NSLS-II IR ring will have world-leading brightness and be at or near the diffraction limit throughout the near- to far-IR spectral region.

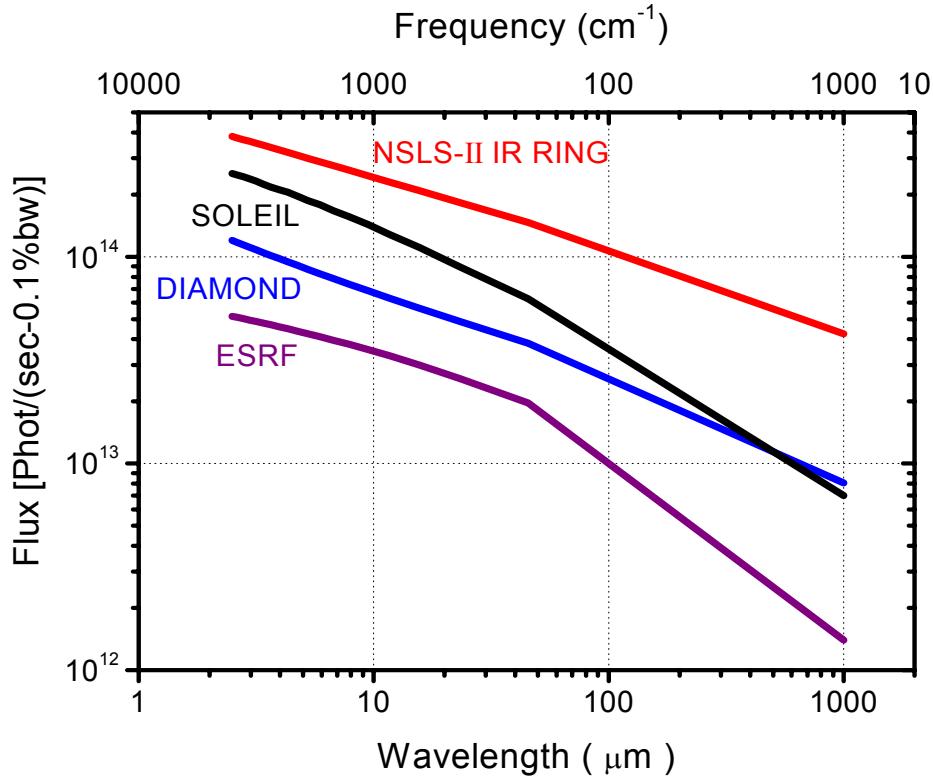


**Figure 3.3.8** Photon flux in the infrared of the NSLS-II IR ring compared with typical 3<sup>rd</sup> generation synchrotron sources. The high stored current and large opening angles (90 mrad<sup>2</sup>) possible on the NSLS-II IR ring result in world leading IR flux and brightness.

on the IR ring will result in world leading brightness throughout the IR spectral region, as shown in Figures 3.3.7 and 3.3.8. The upgraded higher frequency RF system will also result in significantly shorter (10s of picoseconds) electron bunches than the current VUV/IR ring, benefiting the time-resolved spectroscopy program. The high RF frequency also creates exciting possibilities for producing super-radiant THz radiation [3], which will be explored further during development of the Conceptual Design.

#### REFERENCES

- [1] <http://www.sc.doe.gov/bes/besac/20yearagenda.pdf> and unpublished. APS has proposed a 4 stage upgrade. The performance improvements resulting from stages I and II were used as a basis for calculating the upgraded APS performance shown in Figure 3.3.4.
- [2] <http://www-als.lbl.gov/als/20/ALStext.html>
- [3] M. Abo-Bakr, J. Feikes, K. Holldack, P. Kuske, W.B. Peatman, U. Schade, and G. Wüstefeld, H.-W. Hübers, Phys. Rev. Lett. 90, 094801-1 (2003).

### 3.4 Design Considerations and Challenges

The main figures of merit for NSLS-II and their primary determinant factors are:

- *High Brightness*: Current, number of undulator periods, electron beam emittance
- *High Flux*: Current, number of undulator periods
- *Photon Spectrum*: Electron energy, period of undulators
- *Beam Quality*: Position, energy, and intensity stability, reliability, Mean Time Between Failures

To maximize these figures of merit, NSLS-II should have the highest possible stored current, long straight sections for a large number of undulator periods, the lowest possible electron emittance, and well chosen electron energy, while at the same time achieving record setting stability and reliability at a reasonable cost. These are the same requirements confronted in the design of any modern synchrotron and as we discuss, many of them are contradictory. By taking advantage of the experience of current synchrotrons and also of recent and forthcoming technological advances, we believe that NSLS-II will out-perform any other medium energy synchrotron. In this section, the design considerations, initial choices, and future challenges encountered in achieving these ambitious goals are discussed in detail.

#### 3.4.1 Introduction

We begin by reviewing the factors that determine the brightness from undulator insertion device sources in an electron storage ring. When an electron traverses an undulator insertion device in the z direction, with a periodic magnetic field  $\vec{B} = B_u \cos(k_u z) \vec{y}$  in the y direction, it undulates in the horizontal plane (x direction) as shown in Figure 3.4.1. The undulator is characterized by its period,  $\lambda_u$ , and its strength parameter,  $K \equiv (eB_u \lambda_u)/(2\pi mc)$ .

The accelerated electron emits radiation at odd harmonics of the fundamental undulator period but reduced in wavelength by the relativistic factor of  $2\gamma^2$ , where  $\gamma = 1957 E$  [GeV]. The wavelength of radiation emitted in the forward direction is

$$\lambda_n = \frac{\lambda_u}{2n\gamma^2} (1 + K^2/2), \quad n = 1, 3, 5, \dots,$$

The central cone flux of the radiated photons,  $\Phi$ , is proportional to the number of periods of the undulator,  $N_u$ , and the stored electron current,  $I$ ,

$$\Phi \sim N_u I$$

The on axis brightness (sometimes also referred to as brilliance),  $B$ , of the radiated photons is defined

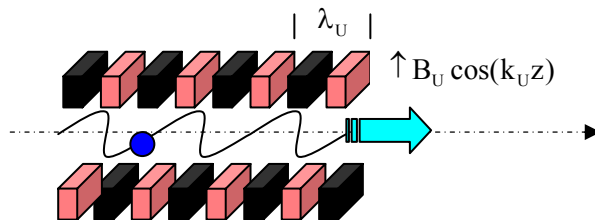


**Figure 3.4.1** Schematic illustration of an electron radiating in an undulator.

as  $\Phi$  divided by the phase space area of the source, which is determined by the horizontal and vertical photon beam source sizes,  $\Sigma_{x,y}$ , and divergences,  $\Sigma'_{x,y}$ ,

$$B = \frac{\Phi}{4\pi^2 \Sigma_x \Sigma'_x \Sigma_y \Sigma'_y}$$

Both the electron beam source sizes,  $\sigma_{x,y}$ , and divergences,  $\sigma'_{x,y}$ , as well as the natural (diffraction limited) photon source size,  $\sigma_r$ , and divergence,  $\sigma'_r$ , for photons emitted by an undulator of length  $L$  contribute to  $\Sigma_{x,y}$  and  $\Sigma'_{x,y}$ ,

$$\Sigma_{x,y} \equiv \sqrt{\sigma_{x,y}^2 + \sigma_r^2} \qquad \Sigma'_{x,y} \equiv \sqrt{\sigma_{x,y}'^2 + \sigma_r'^2}$$

where

$$\begin{aligned} \sigma_x &= \sqrt{\varepsilon_x \beta_x + \sigma_\varepsilon^2 \eta_x^2} & \sigma_x' &= \sqrt{\varepsilon_x \gamma_x + \sigma_\varepsilon^2 \eta_x'^2}, \\ \sigma_y &= \sqrt{\varepsilon_y \beta_y} & \sigma_y' &= \sqrt{\varepsilon_y \gamma_y}, \\ \sigma_r &= \sqrt{\lambda 2L} / (4\pi) & \sigma_r' &= \sqrt{\lambda / 2L}, \end{aligned}$$

Here  $\gamma_{x,y} \equiv (1 + \alpha_{x,y}^2) / \beta_{x,y}$ ,  $\alpha_{x,y} \equiv -\beta'_{x,y} / 2$ ,  $\varepsilon_x \equiv \varepsilon / (1 + \chi)$ ,  $\varepsilon_y \equiv \chi \varepsilon / (1 + \chi)$ , and  $\beta$ ,  $\chi$ ,  $\sigma_E$  and  $\eta_{x,y}$  are the betatron functions, vertical emittance coupling, electron energy spread, and energy dispersion factors, respectively.

The peak brightness is simply the brightness per pulse,

$$B_p = \frac{B}{f \tau}$$

where  $f$  is the number of electron bunches per second and  $\tau = 2.35\sigma_\tau$  is the FWHM pulse length ( $\sigma_\tau$  is the rms pulse length).

Another important figure of merit is the flux of photons that are transversely coherent,  $\Phi_c$ . This is given by

$$\Phi_c = B \left( \frac{\lambda}{2} \right)^2$$

The fraction of photons that are transversely coherent,  $F_c$ , is given by

$$F_c = \frac{\Phi_c}{\Phi} = \frac{\lambda^2}{(4\pi)^2 \Sigma_x \Sigma'_x \Sigma_y \Sigma'_y}$$

Since  $\Sigma_{x,y}$  and  $\Sigma'_{x,y}$  include the contributions of the electron and the photon emittances, the coherent fraction,  $F_c$ , only approaches unity when the electron emittance is much smaller than the photon emittance.

The design of the magnetic lattice of the storage ring determines  $\varepsilon$ ,  $\alpha$ ,  $\beta$ ,  $\chi$ ,  $\sigma_E$  and  $\eta_{x,y}$ . Since the goal in designing NSLS-II is to produce high brightness photon beams, we want to make the electron emittance,  $\varepsilon$ , be small compared to the natural photon emittance,  $\varepsilon_r = \sigma_r \sigma_r' = \lambda/(4\pi)$ . Thus, for diffraction limited X-rays at an energy of 12 keV ( $\lambda \sim 1 \text{ \AA}$ ), the electron emittance,  $\varepsilon$ , should be  $\sim 8$  picometer.

The very low horizontal emittance of NSLS-II of  $\sim 1.5$  nm, together with vertical emittance coupling,  $\chi$ , of 0.5%, means that the vertical emittance will, in fact, be  $\sim 8$  picometer. Thus, the radiation in the vertical direction should be essentially diffraction limited below  $\sim 12$  keV, which is indeed the case, as shown in Figures 3.3.5 and 3.3.6.

### 3.4.2 Lattice

The equilibrium emittance in an electron storage ring results from a balance between the quantum excitation of the electron beam during the emission of radiation in the dipole magnets and the damping of these oscillations by the acceleration in the RF system. For a ring made up of isomagnetic dipole magnets, the horizontal emittance,  $\varepsilon$ , of the electron beam can be written as

$$\varepsilon = \mathbb{F} \frac{\gamma^2 \theta_d^3}{J_x},$$

where  $\mathbb{F}$  depends on the choice of lattice and how it is tuned, and  $\theta_d$  and  $J_x$  are the bend angle of the dipole magnets and the horizontal damping partition function, respectively. The dependence on  $\gamma^2$  shows why it is harder to make a low emittance storage ring as the electron energy increases.

The basic approach to constructing a low emittance light source is thus to use a large number of short magnets (small  $\theta_d$ ), make a wise choice of the lattice type and tuning to minimize  $\mathbb{F}$ , and increase the value of  $J_x$  with combined function dipoles if needed (in which case  $J_x$  increases from 1 to 2). In general, a light source lattice is constructed from ‘basic cells’, containing dipoles, quadrupoles and sextupoles, which are usually bounded by dispersion free drift spaces for insertion devices. Since  $\theta_d$  decreases as the number of cells and the number of magnets per cell increases, the emittance is minimized by having a large number of cells and a large number of bends per cell. This tends to increase the circumference of the storage ring, which makes the cost increase. The dependence on  $\gamma^2$  means this is even more necessary for a high energy storage ring and explains why SPRING-8, APS, and ESRF all have the largest circumferences in Table 3.2.1.

*This also explains why it is not possible to obtain the required gains in performance simply by rebuilding the existing NSLS storage ring. Even if this were done (which would require a two to three year shutdown), it is constrained by its small (170 m) circumference to have too few cells and too few straight sections for insertion devices so that the gains would be minimal.*

In our pre-conceptual design work, we have considered a 24 cell Triple Bend Achromat (TBA) with 7 m long straight sections. This is a relatively large number of cells compared to other recent synchrotrons, (see Table 3.2.1). The only exceptions are Diamond, which also has 24 cells, and the higher energy rings, SPRING-8, APS, and ESRF. Twenty-four cells is chosen to give us a smaller emittance and is also considered to be the minimum number of straight sections (i.e., insertion devices) required to serve the needs of the broad range of scientific problems described in Section 2.

A TBA lattice is chosen for three reasons. First, it gives us more magnets per cell, which, while slightly more expensive, gives us a smaller emittance for a given circumference. This is again in contrast to the choice most synchrotrons have made, which is to employ a Double Bend Achromat (DBA) lattice

(see Table 3.2.1). The exceptions are the Pohang Light Source (PLS), the Swiss Light Source (SLS), the Advanced Light Source (ALS), and the proposed Synchrotron Light Laboratory at Barcelona (LLS). All of these are relatively small circumference machines that have a relatively low emittance for their number of cells and circumference. Second, it provides the ability to tune the momentum compaction while still maintaining zero dispersion ( $\eta = 0$ ) in the straight sections. This is a key requirement to preserve the ability to upgrade NSLS-II to operate in an ERL mode in the future (see Section 3.5.2). Third, it is much easier to add so-called ‘SuperBends’ to a TBA lattice. This is under consideration as an additional means of providing high energy photons from superconducting bending magnets.

The last of the basic defining parameters, the straight section length, is chosen to be a relatively long 7 m to permit long undulators (large number of periods and hence higher brightness) and to meet the needs of injecting into the ring (see Section 3.4.10).

Altogether, these basic design parameters determine the overall storage ring circumference, which, at 620 m, will be the largest medium energy storage ring in the world (see Table 3.2.1).

There are many challenges to be overcome in actually realizing such an ultra-low emittance storage ring. Achieving low emittance requires segmenting the ring into many cells with short dipoles interspersed with lots of strong quadrupoles to focus the electron beam. The strong quadrupoles contribute strong chromatic aberrations that must be corrected with nonlinear sextupole magnets and the short dipoles result in small dispersion so the sextupoles must be very strong and this makes the lattice

Lattice Type	TBA
Circumference [m]	620.4
Superperiods	24
Straight Section Length [m]	7
Energy [GeV]	3
Horizontal Emittance, $\epsilon_x$ [nm]	1.54
Vertical Emittance, $\epsilon_y$ [nm]	0.008
Emittance coupling, $\chi$	0.5%
Momentum Compaction, $\alpha$	0.0000815
Dipole Radius, $\rho$ [m]	7.64
Bending Magnet Critical Energy [eV]	7840.6
Field Index	21.5
Betatron Tunes $Q_x, Q_y$	37.3 , 17.25
Uncorrected Chromaticity, $\xi_x, \xi_y$	-108.8 , -31.6
ID Beta Functions, $\beta_x, \beta_y$ [m]	4.65 , 2.37
Damping Partition Functions, $J_x, J_e$	1.044 , 1.956
Energy Loss in Dipoles $U_o$ [MeV/turn]	0.938
$V_{rf}$ [MV]	1.55
RF Frequency [MHz]	500
RF Acceptance, $\epsilon_{RF}$ [%]	3
Current [mA]	500
Revolution frequency [kHz]	483.9
Orbit Time [ $\mu$ sec]	2.07
Maximum number of RF buckets	1035
Filled RF buckets (2/3 filling)	690
Single Bunch Current (2/3 filling) [mA]	0.72
Single Bunch Charge (2/3 filling) [nC]	1.48
Bunch length, $\sigma$ [mm, ps]	3.3, 11
Natural Energy Spread [%]	0.094

**Table 3.4.1** Initial TBA lattice parameters for NSLS-II.

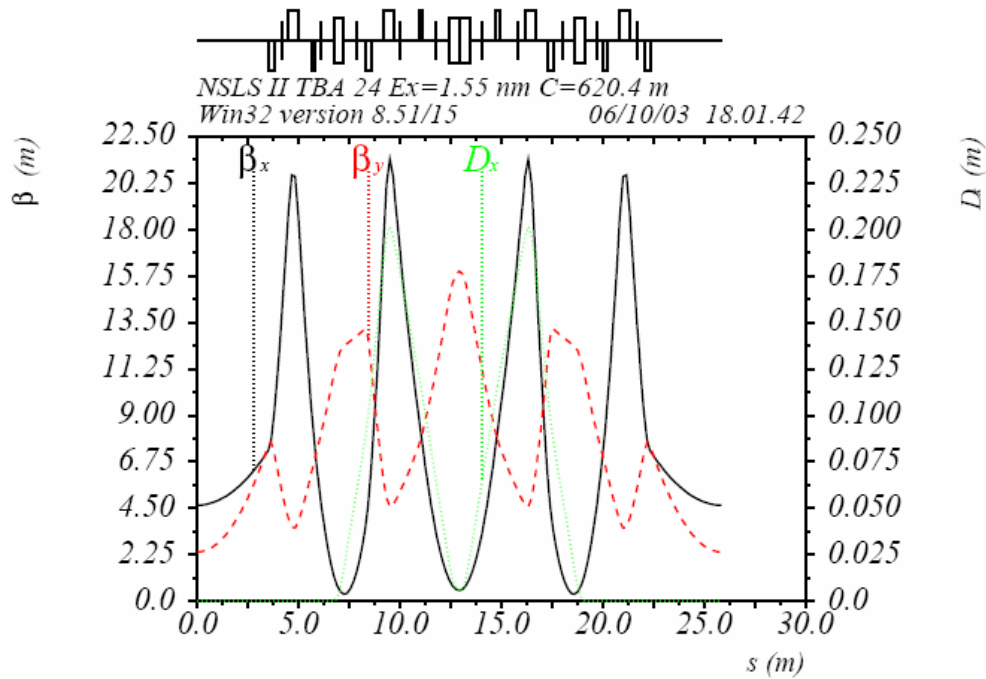


**Figure 3.4.2** Betatron and dispersion functions for one superperiod of the TBA lattice for NSLS-II.

highly nonlinear. The resulting stable phase space available to inject the electrons into the machine and to maintain a good lifetime is compromised (i.e., the dynamic aperture is reduced).

Achieving this leads to small beams (and hence a need for *high beam stability*), low dynamic and physical aperture and low lifetime (and hence the need for a *low emittance, high rep rate injector*), and potential collective effects and instabilities (and hence *sophisticated feedback systems* to cope with them). In addition, all of this must be achieved at a reasonable cost.

The parameters for our preliminary design of the lattice are listed in Table 3.4.1 and Figure 3.4.2 displays the betatron and dispersion functions for one superperiod. Analysis is underway to determine the optimal sextupole placement to maximize the dynamic aperture. Three families of sextupoles located inside the achromats are being used to correct the chromaticity and two or more families are located outside the achromat to improve the dynamic aperture, betatron tune shift with amplitude and nonlinear chromaticity. State of the art lattice and tracking tools such as OPA, TRACY, ACCELERATOR TOOLBOX and FREQUENCY MAP ANALYSIS are being employed.

The complex task of nonlinear optimization of the storage ring lattice is in its very early stages and much work remains to be done during the development of the full conceptual design. Future tasks include determining optimum betatron tunes and straight section betatron functions; determining the optimum number of sextupole families and locations; considering lattices with reduced superperiodicity to incorporate different straight sections; performing dynamic aperture tracking, including the effects of magnet errors and insertion devices; optimization of the off energy behavior of the lattice to ensure a good Touschek lifetime and injection efficiency.

At the present stage of the machine design all of the straight sections are taken to be of equal length at 7 meters to maximize the superperiodicity and thereby optimize the dynamic aperture of the ring. As the machine design evolves we envision reducing the periodicity of the ring and incorporating perhaps four longer straight sections  $\sim 20$  m in length. These would allow for a more optimum injection straight as well as accommodate very long large gap devices used for soft X-ray or VUV production. Longer straights would also facilitate the possible future conversion of the ring to an energy recovery linac mode of operation. Depending on the desired gap of the insertion device in the long straight section it may be necessary to segment the undulators with quadrupoles in between sections to control the growth of the

betatron functions. These issues will be explored further during development of the full conceptual design.

### 3.4.2.1 Lattice Magnets

In designing the lattice magnets several advantageous features will be utilized. Since the ring energy is fixed, the magnetic field will not be ramped with beam stored, so solid, rather than laminated, low-carbon steel may be used for the yokes. Attention will need to be paid to homogeneity and magnetic field uniformity of the steel. The dipoles will be open on the outside of the ring to allow synchrotron radiation from the dipoles to be brought out tangentially and so can have C-frame yokes. The quadrupoles and sextupoles may also be split into C-frames (dipoles into halves, sextupoles into thirds). Design studies will be conducted to optimize the magnet designs from the standpoint of magnetic, mechanical, thermal, and assembly considerations. The long and short dipoles can use a gradient design to provide a modest amount of vertical focusing by a radial taper in the magnet gap. Angled vertical magnet faces can also be used to provide horizontal focusing.

During development of the full conceptual design, we also plan to explore the following three design alternatives for the lattice magnets: conventional discrete electromagnets, integrated common-yoke magnet assemblies, and permanent magnet-driver dipoles.

The ring magnets may be realized with conventional, iron-core, water-cooled electromagnets. The required dipole fields, dipole gradients, quadrupole gradients, and sextupole fields are all readily achievable. The vertical stay-clear apertures, and therefore the magnet gaps, are about 40% smaller than in the present NSLS, so the required ampere-turns will be less and the resulting magnets will be more compact.

Several magnets may be integrated into a single, monolithic unit by machining mirror-image upper and lower yoke halves, each with poles for several magnets. For example, a sector unit may consist of a dipole flanked by a pair of sextupoles and quadrupoles. Channels are cut around each pole for coils, leads and cooling lines. The yoke halves are also machined to accept a sector vacuum chamber. The two halves are then bolted together to form a self-supporting unit. One important advantage of this approach is that the magnets in the assembly are aligned relative to each other with CNC precision. Such an approach was used in the MAX-III ring in Lund, Sweden.

For fixed energy operation, permanent magnet (PM) driven dipoles offer an attractive energy-saving option. Trim coils would be incorporated for fine-tuning the field and even for varying machine energy over a limited range. Magnetic modeling of a gradient dipole using NdFeB has shown this approach to be feasible. A large volume of PM material would be required, so the initial cost is higher than for a conventional electromagnet. Assembly of magnets with large PM blocks is also more difficult because of the large magnetic forces that must be dealt with. However, life-cycle cost, factoring in the rising cost of electricity on Long Island, may make this option worth serious consideration.

### 3.4.3 Stored Current

The design goal for NSLS-II is a stored current of 500 mA to provide very high flux. There are several issues that arise as the stored current is increased. First, the heatload on vacuum chambers, absorbers, and beamlines increases. The heatload on accelerator components is considered in Section 3.4.8 and on beamline optics in Section 4.1. A second set of effects that become significant with increased stored current are various collective effects such as coupled and single bunch instabilities. These can lead to longitudinal oscillations (resulting in increased energy spread) and transverse oscillations (giving an increased effective emittance). Coupled bunch instabilities are discussed in detail in Section 3.4.5.1. We anticipate taking several steps to combat coupled bunch instabilities, including employing superconducting RF cavities, adding a harmonic cavity, and employing sophisticated feedback systems. RF systems are discussed Section 3.4.9 and feedback systems are discussed in Section 3.4.11.

At this point, we are confident we can achieve 500 mA. Further investigation during the conceptual design phase will be pursued to determine whether we can exceed this value.

### **3.4.4 X-ray Pulse Length**

The natural electron, and therefore X-ray, pulse length for the current design of NSLS-II is expected to be only 11 psec (rms). This is shorter than any other storage ring and will be well suited to the range of timing experiments described in Section 2. However, as discussed below, these very short pulses combined with the high average current of NSLS-II result in very high peak currents per bunch. This has several negative consequences, including lower collective effect instability thresholds, shorter stored electron beam lifetimes, and increased heating of insertion devices.

Since the percentage of experiments that require such short pulses is expected to be relatively small, we currently envision running NSLS-II in two different operating modes. In fast timing mode, NSLS-II would be operated with the short pulses. However, in the normal operations mode that is expected to be the dominant operating mode, a passively powered third harmonic RF system (described in Section 3.4.9.1) would be used to stretch the electron bunch length. With this system, we expect the bunch length to roughly triple, resulting in an electron bunch length (and X-ray pulse time) of 33 psec (rms), which, while still quite short, greatly alleviates the effects mentioned above.

### **3.4.5 Collective Effects**

NSLS-II will operate with electron bunches having both very low emittance and large charge per bunch. The bunches interact with themselves and with each other, coupled by the impedance of the vacuum chamber and other storage ring components, higher order modes (HOMs) of the RF cavities, coulomb scattering, and residual gas ions. This gives rise to various collective effects that can limit the stored current due to instabilities, reduce the lifetime of the stored current, and lead to energy spread or emittance blowup. The NSLS-II design parameters are aggressive and the design is especially challenging in this regard. In addition, NSLS-II will employ a large number of small gap undulators that significantly contribute to, and for the vertical plane even dominate, the impedance seen by the electron beam. Finally, since the electron energy of NSLS-II is intermediate at 3 GeV, it provides high brightness hard X-rays by utilizing the higher harmonics of the undulator radiation. This limits the allowable energy spread growth of the electron beam.

The collective effects are driven by interaction of the bunch with the electromagnetic field supported by the ring components, which is modeled as an impedance seen by the beam. As we develop the full conceptual and engineering design of the storage ring and its components, the full impedance will be calculated and the collective effects will be analyzed in detail. This process is typically iterative, whereby some of the components will be modified to reduce their contribution to the impedance and therefore raise the thresholds for various instabilities.

Here we present conclusions from our preliminary analysis of the collective effects based on estimates of the largest contributions to the impedance and the worst case situation corresponding to the higher peak currents encountered in fast timing mode.

#### **3.4.5.1 Coupled Bunch Instabilities**

Coupled bunch instabilities can be driven by the resistive wall impedance of MGUs and the rest of the vacuum chamber. The corresponding instability thresholds have been calculated analytically using some simplifying assumptions, such as infinite thickness of the vacuum chamber wall. If the MGUs are operated at room temperature, the shortest growth time of the longitudinal coupled-bunch modes is  $\sim 50$  seconds and even longer if the MGUs are operated at 4.2 K. This is far greater than the damping time and therefore unimportant.

In the transverse case, the situation is quite different. This is primarily due to the MGU transverse impedance, which scales as  $1/a^3$ , where  $2a$  is the MGU gap and can be as small as 5 mm. If the MGUs are operated at room temperature or 4.2 K, the instability growth time is found to be 0.25 ms or 2.9 ms, respectively. Both of these are shorter than the damping time, indicating that the transverse resistive wall instability may have to be stabilized by dedicated transverse feedback dampers.

Coupled bunch instabilities can also be driven by HOMs of the RF cavities. The instability thresholds due to longitudinal and transverse HOMs of several RF cavity designs have been estimated with simplified expressions and compared with growth rates calculated by ZAP. The PEP-II normal conducting cavities, and the KEK-B, CESR and SOLEIL superconducting cavities have been analyzed for longitudinal stability and the KEK-B superconducting cavity has been analyzed for transverse stability.

The results show that all of the cavities result in longitudinal coupled bunch instability threshold currents above the NSLS-II design values. The worst case is for the PEP-II cavity, where the HOM impedance is quite close to the threshold and some care is needed to ensure that the modes are stagger-tuned among the up to three cavities NSLS-II, which is easily satisfied. We conclude that any of the cavities appear to satisfy the requirements, although the superconducting cavities have a factor of 5-10 margin over normal conducting cavities.

Similarly, for the transverse coupled bunch instability the growth time of  $\sim 34$  ms is about three times higher than the transverse damping time and so the KEK-B superconducting cavity does not cause transverse coupled bunch instability for up to 2 cavities in the ring. In the case that three cavities are required, the modes are of such low Q that it is no longer possible to stagger tune the HOM's and a feedback system may have to be added to damp this instability. In principle this could be the same system as the one that damps the resistive wall driven instability described above.

In summary, by utilizing feedback damping systems and superconducting RF cavities, coupled bunch instabilities are not expected to present any difficulties for NSLS-II operating in fast timing mode. When operated in normal mode with the harmonic cavities, the reduced peak current (as well as Landau damping from the harmonic cavities) is likely to make the feedback damping system unnecessary.

### 3.4.5.2. Single Bunch Instabilities

Single bunch instabilities can be driven by the broad band impedance of the vacuum chamber. Typically, this comes from many elements, including Beam Position Monitors (BPMs), scrapers, vacuum slots, various transitions, etc. Analyses to date have been based on scaling this impedance from other rings using simplified models. For example, measurement data from the current NSLS VUV/IR ring is well described by a  $Q = 1$  broad-band resonator model with resonance frequency  $f_{BB} = 1.8$  GHz, and  $R_{shunt}/n \sim 1$  Ohm, where  $R_{shunt}$  is the shunt impedance. Scaling this with the effective vacuum chamber radius gives, for the NSLS-II ring,  $f_{BB} = 2.9$  GHz, and  $R_{shunt}/n \sim 1.6$  Ohms.

In the case of NSLS-II with many MGUs, small gap transitions are expected to dominate the transverse impedance in the vertical plane. It has also been confirmed by recent NSLS measurements that the geometric contribution greatly exceeds the contribution from the resistive wall. In the limit of low frequencies, the transverse impedance of a linear taper is essentially inductive and scales quadratically with the tapering angle. To be in this regime, however, the taper should be long,  $L_{taper} \gg h a / \sigma_z$ , where  $h$  is the nominal vacuum chamber height,  $\sigma_z$  is the bunch length, and a small transverse aspect ratio is assumed for simplicity. Estimates for the parameters of NSLS-II result in a minimum taper length of about 15 cm, however longer tapers should be planned to lower the magnitude of the impedance. Design of a tapered variable gap chamber will be more complex. To develop these designs, we intend to embark on an R&D program that includes wake-field calculations with 3D EM field solvers, bench measurements of impedance for a prototype chamber, as well as detailed analysis of single bunch transverse instability thresholds.

We have also made preliminary estimates of the longitudinal instability threshold. Estimates in the mode coupling regime,  $\lambda_{wake}/\sigma_z \gg 1$ , indicate that the above estimated impedance gives a current

instability threshold that is rather close to the NSLS-II single bunch current. Note, however, that the NSLS VUV/IR vacuum chambers were constructed without detailed impedance considerations, and it is expected that the NSLS-II impedance values will be lower by an order of magnitude or more.

In the microwave instability regime,  $\lambda_{\text{wake}}/\sigma_z \ll 1$ , the well-known Boussard criterion for the onset of the microwave (MW) instability indicates that the broad-band impedance,  $|Z_n/n|$ , must be less than  $\sim 0.1$  Ohms. It is widely believed that such impedance values are achievable. For example, detailed calculations of the damping ring impedance of the Next Linear Collider produce  $|Z_n/n|$  numbers an order of magnitude lower [1]. Also, it is important to note that the longitudinal impedance is not expected to be affected much by the MGUs. Furthermore, if the impedance is purely inductive rather than resistive, the beam is stable for all currents. In principle, CSR impedance might also contribute to the MW instability. However, our preliminary estimates for the CSR induced instability at NSLS-II indicate a relatively high threshold, so this is not a problem.

In summary, by careful control of the taper of the MGU transitions and the broadband impedance of the NSLS-II storage ring components, single bunch instabilities should not present any difficulties for NSLS-II operating in either fast timing mode or in normal mode.

### 3.4.5.3 Intra-Beam Scattering

While strictly speaking not a collective effect, intra-beam scattering (IBS) is often considered together with collective effects. IBS may degrade beam quality since it generally results in six-dimensional phase-space growth of the beam. The magnitude of the effect is proportional to the particle phase-space density and scales inversely with the square of beam energy. We have done SAD simulations that indicate that the maximum relative blow-up is only a few percent at 1.5 mA single bunch current, which is about twice the nominal single bunch current for standard multi-bunch operation. This and other considerations give us reasonable confidence that IBS should not be a factor for NSLS-II operating in fast timing mode and even less so for normal mode operations. However, IBS may become important for some very specialized modes of operation, such as very high single bunch charge.

### 3.4.5.4 Ion-related Instabilities

Finally, we note that there also exists yet another class of instabilities due to the interaction of beam electrons with ions and low energy electrons in the vacuum chamber, which are produced by various mechanisms. Although these instabilities have not been considered to date, they will be analyzed in detail during conceptual design. This is especially important for MGU locations, where the small transverse beam size may drive ion-related instabilities and providing adequate pumping in a long small gap presents a challenge.

## 3.4.6 Effects of Insertion Devices

The impact of individual undulators on the electron beam properties can usually be ignored. However with as many as 20 small gap undulators installed in the ring the impact on the electron beam needs to be considered. We have estimated the impact assuming the worst case of maximum K, and hence maximum magnetic field, B. The undulators considered are the superconducting undulators U14 ( $\lambda = 14$  mm,  $K_{\text{max}} = 2.24$ , length = 5 m) described in section 3.4.12. We find that the energy losses will be easily handled by the RF system since even with 20 U14 undulators operating at  $K_{\text{max}}$ , the loss is only 66 % of the dipole loss.

A second potential impact is a change in the electron emittance. This is always to lower values and is related to the ratio of  $[\rho_{\text{dipole}}/\rho_{\text{undulator}}]$  as well as the integral of the dispersion emittance over the undulator. For the U14, this ratio is  $\sim 1.25$ . While the emittance reduction is small per undulator ( $\sim 1$  to 2 %), 20 undulators could result in a significant reduction of  $\sim 40\%$ . This has the potential to drive the emittance

below 1 nm for even higher brightness. The energy spread is also related to this ratio and therefore a small increase may occur for 20 U14 undulators all operating at  $K_{\max}$ , but this is not expected to be significant.

Finally, the tune shifts are quite small and shouldn't be a problem even with 20 U14 undulators. However, if they are all operating at  $K_{\max}$  some tune correction may be required with the quadrupoles.

### 3.4.7 Electron Beam Lifetime

Electron losses due to finite energy acceptance or limited transverse dynamic or physical apertures contribute to limit the lifetime of the stored electron beam. We consider these in turn to arrive at the expected overall lifetime for NSLS-II.

#### 3.4.7.1 Quantum Lifetime

Photon emission by synchrotron radiation generates electron energy spread, with rms value  $\sigma_\epsilon$ . This results in the so-called quantum lifetime,  $\tau_q$ , which is given by

$$\tau_q = \frac{\tau_\epsilon e^\xi}{2 \xi},$$

where  $\tau_\epsilon$  is the energy damping time and  $\xi \equiv \epsilon_{RF}^2 / 2\sigma_\epsilon^2$  is the scaled RF energy acceptance,  $\epsilon_{RF}$ . Similar expressions, with corresponding damping times and limiting half apertures, hold for the transverse dimensions. Unless the apertures are extremely small (<10 times the beam size) the quantum lifetime is essentially infinite. Since for NSLS-II, both the RF acceptance and the transverse limiting apertures will significantly exceed the beam dimensions the quantum lifetime can be ignored.

#### 3.4.7.2 Gas-Scattering Lifetimes

The gas scattering lifetime due to elastic collisions between the stored electrons and gas nuclei is given by

$$\frac{1}{\tau_{\text{scat}}} = \frac{4r_e^2 Z^2 \pi n c}{2\gamma^2} \left[ \frac{\langle \beta_x \rangle \beta_{x,\max}}{a^2} + \frac{\langle \beta_y \rangle \beta_{y,\max}}{b^2} \right]$$

where  $n$  and  $Z$  are the nuclei concentration and charge respectively, and  $a$  and  $b$  are the horizontal and vertical stay clear apertures. In case of NSLS-II, the vertical acceptance (defined as the minimum value of  $b^2/\beta_y$  over the circumference) is limited by the MGUs. Since it is expected to be significantly smaller than the horizontal acceptance we will consider the vertical contribution to the lifetime only. For the TBA lattice and 2 m long, 5 mm full gap NSLS-II MGUs, the vertical acceptance is 2.24  $\mu\text{m-rad}$ . Calculating  $n$  from the usual conservative assumption of 1 nTorr  $\text{N}_2$ -equivalent pressure gives the elastic gas-scattering lifetime of  $\tau_{\text{scat}} \approx 61$  hours.

It should be noted that the largest acceptance is reached when the beta function in the center of the straight,  $\beta^*$ , equals half the length of the insertion device (ID). Therefore, for given ID length, the gas scattering lifetime could be lowered further by reducing the vertical beta function. Alternatively, for the present lattice with  $\beta^* = 2.37$  m IDs of up to  $\sim 5$  m in length (again assuming 5 mm full gap) could be used without compromising gas-scattering lifetime.

Bremsstrahlung on nuclei of residual gas, or inelastic gas scattering, may lead to particle loss when the momentum of the scattered electron is outside the limiting momentum aperture  $\epsilon_{\max}$ . The corresponding lifetime can be written as

$$\frac{1}{\tau_{\text{brem}}} = \frac{16r_e^2 Z^2 n c}{411} \ln \left[ \frac{183}{Z^{1/3}} \right] \left[ -\ln \epsilon_{\max} - \frac{5}{8} \right]$$

In principle, either physical aperture, dynamical aperture, or the RF bucket height may set the momentum aperture. The bremsstrahlung lifetime, when calculated for 1 nTorr N<sub>2</sub>-equivalent pressure and a 3% limiting momentum aperture, is  $\tau_{\text{brem}} \approx 72$  hours.

As discussed in Section 3.4.12.4, the present superconducting MGU concept assumes cold-bore devices operating at liquid He temperatures with cold surfaces directly facing ring vacuum. Inside the superconducting MGU chamber the above assumption of 1 nTorr N<sub>2</sub>-equivalent pressure is irrelevant, since most gas species (including N<sub>2</sub>) will likely cryopump to much lower pressures. This however, does not apply to He itself, which in principle may contaminate the ring vacuum inside the superconducting MGU chamber. He is hard to remove and even with state-of-the art vacuum technology one should expect the residual pressure to remain in the 10<sup>-8</sup>-10<sup>-7</sup> Torr range. Assuming the most pessimistic pressure of 10<sup>-7</sup> Torr He-equivalent, the gas scattering lifetime estimates given above would be lower by a factor of ~4. However, this reduction hardly changes the overall gas scattering lifetime, since the superconducting MGUs occupy only a small fraction of the ring circumference. Therefore, for practical purposes, the effect of the superconducting MGUs on the gas scattering lifetimes can be ignored and the estimates above based on 1 nTorr N<sub>2</sub>-equivalent pressure estimates can be used.

### 3.4.7.3 Touschek Lifetime

Coulomb scattering of charged particles in a stored beam causes an exchange of energy between the transverse and longitudinal oscillations. The Touschek effect is the transformation of a small transverse momentum into a large longitudinal momentum due to scattering and can lead to loss of particles that fall outside the momentum limiting aperture. Unlike gas scattering, the time dependence of the number of stored particles is not exponential but is rather described by

$$N_b(t) = \frac{N_b(0)}{1 + t / \tau_{\text{tous}_{1/2}}}$$

Here,  $\tau_{\text{tous}_{1/2}}$  is the so-called Touschek half-life. For short time intervals, such as the ones that occur between top-off injection pulses, the inverse half-life directly gives the slope of  $N_b(t)$ . Alternatively, for longer time periods, when  $N_b(t)$  can no longer be considered linear, its time dependence can be approximated by an exponential with lifetime  $\tau_{\text{tous}} = \tau_{\text{tous}_{1/2}} / \ln(2) \approx \tau_{\text{tous}_{1/2}} / 0.693$ . This regime is less relevant for NSLS-II, and therefore we will use  $\tau_{\text{tous}_{1/2}}$  to estimate particle losses.

The Touschek lifetime for NSLS-II was calculated with three different codes, SAD, ZAP, and MAD, which showed good agreement. So far, no physical or dynamic apertures have been explicitly put in. The lifetime versus RF bucket height for 500 mA current and 3 GeV ring energy is shown in Figure 3.4.3 (top). The Touschek half-life also has a strong dependence on ring energy, as shown in Figure 3.4.3 (bottom) assuming 3% RF bucket height and 500 mA total current. At 3 GeV,  $\tau_{\text{tous}_{1/2}} = 2.4$  hours; it quickly grows at higher energies.

The Touschek lifetimes estimated above are for NSLS-II operating in fast timing mode (see Section 3.4.4). Since the Touschek lifetime is proportional to the bunch length, it is expected to triple to around 7.2 hours in the normal operating mode.

Finally, we note that these lifetime estimates are preliminary as several mechanisms may substantially modify the Touschek numbers above. These will be studied further during the full conceptual design for NSLS-II. Specifically, the momentum acceptance may be limited due to dynamic aperture (which is momentum dependent and has to be calculated for large momentum deviations), non-linear momentum compaction, synchrotron oscillations (which reduce the dynamic aperture due to higher order chromaticity), magnet alignment errors (which affect the emittance coupling), and small gaps of the MGUs (due to coupling, Touschek scattered particles in the beam halo may get lost on vertical apertures). In the future, particle tracking with some or all of the above will be performed with the full lattice, magnet errors, and physical apertures.

#### 3.4.7.4 Total Lifetime

While all the mechanisms considered so far contribute to the overall lifetime, the Touschek losses are clearly the dominate ones for NSLS-II. In fact, adding all the contributions considered so far, and assuming 3% limiting momentum acceptance, gives an overall lifetime when operating in fast timing mode of 2.2 hours or, using  $\tau_{\text{tous}}$  rather than  $\tau_{\text{tous}_{1/2}}$ , of 3.1 hours for longer time-scales. In the normal mode of operations, the overall lifetime will be 5.9 and 7.9 hours for short and long time-scales, respectively. Since the overall lifetime is very close to the Touschek-only number, longer IDs should be possible without significantly impacting the overall lifetime.

#### 3.4.8 Heat Loads

To achieve its aggressive brightness and flux goals, NSLS-II will utilize high stored current and long small-gap undulators. This can result in a substantial heat load on accelerator components from a number of mechanisms, including both incoherent and coherent synchrotron radiation from the bending magnet dipoles and undulators, ‘geometric wake heat’, image current (also known as resistive wall, or Ohmic) heating, and others. These will be carefully taken into consideration during the engineering design stage once the ring components become better defined.

At the present time, we have considered only one component, specifically the superconducting undulator chamber, as this component is one of the most challenging in terms of handling the heat load. Present superconducting undulator design (see Section 3.4.12.4) includes a Cu-coated inner chamber cooled to liquid He temperature (4.2 K) with  $2a = 5$  mm full vertical gap. The amount of heat induced by the beam in this chamber affects the feasibility of the cryogenic design. Of the many mechanisms of beam energy transfer into the ID vacuum chamber, at this point image current heating is believed to be the most important.

We estimate the image current induced power per unit length,  $P/L$ , for undulators at room temperature. Using the normal skin effect surface impedance and Gaussian electron bunches of rms length  $\sigma_z$  we find  $P/L \sim I^2/(\sigma_z^{3/2} a)$ , where only the dependence on current, bunch length, and chamber aperture is expressed. A conservative estimate of the power deposited per unit length results in  $\sim 25$  W/m in fast timing mode (short  $\sigma_z$ ) and  $\sim 5$  W/m in normal operating mode. Either of these values is insignificant for a superconducting undulator in a warmed-up state.

The situation is different when the superconducting undulator is cold and for the frequencies corresponding to the few mm bunch-length of interest. In that case, the Cu coating of the superconducting undulator chamber is expected to be in the extreme anomalous skin effect regime and we find  $P/L \sim I^2/(\sigma_z^{5/3} a)$ . When estimated for NSLS-II parameters we find  $P/L \sim 5$  W/m in fast timing mode and  $\sim 0.8$  W/m in normal operating mode. While these power levels are significantly down from the room temperature values, they now have to be removed cryogenically. Currently, commercial cryo-coolers are available with a capacity of up to 1.5 W. Thus it will likely be necessary to combine several cryo-coolers, provide dedicated refrigerators for each superconducting undulator, or perhaps have a central cryo-plant, with liquid He plumbed around the ring to all superconducting undulators.

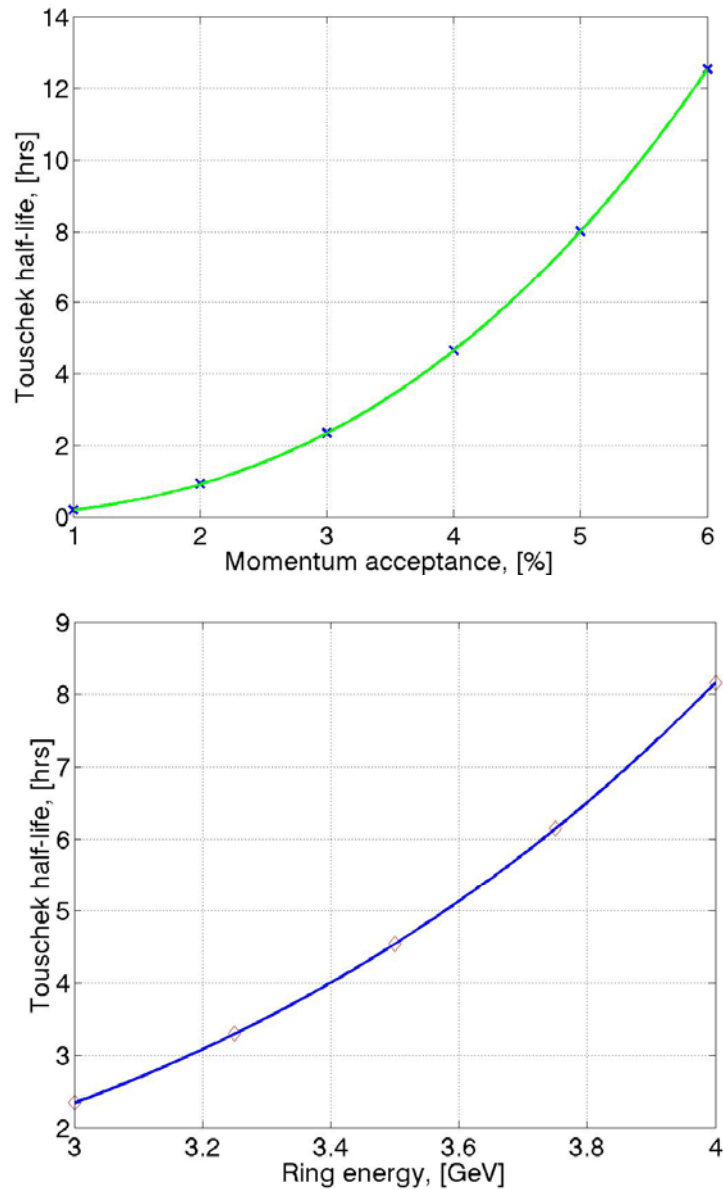


**Figure 3.4.3** *Touschek half-life versus momentum acceptance (i.e., RF bucket height) (top) and versus X-ray ring energy (bottom).*

It is important to note that, while encouraging, these results are preliminary and are based on a simplified treatment that will be further refined during conceptual and engineering design.

### 3.4.9 RF

The NSLS-II RF system must provide sufficient voltage to deliver an acceptance greater than the beam size throughout the operating regime, and power to the beam to make up the synchrotron radiation losses. This amounts to 2.8 MV for a 3 % momentum acceptance in a 500 MHz RF system assuming 870 kW for radiation losses with the full complement of insertion devices.

Both normal conducting and superconducting cavity systems have been considered, with a superconducting system being the preferred choice at this point for several reasons: fewer cavities are

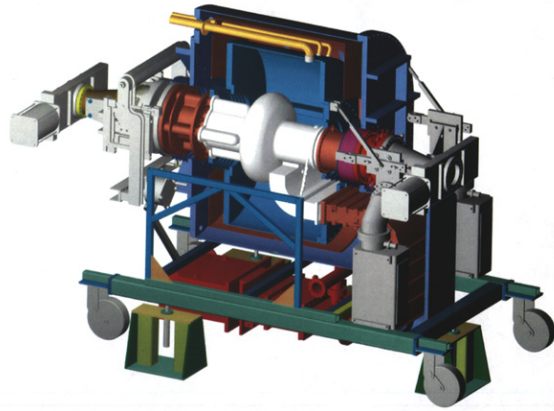


**Figure 3.4.4** *Superconducting 500 MHz CESR RF cavity developed at Cornell.*

required resulting in fewer straight sections being used to house the cavities; lower installation and operating costs; and lower HOM impedances that result in a stable electron beam without the need for additional complexities in the feedback systems in order to tame HOM driven coupled bunch instabilities

Both the KEK-B and Cornell CESR-B superconducting RF cavity designs were analyzed for HOM impedance contributions to coupled bunch instabilities and found to be unconditionally stable (see Section 3.4.5.1). The CESR cavity is shown in Figure 3.4.4. Both have similar power coupling capability and both are available commercially. Either system will meet the requirements for NSLS-II. For purposes of illustration, a KEK derived system is outlined in the following paragraphs.

The KEK-B cavity easily meets the voltage requirement of 2.8 MV with a single cavity, however a minimum of two cavities are required to meet the 800 kW beam power. Existing fundamental power couplers have been operated at 380 kW each, and bench tested higher. Since the superconducting RF cavities with 500 mA of beam loading cannot be always operated as a matched load the couplers must exceed this power level. We are investigating adopting the KEK-B cavity design to add a second input coupler to each cavity. This would give us ample margin to fully power each cavity. Therefore, two cavities are anticipated at this time. The total length of two cavities is  $\sim 5.4$  m, so they will fully occupy one of the 7 m straight sections.

Each cavity will have its own RF power source. CW klystrons with output power between 500 and 1000 kW are commercially available. Alternatively, Inductive Output Tubes (IOT's), which have higher efficiency although at lower gain, have been built at 700 MHz with an output power of 700 kW and can be easily scaled to operate at 500 MHz. These tubes have the important advantage of being able to provide very high instantaneous output power that, when coupled with their low group velocity, allows them to be designed into feedback loops around the cavity for control of the cavity fundamental impedance, greatly improving the beam-loading problem. A single IOT per cavity is thus anticipated.

### **3.4.9.1 Third Harmonic Superconducting RF Cavity for Bunch Lengthening:**

The short bunches (11 psec, rms) produced by the low momentum compaction of the low emittance lattice result in a short Touschek lifetime (see Section 3.4.7.3) and increased image current heating of superconducting undulators (see Section 3.4.8). As explained in Section 3.4.4, we plan to operate in two modes: a fast timing mode with 11 psec (rms) pulses and the normal operating mode with 33 psec (rms) pulses. This longer pulse length will be obtained by installing a third harmonic RF cavity to stretch the electron bunch. A third-harmonic cavity of the type developed for BESSY II by Accel Instruments will be sufficient for this purpose.

### 3.4.10 Injection System

The low emittance of the high brightness lattice of NSLS-II results in quite a short lifetime. This makes operation in top-off injection mode a necessity. Some of the other benefits of top-off operation include constant heat load on accelerator components and beamline optics for increased stability, and constant intensity delivered to experiments.

We begin discussion of the injection system for NSLS-II by considering the requirements for top-off operation of NSLS-II. Our goal is to maintain the storage ring current constant to within 1%. The lifetimes in fast timing and normal operating modes were estimated in Section 3.4.7.4 to be 2.2 and 5.9 hours. As discussed there, these preliminary lifetime estimates may become even shorter as additional development is done during the conceptual design. From the parameters listed in Table 3.4.1, we thus need to replenish about 1% of the charge, or about 0.015 nC, in each filled bunch about once per minute. If we inject at 10 Hz, we could top-off each bunch with this charge once per minute and maintain the bunch charge constant to within 1%. Alternatively, if we accept bunch-to-bunch charge variations of 10% while still maintaining the average current constant to 1 %, we could inject 0.15 nC at a 1 Hz rate. We note that even at the faster 10 Hz injection rate, the 100 ms between injections is still more than 10x greater than the damping time required for the injected charge to reach equilibrium.

In addition, the expected small dynamic aperture and low emittance of the NSLS-II storage ring also implies that the emittance of the injected beam must not be much larger than that of the stored beam to achieve acceptable injection efficiency. Based on experience at the Swiss Light Source and elsewhere, we plan for the emittance of the injected electrons to be no more than a factor of ten larger than the equilibrium emittance in the main ring, i.e., it should be less than 15 nm.

These injection charges, rates, and emittances can be achieved with either a low energy linac driving a full energy booster synchrotron or a full energy linac, and we consider both below. We conclude that there may be advantages to utilizing a full energy linac injection system and this is included in our current plans.

#### 3.4.10.1 Booster Synchrotron

If we use a booster synchrotron injection system, we envision an 800 MeV linac feeding a full energy booster for acceleration of electrons to the 3 GeV energy of the X-ray ring. The linac provides full energy injection of the IR ring as well as serving as an injector for the booster. The booster design has to provide rapid filling of the X-ray ring, flexible repetition rate and ramping profile, and meet the injection charge, efficiency, rep rate, and emittance requirements outlined above. Our preliminary design of a booster injection system that meets these requirements includes a thermionic gun, prebuncher and buncher cavities, linac, linac to booster transfer line, and booster lattice.

A gridded cathode thermionic gun can provide 1 nsec, 1.5 nC electron pulses for single bunch operation. Provision for 500 MHz modulation of long (~100 ns) macropulses for bunch-train injection to the ring will also be explored. A gridded thermionic gun has the advantage of easily varying the charge per bunch between 0.1 and 1.5 nC by varying the bias voltage, allowing the top-off charge per bunch to be continuously adjusted to achieve steady state currents.

Since the thermionic gun cannot make pulses less than 1 ns, and a linac RF bucket is a maximum of 0.33 nsec long a minimum of 3 linac bunches are created. A 500 MHz prebuncher is used to modulate the energy of the electron pulse such that a subsequent drift will create a high-density central bunch at the expense of the two outside bunches. In long-pulse operation the prebuncher acts to sweep particles away from the ends of the separatrix where there is zero bucket height, towards the center where phase errors will result in smaller energy oscillations as the off-center linac bunches undergo coherent synchrotron oscillations.

A 2.997 GHz RF buncher is used to improve the capture efficiency of the linac by moving particles away from the edges of the separatrix. This will be a few cells of 2.997 GHz structure fed either from a

small independent amplifier, or with a few kW siphoned off parasitically from the first klystron waveguide feed to a linac tank with high-power phase and amplitude control.

A linac frequency of 2.997 GHz is chosen, which is a 6<sup>th</sup> harmonic of the RF ring frequency of 499.654 MHz. It is constructed of iris-coupled traveling wave structures similar to the SLAC MK IV linac. Each tank will be driven by a 45 MW peak power klystron. Full turn injection into the booster requires a macropulse length of 500 ns, which is easy to accommodate into the flat top of the klystron Pulse Forming Network. Actual pulse length will be less due to injection and extraction kicker rise and fall times.

The requirements for the linac to booster and linac to IR ring transfer lines are very similar to those for the one at the existing NSLS. An energy analyzing slit will be placed in the bend to limit the energy. A thermionic gun cannot produce pulse lengths shorter than ~1ns, and so the booster RF bucket must accept a linac bunch train of 3 successive bunches, which are within the longitudinal acceptance of the 500 MHz booster bucket.

To achieve the desired low emittance in a compact space the booster design is based on a simple “gradient FODO cell” that makes use of a combined function dipole to provide bending and to also serve as an effective defocusing quadrupole for the cell. Dispersion suppressors are added to the arcs to produce dispersion free straight sections for injection, extraction and the RF system. Even with this compact design, the booster has a substantial circumference of 165 m.

A schematic layout of this design is shown in Figure 3.4.5. While this design meets most of the requirements, its rep rate will only be 3 Hz, which is marginal. Even at this rate, the booster is essentially

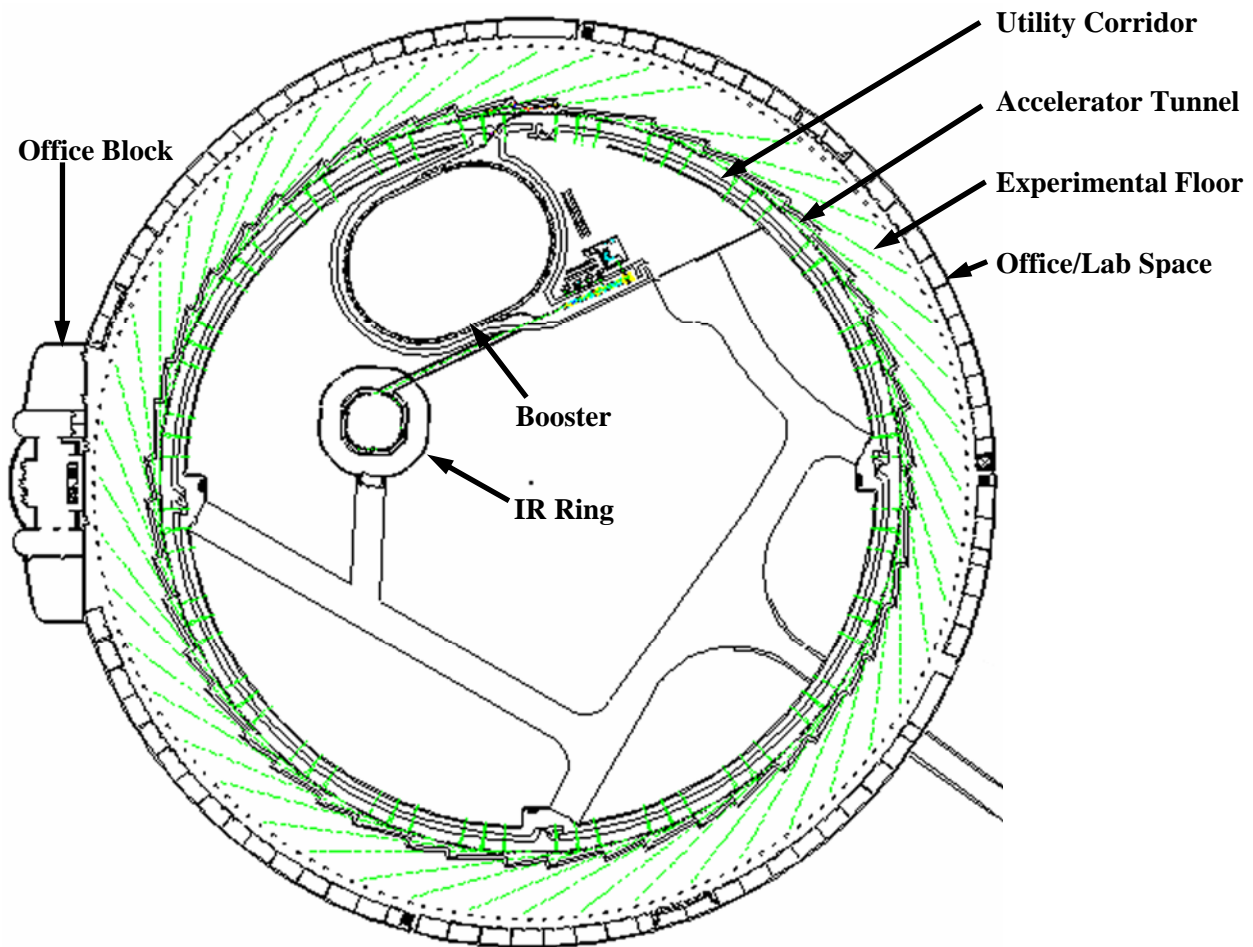


**Figure 3.4.5** Schematic of NSLS-II with a full energy booster synchrotron and linac pre-injector. The linac pre-injector also serves as a full energy injector for the IR ring.

continuously ramping, which creates increased operating cost and reliability concerns. The possibility of using multi-bunch injection to lower the injection frequency will be explored during development of the full conceptual design.

### 3.4.10.2 Full Energy Linac Injector

An attractive alternative to a booster synchrotron is a full energy linear accelerator. As shown in Table 3.2.1, two existing light sources use full energy linacs as injectors, and one of these (Pohang Light Source, PLS) uses it in the more demanding top-off mode. A full energy linac is also used as a full energy injector for three storage rings dedicated to high energy physics (KEK ATF, KEK B-Factory, PEP-II B Factory) and all of these also operate in top-off mode.

A full energy linac injector for NSLS-II has the following potential advantages:

- **Higher Rep Rate:** A linac can be operated from a few Hz up to 120 Hz with more or less the same hardware, while a booster becomes increasingly difficult for rep rates beyond a few Hz due to eddy currents in the vacuum chamber and the complexity and cost of fast ramping power supplies.
- **Better Beam Quality:** If the linac is coupled to a laser driven photoinjector that produces a 1.5 nC/bunch electron beam with a normalized emittance of 6  $\mu\text{m}$ , the geometric emittance of this electron beam at 3 GeV would be  $\sim 1$  nm, which is smaller than the horizontal emittance of the storage ring ( $\sim 1.5$  nm) and an order of magnitude smaller than the emittance from the booster presently under consideration.
- **Better Injection Efficiency:** The better beam quality discussed above will result in better injection efficiency. The KEK ATF recently demonstrated nearly 100% injection efficiency with a photoinjector/linac system. Better injection efficiency is especially important for a high current storage ring operating in top-off mode. It can provide a significantly lower radiation background during ‘shutters open’ top-off injection, resulting in minimized radiation damage to undulators and reduced shielding (and hence reduced cost) requirements.
- **Flexibility in Ring Filling Patterns:** Both single pulse and pulse train injection has been experimentally demonstrated with full energy linac injectors. Furthermore, variable fill patterns and charge/bunch can be easily implemented for the linac with a photoinjector.

Historically, a low energy linac with a full energy booster has been the choice for most light source injection systems because of its perceived advantages in cost and reliability. However, as pointed out above, these are much less compelling at the injection rates required for NSLS-II. In addition, developments in normal conducting linac technology, such as SLED, high power klystrons, and solid state modulators, make a full energy linac injector a very attractive alternative. Recent developments in photocathode RF gun technologies, especially in stability and reliability, make it compatible with storage ring operation. Diode-pumped, all solid state lasers and semiconductor, saturable absorber based passive mode locked oscillators have improved the laser system stability and reliability tremendously. Both metal cathodes (Mg) and semiconductor cathodes ( $\text{Cs}_2\text{Te}$ ) have demonstrated lifetimes of more than several months with a quantum efficiency better than 0.1%. A photocathode RF gun injector is now in routine operation for the damping ring at KEK ATF.

In view of these considerations, we see this as an attractive choice. However, we will continue to evaluate the relative merits of both booster and full energy linac injection systems as part of the conceptual design phase of the NSLS-II project.

### 3.4.11 Photon Beam Stability

To realize the benefits of the high brightness and small beam sizes of NSLS-II, it is essential that the photon beams be exceedingly stable. The stability requirements include constant intensity after apertures, constant photon energy after monochromators, and minimal photon source size and highly precise steering accuracy for focusing on small samples. These requirements directly translate to electron beam current and orbit stability (considered here) combined with stability of beamline components (considered in Section 4.1).

Disturbances with frequencies higher than the experimental sampling rate are generally less harmful since they usually average out and only linearly increase the effective emittance  $\epsilon_{\text{eff}} = \epsilon_0 + \epsilon_{\text{cm}}$ , where  $\epsilon_0$  is the emittance without noise and  $\epsilon_{\text{cm}}$  is the emittance defined by the ellipse of the centroid motion. For example, 5 % fluctuations in centroid motion and divergence results in a 0.25 % increase in effective emittance. However, when disturbances are on a frequency comparable to the sampling rate, their contribution to the effective emittance is more pronounced,  $\epsilon_{\text{eff}} \sim \epsilon_0 + 2 (\epsilon_0 \times \epsilon_{\text{cm}})^{1/2} + \epsilon_{\text{cm}}$ , so that the same 5% motion result in a 10% increase in emittance. Finally, while beam motion on timescales longer than the duration of an experiment have little effect on it, reduction of such motions is still desirable in order to eliminate or reduce realignments.

From these considerations we arrive at our stability requirements of no more than 10% beam motion, both positional as well as angular, particularly in the frequency range from  $\sim 10$  mHz to 1kHz. For the current NSLS-II design parameters, this implies that the rms beam position is stable to within 5 (0.4)  $\mu\text{m}$  and the rms beam angular direction is stable to within 3 (0.4)  $\mu\text{rad}$ , in the horizontal (vertical) directions, respectively.

Achieving the requirements for NSLS-II will require advancing the state of the art, with improved construction and feedback stabilization techniques. However, NSLS is well qualified to accomplish this. NSLS has a rich history of accomplishments in the area of orbit stability, including the invention of switched beam position monitor (BPM) receivers, global orbit feedback, novel compensation techniques for fast switching IDs, and pioneering developments in digital orbit feedback, among others. The digital orbit feedback systems we have recently implemented have the world-highest update rate and correction bandwidth, and maintain the vertical beam position stable to within a few microns in a 0.25-150 Hz bandwidth.

Common sources of orbit motion that must be overcome include: ground motion; floor vibrations due to in-house machinery; thermally induced motion of ring components; injector induced electrical noise; magnet power supply noise; and the effects of a large number of independently controlled IDs (including some that are fast switching). Fortunately, due to extremely well settled glacial sands, ground stability at the proposed NSLS-II site is extremely good, and is definitely superior to that at many existing light sources. This applies both to the natural settlement/noise as well its ability to damp noise sources such as vehicular traffic.

Top-off operation of NSLS-II will be essential in providing good beam stability on slower timescales. Some of the major benefits of topoff injection for stability include: constant heat load on beamline optics and ring components; elimination of magnet ramping and associated effects (heat transients, hysteresis, eddy current induced stresses and mechanical motion, etc); and relaxed requirements for BPM accuracy versus beam current.

One drawback that accompanies topoff injection is a constantly running injection bump that can never be perfectly closed. For example, at the Swiss Light Source, the residual vertical orbit distortion in the undulators is  $\sim 30 \mu\text{m}$ . This motion is present only with the bump on and dies away on the timescale of a damping time when the bump is off, so its contribution to the orbit stability to a large extent averages out. Nevertheless, NSLS-II will likely have to employ sophisticated active compensation systems to reduce or minimize the residual beam motion elsewhere in the ring.

At this point, the most significant orbit stability issue for the NSLS-II appears to be the ability to measure extremely small orbit motions. This will require novel BPMs with full bandwidth resolution of

0.1  $\mu\text{m}$  or better, as well as mechanical innovations for BPM mounting (starting from the girders and up). Reducing thermal expansion of ring components such as BPM mounting stands to acceptable levels will require maintaining the temperature in the storage ring tunnel to 0.1° C or better. Minimizing vibrations will require techniques such as designing mechanical components to avoid low frequency resonance modes, using viscoelastic dampers, and using girders to support entire sections of the ring components.

Advanced orbit position measurement techniques and advanced mechanical construction techniques will enable sophisticated feedback/feedforward systems. In addition to electron beam parameters and accelerator settings, these systems will monitor and control mechanical motions of various accelerator and beamline components. Together, these approaches will achieve the required beam position and angular stability at NSLS-II.

### 3.4.12 Insertion Devices

#### 3.4.12.1 High-Energy Undulator Sources

The most challenging requirements for high energy undulators come from programs that require high brightness, narrow-band, tunable, multi-kilovolt X-rays. Ideally, these photon energy ranges should be obtainable from undulators using the fundamental mode and the first few (odd) harmonics in overlapping bands, with no gaps in the coverage. However, with existing or anticipated magnet technologies, the requirement of fundamental resonance at 5 keV with wide tunability can be met only for electron beam energies of 6 GeV or higher (as at APS, ESRF and Spring8). In a medium-energy storage ring, tunable radiation at energies above 5 keV can be obtained from an undulator with a lower fundamental resonance energy, using its higher harmonics.

Insight into these constraints can be elicited from a few basic relationships governing planar undulators. The resonant fundamental wavelength,  $\lambda_1$ , of a planar undulator is given by

$$\lambda_1 = (\lambda_u / 2\gamma^2)(1 + K^2/2)$$

where  $\lambda_u$  is the undulator period,  $\gamma$  is the relativistic factor,  $B_0$  is the peak magnetic field, and the K factor is given by

$$K = 0.934 \lambda_u [\text{cm}] B_0 [\text{Tesla}]$$

The resonance condition can alternatively be expressed in terms of the fundamental photon energy:

$$E_1 [\text{keV}] = 1.24 / \lambda_1 [\text{nm}] = 2.48 \times 10^{-7} \gamma^2 / [\lambda_u [\text{cm}] (1 + K^2/2)]$$

For 3 GeV electrons ( $\gamma = 5871$ ) and K of order 1, to obtain  $E_1 = 5$  keV would require an undulator period,  $\lambda_u$ , on the order of 1 cm. In fact, the first in-vacuum undulator (IVUN) installed at NSLS did have a period of 1.1 cm. However, a second key requirement for undulators is tunability, embodied in the factor  $(1 + K^2/2)$ , which varies with the magnetic field. For full spectral coverage between the fundamental and third harmonic this factor must vary by 3:1 for  $K_{\min} \leq K \leq K_{\max}$ . Since useful radiated power is only obtained for  $K_{\min} \geq 0.5$ , a 3:1 tuning range requires  $K_{\max} \geq 2.2$ . Thus, if we want the lowest energy of the tuning curve of the undulator fundamental to be 5 keV when  $K = 2.2$ , then we need a period of 0.5 cm. With this period, we then need a peak field of  $B_0 = 1.66$  Tesla in order to reach  $K = 2.2$ . To achieve such a high field with any currently available technology would require an unrealistically small magnetic gap on the order of 1 mm! At NSLS, both IVUN and its successor, the Mini-Gap Undulator (MGU), operate at an unprecedented minimum gap of 3.3 mm, which is permitted by an unusually small beta function (0.3 m).

Current lattice designs for NSLS-II call for a larger beta function (2.4 m) in the center of the straight. For undulators of length 5 m, a safe vertical stay-clear aperture of 5 mm has been specified. No existing technology can produce a (DC) magnetic field of 1.66 Tesla in a planar periodic structure with 0.5 cm period and 0.5 cm gap. However, if we allow a longer period of 1.4 cm or more, we can obtain both higher fields and adequate tunability, but with a lower fundamental energy. The 5-20 keV range may then be covered by the third and higher harmonics. We next describe two candidate undulator designs, one based on proven in-vacuum permanent magnet technology and the other on still-developing superconducting technology.

### 3.4.12.2 In-Vacuum Permanent Magnet Undulators

NSLS pioneered in-vacuum permanent magnet (PM) undulator technology nearly a decade ago. By placing the magnet arrays inside the vacuum envelope, the conventional vacuum chamber can be removed and the magnet gap can be reduced to the minimum stay-clear aperture. Since the peak undulator field increases exponentially as the ratio of the gap to period,  $g/\lambda_u$ , decreases, the period can also be reduced, raising the fundamental energy. Short-period, small-gap, in-vacuum PM undulators have thus brought kilovolt-level photon sources to medium-energy storage rings. Both pure-PM and PM-hybrid in-vacuum undulator designs are in service in many storage rings around the world. PM-hybrid (employing high-permeability poles driven by PM's) in-vacuum designs offer higher fields than pure-PM, and they have been proven in NSLS Mini-Gap Undulators (MGUs) and elsewhere.

For 5-20 keV coverage, we can allow the third harmonic to start at 5 keV. The lower fundamental energy,  $E_1$ , is then 1.67 keV. We may further relax the tunability requirement by allowing a gap between the first and third harmonics and only requiring continuous coverage between higher harmonics starting with the third harmonic. This reduces the necessary tuning range to 1.67:1, which can be obtained with  $K$  varying between 0.5 and 1.32. This constraint leads to  $\lambda_u \leq 2.7$  cm.

A second constraint comes from achievable field with a given  $g/\lambda_u$  ratio. An updated version [2] of the Halbach design formula for peak field in a PM-hybrid undulator using modern NdFeB permanent magnets is

$$B_0 = 3.694 \exp [ -5.068 (g/\lambda_u) + 1.52 (g/\lambda_u)^2 ]$$

From this, we obtain a realizable PM-hybrid undulator design, designated MGU-19, with 19 mm period, 5 m length, and peak field of 1.06 T, giving a  $K_{\max}$  of 2.24. The fundamental covers 1.63 to 4.0 keV, a tuning range of 2.44:1. However, continuous tuning is obtained from 4.9 to over 20 keV, using the third through eleventh harmonics. This model has been verified with the 3D magnetostatics code Radia.

In-vacuum MGUs can be tailored to other energy ranges as well. Another example, designated MGU-21, has a 21 mm period, 5 m length, peak field of 1.14 T and  $K_{\max}$  of 2.24. This gives a tuning range of 3.13:1 and does provide full coverage from 1.15 to over 10 keV using the fundamental through the seventh harmonic.

Yet another option is an MGU optimized to maximize the brightness at a particular energy, e.g., 8 keV. A device with period length of 17.5 mm and 5 m length, designated MGU17.5, reaches 8 keV with the third harmonic. The shorter period allows more periods in a nominal 5 m length, giving higher brightness. A smaller  $K$  may be acceptable, since wide tunability is presumed to not be a requirement.

The reliance on high harmonics (up to the eleventh) puts a premium on magnetic field quality, requiring optical phase error of  $<2$  degrees rms at the fundamental to prevent degradation of brightness of the highest harmonics. We have achieved this level of phase error in the short MGU now installed in the X13 and X29 straights. This level of field quality has also been achieved in longer ID's at other institutions, so it is within the state-of-the-art.

### 3.4.12.3 Consideration of Radiation Damage in Permanent Magnets

The very low emittance lattices being considered for NSLS-II will have higher beam losses due to lower Touschek lifetimes than the present X-ray ring. The small-gap, in-vacuum MGUs can be expected to intercept a significant fraction of the scattered electrons. Most will be blocked by electron and gamma absorbing apertures placed just upstream of the MGUs. Nevertheless, experience with degradation of permanent magnets reported at APS and ESRF requires that beam loss rates be kept to a minimum, even with the availability of top-off injection.

To deal with permanent magnet degradation, ESRF has abandoned NdFeB in favor of  $\text{Sm}_2\text{Co}_{17}$  for in-vacuum undulators because of its higher radiation resistance. The designers of DIAMOND are following the ESRF lead. Unfortunately,  $\text{Sm}_2\text{Co}_{17}$  has a remanence ( $B_r$ ) of  $\sim 1.05$  T, compared to 1.2 to 1.3 T for NdFeB grades currently used in our MGUs and in many out-of-vacuum undulators. Such a low value of  $B_r$  would be insufficient to realize the MGUs we are proposing.

Sumitomo Special Metals recently reported their experimental measurement of demagnetization of their type 35EH NdFeB magnets (a high  $H_{ci}$  grade used in Spring-8 in-vacuum undulators) when exposed to a 2 GeV electron beam at the Pohang injection linac. After a standard pre-bake at  $142^\circ\text{C}$  for 24 hours, the samples showed a 0.4 % field loss after exposure to  $10^{15}$  electrons. The decrease was linear with exposure. Without pre-bake the losses were even higher. The loss appears to be thermal-like. Experts on permanent magnets in the BNL Materials Science Department confirm that demagnetization by electrons and gammas is probably thermal and, in principle, reversible. (Re-magnetization is, of course, impractical in an assembled undulator, unless one disassembles it and re-magnetizes each magnet individually.)

In another study, Sumitomo found that type 27VH, a super-high  $H_{ci}$  grade of NdFeB, degraded about 0.1% at the same exposure, similar to  $\text{Sm}_2\text{Co}_{17}$ . Both 27VH and  $\text{Sm}_2\text{Co}_{17}$  have a remanence of 1.05 Tesla, and similar values of  $H_{ci}$ . We can expect that NdFeB with high values of  $H_{ci}$  will exhibit equally high radiation resistance as  $\text{Sm}_2\text{Co}_{17}$ .

Fortunately, the mature NdFeB material technology is continuing to improve. Sumitomo Special Metals recently announced the AH series of materials that offer  $B_r > 1.3$  T with intrinsic coercivity ( $H_{ci}$ ) comparable to  $\text{Sm}_2\text{Co}_{17}$ . We therefore expect we can realize the high-performance, radiation resistant, in-vacuum undulators discussed in this proposal.

### 3.4.12.4 Superconducting Undulators

While the PM based MGUs described in Section 3.4.12.2 meet many of the requirements for NSLS-II, even higher brightness would be possible if the period could be reduced further while still maintaining sufficiently high magnetic field to ensure full tunability. The goal of high brightness and full tunability from the fundamental through the higher harmonics in the 2 to 20 keV spectral range may be achievable with superconducting undulator technology. R&D on superconducting undulators was carried on at the NSLS during the 1990's, in connection with the Superconducting High-Gain Harmonic Generation experiment (collaboration with Grumman Corp) and a Visible Free-Electron Laser project. Superconducting undulator with periods of 26, 18 and even 8.8 mm were built and tested. Figure 3.4.6 shows sections of the 18 mm and 8.8 mm period superconducting undulators.

Recent superconducting undulator designs, derived from this basic concept, have been prototyped at ANKA, LBL and APS. An ANKA innovation is a bifilar helical winding configuration that avoids the multiple  $180^\circ$  bends in the conductor to reverse the winding direction from slot to slot. ACCEL GmbH is now building full-scale superconducting undulators with this design for the Singapore and ANKA light sources

We have used Radia to analyze a magnetic model of a superconducting undulator. The truncated windings are magnetically equivalent in both the parallel and bifilar configurations, as far as field in the gap is concerned. From the model, we find that a period of 14 mm, a gap of 5 mm and an average current density  $J_c$  of  $1300\text{ A/mm}^2$  will give 1.6 T peak field, for a K value of 2.28, sufficient for 3:1 tuning range

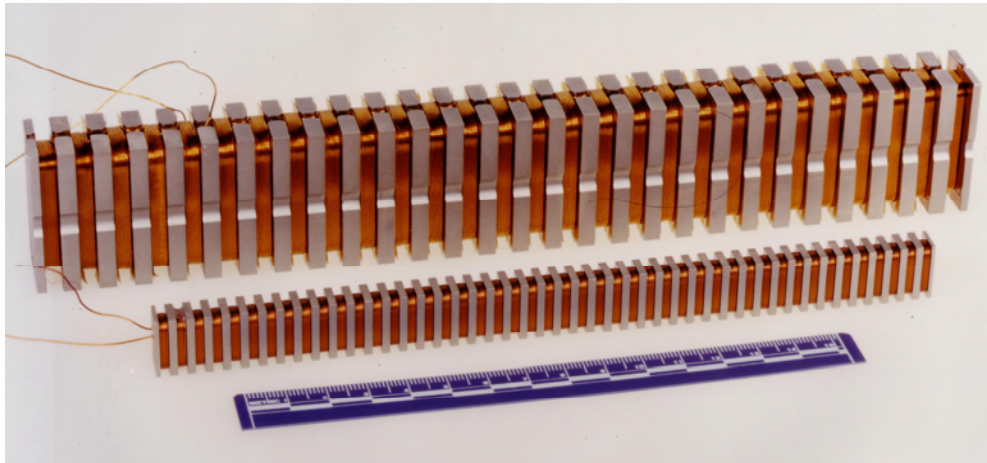


**Figure 3.4.6** Sections of superconducting undulators built at NSLS in the 1990's. The superconductor is wound in machined slots around the iron yokes. The windings are continuous, reversing direction from slot to slot to generate a field of alternating polarity in the iron poles. A pair of such windings facing each other forms an undulator.

and full spectral coverage. The fundamental energy is 1.58 keV. For coverage of 2 to 20 keV we can utilize the first through the ninth harmonics. The 5 mm gap assumes a thin foil barrier between machine vacuum and insulating vacuum.

An average  $J_c$  of  $1,300 \text{ A/mm}^2$  is near the limit for conventional NbTi conductors. Higher  $J_c$  may be

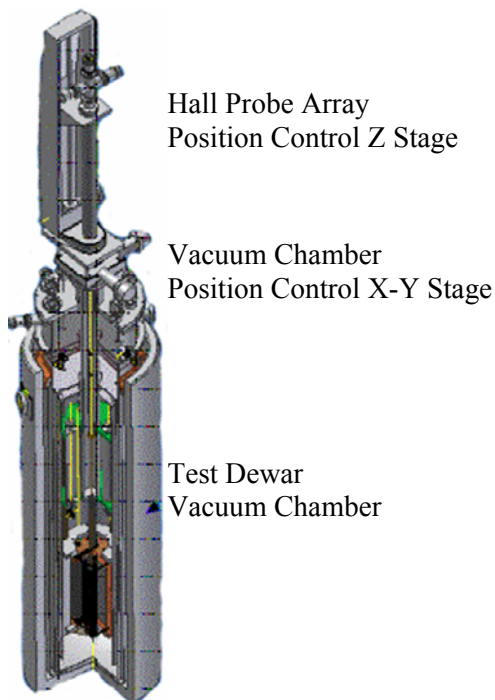


**Figure 3.4.7** (left) Drawing of measurement apparatus for short superconducting undulator models, shown with the Hall probe mapping insert. An interchangeable pulsed wire insert is also being designed. Three helium calorimetric circuits are included for detailed heat loss measurements. (right) Photo of measurement apparatus in assembly stand.

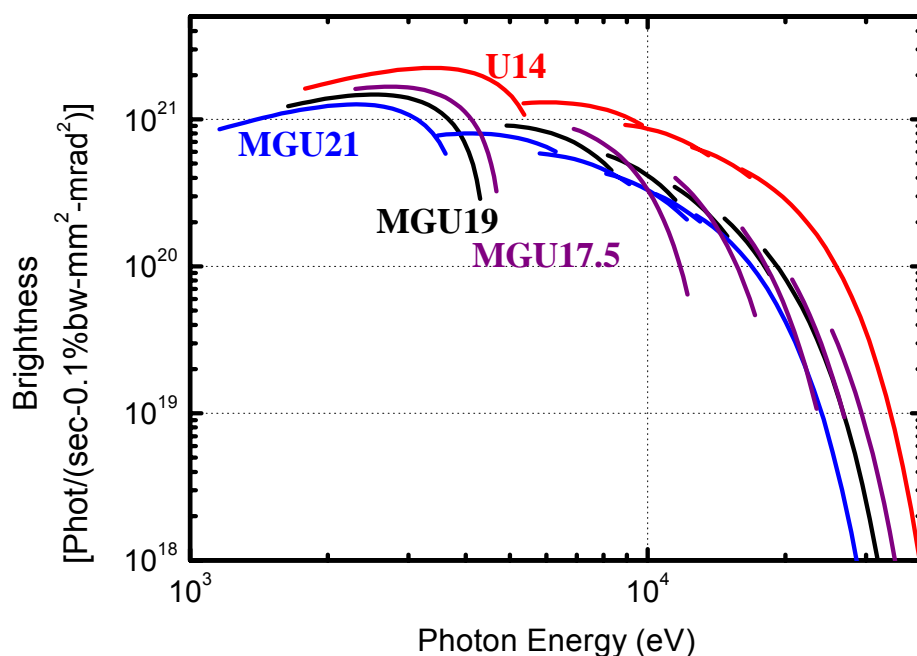


**Figure 3.4.8** Relative performance of the superconducting undulator, U14, compared to that of the permanent magnet undulators MGU17.5, MGU19, MGU21. The superconducting undulator is both brighter and continuously tunable from 2 to more than 20 keV. The first through ninth harmonics are shown for U14 while the first through eleventh harmonics are shown for the MGU devices.

obtained in NbTi with artificial pinning centers (APC-type), but it is not yet available commercially. NbSn<sub>3</sub> is also capable of higher J<sub>c</sub>, and practical conductors are becoming available. We will explore conductor options jointly with the BNL Superconducting Magnet Division.

NSLS is continuing its superconducting undulator R&D effort. We are now constructing a magnetic measurement apparatus for magnetic measurement of short superconducting undulator models by both Hall probe and pulse wire techniques. The apparatus will contain calorimetric instrumentation. Both immersion in liquid helium and conduction cooling can be accommodated. It will fit into an existing dewar that we previously used to test our early superconducting undulator models. A schematic drawing and photo of the apparatus is shown in Figure 3.4.7. NSLS is collaborating with BNL's Superconducting Magnet Division, to draw on their expertise and vast experience in superconducting magnet design and construction. Testing and measurement of superconducting undulator models will be performed in the Magnet Division's cryogenic test facilities.

The brightness of a 5 m long superconducting undulator with 14 mm period, designated U14, is compared in Figure 3.4.8 against that of the permanent magnet undulators discussed in Section 3.4.12.2. It is clear that the superconducting undulator is both brighter, by virtue of having shorter periods and hence more periods in a given length, and continuously tunable.

While permanent magnet undulators are today's state of the art, superconducting undulators are tomorrow's state of the art and will be developed as part of the NSLS-II project. The brightness and flux curves for U14 on NSLS-II are shown in Figures 3.3.3 and 3.3.4.

### 3.4.12.5 Soft X-ray Undulators

Several options are being studied as soft X-ray sources in the 0.2-2 keV range. They include both conventional planar, quasi-periodic and variable polarization undulators. These will be out-of-vacuum

devices. APS-type extruded vacuum chambers may be used, having 5 mm vertical aperture. Allowing for 1 mm chamber walls and 0.5 mm clearance, the minimum magnetic gap for a 6 m long device will be about 8 mm. Extrusions with larger apertures are available for longer ID's.

A conventional planar PM-hybrid undulator with a 40 mm period and 8 mm gap can produce a peak field of 1.27 Tesla for a peak K of 4.7 and fundamental energy of 0.2 keV. A 6 m long device would have 150 full periods. The fundamental, third and fifth harmonics would be used to cover the 0.2-4 keV range. This device is designated U40. Its brightness and flux curves on NSLS-II are shown in Figures 3.3.3 and 3.3.4.

Alternatively, if a somewhat higher energy is range is desired, a similar 6 m long planar PM-hybrid undulator, but with 28 mm period instead of 40 mm period, designated U28, would provide fully tunable high brightness radiation from 0.3 keV to ~ 7 keV from its fundamental, third and fifth harmonics. The brightness and flux of this device on NSLS-II is also shown in Figures 3.3.3 and 3.3.4.

The quasi-periodic undulator (QPU) has the interesting property that higher harmonics are shifted away from integer multiples of the fundamental. This may make it easier to separate higher orders in a monochromator. A pure-PM structure is employed. The quasi-periodicity can be realized in several ways. For example, selected axially polarized magnets may be shorter, or they may be retracted to locally increase the gap.

Variable-polarization undulators come in several varieties. The APPLE-II undulator can provide linear, right- and left circular, as well as any degree of elliptical polarizations. This is accomplished by splitting the conventional pure-PM arrays longitudinally and moving ("phasing") diagonally opposite semi-arrays longitudinally relative to their partners. The lowest energy is reached in the planar, horizontally polarized mode (phase = 0). For other phases that produce elliptical, circular (phase = 90°) and vertical (phase = 180°) polarization modes, the on-axis fields are reduced, so the fundamental resonance occurs at higher energies.

### **3.4.12.6 Ultraviolet Sources**

For vacuum ultraviolet users requiring ten to several hundred eV photons, undulators with very large K values are necessary. The high K also results in very high radiated power in higher harmonics that has to be absorbed by the first optical element in a beamline. The Figure-8 undulator design displaces the radiation of all harmonics above the fundamental off-axis, allowing the possibility of absorbing the unwanted harmonics in a suitable beamstop, while allowing the fundamental to pass through the central aperture. A Figure-8 undulator with 10 cm period can provide photons from 10 to 300 eV in the fundamental. Such a device, 6 m in length and with 10 cm period, is designated U100. Its brightness and flux curves on NSLS-II are shown in Figure 3.3.3 and 3.3.4.

### **3.4.12.7 Superconducting Wigglers**

The highest energy photons (up to 100 keV) are produced by very high field, superconducting wigglers. The radiation is broadband with very high power. Such devices are available commercially with a peak field of up to 5 Tesla. A 1 m long superconducting wiggler with 60 mm period is designated W60. Its brightness and flux curves on NSLS-II are shown in Figures 3.3.3 and 3.3.4.

## **REFERENCES**

- [1] Wolski, S. de Santis, Proceedings of EPAC 2002, 524, Paris, France (2002).
- [2] P. Elleaume, Nuclear Instruments and Methods, A455, 503-523 (2000).

## 3.5 Future Upgrade Opportunities

### 3.5.1 Storage Ring Upgrades

At the present time an electron storage ring is the best steady state source for synchrotron radiation, yielding both high brightness as well as high flux. Most existing storage ring light sources have evolved along several upgrade pathways such as:

- top-off operation
- emittance reduction through the introduction of dispersion into the insertion device straight sections
- richer complement of insertion devices
- higher currents
- longer straight sections

The NSLS-II machine design concept currently incorporates all of these features except the second. Introduction of dispersion in the straight section, which might potentially lower the emittance from 1.5 to  $\sim 1$  nm, will be explored as the lattice design matures. In addition, as discussed in Section 3.4.6, 20 small gap insertion devices are likely to further damp the beam, lowering the emittance. Together, these suggest that it is likely that we will be able to achieve the world's first sub-nm emittance light source.

However, for a major upgrade a new avenue must be pursued. We are exploring the possibility of a converting the storage ring to an energy recovery linac mode of operation in the future as that technology becomes available and mature.

### 3.5.2 Compatibility with Future Upgrade to Operation as an Energy Recovery Linac

The state of the art NSLS-II is being optimized first and foremost to operate as an ultra high brightness electron storage ring. However, we are exploring the possibilities of upgrading the NSLS-II to an ERL in the future if and when the technology has proven itself and the performance characteristics of the ERL are suitable for our user community.

To function as an ERL, a superconducting linear accelerator would have to be introduced into the NSLS-II complex. Figure 3.5.1 is a schematic illustration of how this might be done in a manner that minimizes the impact on the operation of the NSLS-II storage ring and has the electron beam traversing the linac in the same direction for both acceleration and deceleration as is done in the present generation of ERL prototypes. In addition to the superconducting linac, a recirculating loop consisting of two arcs and transport lines to and from the storage ring would be required, as well as a photoinjector electron source. In this configuration nearly all the beamlines of the NSLS-II could be used "as is" and additional very long insertion devices, able to benefit from the potentially reduced energy spread of an ERL could be added into the recirculating loop.

Some of the technical challenges presented by such an upgrade scheme that will be explored further during the conceptual design phase of the NSLS-II project include:

- the storage ring components (vacuum chamber, IDs, etc) must be capable of accommodating the inherently shorter bunches in an ERL ( $\sigma \leq 1$  psec) without damaging the ring or degrading the quality of the electron beam, e.g., heating of small gap IDs in particular superconducting undulators, energy spread increases due to wakefields, coherent synchrotron radiation in the arcs, etc.,

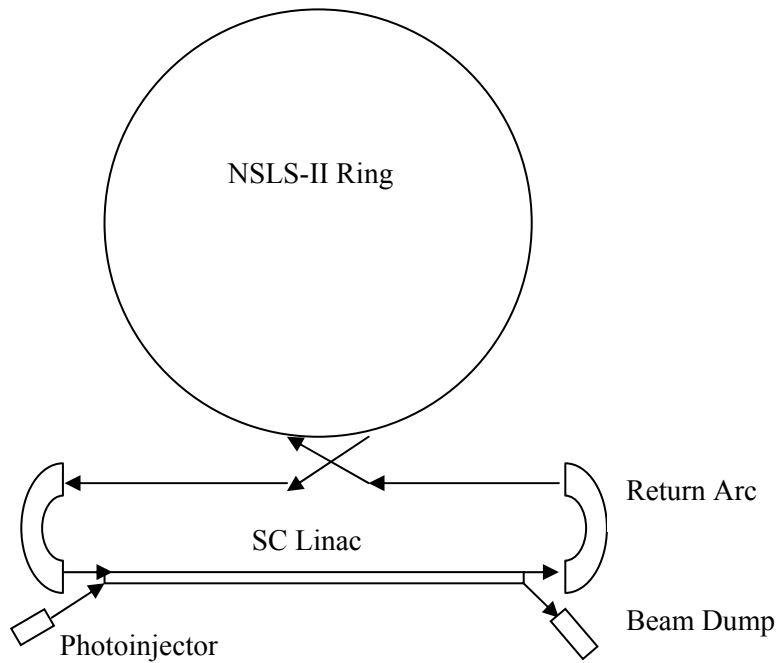


**Figure 3.5.1** Schematic illustration of the general approach which might be used to upgrade the NSLS-II storage ring in the future to operate as an Energy Recovery Linac.

- the storage ring lattice must have the flexibility to vary the linear and nonlinear momentum compaction in order to control the longitudinal phase space of the ERL beam,
- the shielding and safety systems of the ring must be able to accommodate the “infinite source of charge” characteristic of an ERL,
- the possibility of a “multiturn ERL” in which the beam is kicked into the ring to fill it with charge that is then stored for a fraction of a damping time (a few hundred turns) before being kicked out of the ring and energy recovered; if feasible, this mode of operation can greatly reduce the demand on the photoinjector.

### 3.6 Facility Siting and Compatibility with BNL's Master Plan

Since NSLS-II is designed to be at the state of the art in terms of photon beam brightness, stability is a significant factor in selecting the site. Because it will be the locus for many lines of cross-disciplinary research at BNL, locating the facility in close proximity to the core research departments is also very valuable. NSLS-II will be a fairly large structure. The preliminary design envisions a building with nearly 350,000 gross square feet (GSF) and a building envelope about 800 feet in outside diameter. Taken together, these factors favor a site just to the southwest of the present NSLS building, as shown in Figure 3.6.1.

The entire area is relatively flat, with less than 20 feet in elevation change from one end to the other. Most of the area is at the same grade within 4 feet of the same elevation, so excavation and filling can be minimized. The soil is undisturbed glacial till, and has few existing utilities running through the area. Locating the building 50 to 100 feet south of Brookhaven Avenue (as shown) is beneficial from the standpoint of minimizing road induced vibration.

The proposed area for NSLS-II is free of any other anticipated program encumbrances. While the 2000 BNL Site Master Plan did not specifically anticipate NSLS-II, it did establish a framework for the development of future scientific buildings, such as the Center for Functional Nanomaterials and NSLS-II, and identified the area shown in Figure 3.6.1 for that development. The BNL Site Master Plan is currently being updated to reflect the intended location of NSLS-II shown in Figure 3.6.1.

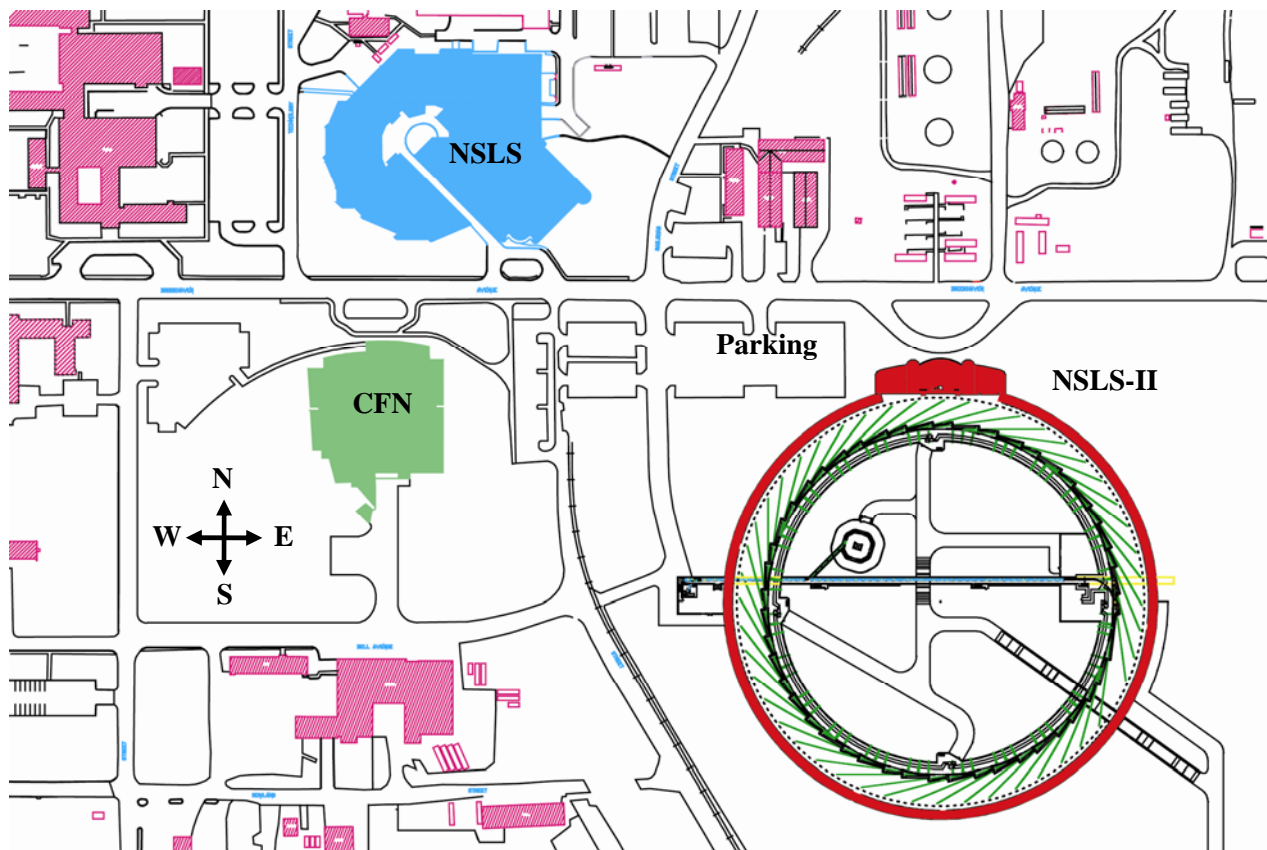


**Figure 3.6.1** Preliminary siting of NSLS-II (outlined in red), located to the southeast of the current NSLS building (in blue) and just east of the BNL Center for Functional Nanomaterials (CFN) (in green). The area to the south and east of NSLS-II is vacant and available if extra long beamlines extending out from NSLS-II are desired. The Physics, Chemistry, Materials Science, Biology, and Medical Departments and the Instrumentation Division are all nearby.

## 4 Experimental Facilities

Fully capitalizing on the superlative performance of NSLS-II will require equally advanced beamlines and optimized and unique endstation instrumentation. In this section, we outline our current plans for beamlines, sample environments, automation and robotic control of beamlines and endstation hardware, and advanced detectors. In each area, there are challenges associated with utilizing the full performance of NSLS-II. For example, advances in mirror technology and nanoprobe optics, as well as advanced, efficient, high throughput, area detectors, are necessary to take full advantage of the high brightness and high flux of NSLS-II. There are a number of developments which hold great promise for providing these advanced capabilities and these are also discussed.

### 4.1 Beamlines

We have developed a preliminary estimate of the type and number of insertion device beamlines which will be necessary to satisfy the needs of the science programs outlined in Section 2. These are shown in Table 4.1.1 and indicate that NSLS-II will be able to support a sufficient number and variety of beamlines to support a large and diverse scientific program well matched to that described in Section 2.

We have included provision for four complete insertion device beamlines in the initial NSLS-II project, including front-ends and undulators. It is expected that the rest of the beamlines will be developed in response to scientific proposals from the user community. These proposals will be selected based on scientific merit and will define the scientific mission of a beamline and the requirements that the beamline and endstation instrumentation must meet in order to fulfill that mission. Some of these beamlines are likely to be built and operated by the users but the majority is expected to be built and operated for the user community by the facility.

The science programs supported by NSLS-II have widely varying requirements for the photon energy range and control of the photon polarization. There is no single insertion device which can satisfy all of these requirements, and so it is essential that the insertion device be thought of as part of the beamline in order to provide an optimum photon spectrum. As outlined in Section 3.4.12, there are several types of insertion devices to choose from that are optimized to provide differing energy ranges and polarization capabilities. Thus, the rest of the insertion devices and associated front ends for the remaining beamlines beyond the initial four mentioned above will be included as components of the individual beamline construction projects.

Type of Beamline	Number
Macromolecular Crystallography	5
X-ray Microdiffraction	1
Materials Science/time-resolved	1
Resonant/Magnetic Scattering	1
Soft X-ray	4
Coherent X-ray Scattering	1
Small Angle X-ray Scattering	1
Inelastic X-ray Scattering	1
Superconducting Wiggler (High Energy)	2 (Split into 6 tandem beamlines)
To Be Determined	4
<b>TOTAL</b>	<b>21</b>

**Table 4.1.1** Preliminary insertion device beamline plan. Each beamlines may have multiple hutches, some of which may be able to operate in tandem, simultaneously. This plan assumes a single insertion device beamline per straight section. However, the possibility of chicaning two undulators in a single straight section to provide photons to two independent beamlines per straight will also be investigated.

## 4.1.1 X-ray Beamlines

### 4.1.1.1 X-ray Scattering/Crystallography Beamlines

The ultra-low emittance of NSLS-II in combination with 5m long 14 mm-period superconducting undulators (undulator U14) will provide a very intense and well-collimated source of X-rays that are ideal for X-ray scattering and crystallography applications. The small angular divergence of the X-ray beam emitted by NSLS-II undulators will allow the collection of the entire photon beam with a relatively compact Kirkpatrick-Baez (KB) mirror assembly. For example, at ~30 m from an undulator source, the width of the horizontal fan of X-rays will only be ~ 2.4 mm [ $4\sigma$ ] and an 80 cm long horizontally focusing mirror will intercept the full beam at a grazing incidence angle of 3 mrad. These optics will allow the X-rays to be focused onto small crystals that are a few tens of microns in diameter with relatively small convergence angles (<100  $\mu$ rad vertically). Using typical mirror coatings, e.g., rhodium or platinum, X-ray energies up to and surpassing 30 keV will be covered with very high photon intensity at this grazing angle. For comparison, this mirror acceptance is simply not possible on an undulator or wiggler beamline on the existing NSLS X-ray ring. At best, such a mirror could intercept only about 15 % of the horizontal beam fan.

We expect that all NSLS-II macromolecular crystallography beamlines will employ undulator sources, allowing coverage of photon energies up to 30 keV with unprecedented brightness. The NSLS-II shield wall will be positioned at 25 meters from the source point, and our preliminary design is to position the monochromator/slit/filter assembly (double or four-bounce crystal monochromator based either on cryogenically-cooled silicon crystals or water-cooled diamond crystals) immediately thereafter, followed by a KB focusing mirror assembly. The KB mirrors will be outfitted with dynamical curvature adjustments that will allow them to produce a micro-focus X-ray beam over a range of demagnifications from approximately 2:1 to ~10:1, depending on experimental requirements. The parameters of the KB mirror system are given in Table 4.1.1 and the optical arrangement is shown in Figure 4.1.1. A long experimental hutch will be used to provide sufficient space for a diffractometer and area detector, and will allow the instrument to translate along the beam path to permit use of different demagnifications while maintaining the sample at the focal position.

The expected “real world” performance of an NSLS-II undulator X-ray crystallography/scattering beamline employing a Si(111) double crystal monochromator and KB focusing optics is shown in Table 4.1.2. Blurring of the focal spot (calculated by ray tracing) due to an assumed mirror figure error of 0.5  $\mu$ rad and transmission losses due to the monochromator, mirrors, and beamline windows have all been included in the estimated performance of the NSLS-II beamline in order to compare it to actual measured

Mirror Coating	Rhodium and/or Platinum			
Grazing Incidence Angle	3 mrad			
Operating Energy Range	~ 3 – 30 keV			
Efficiency of KB system at 12 keV	90% (Rh coating), 75% (Pt coating)			
VFM Length	30 cm			
HFM Length	80 cm			
	<u>High Demagnification Mode</u>		<u>Low Demagnification Mode</u>	
VFM (undulator-mirror distance, 30 m)	Focal Length	5 m	Focal Length	12 m
	Demagnification	6:1	Demagnification	2.5:1
HFM undulator-mirror distance, 31 m)	Focal Length	4 m	Focal Length	11 m
	Demagnification	7.75:1	Demagnification	2.8:1

**Table 4.1.1** KB system parameters for NSLS-II X-ray scattering/crystallography beamline. VFM is vertical focusing mirror, HFM is horizontal focusing mirror.

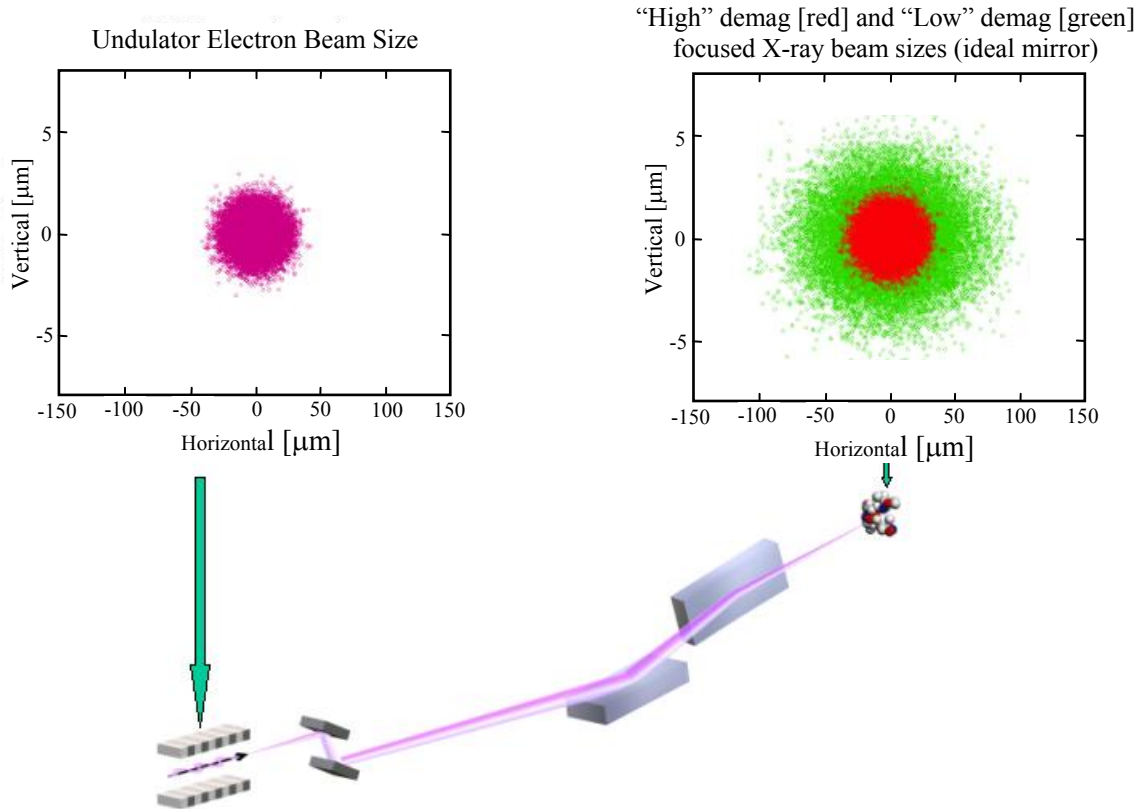


**Figure 4.1.1** Optical arrangement of the KB mirror system for an NSLS-II superconducting undulator X-ray scattering/crystallography beamline. Top-left plot: electron source dimensions. Top-right plot: high demagnification (red) and low demagnification (green) focused X-ray beam dimensions for ideal KB mirrors. A two bounce monochromator is placed upstream of the KB mirrors to enable energy selection.

performance of beamlines at existing facilities. The existing beamlines listed for comparison in Table 4.1.2 are the NSLS X25 wiggler beamline, the new NSLS X29 undulator beamline that is under construction, and a typical “Undulator A” (UA) macromolecular crystallography beamline at the APS [1]

Undulator/Wiggler	NSLS X25	NSLS X29	APS UA	NSLS-II
Monochromatic flux at 12 keV (ph/sec)	$3 \times 10^{12}$	$3 \times 10^{12}$	$1.5 \times 10^{13}$	$2.4 \times 10^{14}$
Energy resolution w/ Si(111) (eV)	12	4	1.8	1.8
Vertical focus size, FWHM ( $\mu\text{m}$ )	200	100	30	11.9/28.5
Horizontal focus size, FWHM ( $\mu\text{m}$ )	700	250	60	27/77.5
Vertical convergence angle (mrad)	0.15	0.2	0.1	0.17/0.07
Horizontal convergence angle (mrad)	1.0	1.0	0.35	0.58/0.22
Monochromatic intensity at 12 keV (ph/sec/ $\mu\text{m}^2$ )	$2 \times 10^7$	$1.2 \times 10^8$	$8 \times 10^9$	$7.5 \times 10^{11}/1.1 \times 10^{11}$

**Table 4.1.2** Expected “real-world” performance of an NSLS-II X-ray crystallography/scattering beamline (including  $0.5 \mu\text{rad}$  mirror figure error and transmission losses for the monochromator, mirrors, and beamline windows) and comparison with actual performance of existing beamlines at the NSLS and APS. The expected performance for NSLS-II in both high and low demagnification modes of operation of the KB assembly is shown as high/low values.

RMS mirror figure error [ $\mu\text{rad}$ ]	0.0	0.1	0.5	1.0	2.0
Vertical focus size, FWHM ( $\mu\text{m}$ )	1.7 / 4.0	2.9 / 6.9	11.9 / 28.5	23.6 / 56.5	47.0 / 112.9
Horizontal focus size, FWHM ( $\mu\text{m}$ )	25.7 / 70.5	25.7 / 70.7	27.3 / 75.1	31.8 / 87.5	45.5 / 125.2
Monochromatic intensity at 12 keV ( $\text{ph}/\text{sec}/\mu\text{m}^2$ )	$5.5 \times 10^{12}$ / $8.5 \times 10^{11}$	$3.3 \times 10^{12}$ / $5.0 \times 10^{11}$	$7.5 \times 10^{11}$ / $1.2 \times 10^{11}$	$3.3 \times 10^{11}$ / $5.0 \times 10^{10}$	$1.1 \times 10^{11}$ / $1.6 \times 10^{10}$

**Table 4.1.3** Expected “real-world” performance of an NSLS-II X-ray crystallography/scattering beamline (including mirror figure error and transmission losses for the monochromator, mirrors, and beamline windows) for different values of mirror figure error. The expected performance in both high and low demagnification modes of operation of the KB assembly is shown as high/low values.

(e.g. SBC-CAT, which is operational, and GM/CA-CAT, which is under construction). NSLS X25 and APS UA values are based on measurements, and the NSLS X29 data are expected values.

A critical physical parameter determining the image quality of the focused beam in the NSLS-II superconducting undulator beamlines will be the residual figure errors of the KB mirror surfaces. At the present state-of-the-art for fabrication of grazing-angle X-ray optics, the beam parameters at the focus of an ultra-low-emittance source such as the NSLS-II would be limited by aberrations resulting from this residual surface figure error. Indeed, one reason to keep the distance from these KB mirrors to the focus relatively short is to prevent their surface figure errors from contributing excessively to the focused spot size. On the other hand, we expect that the state-of-the-art in X-ray optics fabrication will continue to improve significantly between now and the start of NSLS-II operations [2-4]. Table 4.1.3 shows the expected improvement in focused X-ray beam parameters for the undulator X-ray beamline described above as a function of rms surface figure error of the KB mirrors in these beamlines. The perfect-mirror case (0.0  $\mu\text{rad}$  figure error) is included as a point of reference. As was done for Table 4.1.2, transmission losses due to the monochromator, mirrors, and beamline windows were taken into account.

#### 4.1.1.2 Small Angle X-ray Scattering

The small-angle X-ray scattering (SAXS) beamlines to be built for NSLS-II, schematically shown in Figure 4.1.2, will utilize a bendable KB focusing mirror pair for primary focusing and will have the flexibility of being tailored for different applications by using slits and secondary focusing mirrors.

Owing to the low emittance of NSLS-II, the full beam from the undulator will be able to be used for SAXS measurements down to very low  $q$  without any collimating slits. The divergence of the X-ray beam at the sample is limited by the acceptance angle of the KB mirrors and translates into a minimum accessible scattering angle ( $2\theta$ ) of 0.033 mrad. At an X-ray energy of 8 keV ( $7.4 \times 10^{15}$  photons/sec/0.1%bw), the lowest  $q$  is  $\sim 1.4 \times 10^{-4} \text{ \AA}^{-1}$ , corresponding to 4.7  $\mu\text{m}$  in real space. In practice, to

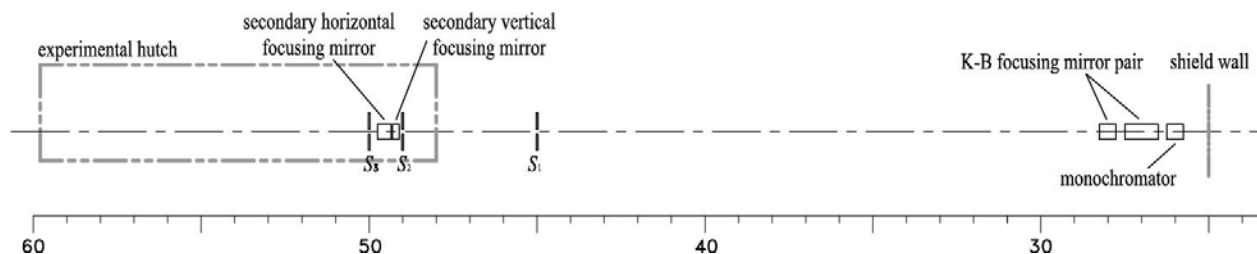


**Figure 4.1.2** Schematic design of the SAXS beamline. The beamline will be equipped with primary K-B focusing mirrors and two secondary cylindrical focusing mirrors. While the primary pair is sufficient for routine experiments, the secondary mirrors can be combined with the primary pair to provide the capability of grazing incidence scattering off liquid surfaces and SAXS within a spot size of a few microns.

S <sub>1</sub> and S <sub>2</sub> (μm)	S <sub>3</sub> (μm)	Beam size at downstream end of expt'al hutch	Lowest q	Flux at the sample (ph/sec/0.1%bw)
100	150	2.2 mm @ 8 m	$0.6 \times 10^{-3} \text{ \AA}^{-1}$	$1.3 \times 10^{15}$
400	600	2.6 mm @ 2 m	$2.8 \times 10^{-3} \text{ \AA}^{-1}$	$7.0 \times 10^{15}$

**Table 4.1.4** Typical microbeam SAXS performance at 8 keV, assuming 1 μrad mirror figure error.

S1 (μm)	S2 (μm) horizontal only	FWHM beam size (μm)		FWHM beam divergence (mrad)		Flux at the sample (ph/sec/0.1%bw)
		horizontal	vertical	horizontal	vertical	
200 (h) x 100 (v)	open	14	13	0.7	0.2	$6.4 \times 10^{15}$
200 (h) x 100 (v)	200	13	13	0.5	0.2	$4.0 \times 10^{15}$
50 (h) x 25 (v)	open	5	4	0.6	0.2	$6.2 \times 10^{14}$

**Table 4.1.5** Typical microbeam SAXS beam size, divergence, and flux at the sample at 8 keV, assuming 1 μrad mirror figure error.

achieve low scattering background and compensate for the divergence created by the figure error of the optical elements, collimating slits will be used (see Table 4.1.4).

Ideally, the secondary horizontal focusing mirror can further focus the full beam to under 10 μm (FWHM) in both horizontal and vertical extent at the sample, even without additional focusing in the vertical direction. Owing to the imperfection of the optical elements, a secondary KB focusing mirror pair will be used to obtain very small beam sizes. To do this, the primary KB pair focuses the beam at S<sub>1</sub> as a virtual source and the secondary mirrors then focus the beam again at the sample. Use of the variable aperture at S<sub>1</sub> to limit the size of the virtual source can further reduce the beam size at the sample. Typical performance values for a few selected choices of S<sub>1</sub> and S<sub>2</sub> slit sizes are shown in Table 4.1.5. By varying the figure of the secondary vertical mirror, e.g. by use of a tangential bender mechanism, one can also deflect the beam downward and focus it on a liquid sample cell (bath) in order to perform grazing incidence scattering measurements on liquid surfaces.

### 4.1.1.3 Nanoprobes

Several X-ray nanoprobes are planned for NSLS-II undulator beamlines. These will provide unprecedented spatial resolution and intensity for imaging, diffraction and fluorescence based applications. X-ray nanoprobes beamlines are not significantly different from a standard X-ray scattering/crystallography beamline, described in Section 4.1.1.1. The main difference is that the optics are designed to focus the incident X-ray beam into nanometer sized X-ray spots at the expense of angular beam convergence on the sample.

Fluorescence and diffraction measurements differ in their requirements on the angular convergence of the photon beam on the sample: the fluorescence technique is insensitive to this, whereas the increased convergence due to the larger demagnifications delivered through the nanofocusing X-ray optics results in a broadening of the diffraction peaks from the sample and hence a reduced sensitivity to strain. The important figures of merit for X-ray nanoprobes are the focused beam size, angular convergence, total flux into the focused image, the ratio of flux in the focused spot to the unfocused background, and beam stability. These factors have to be carefully considered in the design of a nanoprobes instrument.

The emphasis for these beamlines will be obtaining high quality optics that conserve the source brightness and focus the beam to nanometer sized dimensions. Ten years ago the quality of focusing optics was such that a 5-10 μm spot was an expensive and heroic achievement. The present state-of-the-art X-ray optics employed at synchrotron radiation sources can deliver focused X-ray beams of order 100

nm using KB mirror systems [5, 6], diffractive zone plates [7] or refractive lenses [8]. As technological advancements continue, we believe that by the time NSLS-II is commissioned, these optics will be able to deliver X-ray nanobeams with dimensions of ~10 nm and below.

A variety of advanced optics for nanoprobe applications are described in Section 2.4.3.1. As a general rule, the absolute precision with which these demanding optical elements can be fabricated improves as the size of the optic decreases. The small aperture of current micro-focusing optics relative to the fan of radiation at existing, less bright sources such as the present NSLS means that they intercept only a small fraction of the source flux and hence the radiation is inefficiently utilized. The brightness of NSLS-II provides the important advantage that it will be a much better match to the acceptance of small, more precisely shaped, optical elements.

We also anticipate a complement of scanning transmission X-ray microscopes (STXM), which are rapidly becoming workhorses in the synchrotron radiation community. In the standard STXM configuration, the zone plate, which is 10-20% efficient, is located upstream, rather than downstream, of the specimen in the X-ray beam path, thereby minimizing the radiation dose to the sample. This minimization is particularly advantageous in the study of biological samples. STXM instruments are well suited to acquiring near-edge absorption spectra, both from specific points in a specimen and from whole image fields. The STXM user community at the NSLS has led the development of multivariate statistical analysis methods to exploit the information these spectromicroscopy data provide for studies in biological, soft matter, and environmental science [9].

The highest resolution microprobes now operating at NSLS (X1A1 and X1A2) are a pair of soft X-ray scanning transmission X-ray microscopes (STXMs) with a 36 nm Rayleigh resolution [10]. These microscopes are presently being equipped with laser interferometer feedback on the scanning stage motion, and are outfitted with unique segmented detectors that can be used to obtain both absorption and phase contrast images in a single scan. Since the present NSLS has a source phase space of about  $100 \lambda$  horizontally and  $3 \lambda$  vertically for 300 eV photons, the undulator source must be imaged to a secondary focus that is then apertured to deliver the required phase space area in the manner of a laser spatial filter. Moreover, the NSLS X1 undulator provides radiation to three endstations (STXMs at X1A1 and X1A2, and either soft X-ray diffraction or spectroscopy at X1B) simultaneously, so neither of the two STXMs is able to collect radiation from the on-axis undulator peak. The combined effects of off-axis viewing and efficiency losses from the additional optics required to re-image the source reduce the throughput of these microscopes considerably.

STXM-based soft X-ray research will benefit greatly from NSLS-II, which will provide ultra-high brightness in the soft X-ray range with 40 mm period Soft X-ray Undulators (SXU). The STXM beamlines will be based on spherical grating monochromators, which will be designed to demagnify the undulator source to an exit slit/pinhole in order to define the virtual source for the zone plate focusing optics. We propose to employ a pair of mirrors to direct the X-ray beam to one of two end stations, thereby allowing two microscopes to be operated in turn (or even in parallel if desired). By incorporating two microscopes in one SXU beamline, one of them can operate while upgrades or novel optical configurations are explored on the other (a pattern that has worked extremely well at the present X1A1 and X1A2 beamlines). In fact, since it is expected that the existing STXMs will be continuously upgraded between now and NSLS-II commissioning, these microscopes should be able to effectively make use of first light from NSLS-II.

#### **4.1.1.4 High-resolution Inelastic X-ray Scattering**

Inelastic X-ray Scattering (IXS) determines the scattering amplitude,  $S(\mathbf{q}, \omega)$ , by measuring the intensity and energy loss of photons scattered by the sample into a small element in angular space. Ideally, the energy resolution of the monochromator and the analyzer are of the order of 1-100 meV, depending on the system under investigation. If the energy of the incident photons is tuned to an absorption edge of the sample, resonant processes can increase the intensity by a few orders of magnitude compared to non-resonant experiments. The cross section of IXS is fairly small, and including the

geometry of the experimental set-up, efficiency of detectors, and reflectivity of analyzer crystals, just 1 out of approximately  $10^6$  photons is detected if the white line is studied in resonant experiments using the  $K_\alpha$ -fluorescence lines. Experiments in the pre-edge region lower the signal by another factor of 10-50 and studies using other fluorescence lines,  $K_\beta$  and  $K_\gamma$ , reduce the signal by another factor of 60-300. This reduces the signal in a typical experiment to  $10^3 - 10^5$  photon/sec for an incident flux of  $10^{12}$  photon/sec. Non-resonant experiments devoted to the study of band-gaps in insulators or semiconductors may even have count rates as low as 50 photon/sec and non-resonant experiments examining the absorption-edges of low Z elements (Raman scattering) will be of the order of  $10^2$ - $10^4$  photon/sec for an incident flux of  $10^{12}$  photon/sec.

The purpose of the high-resolution inelastic X-ray scattering beamline is to deliver highly monochromatic X-rays with a monochromaticity of 100 meV and 1 meV between 5 keV and 20 keV, large tunability, and highest possible intensity. A high resolution IXS instrument operating on an NSLS-II undulator beamline will be provided with a highly intense and extremely well-collimated source of X-rays, thus allowing the delivery of highly monochromatic X-rays with good efficiency. It is expected that a resolution of 10 meV will be achievable in the 5 to 20 keV photon energy range with a flux of about  $10^9$  photons/sec.

The main optical components of a high-resolution inelastic X-ray scattering beamline are similar to a conventional scattering beamline. The first optical component is a high-heatload cryogenically cooled monochromator that reduces the power on the optical components downstream, especially on the high-resolution monochromator. The bandwidth of this first pre-monochromator is on the order of 1-2 eV. To increase the efficiency of the high-resolution monochromator, the beam is collimated by a spherical mirror downstream of the pre-monochromator. Several different types of monochromators can be considered to obtain high monochromaticity of order either 100 meV or 1 meV, as shown in Figure 4.1.3.

The low-resolution (100 meV) monochromator can be either a four-crystal in-line [11-13] or nested monochromator with high-order reflections and a dispersive arrangement of reflections. Several monochromators of this type are already in use at various synchrotron radiation facilities around the world, and do not present any technical challenge. The loss in intensity due to the smaller energy width and the reflectivity of the crystals will be of the order of 50 compared to the intensity of the pre-monochromator. From Table 4.1.2, the Si(111) double crystal pre-monochromator will provide a monochromatic intensity at 12 keV of  $2.4 \times 10^{14}$  ph/sec with an energy resolution of 1.8 eV. Thus, we expect that the low-resolution monochromator will provide a flux of about  $5 \times 10^{12}$  ph/sec at 12 keV with an energy resolution of 100 meV.

The high-resolution (1 meV) monochromator for the energy range 5 to 20 keV with large tunability will be a technical challenge. Backscattering monochromators operating at Bragg-angles of  $89.9^\circ$  have a small tuning-range of a few meV and operate only at specific high energies if Si-crystals are used [14]. Sapphire ( $Al_2O_3$ ) significantly increases the tuning range and the energy-range, but so far, sapphire crystals of the required quality and size are not available. Nested monochromators can reach an energy-resolution of 5-10 meV with a tunability of a few eV, but only at a few energies close to the backscattering energies of specific reflections of Si [15-17]. A third option was recently proposed by

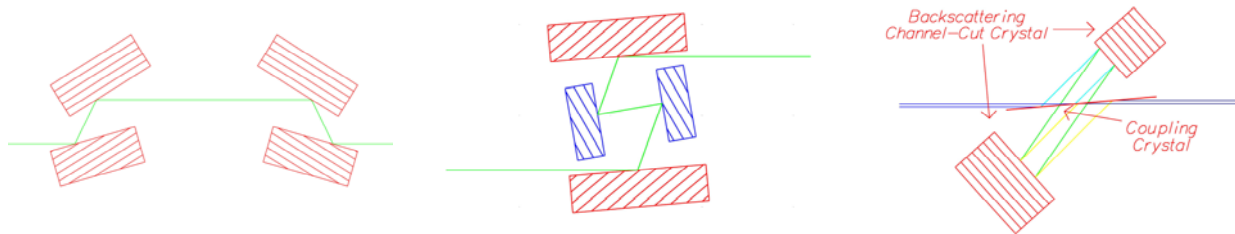


**Figure 4.1.3** Example types of monochromators for medium and high energy resolution for IXS applications. Left: In-line monochromator for medium energy resolution of 50-200 meV. Center: Nested monochromator for high energy resolution (5-10 meV). Right: Compact coupling-crystal backscattering monochromator for ultra-high energy resolution (0.5-1 meV).

Shvyd'ko: Three crystals collimate the beam, monochromatize it, and focus it again. This arrangement has a theoretical energy resolution of about 1 meV with large energy tunability but has not yet been tested under real conditions. The loss in intensity from that provided by the pre-monochromator will be about a factor of 1000 due to the smaller energy-width, and an additional factor of 10 due to several additional reflections, so an intensity of  $\sim 2 \times 10^{10}$  photons/sec at an energy resolution of 1 meV should be possible with this arrangement.

Downstream of the high-resolution monochromator in the IXS beamline, a pair of focusing mirrors (vertical and horizontal) is used to focus the beam onto the sample.

The spectrometer that analyzes the scattered X-rays with high energy resolution is another crucial part of the beamline. Several back scattering analyzer systems with energy-resolution of 100 meV (1 meV) using spherically bent analyzers with radii of curvature of 3 m (7-11 m) have demonstrated their high efficiency over the past decade [11, 16-19]. The future challenge will be to build a spectrometer that will be capable of determining the energy of scattered photons with high energy resolution at angles smaller than backscattering, e.g., the fluorescence lines of 3d and 4f elements, which are not close to backscattering energies of either Si or Ge reflections. One alternative might again be sapphire, but the availability of large perfect single crystals and its elastic properties pose a significant challenge. Again, the proposal by Shvyd'ko with an arrangement of a collimating mirror and three crystals (collimation, monochromatization, focusing) might be an interesting alternative, albeit one that is quite challenging for stability.

The analyzer system offers the only way to increase the signal by increasing its area and using separate detectors for each individual analyzer. Since each individual analyzer sees the scattered photons at a different scattering angle, each one measures its own  $S(q_i, \omega)$ , which will save time, and deliver the signal under identical conditions.

#### 4.1.1.5 Superconducting-wiggler-based High Energy Beamlines

A small but important subset of the programs outlined in Section 2 have a need for high energy X-rays (e.g.  $> 30$  keV) for X-ray scattering in order to probe a larger  $q$  range or to better accommodate special sample environments. A major advantage of using high energy radiation is the reduction in the absorption of X-rays, allowing the study of large samples and samples inside specialized environmental chambers. Focused high-energy X-rays are essential for high-resolution X-ray scattering of samples in multi-anvil and sometimes in diamond anvil cells, for larger  $q$  range, and to better accommodate the special high-pressure/temperature sample environment. Newly developed X-ray focusing optics and

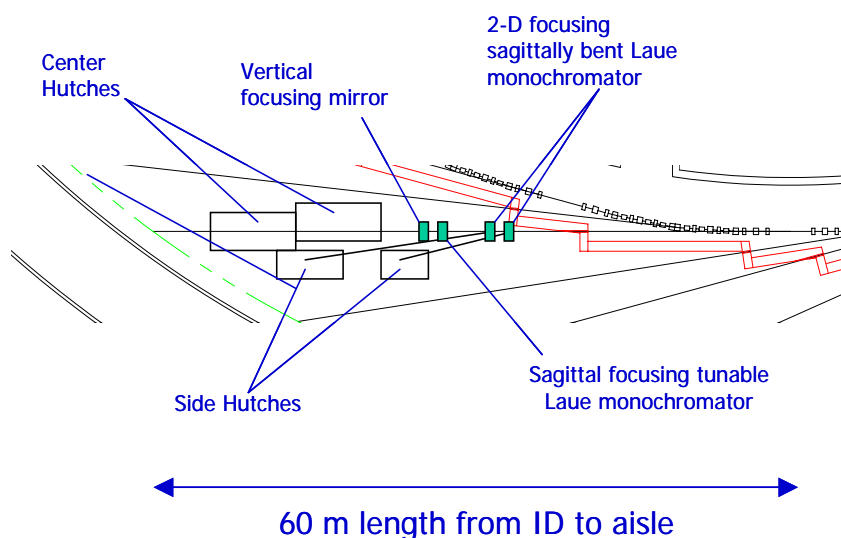


**Figure 4.1.4** Layout of NSLS-II superconducting wiggler beamlines.

detectors are already poised to take advantage of the enhanced flux and brightness of the NSLS-II superconducting wiggler source to enable a myriad of crystallographic and spectroscopic measurements.

The superconducting wiggler beamlines will provide X-rays in the energy range 30 keV to 150 keV. At NSLS-II, the machine energy is 3 GeV, compared to 6 GeV, 7 GeV and 8 GeV respectively for ESRF, APS and SPRING8. Superconducting wigglers are therefore chosen to provide the desired high-energy X-rays. For wiggler radiation, the fan is about 10 mrad wide. Focusing of the hard X-rays is thus crucial to collect this large horizontal fan and utilize it for experiments.

Figure 4.1.4 shows a sketch of a possible arrangement for beamlines utilizing a high-field wiggler source on NSLS-II. The experimental stations include two fixed-wavelength side stations and two center stations that can utilize either white beam or focused monochromatic beam (or both).

Sagittal focusing using Laue crystals was pioneered at the NSLS [20-23]. The concept is shown in Figure 4.1.5. This new X-ray optics concept makes it possible to focus a large divergence of high-energy X-rays produced by the NSLS-II superconducting wiggler. The extent of such focusing is similar to that of sagittal focusing by a Bragg crystal, except for a factor related to the asymmetry angle. The anticlástico bending facilitates the use of inverse-Cauchois geometry in the meridional plane to provide better energy-resolution and to increase the photon flux by an order-of-magnitude compared to traditional sagittal

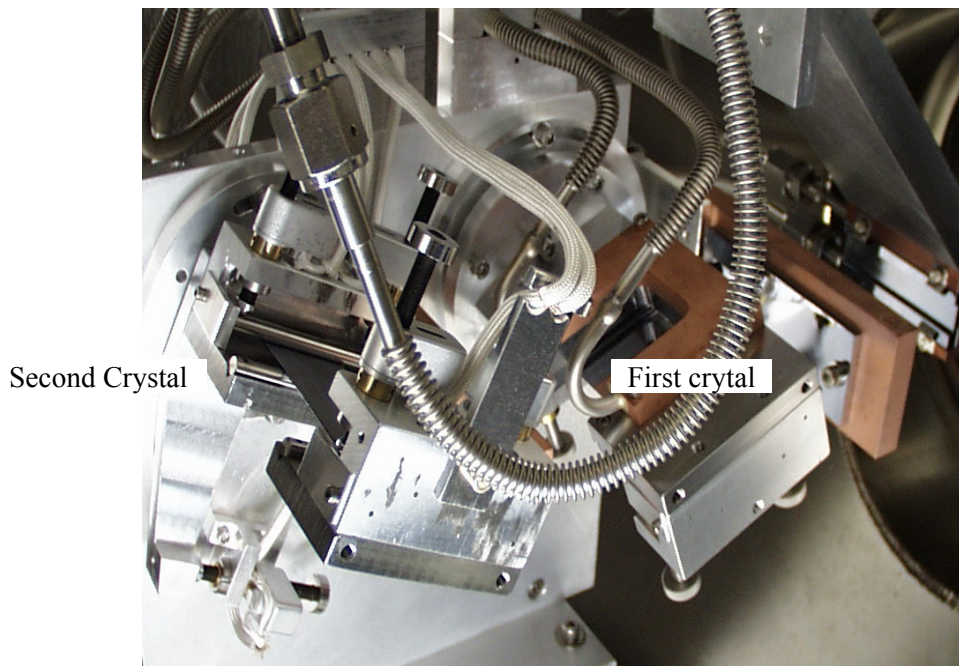
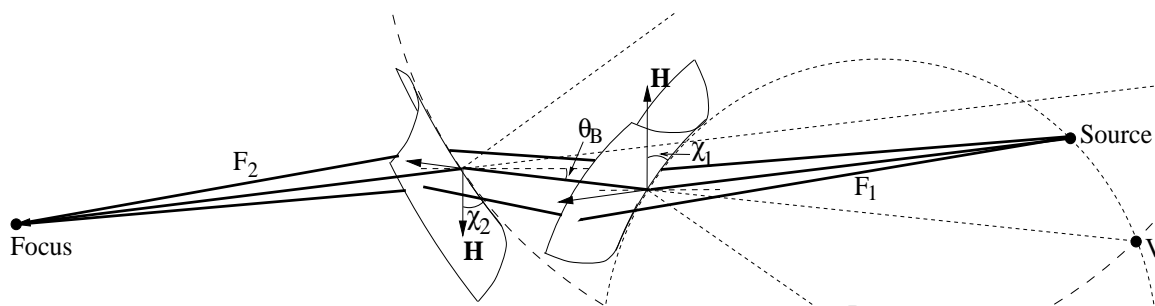


**Figure 4.1.5** Top: Schematic layout of the sagittal focusing mechanism using asymmetric Laue crystals. Bending of the crystals causes precession of the diffraction vector ( $H$ ) around the axis of sagittal bending and results in focusing of the diffracted beams. Bottom: Photograph of such a monochromator installed at the NSLS X17B1 beamline.

focusing with Bragg crystals. Furthermore, sagittal focusing by a Laue crystal is preferred over a Bragg crystal at X-ray energies above 30 keV because, since, unlike Bragg crystals, the length of the beam's footprint on a Laue crystal is small and insensitive to energy. For many experiments, beam divergences of order 1 mrad at the sample will be tolerable. For diffraction experiments in a vertical scattering plane, a larger divergence in the horizontal plane can also be tolerated.

A double-crystal sagittally focusing monochromator, based on this concept, has been constructed, tested, and in use at the X17B1 beamline for two years, providing 67 keV X-rays (Figure 4.1.5). It focuses a horizontal divergence of 3 mrad to a brightness-limited horizontal dimension of 0.2 mm. The X-ray flux density at the focus is a few hundred times larger than that of unfocused X-rays. Currently, using this device, the flux on a small sample in a diamond-anvil cell is limited by the brightness of the NSLS storage ring. Combined with a vertically focusing mirror, the same monochromator can be implemented at the NSLS-II superconducting wiggler beamlines to provide 50-100 keV photons of about  $10^{12}$  ph/s, with an energy resolution of  $10^{-4} \Delta E/E$ , in a spot of less than 50 microns in diameter. This intensity is two orders of magnitude larger than the current state-of-art at NSLS X17B1 and APS. For example, currently at APS 1-ID beamline, using bent Laue crystal optics that are best suited for the undulator, a flux of  $10^{11}$  ph/s with an energy resolution of  $10^{-3}$  is delivered to a similar spot of 100 microns in diameter at 67 keV [24].

The conditions imposed on the asymmetry angle of a sagittally bent Laue crystal to achieve two-dimensional focusing have been derived by NSLS scientists. This simple high-efficiency design diffracts high-energy X-rays into side stations providing a high-flux fixed-energy beam of 67 keV with moderate ( $\Delta E/E \cong 10^{-3}$ ) energy resolution and a flux of  $\sim 10^{13}$  ph/s/mm<sup>2</sup> in a spot of less than 50 microns vertical by 100 microns horizontal. This, when coupled with a matching bent-Laue crystal analyzer, allows high-resolution scattering experiments at high energies. This arrangement is suitable for pair distribution function measurements and powder diffraction measurements in difficult environments, e.g., stainless steel reaction tubes and high temperature capillaries. It will also be valuable for certain single crystal experiments such as charge density studies, where data must be collected to very high  $q$  values.

The use of white radiation and energy sensitive detectors for energy dispersive diffraction is an established technique for kinetic experiments in high pressure (large volume press) and high temperature experiments. With the optical elements withdrawn from the center beam, the end station will accept white radiation, thus allowing for energy dispersive experiments.

### 4.1.2 Soft X-ray Beamlines

The 4.0-cm period, 5.0m-long soft X-ray undulator (SXU) provides high brightness radiation in the soft and intermediate X-ray ranges, from 0.2-7 keV. This large photon energy range will naturally lead to a combination of grating-based and crystal-based beamlines in order to provide efficient utilization.

Above 2.5-3.0 keV photon energy, the range where crystals function robustly and efficiently, the extremely narrow angular width of the central cone emission from the SXU will not overfill the angular acceptance of the highest quality crystals. Furthermore, sagittal focusing will not be required of these crystals, since reasonable-length focusing mirrors will still collect the entire central cone even at 30-40 m meters from the source point (see Section 4.1.1.1). Depending on the application, either single mirror or Kirkpatrick-Baez pair designs will be used to refocus the diffracted radiation onto the sample.

Below 2.5-3.0 keV photon energy, the domain of grazing-incidence diffraction gratings, the extremely high brightness of the SXU beam will provide a very efficient source for the grating, whether it should be real (i.e. focused through an entrance slit) or virtual (e.g. in the SX700 monochromator design [25]). The maturation of variable-line-space grating technology and the superior control over groove shape now provided by the grating manufacturers has pushed the resolving power of soft X-ray monochromators well beyond  $10^4$  while also providing a fixed exit position and angle [26]. The advent of accurate bendable gratings [27] provides another variable parameter to the soft X-ray monochromator

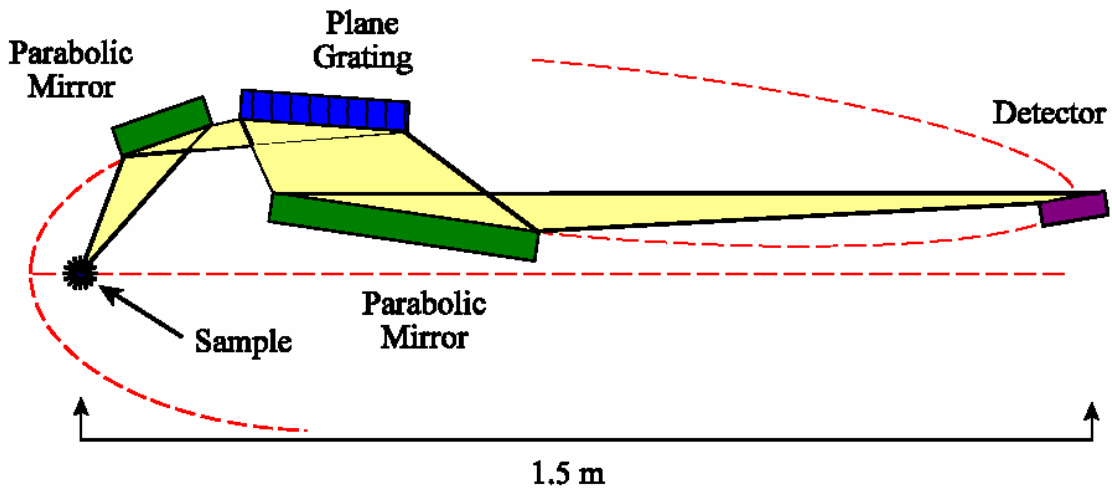


Figure 4.1.6 Soft X-ray emission spectrometer.

designer. The magnification of the monochromator does not differ greatly from unity, so the design of the refocusing mirror(s) is similar to the double-crystal cases above: either a single asphere or a KB pair.

The tiny vertical extent of the refocused monochromatized SXU beam incident on the sample will create a source of soft X-ray emission that will be an ideal match to high-resolution soft X-ray emission spectrometers. One such spectrometer is that being designed by Josef Nordgren (Uppsala) (Figure 4.1.6), in which scattered 50-200 eV soft X-rays from the sample are collected by a parabolic mirror and collimated onto one of three interchangeable plane gratings. The diffracted X-rays are focused by a second parabolic mirror onto a micro-channel-plate detector. This instrument should be able to achieve the super high resolution of  $< 10$  meV at a photon energy of 75 eV. It is, however, a very brightness-hungry instrument, requiring micron-sized beams on the sample since the photon beam on the sample acts as a virtual entrance slit for the emission spectrometer. Thus, the high brightness of NSLS-II in the soft X-ray energy range is essential in order for this instrument to reach its full capability.

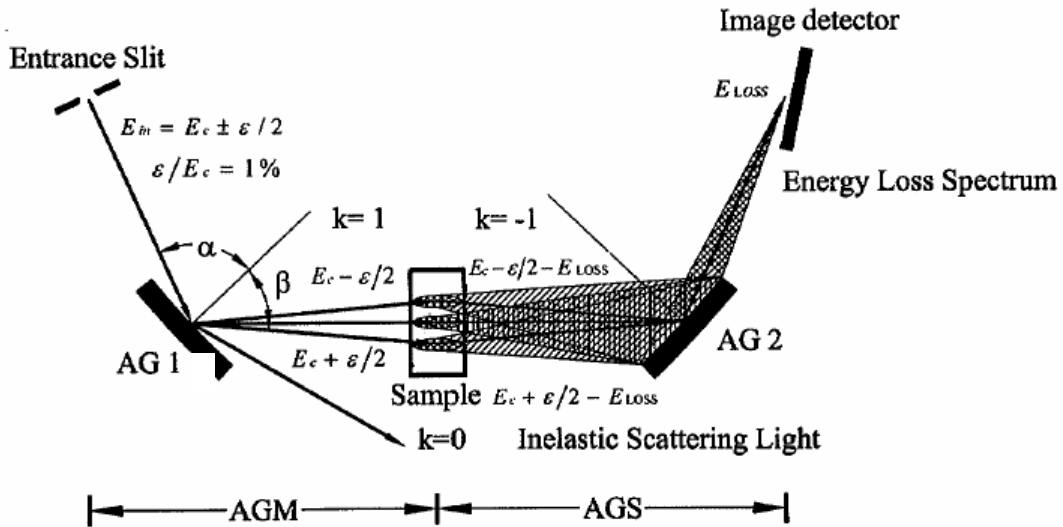


Figure 4.1.7 Conceptual diagram of the SRRC parallel-detection soft x-ray emission system. The active grating monochromator (AGM) and active grating spectrometer (AGS) are time-reversed images of each other, thereby compensating aberrations to achieve high energy resolution.

The SXU will also be an ideal source for the newly designed [28] dispersion-compensated combination of soft X-ray monochromator and soft X-ray emission spectrometer, shown in Figure 4.1.7. This world-leading design, to be commissioned in 2004, will greatly increase the effective count rate of soft X-ray emission spectroscopy by acquiring an entire energy-loss spectrum at once, i.e. without having to scan either the beamline monochromator or the emission spectrometer.

### 4.1.3 High-K-undulator-based VUV Beamlines

Despite the hard X-ray critical energy (7.8 keV) of the NSLS-II X-ray storage ring, the VUV (10-100 eV and above) users will be served very well by long-period high-K undulators (See Figure 3.3.3). These insertion devices could be either planar or of a more exotic magnetic structure such as the Figure-8 [29] or Pera [30] designs. One advantage, especially for the planar high-K undulator, is the very large photon energy range covered by the first, third, and fifth harmonics: from ~10 eV to 1 keV. Thus, high resolution spectroscopy will be able to be performed over a very wide energy range at one endstation, a capability desired by both XPS and angle-resolved photoemission spectroscopists. The disadvantage of high-K planar undulators is the associated extremely high power levels, both total power and angular power density. This power load may be compatible with modern integrally-cooled optics, albeit with some degradation owing to the inevitable thermally-induced surface figure error on the first beamline optical element. One attractive solution to this problem is the Figure-8 undulator design, or similar variants such as the Pera design, in which the high energy harmonics are for the most part missing in a narrow cone on axis that encompasses the low harmonics (e.g. first, third, and fifth). In this case, the first beamline element is a cooled circular aperture that acts as a cost effective energy filter, allowing only the relatively low power but very high brightness fundamental and next few harmonics to pass.

The design of beamlines for these 10-1000 eV sources must necessarily involve combinations of monochromators, each of which covers only a fraction of this range with optimized parameters. For example, the 10-40 eV photon energy range requires a normal incidence monochromator (NIM) design in order to achieve high resolution with high throughput, whereas the 40-1000 eV range can be handled by any of the high-resolution soft X-ray monochromator designs. With careful consideration to proper layout, both the VUV and soft X-ray monochromators can be served alternately by the same undulator source and their output beams directed to a common focused spot on the sample. The achievable resolving power in both the VUV and soft X-ray range continues to increase as the quality of optics, in particular diffraction gratings, improves. In the VUV range, NIM monochromators can achieve well above  $10^5$  resolving power [31]. In the soft X-ray range, resolving powers are above  $10^4$  over large ranges of photon energy, and approaching  $10^5$  at particular photon energies.

### 4.1.4 Infrared

Infrared synchrotron radiation (IRSR) serves a diversity of scientific disciplines in biology, chemistry, materials, physics, geology, environmental and space sciences. As a source, IRSR spans the entire range from  $1 \text{ cm}^{-1}$  up to  $4000 \text{ cm}^{-1}$  (and beyond) with characteristics that enable measurements that otherwise would be impossible [32]. The key aspect to infrared synchrotron radiation is the high brightness (2 to 3 orders of magnitude higher than conventional laboratory spectroscopy sources) that allows throughput limited experiments to be performed with ease. A primary example of this is infrared microspectroscopy, where synchrotron radiation extends the spatial resolution by about 1 order of magnitude (to the diffraction-limit) while still delivering high signal-to-noise. Many other techniques have similar throughput limitations, e.g. ellipsometry, precision reflectance spectroscopy, and grazing incidence reflection spectroscopy, all of which have restrictions placed on the acceptable angle of incidence at the specimen. Techniques such as high-pressure spectroscopy and magnetospectroscopy are constrained by the instruments and their limited optical access. Lastly, a high brightness source is necessary to achieve proper modulation (absence of skew rays) over the very large path lengths of a high-

resolution spectral resolution interferometer. Each of these throughput limited techniques are problematic at mid-infrared frequencies and become increasingly difficult as the spectral range reaches into the very far-infrared and THz region. Infrared synchrotron radiation has overcome some of these problems and efforts continue to improve the source capabilities, especially at the more difficult long-wavelength end of the spectrum.

Another less exploited quality of IRSR is the pulse structure that can be used in time-resolved studies of dynamics [33]. Though the pulse duration (10s to 100s of picoseconds) is significantly longer than what can be achieved with ultra-fast lasers (10s to 100s of femtoseconds), the synchrotron is a “white” source that allows complete spectral information to be acquired. This provides a unique opportunity to study dynamics associated with chemical bonds (vibrational spectra), both charge transfer and interband electronic transitions, and even intraband absorption (by free carriers) all in a single experiment.

Many of the scientific programs described in Section 2 require a high brightness, white source of pulsed infrared – the characteristics which the NSLS-II IR ring described in Section 3 will excel at.

The infrared beamlines will be designed to span the spectral range from about 0.5 eV ( $4000\text{ cm}^{-1}$ ) down to 10 meV ( $80\text{ cm}^{-1}$ ), and in some cases to as low as 250  $\mu\text{eV}$  ( $2\text{ cm}^{-1}$ ). The NSLS presently offers a suite of 6 infrared beamlines, several of which are heavily oversubscribed. The IR community is also among the fastest growing user communities at the present NSLS. Thus, we anticipate expanding this to at least 8 to 10 beamlines on the NSLS-II IR ring to meet the great demand for high brightness, short pulse, broad spectrum IR radiation.

Currently we envision beamlines serving the following scientific needs:

- Materials at extremely high pressure and temperatures (diamond anvil cells)
- Biological microspectroscopy and imaging.
- Environmental and Space materials (microprobe spectroscopy, including far-IR).
- Far-infrared magnetic resonance spectroscopy in high fields
- Fast material dynamics / time-resolved IR spectroscopy
- Precision reflectance spectroscopy and ellipsometry of new and complex materials
- Custom microscopy configurations for nanomaterials, quantum wells and quantum dots.

The useful spectral range is often limited by the extraction port dimensions, rather than downstream optical components (and even the spectrometer endstations). Therefore, the ports for infrared beamlines will all be as large as practical (at least  $90\text{ mrad}^2$ ). This is particularly important for reaching into the THz spectral range, an area of increasing interest. At least two beamlines will be optimized for performance in this low frequency range. The technology for providing radiation at THz frequencies is rapidly evolving, and accelerator-produced THz pulses are no exception. The proposed long wavelength beamlines will be compatible with such technologies as they become available.

#### REFERENCES:

- [1] R. Fischetti, private communication
- [2] D. Hausermann et al., *Synchrotron Radiation and Instrumentation 2003 Conference Proceedings, San Francisco, Ca, 2003, in press.*
- [3] R. Signorato and T. Ishikawa, Nuclear Instruments and Methods in Physics Research A (467-468), 271-274, 2001.
- [4] P. Eng et al., *Test Results of GSECARS Large KB Mirror Focusing System*, <http://cars9.uchicago.edu/gsecars/mirrors/index.html>
- [5] Hignette, G. Rostaing, P. Cloetens, A. Rommeveaux, W. Ludwig, A. Freund, Proceedings of SPIE, X-ray Micro- and Nano Focusing: Applications and Techniques II, 105-116, 2001.

- [6] Hignette, P. Cloetens, W.-K. Lee, W. Ludwig and G. Rostaing, *J. Phys. IV France* **104**, 231-234, 2003.
- [7] W. Yun, B. Lai, Z. Cai, J. Maser, D. Legnini, and E. Gluskin, *Rev. Sci. Instrum.* **70**, 2238-2241, 1999.
- [8] C.G. Schroer, M. Kuhlmann, U.T. Hunger, T.F. Gunzler, O. Kurapova, S. Feste, F. Frehse, B. Lengeler, M. Drakopoulos, A. Somogyi, A.S. Simionovici, A. Snigirev, I. Snigireva, C. Schug and W. H. Schroder, *Appl. Phys. Lett.* **82** (9) 1485-1487, 2003.
- [9] C. Jacobsen, M. Feser, M. Lerotic, S. Vogt, J. Maser, and T. Schäfer, *Journal de Physique IV* **104**, 623 (2003). M. Lerotic, C. Jacobsen, T. Schäfer, and S. Vogt, *Ultramicroscopy* (submitted).
- [10] M. Feser, C. Jacobsen, P. Rehak, and G. De Geronimo, *Journal de Physique IV* **104**, 529 (2003).
- [11] Y.Q. Cai, P. Chow, C.C. Chen, H. Ishii, K.L. Tsang, C.C. Kao, C.T. Chen, *Optical Design and Performance Of The Taiwan Inelastic X-ray Scattering Beamline (BL12XU) At SPring-8*, Proceedings of the Eight International Conference on Synchrotron Radiation Instrumentation, San Francisco, California, August 25-29 2003.
- [12] G. Faigel, D. P. Siddons, J. B. Hastings, P. E. Hausteijn, J. R. Grover, J. P. Remeika and A. S. Cooper, *Phys. Rev. Lett.* **58**, 2699-2701 (1987)
- [13] W. A. Caliebe, C.-C. Kao, M. Krisch, T. Oversluizen, P. Montanez, and J. B. Hastings, *AIP Conference Proceedings*, Volume 417, 6-9 (1997).
- [14] R. Verbeni, F. Sette, M.H. Krisch, U. Bergmann, B. Gorges, C. Halcoussis, K. Martel, C. Masciovecchio, J.F. Ribois, G. Ruocco, and H. Sinn, *J. Synchrotron Rad.* **3**, 62-64, (1996).
- [15] Alfred Q. R. Baron, Yoshikazu Tanaka, Daisuke Ishikawa, Daiwo Miwa, Makina Yabashi, and Tesuya Ishikawa, *J. Synchrotron Rad.* **8**, 1127-1130, (2001).
- [16] Tetsuya Ishikawa, Yoshitaka Yoda, Koichi Izumi, Carlos Kenichi Suzuki, Xiao Wei Zhang, Masami Ando, Seishi Kikuta, *Rev. Sci. Instrum.*, **63**, 1015-1018, (1991).
- [17] E. Ercan Alp, H. Sinn, A. Alatas, W. Sturhahn, T. Toellner, J. Zhao, J. Sutter, M. Hu, D. Shu, Y. Shvydko, *Nucl. Instr. and Meth. in Phys. Res. A*, 467-468, 617-622, (2001).
- [18] C. Masciovecchio, U. Bergmann, M. Krisch, G. Ruocco, F. Sette, R. Verbeni, *Nucl. Instr. And Meth. in Phys. Res. B*, **111**, 181-186, (1996).
- [19] C. Masciovecchio, U. Bergmann, M. Krisch, G. Ruocco, F. Sette, R. Verbeni, *Nucl. Instr. and Meth. in Phys. Res. B*, **117**, 339-340, (1996).
- [20] Z. Zhong, C.C. Kao, D.P. Siddons and J. B. Hastings, *J. Appl. Cryst.* **34** (2001) 504-509.
- [21] Z. Zhong, C.C. Kao, D.P. Siddons and J. B. Hastings, *J. Appl. Cryst.*, **34** (2001) 646-653.
- [22] Z. Zhong, C. Kao, D.P. Siddons and J.B. Hastings, *Acta Cryst, A* **58** (2002) 487-493.
- [23] Z. Zhong, C. Kao, D.P. Siddons, H. Zhong, and J.B. Hastings, *Acta Cryst. A* **59** (2003) 1-6.
- [24] S.D. Shastri, K. Fezzaa, A. Mashayekhi, W.K. Lee, P.B. Fernandez and P.L. Lee, *J. Syn. Rad.* **9** (2002) 317-322.
- [25] H. Petersen, C. Jung, C. Hellwig, W.B. Peatman, and W. Gudat, *Rev. Sci. Instrum.* **66**, 1 (1995).
- [26] M. Koike and T. Namioka, *Rev. Sci. Instrum.* **66**, 2144 (1995), and references therein.
- [27] T.C. Tseng, D.J. Wang, S.Y. Perng, C.K. Kuan, J.R. Lin, S.H. Chang, and C.T. Chen, *J. Synchrotron Radiation* **10**, 450 (2003).
- [28] H.S. Fung, C.T. Chen, et al., "A Novel Active Grating Monochromator – Active Grating Spectrometer Beamline System for Resonant Inelastic Soft X-ray Scattering Experiments", in the proceedings of the 8th International Synchrotron Radiation Instrumentation Conference, San Francisco, CA, 2003.
- [29] T. Tanaka, H. Kitamura, *Nucl. Instrum. Methods* **A364**, 368 (1995); T. Tanaka, H. Kitamura, *J. Synchrotron Radiation* **3**, 47 (1996).
- [30] S. Sasaki, B. Diviacco and R. P. Walker, "Brainstorming on New Permanent Magnet Undulator Designs", in proceedings of the 1998 IEEE Particle Accelerator Conference, Stockholm, Sweden.
- [31] C. Masciovecchio, D. Cocco, and A. Gessini, "Inelastic Ultra-Violet Scattering as a Tool to Investigate Collective Excitation in Condensed Matter Physics", in the proceedings of the 8th International Synchrotron Radiation Instrumentation Conference, San Francisco, CA, 2003.

- [32] G. L. Carr, P. Dumas, C. J. Hirschmugl, and G. P. Williams, *Nuovo Cimento*, 20D, 375 (1998).
- [33] R. P. S. M. Lobo, J. D. LaVeigne, D. H. Reitze, D. B. Tanner, and G. L. Carr, *Rev. Sci. Instrum.* 73, 1 (2002).

## 4.2 Extreme Sample Environments

A major challenge in the physical sciences is to expand our understanding of nature by finding new material phases that are predicted to occur, such as quantum critical phenomena and exotic correlations. Very often, this requires tuning parameters such as pressure, magnetic field, and temperature to extreme values to access the novel phenomena. We intend to equip NSLS-II with associated facilities for obtaining as extreme of environments as possible in synchrotron experiments so that one can perform structural and spectroscopic studies that are not possible at non-synchrotron-based facilities. Our plans for providing experimental facilities at NSLS-II to attain world leading extremes of pressure, magnetic field, and temperature are described in this Section.

### 4.2.1 High Pressures

Ground-breaking high-pressure experiments reveal numerous new phenomena. We are at the exciting moment when high-pressure research is emerging to become a major branch of modern science. The high-pressure environment drastically and ubiquitously alters all material properties, thus opening new frontiers in fundamental physics and chemistry, as well as applications to planetary, Earth, biological, and materials sciences.

To investigate novel phenomena in-situ in high-pressure environments, powerful probes must be developed to reach minute samples through the strong wall of the pressure vessel and to separate the weak sample signals from those of the surrounding vessel materials. High-energy synchrotron radiation enjoys a unique advantage in this regard, as other conventional methods are unsuitable. For instance, pressure vessels are impenetrable by electrons or VUV to soft X-ray photons; on the other hand, the spatial resolution and intensity of conventional X-ray or neutron sources is insufficient for accurate studies at megabar pressures. A vast frontier has opened for high-pressure synchrotron radiation applications. The symbiotic evolution of high pressure and synchrotron radiation science has produced bountiful results in the past and showed boundless future for scientific exploration.

Parallel to three generations of synchrotron radiation advances, the marriage of high pressure environments with synchrotron facilities has also gone through three distinctive phases. At the beginning in the 1980's, users brought high pressure cells loaded with samples and experimental hardware and software, including X-ray optics, sample-handling stage, diagnostic probes, detectors, etc., to basically empty hutches at synchrotron facilities. Research projects were limited by the relatively primitive instrumentation that could be brought in, set up, and dismantled afterward within the assigned beam time.



**Figure 4.2.1** Megabar diamond anvil cell with natural diamonds sitting on the penny, and an anvil representative of the next generation of synthetic diamonds.

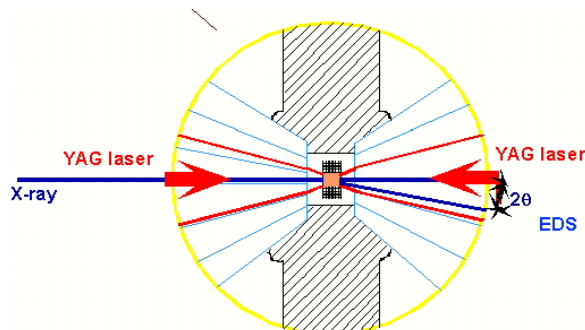


**Figure 4.4.2** Arrangement for heating sample at high pressure. Focused laser beams are capable of creating temperatures of several thousand K.

Nevertheless, exciting pioneering results demonstrated the potential (e.g., pressure-induced amorphization, metallization, and diffraction of ultralight elements, ultrahigh-pressure diffraction above 300 GPa). In the 1990's, single-task (X-ray diffraction) beamlines were constructed and dedicated for high pressure experimentation at X17 of NSLS, ID9 and ID30 of ESRF, and other synchrotron facilities. Dedicated high pressure beamlines allowed the establishment of multianvil apparatus, high-precision diffraction systems, and combined high pressure and high temperature environments that required years to build and optimize, and enabled the extraordinary scientific growth that we have witnessed. In the current decade, the multitasked HPCAT sector at APS combines myriad compatible and complementary synchrotron diffraction and spectroscopy techniques for dedicated high P-T studies. This comprehensive and integrated approach is enabling the next level of advancement.

All existing high-pressure/synchrotron radiation programs, however, were developed after the completion of the synchrotron rings. Consequently, they were restricted by the preset, backward conditions. For the first time, we now have the rare opportunity to plan high pressure synchrotron science for the next decade at NSLS-II. We will be able to consider high pressure as a key sample environment and build an overall infrastructure that combines high pressure with high temperature, cryogenic, and high magnetic field environments. We may build an ideal high pressure synchrotron radiation program that includes both HPCAT-type, multitask beamlines optimized for extensive sample environments and single-task beamlines optimized for special X-ray techniques, but accommodating the P-T-magnetic field conditions. Most importantly, the forward-looking infrastructure can incorporate next-generation high pressure devices.

Major breakthroughs in high pressure technology that will completely change the status quo are looming on the horizon. For instance, high pressure synchrotron studies have been previously limited to small access angles in the forward-scattering geometry. With the invention of panoramic diamond-anvil cells, the nearly complete spherical coverage of reciprocal space and momentum space has become accessible for single-crystal X-ray diffraction and inelastic studies. With the improvement of transparent beryllium and diamond gaskets, the conventional wisdom that only high-energy photons significantly above 10 keV could penetrate the high pressure vessel has been changed. Inelastic X-ray scattering has eliminated the blind spot between 5 eV and 5 keV where the high pressure vessels were opaque, and has opened the full, continuous range from meV to 100 keV. Micro- and nano-diffraction and spectroscopy allow us to investigate the elasticity and rheology of single grains as small 100 nm at multimegabar pressures. On the other hand, the development of giant CVD single-crystal diamonds holds the promise of mm-size sample volumes, 1 eV temperatures, and multimegabar pressures. As high pressure X-ray, high pressure neutron, and related initiatives (e.g., HPCAT, SNAP, COMPRES, and CDAC) continuously push the envelope, these breakthroughs will enable a new generation of scientific advancement in the high-pressure environment that will require considerably different planning than in previous high pressure synchrotron facilities.

The next five years will see continued developments in this area coupled with the creation of new high-pressure devices capable of higher pressures, larger sample volumes, hydrostatic sample conditions, higher and lower temperatures, and multiple analytical probes. These developments will allow measurements to be carried out to the most extreme conditions with an accuracy, precision, and sensitivity approaching studies at ambient conditions. Most important is an initiative aimed to increase sample size at megabar pressures using new gem anvil technology. Depending on the hardness of the gemstones, maximum pressures of 16.7, 25.8, 52, and 300-550 GPa have been reported for cubic zirconia, sapphire, moissanite, and diamond anvils, respectively. The transparency of gem-quality, diamond single crystals over a wide range of the electromagnetic spectrum -- including X-rays, ultraviolet, visible light, and most of the infrared -- permits the application of an unusually large number of complementary analytical techniques for probing samples at multimegabar pressures. This transparency makes it also possible to introduce laser beams that can heat samples from ambient temperature up to electron volt range while at multimegabar pressures.

The fabrication of large, perfect single-crystal diamond using high-growth rate chemical vapor deposition (CVD) stands to revolutionize the field of high-pressure research with the prospect of creation of large perfect anvils employed in a new generation of high-pressure cells. X-ray diffraction measurements carried out at the NSLS indicate that the CVD diamonds can generate multimegabar pressures. Moreover, high P-T annealing of single-crystal CVD diamond has produces material that is significantly harder than any other diamond-based material. Vickers hardness and fracture toughness tests show that the annealed CVD diamond is ultrahard (>160 GPa), beyond that of both type IIa natural diamond and polycrystalline diamond. This ultrahard CVD diamond, together with its high growth-rate synthesis, should find a variety of applications beyond high-pressure technology.

## 4.2.2 High Magnetic Fields

To address the broad range of topics which require extreme magnetic fields for their study, a dedicated beamline with a state-of-the-art high-field steady state magnet will be built. A picture of one of the high field magnets in use at the current NSLS is shown in Figure 4.4.3. The much smaller source size of the high brightness NSLS-II ring will allow a smaller vertical split, increasing the highest attainable field strength. Existing technology should make it possible to build a vertical-field split-coil superconducting magnet with a maximum field of 20 Tesla or more (at present, the largest field at a synchrotron source is 15 T at Spring-8). Most of the systems of interest mentioned in Section 2 can be successfully studied using such a magnet. The magnet should possess a large bore to allow use of sample environment devices (such as high-pressure cells), temperature range of at least 0.3-300 K (or higher T), and windows suitable for small-angle scattering and inelastic experiments (low background). An additional consideration that will be taken into account is to make the windows with as little absorption as possible for lower energy resonant scattering experiments.

The beamline will be equipped for general diffraction, resonant diffraction, and common X-ray spectroscopy techniques, such as XAS. In certain cases, somewhat smaller field magnets will be available on dedicated specialized beamlines, for example small angle scattering, to complement the large field techniques. These combined capabilities will form a unique experimental facility, both in terms of the available magnetic field, and in terms of the broad range of the available experimental techniques.

Finally, we note that in high magnetic field research, no field is ever "high-enough" -- new opportunities continually arise as the field is increased. It is clear that today the highest conceivable DC field compatible with a scattering experiment is the 20 T proposed here. Nevertheless, there are routes to higher fields, in particular through pulsed magnets, which can reach 60 T for periods of milliseconds. Such facilities will be highly desirable and will make an important contribution on the world scene to high-field research. It is envisioned that an auxiliary laboratory might be built to provide such fields, taking advantage of the high brightness beams from NSLS-II to bring X-rays into the adjoining laboratory, perhaps 100 m from the source, and carry out pump-probe experiments.



**Figure 4.4.3** *The superconducting magnet installed at X22B, NSLS. At NSLS-II, steady-state magnetic fields 20 T or more will be available on a beamline with more than two orders of magnitude more flux than at X22B, allowing entirely new classes of problems to be studied.*

### **4.2.3 Ultra-Low Temperatures**

At NSLS-II, a program in ultra-low temperature physics is anticipated, focusing in particular on scattering techniques, including resonant and non-resonant magnetic X-ray scattering, to address these and other questions. A dilution refrigerator will be installed as a dedicated end-station with appropriate technical support, such that routine operation in the 300 mK range will be available to users. There are significant heat load problems that will need to be solved in order to reach such temperatures at NSLS-II. These problems will be addressed in a pilot program which has already begun at the present NSLS in a collaboration between the NSLS, Lucent Technologies, and the Advanced Photon Source.

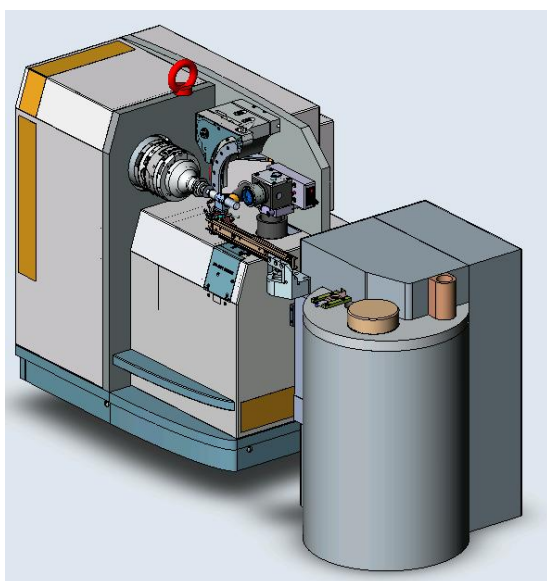
### 4.3 Automation and Robotics

New Synchrotron Facilities are being faced with an ever increasing number of users whose principle focus is not on synchrotron radiation methods. A typical example can be found in the bio-molecular, bio-medical community, which is driving the automation process in the field. These researchers employ synchrotron radiation as a routine tool in their research.

To meet the needs of this community, the structure determination process must be streamlined. A production pipeline for high volume determination of structures requires optimization and automation of current processes in use at synchrotron facilities. The ultimate goal is to arrive at a system that, with little more input than a sample, will provide the researcher with the final molecular structure.

Structure determination by X-ray diffraction is a procedure that involves multiple steps, from beam alignment to sample handling, data acquisition and finally model building. Several groups have been addressing the sample environment, data processing and model building [1]. To expedite sample exchange, which can take from 5 to 30 minutes per sample, robotic sample exchangers have been under development at several synchrotron facilities and are now also commercially available. The goal is to put in place an end-to-end, sample-to-structure, automated bio-molecule characterization capability (Figure 4.3.1).

Automated systems with emphasis on remote access and control have been in development and use for several years at different facilities. The so called FEDEX, or MAIL IN, system developed by the structural biology group in the BNL Biology Department for their NSLS stations has found success with users who do not want to spend the time or money to travel to a Synchrotron Facility to collect their structural data. The main goal of the Material Microcharacterization Collaboration [2] is to provide researchers with a virtual laboratory at their home institutions that will allow the ultimate characterization of their samples at different member laboratories over the internet. The mission of the CmolS, an X-ray diffraction collaboration for research, education and training funded by the W.M. Keck Foundation [3] is



### DNA Project

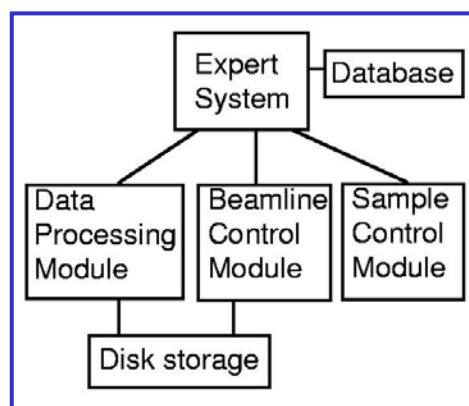


**Figure 4.3.1** The first step towards high sample throughput in structural biomolecular crystallography community was driven by Structural Genomic Initiatives. The goal is to arrive in the future to an end-to-end sample-to-structure, automated bio-molecule characterization machine. Shown here is a sketch of the Microdiffractometer and Automated Sample Changer developed by the EMBL (European Molecular Biology Laboratory) and the ESRF (European Synchrotron Radiation Facility) to be operational on the Protein Crystallography beam lines at the ESRF in 2004.

to provide faculty and students with the opportunity for joint research and teaching activities directed at the determination of molecule structures. At the present NSLS, a first step towards an end-to-end molecular structure determination facility is to integrate an automated sample changer with a neural network pattern recognition algorithm to control the quality and the radiation damage to bio-molecular crystals [4].

To address the users' demands, the NSLS-II beam lines will incorporate fully automated controls. This will be achieved in two parts: one addressing the automated alignment of the optical elements in the beam line, and another addressing the full automation of the end-station, data collection, and data analysis; the goal is an end-to-end characterization capability. A possible approach is to design, demonstrate, and deploy a two layer system in which the top (artificial intelligence) layer reasons symbolically about what the monitoring and diagnostic sensors are saying about the state of the alignment, and the bottom (procedural control) layer translating these into a set of actuator adjustments needed to align the system. This approach will be used at as many facility beamlines as practical. Even though end-stations may differ in specifics, most are fitted with a series of sensors, mechanical slits, and rotation and translation stages, and can profit from sharing development efforts. For example, automated sample changers developed for structural biology end-stations will be adapted to sample changers for other sample intensive methods such as EXAFS or powder diffraction.

Several groups in Europe are collaborating to fully automate protein crystallography beam lines. In the DNA project [5], groups from ESRF, Daresbury, and Diamond are collaborating to develop prototypes of an automated data acquisition system, as shown in figure 4.3.1. In collaboration with the Trieste synchrotron, R. Pugliese developed a fuzzy logic expert system for beam line alignment. This system has been tested only with a toroidal mirror as optical element [6]. At Diamond and Soleil synchrotron facilities, the inclusion of beam line automation is under consideration.

Recently the explosion observed in the development of new technologies applied to the construction of ever smaller and smarter sensors and micro-machines has led to second generation MEMS (micro-electro-mechanical systems) devices where automation is a requisite. Monolithically-Integrated MEMS devices allow for an independent integrated IC and passive/mechanical component design with an integration complexity similar to board level designs. Current MEMS applications include optical devices, mirrors, collimators and alignment aids; sensors and actuators, shutters, rotation and translation stages; electromagnetic devices, motors, solenoids and generators. The combination of several devices can lead to complex applications such as a MEMS micro-microscope shown in Figure 4.3.2.

Further technological developments aim to integrate a complete sensor/communication system into a cubic millimeter package. The goal of the "Smart Dust" project, initially developed by Kris Pister at UC Berkley [7], is to pack in a device the size of a grain of sand, sensors, computational ability, bi-directional wireless communications, and a power supply. While the goal is to attain a 1 mm<sup>3</sup> size device the current state-of-the-art Smart Dust devices are of the order of one hundred cubic millimeters.

Beam lines at the NSLS-II will be designed to take full advantage of the state-of-the-art developments in the area of artificial intelligence, robotics, neural networks, and sensor development. In broad strokes, it is possible to envision that the "Smart Beam Line" architecture would include a top layer based on artificial intelligence and pattern recognition systems and a bottom layer composed by sensors and actuators. The artificial intelligence layer will be used to handle tasks such as sample alignment, beam line control, and data collection and analysis. It will work concurrently with pattern recognition systems that will monitor the quality of data based on the actual images such as the diffraction pattern or beam profile. This top layer will control the beam line elements using actuators and sensors based on emerging technologies that include elements developed in MEMS and Smart Dust.

The challenge that lies ahead is to establish clear development paths for each of these components and the communication protocols between them. Expert systems and neural network techniques can be developed and implemented at the present time at existing beam lines. Collaborations with computer science and robotics research groups will be established to accelerate this development. User input and feedback will be crucial to the development and will provide the ultimate benchmark. The situation in the actuator and sensor front is slightly different and may require an aggressive development path. Devices

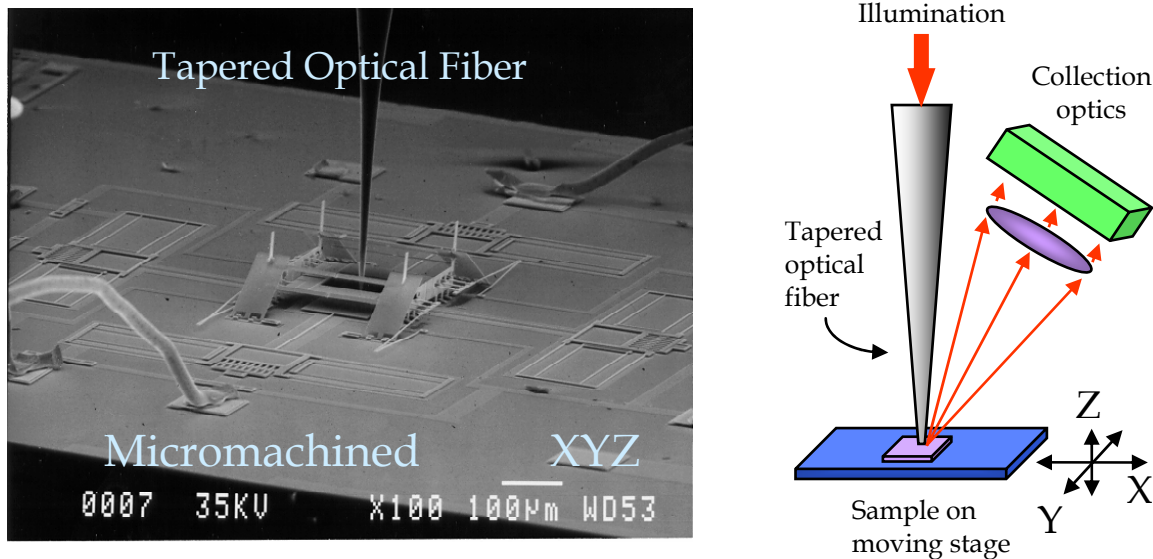


**Figure 4.3.2** MEMS micro-microscope; (a) Scanning Electron Microscopy of an XYZ stage (b) schematics of the micro-microscope [8].

such as Smart Dust are being developed for general applications and specific development for beam lines may be required. Ionizing radiation, vacuum operation, and cryogenic temperatures may lead to custom development. However use of these new technological devices is not essential to the implementation of the “Smart Beam Line”. Conventional actuators such as linear motors with  $\frac{1}{4}$  micrometer precision are available today and are being further developed to attain higher precisions.

Finally, the “modus operandi” for the beam lines needs to be established. The data acquisition and data analysis will be controlled by the artificial intelligence layer and will provide at least a preliminary analysis of the collected data. In this sense the user may or may not be present physically at the beam line while data are being collected.

Taken together, development and use of these approaches at NSLS-II will set a new standard for beamline automation and control and facilitate high throughput usage of NSLS-II.

## REFERENCES

- [34] Interdisciplinary Workshop promoting collaboration in High-throughput X-ray Structure Determination, march 22-23, 2002, Santa Fe, NM, USA.
- [35] <http://tpm.amc.anl.gov/MMC/>
- [36] <http://www-structure.llnl.gov/scaurcon99/cmols2.html>
- [37] Berntson, V. Stojanoff and H. Takai, “Application of a neural network in high-throughput protein crystallography”, *Journal Synchrotron Radiation* (2003) 10, 445-449.
- [38] <http://www.dna.ac.uk/> and <http://www.e-htpx.ac.uk/>
- [39] <http://www.aps.anl.gov/conferences/icalepcs/97/paper97/p146.pdf>
- [40] <http://robotics.eecs.berkeley.edu/~pister/SmartDust/>
- [41] David Bishop, Lucent Technologies, private communication.

## 4.4 Detectors

### 4.4.1 Overview

Advanced detector systems will be required to take full advantage of NSLS-II's superlative performance. For a synchrotron experiment, the detector system is an especially critical component that often enables new science. One outstanding example is that of macromolecular crystallography. When the only viable area detector capable of quantitative interpretation was film, macromolecular crystallography was an esoteric pursuit, involving an exorbitant amount of labor to wet-process thousands of films for each experiment. The availability of synchrotron radiation sources made little impact. The development of new, large area, electronic detectors have transformed macromolecular crystallography into a high-throughput research powerhouse, providing key knowledge for the understanding of disease mechanisms and drug design.

### 4.4.2 Advances

#### 4.4.2.1 Architecture

In general, it is clear that the trend is towards higher levels of functionality integrated into the detector elements and readout systems. This will include digital signal processing (DSP) of the analog sensor output as well as digital post-processing of events. These trends are already visible in the high energy physics field, and are beginning to be seen in synchrotron radiation systems. We can expect that pulse-height histogramming, time and space correlations and spectral corrections will all be integrated at the chip level in future detectors.

Conventional computing resources are also beginning to be embedded in more application-specific integrated circuits (ASICs). At least one programmable gate-array device manufacturer is selling a product with up to four PowerPC processors embedded in the center of a large programmable gate array. In the 10 year process leading to NSLS-II, even more powerful devices can be expected. It is now almost as easy to embed a CPU into an ASIC as it is to include a subroutine in a software program. Modern simulation programs can accurately simulate the performance of a complete ASIC before manufacture, giving a high degree of confidence that the final device will work as specified.

More sophisticated devices will inevitably lead to increased data rates. This is already a limitation for existing detectors, particularly those that deal with images. Add to the large pixel count, the need for energy spectra and/or time-correlation spectra per pixel, plus the need for tomographic information, data set sizes can easily expand to terabytes. It is not yet clear how to handle the gigabyte/second data rates expected from the next generation of area detectors, so these more sophisticated devices will need real innovation in data movement technology, or a great deal more customizing of readout systems to reduce data in real time, probably using the embedded intelligence described above. A more detailed discussion of these issues follows.

Current detectors suitable for acquiring single-crystal and powder diffraction images are rather slow, with readout times of order one second or more. This aspect of 2-dimensional position-sensitive detectors is receiving significant attention due to the large ready market offered by macromolecular crystallography. If we imagine a modest device, with its readout rate increased one thousand fold, i.e. readout times of order 1 millisecond, with 2000 x 2000 pixels, we can see that we will rapidly saturate almost all present computer systems in digesting the 8 Gb/second that it will generate. Fortunately, such detectors will also be highly parallel in nature, in contrast to current charge-coupled device (CCD) technology. Thus, it should be a straightforward (but not simple) strategy to increase the number of CPUs dedicated to its readout. The combined FPGA/CPU device mentioned above is ideally suited to this task. Its FPGA could be programmed to accept and sort the raw data streaming from each column ADC and placed in local memory for later downloading or local processing. If we assume 8 ADC's per processor,

with each ADC digitizing at 2 MHz (a modest value, but consistent with low-noise operation) and providing 2 bytes per conversion, then we would require 256 FPGA/CPU chips to handle the 2048 columns, each one reading out the data at 32 Mb/second. If each CPU is provided with 1 Gb of local memory, then they could hold 32 seconds of data. The 256 systems would hold a total of 256 Gb of data.

It is impractical to move this amount of data around, so the most logical thing would be to analyze it in situ. This may seem like complexity for its own sake, but its potential impact could be huge. Many of the crystals studied by soft-condensed matter and biology scientists are extremely radiation-sensitive. The radiation damage is often diffusion driven and could be alleviated by reducing the total exposure time. The system described above could collect an entire data set in under one second, and a great many systems could survive this long, even at room temperature. This could remove the need to develop a freezing strategy for each new crystal, and could produce better data since the freezing operation lowers the crystalline perfection of most organic materials. It would be impractical to collect such data by collecting discrete frames, as is currently the fashion. Instead the sample would rotate continuously and the data would be read out continuously. Part of this local post-processing would be to unscramble these data streams to provide peak intensities and pattern indexing. Ideally, the output of such a detector would be  $I(h,k,l)$ , the integrated intensities of all of the peaks, rather than raw images; a much smaller data set.

Another big advantage of such a detector readout scheme would be that it would have an arbitrarily large dynamic range. Present framing detectors have a finite capacity per pixel. This is currently mitigated by essentially throwing away signal (by using an X-ray phosphor and collecting the visible light very inefficiently) such that a full pixel corresponds to  $10^5 - 10^6$  X-ray photons. The noise level of such a system is at the 5-50 X-ray photon level. Direct detection of X-rays by a CCD typically results in a full-well of only 100 - 1000 X-ray photons, but the noise level is much less than 1 photon. The proposed XAMP detector full well corresponds to  $10^4$  X-ray photons. Reading out this detector continuously (e.g., every ms) would allow an instantaneous per-pixel rate of  $10^7/s$ , and acquisition could continue as long as needed to provide the required statistical precision for the weakest signals.

As coherence becomes more a part of data collection strategies, detectors designed to measure efficiently the various correlations, spatial and temporal, will be required. One might expect that experiments traditionally considered small-angle scattering (SAXS) will become speckle experiments with the new source, providing dynamic structural information as well as static. The current state of the art provides single-point time correlation measurements down to the microsecond scale, and multipoint measurements at the 10 millisecond scale. The wish is for microsecond scale multipoint measurements, or even faster in the future. The ideal detector for such tasks is the fully-pixelated detector, although prototype experiments are currently carried out using other types of detector. This will have complete readout electronics for every pixel. The simplest system for generating correlations is a photon-counting system, but integrating systems should be able to adopt similar strategies if the intensity prohibits photon counting. Each photon will be tagged with its position and time coordinates. Time autocorrelation will be performed by on-chip logic, following one of the various multiple-time-domain algorithms to provide correlation information over the widest possible time scales. For large numbers of pixels and high count rates this will be the only possible approach. Spatial and temporal cross-correlations will be a much bigger challenge, since the interconnection scheme becomes highly complex. To date there are no examples of such systems outside of high-energy physics. NSLS-II will provide beams with a high degree of spatial coherence. In fact it will be diffraction-limited at 0.1 nm in the vertical plane. So-called speckle experiments will be greatly facilitated by this source, but full utilization will only come with the new detectors discussed here.

Pixel detectors equipped with energy-resolving capability will require the ability to put a complete energy-histogramming subsystem on each pixel of a large array. Such detectors will be the logical extension of devices currently reaching the experimental floor, which have hundreds of pixels each with a complete signal-processing chain. These systems were designed for fluorescence detection in absorption spectroscopy experiments with dilute samples, when the experiment feasibility is dominated by the presence of a high parasitic flux of uninteresting radiation. This results in premature saturation of the detector chain, enforcing long acquisition times and eventually preventing a successful experiment. This

situation will be worse with NSLS-II, and so we must plan for remedies. Increasing the parallelism even further is one way forward, and on-chip intelligence to deconvolve acquired spectra on a photon-by-photon basis will be a significant enhancement, bringing enhanced separation between the desired and parasitic radiation.

One could also imagine such a detector bringing a new lease of life to the Laue diffraction technique, since it becomes much simpler to perform the necessary diffracted intensity corrections if one knows the energy of the photon directly. This same knowledge also helps in indexing Laue patterns, and removes the problem of harmonic overlap. Nevertheless, fabrication of such a detector is no simple undertaking. A high-speed ADC is power-hungry, and one would need about 1 million of them for a reasonably sized detector. As CMOS technology continues to shrink, this will eventually be possible, at least for pixels of dimension 100 micrometers or more. Applications of such a detector might be in microbeam grain-mapping of polycrystalline materials, or high-pressure diffraction experiments. Such studies are important to provide a firmer basis for understanding the properties of real materials on all scales, and are ideally suited to a machine like NSLS-II.

#### 4.4.2.2 Sensors

Currently, the highest performance detector elements are based on pure elemental semiconductors, either silicon or germanium. This is true across the detector spectrum, and is largely a consequence of the high commercial value semiconductor devices have yielded, with the consequent large investment in materials and processes. Sensor technology that is currently considered esoteric will become routine in the next decade, so we can anticipate high-speed devices with good energy resolution based on charge drifting techniques in large arrays, probably up to the sizes currently offered only by CCD devices.

Figure 4.4.1 shows a prototype 384-element array of drift-detectors that is part of a BNL development currently underway. These devices provide enhanced energy resolution by minimizing the capacitance seen by the amplifier by drifting the charges through large distances within the bulk of the silicon to a small collection electrode. It also illustrates another important aspect of silicon-based technology: the ability to make essentially arbitrarily shaped sensor arrays. The one illustrated will have a central hole. This allows an incident probe beam to pass through the detector and impinge on a sample. The scattered radiation is then efficiently detected by this array since there is no restriction on how close the detector can come to the sample. Thus a large fraction of the full sphere of radiation can be collected, even though the array is not very large (the pixels are 1mm diameter). It is simply an engineering problem to add further detector planes around a sample to increase even further the collection efficiency.

Various schemes are under development to provide rapid-readout area detectors for time-resolved studies. These range from intermediate solutions involving a reduction of the readout time to one dimension, similar to active matrix computer screens, all the way to dedicated per-pixel parallel readout

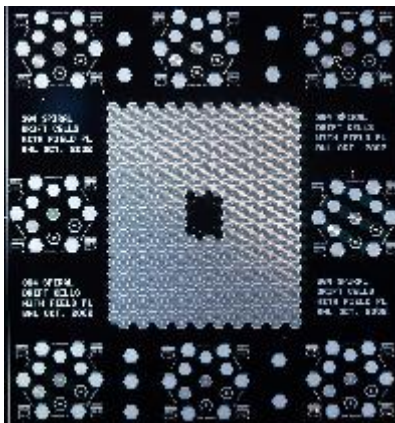


**Figure 4.4.1** *Prototype 384-element array of drift detectors.*

of a sensor array typically separate from the readout array. Such devices will offer readout times less than one millisecond for active matrix devices, to a few microseconds for pixel arrays. Some of the issues with such devices are discussed above. We will surely see these developments continue and bear fruit. We will also see the next level of development where each pixel is also a spectrometer. The difficulties there are more of an engineering nature than any fundamental constraints.

Silicon is only useful up to energies of 15 keV or so, but the thrust of much of detector related materials science research is moving up towards 30 keV and more. Germanium is suitable for this range, but requires cryogenic technology, which is very restrictive. Cadmium Zinc Telluride is a promising material for room-temperature operation in non-spectroscopic applications, but it suffers from material problems that are proving difficult to overcome. Other high-Z semiconductor compounds are also under active development, GaAs or HgI for example. Such materials are particularly attractive in the context of pixel array detectors, where the ability to tailor the sensor properties for the radiation being detected will be valuable. Since the sensor array and the readout electronics are separate objects connected by flip-chip or bump bonding, both components can be optimized for the job in hand. This bonding technique, illustrated in Figure 4.4.2 is still in its infancy and much work needs to be done to make large detector arrays a reality.

A truly new detector principle is making its appearance based on superconductivity. There are two basic types, microbolometers and tunneling junction detectors. Each has its good points and its problems, but they both offer energy resolution in the eV range, with the bolometers having a slight advantage in resolution and energy range, but losing in count rate capability to the tunneling junction devices. Both types are physically small and hence have poor detection efficiency and low solid angle, but it is anticipated that large arrays will eventually be feasible that will mitigate most of these problems. Optimized readout ASICs have yet to be developed for such detectors, but even now they have achieved close to their theoretical limits, and have begun to be used for soft X-ray spectroscopy applications with excellent results. They operate at temperatures below 1 degree Kelvin, and so require advanced cryogenic techniques for their operation. Nevertheless, a reasonably portable and easily-operated tunneling junction device has been made at LLNL and has been used at synchrotron sources. It is shown in Figure 4.4.3.

#### 4.4.2.3 Readout Electronics

Currently, CMOS is proving to be the most valuable technology for detector developers, since it is capable of both relatively high-speed digital and low-noise analog functions on the same chip. Current technology is 0.18 micron design rules (roughly the size of the smallest feature that can be fabricated), but

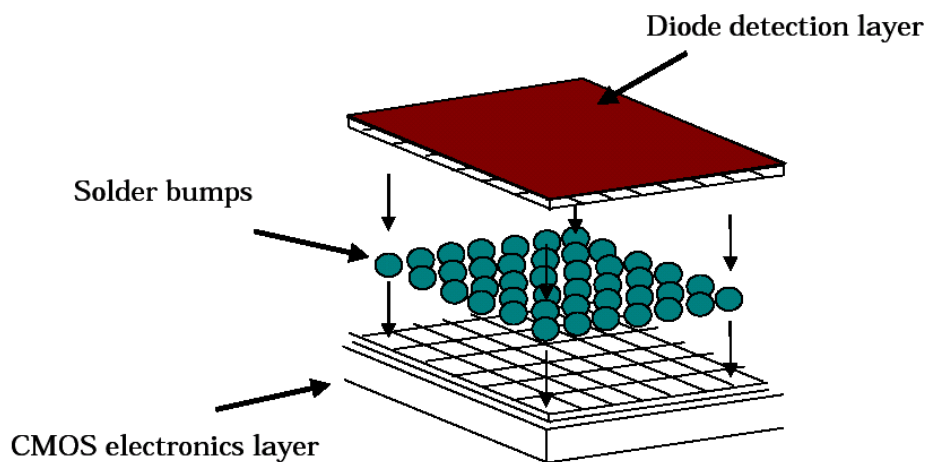


**Figure 4.4.2** Illustration of the bump bonding, a high density interconnection technique which makes possible so-called Pixel Array Detectors, where each pixel is directly connected to its own readout circuit in an underlying CMOS electronics layer.



**Figure 4.4.3** *Prototype superconducting tunnel junction detector, which offers eV energy resolution and high count rate capability.*

it will inevitably decrease. Although the analog circuitry consumes a lot of real estate that will not reduce as rapidly as digital circuitry due to the need for large capacitors, digital circuitry real estate diminishes as the square of the design-rule dimension. Thus a 0.18 micron circuit can pack four times the circuitry of a 0.35 micron device, with reduced power consumption and higher operating speed.

#### **4.4.2.4 Software**

There is an almost insatiable need for application software to bring advanced detectors to the point of being an asset in an experiment, rather than an experiment in its own right. A well-designed user interface can make possible experiments that would otherwise not be attempted. A good example is a scanning X-ray microprobe. In this experiment a small X-ray spot is raster-scanned over the surface of a sample, and an X-ray emission spectrum acquired at each point. Analysis of this three-dimensional data set ( $x$ ,  $y$ , energy) is time-consuming and error-prone. Add to this a multi-element detector with perhaps thousands of channels and anything but an automated system becomes unthinkable. It is in principle possible to perform the analysis in an automated way, adjusting each element's setting for optimal operation, collecting reference spectra and then deconvolving the instrument function and providing elemental mapping corrected for background and peak overlap, on a photon-by-photon basis.

# 5 Budget for Conceptual Design of NSLS-II and Preliminary Budget for the Project

## 5.1 Project and Operating Costs

Based on the pre-conceptual design outlined in this proposal, the preliminary total estimated cost (TEC) is \$392.8M and the preliminary total project cost (TPC) is \$423.5M, in FY04 dollars. The breakdown of these costs is shown in Table 5.1.1. They include all costs associated with R&D, CDR preparation, project management, project engineering and design (PED), technical and conventional construction, contingencies, and commissioning. The costs also include provision for four insertion device beamlines, including front ends and undulators. The preliminary funding profile for this TPC extends over eight years (FY2005-FY2012). The performance cost baseline will be established at CD-2b. The complete project funding profile, TEC, and TPC will be developed during Title I design and will be approved at CD-2b.

The preliminary annual operating costs are estimated to be \$70M, which includes staff, and facility and equipment operating and maintenance costs. This is estimated based on experience with operating the present NSLS, taking into consideration the significantly larger and more complex NSLS-II complex compared to the present NSLS. It is expected that the facility will be responsible for operating, maintaining, and upgrading the majority of the beamlines at NSLS-II and those costs are also included in the estimated operating costs.

<b>Project Support</b>	<b>48.2</b>
Project Management	10.6
Project Engineering	32.6
Construction Management	2.1
ESH Management	2.6
<b>Technical Construction</b>	<b>145.3</b>
Injection System	32.7
Storage Ring	94.1
Machine Service Systems	16.1
<b>Conventional Construction</b>	<b>120.2</b>
Improvements to Land	1.6
Buildings	83.6
Utilities	33.4
Standard Equipment	1.6
<b>ESH</b>	<b>0.5</b>
<b>Contingency (25%)</b>	<b>78.6</b>
<b>TOTAL TEC</b>	<b>\$392.8</b>
<b>R&amp;D &amp; CDR</b>	<b>3.2</b>
<b>Commissioning</b>	<b>27.5</b>
<b>TOTAL TPC</b>	<b>\$423.5</b>

**Table 5.1.1** Breakdown of preliminary total estimated cost and total project cost for NSLS-II in FY04 M\$.

## 5.2 Schedule

A preliminary schedule for the project's Critical Decision (Level 1) milestones is shown in Table 5.1.2. It is planned that R&D and development of the conceptual design report (CDR) take place in FY2004-FY2005. Project engineering and design of NSLS-II would occur during FY2006 and FY2007. Detailed baseline schedule milestones will be developed during Title I design and approved at CD-2b. During the PED phase, the schedule will be tracked and performance will be measured against PED schedule milestones. CD-2 and CD-3 are phased to permit long-lead procurements to be initiated in FY2008. Actual construction would occur during FY2009 through FY2012.

During FY2012, activities would shift from construction to commissioning. A commissioning plan will be prepared to test and evaluate system performance, both individually and collectively, as compared to approved design criteria. Functional performance tests will be established and all designated systems will be tested against the performance criteria. NSLS-II will be commissioned in phases starting with the NSLS-II injection system. As each stage is completed, it will be commissioned. The top-level commissioning goal is to generate x-rays in an NSLS-II undulator and detect them in an x-ray endstation enclosure.

When inspection, acceptance, and commissioning have been completed, technical equipment is installed and operational, and CD-4 has been approved, the project will formally transition to the operational phase. This is expected to occur in late FY2012.

<u>Milestones</u>	<u>Milestone Description</u>	<u>Scheduled Date</u>	<u>Phase</u>
CD-0	Mission Need	May, 2004	Conceptual
CD-1	Preliminary Baseline Range	September, 2005	PED
CD-2a	Long-Lead Procurement Baseline	February, 2006	PED
CD-2b	Performance Baseline	April, 2007	PED
CD-3a	Start Long-Lead Procurement	August, 2007	PED/LLP
CD-3b	Start Construction	July, 2008	Construction
CD-4	Start Operations	June, 2012	Operation

**Table 5.1.2** *Preliminary Critical Decision Milestones.*

## 5.3 Acquisition Plan

The acquisition of NSLS-II will be conducted through Brookhaven Science Associates as the management and operation contractor. BNL management will be responsible for the research and development, conceptual and engineering design, construction, and operation of NSLS-II. The project will make extensive use of existing expertise at the present NSLS facility. The installation must be carefully coordinated with other research activities at Brookhaven National Laboratory (BNL). Therefore, it is infeasible to have a separate subcontract with another organization to manage the project. The project is similar in scope to the recently completed RHIC facility at BNL, which was conducted successfully by BNL management. BNL has the resources to direct and execute the project.

At BNL, the Light Sources Division, in close cooperation with the Facilities and Operations Division, will be responsible for accomplishing the project under the terms of BSA's contract with DOE. BNL will execute all parts of the project.

Project activities will be accomplished to the extent feasible using fixed-price subcontractors selected on the basis of best value, price, and other factors.

## **5.4 Environment, Safety, and Health**

### **5.4.1 Integrated Safety Management System**

Environment, safety and health (ES&H) requirements will be systematically integrated into management and work practices at all levels so that the NSLS-II project is executed while protecting the public, the worker, and the environment. NSLS-II Safety Management System documents and policies will make it clear that the responsibility for safety and environmental protection starts with the NSLS-II Director and flows through the management chain to Associate Directors, to Department Heads and Group Leaders, to line supervisors, and finally to the workers. It is the responsibility of NSLS-II management to ensure that staff are trained and are responsible for ES&H in their assigned areas.

The NSLS-II project work at BNL will be executed in accordance with BNL ES&H policies to ensure hazards are identified and mitigated; work is authorized after ES&H analysis is completed; and oversight of work is conducted by NSLS-II management and staff. The BNL ES&H Division will provide technical support to the project and conduct independent oversight and review of project activities.

### **5.4.2 National Environmental Policy Act**

In compliance with the National Environmental Protection Act (NEPA), DOE will issue a determination to prepare an Environmental Assessment (EA). The effects of the NSLS-II project on the environment will be assessed in the EA. This project will be executed in conformance with existing BNL ES&H policies, systems and procedures to assure a minimum impact on the environment. The EA will serve as the basis for determining whether the NSLS-II project will require an Environmental Impact Statement (EIS) or a Finding of No Significant Impact (FONSI) will be issued. The EA is currently planned to be completed by the end of 2005.

### **5.4.3 Fire Hazard Analyses**

A fire hazard analyses (FHA) will be developed to determine the fire safety risks associated with the NSLS-II project. The conclusions of the FHA should be incorporated into the Safety Assessment Document and into the design of the NSLS-II.

### **5.4.4 Safety Assessment Document**

Specific ES&H hazards and the means for their mitigation will be detailed in the NSLS-II safety assessment. The NSLS-II Preliminary Safety Assessment Document (PSAD) will address the ES&H considerations in the design, fabrication, and installation of NSLS-II. The PSAD will be completed prior to starting NSLS-II construction (i.e., before CD-3b). The PSAD will form the basis for the NSLS-II Final Safety Assessment Document (FSAD). The FSAD will evaluate the ES&H considerations for operation of NSLS-II. The FSAD will be completed prior to operation and will serve as the basis for the Accelerator Readiness Review (ARR). The ARR will be accomplished in phases prior to commissioning and completed prior to starting operations (i.e., before CD-4).

## **Appendix: List of Workshops**

The user community has been actively involved in defining the scientific case for, and requirements to be met by, NSLS-II. As one expression of this, members of the user community worked with NSLS and other BNL staff to organize and host a series of focused user science workshops to explore scientific opportunities that will be enabled by NSLS-II and the requirements that NSLS-II must meet to best serve that science. The workshops are listed below and described more fully at <http://www.nsls2.bnl.gov/newsroom/workshops/2003/Default.htm>.

### **Scientific Opportunities in Macromolecular Crystallography at NSLS-II**

Organizers: Leemor Joshua-Torr - Cold Spring Harbor  
Wayne Hendrickson - Howard Hughes Medical Institute / Columbia University

Date: July 9-10, 2003

Attendees: 24 Participants from the following institutions: Argonne National Laboratory, Brookhaven National Laboratory, Cold Spring Harbor Laboratory, Columbia University, Harvard Medical School, Harvard University, Howard Hughes Medical Institute, Merck Research Labs, National Cancer Institute, National Institutes of Health, Rockefeller University, Stanford University, University of Pennsylvania, Yale University

### **Environmental Sciences at NSLS-II**

Organizers: Richard Reeder – Stony Brook University  
Chris Jacobsen - Stony Brook University  
Tony Lanzirotti - University of Chicago  
Jeff Fitts - Brookhaven National Laboratory

Date: August 21, 2003

Attendees: 12 Participants from the following institutions: BNL, Dartmouth College, Princeton University, Stony Brook University, University of Chicago, University of Delaware, Westinghouse Savannah River

### **Strongly Correlated Electrons, NSLS-II and the Future**

Organizers: John Hill – Brookhaven National Laboratory  
Christy Nelson - Brookhaven National Laboratory  
Peter Abbamonte - Brookhaven National Laboratory  
C. C. Kao – Brookhaven National Laboratory  
Peter Johnson - Brookhaven National Laboratory

Date: August 28-29, 2003

Attendees: 43 Participants from the following institutions: Argonne National Laboratory, BNL, Carnegie Institute of Washington, Columbia University, Cornell University, Florida State University National High Magnetic Field Lab, Lucent Technologies, Princeton University, University of British Columbia, University of California – San Diego, University of Washington

### **Scientific Opportunities in Soft Matter and Biophysics at NSLS-II**

Organizers: Ron Pindak – Brookhaven National Laboratory  
Ben Hsiao - Stony Brook University  
Ben Ocko – Brookhaven National Laboratory  
Ben Chu - Stony Brook University  
Helmut Strey - Stony Brook University

Date: September 5-6, 2003

Attendees: 31 Participants from the following institutions: University of California – Berkeley, Brookhaven National Laboratory, Cornell University, Massachusetts Institute of Technology, Princeton University, Stony Brook University, University of Akron, University of Colorado – Boulder, University of Illinois – Urbana-Champaign, University of Minnesota, University of Pennsylvania, Yale University

### **Biomedical Imaging at NSLS-II**

Organizers: Lisa Miller – Brookhaven National Laboratory  
Zhong Zhong - Brookhaven National Laboratory

Date: September 22, 2003

Attendees: 25 Participants from the following institutions: Albert Einstein College of Medicine, Brookhaven National Laboratory, Harvard Medical School, Rush Medical College, Rutgers University, Stony Brook University, Temple University, University of North Carolina, University of Chicago

### **Nanoscience Opportunities at NSLS-II**

Organizers: Robert Hwang – Brookhaven National Laboratory  
Jim Misewich - Brookhaven National Laboratory  
Chi-Chang Kao - Brookhaven National Laboratory  
Ron Pindak - Brookhaven National Laboratory  
Doon Gibbs - Brookhaven National Laboratory

Date: October 3, 2003

Attendees: 25 Participants from the following institutions: Brookhaven National Laboratory, Columbia University, Cornell University, General Electric, Lucent Technology, New Jersey Nanotechnology Consortium, Rensselaer Polytechnic Institute, Rutgers University